



Max-Planck-Institut für extraterrestrische Physik  
Garching bei München

# POSITRON-ANNIHILATION SPECTROSCOPY THROUGHOUT THE MILKY WAY

THOMAS SIEGERT

Vollständiger Abdruck der von der Fakultät für Physik der Technischen Universität München zur Erlangung des akademischen Grades eines

**Doktors der Naturwissenschaften**

genehmigten Dissertation.

Vorsitzender: Prof. Dr. Alejandro Ibarra  
Prüfer der Dissertation: 1. apl. Prof. Dr. Roland Diehl  
2. Prof. Dr. Lothar Oberauer  
3. Prof. Dr. Karl Mannheim (nur schriftliche Beurteilung)

Die Dissertation wurde am 19.12.2016 bei der Technischen Universität München eingereicht und durch die Fakultät für Physik am 20.02.2017 angenommen.

## Kurzfassung

Mithilfe des Gammastrahlenteleskops SPI wurde der Ursprung von Positronen in der Milchstraße untersucht. Dafür sind hochaufgelöste Spektren der Annihilationsstrahlung von Positronen mit Elektronen sowie radioaktive Zerfälle von  $\beta^+$ -Strahlern aus dem Weltraum aufgenommen worden. Eine Vielzahl von Positronenquellentypen und verschiedene Regionen der Annihilation in der Galaxie konnten durch detaillierte bildgebende und spektroskopische Analysen charakterisiert werden. Dunkle Materie ist als Hauptquelle für Positronen ausgeschlossen wohingegen Mikroquasare einen signifikanten Beitrag leisten.

## Abstract

Using the gamma-ray telescope SPI, the origin of positrons in the Milky Way was investigated by measuring high-resolution spectra of electron-positron annihilation as well as radioactive decay from  $\beta^+$ -unstable nuclei in space. The variety of positron source types and different annihilation regions in the Galaxy have been disentangled by detailed imaging and spectroscopic analyses. Dark matter could be excluded as dominant source whereas microquasars have been consolidated as significant contributors.

# Contents

<b>List of Figures</b>	<b>vi</b>
<b>List of Tables</b>	<b>x</b>
<b>List of Acronyms</b>	<b>xi</b>
<b>1 Introduction</b>	<b>2</b>
<b>2 Positron Physics</b>	<b>5</b>
2.1 What are Positrons? . . . . .	5
2.1.1 The Positron as Elementary Particle . . . . .	5
2.1.2 Bound States with Positrons . . . . .	6
2.1.2.1 Anti-Atoms . . . . .	6
2.1.2.2 Positronium . . . . .	7
2.1.2.3 Ions and Molecules with Positrons . . . . .	9
2.2 Positron Production Mechanisms . . . . .	10
2.2.1 Radioactive Beta-Plus-Decay . . . . .	10
2.2.2 Decay of Leptons . . . . .	11
2.2.3 Decay of Mesons . . . . .	12
2.2.4 Electron-Positron Pair Production . . . . .	14
2.2.4.1 Photon-Photon Interactions . . . . .	14
2.2.4.2 Photon Interactions with Electric Fields . . . . .	16
2.2.4.3 Photon Interactions With Magnetic Fields . . . . .	18
2.2.5 Exotic Positron Production Mechanisms . . . . .	20
2.2.5.1 Dark Matter Self-Interaction . . . . .	20
2.2.5.2 Other Reactions . . . . .	23
2.2.6 Summary of Positron Production Mechanisms . . . . .	23
2.3 Positron Annihilation . . . . .	24
2.3.1 Annihilation in Flight . . . . .	25
2.3.2 Positronium Formation and Annihilation . . . . .	27
2.3.3 Direct Annihilation with Bound Electrons . . . . .	33
2.4 Gamma-Ray Spectra from Positron Annihilation . . . . .	35
2.4.1 Considerations from Kinematics . . . . .	35
2.4.2 From Cross Section to Spectrum . . . . .	38
2.4.2.1 Annihilation Rate . . . . .	39
2.4.2.2 Gamma-Ray Spectra for Direct Annihilation . . . . .	41
2.4.2.3 Gamma-Ray Spectra from Positronium Annihilation . . . . .	42
2.4.3 Environmental and Geometrical Influences . . . . .	44
2.4.3.1 Positron Energy Losses . . . . .	45
2.4.3.2 Annihilation Spectra from Cosmic-Ray Positrons . . . . .	49

2.4.3.3	Annihilation Spectra from Pair-Plasma . . . . .	50
2.4.3.4	Spectra from Annihilation in Interstellar Gas . . . . .	52
2.4.3.5	Bulk Motion Effects . . . . .	55
<b>3</b>	<b>Measuring Galactic Gamma-Ray Signals with INTEGRAL/SPI</b>	<b>57</b>
3.1	High-Energy Astronomy . . . . .	57
3.1.1	Interaction of Light with Matter . . . . .	57
3.1.2	Gamma-Ray Detectors . . . . .	58
3.1.3	Gamma-Ray Telescopes . . . . .	61
3.2	INTEGRAL and its Spectrometer SPI . . . . .	63
3.2.1	The INTEGRAL Mission . . . . .	63
3.2.2	The Spectrometer SPI . . . . .	66
3.2.2.1	Camera . . . . .	66
3.2.2.2	Anticoincidence systems . . . . .	68
3.2.2.3	Calibration and Performance . . . . .	70
3.2.3	High-Precision Background Modelling . . . . .	72
3.2.3.1	Instrumental Gamma-Ray Background Origins . . . . .	72
3.2.3.2	Self-Consistent Background Modelling . . . . .	74
3.2.3.3	Spectral Description of SPI Data . . . . .	76
3.2.3.4	Instrumental Background Parameters . . . . .	79
3.2.4	SPI-light . . . . .	84
3.2.4.1	Single Energy Bin . . . . .	85
3.2.4.2	Detector Response, Line and Continuum Backgrounds . . . . .	88
3.2.4.3	Application and Extension to SPI . . . . .	93
<b>4</b>	<b>The 511 keV Electron-Positron Annihilation Signal in the Milky Way</b>	<b>96</b>
4.1	The Positron Puzzle . . . . .	96
4.2	Data Set . . . . .	100
4.3	Treating the Background Near 511 keV . . . . .	101
4.4	Celestial Emission . . . . .	103
4.4.1	Unbiased Imaging Methods . . . . .	105
4.4.2	Astrophysical Modelling . . . . .	112
4.5	Testing Astrophysical Tracers . . . . .	118
4.5.1	Tracing by Photon Energy . . . . .	118
4.5.2	Tracing by Physical Mechanism . . . . .	121
4.6	Spectral Analysis . . . . .	122
4.6.1	The Bulge Component . . . . .	123
4.6.2	The Disk Component . . . . .	125
4.6.3	The Galactic Centre Source . . . . .	128
4.6.4	Continuum Sources . . . . .	129
4.6.5	Additional Sources . . . . .	131
4.6.6	Galactic Positron Annihilation Portrayal . . . . .	131
4.7	Kinematics of the Galaxy Traced by Gamma-Rays . . . . .	142
4.7.1	Position-Velocity Diagrams . . . . .	144
4.7.2	Kinematics from Al-26 Gamma-Rays . . . . .	146
4.7.3	Positron Annihilation Longitude-Velocity Diagram . . . . .	153

<b>5</b>	<b>Candidate Positron Sources</b>	<b>157</b>
5.1	Nucleosynthesis Origins . . . . .	157
5.1.1	Positrons from Stars . . . . .	158
5.1.1.1	Stellar Evolution . . . . .	158
5.1.1.2	Beta-Unstable Al-26 as Natural Positron Producer . . . . .	162
5.1.1.3	Large- and Small-Scale 1809 keV Emission . . . . .	166
5.1.1.3.1	Galactic Structure . . . . .	166
5.1.1.3.2	Disentangling Gamma-Ray Foregrounds . . . . .	170
5.1.1.3.3	Characterising the Orion OB1 Association . . . . .	174
5.1.1.4	Determining the Al-26 Mass in the Galaxy . . . . .	178
5.1.2	Core-Collapse Supernovae . . . . .	179
5.1.2.1	More Naturally Positron Producing Isotopes . . . . .	182
5.1.2.2	Measuring Ti-44 in Cassiopeia A . . . . .	183
5.1.3	Thermonuclear Explosions . . . . .	189
5.1.3.1	Measuring the Ni-56 Decay-Chain in SN2014J . . . . .	193
5.1.3.1.1	Early Time Spectra of Ni-56 . . . . .	194
5.1.3.1.2	Variable Spectra of Co-56 Emission . . . . .	196
5.1.3.2	Positron Annihilation in SN2014J . . . . .	201
5.1.3.3	Positron Contribution from Type Ia Supernovae . . . . .	202
5.1.3.4	Novae . . . . .	205
5.1.4	Exotics . . . . .	207
5.2	Compact Objects . . . . .	208
5.2.1	X-Ray Binaries . . . . .	210
5.2.1.1	Microquasar V404 Cygni . . . . .	217
5.2.1.2	Positron Contribution from Microquasars . . . . .	224
5.2.2	Supermassive Black Holes . . . . .	226
5.3	Cosmic Rays . . . . .	227
5.4	Pulsars . . . . .	230
5.5	Dark Matter . . . . .	232
5.5.1	Appearance of Dark Matter . . . . .	233
5.5.2	Testing the Dark Matter Scenario with SPI . . . . .	235
5.6	A Galactic Centre Excess in 511 keV . . . . .	245
5.6.1	Sagittarius A* . . . . .	245
5.6.2	Central Molecular Zone . . . . .	246
5.6.3	Dark Matter Annihilation . . . . .	247
5.7	Balancing the Galactic Positron Content . . . . .	247
5.8	Implications for the Positron Puzzle . . . . .	249
<b>6</b>	<b>Summary and Conclusion</b>	<b>251</b>
<b>A</b>	<b>Additional Figures and Tables</b>	<b>I</b>
<b>B</b>	<b>Additional Equations and Derivations</b>	<b>VI</b>
<b>C</b>	<b>Energy Calibration of SPI</b>	<b>XVIII</b>
<b>D</b>	<b>Bibliography</b>	<b>XX</b>

## List of Figures

2.1	Feynman diagram of the $\beta^+$ -decay. . . . .	10
2.2	Photon-photon pair production. . . . .	15
2.3	Photon-photon pair production cross section. . . . .	15
2.4	Pair production in the field of a nucleus. . . . .	17
2.5	Positron production by dark matter interactions. . . . .	22
2.6	Feynman diagrams for electron-positron annihilation. . . . .	25
2.7	Electron-positron annihilation cross section. . . . .	27
2.8	Cross sections for different reactions of positrons. . . . .	31
2.9	Feynman diagrams of three-photon annihilation. . . . .	32
2.10	Positron annihilation on bound electrons. . . . .	34
2.11	Pair annihilation in the centre of momentum frame. . . . .	36
2.12	Three-photon annihilation in the centre of momentum frame. . . . .	37
2.13	Direct annihilation rate as a function of electron and positron energy. . . . .	40
2.14	Annihilation in flight spectra. . . . .	43
2.15	Positronium annihilation spectra. . . . .	44
2.16	Energy losses of positrons in interstellar space. . . . .	49
2.17	Cosmic-ray positron annihilation in flight spectrum. . . . .	50
2.18	Thermal pair-plasma annihilation spectrum. . . . .	52
2.19	Positronium formation in flight. . . . .	54
2.20	Effective 511 keV line width as a function of gas parameters. . . . .	55
3.1	Interaction strengths of photons with matter. . . . .	59
3.2	Photon interactions and spectral response of a germanium detector. . . . .	61
3.3	The function principle of a coded-mask system. . . . .	62
3.4	Field of view definition of coded-mask telescopes. . . . .	63
3.5	The INTEGRAL spacecraft. . . . .	64
3.6	The INTEGRAL orbit. . . . .	64
3.7	Schematic drawing of the detector numbering of the SPI camera. . . . .	67
3.8	The SPI camera system. . . . .	68
3.9	SPI anticoincidence systems. . . . .	69
3.10	Cut-out view of the SPI spectrometer. . . . .	70
3.11	Imaging response generation process on ground. . . . .	71
3.12	SPI effective area and point-spread-function. . . . .	72
3.13	Schematic drawing of a neutron capture process and outcomes. . . . .	73
3.14	Typical SPI spectra on different time scales. . . . .	75
3.15	Line shapes and calibration impact on line positions. . . . .	78
3.16	Continuum detector pattern on short time scales. . . . .	79
3.17	Background intensities as a function of time. . . . .	80
3.18	Instrumental background line widths as a function of time. . . . .	81
3.19	Instrumental background line peak energies. . . . .	82
3.20	Background detector patterns as a function of time. . . . .	83
3.21	Schematic drawing of SPI-light. . . . .	85

3.22	Data structure of SPI-light. . . . .	86
3.23	Background model reconstruction and scaling procedure. . . . .	88
3.24	Line and continuum background data structure. . . . .	90
3.25	Reconstruction of line and continuum background patterns in blocks. . . . .	92
3.26	Dithering strategy of SPI in $5 \times 5$ rectangular grid. . . . .	94
3.27	Detector pattern and shadowgram of a celestial source. . . . .	95
4.1	First galactic 511 keV map from OSSE on GCRO. . . . .	97
4.2	"Life" of a positron in the Milky Way. . . . .	98
4.3	Sky exposure map for the 511 keV data set. . . . .	101
4.4	Background spectrum in the vicinity of 511 keV. . . . .	101
4.5	Imaging analyses informational contents against astrophysical bias. . . . .	104
4.6	Positron annihilation sky map from Richardson Lucy deconvolution. . . . .	106
4.7	Maximum entropy images of the 511 keV sky. . . . .	107
4.8	Maximum entropy images of the inner galactic ridge in 511 keV. . . . .	109
4.9	Emissivity distribution models for bipolar galactic centre morphologies. . . . .	110
4.10	Image of the celestial model components describing the 511 keV sky. . . . .	114
4.11	Annihilation emission profile in longitude and latitude. . . . .	115
4.12	Maximum likelihood estimate for the disk extent. . . . .	116
4.13	Background model performance per energy bin. . . . .	116
4.14	Detection significance of gamma-rays from positron annihilation. . . . .	117
4.15	Likelihood of tracer maps as a function of photon energy. . . . .	120
4.16	Likelihood ratio in different bands as a function of photon energy. . . . .	121
4.17	Likelihood ratio in for maps with explicit physical mechanism. . . . .	122
4.18	Spectrum of annihilation gamma-rays from the bulge. . . . .	123
4.19	Dependence of the bulge 511 keV line flux as a function of disk size. . . . .	124
4.20	Spectral parameters of the bulge as a function of disk size. . . . .	125
4.21	Spectrum of annihilation gamma-rays from the disk. . . . .	126
4.22	Spectral parameters of the disk as a function of disk size. . . . .	126
4.23	Eastern and western hemisphere annihilation spectra. . . . .	127
4.24	Spectrum from a point-like source in the centre of the Milky Way. . . . .	128
4.25	Centre Source 511 keV line flux as a function of disk size. . . . .	129
4.26	Point source continuum fluxes as a function of disk size. . . . .	130
4.27	Spectrum of the Crab and Cygnus X-1 between 490 and 530 keV. . . . .	130
4.28	Annihilation conditions in different regions of the Milky Way. . . . .	134
4.29	Star count map from the 2MASS survey. . . . .	137
4.30	Comparison of bulge to disk ratios from SPI measurements. . . . .	141
4.31	Longitude-velocity diagram of astrophysical tracers. . . . .	143
4.32	Sketch of $^{26}\text{Al}$ rotation and blow-out geometry. . . . .	144
4.33	Definition of the region of interest in the sliding window method. . . . .	145
4.34	Region of interest scheme in the $^{26}\text{Al}$ data analysis. . . . .	145
4.35	Exposure map of the 13 year $^{26}\text{Al}$ 1809 keV data set. . . . .	146
4.36	Detection significance of gamma-rays from $^{26}\text{Al}$ in the Galaxy. . . . .	147
4.37	Celestial and background spectrum in the range 1745 to 1840 keV. . . . .	148
4.38	Variation of celestial and background lines centroids with longitude. . . . .	150
4.39	Longitude-velocity diagram of 1809 keV line emission in the Milky Way. . . . .	151
4.40	Longitude-flux diagram of $^{26}\text{Al}$ emission in the galactic plane. . . . .	151
4.41	Longitude-latitude-velocity-diagram of the Milky Way at 1809 keV. . . . .	152
4.42	$^{26}\text{Al}$ line flux variations with longitude and latitude. . . . .	152
4.43	Doppler-velocity variations with galactic height. . . . .	153

4.44	Longitude-velocity diagram of 511 keV emission in the Milky Way. . . . .	154
4.45	Dispersion profile of positron annihilation in the inner Galaxy. . . . .	155
4.46	Kinematic profiles of RR Lyrae stars in the galactic centre. . . . .	156
5.1	Main paths of the NeNaMgAl sequence. . . . .	161
5.2	Evolution of massive stars. . . . .	162
5.3	COMPTEL $^{26}\text{Al}$ (1809 keV) maximum entropy map. . . . .	164
5.4	Time profiles of $^{26}\text{Al}$ and $^{60}\text{Fe}$ for a coeval population of stars. . . . .	165
5.5	Decay scheme of $^{26}\text{Al}$ . . . . .	166
5.6	Fit results for $^{26}\text{Al}$ data described by an exponential disk model. . . . .	168
5.7	Spectrum of the 1809 keV $^{26}\text{Al}$ emission in the Milky Way. . . . .	169
5.8	Systematics study of measured $^{26}\text{Al}$ fluxes. . . . .	170
5.9	Fit results for $^{26}\text{Al}$ data described by two exponential disk models. . . . .	171
5.10	Massive star region definitions from the COMPTEL ME7 map. . . . .	173
5.11	False-colour image of the Orion region. . . . .	175
5.12	Spectra from the Orion region. . . . .	177
5.13	Spectrum of $^{26}\text{Al}$ emission in the inner Galaxy. . . . .	179
5.14	Final fates of stars with schematic evolutionary tracks. . . . .	180
5.15	Peak explosion temperature and burning zones in supernovae. . . . .	181
5.16	Decay scheme of the $^{44}\text{Ti}$ decay chain. . . . .	183
5.17	False-colour image of Cas A as seen at different wavelengths. . . . .	184
5.18	Exposure map of the Cas A SPI/INTEGRAL data set. . . . .	185
5.19	Spectra around the expected $^{44}\text{Ti}$ lines from the position of Cas A. . . . .	185
5.20	Comparison of Cas A measurements with different instruments. . . . .	187
5.21	Decay scheme of the $^{56}\text{Ni}$ decay chain. . . . .	191
5.22	Background spectrum for the analysis of $^{56}\text{Ni}$ decay gamma-rays. . . . .	193
5.23	Gamma-ray spectra from SN2014J at maximum light. . . . .	194
5.24	Monte-Carlo analysis of $^{56}\text{Ni}$ spectra from SN2014J. . . . .	195
5.25	Sketch of the SN2014J ejecta configuration. . . . .	196
5.26	Expected model spectra of the supernova belt configuration. . . . .	197
5.27	Spectra of $^{56}\text{Co}$ decay gamma-rays from SN2014J. . . . .	197
5.28	Spectral complexity in SN2014J revealed by different energy binning. . . . .	198
5.29	SN2014J signal intensity variations. . . . .	199
5.30	Gamma-ray line light curve of $^{56}\text{Co}$ in SN2014J. . . . .	200
5.31	Annihilation line spectrum of SN2014J. . . . .	201
5.32	Annihilation line light curve of SN2014J. . . . .	202
5.33	Type Ia supernova positron contribution. . . . .	204
5.34	Evolution of gamma-rays emission from nova explosions. . . . .	206
5.35	Compactness as a function of luminosity and size. . . . .	210
5.36	Scheme of the quasi-periodic hydrogen ionisation instability. . . . .	212
5.37	Typical light curves of X-ray binary outbursts. . . . .	213
5.38	Classical definition of spectral states in X-ray binaries. . . . .	214
5.39	Spectral states of an outburst of GRO J1655-40. . . . .	215
5.40	Measured high-energy spectra of microquasars. . . . .	216
5.41	Radio maps of 1E1740.7-2942 at 6 and 20 cm wavelength. . . . .	217
5.42	Light curve of hard X-rays during the V404 Cygni outburst. . . . .	218
5.43	Spectral evolution of V404 Cygni during outburst. . . . .	219
5.44	Alternative model spectra for V404 Cygni outburst epoch 3. . . . .	221
5.45	Annihilation flux light curve of V404 Cygni. . . . .	222
5.46	Correlation between X-ray and annihilation flux in V404 Cygni. . . . .	223

---

5.47	Scenarios for Sgr A* as positron producer in the galactic centre. . . .	226
5.48	Cosmic-ray spectrum measured at Earth. . . . .	228
5.49	Rotation curve of the Milky Way. . . . .	235
5.50	Angular profiles for 511 keV and dark matter. . . . .	235
5.51	Simulated all-sky maps for dark matter annihilation signals. . . . .	236
5.52	Distribution of Milky Way satellite galaxies. . . . .	237
5.53	Spectrum from the position of Reticulum II. . . . .	238
5.54	Annihilation flux of dwarf galaxies as a function of exposure time. . .	239
5.55	Mass-to-luminosity ratios in visible and 511 keV light. . . . .	243
5.56	Schematic view of components in the inner Galaxy. . . . .	246
A.1	Compilation of annihilation in flight spectra. . . . .	I
A.2	Dependence of GCS spectral parameters as a function of disk size. . .	I
A.3	Likelihood as a function of photon energy for the $^{26}\text{Al}$ line. . . . .	II
A.4	Astrophysical tracer maps 1-21. . . . .	III
A.5	Astrophysical tracer maps 21-42. . . . .	IV
A.6	$^{26}\text{Al}$ decay gamma-ray spectra from massive star groups. . . . .	V

# List of Tables

2.1	Summary of positron production mechanisms. . . . .	24
2.2	Possible positron reactions with species of the interstellar medium. . . . .	28
2.3	Kinematic parameter definitions in different frames. . . . .	38
2.4	Descriptive parameters of the interstellar medium. . . . .	53
2.5	Annihilation line widths in different phases of interstellar gas. . . . .	54
3.1	SPI instrument characteristics. . . . .	66
4.1	Exposure times for different regions in the sky. . . . .	101
4.2	Identification of background lines in the vicinity of 511 keV. . . . .	103
4.3	Measured 511 keV bulge extents from previous studies. . . . .	112
4.4	Characteristics of empirical sky model components. . . . .	114
4.5	Correlation coefficients for the six simultaneously fitted sky components	117
4.6	Summary of astrophysical tracer maps. . . . .	119
4.7	Summary of tracer maps with explicit physical mechanism. . . . .	121
4.8	Flux limits on 511 keV emission from detected continuum sources. . . . .	131
4.9	Spectral parameters for each 511 keV sky model component. . . . .	132
4.10	Spectral model comparisons of the celestial components. . . . .	132
4.11	Doppler-velocity diagnostics of the celestial emission model components.	139
4.12	Positron annihilation rates in the Milky Way. . . . .	142
4.13	Exposure time in massive star regions. . . . .	147
5.1	Astrophysically important positron emitting nuclei. . . . .	158
5.2	Excerpt of nuclear reactions inside stars. . . . .	160
5.3	Spectral parameters of the $^{26}\text{Al}$ 1809 keV lines in massive star groups.	173
5.4	Characteristics of the Orion OB1 stellar subgroups. . . . .	174
5.5	Estimates of the galactic $^{26}\text{Al}$ mass. . . . .	179
5.6	Spectral parameters of the detected $^{44}\text{Ti}$ line in Cas A. . . . .	186
5.7	Spectral fit parameters for the flaring epochs of V404 Cygni. . . . .	220
5.8	Characteristic properties of pulsars. . . . .	231
5.9	List of Milky Way satellites tested for 511 keV emission. . . . .	241
5.10	Comparison of positron annihilation and production in the Galaxy. . . . .	248
A.1	Additional gamma-ray lines from astrophysical positron emitters. . . . .	II

## List of Acronyms

ACS	-	Anticoincidence shield
BB	-	Broad bulge
BGO	-	Bismuth germanate ( $\text{Bi}_4\text{Ge}_3\text{O}_{12}$ )
BH	-	Black hole
B/D	-	Bulge-to-disk ratio
CGRO	-	Compton Gamma Ray Observatory
CCSN	-	Core-collapse supernova
COMPTEL	-	Compton telescope
dof	-	Degree of freedom
DSG	-	Dwarf satellite galaxy
D <sup>3</sup> PO	-	Denosing, Deconvolving, and Decomposing Photon Observations
FWHM	-	Full width at half maximum
GCS	-	Galactic centre source
INTEGRAL	-	International Gamma-Ray Astrophysics Laboratory
IRF	-	Imaging response function
ISM	-	Interstellar medium
$\Lambda$ CDM	-	Cord dark matter cosmology with dark energy
LMXRB	-	Low-mass X-ray binary
ME	-	Maximum entropy
NB	-	Narrow bulge
NFW	-	Navarro Frenk White
NS	-	Neutron star
o-Ps	-	Ortho-positronium
p-Ps	-	Para-positronium
PSAC	-	Plastic Anti Coincidence Scintillator
RL	-	Richardson-Lucy
ROI	-	Region of interest
RRL	-	RR Lyrae
SN	-	Supernova
SPI	-	Spectrometer aboard INTEGRAL
TPA	-	Thermal pair-annihilation
WIMP	-	Weakly interacting massive particle
WD	-	White dwarf
XRB	-	X-ray binary

## Danksagung

Als erstes möchte ich mich bei meinem Doktorvater Prof. Dr. Roland Diehl bedanken, dass er mir die Möglichkeit gegeben hat bei ihm zu promovieren. Ich habe von ihm gelernt, wie man wissenschaftlich arbeitet und argumentiert. Für die Erfahrungen, die ich auf verschiedenen Konferenzen sammeln konnte, bin ich sehr dankbar. Ich bedanke mich bei Xiao-Ling Zhang für die Bereitstellung der INTEGRAL Daten und die Hilfe, die ich von ihr bekommen habe, wenn Probleme damit auftraten. Ich danke meinen Kollegen am Max-Planck-Institut für extraterrestrische Physik, insbesondere Fabrizia Guglielmetti, Andrew Strong, Martin Krause und Jochen Greiner für die Unterstützung bei wissenschaftlichen und nichtwissenschaftlichen Angelegenheiten. Meinen Freunden am Institut, Michael Opitsch, Philipp Lang und Christoph Weinberger möchte ich besonders danken, da ich durch sie nicht die Freude an der Arbeit verloren habe.

Der größte Dank gehört der wichtigsten Person in meinem Leben, meiner Liebsten, Tanja. Ohne sie hätte ich die letzten Jahre nicht durchstehen können. Ich danke ihr sehr für die Unterstützung und die Motivation, die ich besonders gegen Ende meiner Doktorarbeit brauchte. Danke Tanja, dass du immer an mich geglaubt hast.

*It is the outlier which is interesting.*

**Fabrizia Guglielmetti**

# 1 Introduction

Since the dawn of particle physics and the awareness that for each particle there exists an anti-particle, the imagination of antimatter being part of the Universe was and is fascinating. The concept of a mirror ensemble of elementary particles is included in the well-established standard model of particle physics, predicting the properties and interactions of particles and anti-particles, and which is impressively confirmed at great precision. The pioneering identification (Dirac 1928; Anderson 1933) of two possible but opposite charges for one and the same species of particles, i.e. particles with identical mass, led to the unification of quantum theories, with electromagnetism (quantum-electrodynamics), later including the weak nuclear force, and finally the strong nuclear force. Gravitation, however, does not conform with this description, as there is no theory to predict gravitational forces on the quantum level, also because gravity is of the order  $10^{40}$  times weaker than the electromagnetic force. The interaction strength between charged particles, expressed by the Sommerfeld-constant  $\alpha$ , is among the most precisely measured and predicted natural constants, and consistent between model and theory to the tenth digit (Mohr et al. 2015).

In the standard model of cosmology, the Universe consists of only  $\sim 5\%$  of baryonic matter, and is dominated by gravity on very large scales. In this picture, a Big Bang (Friedman 1922; Lemaître 1927) created the Universe 13.8 billion years ago (Planck Collaboration et al. 2014b), with presumably an equivalent amount of matter and anti-matter. The remaining  $\sim 95\%$  are thought to be shared among a phenomenon called "dark energy" ( $\sim 70\%$ ), which is made responsible for the apparently-accelerated (Riess et al. 1998; Perlmutter et al. 1999) expansion of the Universe (Hubble 1929), but whose nature is entirely unknown, and another type of matter which is not seen but apparently acting gravitationally, hence called "dark matter" ( $\sim 25\%$  Zwicky 1933, 1937). Today, astronomers believe that the visible Universe contains only matter - and not antimatter - in the form of gas, stars, and galaxies. But there is no way to distinguish light from matter between light from anti-matter, if quantum-electrodynamics is the proper theory (Andresen et al. 2010). The question arises why there is matter at all (Leibniz 1714) if the Big Bang produced the same amount of matter and antimatter, which should have annihilated with each other. This baryon asymmetry of the Universe (Sakharov 1967) assumes a thermal equilibrium (Gamow 1946; Alpher et al. 1948) of protons, anti-protons, and photons shortly after the Big Bang, for a residual freeze-out asymmetry of the order  $10^{-18}$ . The measured asymmetry is about  $10^{-10}$ . This is derived from measurements of the cosmic microwave background (e.g. Komatsu et al. 2011), which is thought to be a witness of the Big Bang, or from local measurements of cosmic-ray abundances (e.g. Fields & Sarkar 2006; Steigman 2010). The baryon asymmetry of the Universe requires additional effect, linked to the annihilation of particles. Quantum mechanical charge-parity violation is discussed as it may lead to a spontaneous symmetry breaking, and a preferred domain (e.g. Stecker 2002). Alternatively, the theory of

gravity may also lead to an effect in which particles and anti-particles are not behaving as expected from general relativity (Milgrom 1983). A common assumption in the standard models of particle physics and cosmology is that both, particles and anti-particles have a positive mass. This has not yet been proven, and may not be true (e.g. Charman 2013; Crivelli et al. 2014). If gravity could also be repulsive like the electromagnetic force, many "known" conceptions of astro- and particle-physics (astroparticle physics) could be enriched by a missing link.

The most straightforward approach to proceed may be to study the nature of a well-known lepton, and how it interacts with its anti-particle throughout the Universe. The annihilation of particles with anti-particles, in particular the conversion of electrons and positrons to gamma radiation at 511 keV (Klempner & Chadwick 1934), takes place in great numbers and steadily (Purcell et al. 1997) in the Milky Way galaxy (Leventhal et al. 1978). Understanding this annihilation radiation, the origin of positrons, and the influence of antimatter in the Galaxy has been a challenge for more than four decades, and is still unsolved (Prantzos et al. 2011). A solution of the galactic positron puzzle may then also provide clues to even greater questions concerning the structure of galaxies and the entire Universe.

In this thesis, the gamma-ray line signal from electron-positron annihilation in the Milky Way is discussed. This is of great interest because literally all astrophysical sources can produce positrons. The unique gamma-ray signature of positron annihilation then presents an efficient and direct tool to study positron astrophysics in this observational window. The positrons which are seen to annihilate now are presumably not primordial, as there is a steady supply of positrons of the order  $10^{43} \text{ e}^+ \text{ s}^{-1}$  (Leventhal et al. 1978), at least on the time-scale of gamma-ray astronomy. But they could originate in, for example, dark matter (e.g. Boehm et al. 2004) which must have also formed during the Big Bang.

The work presented in this thesis includes refined measurements of the positron annihilation emission morphology in the Milky Way, using the gamma-ray spectrometer telescope SPI (Vedrenne et al. 2003) aboard the ESA satellite INTEGRAL (Winkler et al. 2003), and a new elaborate procedure to cope with instrumental background in space. The SPI coded-mask imaging capabilities and the ten year exposure of INTEGRAL observations can answer the question of a 511 keV disk in the Galaxy in addition to the asymmetric bulge component. A disk with its very low surface-brightness was not seen in this large extent before. In addition, a point-like source in the galactic centre has emerged on top of the bulge emission. The morphology which is found is more consistent with galactic positron sources distributed in bulge and disk, and favours scenarios in which positrons propagate far away from their sources, thereby slow down, and annihilate in gas which is ionised, at least to a degree of a few per cent. The specific annihilation conditions may vary across the Galaxy, as the spectral shapes of different galactic components are not found to be identical. It is discussed where the positrons prefer to annihilate, by using astrophysical tracers, such as the emission morphologies at different wavelengths. Also a look at the kinematics of positron annihilation in the inner radian of the Galaxy was exploited. The possibility of annihilation in stellar atmospheres is suggested based on these tracers, instead of annihilation in interstellar gas. The positron budget, separated into bulge and disk, is then compared to estimates from direct observations of positron-producing sources such as massive stars, core-collapse supernovae,

thermonuclear supernovae, black hole binary systems, and dark matter. Massive stars and their supernovae cannot account for all the positrons (via  $\beta^+$ -decay of proton-rich nuclei), but contribute to about 10%. Additional sources are required, and found to account probably for the bulk of positrons. These source have been measured in this thesis by the synthesised mass in type Ia supernovae and the ejected positrons, as well as by photon-photon pair-creation in the vicinity of a stellar mass black hole in a binary system. All these source types can already account for the total number of positrons seen to annihilate in the Milky Way, if a steady state production and annihilation is assumed, their present populations and rates are evaluated. The case of dark matter being responsible for the majority of positrons in the Galaxy can be closed: The study of 511 keV emission from satellite galaxies of the Milky Way yields a negative hypothesis test, and limits the dark matter contribution in the Milky Way itself to less than 1%. Other sources for which no measurements are available but potentially contribute to the total positron content, such as pulsars, novae, and cosmic-rays, are presented and discussed in the limits of the measurements uncertainties.

This thesis is structured as follows: In chapter 2, the physics with positrons is assembled and discussed in detail, starting by characterising the positron in terms of particle physics, then describing the possibilities of creating positrons in general. The chapter ends with a description of the ultimate annihilation with electrons, which focusses on environmental conditions, especially in interstellar space, and the resulting spectral shapes. Chapter 3 first provides an overview of astronomy with gamma-rays, introduces the SPI instrument which is used in this thesis, and then delivers a detailed description of how cosmic-ray background is treated in gamma-ray data analysis. Such comprehensive understanding of the instrument and its data is then used to determine the 511 keV electron-positron annihilation signal in the Milky Way in chapter 4, analysing the image as well as the spectral domain towards a refined view of the positron puzzle. In addition, the kinematics of the Milky Way are determined and discussed, as seen in gamma-rays from the decay of  $\beta^+$ -unstable nuclei as well as from electron-positron annihilation. The astrophysical candidate positron sources are discussed in detail, one-by-one in chapter 5. Here, also the relevant other measurements with SPI are presented, for massive stars, core-collapse supernovae, thermonuclear supernovae, microquasars, and dark matter, towards an attempt to balance the measured annihilation rate with the production rate. The point-source in the galactic centre is discussed in terms of the plausible sources. Chapter 6 summarises the principal parameters of the 511 keV emission in the Milky Way, its possible origins, and concludes with an overview of what is left of the positron puzzle.

## 2 Positron Physics

### 2.1 What are Positrons?

#### 2.1.1 The Positron as Elementary Particle

A positron is identical to an electron, except for its opposite charge. The electron has been identified in 1897 by Sir Joseph John Thomson, as a negatively electrified particle constituent of the "Cathode Rays" in vacuum tubes (Thomson 1897). Thirty years later in 1928, the positron was described theoretically by Paul Dirac. He did actually not propose a positively charged particle besides the electron, but predicted a positive and a negative energy state as the solutions of the special relativistic quantum mechanical equations (Dirac 1928). It was also Dirac himself who questioned the negative energy solution, because in quantum mechanics, such a case cannot be ignored since state transitions between the positive and negative state should have been observed then. To avoid the flaw in his theory, he interpreted the negative energy solution as an electron behaving like it holds a positive charge in an external field (Dirac 1930). This is related to the "Dirac Sea" which was invented to capture *all* the negative energy particles in a vacuum model. A hole in the sea would correspond to one realisation of a positively charged electron. Dirac falsely attributed this to the possibility of the proton to be an island in this sea.

The discovery of the positron is assigned to Carl David Anderson in 1932 who measured the curvatures and track lengths of cosmic-rays in a vertical cloud chamber (Anderson 1933). Anderson was awarded the Nobel Prize in 1936 for his discovery of the positron, as it was then named. It may have been detected earlier if only other scientists had followed up their works, or did not dismiss the positive curvature as coming from protons (see Filk & Close 2010). The detection of the positron was the first step to the development of the standard model of modern particle physics.

In terms of elementary particle physics, electrons and positrons are charged leptonic fermions. This means they are elementary, spin-1/2 particles which follow the Fermi-Dirac statistics and thus obey the Pauli exclusion principle. In particular their charge is  $\mp 1e = \mp 1.6021766208(98) \times 10^{-19} \text{ A s}$ , and their mass  $m_e = 9.10938356(11) \times 10^{-31} \text{ kg} = 510.9989461(31) \text{ keV c}^{-2} \approx 511 \text{ keV c}^{-2}$  (Mohr et al. 2015). In a system of identical fermionic particles with chemical potential  $\mu$ , the mean number  $n$  of particles in a particular energy state  $E$  at temperature  $T$  is described by the Fermi-Dirac-distribution

$$n = \frac{1}{\exp((E - \mu)/kT) + 1}, \quad (2.1)$$

where  $k = 1.38064852(79) \times 10^{-23} \text{ J K}^{-1}$  is the Boltzmann constant (Fermi 1926; Dirac 1926; Zannoni 1999). At absolute zero temperature ( $T \rightarrow 0$ ), at most one particle may populate one given energy level at a time. This is the Pauli exclusion principle, which is realised, for example, in the quantum energy states of electrons in atoms (Pauli 1925), or in the stabilising degeneracy pressure in white dwarves (Chandrasekhar 1931) and neutron stars (Tolman 1939; Oppenheimer & Volkoff 1939). As the positron is of leptonic origin, it only interacts gravitationally, electromagnetically, and weakly, and so does not couple to quarks via the strong force.

With the description and detection of the positron, the proof of the hypothesised "negative matter" was brought up, and the positron was the first antimatter particle that was discovered, with apparently negative energy. The basic idea of Dirac was to prevent an isolated electron in an electromagnetic field from producing an infinite amount of energy in the form of photons, because there is no lower bound, or zero energy level, if there are also negative energy electrons. But if the sea is completely filled and *all* states are populated, the electron cannot drop below the zero level because of the Pauli exclusion principle: *all* negative states in the sea are already occupied. If there is a hole in the sea, this is interpreted as being a positron. Then, an electron can occupy this empty state in the sea when emitting two photons of mass-equivalent energy of 511 keV each. This is today known as matter-antimatter annihilation (see Sec. 2.3).

But the Dirac-Sea involved major physical problems, because the infinite sea contains an infinite amount of negative energy and an infinite mass which does not interact gravitationally. It was Ernst Stückelberg who first revised this picture, and explained the antimatter particles as having the same mass, the same spin, but opposite charge. As a result, in modern particle physics this led to the description of antiparticles moving backwards in time. Richard Feynman crowned this "Stückelberg-Feynman-interpretation": The Feynman diagrams are now the most-common visualisation of quantum-electrodynamics perturbation theory (Feynman 1949).

## 2.1.2 Bound States with Positrons

### 2.1.2.1 Anti-Atoms

The simplest antimatter atom is antihydrogen, made of an anti-proton as the nucleus, and the positron "orbiting" it. It is commonly believed that antihydrogen does not occur naturally on Earth because it would immediately find other protons and electrons to annihilate with. In astrophysical and even more so cosmological sense, antihydrogen and hydrogen are spectroscopically indistinguishable from each other because its constituents have identical mass, charge, and magnetic moment with respect to hydrogen. Atomic emission lines from antihydrogen (excited lines e.g. from Lyman series, Balmer series, ..., or neutral HI line at 21 cm from hyperfine transition) should therefore be identical to hydrogen. This has not yet been proven experimentally to be true, but such a degeneracy involves great uncertainties in the interpretation of astrophysical observations. Whenever hydrogenic emission lines are observed from a star, for instance, the star may either consist of normal hydrogen or antihydrogen. Only rationality arguments lead to the conclusion that *everything*

we see is made of matter - and not antimatter. The question then of course remains: Why is there something and not nothing (Leibniz 1714), if all matter annihilated with all antimatter after the big bang?

On Earth, antihydrogen has to be produced artificially in particle accelerators. It was first synthesised at the Low Energy Antiproton Ring at CERN (Baur et al. 1996) but its storage is very expensive and, because of its charge neutrality, can only be confined magnetically (Pritchard 1983; Madsen 2010). Also other anti-nuclei, up to anti- $^4\text{He}$ , have been produced in accelerator experiments but at such high temperatures (velocities) and at such low numbers that they did not find positrons to form complete anti-atoms (Cork et al. 1956; Massam et al. 1965; Dorfman et al. 1965; Antipov et al. 1970; Vishnevsky et al. 1974; Arsenescu et al. 2003; Star Collaboration et al. 2011).

### 2.1.2.2 Positronium

The first exotic positronium (Ps) atom was theorised by Mohorovičić already in 1934 (Mohorovičić 1934) and was finally discovered in 1951 by Martin Deutsch at the Massachusetts Institute of Technology (Deutsch 1951, announced at a scientific meeting at Brookhaven National Laboratory). It consists of an electron and a positron and is therefore the simplest and lightest purely electromagnetically bound state of elementary particles (Berko & Pendleton 1980). It is related to the hydrogen atom in a sense that the proton is replaced by the positron to be the nucleus which the electron is orbiting. Now, in the Ps atom, the masses of the constituents are identical and hence the reduced mass,  $\mu_{Ps} = \frac{m_- m_+}{m_- + m_+} = 0.5m_e$ , is about half of the reduced mass of the hydrogen atom ( $\mu_H \approx 0.9995m_e$ ). Thus spectroscopically, Ps shows the same neutral and excitation lines as atomic hydrogen but at twice the wavelength for a particular transition. In consequence, also the binding energy,  $E_B$ , of the Ps atom is about half the binding energy of the hydrogen atom, at  $E_B = \frac{m_e e^4}{16h^2 \epsilon_0^2} = 6.80284651(22) \text{ eV} \approx 6.8 \text{ eV}$ , where  $h = 6.626070040(81) \times 10^{-34} \text{ J s}$  is the Planck constant and  $\epsilon_0 = \frac{1}{\mu_0 c^2} = 8.845187817 \dots \times 10^{-12} \text{ A}^2 \text{ s}^4 \text{ kg}^{-1} \text{ m}^{-3}$  is the electric constant (Mohr et al. 2015). This corresponds to a temperature of  $T_B = 118415.674(68) \text{ K} \approx 0.12 \text{ MK}$ , assuming kinetic theory of gases. So, Ps is stable in terms of terrestrial temperatures but as it consists of a matter-antimatter pair, it has a certain decay width and thus lifetime (see Sec. 2.3).

Because of the spin quantum numbers of the electron ( $S_- = 1/2$ ) and the positron ( $S_+ = 1/2$ ), Ps is a boson ( $S_{Ps} = \{-1, 0, 1\}$ ), and may thus occur either in a singlet state with "anti-parallel" spins, called para-positronium (p-Ps), or in a triplet state with "parallel" spins, called ortho-positronium (o-Ps). In particular, the spin part of the wave function of electron and positron can be written as  $|S_-, m_- \rangle$  and  $|S_+, m_+ \rangle$ , respectively, where  $S_{\pm} = 1/2$  denote the spins, and  $m_{\pm} = \pm 1/2$  their projections on the spin axis (chosen as the z-axis). The composite spin wave function of Ps is then

$$\begin{aligned}
|S_{P_s}, m_{P_s}\rangle &= |S_-, m_-\rangle \otimes |S_+, m_+\rangle = \\
&= \sum_{m_{P_s}=m_-+m_+} C_{m_- m_+ m_{P_s}}^{S_- S_+ S_{P_s}} |S_-, m_-\rangle |S_+, m_+\rangle, \quad (2.2)
\end{aligned}$$

where  $C_{m_- m_+ m_{P_s}}^{S_- S_+ S_{P_s}}$  are the Clebsch-Gordan coefficients for adding up angular momenta in quantum mechanics. This obtains a four-dimensional space of basis states

$$\begin{aligned}
&|1/2, +1/2\rangle |1/2, +1/2\rangle \\
&|1/2, +1/2\rangle |1/2, -1/2\rangle \\
&|1/2, -1/2\rangle |1/2, +1/2\rangle \\
&|1/2, -1/2\rangle |1/2, -1/2\rangle \quad (2.3)
\end{aligned}$$

in which three (combinations of) states add up to spin 1 (triplet) and one to spin 0 (singlet). For illustration purpose, the spin of a spin-1/2 particle is symbolised with vertical arrows, following the convention that up means  $m = +1/2$  and down means  $m = -1/2$ :

$$\text{Triplet state o-Ps: } |S_{oP_s}, m_{oP_s}\rangle = \begin{cases} |1, +1\rangle & = \uparrow\uparrow \\ |1, 0\rangle & = \frac{1}{\sqrt{2}}(\uparrow\downarrow + \downarrow\uparrow) \\ |1, -1\rangle & = \downarrow\downarrow \end{cases} \quad (2.4)$$

$$\text{Singlet state p-Ps: } |S_{pP_s}, m_{pP_s}\rangle = \begin{cases} |0, 0\rangle & = \frac{1}{\sqrt{2}}(\uparrow\downarrow - \downarrow\uparrow) \end{cases} \quad (2.5)$$

Positronium decays to integer multiples of two photons ( $2n$ ,  $n \in \mathbb{N}$ ) in case of p-Ps, or to an odd number of photons ( $2n + 1$ ,  $n \in \mathbb{N}$ ) in case of o-Ps, due to energy-momentum conservation and quantum mechanical selection rules. Its wave function is an eigenstate of parity ( $P = (-1)^{L+1}$ ) and charge conjugation ( $C = (-1)^{L+S}$ ) which can be derived from the constituents' parities and the requirement that the final wave function must be asymmetric. The charge-conjugation eigenvalue of  $n$  photons is  $C(n\gamma) = (-1)^n$  and the selection rule to obtain the number of photons for p-Ps and o-Ps decays is  $(-1)^{L+S} = (-1)^n$ . Thus, for the singlet (ground) state  $P_s(^1S_0)$  ( $L = 0$ ,  $S = 0$ ,  $2S + 1 = 1$ ,  $J = L + S = 0$ ), only the decay into two photons is possible. The triplet state  $P_s(^3S_1)$  ( $L = 0$ ,  $S = 1$ ,  $2S + 1 = 3$ ,  $J = L + S = 1$ ) is allowed to decay into at least three photons. The one-photon case is excluded because of momentum conservation.

Because of this, also the decay rates (lifetimes) between p-Ps and o-Ps differ. At tree-level, considerations of the positronium wave functions and counting the vertices in the annihilation Feynman-diagrams (see Fig. 2.6, see also Sec. 2.3) are enough to get a measure of the lifetimes. The calculation by Wheeler and Pirenne (Wheeler 1946) formulate the p-Ps decay rate as

$$\Gamma(Ps \rightarrow n\gamma) = \frac{1}{2J+1} |\Psi_{Ps}(r=0)|^2 (4v_{rel}\sigma(e^-e^+ \rightarrow n\gamma))_{v_{rel} \rightarrow 0} \quad (2.6)$$

with  $\Psi_{Ps}(r=0) = \sqrt{\frac{m_e^3 c^3 \alpha^3}{8\pi \hbar^3}}$  being the wave function of the positronium atom (equivalent to the hydrogen atom) at zero separation (annihilation),  $v_{rel}$  the relative velocity of the particles, and  $\sigma$  the cross section of the process, so that applied to the dominant two-photon case  $\Gamma(p-Ps \rightarrow \gamma\gamma) = \frac{1}{2}\alpha^5 \frac{m_e c^2}{\hbar} \approx 8.0325 \times 10^9 \text{ s}^{-1}$  ( $\alpha = \frac{e^2}{4\pi\epsilon_0 \hbar c} = 7.2973525664(17) \times 10^{-3} = (137.035999139(31))^{-1}$  is the Sommerfeld constant, and  $\hbar = \frac{h}{2\pi}$  (Mohr et al. 2015)). Ore and Powell calculated the case for o-Ps to three photons and found  $\Gamma(o-Ps \rightarrow \gamma\gamma\gamma) = \frac{2(\pi^2-9)}{9\pi}\alpha^6 \frac{m_e c^2}{\hbar} \approx 7.211 \times 10^6 \text{ s}^{-1}$  (Ore & Powell 1949). From an investigation of the Feynman diagram, by counting the vertices (see Fig. 2.9, see also Sec. 2.3), the additional factor of  $\alpha$  is obvious. A thorough calculation of the phase space (coefficients, see Sec. 2.3.2) leads to a  $\approx 1000$  times ( $10/\alpha \approx 1000$ ) shorter lifetime for p-Ps ( $\tau_{pPs} \approx 0.124 \text{ ns}$ ) compared to o-Ps ( $\tau_{oPs} \approx 138.67 \text{ ns}$ ). These values are only first order calculations and are sensitive to radiative corrections. The experimentally accepted values for the decay rates and lifetimes are  $\Gamma(p-Ps \rightarrow \gamma\gamma) = 7.98950(2) \times 10^9 \text{ s}^{-1}$  ( $\tau_{pPs} \approx 0.1251643(3) \text{ ns}$ ), and  $\Gamma(o-Ps \rightarrow \gamma\gamma\gamma) = 7.0398(29) \times 10^6 \text{ s}^{-1}$  ( $\tau_{oPs} \approx 142.049(59) \text{ ns}$ ), respectively (Billoire et al. 1978; Muta & Niuya 1982; Adkins & Brown 1983; Karshenboim 1993; Al-Ramadhan & Gidley 1994; Asai et al. 1995; Czarnecki et al. 1999; Czarnecki & Karshenboim 1999; Adkins et al. 2000; Karshenboim 2002; Vallery et al. 2003; Jinnouchi et al. 2003; Penin 2004; Karshenboim 2004; Gninenko et al. 2006; Kataoka et al. 2009; Namba 2012).

### 2.1.2.3 Ions and Molecules with Positrons

Although Ps has a very short lifetime, excited states exist. This is similar to the hydrogen atom, and hence transitions can occur. The spin-flip ( $1^3S_1 \rightarrow 1^1S_0$ ), leading to the 21 cm line for neutral hydrogen, has been measured for positronium at a wavelength of 1.4739849(54) mm ( $\nu = 203.38910(74) \text{ GHz}$ ). Lyman- $\alpha$ -like (e.g.  $2^1P_1 \rightarrow 1^1S_0$ ,  $2^3P_2 \rightarrow 1^2S_1$ , ...) and Lamb-shift-like ( $2^3S_1 \rightarrow 2^3P_2$ ) transitions have also been theorised and measured (see e.g. Karshenboim 2004, and references therein).

Positronium is able to capture also other particles, forming ion-like structures, or even compounds to form exotic molecules. The negative positronium ion  $Ps^-$ , for example, which captures another electron, has already been observed (Mills 1981, 1983; Mills & Crane 1985). If two Ps atoms find each other before annihilation, they can form dipositronium, a molecule similar to the hydrogen molecule with a covalent bond. This was predicted already in 1946 (Wheeler 1946), and discovered in 2007 (Cassidy & Mills 2007). Also excited states of dipositronium have been measured (Cassidy et al. 2012). Other exotic molecules that have been observed are positronium hydride (which is made of positronium and hydrogen Schrader et al. 1992) or positronium deuteride (with a deuterium atom bound to Ps Monge et al. 1996).

Multiple other compounds with positrons or positronium atoms have been invest-

igated theoretically. Also more complex molecules have been measured so far (e.g. Tao & Green 1969; Mogensen et al. 1982; Saito 2000, and references therein).

## 2.2 Positron Production Mechanisms

### 2.2.1 Radioactive Beta-Plus-Decay

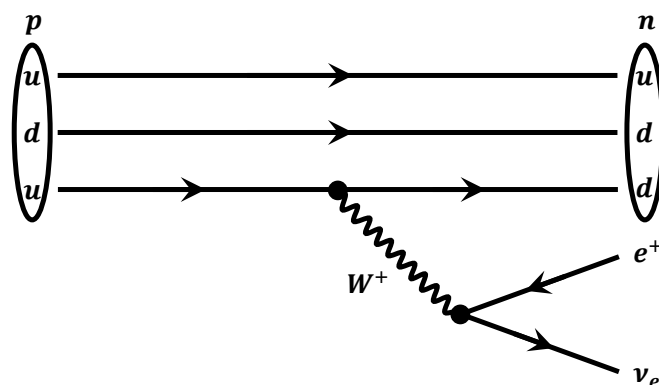


Figure 2.1: Feynman diagram of the  $\beta^+$ -decay. A free proton cannot decay to a free neutron, but bound to a nucleus, the proton may "decay" to a neutron via the emission of a positron and an electron-neutrino if the daughter nucleus obtains a lower ground state energy than its parent. The fundamental transition converts an up-quark of the proton to a down-quark by the emission of a  $W^+$ -boson.

Positrons can be created through electromagnetic and weak interactions. In  $\beta^+$ -decays, radioactive nuclei decay by emitting a positron and an electron-neutrino, because they have too few neutrons to be stable. In the table of nuclides after Emilio Sergè (plotting proton number  $Z$  against neutron number  $N$ ), the  $\beta^+$ -unstable isotopes are located "above" the stable nuclei, and titled "proton rich" although many of them have a larger number of neutrons (see NNDC 2016). Energetically, a  $\beta^+$ -decay is only possible if the mass of the parent atom is higher than its daughter nucleus by at least  $1022 \text{ keV } c^{-2}$ , i.e. two times the mass of a  $\beta$ -particle. The parent atom has to lose one electron to conserve the charge number  $Z$ , and to account for the mass of the positron<sup>1</sup>. If this is not the case, the alternative and competing decay channel is the electron-capture (EC) reaction. The large family of  $\beta^+$ -decays in radioactive nuclei can be described by the basic equation

$${}^A_Z\mathbf{X}_N \longrightarrow {}^A_{Z-1}\mathbf{Y}_{N+1} + {}^0_{+1}\mathbf{e} + {}^0_0\nu_e, \quad (2.7)$$

where  ${}^A_Z\mathbf{X}_N$  is the parent isotope  $\mathbf{X}$  with  $Z$  protons and electrons,  $N$  neutrons, and  $A = Z + N$  nucleons.  $\mathbf{X}$  decays to its daughter  $\mathbf{Y}$  with one proton less, and one neutron more, and emits a positron,  $e^+$ , and an electron-neutrino,  $\nu_e$ , to account for energy and momentum conservation in this three-body decay. Energy,  $Q$ , is released in the form of kinetic energy or gamma-rays, such that

<sup>1</sup>This is counterintuitive since the atomic shells do not participate in a nuclear reaction. But because the masses of fully ionised, i.e. electron-free, nuclei are hard to measure, the atomic weights of parent and daughter are used to calculate  $Q$ -values in general.

$$Q = [m({}_Z^A\mathbf{X}_N) - (m({}_{Z-1}^A\mathbf{Y}_{N+1}) + 2m_e + 2m_\nu)] c^2. \quad (2.8)$$

Inside a  $\beta^+$ -unstable nucleus, this may be considered as the conversion of a proton to a neutron, see Eq. (2.9). In this view, it is obvious that such a decay can only occur in a composite nucleus because the mass of the neutron is larger than that of the proton ( $m_n - m_p \approx 1.293 \text{ MeV c}^{-2}$ , Mohr et al. (2015)), and thus energetically prohibited (Krane 1987).



The reaction in Eq. (2.9) can be reduced to the emission of a  $W^+$ -boson by the one of the up-quarks of the proton (valence quarks:  $uud$ ), thereby converting to a down-quark to form the neutron (valence quarks:  $udd$ ), and followed by the immediate "decay" of the  $W^+$ -boson to a positron and an electron-neutrino (see Eq. (2.10) and Fig. 2.1)

$$u \longrightarrow d + e^+ + \nu_e. \quad (2.10)$$

The lifetimes of  $\beta^+$ -unstable nuclei range from a few nanoseconds to several billions years (Firestone et al. 1996). This reflects the differences in stability of the particular neutron-proton combination. Different time-scales, especially in the astrophysical context, can be traced by the measurement of positrons.

### 2.2.2 Decay of Leptons

Electron and positron, respectively, are the lightest lepton. Therefore, they cannot decay into smaller elementary particles, on time scales of the order of the age of the universe (mean lifetime  $\tau(e^\pm) > 4.6 \times 10^{26} \text{ yr}$  Olive & Particle Data Group 2014). The second and third family of leptons, the muons ( $\mu^\pm$ ) and tauons (tau leptons,  $\tau^\pm$ ), have shorter lifetimes and larger masses, and decay only weakly.

Muons have a mass of  $m_\mu = 105.6583715(35) \text{ MeV c}^{-2}$ , and a lifetime of  $\tau_\mu = 2.1969811(22) \mu\text{s}$ . The dominant decay channel for muons is

$$\begin{aligned} \mu^+ &\longrightarrow e^+ + \nu_e + \bar{\nu}_\mu \\ \mu^- &\longrightarrow e^- + \bar{\nu}_e + \nu_\mu \end{aligned} \quad (2.11)$$

with an almost 100% branching ratio (Olive & Particle Data Group 2014). Muons are created in space as secondary products of cosmic-ray interactions with the interstellar medium (ISM) or the atmosphere of Earth (e.g. Shapiro 2012). In cosmic-ray proton-proton or proton-nuclei reactions, among many other particles, charged pions can be created (see Sec. 2.2.3), which predominantly decay into muons. In principle, muons could be created during radioactive decay, similar to the  $\beta^+$ -decay described

in Eq. (2.10), but with an antimuon and muon-neutrino instead. The rest mass of the muon is larger than all known decay energies and can therefore never be created during a radioactive decay (Firestone et al. 1996). If high-energy cosmic-rays interact with the atmosphere of the planet, relativistic muons can be created and detected on ground with bubble chambers, for example (Street & Stevenson 1937).

Tau leptons are even heavier ( $m_\tau = 1776.82(16)$  MeV  $c^{-2}$ ), and hence even shorter lived  $\tau_\tau = 290.3(5) \times 10^{-15}$  s. They have more decay channels with distinguished branching ratios. The dominant channel ( $\approx 65\%$ ) for tau leptons is the decay into hadrons, mainly charged mesons (kaons and pions, see Sec. 2.2.3), which on their side again decay predominantly to muons but also to electrons/positrons. Tauons have an almost equal share in their branching ratios to also decay directly either to muons (17.41(4)%) or electrons/positrons (17.83(4)%). In most of the decay channels, one of the final products will be in the lightest charged lepton family, electrons or positrons (Olive & Particle Data Group 2014). For the discussion of the galactic positron content, the creation and decay of tauons is probably unimportant, also because they have only been measured in accelerator experiments (first evidence by Perl et al. 1975).

### 2.2.3 Decay of Mesons

Mesons are bound states of different quark-antiquark combinations. Pions belong to the lightest meson family with three different combinations of up, down, anti-up, and anti-down quarks, forming either a positively, negatively, or non-charged particle (isospin triplet). In the quark model, the  $\pi^+$  meson is described by  $|\pi^+\rangle = |u\bar{d}\rangle$ , its antiparticle is the  $\pi^-$  and is described by charge conjugation of the  $\pi^+$ , so that  $|\pi^-\rangle = |d\bar{u}\rangle$ . The neutral pion,  $\pi^0$ , consists of a combination of up-antiup quarks, and down-antidown quarks,  $|\pi^0\rangle = \frac{1}{\sqrt{2}} (|u\bar{u}\rangle - |d\bar{d}\rangle)$  (e.g. Griffiths 1987).

Charged pions have a mass of  $m_{\pi^\pm} = 139.57018(35)$  MeV  $c^{-2}$ , and a mean lifetime of  $\tau_{\pi^\pm} = 2.6033(5) \times 10^{-8}$  s. The  $\pi^0$  meson has a mass of  $m_{\pi^0} = 134.9766(6)$  MeV  $c^{-2}$ , and a considerably shorter lifetime of  $\tau_{\pi^0} = 8.52(18) \times 10^{-17}$  s, due to the dominant electromagnetic decay mode (Olive & Particle Data Group 2014).

Another family of mesons with strange quark constituents are the kaons. Charged kaons are  $|K^+\rangle = |u\bar{s}\rangle$ , and  $|K^-\rangle = |s\bar{u}\rangle$ , with a mass of  $m_{K^\pm} = 493.677(16)$  MeV  $c^{-2}$  and a lifetime of  $\tau_{K^\pm} = 1.2380(21) \times 10^{-8}$  s (Olive & Particle Data Group 2014). Due to neutral kaon mixing (CP-violation, see Griffiths (1987) for example), there exist two distinct neutral kaon states, named  $K_L^0$  ("K-long") and  $K_S^0$  ("K-short"), with largely different lifetimes, and decay channels:  $|K_L^0\rangle = \frac{1}{\sqrt{2}} (|d\bar{s}\rangle + |s\bar{d}\rangle)$  with a lifetime of  $\tau_{K_L^0} = 5.116(21) \times 10^{-8}$  s, and  $|K_S^0\rangle = \frac{1}{\sqrt{2}} (|d\bar{s}\rangle - |s\bar{d}\rangle)$  with a lifetime of  $\tau_{K_S^0} = 8.954(4) \times 10^{-11}$  s. Neutral kaons<sup>2</sup> have a mass of  $m_{K^0} = 497.614(24)$  MeV  $c^{-2}$  (Olive & Particle Data Group 2014).

Pions and kaons are produced as secondary particles in cosmic-ray interactions (e.g. Shapiro 2012). Highly relativistic cosmic-rays (kinetic energies  $> 1$  GeV, see

<sup>2</sup>In the definitions of  $|K_L^0\rangle$  and  $|K_S^0\rangle$  a CP-violating asymmetry factor when mixing the states is omitted. Likewise, due to this factor,  $K_L^0$  and  $K_S^0$  have a mass difference of  $m_{K_L^0} - m_{K_S^0} = 3.484(6) \times 10^{-12}$  MeV  $c^{-2}$ . For the discussion of positrons production, this is irrelevant and only mentioned for completeness.

Sec. 5.3) react with atoms or molecules of the ISM or Earth's atmosphere, and create a large number of secondary particles, among them pions, kaons, neutrons, protons, and photons. These particles carry parts of the incident kinetic (centre of mass) energy away, creating more secondary particles, and also decay very fast. In the end, a cascade of decay particles is created, which, in case of Earth's atmosphere, can be traced back with Cherenkov telescopes, for example, to measure the direction and energy of the incident cosmic-ray (see Sec. 5.3).

Charged pions predominantly decay to muons with a branching ratio of 99.98770(4)%, and only a small fraction (0.0123(4)%) is directly converted to electrons/positrons (Olive & Particle Data Group 2014). However, muons inevitably decay to electrons/positrons, Eq. (2.11), so that after a  $\pi^+$  has decayed at least one positron is created. The decay is related to the  $\beta^+$ -decay as the positive charge is carried away by a  $W^+$ -boson to create an antimuon or positron, so that

$$\begin{aligned}\pi^+ &\longrightarrow \mu^+ + \nu_\mu \longrightarrow e^+ + \nu_e + \bar{\nu}_\mu + \nu_\mu \\ \pi^+ &\longrightarrow e^+ + \nu_e.\end{aligned}\tag{2.12}$$

Pi-zeros are the lightest quarkonia, i.e. bound states of quark and related antiquark, and, unlike charged pions, only decay electromagnetically. Their dominant decay channel (98.823(34)%) is the annihilation of its quark constituents to two gamma-ray photons, each of energy  $E_{\gamma(\pi^0)} = 67.4883(3)$  MeV in the centre of mass frame. However, it is also possible for  $\pi^0$  to decay into (multiple) electron-positron pairs (or Ps directly), possibly accompanied by another photon (Olive & Particle Data Group 2014).

Due to its larger mass compared to pions, kaons have more possible decay channels. Similar to the  $\pi^+$ -decay,  $K^+$ s favour to convert to anti-muons with a probability of 63.55(11)% and only seldom decay into positrons directly (0.001581(7)%). Their hadronic decay modes also produce charged pions, which decay to muons and electrons/positrons, Eq. (2.12), in a second step. It is also possible for charged kaons to decay in a semileptonic way, producing neutral pions, accompanied by charged leptons. In any of the described cases, the final result will be at least one positron (Olive & Particle Data Group 2014), e.g.

$$\begin{aligned}K^+ &\longrightarrow \mu^+ + \nu_\mu \longrightarrow e^+ + \nu_e + \bar{\nu}_\mu + \nu_\mu \\ K^+ &\longrightarrow \pi^+ + \pi^0 \longrightarrow \dots \longrightarrow e^+ + \nu_e + \bar{\nu}_\mu + \nu_\mu + 2\gamma \\ K^+ &\longrightarrow \pi^0 + e^+ + \nu_e \longrightarrow 2\gamma + e^+ + \nu_e.\end{aligned}\tag{2.13}$$

The energy spectrum of galactic cosmic rays reaches up to  $\sim 10^{15}$  eV (Ackermann et al. 2013). The highest energies measured so far are of the order  $10^{21}$  eV (Watson et al. 2011), which makes it in general possible to create any kind of meson species, which may decay into positrons in the end. Forming other species involving charm, bottom, and top quarks is less likely and mesons made of such quarks will not be considered further.

## 2.2.4 Electron-Positron Pair Production

The time-energy uncertainty principle allows the existence of particle-antiparticle pairs for a limited time, out of the vacuum (virtual particles). If the vacuum is influenced by the available internal energy in an arbitrary system, the emergence of real particles may be possible. In such a system, pair production may arise as another degree of freedom, if the internal energy exceeds  $2mc^2$ . In high-energy environments ( $E > 1022$  keV), electron-positron pair production is hence inevitable.

### 2.2.4.1 Photon-Photon Interactions

If two photons with a total energy of at least the rest mass of two electrons interact with each other, it is possible to produce electron-positron pairs. This is related to the conversion and conservation of energy (equivalence of mass and energy),

$$E = mc^2 \quad (2.14)$$

which means that any form of energy can be used to create real particles - and vice versa (Einstein 1905, see also pair annihilation Sec. 2.3). The photon-photon pair-production,

$$\gamma + \gamma \longrightarrow e^+ + e^-, \quad (2.15)$$

is illustrated by the Feynman diagrams in Fig. 2.2. The  $\gamma\gamma$ -pair-creation cross section,  $\sigma_{\text{pair}}$ , is related to the annihilation cross section ( $\sigma_{\text{ann}}$ , Sec. 2.3) and the cross section for the Compton effect ( $\sigma_{\text{comp}}$ , Sec. 3.1.1), by considering the crossing symmetry (i.e. the correct exchange of the Mandelstam variables or the four-momenta in the Feynman diagrams, Fig. 2.2, respectively; Greiner et al. (see 2012), and Appendix B). The total pair creation cross section is given by

$$\sigma_{\text{pair}} = \frac{\pi}{2} \frac{\alpha^2}{m_e^2} (1 - \beta^2) \left[ (3 - \beta^4) \ln \left( \frac{1 + \beta}{1 - \beta} \right) - 2\beta(2 - \beta^2) \right] \quad (2.16)$$

where  $\beta = (|p|/E)_{\text{CM}}$  is the dimensionless velocity in the centre of mass (CM) frame,  $|p|$  is the momentum of the CM frame, and  $E$  the CM energy (Olive & Particle Data Group 2014, note that in Eq. (2.16) natural units, i.e.  $\hbar = c = 1$ , have been used for clarity). In the non-relativistic limit,  $\beta \rightarrow 0$ , Eq. (2.16) can be approximated by  $\sigma_{\text{pair}}^{\text{NR}} \approx \pi \frac{\alpha^2}{m_e^2} \beta$ , from which it is clear that photon-photon pair-production is only possible for  $\beta > 0$ . The ultra-relativistic limit,  $\beta \rightarrow 1$ , can be expressed as  $\sigma_{\text{pair}}^{\text{UR}} \approx \pi \frac{\alpha^2}{m_e^2} \frac{1}{\gamma^2} (2 \ln(2\gamma) - 1)$ . Fig. 2.3 shows the total pair creation cross section as a function of the CM photon "Lorentz factor". The function has a maximum at  $\beta_{\text{max}} \approx 0.701$ , equivalent to an incident photon energy of  $E_\gamma \approx 716.5$  keV, for a cross section of  $\sigma_{\text{pair}}^{\text{max}} \approx 1.70 \times 10^{-25}$  cm<sup>2</sup>. The process in Eq. (2.15) is kinematically only allowed if the incident photon energies are above the pair creation threshold, Eq. (2.17).

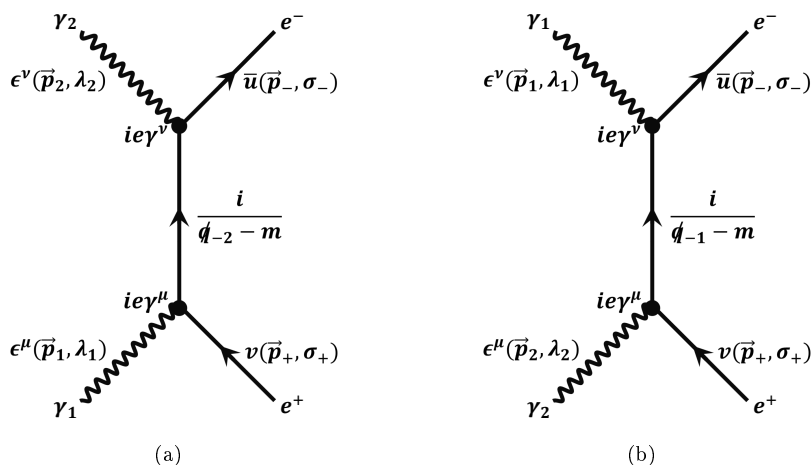


Figure 2.2: Feynman diagrams of electron-positron pair production by photon-photon interactions. The incoming photon polarisation vectors are denoted by  $\epsilon^{\nu}(\vec{p}_i, \lambda_i)$ , where  $i = 1, 2$  and  $\lambda = +, -$ , and the outgoing anti-spinors and spinors for the electron and positron are denoted by  $\bar{u}(\vec{p}_-, \sigma_-)$  and  $v(\vec{p}_+, \sigma_+)$ , respectively, where  $\sigma_{\pm} = 1, 2$  is the spin of the particles.

Because the photons are interchangeable, the energy of one photon can be chosen as an independent variable, here  $E_1$ , so that  $E_2$  becomes a function of  $E_1$ ,

$$E_2 > E_{\text{thresh}}(E_1, \phi) = \frac{2m_e^2 c^4}{E_1(1 - \cos(\phi))}, \quad (2.17)$$

where  $\phi$  is the scattering angle (De Angelis et al. 2013, see also Appendix B). In the case of head-on collisions between the photons,  $\phi = \pi$ , Eq. (2.17) reduces to  $E_1 E_2 \geq m_e^2 c^4$ , which would be naturally expected from the conversion of energy to mass, Eq. (2.14).

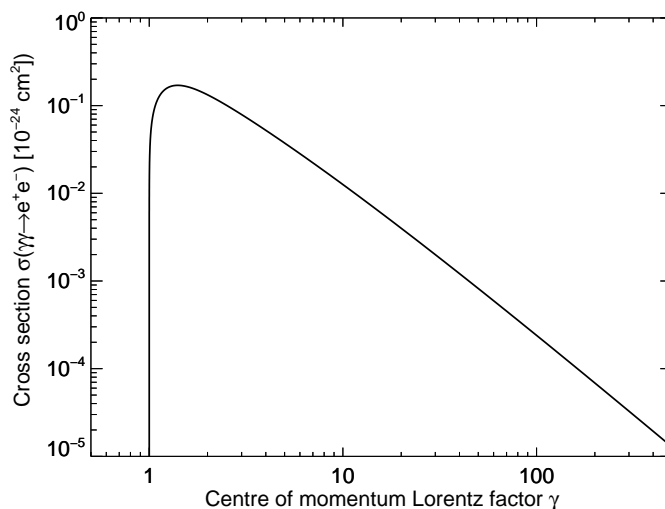


Figure 2.3: Photon-photon pair production cross section as a function of centre of momentum "Lorentz factor",  $\gamma = \frac{E cm_0}{m_e c^2}$ , of either photon. Pair creation is only possible for  $\gamma > 1$ , i.e. if the total energy of both photons together exceeds two times the rest mass of an electron. The pair creation cross section by photons reaches a maximum at  $\beta \approx 0.701$ , corresponding to  $\gamma \approx 1.4$ , and then declines  $\propto \ln(2\gamma)/\gamma^2$ ; see text for details. Although  $\sigma_{\text{pair}}$  is of the order of the Thomson cross section, experimental proofs are difficult to achieve because of the necessity of high-energy photon beams and large photon densities.

With  $\sigma_{\text{pair}} \sim 10^{-25} \text{ cm}^2$ , it is of the order of the Thomson cross section,  $\sigma_T =$

$6.6524587158(91) \times 10^{-25} \text{ cm}^2$  (Mohr et al. 2015), but experimentally, photon-photon pair-production has never been observed. Pair production is only efficient at very high photon densities, but in terrestrial laboratories, such intense beams of high-energy photons are not achievable (Greiner et al. 2012). However, in compact astrophysical sources, the optical depth of gamma-ray sources can be large enough to efficiently absorb themselves (see Sec. 5.2). The CM velocity can be written as

$$\beta = \left( \frac{|p|}{E} \right)_{\text{CM}} = \frac{\sqrt{E_{\text{CM}}^2 - 4m_e^2}}{E_{\text{CM}}} = \sqrt{1 - \frac{2m_e^2}{E_1 E_2 (1 - \cos(\phi))}}, \quad (2.18)$$

so that at the maximum of  $\sigma_{\text{pair}}$ , at  $\beta_{\text{max}} \approx 0.701$ , is reached if

$$E_2 = \frac{2m_e^2}{(1 - \beta_{\text{max}}^2)(1 - \cos(\phi))E_1} \approx \left( \frac{1}{(1 - \cos(\phi))E_1 [\text{TeV}]} \right) \text{ eV}. \quad (2.19)$$

At very high energies ( $E_\gamma \gtrsim 1 \text{ TeV}$ ), the process described in Eq. (2.19) leads to the effect that the Universe becomes opaque, because such photons rapidly find low-energy photon partners to interact with. These are much more numerous, e.g. from star light (visible light at 500 nm wavelength equivalent to 2.5 eV photon energy) or from the cosmic microwave background (1 mm equivalent to 1 meV), so that electron-positron pairs are inevitably created, preventing high-energy photons to travel far. In particular, very-high-energy photons in the energy range between  $10^{-2}$  and  $10^2 \text{ TeV}$  are most efficiently absorbed by extragalactic background light at infrared, visible, and ultraviolet wavelengths. Between  $10^2$  and  $10^7 \text{ TeV}$ , cosmic microwave background photon interactions dominantly suppress the detectability, and above  $10^7 \text{ TeV}$ , radio background photons absorb such emission (De Angelis et al. 2013). Therefore, if such very-high-energy emission is measured, it can be considered to originate mainly in the Milky Way.

#### 2.2.4.2 Photon Interactions with Electric Fields

For a single photon in the vacuum, it is not possible to spontaneously produce an electron-positron pair. Kinematically, energy and momentum of the photon are not conserved at the same time, so the photon needs an electromagnetically charged partner to interact with, and which is carrying away the excess momentum.

$$\gamma + {}^A_Z\mathbf{X}_N \longrightarrow e^+ + e^- + {}^A_Z\mathbf{X}_N \quad (2.20)$$

Pair creation can therefore happen, e.g., in the field of an atomic nucleus with charge  $-Ze$ , which is exhibiting an external Coulomb field, Eq. (2.20). Fig. 2.4 shows the Feynman diagrams for pair-production in an electric field. The reaction is related to the bremsstrahlung process when considering crossing symmetry. During bremsstrahlung, electrons (or other charged particles) scatter off protons or heavier charged particles (electric fields in general), emit real photons, and lose energy in this way (they decelerate; German "bremsen"). Similarly, a free electron cannot emit a

photon spontaneously, because energy and momentum would not be conserved in this process. In Fig. 2.4, to obtain the diagrams for bremsstrahlung, the external lines for pair production must be exchanged: The incident photon becomes the outgoing photon, and the outgoing positron becomes the incident electron (Jauch & Rohrlich 1955; Greiner et al. 2012).

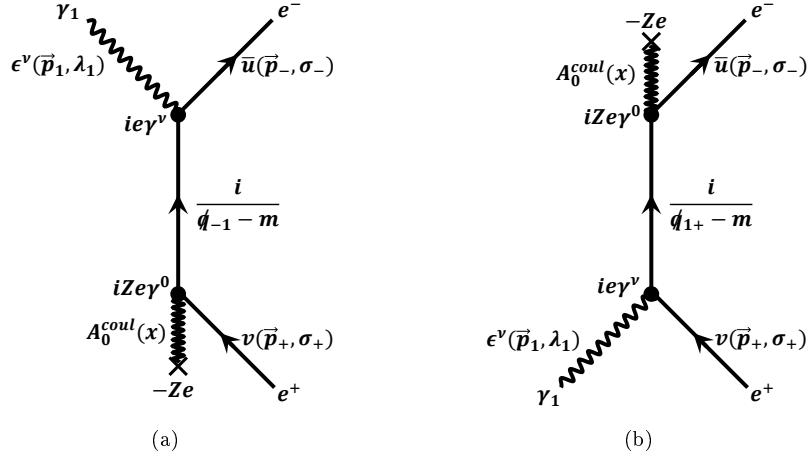


Figure 2.4: Feynman diagrams of electron-positron pair production in the external field of a nucleus of charge  $-Ze$ . The incoming photon polarisation vector is denoted by  $\epsilon^\nu(\vec{p}_1, \lambda_1)$ , where  $\lambda = +, -$ , and the outgoing anti-spinors and spinors for the electron and positron are denoted by  $\bar{u}(\vec{p}_-, \sigma_-)$  and  $v(\vec{p}_+, \sigma_+)$ , respectively, where  $\sigma_\pm = 1, 2$  is the spin of the particles. The external Coulomb field,  $A_0^{\text{coul}}(x) = -\frac{Ze}{|\vec{x}|}$ , for the position vector  $\vec{x}$  of the nucleus, takes the form  $-4\pi Ze \int \frac{d^3q}{(2\pi)^3} \frac{\exp(-i\vec{q}\cdot\vec{x})}{|\vec{q}|^2}$  in momentum space, where  $\vec{q} = \vec{p}_+ + \vec{p}_- - \vec{p}_1$  is the momentum transferred to the nucleus (e.g. Bethe & Heitler 1934; Jauch & Rohrlich 1955; Greiner et al. 2012).

The total cross section for pair creation of a photon with energy  $E$  in the field of an atomic nucleus with charge  $-Ze$  cannot be written out in a closed form, analytically, as stepping from the differential cross section (Bethe & Heitler 1934) to the total one involves elliptical integrals. A compact form is given by Racah (1936), Jost et al. (1950), and Jauch & Rohrlich (1955),

$$\sigma_{Z,\text{pair}}(E) = \alpha Z^2 r_e^2 \left\{ 2\eta^2 [2C_2(\eta) - D_2(\eta)] + \right. \\ \left. - 2/27 [(109 + 64\eta^2)E_2(\eta) - (67 + 6\eta^2)(1 - \eta^2)F_2(\eta)] \right\}. \quad (2.21)$$

In Eq. (2.21),  $\eta^{-1} = \frac{E}{2m_e} \geq 1$  is the dimensionless energy of the photon, scaled by the threshold of  $2m_e$  for pair creation, and  $r_e = \frac{1}{4\pi\epsilon_0} \frac{e^2}{m_e c^2} = 2.8179403227(19)$  fm is the classical electron radius (Mohr et al. 2015). The functions  $C_2(\eta)$ ,  $D_2(\eta)$ ,  $E_2(\eta)$ , and  $F_2(\eta)$  are given in Appendix B. The pair-creation cross section in the field of a nucleus,  $\sigma_{Z,\text{pair}}(E)$ , is a strictly increasing function of photon energy so that with increasing photon energy, the production of electron-positron pairs is more and more probable. Near the threshold energy, i.e. in the low-energy limit,  $\sigma_{Z,\text{pair}}$  can be approximated by

$$\sigma_{Z,\text{pair}}^{\text{NR}}(E) = \frac{\pi}{12} \alpha Z^2 r_e^2 \left( \frac{E}{m_e} - 2 \right)^3, \quad (2.22)$$

in the high-energy limit by

$$\sigma_{Z,pair}^{UR}(E) = \alpha Z^2 r_e^2 \left( \frac{28}{9} \ln \left( \frac{2E}{m_e} \right) - \frac{218}{27} \right) \quad (2.23)$$

(Jauch & Rohrlich 1955).

Pair creation is one of the three fundamental interactions of light with matter. The other two, the Compton effect as well as the photoelectric effect will be described in Sec. 3.1.1.

Single photons do not necessarily need to interact with the electric field of the nucleus but rather need any electric field, so pair creation is also possible in the field of free electron,

$$\gamma + e^- \longrightarrow e^+ + e^- + e^-. \quad (2.24)$$

The cross section for creation in the field of an electron is asymptotically identical to Eq. (2.21), omitting the charge number  $Z$  (Haug 1975; Zdziarski 1980). The only difference is in the low-energy limit because the threshold for pair creation in the field of a single electron in the laboratory frame is  $E_\gamma \geq 4m_e c^2$ , and in the field of a nucleus it is  $E_\gamma > 2m_e c^2$ , see Appendix B.

If in electron-electron (e-e), electron-proton (e-p), or proton-proton (p-p) collisions, the kinetic energies of interacting particles are large enough, also electron-positron pairs can be created. Kuraev & Lipatov (1974) approximated the cross section for pair creation in inelastic e-e scattering to

$$\sigma_{ee,pair} \approx \frac{\alpha^2 r_e^2}{\pi} (1.03\rho^3 - 6.6\rho^2 - 11.1\rho + 100), \quad (2.25)$$

where  $\rho = \ln \left[ \left( \frac{p_1 + p_2}{m_e c} \right)^2 \right]$ , and  $p_1$  and  $p_2$  are the momenta of the incident electrons, respectively. This process is only possible for highly relativistic electrons as the threshold energy in the lab frame is  $7m_e c^2$  (Appendix B). The cross section for pair production in e-p collisions is similar to Eq. (2.25), see Zdziarski (1980).

#### 2.2.4.3 Photon Interactions With Magnetic Fields

Similar to the case with an (external) electric field, it is also possible for single photons to produce electron-positron pairs in a magnetic field. When the gyro-energy of an electron (or positron) becomes of the order of the rest mass of the particle, spontaneous pair production will be efficient (Erber 1966; Daugherty & Harding 1983). The rate of photons that will convert to electron-positron pairs was found to depend on the parameter  $\chi = \left( \frac{\hbar\omega}{2m_e c^2} \right) \left( \frac{B \sin(\theta)}{B_{cr}} \right)$ , where  $\hbar\omega$  is the incident photon energy,  $B$  the magnetic field,  $\theta$  the angle between the magnetic field vector

and the photon momentum vector, and  $B_{cr} = \frac{m_e^2 c^2}{\hbar e} \approx 4.4 \times 10^{13}$  Gauss (Toll 1952; Erber 1966; Baier & Katkov 1968; Tsai & Erber 1974; Daugherty & Harding 1983). Even though there is no physical particle which takes the excess photon momentum and energy, the "rigidity" of a present magnetic field can retain energy and momentum conservation. The field, which is included in the conservation laws, does not require the momentum of the photon to be conserved orthogonal to the magnetic field direction, Eq. (2.27). If a photon with momentum  $\vec{p}_\gamma = \omega(0, \sin(\theta), \cos(\theta))$  is moving with an angle  $\theta$  through a homogeneous magnetic field  $\vec{B} = B\hat{z}$ , without loss of generality, the conservation of energy and momentum reads ( $\hbar = c = 1$ ):

$$\text{Energy:} \quad \omega = E_+^k + E_-^j \quad (2.26)$$

$$\text{Momentum:} \quad p_{\gamma,z} = p_{+,z} + p_{-,z} \Leftrightarrow \omega \cos(\theta) = p_+ + p_- \quad (2.27)$$

In Eq. (2.27),  $E_+$  and  $E_-$  are the quantised energy states of the positron and electron, respectively, given by the Landau levels of moving charged particles in a uniform magnetic field

$$E_+^k = \sqrt{p_+^2 + m_e^2 \left(1 + 2k \frac{B}{B_{cr}}\right)}, \quad (2.28)$$

$$E_-^j = \sqrt{p_-^2 + m_e^2 \left(1 + 2j \frac{B}{B_{cr}}\right)}, \quad (2.29)$$

with  $p_+$  and  $p_-$  the momenta of the positron and electron, respectively, and  $k, j = 0, 1, 2, 3, \dots$  the quantum levels (e.g. Johnson & Lippmann 1949). From the transition of one photon to an electron-positron with discrete energy levels in a magnetic field, the photon attenuation length  $\alpha(\chi)$  can be derived. This is a measure of how fast (at what distance) photons are being converted into pairs. In general, the number of pairs  $n_\pm$ , created during the photon path length  $x$ , can be calculated from the number of photons,  $n_\gamma$ , by

$$n_\pm = n_\gamma(1 - \exp(-\alpha(\chi)x)). \quad (2.30)$$

The exact attenuation coefficient was calculated first by Toll (1952) and thoroughly discussed by Daugherty & Harding (1983). Because of the quantised energy levels, the attenuation coefficient, depending on the magnetic field and the photon energy, shows a "saw-tooth" behaviour for fixed values of the magnetic field. In astrophysical environments, this effect may not be unimportant (see Sec. 5.4). The saw-tooth shape of the attenuation length may be smoothed out and asymptotic expressions can be derived in the limits  $\chi \ll 1$  and  $\chi \gg 1$ ,

$$\alpha(\chi) = \frac{1}{2} \left(\frac{\alpha}{\lambda_C}\right) \left(\frac{B}{B_{cr}}\right) T(\chi), \quad (2.31)$$

where  $T(\chi) \approx 0.46 \exp(-4/(3\chi))$  for  $\chi \ll 1$ , and  $0.60\chi^{-1/3}$  for  $\chi \gg 1$ , respectively (Erber 1966; Daugherty & Harding 1983). From Eq. (2.31), it can be seen that for fixed values of magnetic fields, the attenuation coefficient has a unique maximum for photon energies  $\hbar\omega_{max} \approx 12(B_{cr}/B)$ . If the photon energy is regarded as fixed,  $\alpha(\chi)$  is a monotonic rising function of  $\omega$ , so that very strong magnetic fields can be very efficient electron-positron pair producers (see Sec. 5.4).

## 2.2.5 Exotic Positron Production Mechanisms

### 2.2.5.1 Dark Matter Self-Interaction

This section focusses on the particle physics aspect of dark matter, whereas a more detailed discussion of dark matter and its implications to galactic astronomy and cosmology will be given in Sec. 5.5. Because dark matter density profiles are strongly peaked towards the centre of the Galaxy, and because the 511 keV electron-positron annihilation emission morphology in the Milky Way is peaked similarly (Sec. 4.4), the elementary particle constituents of dark matter were invoked as a possible source of positrons in space. The "dark matter particle", if assuming it to be an elementary particle, and not an unseen (faint) baryonic mass, has neither been found experimentally in terrestrial laboratories nor have fundamental direct evidences ("smoking gun evidence") from astrophysical observations been provided. There are indeed many more indications of an unseen mass from galactic rotation or cosmology, for example, but these may be explained by other theories as well.

As dark matter is not taking part in electromagnetic interactions, it was intended, for instance, that the particle constituents are only weakly (and gravitationally) interacting. These weakly interacting massive particles (WIMPs, hereafter denoted by the particle symbol  $\chi$ ) have been theorised to explain the current dark matter abundance in the universe<sup>3</sup> by thermal production during the big bang. This requires that the WIMPs may not have a larger "relic" cross section for self-annihilation of  $\langle\sigma_{DM}v\rangle \approx 3 \times 10^{-26} \text{ cm}^3 \text{ s}^{-1}$ , as otherwise the particles would have continued to annihilate and no structure formation could have set in (Jungman et al. 1996). The relic cross section is related to the (present) dark matter mass density of the universe,  $\Omega_\chi$ , in units of the critical density,  $\rho_c = \frac{3H_0^2}{8\pi G} = 1.87847(23) \times 10^{-26} \text{ h}^2 \text{ kg m}^{-3}$ , by

$$\Omega_\chi h^2 \approx \frac{m_\chi n_\chi}{\rho_c} \approx \frac{3 \times 10^{-27} \text{ cm}^3 \text{ s}^{-1}}{\langle\sigma_{DM}v\rangle}, \quad (2.32)$$

where  $h$  is the Hubble constant in units of  $100 \text{ km s}^{-1} \text{ Mpc}^{-1}$  (today's best fit value assuming  $\Lambda$ CDM:  $h = 0.6774 \pm 0.0046$  (e.g. Olive & Particle Data Group 2014; Planck Collaboration et al. 2014a,b)),  $m_\chi$  is the unknown WIMP mass, and  $n_\chi$  is the WIMP particle density (Jungman et al. 1996). Using measurements of  $\Omega_\chi$  from the Planck satellite, for example ( $\Omega_\chi h^2 = 0.1199 \pm 0.0027$  Planck Collaboration

<sup>3</sup>Assuming the universe follows the standard model of cosmology, the universe consists of  $68.5 \pm 1.7\%$  dark energy ( $\Lambda$ ),  $26.1 \pm 1.7\%$  dark matter (DM), and  $4.9 \pm 0.1\%$  baryonic matter. Because dark matter has to be "cold" (C) to form the large-scale structures of galaxies that are seen today, and because the universe is dominated by a "negative" pressure component, the standard cosmological model is called  $\Lambda$ CDM (Planck Collaboration et al. 2014a,b).

et al. 2014a,b), Eq. (2.32) constrains the relic cross section to the before-mentioned value of  $\langle\sigma_{DMv}\rangle \approx 3 \times 10^{-26} \text{ cm}^3 \text{ s}^{-1}$ . This cross section has about the value of what would be expected if a "new" particle, i.e. beyond the standard model of particle physics, with a mass of the order of GeV to TeV would interact only weakly (Jungman et al. 1996). Until now (year 2016), there was no experimental proof of such a particle, neither in accelerator experiments by creating WIMP particles (e.g. Craig 2013), nor in direct detection experiments by measuring the recoil momentum of WIMP-nucleus-interactions (e.g. Fox et al. 2014).

In any case, the WIMPS may either annihilate themselves, decay to lighter particles, or de-excite by the emission of other particles. Any of these branches may lead to the production of positrons at some point during the process. In the minimal supersymmetric standard model of particle physics, for example, the lightest supersymmetric particle may be stable in the mass range of a few GeV to TeV, and therefore a good candidate (Jungman et al. 1996). It is generally named "the neutralino",  $\chi$ . In this theory, there are actually many neutralinos,  $\tilde{\chi}_i^0$ ,  $i = 1, 2, 3, 4$ , and  $\chi$  refers to the lowest mass representative.

The annihilation of the lightest supersymmetric particle with its own kind is possible as neutralinos are Majorana fermions, i.e. they are their own antiparticles, have spin 1/2, and are uncharged. If neutralinos are more massive than  $m_\chi \approx 175 \text{ GeV } c^{-2}$  ( $\approx m_t$ ), they can annihilate directly to all (known) standard model particles, thereby producing either positrons directly or after intermediate production of other particles. Some of the Feynman diagrams which may contribute to the production of fermion-antifermion pairs are shown in Figs. 2.5a and 2.5b. The annihilation cross section,  $\sigma(\chi\chi \rightarrow f\bar{f})$ , where  $f = u, d, c, s, t, b, e, \mu, \tau$ , is proportional to the mass squared of the produced fermion, thus favouring annihilations to top or bottom quarks, rather than to electrons and positrons. In the non-relativistic limit, the neutralino self-annihilation cross section into fermion-antifermion pairs is given by

$$\sigma(\chi\chi \rightarrow f\bar{f})_{v \rightarrow 0} = \frac{c_f \beta_f}{128\pi m_\chi^2} |\mathcal{A}(\chi\chi \rightarrow f\bar{f})|^2, \quad (2.33)$$

where  $c_f$  is a colour factor (3 for quarks, 1 else),  $\beta_f = \sqrt{1 - \frac{m_f^2}{m_\chi^2}}$ , and  $\mathcal{A}(\chi\chi \rightarrow f\bar{f}) \propto m_f^2$  is the annihilation amplitude for different channels (e.g. Drees & Nojiri 1993; Jungman et al. 1996, see also Appendix B).

Any heavier neutralino species may decay to the lightest supersymmetric particle by the emission of fermion-antifermion pairs,  $\tilde{\chi}_2^0 \rightarrow e^+ + e^- + \tilde{\chi}_1^0$ , for example (Ambrosanio & Mele 1996; Djouadi et al. 2001; Olive & Particle Data Group 2014). Some contributing Feynman diagrams of heavy neutralino decay are shown in Figs. 2.5c and 2.5d for three-body decay. As neutralinos have not been detected yet, the decay widths (lifetimes) can only be quoted formally, being proportional to the mass of the heavy neutralino (Ambrosanio & Mele 1996; Djouadi et al. 2001).

Finkbeiner & Weiner (2007) suggested that dark matter is made of WIMPs which may be collisionally excited, and de-excite by the emission of electron-positron pairs.

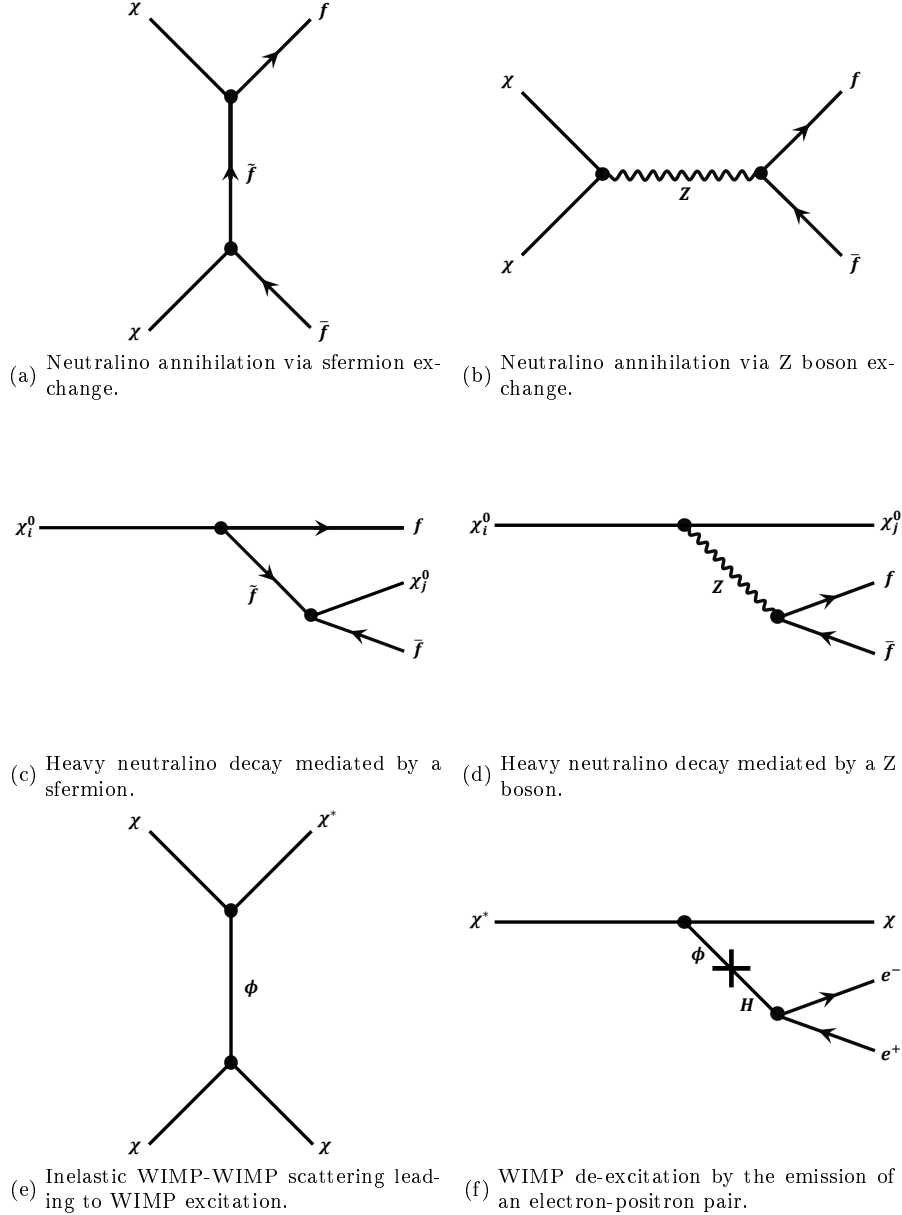


Figure 2.5: Positron production by WIMP dark matter interactions. The top panels show possible Majorana neutralino ( $\chi$ ) self-annihilation diagrams to fermion-antifermion pairs,  $f\bar{f}$ , mediated either by sfermions,  $\tilde{f}$  (a), or by a Z boson (b), respectively. The middle row panels illustrate possible heavy neutralino ( $\chi_i^0$ ) three-body decays into lighter neutralinos ( $\chi_j^0$ , where  $m_{\chi_i} > m_{\chi_j}$  and  $i \neq j$ ) and fermion-antifermion pairs, mediated either by sfermions (c) or a Z boson (d), respectively. The two-body decay of neutralinos is also possible and the Feynman description, not shown here, is straight-forward. The bottom panels show the inelastic WIMP-WIMP scattering to an excited state of the WIMP,  $\chi^*$ , through the exchange of a (another) new (light) scalar particle,  $\phi$  (e), and also the subsequent de-excitation process, accompanied by the emission of electron-positron pairs (f, Finkbeiner & Weiner 2007).

Such excited dark matter (XDM,  $\chi^* \rightarrow \chi + e^+ + e^-$ ) scenario is motivated by the fact that WIMPs would have masses of the order of  $500 \text{ GeV } c^{-2}$ , and if moving at a mean velocity of several  $500 \text{ km s}^{-1}$ , would have a kinetic energy of more than  $511 \text{ keV}$ . If WIMPs can be excited by inelastic WIMP-WIMP scattering, and if the energy splitting between the ground state and the excited state is more than  $2m_e c^2$ , the de-excitation may be accompanied by the emission of an electron-positron pair. The excitation of a WIMP requires the existence of another light scalar particle,  $\phi$ , with  $m_\phi < 1 \text{ GeV } c^{-2}$ , which will mediate the process of excitation and de-excitation by coupling to the WIMP and to the Higgs. The Feynman diagrams in Figs. 2.5e and

2.5f illustrate the excitation by WIMP-WIMP scattering and the de-excitation of an excited WIMP by the emission of an electron-positron pair, respectively. Finkbeiner & Weiner (2007) estimated the excitation cross section to  $\sigma_{XDM} v_{rel} \sim 10^{-30} \text{ cm}^2$  for relative velocities around  $1000 \text{ km s}^{-1}$ , as those are expected from WIMP dispersion in the centre of the Galaxy.

### 2.2.5.2 Other Reactions

The following mechanisms are listed here only for the sake of completeness. These depend on uncertain terrestrial assumptions, and are considered less significant.

- Neutrino pair annihilation:  $\nu_l + \bar{\nu}_l \rightarrow e^+ + e^-$ , where  $l = e, \mu, \tau$ ;  $\sigma \propto G_F^2 \sim 10^{-44} \text{ cm}^2$
- W boson pair creation:  $W^+ + W^- \rightarrow e^+ + e^-$ ;  $\sigma \propto G_F^2 \sim 10^{-44} \text{ cm}^2$
- Z boson decay:  $Z \rightarrow e^+ + e^-$ ;  $\tau_Z \approx 3.8 \times 10^{-25} \text{ s}$  (Olive & Particle Data Group 2014)
- W boson decay:  $W^+ \rightarrow e^+ + \nu_e$ ;  $\tau_W \approx 4.6 \times 10^{-25} \text{ s}$  (Olive & Particle Data Group 2014)
- Antineutron decay:  $\bar{n} \rightarrow \bar{p} + e^+ + \nu_e$ ; only in particle accelerators; ( $n \leftrightarrow \bar{n}$ )-oscillation time  $> 10^{31} \text{ yr}$  (Mohapatra 2009)
- H boson decay:  $H \rightarrow e^+ + e^-$ ;  $\tau_H \approx 1.6 \times 10^{-22} \text{ s}$  (standard model prediction) (Olive & Particle Data Group 2014)
- Superconducting strings,  $X$  in magnetic field,  $B$ :  $X + B \rightarrow e^+ + e^-$ ; no experimental proof (Witten 1985; Ferrer & Vachaspati 2005, 2007)

In general, there are many more possible reactions or processes which may give rise to either positrons or photons at 511 keV directly. For example, there are alternative theories of dark matter being composed of axions (B  hm & Fayet 2004), or "millicharged" fermions (Huh et al. 2008), which may also decay to positrons in the end. Va'vra (2013) discussed the possibility that the 511 keV emission is not from the annihilation of electrons with positrons but rather due to "small hydrogen atoms" in which the proton is capturing an electron on a small and tight orbit leading to the 511 keV emission by recombination directly. In this thesis, the most plausible reactions involving the creation of positrons in astrophysical sources will be discussed in detail and other possibilities are only mentioned for completeness.

### 2.2.6 Summary of Positron Production Mechanisms

Table 2.1 provides an overview of possible positron production mechanism and summarises the previous sections.

The positron production rates for the processes listed in Tab. 2.1 all depend on the

Mechanism	Reaction	Comments
$\beta^+$ -decay	${}^A_Z\mathbf{X}_N \longrightarrow {}^A_{Z-1}\mathbf{Y}_{N+1} + e^+ + \nu_e$	Only possible if Q value high enough (Sec. 2.2.1).
Anti-muon decay	$\mu^+ \longrightarrow e^+ + \nu_e + \bar{\nu}_\mu$	Secondary product in high-energy collisions (Sec. 2.2.2).
Anti-tauon decay	$\tau^+ \longrightarrow e^+ + \nu_e + \bar{\nu}_\tau$	Decay into mesons and muons possible. Probably unimportant astrophysical source (Sec. 2.2.2).
Pion-decay	$\pi^+ \longrightarrow \dots \longrightarrow e^+ + \nu_e + \bar{\nu}_\mu + \nu_\mu$	Primary product in high-energy collisions (Sec. 2.2.3).
Kaon-decay	$K^+ \longrightarrow \dots \longrightarrow e^+ + \nu_e + \bar{\nu}_\mu + \nu_\mu$	Primary product in high-energy collisions (Sec. 2.2.3).
Photon-photon pair production	$\gamma + \gamma \longrightarrow e^+ + e^-$	Photon energies must exceed $2m_e c^2$ (Sec. 2.2.4.1).
Photon-nucleus interaction	$\gamma + {}^A_Z\mathbf{X}_N \longrightarrow e^+ + e^- + {}^A_Z\mathbf{X}_N$	Photon energy threshold $> 2m_e c^2$ (Sec. 2.2.4.2).
Photon-electron interaction	$\gamma + e^- \longrightarrow e^+ + e^- + e^-$	Photon energy threshold $> 4m_e c^2$ (Sec. 2.2.4.2).
Photon-B-field interaction	$\gamma + B \longrightarrow e^+ + e^- + B$	Only efficient for high B-fields (Sec. 2.2.4.3).
Dark matter annihilation	$\chi + \chi \longrightarrow e^+ + e^-$	Hypothetical reaction with small cross section. No experimental proof (Sec. 2.2.5.1).

Table 2.1: Summary of positron production mechanisms.

circumstances and conditions and can therefore not be compared directly but only in the context of astrophysical systems. Many of these processes are efficient sources of positrons only if extreme conditions are fulfilled, e.g. in supernovae, producing  $\beta^+$ -unstable nuclei (Sec. 5.1), microquasars with huge high-energy photon densities leading to pair-production (Sec. 5.2), or pulsars with their large magnetic fields also forming pairs (Sec. 5.4).

## 2.3 Positron Annihilation

In this thesis, the major diagnostic tool is the gamma-rays from the annihilation of positrons with electrons in space. These gamma-rays are measured with the

spectrometer SPI aboard the INTEGRAL satellite (Sec. 3.2.1). Depending on the circumstances, the interstellar environment, particle populations, and kinematics, the resulting spectra do not only show a 511 keV gamma-ray line but rather span a whole range in photon energy. Below the natural annihilation line at photon energies equivalent to the rest mass energy of an electron, the decay of o-Ps (Sec. 2.3.2) yields three photons with energies between nearly 0 and 511 keV. If the kinetic energies of the particles are not zero, i.e. in a non-stationary frame, the annihilation gamma-rays will be distributed according to the kinematics of the particles, into the MeV range and beyond. If the annihilating particles follow a certain distribution, the annihilation spectrum will have incorporated these particle populations. Doppler-shifts and -broadenings will further skew the individual spectra and superpositions of several different effects build up unique diagnostics for different processes in different regions or sources in the sky.

### 2.3.1 Annihilation in Flight

All electron-positron annihilations underlie the process depicted in Fig. 2.6. This is the quantum-electrodynamics electron-positron annihilation Feynman diagram at tree level, also named "direct annihilation" or "annihilation in flight". There are two equivalent diagrams, because of the interchangeability of the produced photons. The electron-positron annihilation into two photons is purely electromagnetic, so that the matrix elements from the Feynman diagrams in Fig. 2.6 are proportional to  $\alpha$ . Annihilations to multiples of two photons is suppressed by factors of  $\alpha$  times the phase space of particular outcomes. The decay of Ps and the "one-quantum annihilation" will be separately discussed in Secs. 2.3.2 and 2.3.3 below).

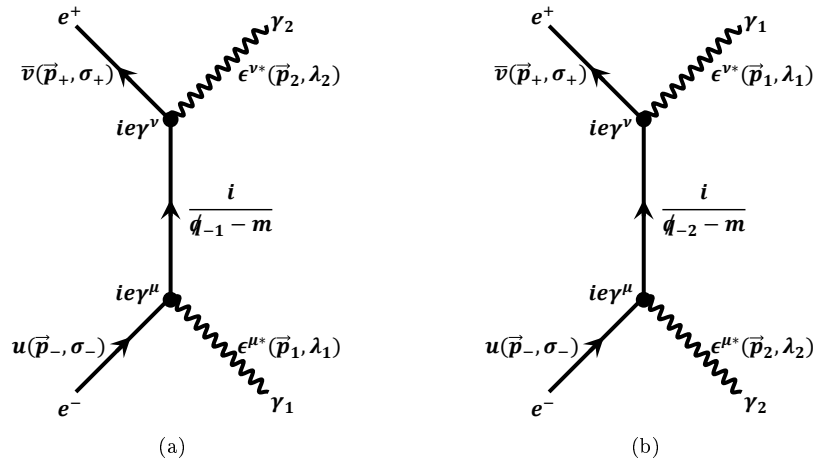


Figure 2.6: Feynman diagrams for electron-positron annihilation (para-positronium decay,  $\vec{p}_+ \approx \vec{p}_- \rightarrow 0$ ) at tree level. The incoming spinors and anti-spinors for the electron and positron are denoted by  $u(\vec{p}_-, \sigma_-)$  and  $\bar{v}(\vec{p}_+, \sigma_+)$ , respectively, where  $\sigma_{\pm} = 1, 2$  is the spin of the particles, and the outgoing photon polarisation vectors by  $\epsilon_i(\vec{p}_i, \lambda_i)$ , where  $i = 1, 2$  and  $\lambda = +, -$  is polarisation of the photon  $i$ .

For the general calculation of annihilation spectra, Sec. 2.4, the differential electron-positron annihilation cross section,  $\frac{d\sigma_{\gamma\gamma}}{d\Omega}(E, \theta)$ , is required. It can be written in a compact form using the Mandelstam variables,  $s$ ,  $t$ , and  $u$ ,

$$\frac{d\sigma_{\gamma\gamma}(E, \theta)}{d\Omega} = \frac{\alpha^2}{2s} \frac{u^2 + t^2}{ut} = \quad (2.34)$$

$$= \frac{\alpha^2}{8E|\vec{p}|} \left[ \frac{3m^2 + |\vec{p}|^2(3 + \cos^2(\theta))}{m^2 + |\vec{p}|^2 \sin^2(\theta)} - \left( \frac{|\vec{p}|^2 \sin^2(\theta) - m^2}{|\vec{p}|^2 \sin^2(\theta) + m^2} \right)^2 \right], \quad (2.35)$$

where  $E = \sqrt{|\vec{p}|^2 + m^2}$  is the energy of the particles with momentum  $\vec{p}$  in the centre of mass frame, and  $\theta$  is the scattering angle between an incoming particle and an outgoing photon (e.g. Heitler 1954; Svensson 1982; Greiner et al. 2012; Olive & Particle Data Group 2014, see also Sec. 2.4.2, and Appendix B for the definition of the Mandelstam variables). In the non-relativistic limit,  $p \rightarrow 0$ , the angle-dependence disappears, and the cross section becomes isotropic,  $\frac{d\sigma_{\gamma\gamma}^{NR}}{d\Omega}(E, \theta) \approx \frac{r_e^2}{4E|\vec{p}|}$  (see also Eq. (2.37)). The ultra-relativistic limit,  $E \approx p \gg m$ , however, shows a high anisotropy, and the cross section is peaked into the forward direction,  $\frac{d\sigma_{\gamma\gamma}^{UR}}{d\Omega}(E, \theta) \approx \frac{r_e^2}{4E^2} \frac{1 + \cos^2(\theta)}{\sin^2(\theta)}$ . The produced photons in the annihilation process essentially carry on the momenta in the direction of the incident particles.

The total annihilation cross section, i.e. the integral of Eq. (2.35) over the solid angle was first derived by Dirac (1930), even though the positron had not been discovered at that time. It is given by

$$\sigma_{\gamma\gamma}(\beta) = \pi r_e^2 \frac{1}{\beta^2 \gamma (\gamma + 1)} \left[ \left( \gamma + 4 + \frac{1}{\gamma} \right) \ln(\gamma + \sqrt{\gamma^2 - 1}) - \beta(\gamma + 3) \right], \quad (2.36)$$

where  $\beta = v/c$  is the dimensionless velocity,  $v = |v_{rel}|/2$  the relative velocities of the electron and the positron, and  $\gamma = (1 - \beta^2)^{-1/2}$  the Lorentz-factor. In the low-energy limit,  $\beta \ll 1$ , Eq. (2.36) reduces to

$$\sigma_{\gamma\gamma}^{NR} = \frac{\pi r_e^2}{\beta}. \quad (2.37)$$

This is plausible since the particles are more likely to annihilate when their relative velocity is slow. Equation (2.37) approaches infinity as  $\beta$  gets close to zero. But since the number of incoming charged particles per unit volume,  $n_{\pm}$ , also approaches zero at nearly zero velocity, the number of annihilation processes per unit time,  $\phi_{\gamma\gamma}$ , is still finite and constant down to lowest energies (Bethe 1935; Jauch & Rohrlich 1955),

$$\phi_{\gamma\gamma} \equiv \frac{1}{\tau_{\gamma\gamma}} = n_{\pm} \beta \sigma_{\gamma\gamma} = n_{\pm} \pi r_e^2. \quad (2.38)$$

Higher order Coulomb corrections are important for the non-relativistic case. Taking these into account, the limit of the direct annihilation cross section takes the form

(e.g. Landau & Lifshitz 1975; Crannell et al. 1976; Gould 1989)

$$\sigma_{\gamma\gamma}^{NR,*} = \frac{\pi r_e^2}{\beta^2} \frac{2\pi\alpha}{1 - \exp(-2\pi\alpha/\beta)}. \quad (2.39)$$

In the ultra-relativistic limit,  $\beta \rightarrow 1$ , the annihilation cross section asymptotically becomes

$$\sigma_{\gamma\gamma}^{UR} = \pi r_e^2 \frac{\ln(2\gamma)}{\gamma}. \quad (2.40)$$

The cross section approaches zero for very large velocities (Jauch & Rohrlich 1955). Fig. 2.7 shows the total direct annihilation cross section as a function of energy.

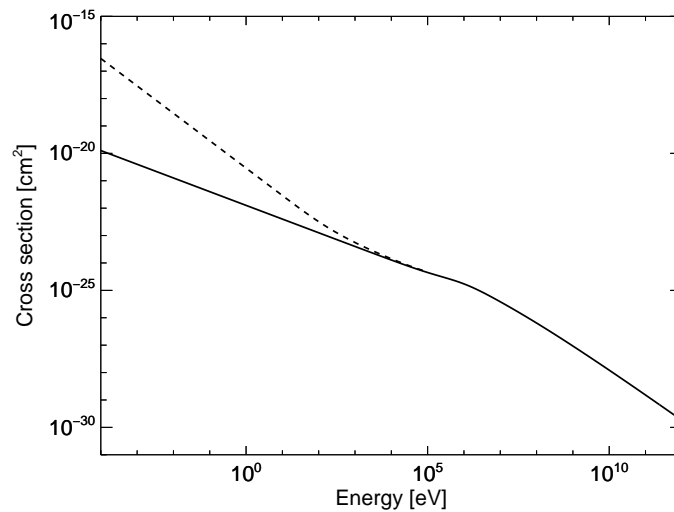


Figure 2.7: Electron-positron annihilation cross section as a function of energy. Shown are the first order direct annihilation cross section (solid line) and its low-energy adjustment due to Coulomb corrections for slow electrons and positrons which becomes important below several tens of keV.

### 2.3.2 Positronium Formation and Annihilation

The process of annihilation in flight is competing with the intermediate formation of Ps (see Sec. 2.1.2.2), followed by annihilation into two or three photons, depending on the Ps spin state. In the astrophysical context, Ps formation may be described by charge exchange reactions with interstellar atoms. The most important ingredient for understanding Ps formation is therefore the correct description of reactions involving the most abundant species in the ISM. Positron-hydrogen- and positron-helium-scatterings, and also reactions of positrons with molecular hydrogen and free electrons are important.

Positrons at very low kinetic energies ( $E_{kin} \lesssim 1$  keV, i.e. cold to warm ISM phases, Tab. 2.4) can react in several different ways with atoms in the ISM, including elastic scattering, atomic excitation and ionisation, and direct annihilation or annihilation after Ps formation, as shown in Tab. 2.2. Higher kinetic energies will be important

for the discussion about energy losses of positrons in the ISM once they have been injected from their sources at energies typically in the MeV range.

	Process	Reaction	Comments
$e^+ + e^-$	$\rightarrow e^+ + e^-$	Elastic Scattering	
	$\rightarrow \gamma + \gamma$	Direct Annihilation	"Annihilation in Flight", see Sec. 2.3.1
	$\rightarrow Ps + \gamma$	Ps Formation	"Radiative recombination" reaction, no experimental value, similar to hydrogen recombination
$e^+ + H$	$\rightarrow e^+ + H$	Elastic Scattering	
	$\rightarrow \gamma + \gamma + H^+$	Direct Annihilation	See Sec. 2.3.3
	$\rightarrow e^+ + H^*$	Excitation	Efficient above $\gtrsim 50$ eV, threshold 10.2 eV
	$\rightarrow e^+ + e^- + H^+$	Ionisation	Efficient above $\gtrsim 50$ eV, threshold 13.6 eV
	$\rightarrow Ps + H^+$	Ps Formation	"Charge exchange" reaction, threshold 6.8 eV
$e^+ + He$	$\rightarrow e^+ + He$	Elastic Scattering	
	$\rightarrow \gamma + \gamma + He^+$	Direct Annihilation	See Sec. 2.3.3
	$\rightarrow e^+ + He^*$	Excitation	Subdominant above $\gtrsim 80$ eV, threshold 21.2 eV
	$\rightarrow e^+ + e^- + He^+$	Ionisation	Dominant above $\gtrsim 50$ eV, threshold 24.6 eV
	$\rightarrow Ps + He^+$	Ps Formation	"Charge exchange" reaction, threshold 17.8 eV
$e^+ + H_2$	$\rightarrow e^+ + H_2$	Elastic Scattering	
	$\rightarrow \gamma + \gamma + H_2^+$	Direct Annihilation	See Sec. 2.3.3
	$\rightarrow e^+ + H_2^*$	Excitation	Dominant between $\approx 35$ and 55 eV, threshold 12.0 eV
	$\rightarrow e^+ + e^- + H_2^+$	Ionisation	Dominant above $\gtrsim 60$ eV, threshold 15.4 eV
	$\rightarrow Ps + H_2^+$	Ps Formation	"Charge exchange" reaction, threshold 8.6 eV

Table 2.2: Possible positron reactions with main species of the interstellar medium for kinetic positron energies below 1 keV. The threshold energies and relative reaction rates / cross sections have been taken from Guessoum et al. (2005).

Figure 2.8 shows several reaction rates of Tab. 2.2 as a function of positron energy. Below  $\lesssim 100$  eV, charge exchange and radiative recombination reactions have the largest cross sections and become the dominant Ps forming processes. The threshold energies given in Tab. 2.2 are the minimally-required kinetic energies of positrons for a particular process. They are equal to the ionisation energy of the atom/molecule minus the binding of the Ps atom of 6.8 eV (Sec. 2.1.2.2). Below kinetic energies of 6.8 eV, positrons may either scatter elastically with interstellar matter, or annihilate directly with free electrons. The energy thresholds will be important for the discussion of the celestial 511 keV line in Sec. 4.6.

The competition of positrons annihilating in flight with the formation of Ps can be expressed as the probability of positrons with initial kinetic energy,  $E_{kin}$ , to find electrons to annihilate with before reaching an energy where Ps formation becomes dominant, e.g. at  $T \approx 100$  eV. This is formulated as the integral over the positron energy from its formation down to  $T$ , and reads

$$P(E_{kin}, T) = 1 - \exp \left( -n_X \int_T^{E_{kin}} \frac{v(E)\sigma_X(E)}{|dE/dt|} dE \right). \quad (2.41)$$

In Eq. (2.41),  $n_X$  is the target particle number density,  $v(E)$  the positron velocity,  $\sigma_X(E)$  the cross section for direct annihilation with free or bound electrons (see Sec. 2.3.3), and  $|dE/dt|$  is the energy loss rate of the positrons (Drachman 1983; Prantzos et al. 2011). Energy losses in interstellar space happen mainly due to Coulomb interactions, such as bremsstrahlung, synchrotron radiation, or ionisation reactions; these processes will be further discussed in Sec. 2.4.3.1. Equation (2.41) therefore depends on the environment in which the positrons are slowed down. The general shape of the probability curve describes the physical intuition, as positrons with small kinetic energies (non-relativistic) are dominantly forming Ps, whereas ultra-relativistic positrons mainly annihilate in flight (see Sec. 2.3.1). Astrophysical sources produce positrons at MeV energies, but the measurements are only explained by almost 100% Ps formation. Hence propagation and energy loss of positrons in the ISM play a crucial role (see Sec. 4.6.6), also for the positron budget in the Galaxy.

The cross section of the charge exchange reaction  $e^+ + H \rightarrow Ps + H^+$  cannot be calculated analytically. It involves the three-body system of positron, proton, and electron. The positive charge of the nucleus is partly shielding the negative charge of the electron (or electrons in multiple electron atoms) so that the positron sees an effective number of electrons, i.e. an effective charge, to annihilate within a particular atom, which also depends on the incident energy of the positron (see e.g. Humberston & Wallace 1972). Furthermore, the hydrogen atom, and the Ps atom are bound states, and interactions also involve excitations of these bound states. In other words, phase space and partial waves play a non-negligible role (Humberston et al. 1997). Different approaches for the calculation of Ps formation in positron-hydrogen collision at low, i.e. near the Ps-formation threshold, and at higher energies can be found in Drachman et al. (1976); Satapathy et al. (1982); Khan & Ghosh (1983); Varracchio & Girardeau (1983); Kuang & Gien (1997), or Ryzhikh & Mitroy (2000), for example. In general, the cross section as a function of energy has a low-energy threshold at 6.8 eV as expected from the binding energy of the Ps atom, then obtains a maximum near  $\gtrsim 10$  eV, and falls off approximately exponentially towards higher energies, so that at energies above  $\gtrsim 50$  eV, ionisation and excitation reactions dominate the cross section.

For He and molecular hydrogen, the energy dependencies of the cross sections for charge exchange, ionisation, and excitation are very similar, but differ slightly in absolute values. The cross sections as a function of energy are shown in Fig. 2.8, and the respective threshold energies for He and H<sub>2</sub> are given in Tab. 2.2.

Positronium can also be formed through radiative recombination of free positrons with free electrons,  $e^+ + e^- \rightarrow Ps + \gamma$ . In general, radiative recombination denotes the process of any (often a hydrogenic ion) particle capturing another particle to a common bound state, thereby releasing a photon equivalent to the binding energy of that bound state. The positronium formation of free electrons with free positrons is related to the well-studied radiative recombination of hydrogenic ions (e.g. the proton) capturing an electron from the continuum (free particle) to a level  $n$  of the hydrogen atom.

For a hydrogenic ion of nuclear charge  $Z$ , the rate of recombinations to an atomic level  $n$  per unit time and unit volume,  $\frac{dN}{dt dV}$ , is given by

$$\frac{dN}{dt dV} = \alpha_n(Z, T) N_e N_I, \quad (2.42)$$

where  $\alpha_n(Z, T)$  is the radiative recombination rate coefficient as a function of the nuclear charge and kinetic temperature of the electron,  $T$ , and  $N_e$  and  $N_I$  are the number densities of free electrons and ions, respectively (e.g. Seaton 1959; Cranell et al. 1976; Gould 1989). The thermally-averaged radiative recombination rate  $\alpha_n(Z, T) (= \langle \sigma_{rr} v \rangle)$  can be calculated from the inverse process, photo-ionisation. It therefore also includes the several ionisation energies,  $I_n = \frac{Ry Z^2}{n^2}$ , for different atomic excitation levels  $n$ . Seaton (1959) calculated the total recombination rate numerically which was then refined by Gould (1989) for higher temperatures. The general form for radiative recombination of hydrogen ions ( $Z = 1$ ) is given by

$$\alpha_H(T) = C \sqrt{\frac{2kT}{\pi m}} y \phi(y) \bar{g}(y). \quad (2.43)$$

Here,  $C = 2^6 3^{-3/2} \alpha^3 \pi a_0^2 \approx 4.21 \times 10^{-22} \text{ cm}^2$ ,  $y = \frac{Ry}{kT}$ ,  $\bar{g}(y)$  is an averaged Gaunt factor, expressing medium properties, and  $\phi(y)$  is a slowly varying function of the temperature (see Appendix B).

Gould (1989) showed from first principles that the radiative recombination process of a proton capturing an electron is directly related to the radiative recombination process of a positron capturing an electron. The only adjustment comes from considering the reduced mass in the bound Ps atom, so that

$$\alpha_{Ps}(T) = \alpha_H(T; m \rightarrow \frac{m}{2}), \quad (2.44)$$

and consequently because  $a_0 \propto m^{-1}$  and  $Ry \propto m$

$$\alpha_{Ps}(T) = 4\alpha_H(2T). \quad (2.45)$$

The radiative recombination rate,  $\alpha_{Ps}(T)$ , can then be used to calculate the cross section for Ps formation from free electrons and positrons in space. Below positron energies of 6.8 eV, radiative recombination is the dominant process in the ISM, see Fig. 2.8.

Once Ps is formed, it will end in annihilation. The life-time of this bound state depends on the spin state of the electron and the positron, as already described in Sec. 2.1.2.2. Para-positronium with "antiparallel" spins decays to two<sup>4</sup> photons after a mean lifetime of

---

<sup>4</sup>Para-positronium can decay to integer multiples of two photons, but annihilations to four or more photons is strongly suppressed by factors of  $\alpha^{2n}$  where  $2n$  is the number of additional photons.

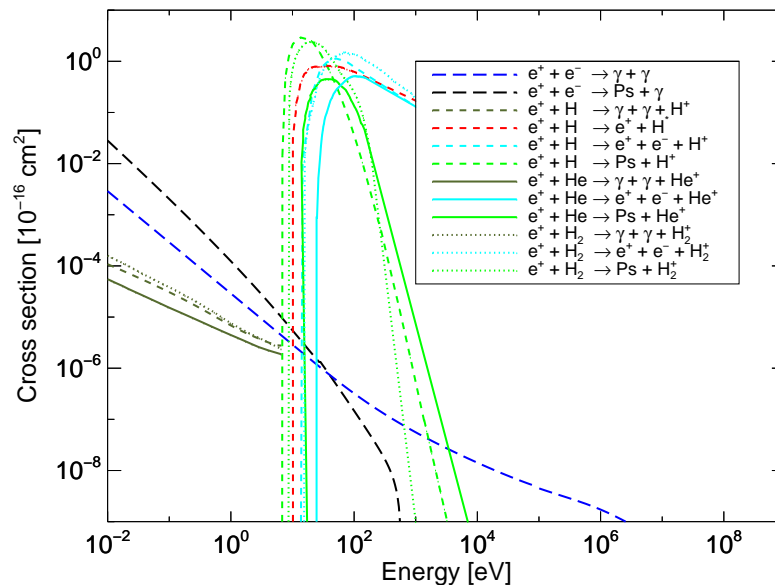


Figure 2.8: Cross sections for different reactions of positrons with other particles or compounds as a function of energy. Below the positronium binding threshold of 6.8 eV, direct annihilation with electrons and atoms, and also radiative recombination with free electrons are the dominant processes. Although direct annihilation with bound electrons has the lowest of all cross sections, the process will become important in environments of large densities and high-Z materials exposed by positrons, e.g. in a space-craft bombarded by cosmic-rays (see Sec. 3.2.3.1). Above 6.8 eV the dominating charge exchange reactions of positrons with H, He, or H<sub>2</sub> lead to the intermediate formation of positronium, and the subsequent decay thereof, if it is not dissociated again. Positronium formation is most efficient up to  $\approx 40$  eV, depending slightly on the species. Annihilation in flight would be the dominant process again above 3 keV if there are sufficient number densities of free electrons available; otherwise, ionisation or excitation reactions with H, He or H<sub>2</sub>, having orders of magnitude larger cross sections, will lead to an energy loss of the positrons (see also Sec. 2.4.3.1). Cross sections not discussed in detail in the text have been taken from Kadyrov & Bray (2002) for H ionisation, Kernoghan et al. (1996) for H excitation, Campbell et al. (1998) for He ionisation and Ps formation with He, Campeanu & Humberston (1977) for direct annihilation with He, Guessoum et al. (2005) for H<sub>2</sub> ionisation and Ps formation with H<sub>2</sub>, and Armour et al. (1990) for direct annihilation with H<sub>2</sub>. Theoretical calculations and measurements for low energy positrons exciting He or H<sub>2</sub> are very imprecise and only the cross section for H excitation by positrons is given.

$$\tau_{pPs} = \frac{2\hbar}{\alpha^5 m_e c^2} \approx 0.125 \text{ ns} \quad (2.46)$$

at tree level (Ore & Powell 1949; Jauch & Rohrlich 1955). The decay rate for p-Ps can be derived from the non-relativistic limit of the direct annihilation rate, Eq. 2.38, by considering that the electron and positron number density  $n_{\pm}$  equals the wave function of the  $1^1S_0$  Ps state at zero separation, and taking into account that there is only one possible state to decay, instead of four possible relative spin states of a free electron-positron pair.

The annihilation of o-Ps with "parallel" spins is illustrated in the Feynman diagrams, Fig. 2.9. Similarly to the p-Ps case, the free electron-positron pair annihilation rate into three photons may be calculated as radiative correction to the two-photon annihilation channel. Then, the result has to be applied to the non-relativistic case of zero separation of the  $1^3S_1$  Ps state. The  $1^3S_1$  spatial wave function is identical to the  $1^1S_0$  state and only differs in the spin wave function. In this calculation, the only changes in the matrix element are an additional vertex for the third outgoing photon and an additional fermion propagator. The phase space integration therefore also involves the third photon momentum. In the non-relativistic limit, the differential cross section is

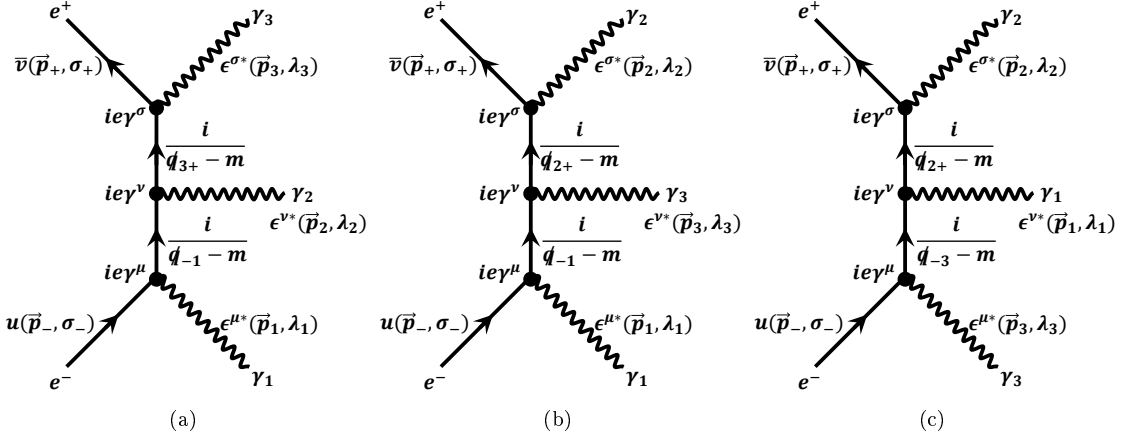


Figure 2.9: Subset of Feynman diagrams of three-photon annihilation (ortho-positronium decay,  $\vec{p}_+ \approx \vec{p}_- \rightarrow 0$ ). Because the three outgoing photons are interchangeable, there are a total of six diagrams,  $(1/2/3)$ ,  $(1/3/2)$ ,  $(2/1/3)$ ,  $(2/3/1)$ ,  $(3/1/2)$ , and  $(3/2/1)$ , respectively. The incoming spinors and anti-spinors for the electron and positron are denoted by  $u(\vec{p}_-, \sigma_-)$  and  $\bar{v}(\vec{p}_+, \sigma_+)$ , respectively, where  $\sigma_{\pm} = 1, 2$  is the spin of the particles, and the outgoing photon polarisation vectors by  $\epsilon_i(\vec{p}_i, \lambda_i)$ , where  $i = 1, 2, 3$  and  $\lambda = +, -$  is polarisation of the photon  $i$ . The fermionic propagators transfer the four-momentum difference  $p_{ij} = p_i - p_j$  to the next electromagnetic vertex,  $ie\gamma^\mu$ .

$$\frac{d\sigma_{\gamma\gamma\gamma}}{d\Omega_1 d\Omega_2 dE_1} = 4 \frac{\alpha r_e^2}{\beta} \frac{(1 - c_{12})^2 + (1 - c_{23})^2 + (1 - c_{31})^2}{2m_e - E_1(1 - c_{12})} \frac{E_1 E_2}{(4\pi)^2 m_e^2}, \quad (2.47)$$

where  $c_{ij} = \cos(\theta_{ij})$  is the cosine of the angle between outgoing photon  $i$  and  $j$ ,  $d\Omega_i = \sin(\theta_i) d\phi_i d\theta_i$  is the solid angle element, and  $E_i$  the energy of photon  $i$  (Jauch & Rohrlich 1955). Integration over the angles, and considering that the outgoing photons span a flat plane, then yields

$$\frac{d\sigma_{\gamma\gamma\gamma}}{dE_1 dE_2} = 8 \frac{\alpha r_e^2}{\beta} \left[ \left( \frac{m - E_1}{E_2 E_3} \right)^2 + \left( \frac{m - E_2}{E_3 E_1} \right)^2 + \left( \frac{m - E_3}{E_1 E_2} \right)^2 \right]. \quad (2.48)$$

This cross section is proportional to the energy spectrum for one photon energy fixed. For a detailed discussion of the o-Ps continuum shape, see Sec. 2.4.2.3. The total three-photon annihilation cross section in the non-relativistic limit is then given by

$$\sigma_{\gamma\gamma\gamma} = \frac{4}{3} \frac{\alpha r_e^2}{\beta} (\pi^2 - 9), \quad (2.49)$$

where a factor  $3!$  has been introduced to account for the indistinguishability of the final states with three photons (Ore & Powell 1949; Jauch & Rohrlich 1955). For a given electron and positron number density,  $n_{\pm}$ , the probability for a free positron to annihilate via the emission of three photons per unit time,  $\phi_{\gamma\gamma\gamma}$ , is given by

$$\phi_{\gamma\gamma\gamma} \equiv \frac{1}{\tau_{\gamma\gamma\gamma}} = n_{\pm} \beta \sigma_{\gamma\gamma\gamma} = \frac{4}{3} n_{\pm} (\pi^2 - 9) \alpha r_e^2, \quad (2.50)$$

similar to Eq. (2.38). Analogous to the p-Ps decay, there is only one final state to decay instead of four relative spin states, so that a factor of 4 has to be introduced to the o-Ps decay rate. However, there are three possible spin states that may decay to three photons<sup>5</sup>, and a factor of 1/3 occurs in the final formula for the o-Ps decay rate

$$\Gamma_{oPs} = \frac{\hbar}{\tau_{oPs}} = \frac{4}{3} \frac{4}{3} (\pi^2 - 9) \alpha r_e^2 \frac{\alpha^3 m_e^3 c^3}{8\pi \hbar^3}, \quad (2.51)$$

and the corresponding lifetime for ortho-positronium is

$$\tau_{oPs} = \frac{9\pi}{2(\pi^2 - 9)} \frac{\hbar}{\alpha^6 m_e c^2} \approx 13.86 \mu\text{s}. \quad (2.52)$$

At tree-level, the o-Ps lifetime is about 1000 times longer than the p-Ps lifetime, as already estimated in Sec. 2.1.2.2 from considerations of vertex counting in Feynman diagrams.

### 2.3.3 Direct Annihilation with Bound Electrons

If positrons slow down to energies below the various threshold energies for charge exchange reactions with atoms or molecules in the interstellar medium, and if there are not enough free electrons present, direct annihilation of positrons with bound electrons is the only possible reaction to take place. Such low energies then correspond to temperatures below several thousand Kelvin (Guessoum et al. 2005).

Because the annihilation then happens in the external field of an atom, the process can either yield two photons, like the general case, or even only one photon, which is called "one-quantum annihilation". In the latter case, the field of the atom absorbs the recoil momentum of the incident positron, similar to pair creation in the field of a nucleus by only one photon (see Sec. 2.2.4.2), and a gamma-ray photon with energy

$$E_\gamma = 2m_e c^2 + E_{kin}^+ - I_S - E_{recoil}, \quad (2.53)$$

may be emitted. In Eq. (2.53),  $I_S$  is the ionisation energy of the atom's shell  $S = K, L, M, \dots$ , and  $E_{recoil}$  is the recoil energy of the target nucleus, which is in general very small and neglected in calculations (see e.g. Sodickson et al. 1961; Weigmann et al. 1963; Johnson et al. 1964; Bergstrom et al. 1996).

The interaction occurs in the field of an atom, for which reason the charge that is "seen" by the incoming positron is screened by the positive charge of the atomic nucleus, and only an effective charge,  $Z_{eff}$ , shows up in the calculation of cross sections. This applies to both, single-quantum and two-quantum annihilations. In

<sup>5</sup>Similar to p-Ps, o-Ps can also decay into  $2n + 1$  photons, whereas each additional pair of photons in the final state introduces a factor of  $\alpha^2$  in the transition probability and is hence also largely suppressed.

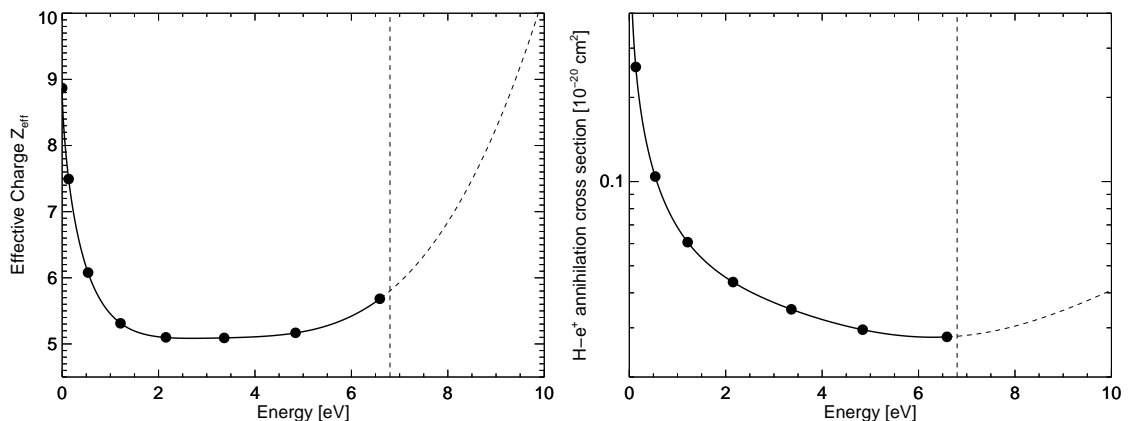
case of the emission of two gamma-rays, the cross section of positron annihilation with a bound electron may be written as

$$\sigma_{\gamma\gamma}^{bound} = Z_{eff}\alpha^3 k^{-1}\pi a_0^2, \quad (2.54)$$

where  $Z_{eff}$ , the effective charge, specific to the atom or molecule which the positron is interacting with (Ferrell 1956; Bhatia et al. 1974, 1977), and  $k = \frac{\sqrt{2m_e E_{kin}^+}}{\hbar}$  is the wave number of the positron in units of the inverse Bohr radius,  $a_0 = r_e/\alpha^2$ . In the case of hydrogen, the effective charge can be formulated as

$$Z_{eff} = \int \int d\vec{r}_1 d\vec{r}_2 |\Psi(\vec{r}_1, \vec{r}_2)|^2 \delta(\vec{r}_1 - \vec{r}_2), \quad (2.55)$$

in which  $\Psi(\vec{r}_1, \vec{r}_2)$  describes the quantum mechanical scattering wave function of the positron-hydrogen system, so that  $Z_{eff}$  is a measure of the probability for the hydrogen-electron and the positron to have zero separation (Bhatia et al. 1974, 1977). It is a convex function of wave number (concave function of energy) with a shallow minimum around  $k = 0.5a_0$ , corresponding to  $E_{kin}^+ = 3.4$  eV. The annihilation cross section with a bound electron in hydrogen is then proportional to approximately  $k^{-5/4}$ , or  $E^{-5/8}$  (Bhatia et al. 1977). Figure 2.10 shows the energy dependence of the effective charge for a hydrogen atom; the resulting cross-sections are of the order  $10^{-26}$ - $10^{-24}$  cm<sup>2</sup> for temperatures below  $\approx 100$  K. Thus, direct annihilation with bound electrons becomes negligible for temperatures exceeding several thousand Kelvin, then being dominated by charge exchange reactions (see Fig. 2.8).



(a) Effective charge,  $Z_{eff}$ , of a hydrogen atom seen by a positron as a function of kinetic positron energy. (b) Cross section of a positron annihilating with a bound electron of a hydrogen atom as a function of energy.

Figure 2.10: Positron annihilation on bound electrons. Shown is the example of positron-hydrogen annihilation. On the left panel, the energy dependency of the effective charge of the hydrogen-atom as seen by a slow positron is shown. The calculated values (black dots in both panels) are taken from Bhatia et al. (1977), together with an empirical six-degree polynomial fit (black solid line in both panels) up to the positronium formation threshold energy of 6.8 eV (vertical dashed line in both panels). On the right panel, the resulting cross section as a function of energy is shown for the calculated values of the left panel, as derived from Eq. (2.54), and the polynomial fit. The screening effects are dominant between 2 and 4 eV and seem to decrease again for high energies. The cross section is then a strictly decreasing function of energy up to the threshold. Extrapolated values from the polynomial fit are shown as dashed lines but should be considered with caution as charge exchange becomes the dominant reaction branch.

The cross section calculated in lowest order Born approximation for the single-

quantum annihilation is given by

$$\sigma_{\gamma}^{\text{bound}} = 4\pi r_e^2 \alpha^4 Z^5 f(\eta), \quad (2.56)$$

where  $\eta = E_+/m_e c^2$  is the dimensionless energy of the incident positron and  $f(\eta)$  is a concave function with a maximum between  $\eta = 1$  and  $\eta = 2$  (e.g. Johnson et al. 1964, see also Appendix B). However, for elements with charge number  $Z$  larger than  $\approx 70$ , this approximation is not valid any more, since the interaction term  $\alpha Z$  is larger than 0.5 and screening effects become more and more important (Sodickson et al. 1961; Weigmann et al. 1963; Johnson et al. 1964; Broda & Johnson 1972).

In principle, one-quantum annihilation can be distinguished from the emission of two photons by a spectral analysis, due to the different possible photon energies considering energy and momentum conservation in each process, see Sec. 2.4. But since the cross sections for both processes are only of the order of  $10^{-26}$ - $10^{-20}$  cm<sup>2</sup>, and become dominant only for high  $Z$  materials, annihilation gamma-rays from reactions of positrons with bound electrons will only contribute a small fraction to an astrophysical signal, though this might be a significant background source in the INTEGRAL satellite (see Sec. 3.2.1).

## 2.4 Gamma-Ray Spectra from Positron Annihilation

In this thesis, the annihilation of positrons with electrons is measured by detecting the emitted gamma-rays from the conversion of rest mass and kinetic energy of massive particles to photon energy, Eq. (2.14). Because the annihilation of electrons with positrons is not isotropic, Eq. (2.35), the exact annihilation spectra, i.e. the differential number of photons per unit time and unit energy for given distributions of interacting particles, are difficult to calculate for the general case. In Sec. 2.4.2, the universal formula for the derivation of annihilation spectra is given in an integral form and discussed for special cases in an astrophysical context. The kinematics of particular positron/electron energies and momenta in general annihilation reactions are necessary for the description of the final photon spectra. The synthesis towards a differential spectrum requires an integration over all possible final photon energies, weighted according to the velocity distributions of the massive particles. Furthermore, kinematics also provide an intuition for extreme or special cases (see Sec. 2.4.1).

### 2.4.1 Considerations from Kinematics

In the centre-of-momentum (COM) frame, the annihilation of a positron with momentum  $\vec{p}_+$  and energy  $E_+ = \sqrt{|\vec{p}_+|^2 + m^2} \equiv \gamma_+ m$  with an electron of momentum  $\vec{p}_-$  and energy  $E_- = \sqrt{|\vec{p}_-|^2 + m^2} \equiv \gamma_- m$ , where  $\vec{p}_+ = -\vec{p}_-$ , yields two photons with energies and momenta,  $E_1, \vec{p}_1$ , and  $E_2, \vec{p}_2 = -\vec{p}_1$ , respectively. The Lorentz-factors  $\gamma_{\pm} = \frac{T_{\pm}}{m} + 1$  describe the kinetic energies  $T_{\pm}$  of the positron and electron with mass  $m = m_e$ , respectively. Figure 2.11 illustrates the reaction in the COM frame;

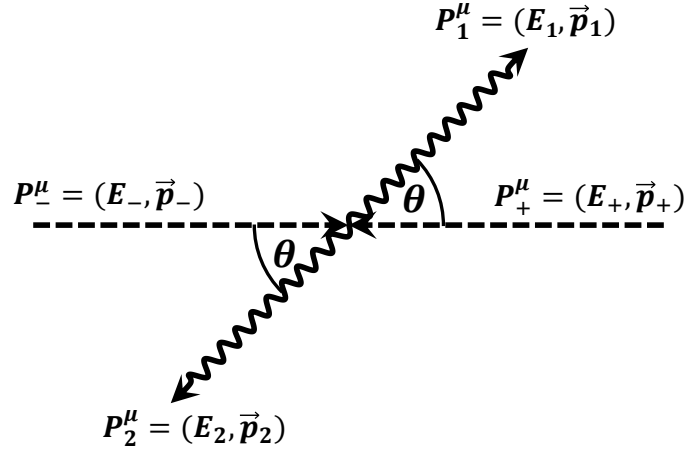


Figure 2.11: Electron-positron pair annihilation in the centre of momentum frame. Shown is the general case for arbitrary electron and positron four-momenta,  $P_-^\mu$  and  $P_+^\mu$ , respectively, annihilating into two photons with four-momenta,  $P_1^\mu$  and  $P_2^\mu$ , respectively. Here, the interaction angle in the centre of momentum frame is defined as the angle between the incoming electron momentum vector,  $\vec{p}_-$ , and the outgoing momentum vector of photon 2,  $\vec{p}_2$ .

the angle between incoming electron/positron and outgoing photon 2/1 is denoted by  $\theta$ . Energy and momentum conservation in the COM frame are then given by

$$\text{Energy:} \quad E_+ + E_- = E_1 + E_2 \quad (2.57)$$

$$\text{Momentum:} \quad \vec{p}_+ + \vec{p}_- = \vec{p}_1 + \vec{p}_2 = 0. \quad (2.58)$$

For a given electron and positron energy, the resulting photon energies can be described as a function of  $m$ ,  $\gamma_+$ ,  $\gamma_-$ , and  $\theta$  (see Appendix. B for detailed calculation). The final result can be written in the form

$$E_1 = m(\gamma_+ + \gamma_-) - E_2 \quad (2.59)$$

$$E_2 = m \left( \frac{1 + \gamma_+ \gamma_- + \sqrt{(\gamma_+^2 - 1)(\gamma_-^2 - 1)}}{(\gamma_+ + \gamma_-) + \cos(\theta)(\sqrt{\gamma_-^2 - 1} - \sqrt{\gamma_+^2 - 1})} \right). \quad (2.60)$$

Equation (2.60) is now used to discuss several special cases for the kinetic energies of the annihilating particles into two photons:

1.  $\gamma_+ = \gamma_- = 1$ :  $E_1 = E_2 = m$

The energies of electron and positron are equivalently distributed to both photons. As there are no kinetic energies involved, only the rest mass energies are converted to photon energies of  $E_{1/2} = m = 511$  keV. This is called annihilation at rest, and conforms to Eq. (2.14).

2.  $\gamma_+ = \gamma_- = \gamma$ :  $E_1 = E_2 = \gamma m$

Electron and positron have the same kinetic energy. The interaction angle  $\theta$  is not important in this case, as the produced photons are emitted diametrically opposed, and as a result also share the equivalent amounts of energy, depending

on the Lorentz-factors of electron and positron.

3.  $\gamma_{\pm} = \gamma, \gamma_{\mp} = 1$ :  $E_{1/2}^{max} \approx E + \frac{1}{2}m, E_{2/1}^{min} \approx \frac{1}{2}m$

For the case of a stationary electron (positron) hit by a moving positron (electron), the interaction angle  $\theta$  regulates the specific energy one photon obtains. For the minimum and maximum energy a photon can carry, the limiting cases  $\cos(\theta) = \mp 1$  can be considered and, assuming  $\gamma \gg 1 \leftrightarrow E \gg m$ , yield a lower photon energy of  $\frac{1}{2}m$  and an upper bound of  $E + \frac{1}{2}m$  (see Appendix. B for more details). For a mono-energetic population of positrons (electron) reacting with stationary electrons (positrons), the differential energy spectrum of resulting photons will be described in Sec. 2.4.2.2.

In case of intermediate Ps formation (Sec. 2.3.2), the result is either the emission of two photons (p-Ps) or three photons (o-Ps). For the case of p-Ps, Eqs. (2.58) and (2.60) can also be used to determine limits in the spectral energy density. The process, however, is conceptionally different, because now, there is a composite bound state which is decaying, rather than two free particles reacting with each other. The "relative" momenta of electron and positron in p-Ps are very small. Hence, (1) can be applied, so that two photons with an energy of  $m = 511$  keV each are emitted. The motion of p-Ps with respect to the observer, and all other cases seen from laboratory frame, will be discussed in Sec. 2.4.3.

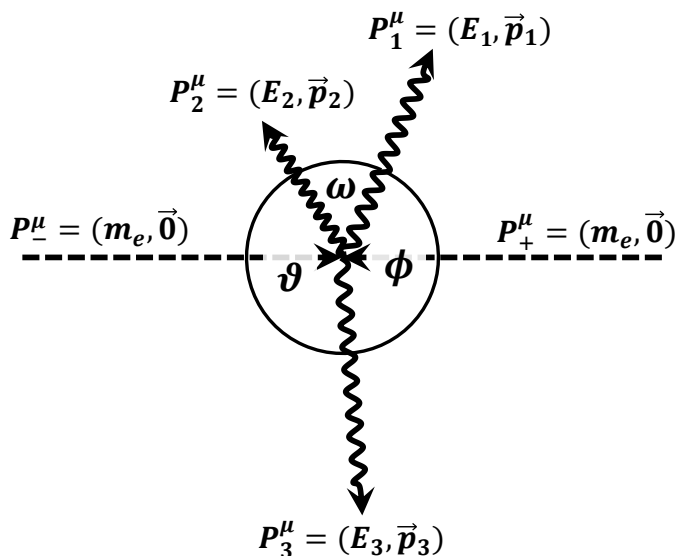


Figure 2.12: Three-photon annihilation in the centre of momentum frame. Shown is the case of ortho-positronium decay, where the momenta of incoming electron and positron,  $\vec{p}_+$  and  $\vec{p}_-$ , respectively, are nearly zero, and only the rest masses,  $m_e$ , contribute to the total energy of the particles. The emitted photons are moving in a flat plane, spanned by the photon momentum vectors  $\vec{p}_1, \vec{p}_2$ , and  $\vec{p}_3$ .

The fundamental energy and momentum conservation equations in three photon annihilation at rest or o-Ps decay are

$$\text{Energy:} \quad E_+ + E_- = E_1 + E_2 + E_3 = 2m \equiv E_{tot} \quad (2.61)$$

$$\text{Momentum:} \quad \vec{p}_+ + \vec{p}_- = \vec{p}_1 + \vec{p}_2 + \vec{p}_3 = 0. \quad (2.62)$$

Momentum conservation confines all particles into a flat plane, Fig. 2.12. The max-

imum energy a particular photon can obtain is one half of the total energy available, i.e.  $1m = 511$  keV. The energies of all three photons now depend on each other,

$$E_1 = 2m - (E_2 + E_3) \quad (2.63)$$

$$E_2 = \frac{m - E_3}{1 + \frac{E_3}{2m} (\cos(\phi) - 1)}, \quad (2.64)$$

where  $\phi$  is the angle between photon 2 and 3. Eq. (2.64) can be tested for consistency by applying special or limiting cases for a fixed energy  $E_3$  of photon 3.

1.  $E_3 = 0$ :  $E_2 = m$ ,  $E_1 = m$

Assuming the photon energy  $E_3$  to be negligible small compared to  $E_{tot}$ , the other two photons share the remaining  $2m$  to equivalent fractions, as expected. This case can be permuted among the photons.

2.  $E_3 = \frac{m}{2}$ :  $E_2 = \frac{\frac{m}{2}}{1 + \frac{m}{4}(\cos(\phi))}$

Depending on  $\phi$ ,  $E_2$  achieves values between  $0.5m$  and  $1.0m$  only, so that the remaining energy is passed to  $E_1$ .

3.  $E_3 = 2m$ :  $E_2 = \frac{-m}{\cos(\phi)}$

This case illustrates that one photon cannot obtain more than one rest mass energy: First of all, photon energy  $E_2$  is divergent for angles  $\phi = \{90^\circ, 270^\circ\}$ , resulting in infinite negative or positive energies. On the other hand, for angles  $\phi = (90^\circ, 270^\circ)$ ,  $E_2$  can indeed obtain positive values, but due to energy conservation,  $E_1$  is always negative in this case. Thus, photon energies above  $1m$  are excluded (see also Appendix B).

Particle / Measure	LAB	COM
Positron	$v_+^\mu = \gamma_+(1, \vec{\beta}_+)$	$v_+^\mu = \gamma_{cm}(1, \vec{\beta}_{cm})$
Electron	$v_-^\mu = \gamma_-(1, \vec{\beta}_-)$	$v_-^\mu = \gamma_{cm}(1, -\vec{\beta}_{cm})$
Photon	$p_\gamma^\mu = k(1, \hat{k})$	$p_\gamma^\mu = k_{cm}(1, \hat{k}_{cm})$
Frame	$v_L^\mu = \gamma_c(1, -\vec{\beta}_c)$	$v_c^\mu = \gamma_c(1, \vec{\beta}_c)$
Angles	$\mu := \cos(\alpha) = \frac{\vec{\beta}_+ \cdot \vec{\beta}_-}{ \vec{\beta}_+   \vec{\beta}_- }$	$x := \cos(\theta) = \frac{\hat{k}_{cm} \cdot \vec{\beta}_{cm}}{ \vec{\beta}_{cm} }$ $y := \cos(\phi) = \frac{\vec{\beta}_{cm} \cdot \vec{\beta}_c}{ \vec{\beta}_{cm}   \vec{\beta}_c }$ $z := \cos(\omega) = \frac{\hat{k}_{cm} \cdot \vec{\beta}_c}{ \vec{\beta}_c }$

Table 2.3: Kinematic parameter definitions of positron annihilation in different frames.

## 2.4.2 From Cross Section to Spectrum

In this section, the ideal theoretical gamma-ray spectra will be derived for the different annihilation processes. In calculations of cross sections, annihilation rates, and differential spectra, three frames are being distinguished: The rest-frame of the positron (REST), COM frame, and the laboratory frame of the observer (LAB). The required four-velocities and four-momenta are defined by  $v^\mu \equiv (\gamma c, \gamma \vec{v})$  and  $p^\mu \equiv (m_e \gamma c, m_e \gamma \vec{v})$ , respectively. For better comprehensibility and convenience in

formulation, the essential parameters are given in natural units and in units of the electron mass, following the form of Svensson (1982). Tab. 2.3 lists important variable definitions in the COM and LAB frame, respectively.

The COM and LAB frame can be in relative motion with velocity  $\vec{\beta}_c$ ; this translates to a Doppler-shift for the observed photons. A simple illustration and derivation of arbitrary Doppler-shifts is given in Sec. 2.4.3.5. In the rest frame of the electron (positron), the positron (electron) is seen at a four-velocity  $v_{\pm}^{\mu} = \gamma_r(1, \vec{\beta}_r)$ , where  $\gamma_r$  (and thus  $\beta_r$ ) can be connected to the COM velocity and the individual LAB frame velocities of electron and positron by evaluating the Lorentz invariant products  $v_+^{\mu}v_{-,\mu}$  in all considered frames,

$$v_+^{\mu}v_{-,\mu} = \gamma_+\gamma_-(1 - \beta_+\beta_-\cos(\alpha)) = 2\gamma_{cm}^2 - 1 = \gamma_r. \quad (2.65)$$

#### 2.4.2.1 Annihilation Rate

In a first step, the annihilation rate, i.e. the number of positrons annihilating per unit time and unit volume,  $\dot{n}_+$ , derived from the annihilation cross section, Eq. (2.36), is calculated. Due to special relativistic effects, the volume elements and thus the number densities of electrons and positrons follow a relativistic length contraction. The Lorentz invariant annihilation rate is then defined by (Landau & Lifshitz 1975; Jauch & Rohrlich 1955; Svensson 1982)

$$\dot{n}_+ = n_+n_- \frac{\sqrt{(v_+^{\mu}v_{-,\mu})^2 - 1}}{\gamma_+\gamma_-} c\sigma(\gamma_{cm}), \quad (2.66)$$

where  $n_{\pm}$  are the particle number densities of positrons and electrons, respectively, for mono-energetic particles with four-velocities  $v_+^{\mu}$  and  $v_{-,\mu}$  as defined in Tab. 2.3, and  $\sigma_{cm}$  is the total annihilation cross section as given in Eq. (2.36) in the COM frame. Using Eq. (2.65), the annihilation rate can be written as

$$\dot{n}_+ = n_+n_- \frac{\gamma_{cm}^2}{\gamma_+\gamma_-} 2\beta_{cm}c\sigma(\gamma_{cm}). \quad (2.67)$$

Using the non-relativistic annihilation cross section, Eq. (2.37), in the COM frame ( $\beta \rightarrow 2\beta$ ), the non-relativistic annihilation rate, as already described in Eq. (2.38), is recovered.

In order to discuss the various spectra that may emerge from the annihilation of arbitrary populations of electrons and positrons, Eq. (2.66) has to be adjusted for the velocity distribution functions of electrons,  $f_-(\vec{\beta}_-)$ , and positrons,  $f_+(\vec{\beta}_+)$ , respectively,

$$\dot{n}_+ = n_+n_- \int \int d^3\vec{\beta}_+ d^3\vec{\beta}_- f_+(\vec{\beta}_+) f_-(\vec{\beta}_-) \frac{\gamma_{cm}^2}{\gamma_+\gamma_-} 2\beta_{cm}c\sigma(\gamma_{cm}). \quad (2.68)$$

For the very general case, the evaluation of the integrals in Eq. (2.68) can be very complicated and might not reduce to analytical expressions. Here, the special case of isotropic and mono-energetic distribution functions will be discussed in order to describe and illustrate order of magnitude estimates and dependencies on energy for pair annihilation rates. A more detailed discussion can be found in Svensson (1982).

The angle- and distribution-averaged annihilation rate can then be written as

$$\dot{n}_+ = n_+ n_- \langle \overline{\sigma v} \rangle, \quad (2.69)$$

where  $\overline{\sigma v}(\gamma_+, \gamma_-)$  describes the angle-averaged reaction rate per electron-positron pair. After a lengthy calculation, it is given by

$$\overline{\sigma v}(\gamma_+, \gamma_-) = \pi r_e^2 c \frac{F(\gamma_{cm})}{\beta_+ \gamma_+^2 \beta_- \gamma_-^2}. \quad (2.70)$$

In Eq. (2.70),  $F(\gamma_{cm})$  is a strictly monotonic decreasing function of  $\gamma_{cm}$ , and given in Appendix B. As expected for the conditions on  $f_+$  and  $f_-$ ,  $\overline{\sigma v}$  is symmetric in  $\gamma_+$  and  $\gamma_-$ , respectively. Figure 2.13 shows the angle-averaged annihilation rate in the plane of electron and positron energies.

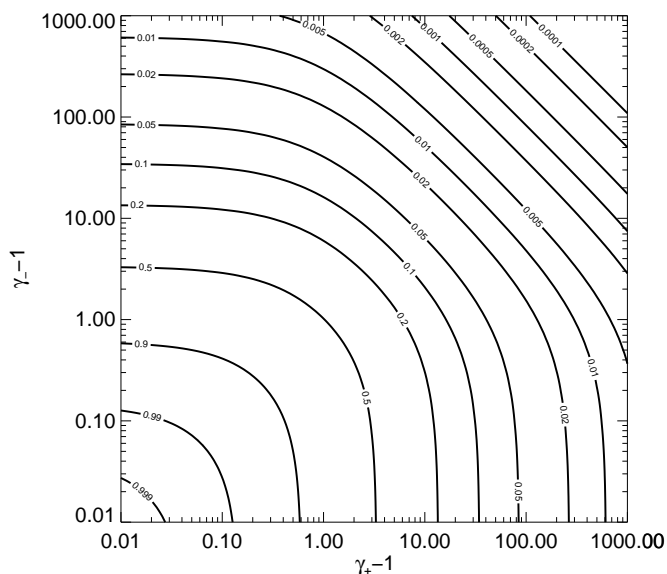


Figure 2.13: Direct annihilation rate as a function of electron and positron Lorentz-factors,  $\gamma_+$  and  $\gamma_-$ , respectively, in units of  $\pi r_e^2 c$  from Eq. (2.70). The contours are symmetric about the diagonal axis  $\gamma_+ = \gamma_-$ . Towards lower energies, the normalised rate approaches 1.0 and is of the same order of magnitude until Lorentz-factors of  $\approx 1.5$ , corresponding to velocities of  $\approx 0.75c$ . At high kinetic energies, the annihilation rate quickly drops  $\propto \ln(\gamma)/\gamma^2$ .

From Fig. 2.13 it can be seen that in the non-relativistic limit ( $\gamma_- \rightarrow 1$ ,  $\gamma_+ \rightarrow 1$ ),  $\overline{\sigma v}$  approaches a constant value of  $\pi r_e^2 c \approx 7.5 \times 10^{-15} \text{ cm}^3 \text{ s}^{-1}$  which is exactly the value derived in Eq. (2.38), confirming the conditions and assumptions from the previous sections. As expected from the ultra-relativistic limit of the annihilation cross section, Eq. (2.40), the annihilation rate drops rapidly for large values of  $\gamma_+$  or  $\gamma_-$ .

### 2.4.2.2 Gamma-Ray Spectra for Direct Annihilation

The annihilation spectrum, i.e. the distribution of photons in the energy interval  $[E, E + dE]$  from annihilating electron-positron pairs per unit time and unit volume (spectral emissivity), is related to the annihilation rate by the differential with respect to the photon energy. For arbitrary isotropic electron- and positron-velocity-distribution functions, the general annihilation spectrum can be calculated by (Svensson 1982)

$$\dot{n}(E)dE = n_+n_- \int d\gamma_+ f_+(\gamma_+) \int d\gamma_- f_-(\gamma_-) \int \frac{d\mu}{2} \frac{\gamma_{cm}^2}{\gamma_+\gamma_-} 2\beta_{cm}c \frac{d\sigma_{\gamma\gamma}}{dE}(E, \gamma_+, \gamma_-, \mu) dE, \quad (2.71)$$

where  $\frac{d\sigma_{\gamma\gamma}}{dE}(E, \gamma_+, \gamma_-, \mu)$  is the differential annihilation cross section as given in Eq. (2.35). Similar to the annihilation rate, the angle-averaged emissivity per annihilating electron-positron pair can be defined as

$$\overline{v \frac{d\sigma_{\gamma\gamma}}{dE}}(E, \gamma_+, \gamma_-) \equiv \frac{1}{\gamma_+\gamma_-} \int \frac{d\mu}{2} 2\beta_{cm}\gamma_{cm}^2 c \frac{d\sigma_{\gamma\gamma}}{dE}(E, \gamma_+, \gamma_-, \mu), \quad (2.72)$$

which describes the shape of any annihilation spectrum for arbitrary Lorentz-factors (particle energies)  $\gamma_+$  and  $\gamma_-$ . Svensson (1982) derived an analytical expression for the spectral shape as a function of  $E$ ,  $\gamma_+$ , and  $\gamma_-$ , respectively. It is given by

$$\overline{v \frac{d\sigma_{\gamma\gamma}}{dE}}(E, \gamma_+, \gamma_-) = \pi r_e^2 c \frac{S(E, \gamma_+, \gamma_-, \gamma_{cm})}{\beta_+ \gamma_+^2 \beta_- \gamma_-^2}. \quad (2.73)$$

Equation (2.73) is similar to Eq. (2.70) for the annihilation rate, but with a function  $S(E, \gamma_+, \gamma_-, \gamma_{cm})$ , containing the energy dependence of the emitted photons (see Appendix B). Similar to the annihilation rate, also the spectral emissivity is symmetric in changes of  $\gamma_+ \leftrightarrow \gamma_-$ , as expected.

Figure 2.14 shows the spectral shapes for various combinations of  $\gamma_+$  and  $\gamma_-$  for isotropic particles of specific energies  $E_+$  and  $E_-$  as a function of photon energy (see also Appendix A). In general, as already considered from energy conservation, Eq. (2.60), the spectra show peaks at  $E_1 = E_+ = \gamma_+ m_e$  and  $E_2 = E_- = \gamma_- m_e$ , where the intensity is also the same for both peaks. The spectrum is always symmetrical about the point  $E = E_{tot}/2$  in this case, and the general shape from peak to peak is described by the angle-dependence of the annihilation cross-section.

When one particle, say the electron, is at rest, this represents the case for cosmic-ray positrons of relativistic energies interacting with (almost stationary) electrons of the ISM. The spectral emissivity for this case, i.e.  $\gamma_+ = \gamma_r$ ,  $\gamma_- = 1$ , reduces to

$$\overline{\frac{d\sigma_{\gamma\gamma}}{dE}}(E, \gamma_r, 1) = \frac{c\pi r_e^2}{\beta_r \gamma_r^2} \left( \frac{-(3 + \gamma_r)/(1 + \gamma_r) + (3 + \gamma_r)/E - 1/E^2}{[1 - E/(1 + \gamma_r)]^2} - 2 \right), \quad (2.74)$$

for energies  $\frac{1}{2}(\gamma_r(1 - \beta_r) + 1) \leq E \leq \frac{1}{2}(\gamma_r(1 + \beta_r) + 1)$  (e.g. Stecker 1969; Svensson 1982; Aharonian & Atoyan 2000; Beacom & Yüksel 2006). This was as already estimated from Eq. (2.60), as  $\frac{1}{2}(\gamma_r(1 \mp \beta_r) + 1) \xrightarrow{\gamma_r \gg 1} \frac{1}{2}m \vee \frac{1}{2}m + \gamma_r m$ , and is illustrated in Fig. 2.14a. For highly relativistic positrons, the broadband spectral behaviour of Eq. (2.74) follows approximately  $E^{-1}$ . In this special case, the spectral peaks, shown in the inset, move outward to lower and higher energies, respectively, by  $\approx 0.5m_e$ .

For the case  $\gamma_+ = \gamma_- = \gamma$ , shown in Fig. 2.14b, the spectrum shows only one peak at the symmetric centre  $E_{tot}/2$ . The spectra show a certain broadening around the peak which originates from the angle-averaging of the emissivity. For the special case  $\gamma \approx 1$ , i.e. annihilation "at rest", the spectrum can be described by a Dirac-delta function.

#### 2.4.2.3 Gamma-Ray Spectra from Positronium Annihilation

Para-positronium has a finite lifetime,  $\tau_{pPs}$ , so there will be a natural line width,  $\Delta E$ , associated with it in the form of a Lorentzian-shaped line profile. This follows directly from Heisenberg's uncertainty principle (Heisenberg 1927):

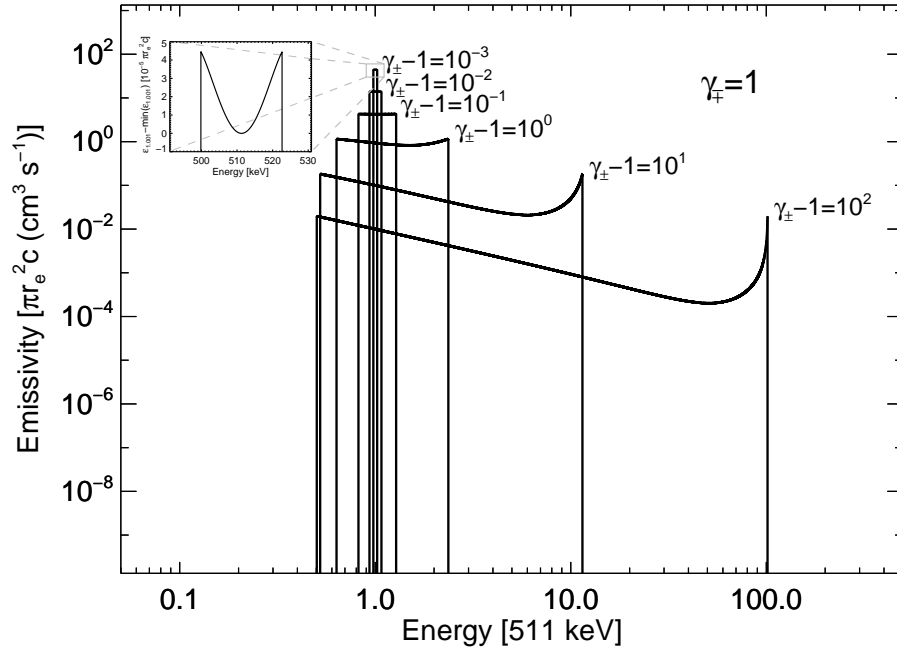
$$\Delta E = \frac{\hbar}{\tau}. \quad (2.75)$$

For p-Ps, the natural line width is  $\Delta E_{pPs} \approx 5.26 \mu\text{eV}$  ( $= 1.27 \text{ GHz}$ ;  $= 23.58 \text{ cm}$ )<sup>6</sup>.

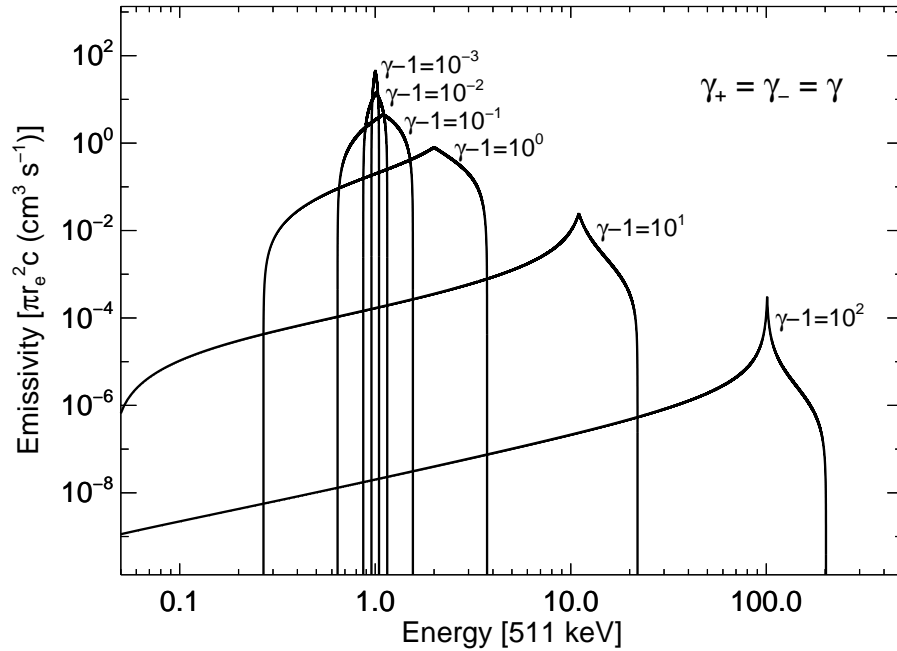
The three photon spectrum from the decay of o-Ps extends from zero to an energy of 511 keV, or almost zero energy, Sec. 2.4.1. The first to calculate the o-Ps annihilation spectrum were Ore & Powell (1949), starting from Fermi's Golden Rule (Fermi 1950), and considering all possible quantum-mechanical intermediate states. The differential cross section for three-photon annihilation, Eq. (2.48), then occurs as an intermediate step. The number of photons per unit time in the energy interval  $[E, E + dE]$  is calculated by integrating over all solid angles, and over energies of the other photons (Ore & Powell 1949),

$$\begin{aligned} \frac{dF_{oPs}}{dE}(E) &= 2 \left[ \frac{E(m - E)}{(2m - E)^2} - \frac{2m(m - E)^2}{(2m - E)^3} \ln \left( \frac{m - E}{m} \right) + \right. \\ &\quad \left. + \frac{2m - E}{E} + \frac{2m(m - E)}{E^2} \ln \left( \frac{m - E}{m} \right) \right], \end{aligned} \quad (2.76)$$

<sup>6</sup>State-of-the-art Germanium detectors, like in SPI (Sec. 3.2.2), have instrumental spectral resolutions of few keV, depending on the energy, and hence the natural line width of para-positronium, and any other similarly short-lived state or transition (see e.g. <sup>26</sup>Al in Sec. 5.1.1.2), will be negligibly small.



(a) Annihilation in flight spectra from Eq. (2.74) for stationary particles hit by isotropic and mono-energetic populations of anti-particles,  $\gamma_{\pm} = \gamma_r$ ,  $\gamma_{\mp} = 1$ , normalised to an emissivity of  $\pi r_e^2 c$ . Shown are spectra (emissivity  $\epsilon_{\gamma_{\pm}}$ ) for different values of  $\gamma_{\pm}$ , representing the total energy of a positron (electron) annihilating with an electron (positron) at rest,  $\gamma_{\mp} = 1$ . As shown in Eq. (2.60), the low- and high-energy cut-off in the spectra from highly relativistic particles is at  $E \approx 0.5$  and  $\approx \gamma_{\pm} + 0.5$ , respectively. For non-relativistic particles, the spectrum shows a rather flat top (see zoomed inset), which is, however, still symmetric and similar to other spectra.



(b) Annihilation in flight spectra from Eq. (2.72) for isotropic and equally energetic populations of electrons and positrons,  $\gamma_+ = \gamma_- = \gamma$ , normalised to an emissivity of  $\pi r_e^2 c$ . Shown are spectra for different values of  $\gamma$ , representing the total (rest mass + kinetic) energy of one particle as a function of photon energy. Each spectrum is symmetric about the peak at  $E = \gamma$  where the two photons share equally the total energy of electron and positron, respectively. The apparent broadening occurs due to the angle-dependence of the annihilation cross section.

Figure 2.14: Annihilation in flight spectra for isotropic and mono-energetic populations of electrons and positrons.

where  $m = m_e$  is the electron mass.

The theoretical gamma-ray spectra from the annihilations of p- and o-Ps, respectively, are shown in Fig. 2.15.

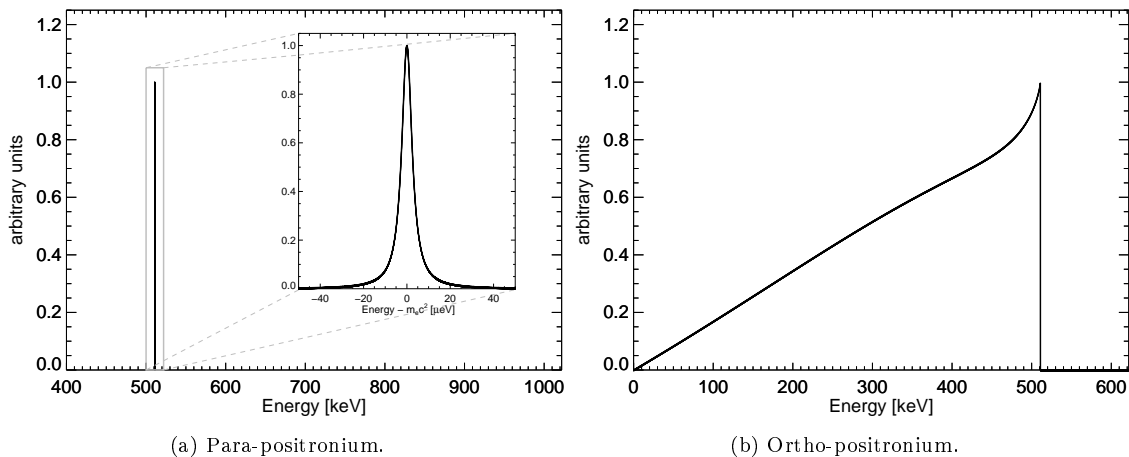


Figure 2.15: Expected photon spectra as a function of energy from the annihilation of para-positronium (left panel) and ortho-positronium (right panel). The para-positronium line appears as a delta-peak like function on the keV energy scale. The inset is zooming into the  $\mu\text{eV}$  scale to illustrate the natural line width of para-positronium. The ortho-positronium spectrum reaches from almost zero energy to 511 keV, distributed according to Eq. (2.76).

### 2.4.3 Environmental and Geometrical Influences

Positrons may be created at almost zero kinetic energy to several GeV. After leaving the local environments of their sources, further acceleration in interstellar space, by diffusive shock acceleration (Baade & Zwicky 1934; Aharonian et al. 2001), for example, may occur. If they escape the astrophysical source where they have been produced, and do not annihilate directly there, they either thermalise with the ISM, or annihilate. The thermalisation is governed by various possible interactions of positrons with the ambient medium, which is accompanied by a slowing-down from large kinetic energies down to the temperature of the ISM. During the loss of kinetic energy via electromagnetic interactions, the positrons can also directly annihilate with free or bound electrons of the ISM, or form Ps in flight.

This description includes microphysics of positrons interacting with electrons, ions, atoms, molecules, solid dust grains, photons, and magnetic fields. These components are the basic constituents of the ISM, and, depending on the initial energy of the positron, have different impacts on the kinetic energy loss. The resulting spectral shapes do also change, depending on the specific annihilation path, and the environmental conditions, such as temperature  $T$ , density  $n$ , ionisation fraction  $x$ , magnetic field  $B$ , or radiation energy density  $u_{rad}$ .

In the following, the electromagnetic energy losses of positrons, depending on the positron energy, will be discussed and details about the resulting spectra, especially for the annihilation line shape, will be given.

### 2.4.3.1 Positron Energy Losses

Positrons can lose kinetic energy by Coulomb scatterings with free electrons or inelastic interactions with atoms or molecules. The non-relativistic differential cross section for Coulomb-scattering is given by the Rutherford scattering formula

$$\frac{d\sigma}{d\Omega} = \left( \frac{\alpha^2}{2mc^2\beta^2} \right)^2 \frac{1}{\sin^4(\frac{\theta}{2})} \quad (2.77)$$

$$\frac{d\sigma}{dE} = \frac{2\pi\alpha^2}{E^2mc^2\beta^2}, \quad (2.78)$$

where  $\theta$  is the scattering angle in the LAB frame (e.g. Landau & Lifshitz 1975). The energy loss during a single scattering in units of eV cm<sup>2</sup> can be calculated by

$$dE = \int_{E_{min}}^{E_{max}} E d\sigma = \frac{2\pi\alpha^2}{mc^2\beta^2} \ln \left( \frac{E_{max}}{E_{min}} \right), \quad (2.79)$$

in which  $E_{min}$  ( $E_{max}$ ) is the minimum (maximum) transferred energy of the scattering particle (Landau & Lifshitz 1975; Olive & Particle Data Group 2014). The important astrophysical issue is then the energy that a particle with velocity,  $v = \beta c$ , loses over time. Multiplying Eq. (2.79) by the density of the scattering target particles,  $n$ , leads to the "stopping-power" for charged particles,  $-\left(\frac{dE}{dx}\right)$ . By multiplication with the velocity of the charged particles, the energy loss rate becomes

$$-\left(\frac{dE}{dx}\right) = -\frac{1}{v} \left(\frac{dE}{dt}\right). \quad (2.80)$$

This heuristic derivation reveals the general analytic form of the energy loss rate for charged particles by Coulomb scattering. For energies between  $\beta\gamma \approx 0.1$  and  $\approx 1000$ , the Coulomb scattering energy loss of a particle with charge  $z$  in a medium composed of particles with charge  $Z$  and relative atomic mass  $A$  is given by the Bethe-Bloch formula

$$-\left\langle \frac{dE}{dx} \right\rangle = 4\pi N_A r_e^2 m_e c^2 z^2 \frac{Z}{A} \frac{1}{\beta^2} \left[ \frac{1}{2} \ln \left( \frac{2m_e c^2 \beta^2 \gamma^2 E_{max}}{I^2} \right) - \beta^2 - \frac{\delta(\beta\gamma)}{2} \right], \quad (2.81)$$

where  $N_A = 6.02214129(27) \times 10^{23}$  mol<sup>-1</sup> is Avogadro's number,  $I$  is the mean excitation potential (determined experimentally),  $E_{max} = \frac{2m_e c^2 \beta^2 \gamma^2}{1+2\gamma m_e/M+(m_e/M)^2}$  is the maximum energy that can be transferred in a single collision, and  $\delta(\beta\gamma)$  describes a density dependent effect on the stopping-power of the material (Landau & Lifshitz 1975; Olive & Particle Data Group 2014).

In a (partially) neutral ISM, positrons transfer most of their kinetic energy by ion-

isation losses during interactions with atomic electrons. Similar to the Bethe-Bloch formula, Eq. (2.81), Berger & Seltzer (1964) calculated the ionisation energy losses for electrons or positrons passing through matter with electron density  $n_e$ , charge number  $Z$ , and relative atomic mass  $A$ ,

$$\frac{dE}{dx} = 2\pi r_e^2 m_e c^2 n_e \frac{1}{\beta^2} \left[ \ln \left( \frac{\beta^2 \gamma^2 (\gamma - 1)}{2(I/m_e c^2)^2} \right) + F^\pm(\beta\gamma) - \delta(\beta\gamma) \right]. \quad (2.82)$$

Equation (2.82) combines the effects of Møller- ( $e^- + e^- \rightarrow e^- + e^-$ ) and Bhabha-scattering ( $e^+ + e^- \rightarrow e^+ + e^-$ ) in the factors  $F^-(\beta\gamma)$  and  $F^+(\beta\gamma)$ , respectively (Møller 1932; Bhabha 1936; Berger & Seltzer 1964; Landau & Lifshitz 1975; Olive & Particle Data Group 2014, see also Appendix B). Comparing Eq. (2.82) for positrons with the Bethe-Bloch formula, Eq. (2.81), the maximum energy that can be transferred by one positron equals its total kinetic energy,  $E_{max}^+ = (\gamma - 1)m_e c^2$ . For a fully ionised plasma of density  $n_e$  in the ISM, i.e. 90% H and 10% He by number, and at rest with respect to a fast-moving positron, the positron loses energy via the interaction with that plasma according to (Landau & Lifshitz 1975)

$$\frac{dE}{dt} = -7.62 \times 10^{-9} \frac{n_e}{\beta} \left[ \ln \left( \frac{\gamma}{n_e} \right) + 73.4 \right] \frac{\text{eV}}{\text{s}}. \quad (2.83)$$

If the positron is not fast compared to the plasma temperature ( $E_{kin}^+ \lesssim 10kT$ ), the energy loss rate depends also on the plasma temperature and can be expressed as

$$\frac{dE}{dt} = -1.7 \times 10^{-8} \frac{n_e}{\beta} \ln(\Lambda) F(\theta) \frac{\text{eV}}{\text{s}}, \quad (2.84)$$

where  $\ln(\Lambda) = \frac{\sqrt{kT/4\pi n_e e^2}}{\max(2e^2/mu^2, \hbar/mu)}$  is the Coulomb-logarithm, cf. Eq. (2.79),  $u = \sqrt{\frac{2E}{m} - \frac{8kT}{\pi m}}$ , and  $F(\theta)$  is a function depending on the energy  $E$  of the positron with respect to the temperature  $T$  of the plasma,  $\theta = \frac{E}{kT}$  (Murphy et al. 2005).

At higher kinetic energies, electrons and positrons mainly lose their energies by bremsstrahlung, i.e. the emission of a real photon during an electromagnetic interaction, either with (screened) nuclei or with other electrons or positrons. Bremsstrahlung is related to pair production in the field of a nucleus (Sec 2.2.4.2) by interchanging one of the outgoing leptons with the incoming photon in Fig. 2.4. The cross section for the emission of a photon with energy  $E_\gamma$  from the interaction of an electron (positron) with a nucleus (antinucleus) of charge  $Z$  is given by the Bethe-Heitler formula (Bethe & Heitler 1934; Sauter 1934; Heitler 1954),

$$\frac{d\sigma^{NR}}{dE_\gamma} = \frac{16}{3} \frac{\alpha Z^2 r_e^2}{E_\gamma \beta^2} \ln \left( \frac{\beta + \beta'}{\beta - \beta'} \right), \quad (2.85)$$

$$\frac{d\sigma^{UR}}{dE_\gamma} = 4 \frac{\alpha Z^2 r_e^2}{E_\gamma} \left( 1 + \left( \frac{\gamma'}{\gamma} \right)^2 - \frac{2}{3} \frac{\gamma'}{\gamma} \right) \left( \ln \left( \frac{2m\gamma\gamma'}{E_\gamma} \right) - \frac{1}{2} \right). \quad (2.86)$$

Here,  $\gamma' = (1 - \beta'^2)^{-1/2}$  is the Lorentz-factor of the electron after the photon emission. The photon energy  $E_\gamma$  is at the same time also the energy lost by the electron, and by integration yields the energy loss rate of the electron for electron-nucleus bremsstrahlung. In the case of significant screening, the bremsstrahlung formula of Tsai (1974) should be used, which also includes the improved wave functions beyond the Born approximation (cf. Elwert factor (Elwert 1939; Haug & Nakel 2004)). The  $(e^- - e^-)$ ,  $(e^+ - e^-)$ , or  $(e^+ - e^+)$  bremsstrahlung calculations do not have to consider those screening effects and cross sections and energy losses can be derived straight-forwardly. In the high-energy limit, the total  $(e^\pm - e^\pm)$  cross section is given by

$$\sigma_{BRee} = 4\alpha r_e^2 \ln(2\gamma). \quad (2.87)$$

However, in the case of positron-nucleus bremsstrahlung, there is a difference in the cross section compared to electron-nucleus bremsstrahlung, because of the opposite sign of the positron interacting with the Coulomb potential of the positively charged nucleus screened by negative electrons. At very high energies, there is almost no difference in the cross sections, but low-energy positrons cannot go deep into the repulsive part of the central potential and therefore bremsstrahlung is strongly suppressed (Haug & Nakel 2004).

The energy dependence in Eqs. (2.85) and (2.86) is essentially given by  $E_\gamma^{-1}$ , and hence the energy loss rate for positrons interacting with a neutral gas is approximately proportional to the total energy of the positron and the gas density  $n_X$ , and only slightly depends on the composition of the gas,

$$\frac{dE}{dt} = A_X n_X \gamma \frac{\text{eV}}{\text{s}}. \quad (2.88)$$

Here,  $A_X = -4.1 \times 10^{-10}$  for  $X = \text{H}$  and  $-1.1 \times 10^{-9}$  for  $X = \text{He}$  (Ginzburg 1979). In the case without screening, i.e. in a fully ionised plasma, the logarithmic terms in Eqs. (2.85) and (2.86) become important. The energy loss of positrons in such a plasma can be approximated by

$$\frac{dE}{dt} = -3.6 \times 10^{-11} Z(Z+1) n_X \gamma \left[ \ln(2\gamma) - \frac{1}{3} \right] \frac{\text{eV}}{\text{s}}, \quad (2.89)$$

in which also the electron-positron collisions ( $Z^2 \rightarrow Z(Z+1)$ ) are taken into account (Ginzburg 1979).

Positrons in interstellar space will also experience the magnetic and radiation fields of the Galaxy. Thus, energy loss may also occur from synchrotron radiation or inverse Compton scattering. The radiation loss of an accelerated charged particle<sup>7</sup> is given by the relativistic Larmor formula

$$-\left(\frac{dE}{dt}\right)_{rad} = \frac{q^2 |\vec{r}|^2 \gamma^4}{6\pi\epsilon_0 c^3}, \quad (2.90)$$

where  $q$  is the charge of the particle and  $|\vec{r}|$  is the acceleration which the particle experiences (Longair 1992). If a positron moves with a constant velocity  $\vec{v} = \frac{\beta}{c}$  in a uniform magnetic field of strength  $B$  at an angle  $\alpha$  to the field lines (pitch angle), the relativistic equation of motion provides the acceleration due to the Lorentz force,  $|\vec{r}| = \frac{e\beta B}{\gamma m} \sin(\alpha)$ , and the energy loss due to synchrotron radiation is given by

$$\left(\frac{dE}{dt}\right)_{syn} = -\frac{e^4 \beta^2 \gamma^2 B^2}{6\pi\epsilon_0 m^2 c} \sin^2(\alpha) = -9.9 \times 10^{-16} \beta^2 \gamma^2 B^2 \sin^2(\alpha) \frac{\text{eV}}{\text{s}}. \quad (2.91)$$

The positron will propagate in the direction of the magnetic field<sup>8</sup> lines, and spiralling around them with an orbit equal to the Larmor (gyro) radius,  $r_g = \frac{m\beta \sin(\alpha)c}{qB}$  (e.g. Rybicki & Lightman 1979; Longair 1992). Energy losses due to the emission of synchrotron radiation are therefore only efficient if the magnetic field is large, or if the particle is highly relativistic. Using the definition of the Poynting vector,  $\vec{S} = \frac{1}{\mu_0}(\vec{E} \times \vec{B})$ , to describe the energy flux rate per unit area, Eq. (2.91) can be generalised towards the energy density of a field,

$$\left\langle \frac{dE}{dt} \right\rangle_{syn} = -\frac{2}{3} \frac{e^4 \beta^2 \gamma^2 B^2}{6\pi\epsilon_0 m^2 c} = \frac{4}{3} \sigma_T c \beta^2 \gamma^2 u_{mag}. \quad (2.92)$$

In Eq. (2.92),  $\sigma_T = \frac{8\pi}{3} r_e^2$  is the Thomson cross section,  $u_{mag} = \frac{1}{2} \epsilon_0 B^2 c^2 = \frac{S}{c}$  is the energy density of the magnetic field; here, averaging over the pitch angle  $\alpha$  has been included.

In analogy to the energy loss by synchrotron radiation, the energy density of the photon field, as viewed from the instantaneous rest-frame of the positron, has to be determined to obtain a measure for the energy loss rate due to inverse Compton scattering of high-energy positrons with low-energy photons ( $E_{kin}^+ \gg E_\gamma$ ). The Lorentz transformation of the flux density,  $u_{rad} = NE_\gamma$ , of mono-energetic photons with photon-density  $N$ , as seen from a stationary positron towards a relativistic positron, yields

$$u'_{rad} = [\gamma(1 + \beta \cos(\alpha))]^2 u_{rad}. \quad (2.93)$$

The energy loss of a positron encountering an isotropic radiation field consequently

<sup>7</sup>This can be considered as an alternative description to the cross section formalism.

<sup>8</sup>In the right term of Eq. (2.91),  $B$  is to be given in units of  $\mu G$ .

reads (e.g. Rybicki & Lightman 1979)

$$\left\langle \frac{dE}{dt} \right\rangle_{IC} = -\frac{4}{3} \sigma_T c \beta^2 \gamma^2 u_{rad}. \quad (2.94)$$

In general, also the emission of Cherenkov radiation by charged particles in media would contribute to the energy loss. But since the refractive index of interstellar space is very close to 1.0, this can be ignored here, even for large distances.

In Fig. 2.16, the radiation losses of positrons are shown as a function of energy for typical values of the interstellar medium.

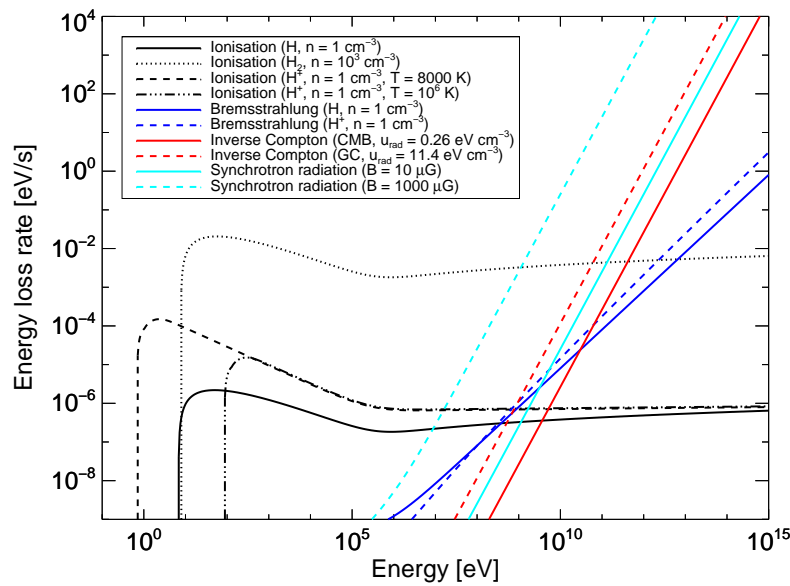


Figure 2.16: Energy losses of positrons in interstellar space as a function of kinetic energy for different values of typical ISM conditions. In general, for an ISM particle density of  $1 \text{ cm}^{-3}$ , whether ionised or not, ionisation losses dominate until the kinetic energy is of the order of the rest mass energy of the positron. For higher energies, synchrotron, bremsstrahlung, and inverse Compton losses mainly reduce the kinetic energy. Apart from the initial kinetic energy of the positron, the magnitude of bremsstrahlung losses is mainly influenced by the particle density, synchrotron radiation mainly depends on the strength of the magnetic field, and inverse Compton losses are scaled by the energy density of the radiation field. Scaling these parameters up or down will have an enormous impact on the energy loss of high-energy positrons. A typical value of the magnetic field in a spiral galaxy like the Milky Way is  $\approx 10 \mu\text{G}$ , although locally, higher values are possible, especially near stars. On their flight through the ISM, positrons experience different (superposed) radiation fields, like the omnipresent cosmic microwave background with a low energy density of  $0.26 \text{ eV cm}^{-3}$ , or a higher energy density like in the galactic centre (GC) with  $11.4 \text{ eV cm}^{-3}$  (Moskalenko et al. 2006). Bremsstrahlung and especially ionisation losses depend on the particle density which can change dramatically in the various phases of the ISM (see Sec. 2.4.3.4), from cold ( $T \approx 10 - 20 \text{ K}$ ) but dense ( $n \approx 10^2 - 10^6 \text{ cm}^{-3}$ ) molecular ( $\text{H}_2$ ) clouds, over warm ( $T \approx 6000 - 10000 \text{ K}$ ) neutral and warm ionised media with densities around  $1 \text{ cm}^{-3}$ , up to the hot and ionised phase ( $T \approx 10^6 \text{ K}$ ,  $n \approx 10^4 - 10^{-2} \text{ cm}^{-3}$ , not shown in graphic), so that in high-density regions, positrons can rapidly lose their kinetic energy.

### 2.4.3.2 Annihilation Spectra from Cosmic-Ray Positrons

Assuming the positrons are injected into the ISM (particle density  $n_X$ ) at an initial energy  $E_0$ , all positrons lose the same amount of energy for the same distance. The relative number of positrons not surviving from an initial energy at a distance  $dx$  (i.e. they annihilated in flight at an energy in the interval  $[E, E + dE]$ ), is given by (e.g. Beacom & Yüksel 2006)

$$\frac{dN(E)}{N(E)} = n_H \sigma_{\gamma\gamma}(E) dx = n_X \sigma_{\gamma\gamma}(E) \left| \frac{dE}{dx} \right|, \quad (2.95)$$

where  $\left| \frac{dE}{dx} \right|$  is the sum of all energy losses from Sec. 2.4.3.1. At injection energies  $\gtrsim 100$  MeV, mainly ionisation and Coulomb interactions are important. From Eq. (2.95), the annihilation probability for a positron at energy  $E$ , cf. Eq. (2.41), can be derived by formal integration. This probability is used as a weighting factor for the general annihilation-in-flight spectrum, Eq. (2.74),

$$\frac{dF_{CR,AIF}}{dE} \propto n_x \int_E^{E_0} \frac{1}{2} P(E_0, E') \frac{d\sigma_{\gamma\gamma}}{dE'}(E', \gamma_r, 1) \left| \frac{dE'}{dx} \right|. \quad (2.96)$$

This is shown in Fig. 2.17 for different values of initial positron energy. In this description, the probability serves as the distribution function of positrons, cf. Eq. (2.71). As the high-energy positrons are cooled down "quickly", the symmetric spectrum degrades towards an asymmetric, power-law like shape, still retaining the  $E^{-1}$  behaviour between the peak, which is still below 511 keV, and the high-energy cut-off of the spectrum.

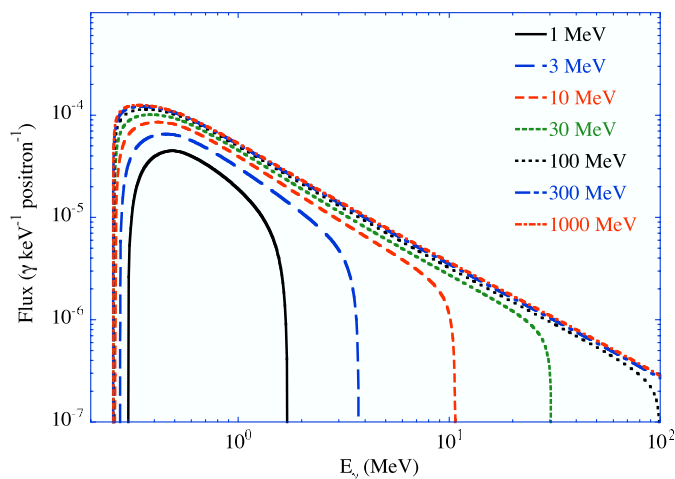


Figure 2.17: Cosmic-ray positron annihilation in flight spectrum for different values of the initial kinetic positron energy. From Prantzos et al. (2011).

### 2.4.3.3 Annihilation Spectra from Pair-Plasma

Particle velocities in an electron-positron pair-plasma are described a relativistic Maxwell-Boltzmann distribution (also called Maxwell-Jüttner distribution)

$$f(\gamma)_{MJ} = \frac{\gamma^2 \beta}{\theta K_2(1/\theta)} \exp\left(-\frac{\gamma}{\theta}\right), \quad (2.97)$$

where  $\theta = \frac{kT}{m_e c^2}$  is the dimensionless temperature of the pair plasma, and  $K_2(x)$  is the modified Bessel function of second kind. Such matter-antimatter plasma may be created in environments opaque to high-energy gamma-ray photons, i.e. if the

optical depth of photon-photon pair production is of the order of unity or larger,  $\tau_{\gamma\gamma} \approx n_{\gamma}\sigma_{\text{pair}}r \stackrel{!}{\geq} 1$ . High-energy gamma-ray photons ( $E \gtrsim 1$  MeV) with a photon density  $n_{\gamma}$  may react with ambient low-energy photons in a confined region of size  $r$ , and can efficiently create electron-positron pairs, building a pair plasma. In equilibrium, the photon-number density may be estimated from the energy density of a photon field with photon energies of order  $m_e c^2$  on average,  $n_{\gamma} = \frac{u_{\text{rad}}}{m_e c^2} = \frac{S}{m_e c^3}$ , cf. Eq. (2.93). The Poynting flux associated with this energy density,  $S$ , measures the power  $P$  per unit area,  $n_{\gamma} \propto \frac{P}{r^2 m_e c^3}$ , so that photon-photon pair absorption is efficient if

$$\tau_{\gamma\gamma} \approx n_{\gamma}\sigma_{\text{pair}}r \propto \frac{P\sigma_{\text{pair}}r}{r^2 m_e c^3} \propto \frac{P}{r} \frac{\sigma_{\text{pair}}}{m_e c^3} \stackrel{!}{\geq} 1. \quad (2.98)$$

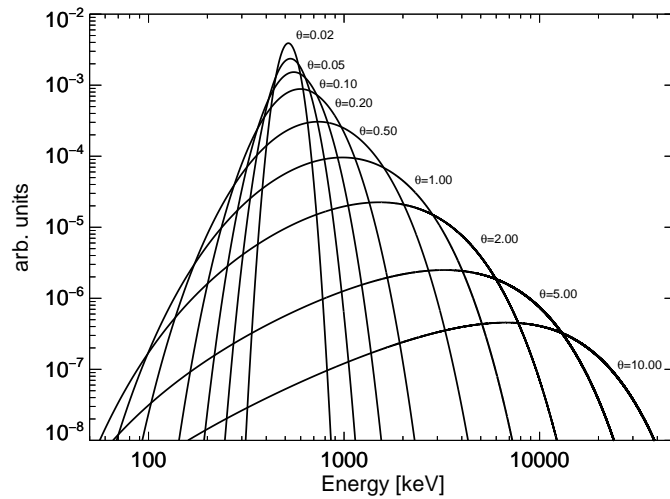
For a source of given power  $P$  (or equivalent to a luminosity  $L$ ), the region in which photon-photon pair absorption is efficient must be small, since  $\tau_{\gamma\gamma} \propto r^{-1}$ . The gamma-gamma pair production cross section,  $\sigma_{\text{pair}}$ , divided by  $m_e c^3$  is of the order of  $10^{-29} \frac{\text{cm s}}{\text{erg}}$ . Thus, the fraction  $\frac{L}{r}$  must be of the order  $10^{29} \frac{\text{erg}}{\text{cm s}}$ , or, in other words, the "compactness parameter"  $l \equiv \frac{L}{r} \frac{\sigma_T}{m_e c^3}$  must be of the order 10 to fulfil the requirement for efficient pair production.

If particles of the pair plasma now annihilate with each other, the spectral shape is given by integrating over their velocity distribution functions, and the differential cross section of pair annihilation (Eq. (2.71), Zdziarski 1980; Aharonian & Atoyan 1981; Ramaty & Meszaros 1981; Svensson 1982; Yahel 1982; Svensson 1983). Svensson (1983) used a detailed balance approach by considering the pair creation and pair annihilation reaction in an equilibrium situation ( $e^+ + e^- \rightleftharpoons \gamma + \gamma$ ) to calculate the spectrum. This can be expressed as a single integral

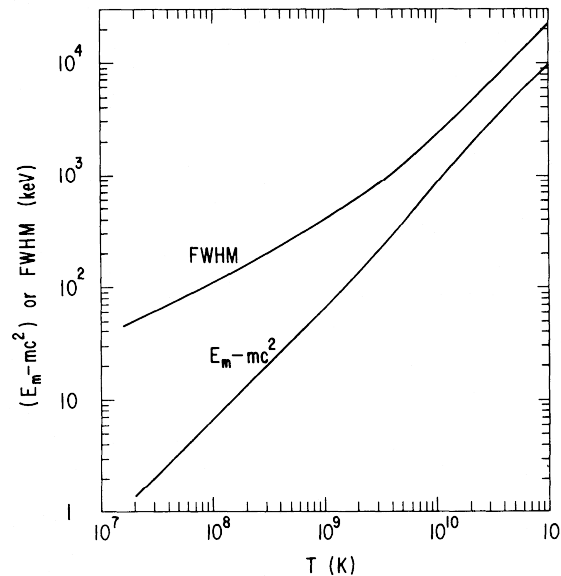
$$\frac{dn}{dt}(x, \Theta)dx = n_+ n_- c dx \frac{2}{\Theta K_2(1/\Theta)^2} \exp\left(-\frac{x}{\Theta}\right) \int_1^{\infty} ds 2(s-1) \sigma_{\gamma\gamma}(s) \exp\left(\frac{s}{x\Theta}\right), \quad (2.99)$$

where  $x = \frac{E}{m_e c^2}$  is the dimensionless photon energy, and  $s = \gamma_{cm}^2$  with  $\gamma_{cm}$  being the particle Lorentz factors in the COM frame. Svensson et al. (1996) derived an excellent approximation formula which can be used for a broad range of plasma temperatures,  $\theta$ , and a wide range of photon energies. This thermal pair annihilation (TPA) spectrum for different values of the pair plasma temperature is shown in Fig. 2.18a. It can be seen that the 511 keV "line" is broadened, depending on the temperature, as expected from thermal Doppler broadening (see Secs. 2.4.3.4 and 2.4.3.5), but the lines are also Doppler blue-shifted. For high temperatures, the spectrum is almost entirely determined by the convolution of the pair annihilation cross section with the particle distribution. Both functions are highly asymmetric, which leads to the dispersion-dominated behaviour of the spectrum at relativistic energies. In Fig. 2.18b, the peak position and the width (FWHM,  $\Delta$ ) of the TPA feature are shown as a function of the pair plasma temperature, respectively. For low temperatures ( $kT \ll m_e c^2$ ; i.e.  $T \ll 5 \times 10^9$  K), the width closely follows thermal Doppler broadening,  $\Delta^{NR} \approx 1.1\sqrt{T_4}$  keV, where  $T_4$  is the plasma temperature in units of

$10^4$  K, see Sec. 2.4.3.4. For high temperatures ( $kT \gg m_e c^2$ ), the width linearly increases with temperature,  $\Delta^{UR} \approx 1.2kT$ . The peak of the TPA feature is always blue-shifted with respect to the laboratory energy of 511 keV, and furthermore is always below the mean energy of the photons. This again reflects the asymmetric distribution functions and the annihilation cross section. For  $kT \ll m_e c^2$  and  $kT \gg m_e c^2$ , the peak energy can be approximated by  $E_{peak}^{NR} \approx m_e c^2 + \frac{3}{4}kT$  and by  $E_{peak}^{UR} \approx 1.2kT$  (see also Zdziarski 1980; Aharonian & Atoyan 1981; Ramaty & Meszaros 1981).



(a) Thermal pair-plasma spectrum.



(b) FWHM and peak position of the TPA feature.

Figure 2.18: Thermal pair-plasma annihilation spectrum for different values of the dimensionless plasma temperature  $\theta$  (a) as calculated from Eq. 2.99, as well as the peak and width (b) of the annihilation feature as a function of  $\theta$ , taken from Ramaty & Meszaros (1981).

#### 2.4.3.4 Spectra from Annihilation in Interstellar Gas

Positron trajectories in interstellar space may pass through different phases of the ISM. For simplicity, a phase may be described by its temperature  $T$ , particle number density  $n$ , and ionisation state  $x$ . The annihilation of positrons in these different

Phase	$T$	$n_X$	$x$	$M$	$h$
Molecular clouds	10-20	$10^2$ - $10^6$	$\leq 10^{-4}$	1.3-2.5	80
Cold atomic	50-100	20-50	$4 \times 10^{-4}$ - $10^{-3}$	} $\geq 6.0$	100-300
Warm atomic	6000-10000	0.2-0.5	0.007-0.05		300-400
Warm ionised	$\sim 8000$	0.2-0.5	0.6-0.9	$\geq 1.6$	1000
H II regions	$\sim 8000$	$10^2$ - $10^4$	1		70
Hot ionised	$\sim 10^6$	$\sim 0.0065$	1		1000-3000

Table 2.4: Descriptive parameters of the interstellar medium. The temperature  $T$  is given in K, the particle number density  $n_X$  in  $\text{cm}^{-3}$ , the ionisation fraction as  $x = \frac{n_e}{n_e + n_X}$ , the total mass of a component in the Milky Way  $M$  in units of  $10^9 M_\odot$ , and the scale-height  $h$  in pc. Adopted from Ferrière (2001).

phases will create different spectral shapes, especially for the annihilation line (and to some extent the o-Ps continuum). An overview of the different ISM phases is given in Tab. 2.4. Such superpositions are difficult to disentangle, and often it is assumed, that a single "average" phase can be assigned (see also Sec. 4.6.6).

In general, the width - or more accurate the shape - of the annihilation line is determined by the velocity distribution of the electron-positron pair at the instant of annihilation into two photons, as the Doppler-shift of many such processes lead to an actual broadening (Drachman 1983).

If positrons are in thermal equilibrium with a gas of temperature  $kT \ll m_e c^2$ , their velocities follow a Maxwell-Boltzmann-distribution,

$$f(v) = \sqrt{\left(\frac{m_e}{2\pi kT}\right)^3} 4\pi v^2 \exp\left(-\frac{m_e v^2}{2kT}\right), \quad (2.100)$$

so that the spectral shape of direct annihilation of thermal positrons with free electrons, Eq. (2.71), is represented by a Gaussian

$$\frac{1}{N_\gamma} \frac{dN_\gamma}{dE}(E) \propto \exp\left(-\frac{(E - m_e c^2)^2}{kT m_e c^2}\right). \quad (2.101)$$

This leads to a line width (FWHM) of  $\Delta^{DA} \approx 1.105\sqrt{T_4}$  keV (Crannell et al. 1976; Murphy et al. 2005). If the gas is not too hot ( $kT \lesssim 100$  eV, see Sec. 2.3.2), Ps can be formed by thermal positrons with free electrons by radiative recombination. The decay of the  $^1\text{Ps}$  (p-Ps) state will obtain the same spectral shape, and thus the same line width as for direct annihilation.

If Ps is formed by charge exchange, the velocities of the formed para-positronia are not Maxwell-Boltzmann-distributed any more, and thus the line shape is not Gaussian. At low energies, annihilation is isotropic, as is charge exchange. The resulting Ps energies follow a flat distribution, extending from 0 to the maximum Ps energy (Stecker 1971; Murphy et al. 2005). Consequently, the line shapes calculated from a Maxwellian plasma also show flattened tops, depending on the species, and line broadenings due to the temperature.

The fraction of Ps formed in flight can be expressed as a function of ionisation, density, and temperature, and thus depends strongly on the conditions in the ISM.

Derivations from Monte Carlo simulations, considering all possible energy losses, and different environments, by several authors (Bussard et al. 1979; Guessoum et al. 2005; Murphy et al. 2005), found consistent results for the fraction of positrons which form Ps in flight. This is shown in Fig. 2.19.

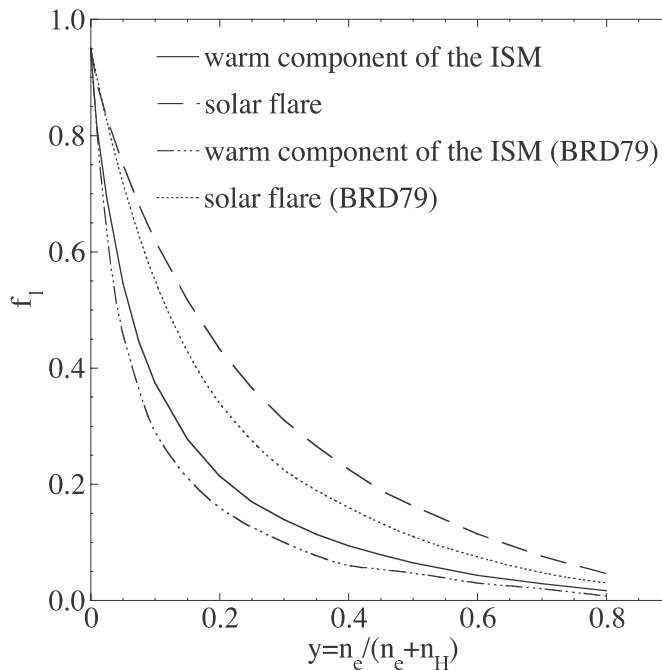


Figure 2.19: Fraction of positrons forming positronium in flight,  $f_1$ , by charge exchange with atomic hydrogen as a function of ionisation fraction,  $y$ , in either a warm ISM component ( $n_e = 0.1 \text{ cm}^{-3}$ ,  $T_e = 8000 \text{ K}$ ), or a solar flare like environment ( $n_e = 5 \times 10^{13} \text{ cm}^{-3}$ ,  $T_e = 11600 \text{ K}$ ); from Guessoum et al. (2005). The results are compared to similar simulations from Bussard et al. (1979) (BRD79). The fraction  $f_1$  is equivalent to 1.0 minus the fraction of positrons annihilated in flight.

Table 2.5 summarises characteristic line widths of the different ISM phases and conditions by assuming Gaussian shapes, although the annihilation line shapes are not Gaussian altogether.

Process / medium	Cold molecular	Warm atomic	Warm ionised	Hot ionised
CEiF / H	5.8	5.8	-	-
CEiF / H <sub>2</sub>	6.4	-	-	-
CEiF / He	7.5	7.4	8.7	-
CEaT / H	-	1.16	-	-
CEaT / H <sub>2</sub>	-	-	-	-
CEaT / He	-	1.22	1.22	-
DA / H	1.56	1.56	-	-
DA / H <sub>2</sub>	1.71	-	-	-
DA / He	2.50	2.50	2.50	-
DA / e <sup>-</sup>	-	-	0.98	11
RR / e <sup>-</sup>	-	-	0.98	11

Table 2.5: Annihilation line widths in different phases of the interstellar medium, parametrised as FWHM of symmetric Gaussians in units of keV. The processes abbreviations are Charge Exchange in Flight (CEiF), Charge Exchange after Thermalisation (CEaT), Direct Annihilation (DA), and Radiative Recombination (RR). The temperatures assumed for cold molecular, warm atomic, warm ionised, and hot ionised ISM phases are 100 K, 8000 K, 8000 K, and 10<sup>6</sup> K, respectively. Adopted from Guessoum et al. (2005).

The intensity of the o-Ps continuum in relation to the intensity of the annihilation line<sup>9</sup>, and parameters of the ISM, provides additional information (Churazov et al.

<sup>9</sup>The annihilation line may be due to p-Ps decay or direct annihilation.

2005; Murphy et al. 2005). A Ps fraction,  $f_{Ps}$ , can be calculated from the statistical weight of Ps decaying into two or three photons, and the number of direct annihilations without Ps formation. The multiplicity of a particular spin state is  $(2S + 1)$ , and p-Ps ( $S = 0$ ) will be formed  $\frac{1}{4}$  of the time, while o-Ps ( $S = 1$ ) will be formed  $\frac{3}{4}$  of the time. Para-positronium will emit two photons, and o-Ps three photons, so that the number of photons per unit time from three-photon annihilation, i.e. intensity  $I_{3\gamma}$ , is proportional to  $3\frac{3}{4}f_{Ps} = \frac{9}{4}f_{Ps}$ . The two-photon intensity is then given by the sum over p-Ps decays and the direct annihilation intensity, weighted with the respective Ps fraction,  $I_{2\gamma} \propto 2\frac{1}{4}f_{Ps} + 2(1 - f_{Ps}) = 2 - \frac{3}{2}f_{Ps}$ . If the total annihilation gamma-ray intensity is measured, the positronium fraction is given by

$$f_{Ps} = \frac{8R_\gamma}{6R_\gamma + 9}, \quad (2.102)$$

where  $R_\gamma = \frac{I_{3\gamma}}{I_{2\gamma}}$ . Thus, if all positrons annihilate via the formation of Ps,  $f_{Ps} = 1$ , and the maximum ratio between the intensities,  $R_\gamma^{max}$ , is 4.5. In Fig. 2.20, the line width as a function of ionisation, temperature, and Ps fraction is shown, also illustrating the partial degeneracy of the line width with ISM parameters.

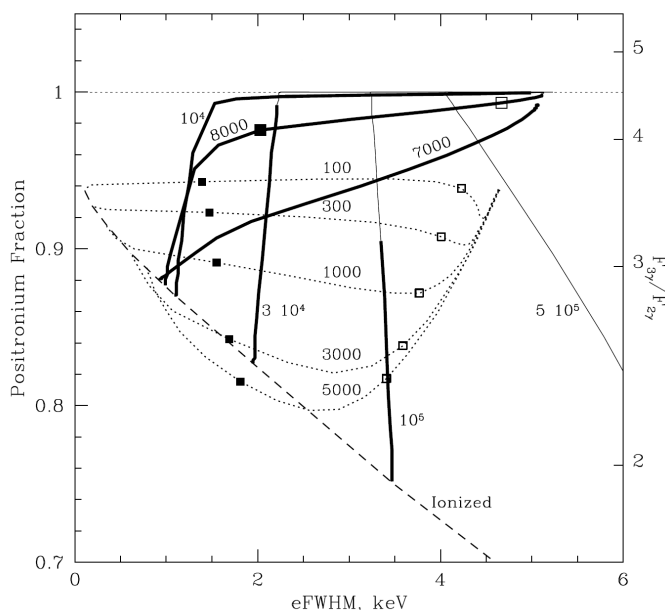


Figure 2.20: Effective 511 keV line width as a function of ISM parameters and positronium fraction. The effective full width at half maximum (eFWHM) is defined as the energy interval containing 76% of the photons (Guessoum et al. 1991). Annihilation in cold ( $T < 5000$  K) media are shown with dotted lines, in warm ( $T > 5000$  K) media by solid lines. Along a temperature curve, the ionisation fraction varies, marked by open squares for an ionisation fraction of 0.01 towards the filled squares indicating an ionisation level of 0.1. The high-temperature curves are separated into two parts, showing either ionisation fractions smaller (thin lines) or larger (thick lines) than what would be expected for collision-dominated plasma at this temperature, respectively. The dashed line is showing the eFWHM and  $f_{Ps}$  as a function of temperature for a fully ionised medium. Adopted from Churazov et al. (2005).

#### 2.4.3.5 Bulk Motion Effects

Relative velocities of source and observer result in the wavelengths of the emitted photons to be "stretched" or "compressed", according to the Doppler formula

$$\frac{\lambda_0}{\lambda_{obs}} = \frac{\nu_{obs}}{\nu_0} = \frac{E_{obs}}{E_0} = \sqrt{\frac{1-\beta}{1+\beta}}. \quad (2.103)$$

The index 0 in Eq. (2.103) indicates the photon energy (wavelength, frequency) in the rest-frame of the source, and the index *obs* what would be measured by an observer moving relative to the source at a velocity  $\beta = \frac{v}{c}$ . For non-relativistic velocities,  $\beta \ll 1$ , the Doppler-shift,  $\Delta E \equiv E_0 - E_{obs}$ , reduces to  $\Delta E^{NR} = \beta E_0$ , which is accurate to 0.2% up to relative velocities of  $\approx 10^3 \text{ km s}^{-1}$ , and to 5% up to  $\approx 3 \times 10^4 \text{ km s}^{-1}$ . Except for the thermal pair annihilation case in which the relative velocities are of the order of  $c/2$ , the non-relativistic Doppler formula is applicable since typical celestial relative velocities are few  $100 \text{ km s}^{-1}$  for galactic rotation, for example, or few  $1000 \text{ km s}^{-1}$  for particular sources of the Milky Way, like kicked neutron stars (e.g. Bray & Eldridge 2016; Wongwathanarat et al. 2016) or stellar winds (Castor et al. 1975), or few  $10000 \text{ km s}^{-1}$  for very young expanding supernova remnants (e.g. Filippenko 1997; Burrows et al. 2000).

Line-of-sight and viewing angle effects, and in particular integrating over large solid angles, will lead to special spectral shapes, as the Doppler-shifts from many directions with different Doppler-velocities will be superimposed and weighted by their intensity and distance. A thin homogeneous and spherically symmetric shell with radius  $R$ , for example, expanding with a velocity  $v_{exp} \ll c$  at a distance  $d \gg R$  to the observer, emitting mono-energetic gamma-rays at energy  $E_0$ , will lead to a rectangular spectrum, with low- and high-energy edges at the minimum and maximum shifted Doppler-velocities,

$$\frac{dF}{dE}(E)^{shell} \propto \Theta \left( v_{exp} - \left| c \left( \frac{E}{E_0} - 1 \right) \right| \right), \quad (2.104)$$

where  $\Theta(x)$  is the heaviside function (Kretschmer, K. A. 2011).

## 3 Measuring Galactic Gamma-Ray Signals with INTEGRAL/SPI

### 3.1 High-Energy Astronomy

#### 3.1.1 Interaction of Light with Matter

Whenever the observation of high-energy (short-wavelength) light is desired, for example from nuclear reactions, or the annihilation of electrons with positrons, the observer is confronted with two problems. First, at such wavelengths, very sophisticated apertures must be used to infer the incident direction of the photons, because they are highly penetrating. And second, if astrophysical observations want to be made, the atmosphere of Earth hinders direct observations, as the reaction rate with atoms and molecules in the dense atmosphere is large, so that high-energy (gamma-ray) photons are efficiently absorbed and down-scattered. Hence, in the case of photon energies between a few keV to several MeV, satellite-based telescopes are unavoidable.

The detection of gamma-ray photons is based on the fundamental interactions of light with matter, the photo-electric effect, the Compton-effect, and pair-production. The lower end of the energy range is dominated by the photo-electric effect (photo-effect). If a photon is energetic enough to exceed the work function of an electron in some material, the electron is kicked out, and holds a kinetic energy which is the difference of photon energy minus the work function. This can be interpreted as the photon being absorbed by a de-localised electron which exceeds its binding energy and leaves the material. The cross section of the photo-effect can be roughly expressed as

$$\sigma_{PE} = \kappa \frac{Z^n}{E^m}, \quad (3.1)$$

where  $Z$  is the charge number of the material which the photon is interacting with, and  $\kappa$  is a material-dependent constant. The pair of exponents  $(n, m)$  vary from low ( $n = 4, m = 3$ ) to high energies ( $n = 5, m = 1$ ). This is due to the effect that at higher photon energies, also K-electrons can be ejected which is then superseding the cross section of L-, M-, ..., -electrons. The strong dependency on the atomic number  $Z$  favours high- $Z$  materials as veto-shields for photons in this energy range.

At photon energies around 500 keV, the Compton effect is the dominant process with matter. Here, a photon is scattered inelastically on an electron causing the photon to lose energy and change its direction. This angle-dependency can furthermore be

used in Compton-telescopes. The cross section was first derived by Klein & Nishina (1929), based also on the work of Compton who quantitatively described the change of electron energy and momentum as an impact on the photon wavelength,

$$\lambda' - \lambda = \frac{h}{m_e c} (1 - \cos(\theta)), \quad (3.2)$$

where  $\theta$  is the scattering angle and  $\lambda' - \lambda$  the change in photon wavelength. In terms of energy, the scattered photon carries an energy of

$$E' = \frac{E_0}{1 + \frac{E_0}{m_e c^2} (1 - \cos(\theta))}, \quad (3.3)$$

where  $E_0$  is the incident photon energy. According to Eq. (3.3), photons can only lose energy when interacting via the Compton effect. However, the inverse Compton effect, in which an ultra-relativistic particle, for example an electron, transfers its energy to a photon, can lead to very high-energy photons. The name "inverse Compton scattering" is misleading, as the effect is still the same, but the rest frame is transformed to a relativistic particle where the photon gets Doppler-shifted to a higher energy. The angle-dependency of the Compton effect cross section is given in differential form as

$$\frac{d\sigma_{CE}}{d\Omega}(\theta) = \frac{1}{2} r_0^2 \left( \frac{k}{k_0} \right)^2 \left( \frac{k}{k_0} + \frac{k_0}{k} - \sin^2(\theta) \right), \quad (3.4)$$

where  $k_0 = \frac{E_0}{m_e c^2}$ ,  $k = \frac{E'}{m_e c^2}$ , and  $r_0 = \frac{\alpha h c}{m_e c^2}$  is the reduced Compton wavelength. The total cross section is then derived by integration over the solid angle (Klein & Nishina 1929). In general, the Compton effect cross section is a linear monotonically decreasing function of  $Z$ .

As already described in detail in Sec. 2.2.4.2, electron-positron pair-production becomes possible above photon energies of  $2m_e c^2$ , and dominates by far over the other interaction processes at very large energies. The pair-production cross section has been shown to increase monotonically with energy, and shows in general a  $Z^2$  dependence, cf. Eq. (2.21).

### 3.1.2 Gamma-Ray Detectors

In many applications, the scintillation method is used to detect gamma-rays by their interactions with matter. In this technique, the excitation of an electron, induced from the photon interaction, from the valence band into the conduction band is used. The resulting electron-hole pair will recombine after a certain time, yielding another but lower energy photon. If, for example, a pure crystal is used for scintillation, the secondary photons may have wavelengths outside the visible band. The light output of a pure crystal is also very low, because the recombination processes are

inefficient. If crystals are doped, which means integrating chosen impurities, there will be additional levels between the valence and the conduction band, making the excitation more probable (Hofstadter 1948). Then, the produced photons from a doped crystal are in the wavelength range 250-650 nm, which makes them usable in photomultiplier tubes or photodiodes. The optical signal which results from one gamma-ray photon is very weak. It has to be transferred into a measurable electronic signal via the amplification of photomultiplier tubes or photodiodes.

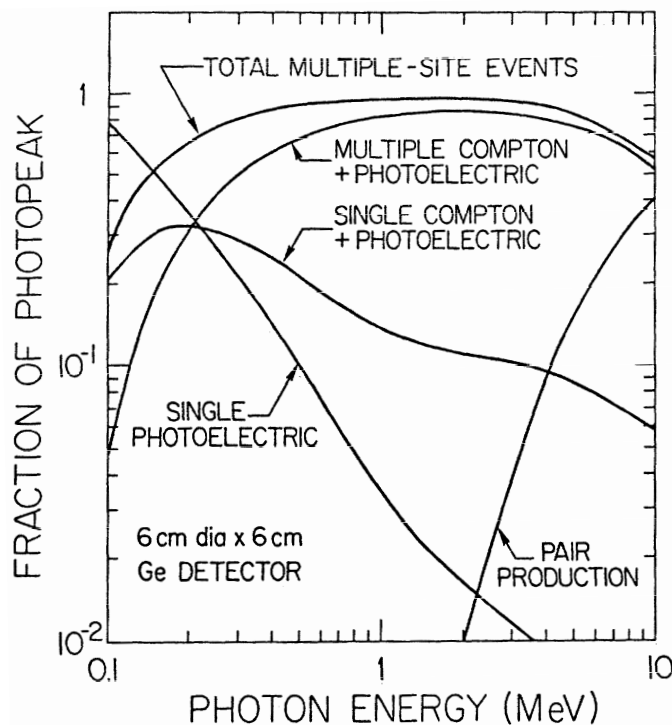


Figure 3.1: Interaction strengths of photons with Ge as a function of energy. Shown is the fraction of full-peak energy contributed by different energy loss mechanism in a 6 cm  $\times$  6 cm high-purity Ge detector. Photo-electric absorption is dominating below photon energies of  $\approx$  140 keV. Above this energy, single and multiple Compton-scattering increases the Compton continuum as shown in Fig. 3.2b. In the energy range of the gamma-ray spectrometer SPI ( $<$  8 MeV, Sec. 3.2.2), pair-production contributes significantly only above 3 MeV. From Roth et al. (1984).

In order to detect gamma-rays, a detector in space must meet the following criteria: The material should have a high enough density for the photons to maximise the cross section for interaction, but at the same time may not be too heavy to lift. Additionally, the light yield should be large enough. In general, organic scintillators have low densities and low light outputs, which makes them not too suitable gamma-ray detectors. Nevertheless, they are used in astrophysics because of their fast response times. For this reason, they are often a favoured choice as anticoincidence shields (Lichti & Georgii 2001). Among the most commonly used inorganic scintillators are NaI(Tl), CsI(Tl), and  $\text{Bi}_4(\text{GeO}_4)_3$  (BGO). BGO has one of the largest densities of scintillator materials, and thus a large stopping power, but the light yield is rather low. It is often used in combination with gamma-ray detectors as anticoincidence shield material. In order to measure high-resolution gamma-ray spectra, scintillators are not the best choice, as most of them have relatively large band gaps of the order 5-9 eV. The creation of electron-hole pairs is then hindered, and the energy resolution is limited by statistical fluctuations to about 10%. Semi-conductors like Si or Ge have small band gaps (Si 1.12 eV, Ge 0.67 eV at room temperature) compared to scintillators, which increases the number of charge carriers for one incident

photon by about two orders of magnitude, resulting in an improvement of spectral resolution of at least one order of magnitude. Furthermore, Ge also has a high density of  $5.33 \text{ g cm}^{-3}$ , so that the interaction probability is large, even for small-sized detectors. A physical signal out of one impinging photon is then created by applying a high voltage of typically 2-9 kV across the detector, meaning between the outer surface and an inner hole. A gamma-ray photon is mainly absorbed in the outer most parts of the detector, creating a secondary electron. This electron is then creating electrons and holes, whose numbers are proportional to the energy of the incident photon. The holes are trapped easily on their way to the cathode. For this reason, an n-type detector is created by doping Li to the Ge lattice to make the holes' paths as short as possible. Although the small band gap of Ge provides best high-resolution gamma-ray spectra, the number of thermal excitations of electron-hole pairs is non-negligible even at room temperature. Consequently, high-purity Ge detectors are cooled down to  $\approx 100 \text{ K}$  in order to avoid disturbing leakage currents. Moreover, solid-state detectors are very sensitive to radiation damage which worsens the resolution, and even changes the instrumental response function over time.

In this work, the spectrometer telescope SPI aboard the satellite INTEGRAL (see Sec. 3.2.1), is used for data analysis. The SPI camera consists of 19 high-purity Ge detectors, surrounded by an anticoincidence shield made of BGO, and a plastic scintillator. The different interaction strengths of photons with a Ge detector are shown in Fig. 3.1. When a gamma-ray spectrometer like SPI is recording photon spectra, the incident spectrum is suffering from the different interactions of light with matter, at different relative strength for different energies. An ideal detector would translate an arbitrary shaped spectrum to the spectrum itself, but a real detector features spectral responses according to the properties of the photon and the detector. In general, a measured spectrum  $D(E)$  is described by a convolution of the incident, true source spectrum  $S(E)$  with the spectral response function  $R(E)$ ,

$$D(E) = S(E) \otimes R(E) \equiv \int_{-\infty}^{+\infty} S(E') \cdot R(E + E') dE', \quad (3.5)$$

which can be seen as a blurring effect of the sharply defined source spectrum. In the case of Ge detectors, the spectral response is composed of a photo-peak, a Compton continuum, and escape peaks. The interaction of an incident mono-energetic beam of photons via the photo-effect leads to the photo-peak at exactly the energy of the photon, but blurred by the instrumental resolution, given by charge carrier statistics. In the case of Compton scattering in the detector, a continuum of energies can be transferred to the charge carriers, ranging from zero ( $\theta = 0$ ) to the maximum ( $\theta = \pi$ ) predicted energy  $E_{e^-}^{max}$  as derived from Eq. (3.3),

$$E_{e^-}^{max} = E_0 - E'|_{\theta=\pi} = E_0 \left( \frac{2 \frac{E_0}{m_e c^2}}{1 + 2 \frac{E_0}{m_e c^2}} \right). \quad (3.6)$$

The gap between the photo-peak and the maximum Compton recoil electron energy,  $E_C$ , is hence given by

$$E_C \equiv E_0 - E_{e^-}^{max} = \frac{E_0}{1 + 2\frac{E_0}{m_e c^2}}, \quad (3.7)$$

which reduces to  $E_C \approx \frac{1}{2}m_e c^2$  in the case of high-energy photons ( $E_0 \gg m_e c^2$ ). In the case of pair-production in the intense electric field of a Ge detector lattice, the incident photon of at least 1.022 MeV energy converts to an electron and a positron with masses of  $511 \text{ keV } c^{-2}$  each, and kinetic energies corresponding to the energy of the photon, so that

$$E_{e^-} + E_{e^+} = E_0 + 2m_e c^2. \quad (3.8)$$

The electron and the positron are slowed down after only a few millimetres in the detector, and deposit their kinetic energies. As their rest masses are not transferred, an additional spectral line at an energy of  $E_0 - nm_e c^2$  is produced in the measured spectrum. When both, electron and positron, have deposited all their kinetic energy to the detector, a double escape peak with  $n = 2$  appears. Once the positron slowed down to thermal energies, it will annihilate or combine with a normal electron in the lattice. This corresponds to the disappearance of both particles, and a conversion to two  $511 \text{ keV}$  photons, virtually at the same time as the incident photon arrived. If one of the  $511 \text{ keV}$  photons again interacts with the Ge detector, and one leaves the system, a single escape peak with  $n = 1$  is measured. In Fig. 3.2a, the possible interactions of high-energy photons with a Ge detector is shown, together with the expected spectrum in the case of  $E_0 \gg 2m_e c^2$  in Fig. 3.2b.

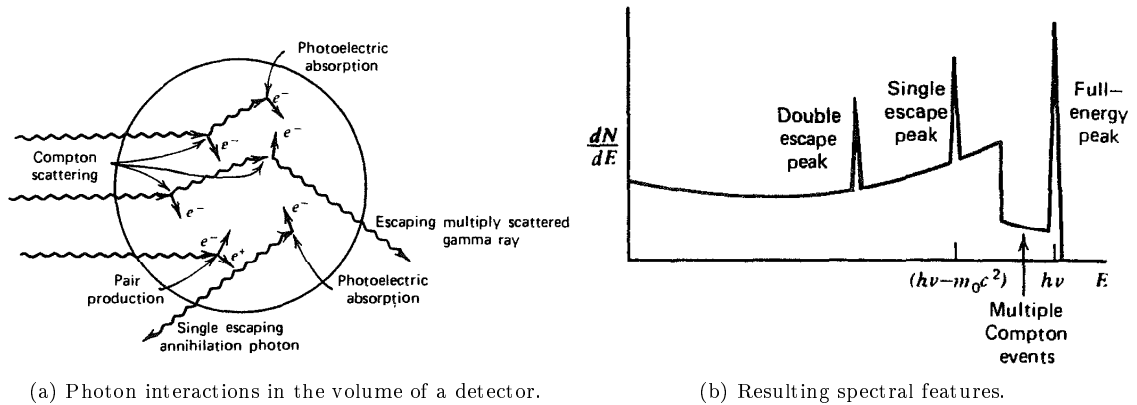


Figure 3.2: Photon interactions and spectral response of a germanium detector. From Knoll (2010).

### 3.1.3 Gamma-Ray Telescopes

Solid-state detectors provide a good energy resolution, but have intrinsically no information about the direction a photon came from. With a spark chamber or a Cherenkov detector, for example, the direction of an incident gamma-ray photon can be measured well, but the energy information and spectral resolution is very restricted. In general, there are many ways to make a gamma-ray telescope out of a gamma-ray detector but since the SPI telescope, which features a Ge detector

camera, is used for the analysis in this thesis, the coded-mask principle and aperture is worked out.

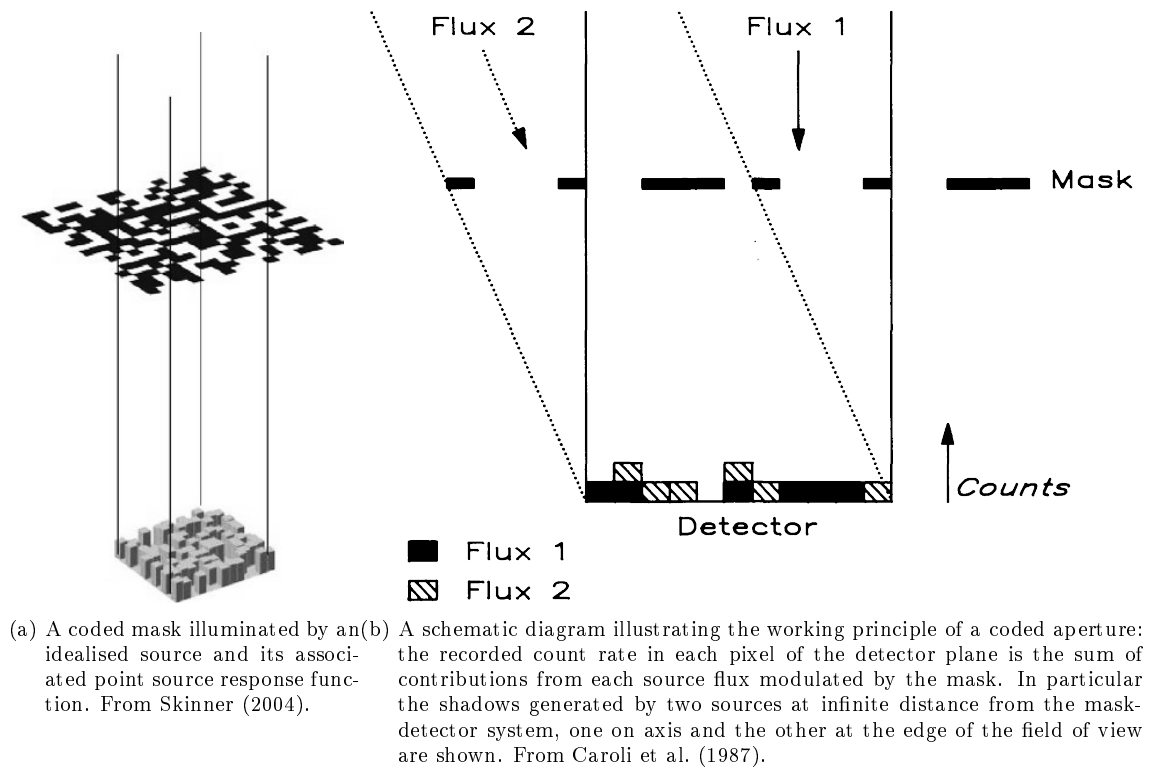


Figure 3.3: The function principle of a coded-mask system.

Whenever a coded-mask system is used, a position-sensitive camera has to be constructed, for example by arranging many Ge detectors in an array. The working principle of such a system is illustrated in Figs. 3.3a and b, in which a point source, located at infinity, is illuminating a mask, consisting of transparent and opaque elements. The mask is situated above the detecting array and transforms the "beam" of photons into a certain shadow pattern (shadowgram), depending on the aspect angle of source and telescope. These known shadowgrams from different directions are then used to reconstruct the position of sources in the field of view of the telescope as defined in Fig. 3.4. For point-sources, this reconstruction is mostly unique, but for diffuse celestial emission, a coded-mask telescope must rely on morphology gradients, as otherwise the mask pattern is identical from all directions.

In general, the reconstruction is better the more pixels there are in the detector array. However, the smaller the detector size, the less efficient will high-energy photons in the MeV range be detected. The apertures of coded-mask systems have a relatively large "fully coded field of view", because the mask plane is often more extended than the detector plane. Only the geometry of the instrument is responsible for the field of view, which is typically in the range of tens of degrees. Also the angular resolution,  $\Delta\theta$ , is only determined by the separation between detector array and mask  $l$ , the characteristic size of transparent elements  $m$ , and the characteristic size of opaque elements  $d$ , to (Skinner 2008)

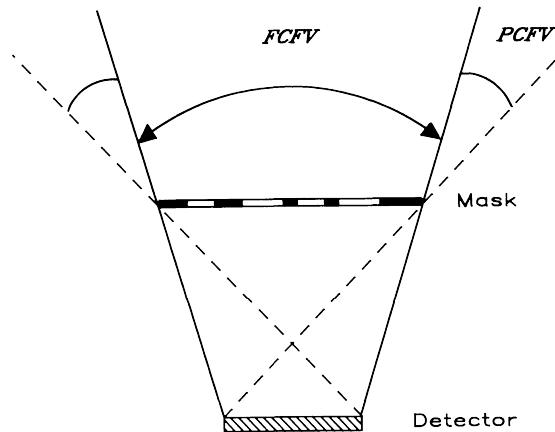


Figure 3.4: Field of view definition of coded-mask telescopes. The fully coded field of view (FCFOV) is defined as comprising all directions for which the recorded flux is entirely modulated by the mask and the partially coded field of view (PCFOV) for which only a fraction of the detected flux is coded by the mask. From Caroli et al. (1987).

$$\Delta\theta = \sqrt{\left(\frac{m}{l}\right)^2 + \left(\frac{d}{l}\right)^2}. \quad (3.9)$$

In fact, it is most efficient to construct a coded-mask instrument for which the transparent and opaque elements have the same size (Skinner 2008), so that the angular resolution is only depends on the ratio  $d/l$ . Decreasing the pixel elements is similar to constructing a pinhole camera but suffers from detection efficiency. Increasing the separation between mask and detector ("focal length") is only possible as far as the instrument fits on a satellite to be launched into space. Typically, the angular resolution of MeV coded-mask telescopes is thus of the order of degrees. In order to resolve ambiguities on the detector plane, due to the fact that there are more "sky pixels" than "detector pixels", the instruments are "dithered" from pointing to pointing around the object in the sky, so that there will be also temporal coding in addition to the spatial coding of the mask. The specifications of the SPI instrument will be discussed further in Sec. 3.2.2.

## 3.2 INTEGRAL and its Spectrometer SPI

### 3.2.1 The INTEGRAL Mission

The INTEGRAL satellite is the INTERnational Gamma-Ray Astrophysics Laboratory of the European Space Agency. The spacecraft was planned during the Compton Gamma Ray Observatory (CGRO) mission as a follow-up instrument to observe the "violent" high-energy universe. INTEGRAL was planned as a three-year mission with possible extension up to five years (Winkler et al. 2003). Due to its great success in deciphering the messages from gamma-ray sources throughout the Milky Way and beyond, the mission duration was extended several times and is still operating and taking data (year 2016).

INTEGRAL was launched on October 17, 2002, from the spaceport in Baikonur,

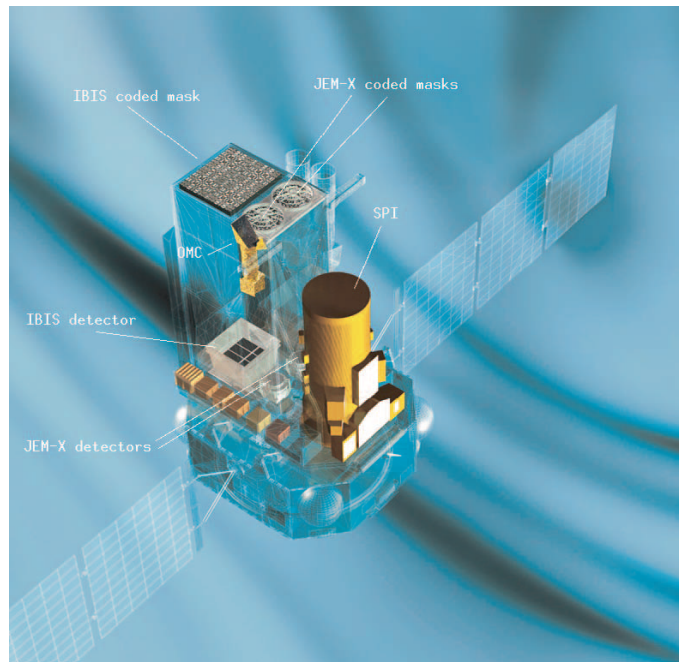


Figure 3.5: The INTEGRAL spacecraft. Dimensions are  $(5 \times 2.8 \times 3.2)$  m. The deployed solar panels are 16 metres across. The mass is 4 t (at launch), including 2 t of payload. The main instruments, the gamma-ray spectrometer telescope SPI and the soft gamma-ray imager IBIS, as well as the complementary instruments, JEM-X for soft X-rays and OMC for visible light, are shown; picture from Winkler et al. (2003).

Kazakhstan, by a PROTON rocket into a high-inclination and high-eccentricity orbit. It carries four co-aligned instruments, the gamma-ray spectrometer telescope SPI (Sec. 3.2.2), the soft gamma-ray imager IBIS, the soft X-ray monitor JEM-X (two identical units), and the optical monitoring camera OMC. The two latter instruments are complementary to the main telescopes SPI and IBIS.

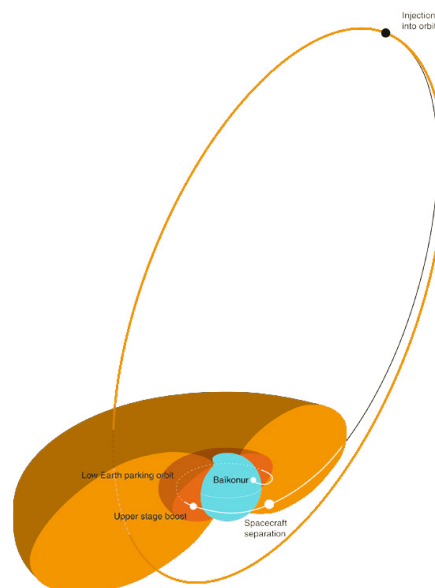


Figure 3.6: Chosen trajectory for the INTEGRAL spacecraft. The Earth is shown as the blue sphere with the launch point in Baikonur, surrounded by the inner and outer Van Allen radiation belts in red and orange, respectively. The low-Earth parking orbit and the final upper stage boosting for the transfer to the high-inclination, high-eccentricity orbit are indicated, as well as the apogee injection towards the final orbit.

The orbit, shown in Fig. 3.6, was chosen to avoid enhanced radiation near Earth, because the planet is surrounded by tori or energetic charged particles, the Van Allen radiation belts. The particles which build the belt are mainly from the solar wind or cosmic rays, captured by the Earth magnetic field, and bound to it due to a magnetic bottle effect of the terrestrial magnetic dipole field. The inner belt is located between  $\approx 3000$  and  $6000$  km above the surface and mainly consists of high-energy protons. The outer belt reaches up to altitudes of  $\approx 25000$  km, thereby bracing the inner belt, and is built up of electrons. Due to the enhanced particle densities, increased electronic malfunctions can occur, and also the radiation damage to the instrument detectors (cameras) would degrade the sensitivity and measurement quality quickly. Therefore, the orbit was chosen highly eccentric with a perigee height of  $\approx 9000$  km and an apogee height of  $\approx 154000$  km, at an inclination of  $52.5^\circ$  with respect to the rotation axis of the Earth. This leads to a  $\approx 3$  day orbital period<sup>1</sup> in which the instruments typically take data between orbital phases  $\approx 0.1$  and  $\approx 0.9$ , corresponding to nominal altitudes of  $\approx 50000$  km, thereby avoiding the radiation belts.

For this thesis, data from the spectrometer SPI were used. SPI is described in detail in Sec. 3.2.2. Nevertheless, the other instruments aboard INTEGRAL will be introduced briefly below.

IBIS is the Imager on-Board the INTEGRAL Satellite, dedicated to observe in the energy range from 15 keV to 10 MeV. In addition to its coded mask aperture, it is using two detector array layers to function also as a Compton telescope. The one layer, called ISGRI (INTEGRAL Soft Gamma-Ray Imager), consists of  $128 \times 128$  pixels made of CdTe, building an area of  $\approx 2600$  cm<sup>2</sup>. Due to the fact that these detectors are very small, they provide an excellent spatial resolution, but their thinness makes them only suitable for energies between 15 and 150 keV. The other layer is called PICsIT (Pixellated Caesium-Iodide Telescope), and is made of  $64 \times 64$  CsI scintillators, doped with Tl, with a total area of 2890 cm<sup>2</sup>. The mask is situated 3.4 m above the detector layer, and enables a fully-coded field of view of  $9^\circ \times 9^\circ$ , and a partially-coded field of view of  $19^\circ \times 19^\circ$ . Due to the large number of detectors, combined with the Compton telescope principle, the spatial resolution is around 12 arcmin; the point source location accuracy is 30 arcsec. The energy resolution of IBIS is 9-10% ( $\Delta E = E/2$ ), and thus focusses on sources with a spectral continuum rather than spectral gamma-ray lines (Ubertini et al. 2003).

The Joint European X-Ray Monitor (JEM-X) is a complementary instrument, providing additional information on the identification of gamma-ray sources. It is made of two co-aligned telescopes, each of them using its own coded mask. Each detector is an imaging microstrip gas chamber and has an area of  $\approx 500$  cm<sup>2</sup>, providing an angular resolution of 3 arcmin over a fully-coded field of view of  $10^\circ \times 10^\circ$ . JEM-X is recording spectra in the energy range 3-35 keV, with an energy dependent resolution of  $\frac{\Delta E^{FWHM}}{E} = 0.40 \sqrt{\frac{1}{E[\text{keV}]} + \frac{1}{60}}$  (Lund et al. 2003).

The Optical Monitoring Camera (OMC) is rounding off the INTEGRAL spacecraft, being a classical camera which is using refraction of optical light around a wavelength

<sup>1</sup>INTEGRAL will be deorbited safely in 2029. For this manoeuvre, the boosters have been used in 2015 to bring the satellite into a lower and thus faster orbit around Earth in order to decelerate again by residual atmosphere at these altitudes. In particular, this leads to a shorter orbital period after INTEGRAL's 1500th revolution around Earth.

Table 3.1: SPI instrument characteristics; values taken from Vedrenne et al. (2003), Winkler et al. (2003), Roques et al. (2003), and Siegert et al. (2016d).

Parameter	
Energy range	20 keV-8 MeV
Detectors	19 high-purity Ge detectors, cooled to $\approx 85$ K
Detector area	508 cm <sup>2</sup> geometrical; 10 – 100 cm <sup>2</sup> effective
Detector thickness	7 cm
Spectral resolution (FWHM)	2.1 keV at 511 keV; 3.1 keV at 1809 keV
3 $\sigma$ Continuum sensitivity	$1.5 \times 10^{-6}$ ph cm <sup>-2</sup> s <sup>-1</sup> keV <sup>-1</sup> at 511 keV
3 $\sigma$ Line sensitivity	$5 \times 10^{-5}$ ph cm <sup>-2</sup> s <sup>-1</sup> at 511 keV
Field of view	16° $\times$ 16° (fully coded); 31° $\times$ 31° (partially coded)
Angular resolution (FWHM)	2.7°
Source location (radius)	10 arcmin
3 $\sigma$ Absolute timing accuracy	$\pm 52$ $\mu$ s
Total mass	1228 kg
Power (max/avg)	385/110 W

of 550 nm, and focussing it on a CCD (charge-coupled device). It is supporting the INTEGRAL mission by observing the optical emission from the prime targets of gamma-ray emission. It provides the brightness and position of the optical counterpart of any gamma- or X-ray transient taking place within the field of view of  $5^\circ \times 5^\circ$ . The angular resolution amounts to 24.5 arcsec, and the point source location accuracy to  $\approx 6$  arcsec. The "1-Megapixel" camera can identify sources down to magnitudes  $V = 18$  (Mas-Hesse et al. 2003).

### 3.2.2 The Spectrometer SPI

SPI is the high spectral resolution gamma-ray spectrometer aboard INTEGRAL and uses a coded-mask aperture to "focus" gamma-rays in the energy range between 20 keV and 8 MeV onto its 19-segmented Ge detector array (Vedrenne et al. 2003). The angular resolution, which SPI can achieve in its fully-coded field of view of  $16^\circ \times 16^\circ$ , is 2.7°. Due to the solid state Ge detectors, SPI obtains a spectral resolution of  $\approx 2.1$  keV at 511 keV, depending also on the temperature, and the current state of degradation of SPI due to cosmic-ray bombardment, Sec. 3.2.3.1. In the following sections, the sub-systems of SPI will be described, that are necessary for high-precision spectroscopy in space. Table 3.1 provides an overview of the key parameters of the instrument.

#### 3.2.2.1 Camera

The centrepiece of SPI is its camera, consisting of 19 high-purity Ge detectors, working as reverse-biased n-type diodes. Each of the detectors has a hexagonal shape with a side length of 3.2 cm and a height of 69.42 mm, for a total geometrical area of 508 cm<sup>2</sup>. The 19 detectors are ordered in a honeycomb structure, and numbered from 00 to 18, beginning with detector 00 in the centre (Fig. 3.7). This design was chosen to provide a large effective area for incoming photons, and at the same time to have a compact setting. In Fig 3.8b, one of the detectors is shown, encapsuled in Al, working as the cathode for the external high-voltage of 4 kV.

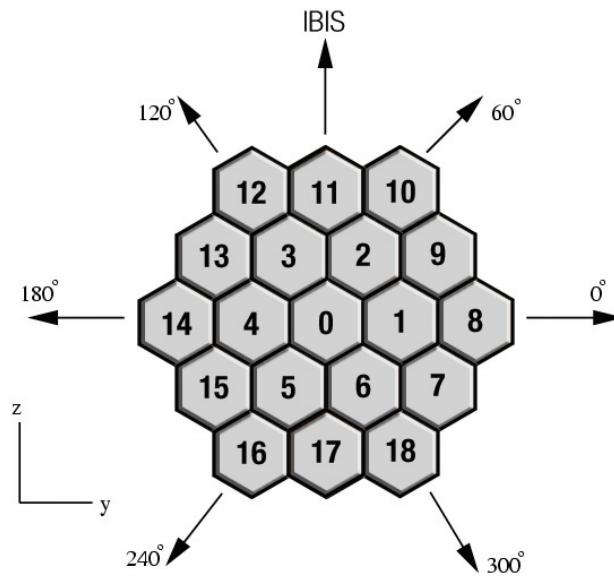
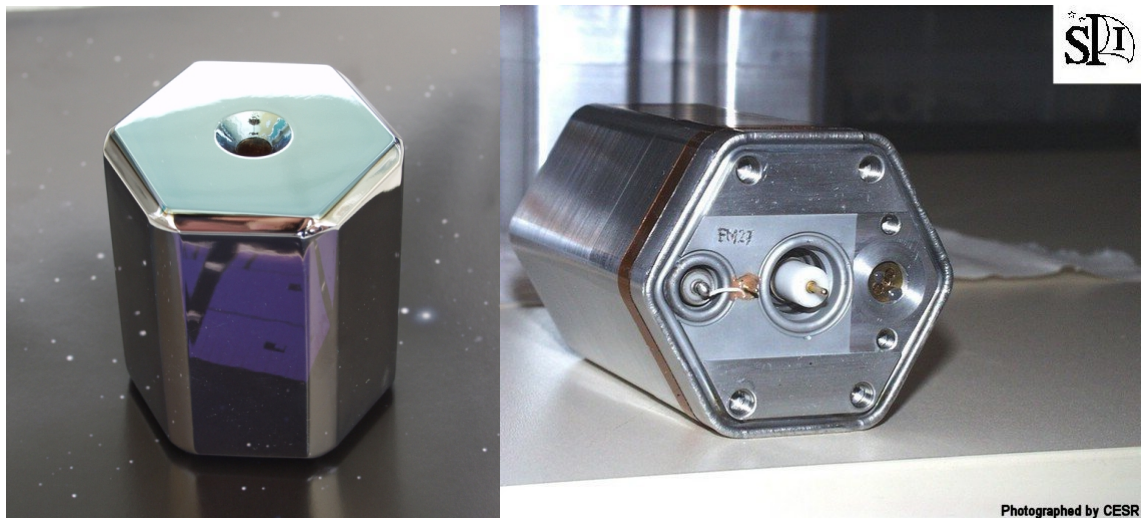


Figure 3.7: Schematic drawing of the detector numbering of the SPI camera. Symmetry-axes and the direction to the IBIS-instrument, Sec. 3.2.1, are shown.

The gradual deterioration of the Ge detectors, due to cosmic rays hitting the spacecraft, is countered by heating up the whole camera twice a year in a so-called "annealing" period. In particular, high-energy cosmic-ray particles interact with the crystalline structure of the Ge detectors and spoil the regular structure. If a relativistic particle hits a Ge atom in the lattice, the recoil momentum may be so large that the atom may be left in another position in the lattice, building either vacancies or interstitials. These irregularities in the lattice structure lead to a decrease in the charge collection efficiency of the detectors, because electrons or holes can be trapped in these imperfections. The event readout time in the instrument is calibrated to be finite, but the trapped charges would invoke a time delay which lengthens the processing time. The resulting pulse shape is consequently different compared to a regular lattice structure. The effect on the spectrum of a monoenergetic source will be a shift of the peak energy, and an asymmetric broadening of the instrumentally resolved line shape (Kretschmer, K. A. 2011).

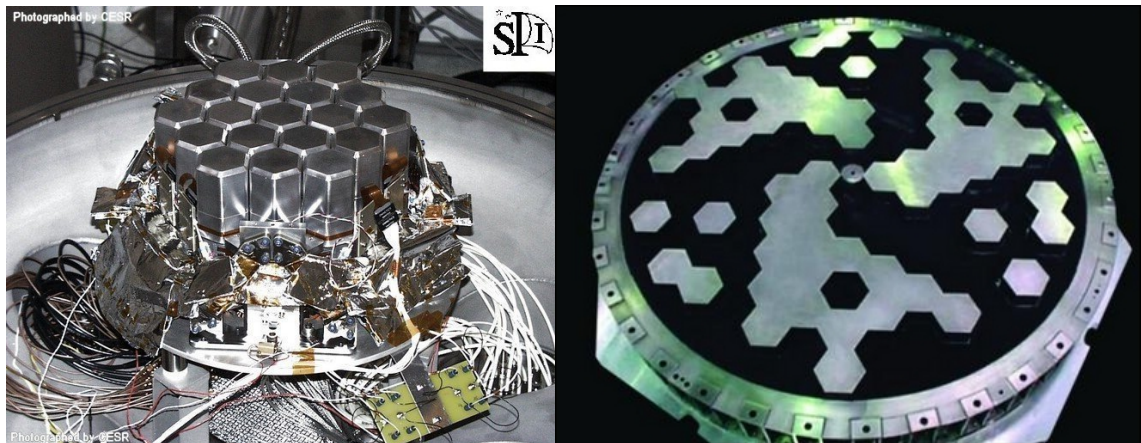
SPI exhibits a Stirling-cycle cooling system in order to cool the entire Ge detector array down to  $\approx 85$  K, so that less thermally excited electrons populate the conduction band of Ge for an almost leakage current free semiconductor detector. Because of the detector degradation, the entire array is heated up to  $105$  °C for about two weeks twice a year. This annealing process, which is related to tempering, repairs the lattice structure and resets the instrumental resolution back to an acceptable value.

In order to function as a gamma-ray telescope, the SPI mask is situated 1.71 m above the detector array with a diameter of 0.72 m which results in a fully-coded field of view of  $16^\circ \times 16^\circ$  and a partially coded field of view of  $31^\circ \times 31^\circ$ . It consists of 127 hexagonal elements, 63 being opaque to gamma-rays, and 64 transparent. The opaque pixels are made of W, are 30 mm thick, and have otherwise the same dimensions as the detectors. The mask pattern is  $120^\circ$ -rotational symmetric about its centre, see Fig. 3.8d. The limiting factor of the spatial resolution is the number



(a) Single Ge detector. The central bore is 0.6 cm in diameter and 5.5 cm in length.

(b) Ge detector flight mode, encapsuled and wired.



(c) Complete detection cold plate assembly in a vacuum box for thermal tests.

(d) SPI mask with opaque W elements.

Figure 3.8: The SPI camera system; pictures from Vedrenne et al. (2003) and the SPI team.

of mask pixels that are used in reconstructing the shadowing pattern in relation to the number of camera "pixels"; in the case of SPI, the angular resolution is  $\approx 2.7^\circ$ . Because the mask is shadowing about 50% of the incoming celestial photons, the geometrical area is reduced. In addition, as high-energy photons are more likely to pass through the Ge detectors without interaction, the area is reduced even further, leading to an effective area between  $\approx 10$  and  $\approx 100 \text{ cm}^2$ . The point-source location accuracy of SPI is  $\approx 10$  arcmin.

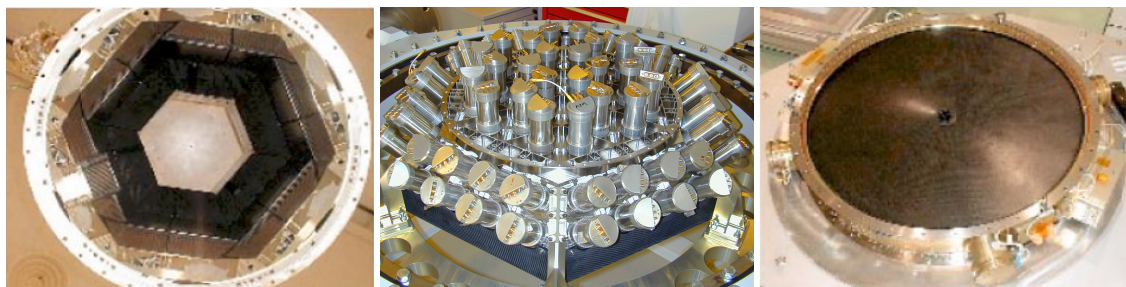
### 3.2.2.2 Anticoincidence systems

Satellite-based nuclear astrophysics telescopes suffer from both the problem of focusing gamma-rays, and cosmic-rays steadily exciting the instrument and spacecraft material. Therefore, the camera system has to be protected against photons from "other" directions than what the mask is trying to focus, and also cosmic-rays. SPI has several anticoincidence systems which try to reduce the photon and particle background.

The SPI "anticoincidence system" (ACS, Figs. 3.9a and 3.9b) is made of 91 separate BGO crystals, arranged in four sub-units, surrounding the camera system, and shielding it from all directions. The upper collimator ring, lower collimator ring, and the side shield assembly, are each made of 18 BGO crystals, and the lower veto shield is made of 36 crystals. The BGO blocks have thicknesses of 16 mm at the top, to 50 mm at the bottom. The additional spacecraft mass due to BGO only is 512 kg.

Scintillating BGO crystals emit photons in the range between  $\approx 375$ -650 nm when exposed by high-energy gamma-rays. Each of the SPI ACS BGO crystals is viewed by two (for redundancy) photomultiplier tubes in order to trigger a veto-signal, if SPI is hit from the "wrong" direction. Because only the total event rates over all SPI ACS crystals are recorded, there is no spectral and no directional information available from this anticoincidence system. However, because it has a large effective area of up to  $\approx 1 \text{ m}^2$ , and fast timing, it is also used for studying gamma-ray bursts (GRB, e.g. von Kienlin et al. 2004; Larsson et al. 2004).

During a typical SPI observation of a  $5 \times 5$  pointing grid (see Sec. 3.2.4.3), the SPI ACS count rate varies a few percent from its mean value, which ranges between  $5 \times 10^4$  and  $10^5 \text{ ph s}^{-1}$ , depending on the state of the solar cycle, and can reach much higher values during solar flares.



(a) SPI ACS BGO blocks in hexagonal arrangement. (b) SPI ACS bottom shield viewed by PMTs. (c) PSAC in a light diffusion chamber, viewed by PMTs.

Figure 3.9: SPI anticoincidence systems; pictures from Vedrenne et al. (2003) and the SPI team.

For further reduction of the instrumental background near the 511 keV line, another veto unit was installed in SPI, directly below the mask, the plastic scintillator anticoincidence subassembly (PSAC, Fig. 3.9c). The PSAC is 5 mm thick and 0.8 m in diameter, and viewed by four photomultiplier tubes. Before launch, Jean et al. (1997) simulated a plastic scintillator veto system below the mask, and estimated a gain of sensitivity in measuring the 511 keV line of factor of 1.4. However, the effect of the real PSAC is only "modest" (Vedrenne et al. 2003), and the sensitivity of the 511 keV line is now (15 of 19 detectors working) around  $5\text{-}6 \times 10^{-5} \text{ ph cm}^{-2} \text{ s}^{-1}$  for an exposure of 1 Ms (Siegert et al. 2016d).

Another system that was implemented in SPI, trying to reduce the background originating in the energy deposition of  $\beta^\pm$ -particles into the detectors, is a pulse-shape discriminator circuit. In contrast to photons, charged particles do not deposit their whole energy at one point in the solid state detector, but rather create a trace of ionisation (Knoll 2010). This changes the pulse shape of the collected charges and should therefore ideally be distinguishable from photons, further reducing particle induced backgrounds by sending veto signals. Mandrou et al. (1997) suggested a

pulse-shape discriminator system for SPI, and Jean et al. (1997) simulated the effect of such a system in association with SPI. The estimated factor of 2 (Jean et al. 1997) was not reached in reality, because there seems to be a relatively low fraction of localised  $\beta$ -decays in the target energy range, between 0.4 and 2.0 MeV, with respect to model predictions (Vedrenne et al. 2003). However, in the energy range between  $\approx 1400$  keV and 1700 keV, there are background features, called "electronic noise", which can be "filtered" efficiently by pulse-shape selections. Although the raw, background-dominated, spectrum is reduced by  $\approx 15\%$ , the systematic uncertainties in this energy range is increased because the instrumental response function, and the real efficiency using these selection criteria, are not well known (see e.g. Appendix of Siegert et al. 2016a).

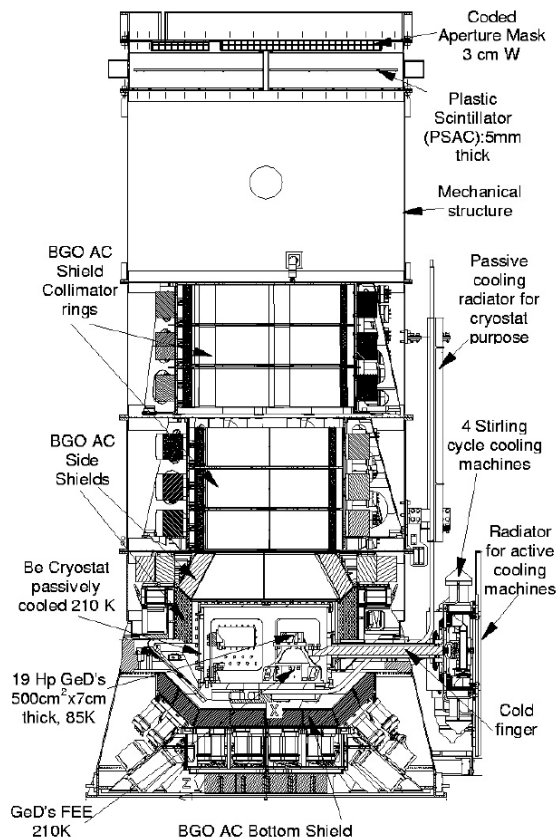
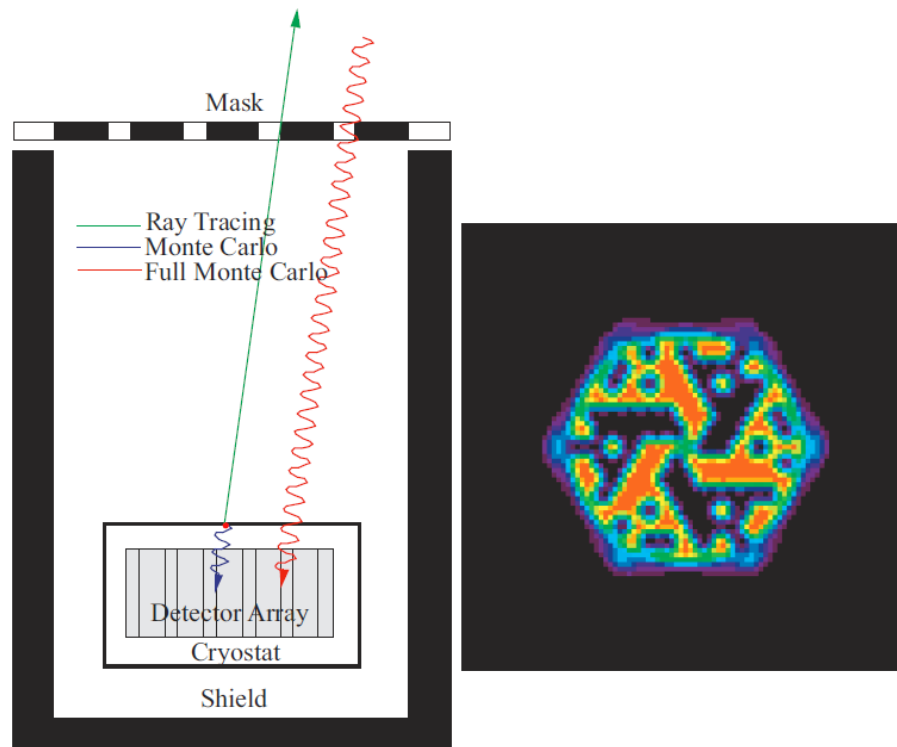


Figure 3.10: Cut-out perspective of the SPI spectrometer viewed from the side. The main systems are shown and indicated with arrows: Ge detector array with front end electronics (FEE), cooling systems, BGO shields, PSAC, and mask; picture from Vedrenne et al. (2003); see text for details.

### 3.2.2.3 Calibration and Performance

The sub-units of SPI have been tested, calibrated, and compared to simulation predictions on ground before launch. The instrumental imaging response function (IRF), i.e. how does a source look like on the Ge detector array if it shines through the mask from a particular direction, has been determined by a combination of Monte Carlo simulations and a ray-tracing method (Sturmer et al. 2003). A full Monte Carlo calculation of the response, at that time, was too CPU-intensive, because a complete coverage for each detector, at each incident photon direction and each photon energy, needs large statistics during such a simulation. As a consequence, the number of simulated photons was reduced by partly performing a

ray-tracing algorithm<sup>2</sup>. A sketch of the used method is shown in Fig. 3.11a, and an example of the SPI imaging capability is shown in Fig. 3.11b.



(a) Schematic illustration of the decomposition of the response generation process into ray tracing and Monte Carlo parts. (b) SPI IRF at 508.33 keV for the photopeak effective area as a function of direction for detector 00. The mask pattern is clearly seen and the hexagonal boundary is a consequence of the shape of SPI's BGO collimator.

Figure 3.11: Imaging response generation process on ground; pictures taken from Stürner et al. (2003).

Four of the 19 Ge detectors failed for unknown reasons during perigee passages of INTEGRAL. Detector number 02 (D02) failed in December 2003, D17 in July 2004, D05 in September 2009, and D01 in May 2010. Consequently, there have to be additional sets of IRFs for each camera configuration. In fact, the number of single events and multiple events<sup>3</sup> in neighbouring detectors changes significantly after a failure. When a detector turns out, photons can still scatter in it, and can be detected by adjacent detectors afterwards. This increases the number of single events in adjacent detectors while the number of multiple events decreases.

These IRFs can then be used to determine the point spread function (Fig. 3.12b) of the SPI telescope on ground, by testing different sources with known energy, intensity, and location. Part of the IRFs are also the effective area of the SPI camera as a function of energy and configuration (see Fig. 3.12a).

The spectral resolution of each Ge detector as a function of photon energy depends sensitively on its temperature. Attié et al. (2003) determined the energy resolution (FWHM) of SPI during the ground calibration as

<sup>2</sup>In general, ray-tracing is the determination of the visibility of a "ray" originating from a three-dimensional object at a particular point in the environment.

<sup>3</sup>Photons which are scattered not only in the volume of one detector, but in more than one are called multiple events. The number of detectors participating in one multiple events varies from two to many, whereas the interaction in two detectors, "double event", is the most probable.

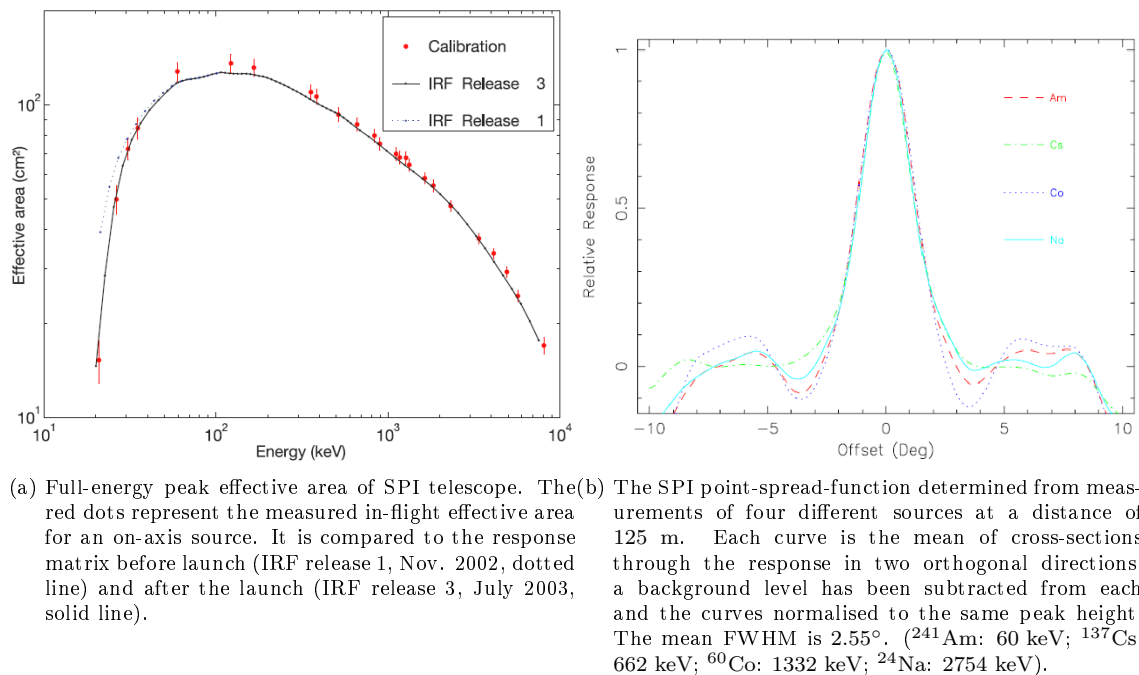


Figure 3.12: SPI effective area and point-spread-function; figures from Attié et al. (2003).

$$\sigma_{FWHM} = F_1 + F_2\sqrt{E} + F_3E, \quad (3.10)$$

where  $F_1 = 1.54$ ,  $F_2 = 4.6 \times 10^{-3}$  and  $F_3 = 6.0 \times 10^{-4}$  at a temperature of 90 K, which should only be taken as a consistency check for the real flight performance. At around 511 keV, the ground calibration, Eq. (3.10), would predict a FWHM of 1.95 keV for instrumental gamma-ray lines, whereas the nominal "best" resolution, i.e. after an annealing period, is about 2.15 keV (see also Sec. 3.2.3.4).

### 3.2.3 High-Precision Background Modelling

#### 3.2.3.1 Instrumental Gamma-Ray Background Origins

Since SPI is a space-based telescope, it is suffering from cosmic-ray bombardment. Cosmic rays in the vicinity of Earth are mainly protons ( $\approx 87\%$ ) and alpha particles ( $\approx 12\%$ ), and only  $\approx 1\%$  heavier elements. These particles react with the material of the telescope and the satellite, and may produce secondary (slow, few MeV) neutrons by spallation processes. The neutrons may be captured by nuclei of the satellite, and form new isotopes in excited nuclear states. A newly built compound nucleus can emit gamma-rays promptly, i.e. on time scales of pico- to nanoseconds, because it was created in an excited state and is de-exciting by photon emission. Then, it is either left as stable or radioactive nucleus which decays after its respective life-time to its daughter nucleus. The latter is most probably also not in its ground state, but in an excited state and de-excites by emitting gamma-rays, often through a cascade of de-excitations. The gamma-rays of long-lived (more than a coincidence window of SPI detectors,  $\approx 160 \mu\text{s}$  Roques et al. 2003) radioactive isotopes are then considered delayed. In Fig. 3.13, the neutron activation of target nuclei in the satellite and

telescope material is illustrated.

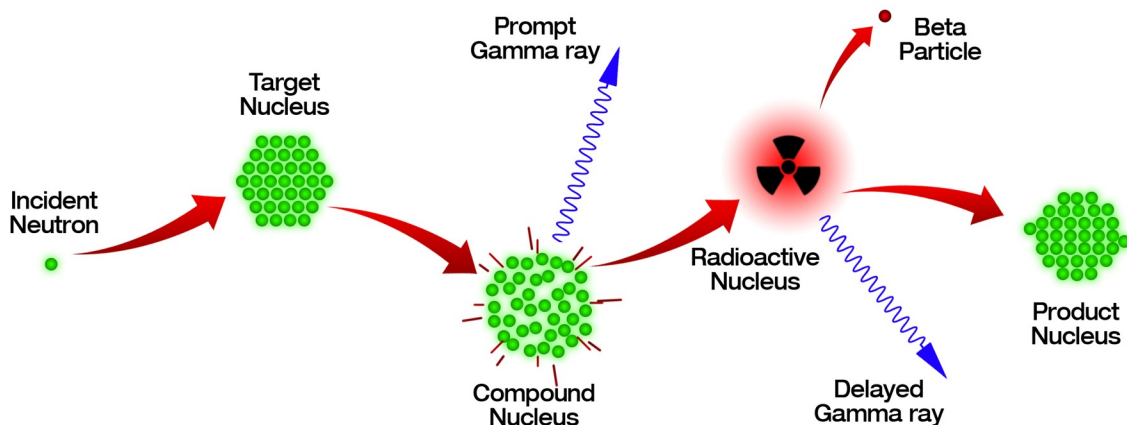


Figure 3.13: Schematic drawing of a neutron capture process, showing possible intermediate states and outcomes. Modified after Firestone (2003).

These gamma-rays account for most of the instrumental background measured with SPI. The instrumental background represents typically 99% or more of the measured data in a single observation. In particular, the ACS vetoes about  $70000 \text{ cts s}^{-1}$ , whereas the rate of photons measured by the Ge detectors, between 20 and 8000 keV, is around  $50 \text{ ph s}^{-1}$ . However, a high background count rate from (secondary) cosmic-ray interactions still remains in the Ge detector spectra. Apart from the cosmic-ray bombardment, nuclear de-excitation gamma-ray lines whose Compton "tails" produce instrumental background continuum at lower photon energies (Sec. 3.2.3.2), there is also general continuum radiation from bremsstrahlung, for example. Annihilation radiation from cosmic-ray or decay positrons with electrons in the satellite produce a strong background feature at 511 keV as expected from the rest mass of the positron. Positron-nucleus bremsstrahlung may also produce continuum along the whole spectral energy range.

Due to the penetrating nature of high-energy cosmic-rays, the entire spacecraft material is exposed to such nuclear reactions, creating secondary gamma-rays. Most of the instrumental background is prompt and follows closely the impinging function of cosmic rays into the space craft. Delayed photons from long-lived radioactive nuclei produce radioactive build-ups, showing a rising gamma-ray flux for particular lines. Cosmic rays steadily create more and more radioactive nuclei of the same species in a much shorter time than the half-life of the nuclei so that a reservoir of radioactivities is filled and more nuclei can decay during the same time (build-up). When the cosmic-ray activation rate and the decay lifetime balance each other, a constant, steady state, gamma-ray flux level of that particular line, greater than in the beginning of the mission, will be established. Examples for this behaviour are  $^{60}\text{Co}$  with a half-life time of 5.27 years emitting gamma-rays predominantly at 1173 and 1333 keV,  $^{22}\text{Na}$  with a half-life time of 2.60 years at a photon energy of 1275 keV, or  $^{65}\text{Zn}$  with a half-life time of 0.67 years and a line at 1116 keV.

In a solar flare event, INTEGRAL is exposed by an enhanced particle dose, so that the instrumental gamma-ray background lines and continuum are rising proportional to the strength of the flare. In such an event, large amounts of charged particles are ejected from the Sun, often accompanied by a coronal mass ejection. Since most of the lines come from prompt de-excitations, the overall background level returns to normal right after the flare. But some species have half-life times of several days to

weeks and stay on a high level according to their half-life times, and the background gamma-ray emission only fades away slowly. With a half-life time of 15.97 days,  $^{48}\text{V}$  is very sensitive to such solar flare events in its strong lines (large branching ratio) at 944, 983, and 1312 keV.

### 3.2.3.2 Self-Consistent Background Modelling

In Figs. 3.14a to c, typical spectra measured with SPI are shown for different accumulation times. In Fig. 3.14c, it is shown that SPI data are statistics limited. Consequently, simple background subtraction is not possible. In particular, celestial signals and background contributions have to be determined simultaneously by correctly considering the Poisson statistics

$$P(d|m) = \frac{m^d \exp(-m)}{d!}, \quad (3.11)$$

which describes the probability that  $d$  events (measured photon counts) are found in a given length of time (exposure time), if the events occur independently at a constant rate  $m$  (complete model). The model  $m_k$ , for a particular energy bin  $k$ , consists of a description of the background in this bin over time, and a description of a possible celestial signal. The background intensity varies according to a superposition of the cosmic-ray incident rate, radioactive build-ups, radioactive decays, and other secondary effects like distance to Earth, solar cycle phase, or cold plate temperatures. A temporal variation of celestial source intensities may exist, depending on the source type. Large scale diffuse emission, for example, can be considered constant on time scales of the satellite mission; particular point sources, such as pulsars or expanding supernova remnants, can show strong time variability.

In general, the model that is used to describe the data in SPI is given by

$$m_k = \sum_t \sum_j R_{jk} \sum_{i=1}^{N_I} \theta_{it} M_{ij} + \sum_t \sum_{i=N_I+1}^{N_I+N_B} \theta_{i,t} B_{ik}, \quad (3.12)$$

where  $m_k$  is one element of the "data cube" referring to the counts in energy bin  $k$  from all detectors and pointings in a particular data set. The contributions from the  $N_I$  celestial sources,  $M_{ij}$ , are convolved by the imaging response function  $R_{jk}$  - the mask pattern - for each image element  $j$ . In the image dimension, pixels  $j$  refer to a particular longitude and latitude, at a particular point (interval) in time. In general, there are  $N_B$  background components,  $B_{ik}$ . These are independent of the mask. Both, sky and background may be time-dependent on different time-scales. The parameters  $\theta_{i,t}$  determine the intensities for all model components  $i$ . By deriving the sky sources' intensities per chosen energy bin size, spectra are derived which are independent of any prior assumption of the spectral shapes of the sources, and hence mostly unbiased.

Given a source at a determined position in the sky, the relative mask patterns, varying from pointing to pointing (see Sec. 3.2.4.3), are known for all source positions. If

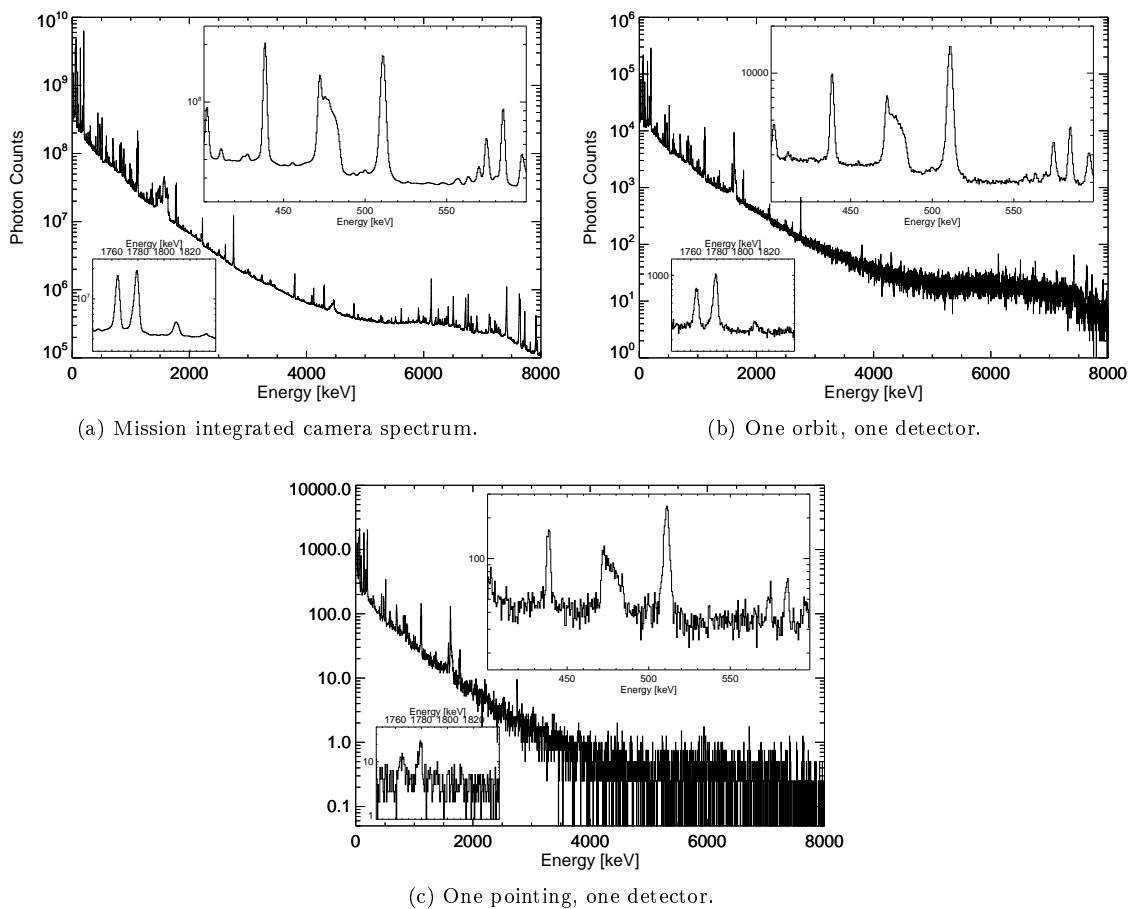


Figure 3.14: Typical SPI spectra on different time scales. Shown are mission integrated spectrum for all 19 detectors summed (a) in 1 keV binning with inlets showing the 511 keV and 1809 keV vicinity, respectively, in 0.5 keV binning. Here, even the weakest instrumental background lines are identifiable whereas for shorter time scales, those features are present but drown in the statistical noise. Panel (b) shows the spectrum of one orbit (here #1000) and one detector (here D00) which is used for determining the spectral background parameters, and panel (c) shows the spectrum of one pointing (within revolution #1000) and one detector (D00) which is to be analysed as part of an observation data set consisting of many pointings, with 4 keV binning in the broadband spectrum for clarity.

a source (extended or point-like) is located at galactic coordinates  $(l/b)$ , it is known which shadowgrams to expect on the SPI Ge detectors, depending on where SPI pointed to. It is, however, not known how strong the source is. In addition, the background intensities are also unknown, a priori. Therefore, the intensity scaling parameters  $\theta_{i,t}$  for both, sky and background, have to be determined by statistical inference. In this thesis, the maximum likelihood method is used to determine the fluxes from predicted, predetermined, models of sky and background. Because the measured photons are Poisson-distributed, the likelihood of a set of model parameter  $\theta_{i,t}$ , given the data set  $D$  with  $n$  data points, is calculated by

$$\mathcal{L}(\vec{\theta}|D) = \prod_{k=1}^n \frac{m_k^{d_k} \exp(-m_k)}{d_k!}. \quad (3.13)$$

The used log-likelihood to determine the scaling parameters in a statistical fit is then given by

$$\mathcal{C}(\vec{\theta}|D) = 2 \sum_{k=1}^n [m_k - d_k \ln(m_k)], \quad (3.14)$$

which is called Cash statistic (Cash 1979). Note that the term  $\ln(d_k!)$  is dropped from  $\mathcal{C}(\vec{\theta}|D)$  as it is model independent, and would vanish anyway when comparing models by likelihood ratio tests. The Cash statistic correctly treats the Poisson distributed data, as the model prediction is always positive definite, and also avoids the problem of zero or negative data counts which may occur by simple background subtraction.

### 3.2.3.3 Spectral Description of SPI Data

The general spectral shape of SPI data can be described by two components: many instrumental gamma-ray lines on top of a power-law like continuum. Although it is not known what the background intensity in a particular energy bin at a particular point in time is, it is known that the background sources inside the satellite have constant origins. This means that the radiation inside the satellite, as measured by the Ge detector array, is coming from the same direction at different times. As a consequence, the background pattern that is measured for a particular isotope is constant over time, no matter where SPI is pointed to. Each instrumental background line has therefore its own background pattern which only changes if a detector fails. Likewise, the instrumental background continuum is also constant in time, as the continuum sources are also spatially constant. However, since the instrumental resolution of SPI is 2.15 keV at photon energies around 511 keV, the background pattern for particular half-keV energy bins is not constant, because the detectors degrade over time and the resolution (instrumental line width, FWHM) changes accordingly.

The only information required to obtain the celestial intensity as a function of energy (spectrum), is the background detector pattern of instrumental continuum and all instrumental lines as a function of energy and time. In addition, the celestial detector pattern is given by the observation strategy and the imaging response function. The intensity of each pattern is then determined by minimising the log-likelihood, Eq. (3.14). The background patterns for each energy bin of interest have to be determined from the data itself, but cannot be determined on time-scales of pointings ( $\sim$  hours, i.e. shortest time unit) as the statistics are not high enough, and the source does also imprint its own shadowgram onto the detectors. Using observations in which the source of interest is not in the field of view of SPI will only work if these "off"-observations are not too far away in time. This is due to the fact that the detectors degrade between different observations and will thus skew the background patterns for particular energy bins. Similar arguments apply for a summation into 19 mission-integrated spectra because this would only resemble a mean degradation, even though the statistics would be enough to wash out any celestial contribution to the background pattern (see also Sec. 3.2.4 for details on the background method).

As a compromise to smear out celestial contributions, at the same time to trace the detector degradation, and also to have enough statistics to determine the back-

ground patterns with high precision, the spectra are combined per detector and three-day orbit of INTEGRAL. In order to measure the relative intensities per detector (detector ratios, patterns), the orbit integrated spectra are described by a power-law and a number of instrumental background lines, thereby separating continuum and line background patterns, which may vary on different time scales. The mission-integrated spectrum (14 years, 19 detectors) shows a large number of instrumental background lines which will have varying widths on the three-day time scale due to the cosmic-ray degradation effects. In a defined energy range of interest, the spectrum per orbit and detector  $j$  is determined by a statistical fit using the function

$$C(E; C_{0,j}, \alpha_j) + \sum_i L_i(E; A_{0,ij}, E_{0,ij}, \sigma_{ij}, \tau_{ij}), \quad (3.15)$$

where the sum over  $i$  is over all instrumental lines in that energy range, and  $C(E)$  and  $L(E)$  are given by

$$C(E) = C_{0,j} \left( \frac{E}{E_m} \right)^{\alpha_j} \quad (3.16)$$

$$G(E) = A_{0,ij} \exp \left( -\frac{(E - E_{0,ij})^2}{2\sigma_{ij}} \right) \quad (3.17)$$

$$T(E) = \frac{1}{\tau_{ij}} \exp \left( -\frac{\tau_{ij}}{E} \right) \quad \forall E > 0 \quad (3.18)$$

$$\begin{aligned} L(E) &= (G \otimes T)(E) = \\ &= \sqrt{\frac{\pi}{2}} \frac{A_{0,ij} \sigma_{ij}}{\tau_{ij}} \exp \left( \frac{2\tau_{ij}(E - E_{0,ij}) + \sigma_{ij}^2}{2\tau_{ij}^2} \right) \\ &\quad \operatorname{erfc} \left( \frac{\tau_{ij}(E - E_{0,ij}) + \sigma_{ij}^2}{\sqrt{2}\sigma_{ij}\tau_{ij}} \right). \end{aligned} \quad (3.19)$$

The continuum  $C(E)$  is represented by a power-law function with amplitude  $C_{0,j}$ , normalised to a fixed (i.e. not fitted) value  $E_m$ , and power-law index  $\alpha_j$ . The line shape  $L(E)$  takes into account the degradation effects of a formerly symmetric Gaussian function  $G(E)$ . The function is parametrised by the amplitude  $A_{0,ij}$ , centroid  $E_{0,ij}$ , and width  $\sigma_{ij}$ .  $L(E)$  is then calculated by a convolution of  $G(E)$  with an exponential tail function  $T(E)$ , which originates in a physical description of the detector degradation and involves the degradation parameter  $\tau_{ij}$ . In general, it is expected that  $\sigma_{ij}$  is constant over time for a particular detector  $j$  and line  $i$ , as it represents the physical property of that detector. Only  $\tau_{ij}$  should vary according to the detector degradation. However, since  $\sigma_{ij}$  and  $\tau_{ij}$  are partly degenerate in the statistical description of the spectra, also their absolute values cannot be disentangled entirely. The line shape  $L(E)$  is shown for different values of  $\tau$  in Fig. 3.15.

Using the description of Eq. (3.19), and as can be seen from Fig. 3.15, a degraded spectral line is not symmetric any more, but rather elongated towards lower photon energies. Furthermore, for constant values of  $A_0$ ,  $E_0$ , and  $\sigma$ , the line centroid does

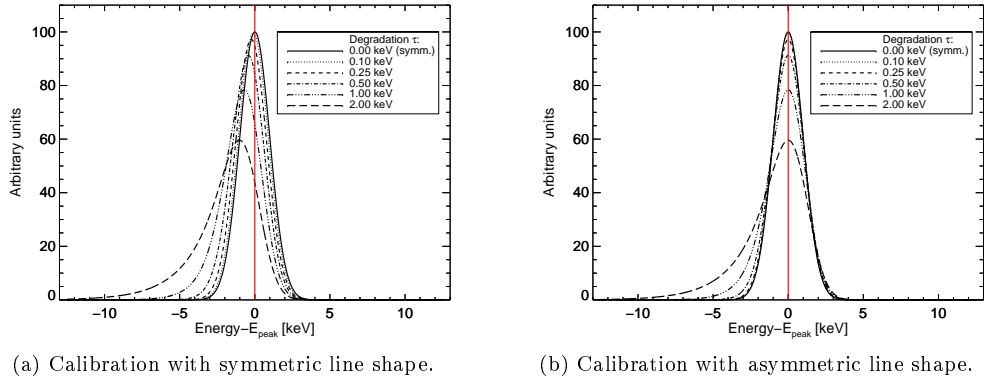


Figure 3.15: Line shapes and calibration impact on line positions. The resulting line peaks are shifted towards lower energies if the calibration is done with a symmetric Gaussian function as shown in (a). The larger the degradation parameter  $\tau$ , the further the peak is shifted. Note that the line peaks for  $\tau \neq 0$  follow the curve for  $\tau = 0$ . If an asymmetric function like Eq. (3.19) is used, or if the peak shift would be corrected by using Eq. (3.20), the peak positions align on the red line as shown in (b).

not peak at  $E_0$ , the amplitude is not given by  $A_0$ , and the FWHM is a function of both,  $\sigma$  and  $\tau$ . In particular, the peak energy  $E_{peak}$  is given by solving the equation

$$\left. \frac{\partial L(E)}{\partial E} \right|_{E=E_{peak}} \stackrel{!}{=} 0, \quad (3.20)$$

which reduces to

$$E_{peak} \approx E_0 - \tau \quad (3.21)$$

for small values of  $\tau$  (see Appendix B). The FWHM,  $\Gamma_L$ , of  $L(E)$  can be approximated by

$$\Gamma_L \approx \Gamma \left[ a_0 + \sqrt{(1 - a_0)^2 + \left( \frac{a_1 \tau}{\Gamma} \right)^2} \right], \quad (3.22)$$

where  $\Gamma = 2\sqrt{2 \ln 2} \sigma$  is the normal FWHM of the symmetric Gaussian  $G(E)$ , and  $a_0 = 0.913735$  and  $a_1 = 0.710648$  are fitted constants (Kretschmer, K. A. 2011). The only but most important measure of the line shape which does not change due to the convolution is the area under the curve, i.e. the intensity, which is reasonable because all charge carriers still reach the cathode so that only the shape is degraded but the total flux remains constant,

$$\int_{-\infty}^{+\infty} L(E) dE = \int_{-\infty}^{+\infty} (G \otimes T)(E) dE = \int_{-\infty}^{+\infty} G(E) dE = \sqrt{2\pi} \sigma A_0. \quad (3.23)$$

As a consequence, the parameters  $E_0$  may vary in time but  $E_{peak}$  should be stable over longer periods of time. However, since the energy calibration is done automated by fitting symmetric Gaussians to a set of strong background lines (see Appendix C),

the peak values of the calibrated and thus all other lines, too, can show offset of the order of 0.1 keV. Not considering the spectral domain by building a background model will thus end in skewed time and detector patterns and produce systematic effects. Likewise, the FWHM of the degraded line shape is rising in time until the annealing sets in and recovers the resolution of the detectors.

### 3.2.3.4 Instrumental Background Parameters

Using this formalism for the whole energy range of SPI, an instrumental background data base is created, providing information about the spectral, temporal, and peculiar behaviour of instrumental lines and continuum. Furthermore, this background data base provides the detector patterns for all energies and all times, separately for lines and continuum, building the basic background model ingredients as will be described in Eqs. (3.33) and (3.34). It can be shown that the detector patterns for particular instrumental background features stay constant on all time scales, as expected from the assumption of spatial constancy of background sources in the space craft. This is illustrated in Fig. 3.16 for the case of the background continuum on a half-hour time scale. For longer time-scales, see Fig. 3.20.

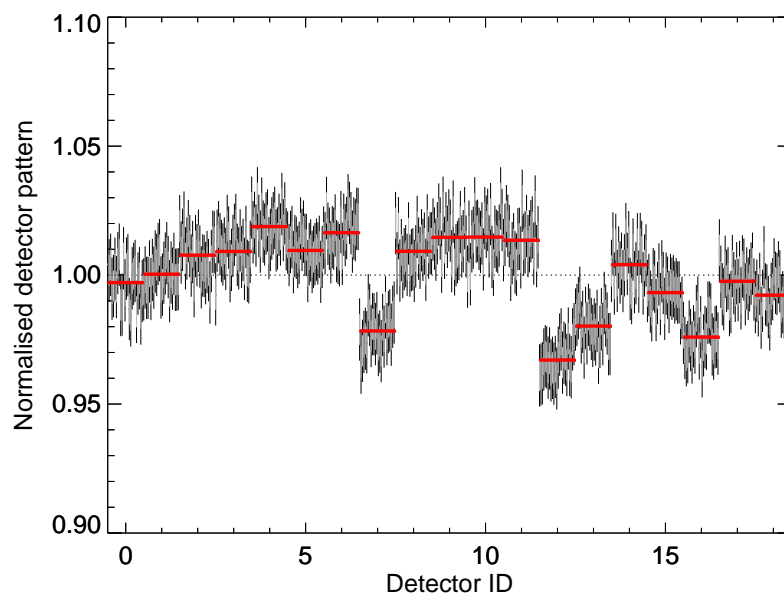


Figure 3.16: Continuum detector pattern on short time scales. Shown is the energy band between 100 and 900 keV for all pointings in revolution 56 (black data points) in which 19 detectors were fully functioning. The means values during that time are given as red bars, serving as a secondary time axis. Note also the similarity to Fig. 3.20d for longer time scales.

In Figs. 3.17a-f, the temporal behaviour of characteristic spectral features are shown as a function of INTEGRAL mission time. In general, the background count rate as a function of time is rising, starting from February, 2003 (INTEGRAL revolution #43), has a maximum near Jan 2010, declines afterwards, shows a minimum in 2014, and starts to rise again. Prompt background lines, as shown in panels (a) and (b) of Fig. 3.17, are anti-correlated to the solar cycle, shown as three-monthly average of the sunspot number. The linear Pearson correlation coefficient,  $\rho$ , between the  $^{69}\text{Ge}$  ( $^{205}\text{Bi}$ ) line intensity and the solar cycle is  $-0.71$  ( $-0.60$ ) on a time basis of three days, showing that the reduced magnetic field of the Sun increases the background flux, as its shielding effect for charged particles is reduced. Background

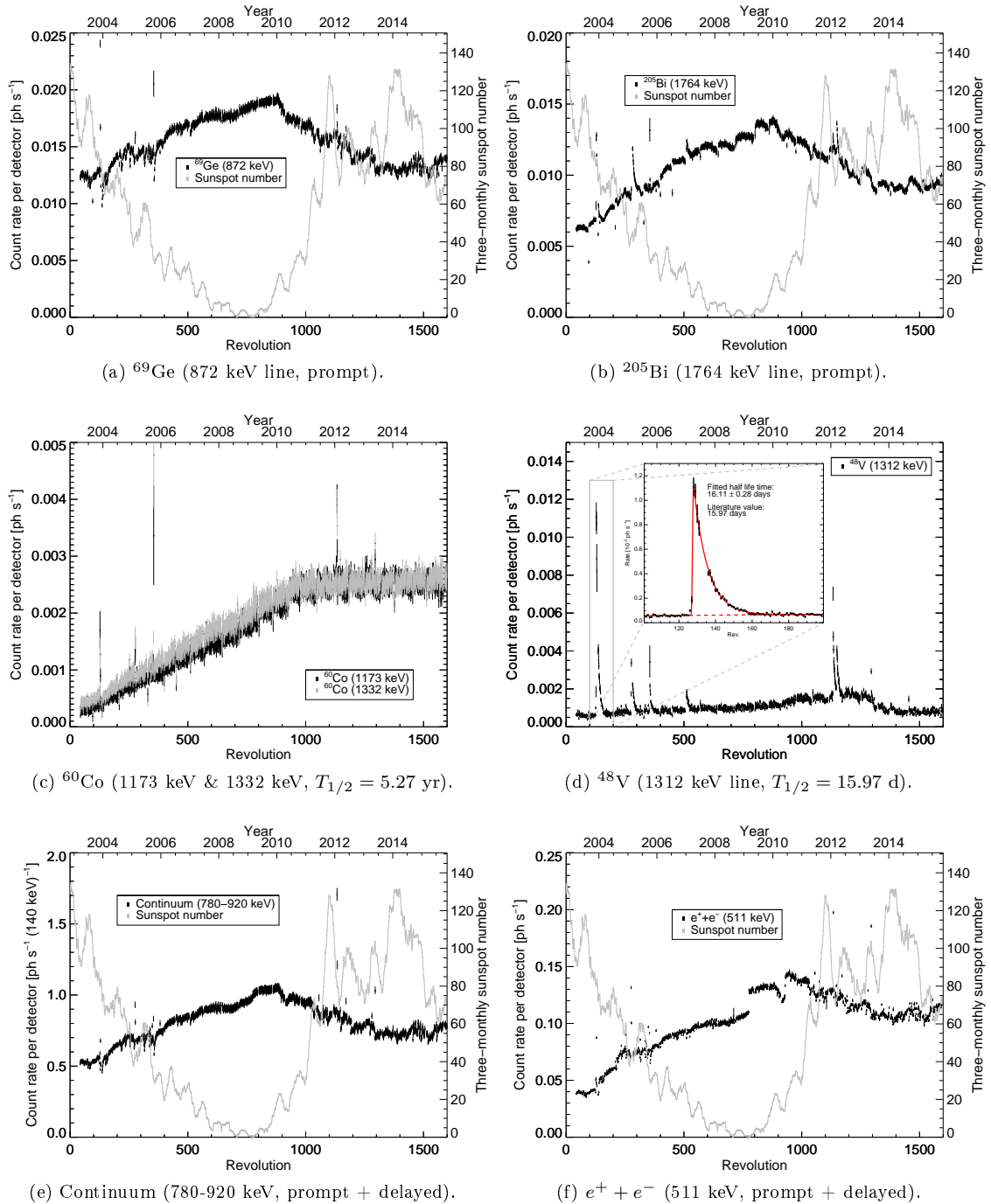


Figure 3.17: Background intensities as a function of time (INTEGRAL revolutions) for different characteristic spectral features. See text for details.

lines with half-life times longer than a few hours show different temporal behaviours, see panels (c) and (d). The half-life time of  $^{60}\text{Co}$  is so long that radioactive build-ups are clearly seen. The background line flux is linearly rising until year 2011, being saturated afterwards and emitting on a constant level. In the case of  $^{48}\text{V}$ , also a radioactive build-up is visible but which decays after the year 2012 to the level it had at the beginning of the mission. Due to the solar maximum in 2012, not enough  $^{48}\text{V}$  is produced to retain a constant flux level like in the  $^{60}\text{Co}$  case. In addition, solar flares create clear signatures of enhanced  $^{48}\text{V}$  abundance in the space craft. This enhancement then decays according to the half-life time, as shown by an exponential fit in the inset of (d), for a solar flare event in Oct 2003. The continuum and the instrumental positron annihilation signal in panels (e) and (f), both contain prompt and delayed instrumental background photons as a combination of prompt responses to cosmic-ray bombardment, and delayed photons and positrons from the decay of longer-lived isotopes. As most of the continuum is dominated by prompt background emission, the anti-correlation with the solar cycle is clearly visible ( $\rho = -0.58$ ). For the instrumental 511 keV line, the correlation is partly visible, but because the camera reacts strongly to detector failures in the case of background positrons, large steps in the total flux are seen.

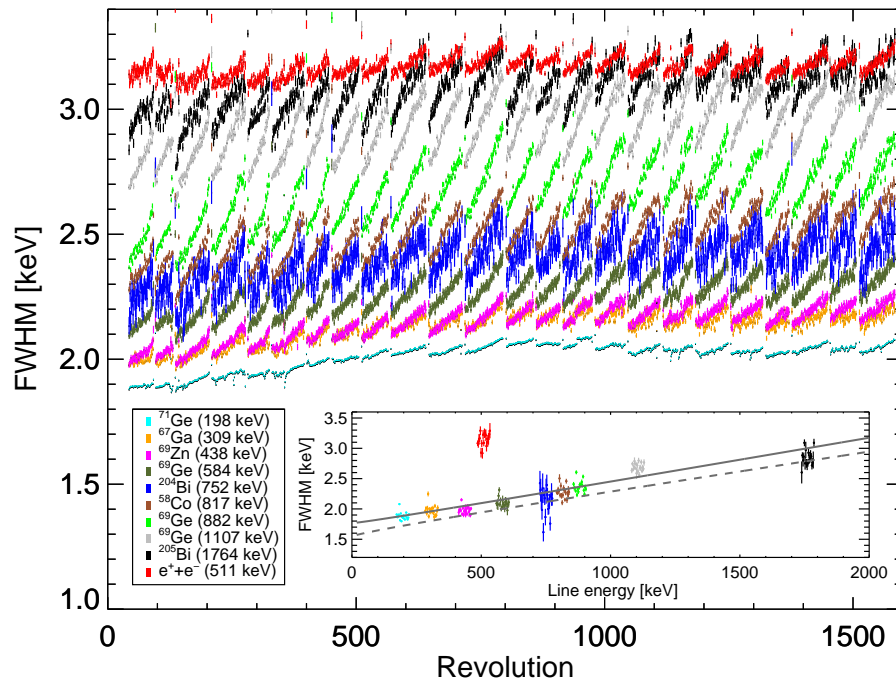


Figure 3.18: Instrumental background line widths as a function of time for different characteristic and strong background lines. The general trend is the gradual degradation of the detectors leading to a worsening of the resolution with time. Twice a year, the camera is heated up (annealing), thereby repairing the lattice structure and resetting the resolution to acceptable values. The inset shows the FWHM after an annealing, i.e. best resolution, of each line for each detector in flight. The data points per detector are shifted around the line energy for illustration purpose only. Except for the instrumental 511 keV line which is Doppler broadened, the data points can be described by Eq. (3.10), providing the resolution as a function of energy in flight (solid grey line) compared to the ground calibrated function (dashed grey line). See text for details.

The line widths as a function of time, Fig. 3.18, show a sawtooth shape. This originates from the gradual degradation of the detectors due to cosmic-ray bombardment, and the annealing activities, which are conducted twice a year to repair the lattice structure of the Ge detectors. Fitting the line widths as a function of time by straight lines, for the different line energies from Fig. 3.18, the average detector degradation per revolution can be estimated to  $\approx 4.5E[\text{MeV}] \frac{eV}{\text{rev}}$ , where  $E$  is the

photon energy in units of MeV. The general Ge detector resolution behaviour as a function of energy for each detector is shown in the inset. The FWHM as a function of energy has been determined by fitting Eq. (3.10) to all data points in the inset, but ignoring the instrumental 511 keV line as it is Doppler broadened with respect to the neighbouring lines. This is probably due to the annihilation of positrons not at rest with respect to the space craft. The fitted parameters of the function are  $F_1^{flight} = 1.77$ ,  $F_2^{flight} = -2.2 \times 10^{-3}$ , and  $F_3^{flight} = 7.5 \times 10^{-4}$ , respectively. The in-flight and ground-calibrated resolution is shown as solid and dashed grey line in the inset, respectively.

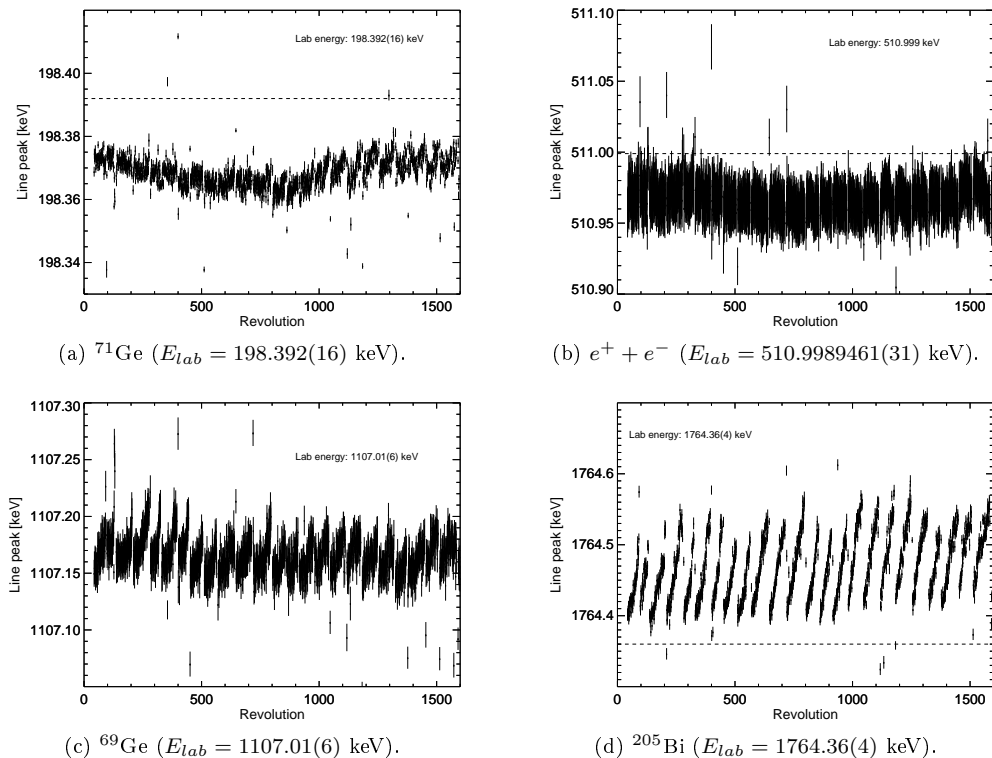


Figure 3.19: Instrumental background line peak energies for different instrumental lines as a function of time. The laboratory energies are marked with dashed lines. The higher the line energy, the more the systematic line drift. See text for details.

The peak values of lines, shown in Fig. 3.19, are varying by about 0.01% between two annealing phases, irrespective of the energy. Due to imprecise energy calibration (ISDC, see Appendix C), most of the lines' systematic drift is much larger than its statistical uncertainty. This effect introduces a systematic uncertainty for celestial gamma-ray line shifts, leading to Doppler-velocity inaccuracies of the order  $\left(\frac{\Delta E}{E}\right)_{calib} c \approx 10^{-4}c \approx 30 \frac{\text{km}}{\text{s}}$ . In the case of the 1808.63 keV line, for example, the systematic uncertainty is of the order 0.2 keV as seen in Fig. 3.19d, equivalent to  $33 \frac{\text{km}}{\text{s}}$ , while the statistical uncertainty on the line shift is only 0.06 keV ( $10 \frac{\text{km}}{\text{s}}$ , see Sec. 5.1.1.4).

The background detector patterns for different isotopes are different, but are the same for the same isotopes, Fig. 3.20. This is another validity proof of the background modelling approach as it provides an additional check of self-consistency. The general shapes of the detector patterns for lines can be summarised as follows: For background sources which surround the Ge camera, the outer detectors (07-18) are illuminated more than the inner ones (00-06), as the inner ones are shielded by

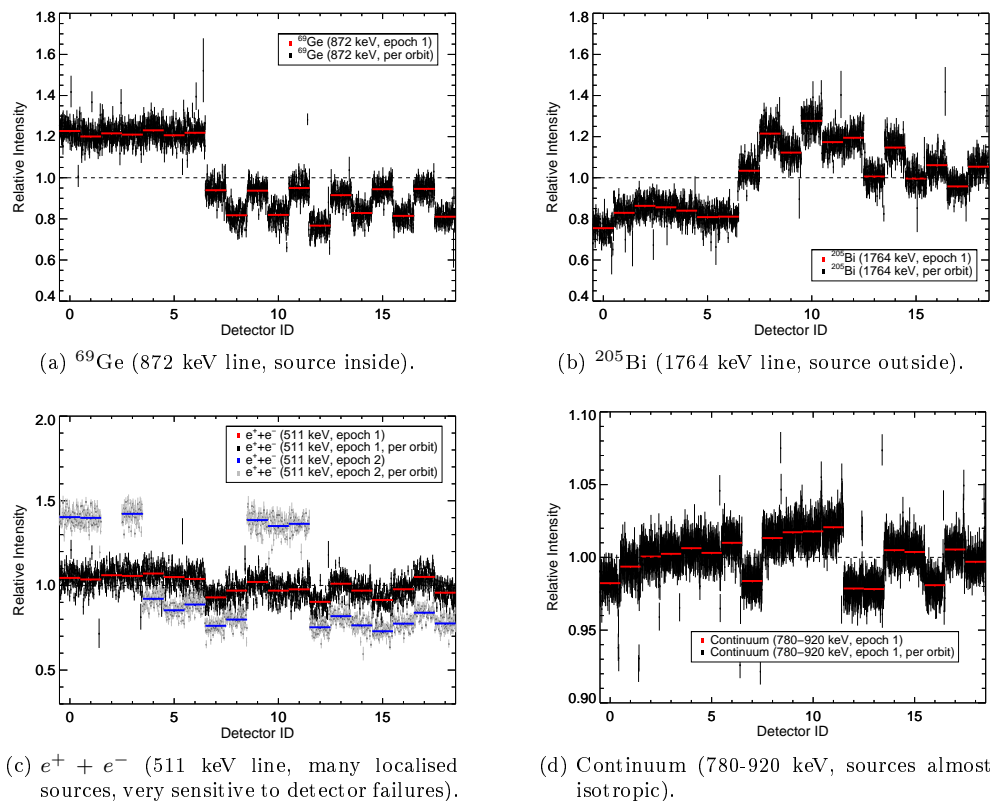


Figure 3.20: Background detector patterns as a function of time for different characteristic background features. The red bars represent the average normalised detector intensity relative to the others for the time scale of the first epoch, i.e. integral revolutions #43 to #140 ( $\approx 290$  days) until the first detector (D02) failed. It also serves as a secondary time axis for the detectors as each set of black data points around the bar ranges from revolution #43 to #140. For each feature, it is evident that the detector patterns stay constant as expected from the spatial constancy of the background sources in the satellite. Note that all Ge-like instrumental background lines show similar patterns like in (a), and all Bi-like lines similar to (b). The continuum, (c), is rather flat, not showing variation from detector to detector, meaning that the background sources are almost isotropically distributed. For the 511 keV background line, (d), also the second epoch with only 18 working detectors is shown for comparison as the line is very sensitive to detector failures. See text for details.

the outer ones. This is true for lines originating in the SPI ACS, made of BGO; all lines from Bi and "neighbouring" elements<sup>4</sup>, like Pb or Ra, lead to a detector pattern like shown in Fig. 3.20b. Another family of background lines come from Ge and associated elements like Ga or Zn. Here, the background source is the Ge detectors themselves, so that the more neighbouring detectors one particular detector has, the more Ge line intensity it will measure. Thus, the inner detectors (00-06), with six neighbours each, have a larger background intensity relative to the detectors, with only four (07,09,11,13,15,17) or three (08,10,12,14,16,18) neighbours. This is shown in Fig. 3.20a for the Ge line at 872 keV. When a detector fails, the neighbouring detectors will receive more counts, because the photons which are actually measured as triggering two detectors (double events) will be converted to single events in these neighbours, as the dead detector does not recognise the second trigger any more. This also reflects in the relative detector patterns, boosting the neighbours' intensities of a dead detector. For example, when detector 02 fails, detectors 00, 01, 03, 09, 10, and 11 show an increased flux like is shown in the extreme case of the instrumental 511 keV line, Fig. 3.20c. This effect occurs for all energies, no matter if in a line or continuum. However, since the continuum is dominating the measured

<sup>4</sup>Neighbouring elements are defined as isotopes connected by electron capture, p, n, or  $\alpha$  reactions in the table of isotopes.

photon counts in one energy bin<sup>5</sup>, treating that energy bin's counts as "one" background source, and not linearly combining the two patterns with different scaling factors, will spoil the inferred fluxes for celestial sources. The continuum detector ratios, i.e. integrating the non-line parts over large energy bands, are very close to 1.0. They differ slightly due to differences in detector volume, which lead to different effective areas to measure photons, Fig. 3.20d. In principle, there are many different background detector patterns from different lines. If there is a peculiar source right next to a particular detector, and only there, this detector will of course show a very large background flux, but is also shielding the neighbours, which also shield the next-to-neighbouring detectors. An example are the lines from Ti or V with aligned structure components inside the instrument. On the other hand, there is a significant amount of Cu in the cables. Apparently, this background is nearly isotropic, since the detector patterns for those lines (and associated elements, Fe, Co, Mn, Cr) are rather flat.

By investigations of all these dependencies and trends, a physically-consistent track of effects such as resolution worsening, detector failures, energy calibration changes, and detector pattern constancy can be asserted. Herein, also the impacts of the solar cycle and flares, and the different physical processes that lead to different spectral shapes have to be accounted for. From such a data base of the behaviour of instrument response and background, a self-consistent background model is built, using the details of the spectral parameters data base.

Typical data sets for large scale emission of the entire Milky Way contain several 10000 observations (pointings). Each of the 19 detectors records photons in several 1000 channels (energy bins). Quickly, an overwhelming data space in these three abstract dimensions accumulates. In order to illustrate the data structure of SPI, and how the background modelling procedure works in combination with a maximum likelihood analysis in detail, an oversimplified two-detector description will be carried out in the following section. Thereafter, the application to the full volume of SPI data will be presented.

### 3.2.4 SPI-light

A two-dimensional mathematical construct may describe the background modelling procedure for the 19-detector SPI camera in an understandable and comprehensible way ("SPI-light"). The hypothetical SPI-light instrument, Fig. 3.21, consists of two detectors, surrounded by an anti-coincidence shield, and a time-variable mask above the detectors. The mask structure and the corresponding shadowgram on the detectors change instantaneously between different pointings of the whole observation.

The parameter space for a particular SPI-light observation consists of  $N_{obs}$  pointings with a source *in* the field of view, and  $N_p$  total (mission) pointings, where  $N_p > N_{obs}$ . The detectors are named  $D1$  and  $D2$ , respectively. The mask produces an idealised, sharp-edged shadow, and is assumed to not create background photons.

---

<sup>5</sup>In most cases the background continuum in a single energy bin is stronger than the background lines. There are only a few exceptions, such as lines at 140 or 198 keV.

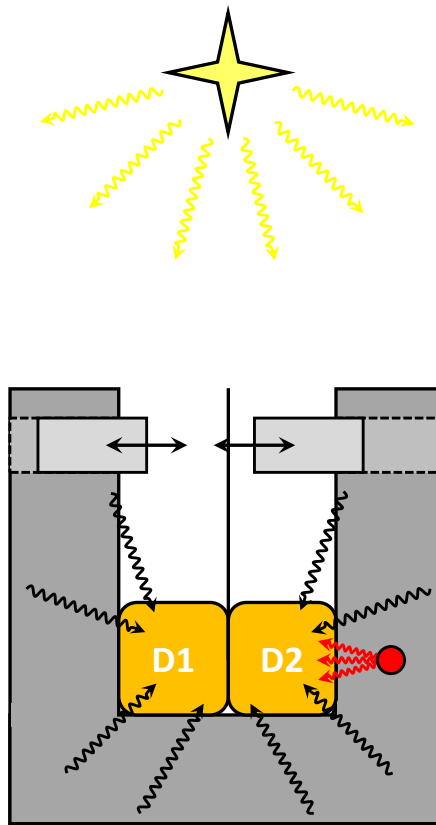


Figure 3.21: Schematic drawing of SPI-light, showing the main components to describe the working principle, background sources, and detectors. The detectors are shown in orange, embedded in the veto-shield (grey), and below the time variable mask (light grey). A source emitting gamma-rays (yellow rays) is shown as star above the instrument. Background sources are marked with black rays representing the continuum radiation, and with red rays indicating a particular line emitting region (red circle). See text for details.

#### 3.2.4.1 Single Energy Bin

First, a single energy (bin)  $E_\gamma$  is considered. Emission may arise from the celestial source, and from the shields of SPI-light as background radiation. The mask totally obscures one detector at a particular pointing  $p$  from the source, so that this detector only measures background<sup>6</sup>. The response function to a celestial source with signal strength  $\alpha$  (in units of photons per second) in the field of view of SPI-light is then given by  $R_S(p)$  in vector-form,

$$R_S(p) = N_S \cdot \begin{pmatrix} \frac{1}{2}(1 + (-1)^{p+1}) \\ \frac{1}{2}(1 + (-1)^p) \end{pmatrix}. \quad (3.24)$$

Here,  $p$  is the number of the pointing, and  $N_S = 2$  a normalisation coefficient<sup>7</sup>. If a photon interacts with a detector, its energy is assumed to be completely deposited in this detector, and may not scatter. Background that originates from the shields of SPI-light is measured in each detector permanently. As the structure of the instrument and its irradiation from cosmic-rays is assumed to not change, the "response function of the background" with intensity  $\beta$  (in units of photons per second) can

<sup>6</sup>If this is known, then there is an easier way to disentangle source and background. As SPI background is not known a priori, this oversimplification will be ignored.

<sup>7</sup>In general the detector ratio/pattern is normalised to the number of detectors,  $N_{det} = 2$ .

be expressed as

$$R_{BG}(p) = N_{BG} \cdot \begin{pmatrix} 1 \\ 1 \end{pmatrix}. \quad (3.25)$$

This is valid for all  $p$ . In Eq. (3.25),  $N_{BG} = 1$  is the normalisation of the response. The background intensity may be taken to be much greater<sup>8</sup> than the celestial intensity,  $\beta \gg \alpha$ . The measured data,  $D(p)$ , also in units of photons per second, is then a superposition of background and sky

$$D(p) = \alpha R_S(p) + \beta R_{BG}(p) = \frac{1}{2} \begin{pmatrix} \alpha(1 + (-1)^{p+1}) + 2\beta \\ \alpha(1 + (-1)^p) + 2\beta \end{pmatrix}. \quad (3.26)$$

This data structure is shown in Fig. 3.22 for  $N_{obs} = 6$  observation pointings with  $\alpha = 1.5$  and  $\beta = 5$ . For a typical observation, only  $D(p)$  is known;  $R_{BG}(p)$  is unknown and needs to be derived from the data. For any position in the sky, i.e. for any pointing  $p$ , the response function  $R_S(p)$  predicts how a signal in a particular direction would look like. All possible solutions of any source during the  $N_{obs}$  observation pointings are incorporated in  $R_S(p)$ , hence the correct sky model can be derived from knowing the background pattern.

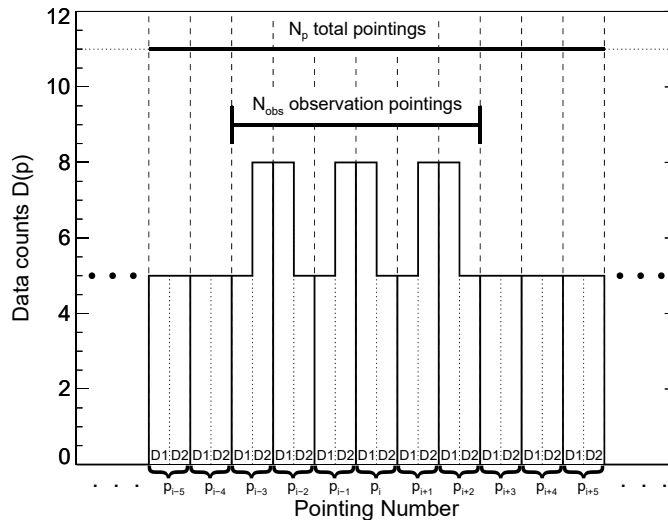


Figure 3.22: Data structure of SPI-light for a single energy bin. The abscissa shows several pointings, separated by dashed lines, from  $p_{i-5}$  to  $p_{i+5}$  out of  $N_p$  pointings with an "observational period" during  $p_{i-3}$  to  $p_{i+2}$ , i.e.  $N_{obs} = 6$ . Each pointing is split by a dotted line, showing the individual counts for each of the two detectors,  $D1$  and  $D2$ . The intensity parameters for background and celestial signal are  $\beta = 5$  and  $\alpha = 1.5$ , respectively.

As illustrated before,  $R_{BG}(p) \equiv R_{BG}$  is independent of  $p$ , which means the pattern of the background radiation, measured by the detectors, is the same for all times. It does not necessarily mean that the amplitude of the background is constant over time, only the ratio between detectors. This is the main assumption for this background modelling approach

<sup>8</sup>This assumption has to be fulfilled if the signal to reconstruct is largely part of the whole observation, i.e. if  $N_{obs} \lesssim N_p$ , and the data set when the real observation was performed ( $N_{obs}$ ) cannot be excluded from the whole mission data set ( $N_p$ ). This is typically the case for SPI when analysing large scale diffuse emission and will be considered as the "standard case".

$$R_{BG} = \text{const.} \quad (3.27)$$

In order to reconstruct the background pattern, the arithmetic mean (or sum) over all mission pointings is used as a mathematical model to (a) circumvent the statistical limitations, and (b) derive the background pattern from the background dominated data.

$$\begin{aligned}
\sum_{p=1}^{N_p} D(p) &= \frac{1}{2} N_{obs} 2\alpha \begin{pmatrix} 1 \\ 1 \end{pmatrix} + N_p \beta \begin{pmatrix} 1 \\ 1 \end{pmatrix} = \\
&= N_p \left( \beta + \frac{N_{obs}}{N_p} \alpha \right) \begin{pmatrix} 1 \\ 1 \end{pmatrix} = \\
&= N_p (\beta + \Delta\beta) \begin{pmatrix} 1 \\ 1 \end{pmatrix} = \\
&= N_p \beta' R_{BG} = \\
&= N_p \beta \cdot \underbrace{\frac{\beta'}{\beta}}_{\text{scaled normalisation}} \cdot \underbrace{R_{BG}}_{\text{reconstructed background pattern}} \quad (3.28) \\
&\quad \underbrace{\hspace{10em}}_{\equiv R_{BGM} \text{ background model pattern}}
\end{aligned}$$

In Eq. (3.28),  $\Delta\beta \geq 0$ , as  $\alpha \geq 0$ , and hence  $\beta' = \beta + \Delta\beta \geq 0$ . In this very special case, the background model pattern,  $R_{BGM}$ , is exactly the initial background pattern  $R_{BG}$ , but with a scaled normalisation which is to be determined by a  $\chi^2$ -minimisation or maximum likelihood fit, for example. For this example, it is sufficient to write down the complete model,  $M(p, \vec{\Theta})$  with scaling parameters  $\Theta_1$  and  $\Theta_2$  for sky and background, respectively, and to equate coefficients:

$$\begin{aligned}
M(p, \vec{\Theta}) &= \Theta_1 R_S(p) + \Theta_2 R_{BGM}(p) = \\
&= \Theta_1 R_S(p) + \Theta_2 \frac{\beta'}{\beta} R_{BG} \stackrel{!}{=} \\
&\stackrel{!}{=} \alpha R_S(p) + \beta R_{BG} = D(p) \\
&\Leftrightarrow \Theta_1 \stackrel{!}{=} \alpha \\
&\Leftrightarrow \Theta_2 \frac{\beta'}{\beta} \stackrel{!}{=} \beta \Leftrightarrow \Theta_2 = \beta \left( \frac{1}{1 + \frac{N_{obs}}{N_p} \frac{\alpha}{\beta}} \right) < \beta \quad (3.29)
\end{aligned}$$

From Eq. (3.29) it is evident that the scaling parameter of the background model,  $\Theta_2$ , will get scaled down with respect to  $\beta$ , as the background model pattern is normalised to the total data counts of the observation, not knowing the intensity of the true background. In Fig. 3.23, one complete "analysis" for the simplest assumptions and configurations is presented.

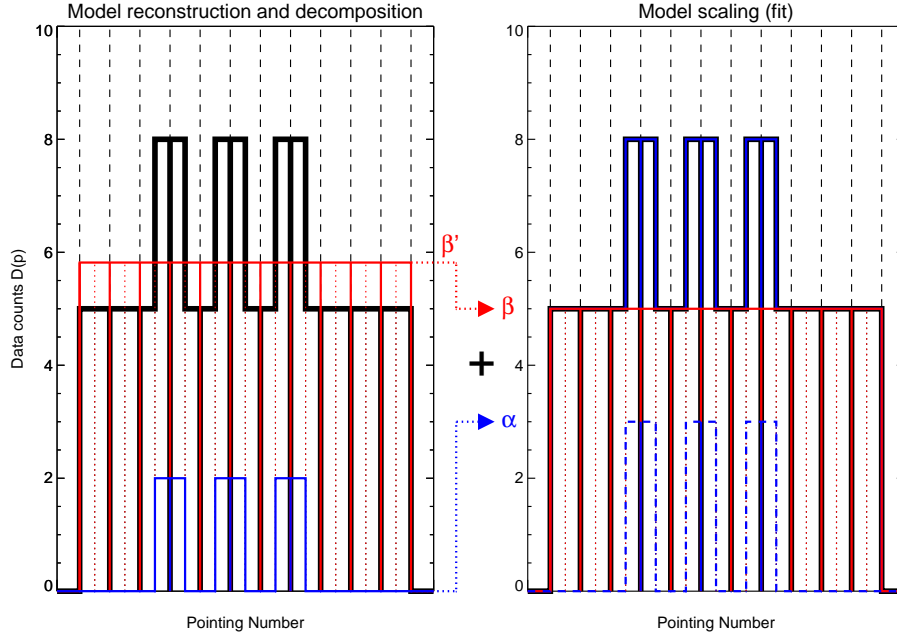


Figure 3.23: Background model reconstruction and scaling procedure. The same data as in Fig. 3.22 are shown for  $N_p = 11$  total observations and  $N_{obs} = 6$  source observations. In the left panel, the reconstructed background model is shown in red as derived from Eq. 3.28, together with the proposed sky model in blue. From the left to the right panel, a fit procedure to adjusting both models to the data (or here by equating coefficients, cf. Eq. 3.29) scales down the background model normalisation  $\beta'$  to the correct intensity  $\beta$  while the sky model obtains its correct amplitude  $\alpha$ .

### 3.2.4.2 Detector Response, Line and Continuum Backgrounds

Complications arise if another background source with a different pattern is introduced. In Fig. 3.21, this is illustrated as a red emission spot. This emission spot in SPI-light is assumed to be a background line emitter in addition to the background continuum. The previous method still works if the two background patterns are assumed to be constant in time. However, the detectors degrade, i.e. the resolution changes with time (pointing), and on different time scales, so that background patterns cannot be considered to be constant for single energy bins any more. The constancy for detector patterns is only fulfilled if all photons for these processes are taken into account, i.e. not only in a single bin but over the full spectral feature. In the following example, the ratio of the area under the same instrumental background line in detectors  $D1$  and  $D2$ , respectively, will be assumed to be constant over time. Similarly, for the continuum background, the pattern is also assumed to be stable. Thus, the assumption in Eq. (3.27) holds for the spectral features as entities, but not for single energy bins. Because the detectors are not identical, their degradations will take shape differently, which will result in time-dependent patterns for single energy bins. This will lead to a violation of Eq. (3.27) because the background patterns in the wings of the instrumental background lines will change, cf. Fig. 3.15.

In this example, the sky response,  $R_S(p)$ , is the same as before, Eq. (3.24). The instrumental background line response,  $R_{BGL}(p)$ , for a particular energy bin which is part of the line, now shows a time dependency. For very long times, this will be an exponential worsening of the detectors (see Sec. 3.2.3.4), but between two annealings (Sec. 3.2.2.1), this can well be approximated by a linear function

$$\frac{1}{N_{BGL}} R_{BGL}(p) = \begin{pmatrix} \lambda_1 \\ \lambda_2 \end{pmatrix} + p \begin{pmatrix} l_1 \\ l_2 \end{pmatrix} \quad (3.30)$$

In Eq. (3.30),  $N_{BGL} = ((\lambda_1 + p \cdot l_1 + \lambda_2 + p \cdot l_2)/2)^{-1}$  is the normalisation of the background line response,  $\lambda_1$  and  $\lambda_2$  represent the initial detector pattern for no degradation ( $p = 0$ ), and  $l_1$  and  $l_2$  determine the temporal behaviour. In general  $\lambda_1 \neq \lambda_2$  and  $l_1 \neq l_2$ . The continuum is assumed to be independent of the detector degradation<sup>9</sup>, and is chosen to be the same as in Sec. 3.2.4.1,

$$\frac{1}{N_{BGC}} R_{BGC}(p) = \begin{pmatrix} 1 \\ 1 \end{pmatrix}, \quad (3.31)$$

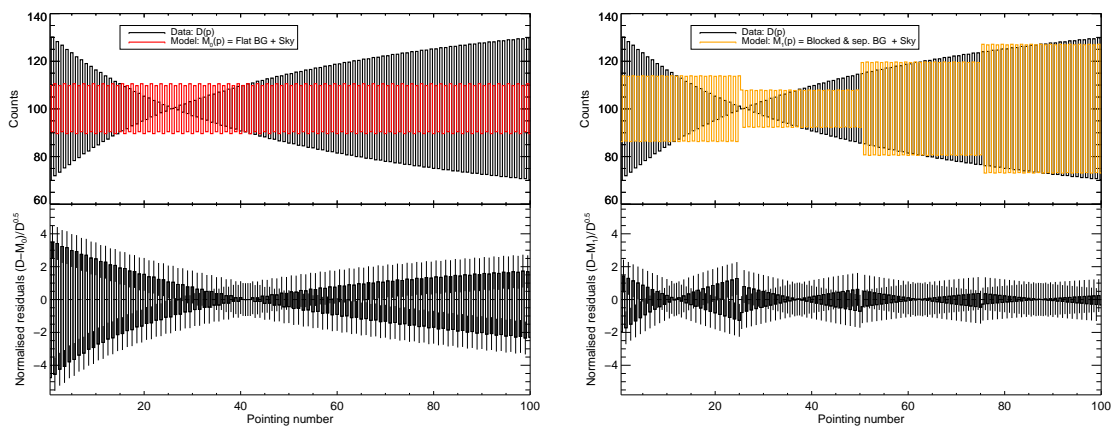
with  $N_{BGC} = 1$ . The measured data during an observation with  $N_{obs}$  pointings is therefore given by

$$\begin{aligned} D(p) &= \alpha R_S(p) + \beta_C R_{BGC}(p) + \beta_L R_{BGL}(p) = \\ &= N_D(p) \begin{pmatrix} 1 \\ 1 + \delta(p) \end{pmatrix}, \end{aligned} \quad (3.32)$$

where  $\alpha$ ,  $\beta_C$ , and  $\beta_L$  are the intensities of the celestial signal, the instrumental continuum background, and the instrumental line background, respectively.  $N_D(p)$  is the proper, time dependent, normalisation of the data which includes a function of the intensities. The time dependent change of the detector pattern of the data is denoted by  $\delta(p)$ .

For this type of data structure, two changes have to be applied to the general treatment of summing individual time bins for a particular energy. Because continuum and line background show different temporal behaviours, **the line part must be treated separately from the continuum part**. It is not possible to distinguish the fraction of an instrumental line and the fraction of the instrumental continuum using a single energy bin. Therefore, the energy spectrum as a whole is to be described by a statistical fit per detector. However, accumulating too many time bins (integration time) to determine the line and continuum patterns will provide false background model patterns, because the only an average degradation would be considered. Therefore, **the integration time to derive the background patterns must balance the integration time to measure the degradation**. In other words, there is a trade-off between the accuracy to measure the degradation of the detectors due to limited statistics, and the accuracy to determine the detector patterns by fitting the integrated spectra per detector. On longer time scales (several revolutions), the detector patterns per energy bin can be very precisely determined but are skewed due to degradation effects; on very short time scales (e.g. 1 pointing) the degradation can be traced easily, but the low count rate per detector may predict wrong detector patterns for the background, because celestial signals do not

<sup>9</sup>This is related to the spectral shapes of gamma-ray continuum and line. Also continuum photons suffer from the effect of charge collection deficiency, but as the continuum is not narrow feature in a photon spectrum like a line, the patterns are nearly constant even for single energy bins.



(a) Background pattern (red histogram) from the arithmetic mean model. The derived detector pattern  $R_{BGM}$  is (1.10/0.90) throughout all pointings, and is fitted to a value of  $\theta = 99.7$ . It can be seen that the model is only good for particular pointings between  $p = 25$  and  $p = 65$  and large residuals occur during other pointings which may falsely be interpreted as a transient celestial source.

(b) Model fit with line-continuum-separated background model in four blocks (orange histogram). The normalised residuals ( $\chi^2$ -contribution) now deviate at most  $1.5\sigma$  from zero. The larger residuals in the first block arise from the large detector ratio gradient and could be further reduced by separating the block into two sub-blocks.

Figure 3.24: Line and continuum background data structure (black histogram) for 100 pointings of SPI-light in one energy bin (black histogram, structure similar to Fig. 3.22). The continuum and line intensities are fixed to  $\beta_C = 50$  and  $\beta_L = 50$ . An additional sky component with an intensity of  $\alpha = 0.1$  has been added to all pointings. Due to the temporal behaviour of the line pattern from Eq. (3.30), here with  $\lambda_1 = 1$ ,  $\lambda_2 = 4$ ,  $l_1 = 0.109$  and  $l_2 = -0.010$ , the ratio between the counts in  $D1$  and  $D2$  changes with time. Different background modelling approaches are shown in the panels.

smear out.

For the example data of SPI-light in Fig. 3.24, four blocks of 25 pointings each are used to determine the patterns. By separating the line from the continuum, the celestial part is distributed with an unknown fraction  $f$ , where  $0 \leq f \leq 1$ , to the continuum and with  $(1 - f)$  to the line part. Considering background continuum pattern, and the averaged celestial pattern,  $f$  turns out<sup>10</sup> to be 1. Similar to the case in Sec. 3.2.4.1, the fitted background parameter for the continuum will get scaled down due to this reason (see also Eq. (3.33)). In general, there will be  $N$  blocks made of  $M_N = \{m_0, m_1, m_2, \dots, m_N\}$  pointings to determine the pattern, where  $m_i \neq m_j$  in general, depending on the concrete observation, and  $m_0 = 0$ . Assuming a perfect separation of continuum data,  $D_C(p)$ , and line data,  $D_L(p)$ , the background continuum model pattern takes the following form, for each block from  $i = 0..N - 1$ :

$$\begin{aligned} \sum_{p=s_i}^{f_i} D_C(p) &= \sum_{p=s_i}^{f_i} (\beta_C R_{BGC}(p) + f \alpha R_S(p)) = \\ &= \beta_C N_{BGC} m_{i+1} \begin{pmatrix} 1 \\ 1 \end{pmatrix} + \frac{\alpha}{2} N_S f'_C \begin{pmatrix} 1 \\ 1 \end{pmatrix} = \end{aligned}$$

<sup>10</sup>For the real SPI case,  $f$  is also very close to 1, because the continuum detector pattern shows almost no structure, i.e. is flat, and also the detector pattern for the sky, averaged over several pointings, smears out to a flat (1/1) pattern.

$$\begin{aligned}
&= \beta_C N_{BGC} m_{i+1} \left( 1 + \frac{\alpha N_S f'_C}{2\beta_C N_{BGC}} \right) \begin{pmatrix} 1 \\ 1 \end{pmatrix} = \\
&= \beta_C m_{i+1} N_{BGC} \begin{pmatrix} 1 \\ 1 \end{pmatrix} (1 + \epsilon_C) = \\
&= \beta_C m_{i+1} \cdot \underbrace{R_{BGC}}_{\text{reconstructed background pattern}} \cdot \underbrace{(1 + \epsilon_C)}_{\text{scaled normalisation}} \quad (3.33) \\
&\equiv R_{BGC}^{i+1} \text{ continuum background model pattern for block } i+1
\end{aligned}$$

In Eq. (3.33),  $f'_C = f \frac{N_{obs}^{i+1}}{m_{i+1}}$  is the share of the signal in block  $i+1$  to the continuum background pattern with  $N_{obs}^{i+1}$  observations, and  $0 \leq f'_C < 1$ . The overestimated scaling,  $\epsilon_C \ll 1$  because  $\alpha \gg \beta_C$ ,  $f'_C < 1$ , and  $m_{i+1} \geq N_{obs}^{i+1}$ . The summation limits are starting from  $s_i = 1 + \sum_{j=0}^i m_j$  until  $f_i = \sum_{j=0}^{i+1} m_j$ , so that the number of pointings in a particular block  $i+1$  is  $m_{i+1}$ .

The background line model pattern is then

$$\begin{aligned}
\sum_{p=s_i}^{f_i} D_L(p) &= \sum_{p=s_i}^{f_i} (\beta_L R_{BGL}(p) + (1-f)\alpha R_S(p)) = \\
&= \sum_{p=s_i}^{f_i} \left[ \beta_L N_{BGL}(p) \begin{pmatrix} \lambda_1 \\ \lambda_2 \end{pmatrix} + \beta_L N_{BGL}(p) p \begin{pmatrix} l_1 \\ l_2 \end{pmatrix} \right] + \alpha N_S f'_L \begin{pmatrix} 1 \\ 1 \end{pmatrix} = \\
&= \beta_L \left[ \Delta_1^{i+1} \begin{pmatrix} \lambda_1 \\ \lambda_2 \end{pmatrix} + \Delta_2^{i+1} \begin{pmatrix} l_1 \\ l_2 \end{pmatrix} + \frac{\alpha}{\beta_L} N_S f'_L \begin{pmatrix} 1 \\ 1 \end{pmatrix} \right] = \\
&= \beta_L m_{i+1} \left[ \underbrace{\langle N_{BGL}^{i+1} R_{BGL}^{i+1} \rangle}_{\text{normalised mean line ratio of block } i+1} + \underbrace{\frac{\alpha}{\beta_L} f'_L N_S \begin{pmatrix} 1 \\ 1 \end{pmatrix}}_{\text{wrong pattern } \sim \frac{\alpha}{\beta_L} f'_L \rightarrow 0} \right] \cdot \\
&\equiv R_{BGLM}^{i+1} \text{ line background model pattern for block } i+1 \quad (3.34)
\end{aligned}$$

In Eq. (3.34), the parameters  $\Delta_1^{i+1}$  and  $\Delta_2^{i+1}$ , given in Appendix B, are weighting functions for the changing line ratios during a particular block  $i+1$ .  $f'_L = (1-f) \frac{N_{obs}^{i+1}}{m_{i+1}}$  is the share of the signal in block  $i+1$  to the line background pattern, where  $0 \leq f'_L < 1$ , and  $f'_L < f'_C$ . This wrong pattern for the line background hardly influences the line background model pattern, as its normalised amplitude is of the order  $\frac{\alpha}{\beta_L} f'_L$  which is close to zero.

For a particular block  $j = i+1$ , the background patterns for the  $m_j$  pointings are constant; the remaining observations,  $N_{obs} - m_j$ , are zero throughout to fulfil number of data points for each block, see Fig. 3.25. The full background model  $M(p, \vec{\Theta})$  with  $N$  continuum background patterns,  $N$  line background patterns, and one celestial source finally reads

$$M(p, \vec{\Theta}) = \sum_{j=1}^N (\Theta_j R_{BGCM}^j) + \sum_{j=N+1}^{2N} (\Theta_j R_{BGLM}^j) + \Theta_{2N+1} R_S(p). \quad (3.35)$$

The block-arranged background model patterns are only "connected" via the sky model, because its pattern populates the whole observation. If there is no sky signal during a particular block, the background model will perfectly fit to the data.

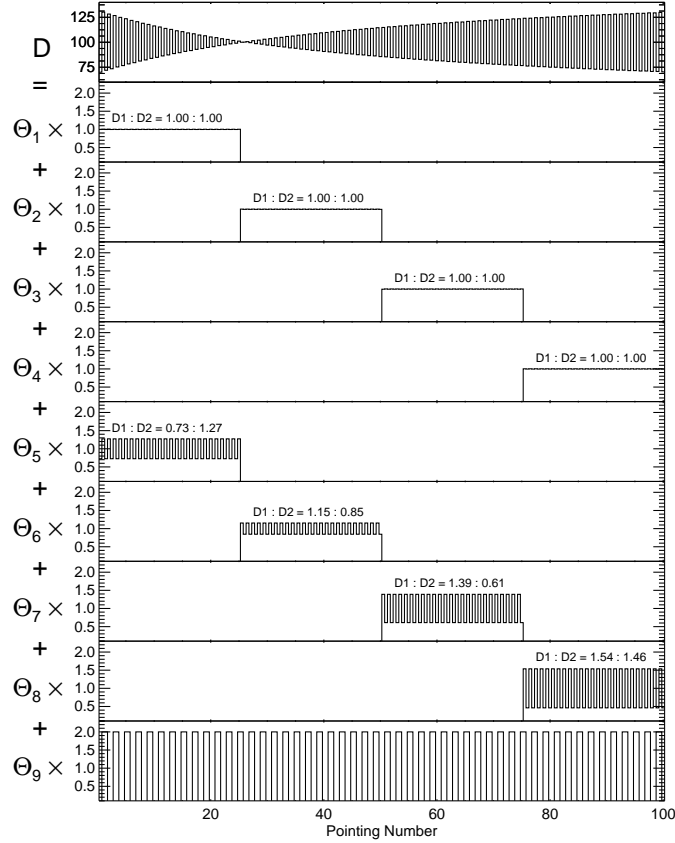


Figure 3.25: Reconstruction of line and continuum background patterns in four equally sized data blocks of 25 pointings each. The top panel shows the data  $D(P)$ , similar to Fig. 3.24a as a function of pointing number. Panels 2 to 5 show the reconstructed background continuum pattern in each data block as derived from Eq. (3.33) with a detector pattern of (1/1) in each case. Panels 6 to 9 contain the reconstructed background line patterns as derived from Eq. (3.34) with varying detector patterns. The bottom panel illustrates the expected sky signal pattern. Each component is scaled with an intensity parameter  $\Theta_j$ ,  $j = 1..9$ , which is determined in a statistical fit to the data.

In the case of the example in Fig. 3.25, 10000 Poisson-distributed realisations of the data set have been created. Two background modelling approaches have been applied to the data: The blocked line and continuum patterns as derived in Eqs. (3.33 + 3.34), and the arithmetic mean model from Sec. 3.2.4.1, see also Appendix B. The mean values of the derived celestial signal strength are 0.12 and 0.40, respectively. The signal for the simple model is overestimated by a factor of  $\sim 4$ , whereas the signal from model Eqs. (3.33 + 3.34) is very close to the input value of  $\alpha = 0.1$ , validating the visual impression of Figs. 3.24a and 3.24b. Also the  $\chi^2$  goodness-of-fit value is  $\approx 10$  times larger than when separating in blocks, and line and continuum. Therefore, the sensitivity and reliability of the celestial signal is strongly increased. In fact, the position, size and number of individual blocks affect the accuracy of the reconstructed signal strength. If the gradient of detector patterns is very large, more

and smaller blocks, if not limited by statistics, should be used to model the background pattern. It is important to mention that the limiting number of blocks  $N$  is given by the number of pointings which are needed to smear out enough the celestial signal. As the number of block  $N$  approaches the number of total pointings  $N_p$ , the signal tends to zero. However, with another assumption (see next paragraph), it is possible to derive the background intensity on the pointing time scale.

SPI-light and the illustrated data are oversimplified but provide a basic understanding of the background modelling approach. Additional complications arise when the different temporal behaviours of line and continuum detector patterns are considered. In general, these follow a function of time  $I(p)$ , which is the response of the detectors to the cosmic-ray bombardment, causing the background. This function determines how the detectors degrade on longer time scales, and also how the prompt background varies with time.  $I(p)$  is unknown a priori, but can be assumed to follow the time sequence of an on-board radiation monitor or the anticoincidence shield count rate. The incident rate of cosmic rays,  $I(p)$ , may be similar or congruent to an instrumental count rate,  $\tilde{I}(p)$ . If  $\tilde{I}(p)$  is taken from such a radiation monitor, the normalised background model detector patterns can be convolved with this function, which may stabilise and improve the fit further. But this only applies for prompt background emission, and larger radioactive decay half-life times require separated treatments. For strong sources it is possible to omit  $I(p)$  completely, because the celestial pattern is very orthogonal to the background patterns, and the background intensities per pointing can be determined directly on this time scale. For diffuse large scale emission, or in general faint sources, the mask pattern is so weak that determining the background on the pointing time scale will completely zero out the celestial signal. In this case, the function  $\tilde{I}(p)$  must be used to stabilise the fit by fixing the relative background variations on shorter time scales.

### 3.2.4.3 Application and Extension to SPI

The transformation of the background model to the full SPI instrument is now straight-forward. The 2D case will be transformed to 3D, where SPI with all its materials, shields, wiring, fixations, etc. is mounted on the INTEGRAL satellite with its solar panels, cooling system, and other instruments. In other words, the background origins are now much more diverse, which in return means more instrumental background lines. The number of detectors is then  $N_{det} = 19$  in case of a fully functioning camera. During the mission, the normalisation changes as four detectors failed. In principle, this background modelling approach also applies to double/multiple detectors and their background patterns, but is limited due to the low number statistics in each multiple-detector.

The optimal integration time to determine the spectral parameters for the input background model, and thus the detector patterns for the energy bins of interest, depends mainly on the energy range. The instrumental background spectrum in SPI roughly follows a power-law with index  $-1$ , and the integration time for higher energies should therefore in principle be larger. In many cases, there are very strong instrumental background lines on top of the background continuum, neighbouring weak background lines. These are harder to identify on times scales which may be optimal for strong lines. Measuring the line shape parameters of instrumental lines in

a very broad energy band is hence always focussing on a particular intensity range of lines for particular integration times. This can be improved by splitting the energy intervals into smaller pieces. This determines the line shapes more accurate and treats each line or line complex separately from each other. However, this may skew the fit parameters again because the (broadband) continuum is then described by an often broken power-law. It turned out that integration times of one INTEGRAL revolution (50-100 pointings) are most useful for background modelling. Energy bands should at least include  $\sim 40$  keV to provide stable fits during one revolution. Details for the energy bands that have been analysed for point sources and diffuse emission will be given in the respective sections.

The response to celestial signals is now directly encoded in the mask pattern which is casting a shadowgram onto the array of the 19 detectors. The alternating mask matter from SPI-I is now a pointing-based mask pattern, depending on the direction and angle with respect to the optical axis of SPI and its field of view. A typical observation with SPI is performed in a  $5 \times 5$  rectangular grid of pointings on the sky, in steps of  $2.1^\circ$  around the target to be observed. Each pointing lasts typically between 30 and 60 min. During one of these observations, the detector pattern of the sky response changes gradually from pointing to pointing which is shown in Fig. 3.26 for a source near the "optical axis" (centre of the observation). Which detectors are being illuminated in particular depends on rotation angle around the optical axis as the SPI mask is symmetric about  $120^\circ$  rotation. The detector patterns also depend on energy, because multiple scatterings may occur, which depend on the incident photon energy.

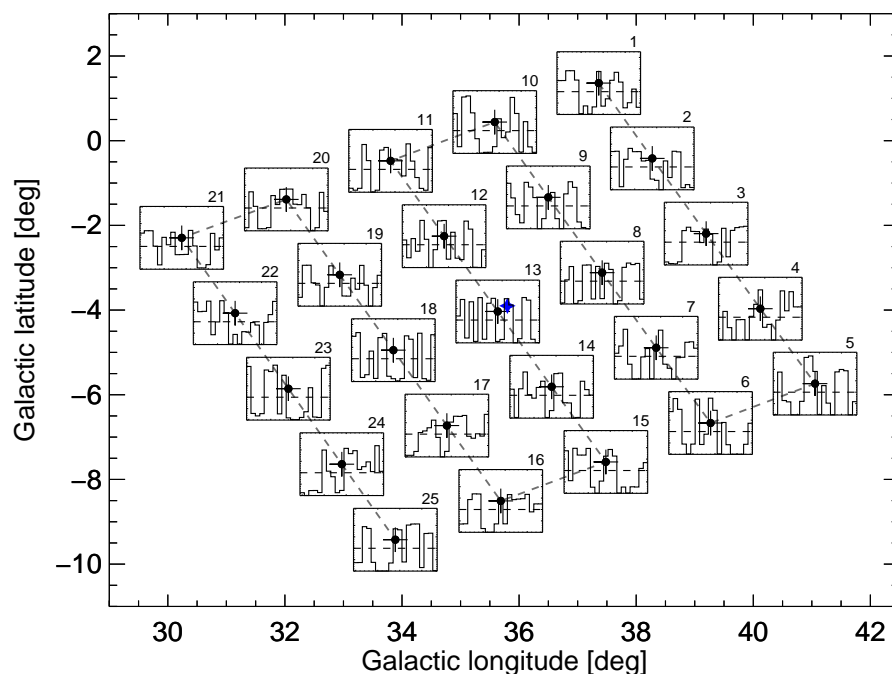
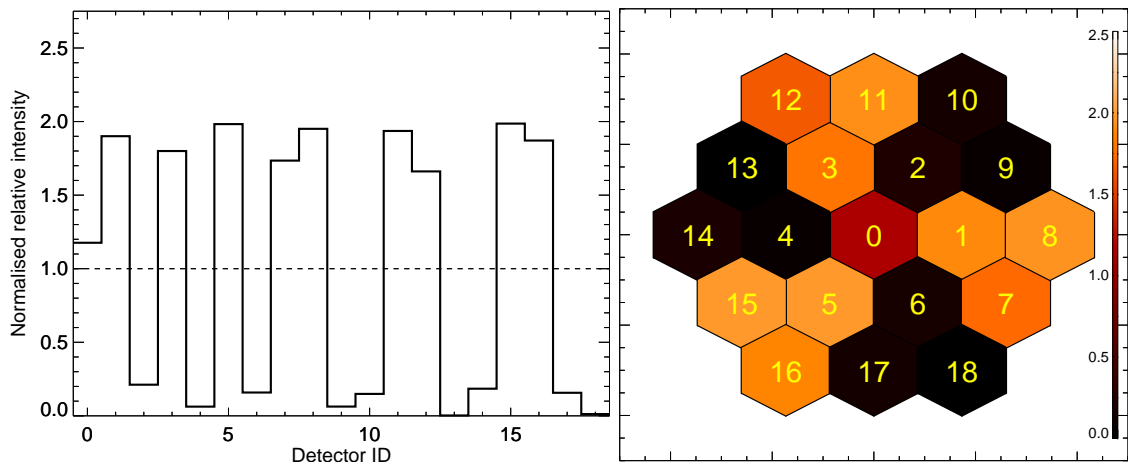


Figure 3.26: Typical  $5 \times 5$  rectangular dithering strategy with SPI, marked with dots and sequenced by number above the insets. Each dot represents one pointing with a field of view of  $16^\circ \times 16^\circ$  and is  $2.1^\circ$  away from the next/neighbouring pointing. The celestial source is marked with a blue star symbol at the position  $(l/b) = (35.8^\circ / -3.9^\circ)$ . In each inset panel, the relative detector pattern, ranging from 0 to 2.75, of how the source would be seen by SPI is shown. The dashed line indicates the equal ratio pattern at 1.0. With respect to this line, the pattern changes drastically from pointing to pointing which is the only way to distinguish between background and sky.

Panel 13, close to the celestial source in Fig. 3.26, exhibits the most intuitive pattern when comparing it with the detector array, Fig. 3.7, and the mask pattern,

Fig. 3.11b. A larger view of this inset is shown in Fig. 3.27a, where it can be seen that the relative intensities between detectors can change by more than 100%. Here, the shadow of the mask directly imprints onto the detector array, which means that only the inner mask has an effect, and sets of three detectors are alternately illuminated or shadowed. In the middle of the array, detector  $D00$  is partly shadowed because of extra material (screws, mounting) directly above it (see Fig. 3.27a). The shadowgram of this detector pattern is shown in Fig. 3.27b.



(a) Zoom of panel 13 in Fig. 3.26. The relative detector pattern is shown; the dashed line at 1.0 marks the equal ratio for all detectors. (b) Shadowgram equivalent to detector pattern of panel 13.

Figure 3.27: Detector pattern and shadowgram of a celestial source near the optical axis of SPI.

The background modelling approach from the previous sections is only applicable and efficient if the celestial signal is smeared out when integrating over long enough observation periods. For the example observation in Fig. 3.26, the integrated detector pattern for only the celestial source is shown. The relative pattern is very close to unity, at most deviating +14% and  $-9\%$  from an equal ratio. The patterns during such a sequence of 25 pointings are dramatically different with respect to the mean pattern - often more than 100%. For comparison, the detector patterns per pointing and its mean of the continuum band between 100 and 900 keV are shown in Fig. 3.16, deviating from the mean pattern at most 1.5% per pointing. Within statistical uncertainties, the detector pattern for the continuum is constant on time scales between pointings and revolutions (several tens of pointings). Similarly, the detector pattern for the background continuum is constant on time scales between revolutions and one epoch, as shown in Fig. 3.20d. In summary, the continuum background pattern, as well as the lines' background pattern have been shown to be constant on all time scales. Furthermore, the celestial contribution to the patterns on time scales of "one" observation ( $5 \times 5 = 25$  dithered pointings) smears out to a rather flat pattern so that it would be recognised as "continuum" when creating the instrumental spectral parameters data base. In a statistical description of the data including background and sky on a pointing time scale, however, the celestial shadowgram is varying according to the observation strategy, while the background pattern is stable. This allows to discriminate celestial contributions from instrumental background dominated data.

## 4 The 511 keV Electron-Positron Annihilation Signal in the Milky Way

### 4.1 The Positron Puzzle

In the years of 1968 to 1970, simple pioneering balloon experiments (Haymes et al. 1969; Johnson et al. 1972) measured the first gamma-ray line signal at an energy of  $473 \pm 30$  keV from outside the solar system, from the direction of the centre of the Galaxy. Later, Leventhal et al. (1978) used a solid-state detector with its higher spectral resolution to unambiguously identify this line as due to positron annihilation, because its centroid was found exactly at 511 keV, which is equivalent to the electron/positron rest mass. The positron annihilation line is the strongest gamma-ray line that is known. Its intensity of the order  $\sim 10^{-3}$  ph cm $^{-2}$  s $^{-1}$  corresponds to a luminosity of  $\sim 10^{37}$  erg s $^{-1}$  in gamma-rays. The problem arises that there are too many possible candidate sources in the Milky Way which could potentially create this amount of positrons. After Leventhal et al. (1978) claimed a significant amount of antimatter to annihilate in the Milky Way, they mentioned in their paper that

*"Undoubtedly, the positrons giving rise to the observed feature come from a variety of processes."*

The identification and contribution of these sources are in fact the goal that this thesis tries to answer. If a steady state between production and annihilation of positrons is assumed, a source is required which can produce  $10^{43}$  positrons per second. Among the sources, which will be thoroughly discussed in Chp. 5, are secondary positrons in the ISM due to cosmic-ray interactions, explosive nucleosynthesis  $\beta^+$ -unstable elements, such as  $^{56}\text{Ni}$ ,  $^{44}\text{Ti}$ ,  $^{26}\text{Al}$ , or  $^{22}\text{Na}$ , and photon interactions with magnetic fields around neutron stars (e.g. Ramaty et al. 1979; Guessoum et al. 2006; Weidenspointner et al. 2008a; Prantzos et al. 2011). The fractional contribution of each of these sources is a matter of debate. Mainly indirect measurements and heuristic arguments can be used to constrain the potential roles of each source type.

With the first gamma-ray imaging telescopes (e.g. OSSE on CGRO Johnson et al. 1989) the positron puzzle became even more complex as the 511 keV emission morphology was different and unique compared to the picture obtained at all other wavelengths. Instead of a typical disk-like structure with an accumulation in the centre of the Galaxy, the bulge, the early observations showed only a strong component in the region of the galactic centre, with a radial extension of about 1.5 kpc. Only a marginal disk was identified in addition, if at all (Purcell et al. 1997; Knödlseder et al. 2005). The suggested sources, however, are mainly located in the galactic disk, so that none of the proposed candidates fitted the observations if the positrons annihilate close to their sources. An exception here may be dark matter. An additional

ingredient in the puzzle is the propagation of positrons as cosmic-rays through the ISM. It is known that positrons travel through interstellar space, and also at relativistic kinetic energies, as this has been measured with space-borne magnetic spectrometer experiments (Adriani et al. 2013; Aguilar et al. 2013). Where the positrons are created, how and how far they propagate through interstellar gas, and where and how the positrons annihilate, is only poorly understood. Simulations may explain the amount of positrons present in some parts, based on a pure nucleosynthesis origin of positrons, and a diffusion-like motion in the Milky Way (Martin et al. 2012; Alexis et al. 2014). But the simulated emission morphology of the 511 keV radiation can hardly be matched to the observations. The large accumulation of positrons in the galactic bulge can only be explained from peculiar environmental conditions, or with major star burst events, then at exactly the correct time, several million years ago (Alexis et al. 2014). Due to the peaked and centred morphology, this peculiarity culminated in the possibility that dark matter particles could be entirely responsible for the production of positrons in the galactic centre, as the density profile of dark matter haloes would just deliver the correct gamma-ray image, assuming that positrons would not travel far (e.g. Hooper & Wang 2004).

For the galactic 511 keV morphology, several different approaches have been applied in previous studies. Knödseder et al. (2005), for example, used the Richardson-Lucy deconvolution method (RL method Richardson 1972; Lucy 1974, see Sec. 4.4.1) to obtain a first high angular resolution map of the 511 keV positron annihilation in the Milky Way with SPI on INTEGRAL. With 15.3 Ms of SPI data, they validated parts of the pioneering work by Purcell et al. (1997) with OSSE on CGRO, who revealed the very first reconstructed morphology of the 511 keV emission. In Fig. 4.1, the OSSE map of the inner Galaxy with an effective angular resolution of  $\approx 10^\circ$  (multiple oriented collimators) is shown. The basic features of the 511 keV morphology are the bright galactic centre and a rather faint disk. In addition, OSSE also saw a positive latitude enhancement which is, however, not seen in any subsequent study.

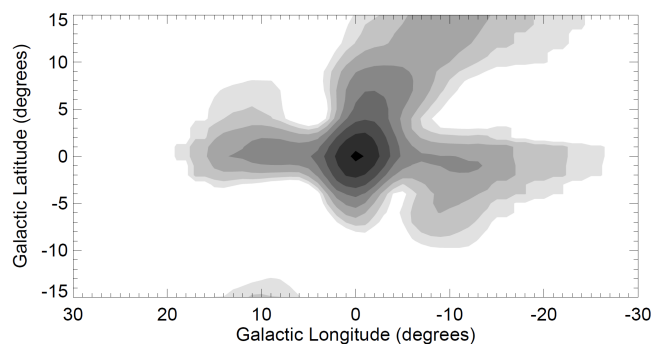


Figure 4.1: First galactic 511 keV map measured by OSSE on GCRO. Contours are exponentially spaced, decreasing from the centre outwards. From Purcell et al. (1997).

Spectral analyses (Kinzer et al. 2001; Churazov et al. 2005; Jean et al. 2006) showed that positrons, no matter at which energies they are created, predominantly form the intermediate Ps state before annihilation. This is only efficiently possible if the positrons slowed down to less than  $\sim 1$  keV (e.g. Crannell et al. 1976). The slowing-down process must be part of the propagation, if the positrons started from relativistic energies, so that they suffer from the galactic environmental conditions like electromagnetic fields, temperature, density, and the composition of interstellar gas (Bussard et al. 1979). If dark matter, for example, is the cause for positrons, the slowing-down is either very fast, or the dark matter particle mass is only of the

order of a few  $\text{MeV c}^{-2}$  (Boehm et al. 2004; Sizun et al. 2006; Beacom & Yüksel 2006). For direct annihilation of slowed down positrons, only a line at 511 keV would be seen, so that the ratio between the Ps continuum and the 511 keV line, in combination with quantum-mechanical statistics and models of interstellar space, the annihilation conditions can be inferred from gamma-ray spectra (Crannell et al. 1976; Bussard et al. 1979; Murphy et al. 2005; Guessoum et al. 2005; Churazov et al. 2005; Jean et al. 2006; Churazov et al. 2011). Positrons are measured to have been created at relativistic energies, slow down by electromagnetic interactions, form Ps with electrons from H, and then annihilate, creating gamma-rays. In fact, such a scenario is based on simple models (e.g. Churazov et al. 2005) which turn out to be ambiguous in their parameter spaces, so that even the most settled preassigned assumptions, like the annihilation of positrons in interstellar gas, can readily be questioned.

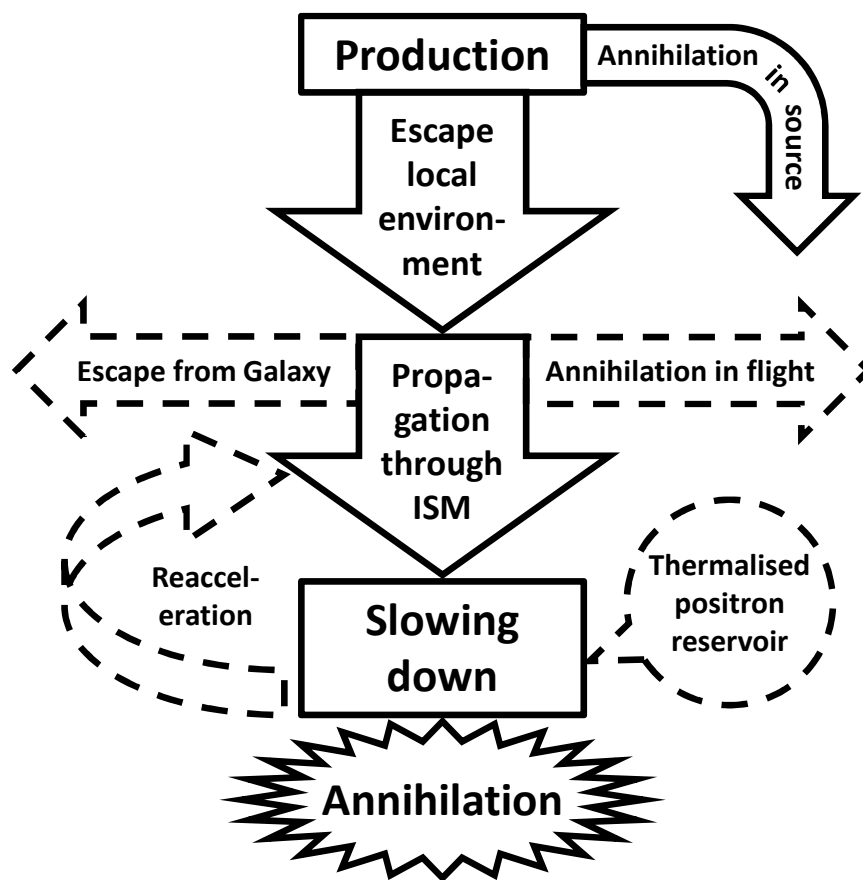


Figure 4.2: "Life" of a positron in the Milky Way, from the production in unknown sources towards annihilation with electrons. Dashed arrows indicate unproven possibilities during the life of a positron.

The relation of the 511 keV morphology from positron annihilation to the sources of positrons and their distributions in the Milky Way (source morphology) was addressed by taking the bulge-to-disk ratio (B/D) of the 511 keV emission and the candidate sources as a very simple basis to identify and choose among them. The B/D of the 511 keV emission was initially set to "infinity", as the disk was not seen at all. The ratio was specified with more observations and more sensitive instruments to a value of 1.4 (Weidenspointner et al. 2008b), and even below, to a value of 1.0, from the analysis of this work. In any case, this number is higher than what is expected for the B/D of the candidate sources: Cosmic rays ( $< 0.2$ ), SNe Ia /

Novae ( $< 0.5$ ), CCSNe / massive stars ( $< 0.2$ ), Pulsars ( $< 0.5$ ). Consequently, the assumption that the positrons annihilate close to their sources is probably not correct, as the emission morphology differs significantly from the source morphology. In addition, the injection energies of the positrons are of the order of MeV or larger. But the spectral details constrain the annihilation to be exclusively due to slow positrons. This is inferred from the annihilation spectra, as most of the positrons annihilate after forming Ps. Measuring the emission morphology is thus not sufficient to identify the sources because an important and potentially time and space consuming process of slowing down must be considered. This is the propagation of positrons in the ISM, and is very uncertain. In total, this became known as the positron puzzle.

The canonical "solution" to the puzzle (actually only one part of it) is usually presented in the way shown schematically in Fig. 4.2:

- A positron is produced by any kind of source with a kinetic energy of the order of MeV or above. For example from the  $\beta^+$ -decay of  $^{26}\text{Al}$ , which is produced in massive stars, Sec. 5.1.1, the positrons emitted have a kinetic energy distribution which peaks at 543.3 keV, and has an end point at 1173.5 keV in the rest frame of the nucleus (Bé et al. 2016). In the case of secondary muons from cosmic-ray interactions, the decay positrons' kinetic energy peaks around 52 MeV with a sharp cut-off right after the peak for stationary muons (e.g. Michel 1950; Dudziak et al. 1959; Bardon et al. 1965).
- If the positron manages to escape its local environment and does not annihilate directly "in" the source, i.e. it does not deposit its total energy in the immediate vicinity of, e.g., a supernova cloud, or in a pair plasma of a microquasar for example, it will propagate through the ISM. Depending on the source type, the source's annihilation spectrum will have characteristic shapes, see Sec. 2.4, which can be used to determine the effective number of positrons trapped and escaping.
- The propagation is then subject to the circumstances the positrons encounters along the path through the ISM, i.e. it depends on the temperature, ionisation state of the medium, density, magnetic field, radiation field, and composition. Positrons then react to the effects of the changing environment.
  - If they are energetic enough, they may escape the Galaxy and enter the intergalactic medium (IGM). Particle number densities in the IGM are believed to be low, of the order  $10^{-6} \text{ cm}^{-3}$  or less (Meiksin 2009), and the IGM is fully ionised, so that the reaction rates of positrons with particles there decrease significantly. Positrons might survive billions of years, or even could form a reservoir of positively charged particles when thermalising with the IGM. Interestingly, such a cloud of equal charges would exhibit a negative pressure on cosmological scales.
  - If the positrons propagate in the ISM and do not escape the Galaxy, they may annihilate in flight with a certain probability. This would result in a continuous cosmic-ray positron annihilation spectrum.
- Measurements showed that most of the positrons do not annihilate in flight.

Here, they must lose their kinetic energy by synchrotron radiation, bremsstrahlung, and inverse Compton scattering for very high kinetic energies ( $\gtrsim 10^9$  eV for typical ISM conditions), and by ionisation and Coulomb scattering for low kinetic energies. Note that this aspect is not proven directly by measurements.

- Below  $\approx 1$  keV, positrons begin to form Ps with free or bound electrons via radiative recombination or charge exchange with ambient atoms. The fraction of Ps formed in flight depends also on the environment, but essentially all positrons form this intermediate state, as shown by the measurements, Secs. 2.4.3.4 and 4.6.6. The exact ISM conditions then determine the shape of the annihilation spectrum of cool positrons, with a 511 keV line and an o-Ps continuum.

In consequence, the gamma-rays from annihilating positrons are most probably not directly associated with the sources which ejected them. The propagation of one positron is usually modelled as a diffusion-like process. It may take several millions of years in typical ISM conditions, so that positrons may be found kiloparsecs away from their sources (e.g. Martin et al. 2012; Alexis et al. 2014). If they do not annihilate during their slowing-down phase, they may reside in the ISM or a thermal pool for a long time, and eventually also get re-accelerated by diffuse shock acceleration. A steady supply of positrons may thus be present. As a result, the emission morphology of the 511 keV in the Milky Way is not representing the source morphology at all.

## 4.2 Data Set

The objective of this thesis is to measure the electron-positron annihilation signal in the Milky Way. This includes refining its spatial morphology with respect to previous studies, and determining spectral parameters to obtain information about the annihilation conditions. Most of the signal has been shown to be contained in the 511 keV line and the ortho-positronium continuum below, while the spectrum of positrons annihilating with electrons in flight was not accurately measured or disentangled from the high-energy, cosmic-ray induced, power-law spectrum (e.g. Kinzer et al. 2001; Churazov et al. 2005; Jean et al. 2006). Therefore in this section, the focus was put on a 40 keV band between 490 and 530 keV with 0.5 keV binning to measure the annihilation line, the ortho-positronium step and the underlying continuum precisely in high resolution. Most of the results have been presented in Siegert et al. (2016c).

The data set used for the analysis comprises almost eleven years of INTEGRAL/SPI data, ranging from revolutions 21 to 1279, with gaps due to annealing periods, in-flight calibration or solar activity contamination. The exposure map is shown in Fig. 4.3; the difference between positive and negative longitudes integrated over all latitudes is less than 7%. For a single, not destroyed detector, the total exposure is 160 Ms, distributed over the entire sky with 73590 telescope pointings, lasting typically 1800 s. The exposure times for particular regions in the sky are given in Tab. 4.1. In total, also taking into account the dead detectors, 1214799 spectra (97183920 data points) were analysed in this data set to obtain detailed celestial gamma-ray emission spectra from positron annihilation in the Milky Way.

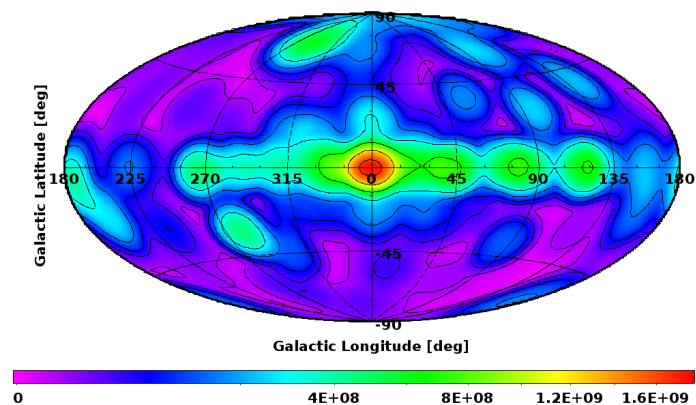


Figure 4.3: Sky exposure with SPI for the data set analysed. The units of the map are given in  $\text{cm}^2\text{s}$ . The equivalent exposure time is calculated for 19 detectors with an effective area of  $\sim 75 \text{ cm}^2$  for photon energies around 511 keV. The contours, starting from the innermost, correspond to exposures of 22 Ms, 16 Ms, 9 Ms, 4 Ms, 2 Ms, 1 Ms, 0.5 Ms, and 0.1 Ms, respectively. The total exposure time is 160 Ms.

$ l $	$< 15^\circ$	$15^\circ\text{-}60^\circ$	$60^\circ\text{-}105^\circ$	$105^\circ\text{-}180^\circ$
$T^+$		21.8	17.6	
$T^-$	30.8	20.4	15.6	30.7

Table 4.1: Exposure times in different regions of the sky. The times have been extracted from the exposure map (Fig. 4.3) in the listed longitude ranges and for latitudes  $|b| < 45^\circ$  in each case.  $T^+$  and  $T^-$  are the exposure times for positive and negative longitudes, respectively, given in Ms.

### 4.3 Treating the Background Near 511 keV

In the energy range between 490 and 530 keV, there are eight instrumental background lines on top of an instrumental background continuum which can be described by a power-law function. In Fig. 4.4, the mission integrated spectrum in that range is shown, together with a statistical fit using function Eq. (3.15). The derived parameters of this fit serve as the starting points for the MCMC fits describing the spectra per revolution and detector, thereby creating the instrumental background data base, as depicted in Sec. 3.2.3.4.

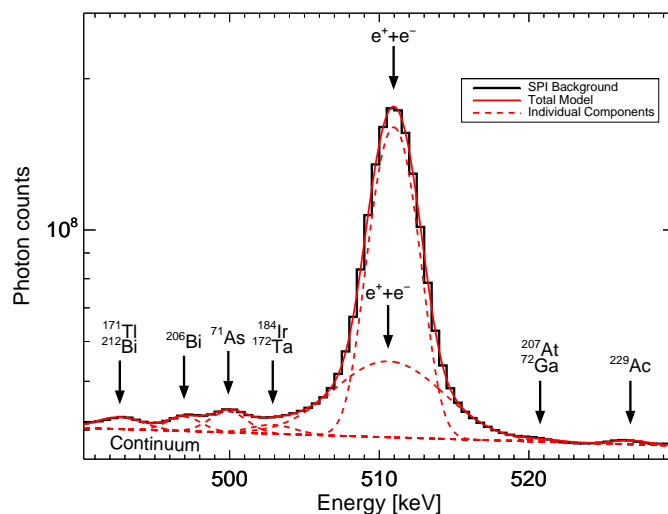


Figure 4.4: Background spectrum (black histogram) in the vicinity of 511 keV. The identified instrumental background features, i.e. lines and continuum, are indicated with dashed red lines; summing them together gives the total model in solid red. Possible line identifications are marked with arrows. See text for further detail.

The used lines for background modelling are listed in Tab. 4.2, together with possible identifications of nuclei which may produce these gamma-ray lines in the INTEGRAL space craft. A priori, a certain gamma-ray line centroid cannot be attributed to a specific process, because there are many nuclear de-excitation gamma-ray lines within the statistical and systematic uncertainties of the measured peak positions. Based on heuristic arguments, like half-life times, abundances in the satellite, branching ratios, and detector patterns, the lines will be attributed a most probable nucleus for that energy. Note that the spectrum of the entire mission combines different calibrations, so that the spread in line peaks combines to an inaccurate peak position and a certain broadening to the instrumental background lines. The spectrum has to be described by two "annihilation lines" in the vicinity of 511 keV, which is probably due to a combination of different line shapes originating in different annihilation conditions. The lines may originate in annihilation of instrumental positrons on low- or high- $Z$  materials at non-zero velocities inside the satellite. Using the description of two asymmetric Gaussian lines, this will yield a "narrow" component with an average width (FWHM) of  $3.15 \pm 0.05$  keV, and a "broad" component with  $8.1 \pm 0.7$  keV. The widths of the narrow and broad component are slightly correlated ( $\rho = 0.38$ ), and seem to follow the solar cycle. This may be caused by improved accuracy in determining the spectral parameters of the background when the background intensity has a maximum. Additionally, there could be an underlying, weak, instrumental o-Ps continuum, and also Compton continuum features, which may add to the spectrum in that range.

The temporal behaviour of the instrumental 511 keV background line was shown in Sec. 3.2.3.4. The final step of background modelling is then the prediction of background for this data set. The database parameters represent essentially the behaviour of the background dominated count rates in the instrument because the varying sky contribution is smeared out as explained in Sec. 3.2.4.3. The database parameters allow to reconstruct a background pattern, i.e. the expected count rate of each detector relative to each others, for instrumental background lines and instrumental background continuum. Due to the nature of these processes, the pattern is different for these two background components, *lines* and *continuum*, for each analysed energy bin as described in Sec. 3.2.4.2. The short-term pointing-to-pointing variations,  $\tilde{I}(p)$ , are traced by the side shield assembly total rate of the SPI instrument, which stabilises the background. The temporal behaviour is imprinted on top of the pre-defined patterns for a coherent description of the background due to cosmic rays. Special care is required to obtain the proper absolute normalisation of this background model. The relative detector contributions to total continuum and line backgrounds may not be properly normalised, as each of these are derived from a data set stretching further in time. Therefore, the background model as re-built from the database is re-normalised to the actual data, by fitting time-dependent scaling parameters,  $\theta_{i,t}$  in Eq. (3.12). This is done per background component, in addition to the proposed sky model scaling parameters (see Sec. 4.4).

In general, the detection of diffuse emission with a coded-mask telescope like SPI, i.e. emission on angular scales comparable to the field of view, relies on the correct comparison of flux in one pointing with that in another. Such emission will add only small variations from its pattern of relative detector ratios to the total signal. Furthermore, the average contribution from extended large-scale emission during the observations around a particular target on the sky will not vary much as the

Line [keV]	Peak	Parent Nuclei (Lab energy [keV])	Production Reaction	Characteristics	$F/F_{511}$
492.66(8)		$^{171}\text{Tl}$ (492.7(1)); $^{212}\text{Bi}$ (492.7(3))	$^{171}\text{W}(\text{EC})^{171}\text{Tl}$ ; $^{212}\text{Pb}(\beta^-)^{212}\text{Bi}$	Bi-like det. pattern; W origin from mask? Thorium series?	1.24%
496.95(8)		$^{206}\text{Bi}$ (497.06(4))	$^{205}\text{Tl}(\alpha, 3n\gamma)^{206}\text{Bi}$	$T_{1/2} = 6.24$ d; $^{205}\text{Tl}$ from Neptunium series;	1.22%
499.91(8)		$^{71}\text{As}$ (499.876(10))	$^{69}\text{Ga}(\alpha, 2n\gamma)^{71}\text{As}$ ; $^{70}\text{Ge}(\text{p}, \gamma)^{71}\text{As}$	Bi-like det. pattern $T_{1/2} = 65.28$ h;	2.92%
502.87(9)		$^{184}\text{Ir}$ (502.94(9)); $^{172}\text{Ta}$ (503.0(5))	$^{184}\text{Pb}(5\text{EC})^{184}\text{Ir}$ ; $^{172}\text{W}(\text{EC})^{172}\text{Ta}$	flat det. pattern; mask and shield contributions?	0.86%
510.59(9)		$e^+, e^-$ (511.00)	many sources; $e^+ + e^-$	kinematically broadened $\approx 4500$ km s $^{-1}$ red-shifted $\approx 235$ km s $^{-1}$	22.75%
510.96(9)		$e^+, e^-$ (511.00)	many sources; $e^+ + e^-$	kinematically broadened $\approx 1500$ km s $^{-1}$	77.25%
520.76(9)		$^{72}\text{Ga}$ (520.74(24)); $^{207}\text{At}$ (520.78(9))	$^{71}\text{Ga}(n, \gamma)^{72}\text{Ga}$ ; $^{207}\text{Rn}(\text{EC})^{207}\text{At}$	flat det. pattern with peaks at det. 08-10; Actinium series?	0.09%
526.79(9)		$^{229}\text{Ac}$ (526.8(2))	$^{229}\text{Ra}(\beta^-)^{229}\text{Ac}$	flat det. pattern; Neptunium series?	0.38%
490-530		Continuum	many processes	flat det. pattern; sources isotropic	497%

Table 4.2: Identification of background lines and continuum in the vicinity of 511 keV. The parent nuclei and their production mechanisms are not definitive answers to the background source origin question but rather suggestions based on heuristic arguments. If more than one species or reaction is plausible based on the table of isotopes (Firestone et al. 1996), at least two possibilities are given. The lines at 497, 500, and 511 keV have already been identified by Weidenspointner et al. (2003); due to the increased mission time, even weaker lines could be identified and used for background modelling. The intensity of the lines are given with respect to the sum of narrow and broad component intensity of the instrumental 511 keV feature. The apparent red-shift of the broad line is probably not real but only occurs due to the decomposition of narrow and broad line. The Doppler-broadening of both 511 keV lines cannot be complete, the continuum is also listed, being about five times stronger than the 511 keV feature in the whole 40 keV band, and about 75% in a 6 keV beneath the line.

$5 \times 5$  dithering is performed (see Fig. 3.26). It will, however, likely change when the target direction of pointings is redirected by a significant fraction of the telescope field of view or more. The fixed relative detector patterns, derived for instrumental background lines and instrumental background continuum, are the key tools allowing the shadowgrams from the mask to be distinguished, as those change between pointings. Systematic mismatches of the celestial and background detector patterns may make it more difficult to find mask-encoded sky signals, and can thus reduce the sensitivity. Therefore, a re-normalisation of background detector patterns whenever the telescope is re-oriented to target a location in the sky that is more distant from the current than  $\sim$  one field of view is performed. Re-scaling by fitting at three-day intervals for each of the two background components is adequate to recover proper normalisation (cf. Sec. 3.2.4.2 and Fig. 3.25).

## 4.4 Celestial Emission

Gamma-ray data from SPI is completely background dominated, so that an inversion of Eq. (3.12) towards the celestial components (deconvolution) is not straight-

forwardly applicable. A projection of the measured photon counts onto a sky map is possible in principle, but would only work if the source is significantly stronger than the background. Otherwise, the complexity of the imaging response function (mask, shadowgram) will produce arbitrary and imprecise results. In general, there are two possibilities to infer information from data in image space. Either the point-spread-function is used to deconvolve the image towards what is actually occurring in the sky, i.e. producing an "unblurred" image, or the forward-folding method is used to compare models with data, i.e. the assumed model is convolved ("blurred") to the data space. The convolution of a model with a precisely known response function is usually easier to apply and to judge than the deconvolution of background dominated data with unknown contributions from celestial signals. However, forward-modelling may be biased by ad hoc assumptions which can not be proven in many cases.

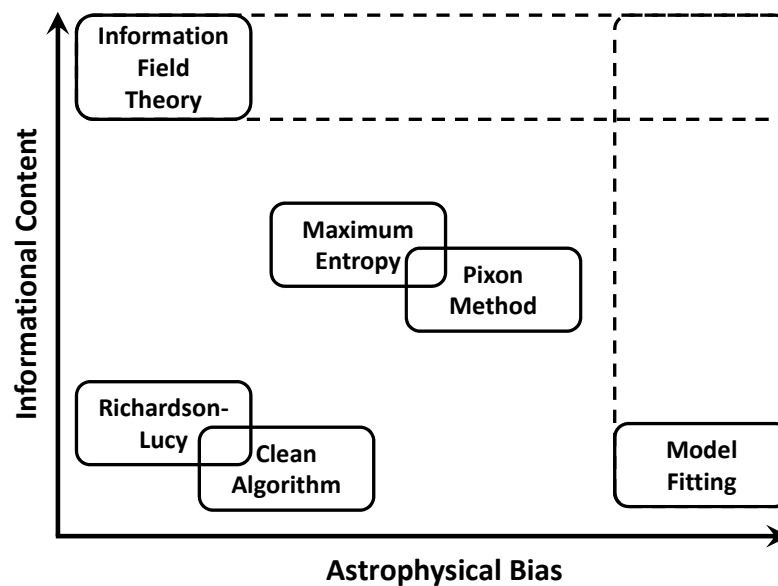


Figure 4.5: Imaging analysis approaches informational content against astrophysical bias. While methods like the Richardson-Lucy or the Clean algorithm can provide an initial guess or first imaginations of how the data space looks like in an image, their astrophysical interpretation is in most cases questionable. Likewise, the Maximum Entropy method decomposes an image based on probabilistic theory but is influenced strongly by the starting point or number of pixels (or pixons) of the iterative algorithm. Information Field Theory is the most modern fully Bayesian approach for the data analysis problem. It starts from very first principles but can also incorporate prior information about astrophysical systems (dashed extended horizontal box) and can answer very specific questions to the data. Likewise, astrophysical model fitting assumes the properties of, for example, a Galaxy made of a bulge and disk, and directly determines the values for the input model components. By incorporating also prior information of the astrophysics that may happen as part of the model, more information can be extracted (dashed extended vertical box).

A degree of bias in gamma-ray image analysis and reconstruction can be defined: Unbiased imaging methods are the RL deconvolution or information field theory (IFT). More bias is added in Maximum Entropy (ME) method which may be biased by the starting point of the iterative algorithm or pixons<sup>1</sup>. Full-forward model-fitting in data space is then biased by the imagination of how an astrophysical system might look like. The IFT, for example, allows to answer very specific questions from the data, typically of the form: "Assuming the spectrum of a population sources has a certain shape, where in the sky can those sources be found?" In other words, where does the sky look like from what is expected from any supposed imagination. This is biased as well from the spectral perspective, but can provide detailed and probabilistic correct answers. On the other hand, model-fitting allows to derive unbiased

<sup>1</sup>Pixons are image objects like wavelets, spline functions or normal pixels.

spectra of what has been input as (astrophysically) biased morphology. In Fig. 4.5, the quantitative informational content of certain imaging analysis approaches is illustrated qualitatively against their bias.

#### 4.4.1 Unbiased Imaging Methods

##### Richardson-Lucy Deconvolution

The RL method assumes that a measured (blurred) image is described by the convolution of a latent (real) image with the point-spread-function of the instrument (see Fig. 3.12b), with photons being Poisson distributed. An observed pixel with value  $d_i$  at a position  $i$  in image space is hence formally written as

$$d_i = \sum_j p_{ij} m_j \leftrightarrow d = p \otimes m. \quad (4.1)$$

Here,  $p_{ij}$  is the point-spread-function which is distributing a fraction of photons with values  $m_j$  originally at the true position  $j$  to the observed position  $i$ . The right-hand side of Eq. (4.1) is equivalent to the left-hand side, using the shorter notation of the convolution operator. The Poissonian likelihood, Eq. (3.13), is then used to obtain a maximum likelihood estimate of the true image value  $m_j$ , which leads to an iterative formulation,

$$m_j^{(r+1)} = m_j^{(r)} \sum_i p_{ij} \frac{d_i}{\sum_j p_{ij} m_j^{(r)}} \leftrightarrow m^{(r+1)} = m^{(r)} \left( p \otimes \frac{d}{p \otimes m^{(r)}} \right). \quad (4.2)$$

It has been shown by Shepp & Vardi (1982) that Eq. (4.2) indeed converges to the maximum likelihood solution for  $m_j$  in cases when the "Poissonian noise" is not dominant. Otherwise, the RL method will amplify this noise by overfitting the data, i.e. squeezing counts into single bins in data space which will produce artefact like images. Consequently, there is no real objective stopping criterion when to interrupt the algorithm. Often, the maximum likelihood or  $\chi^2$  statistics are used to judge whether an image is representative or not.

Knoedlseder (2005) illustrate the performance of the RL algorithm for the 511 keV emission measured with SPI by illustrating the trade-off between maximum likelihood value, derived flux, granularity of image, and comparisons to the exposure map for different iterations steps. As the most plausible sky image, he chose iteration 17, although all iterations between 10 and 25 are similarly well describing the data.

The map in Fig. 4.6a yields an integrated flux of  $\approx 1.4 \times 10^{-3}$  ph cm $^{-2}$  s $^{-1}$  while the map in Fig. 4.6b counts  $\approx 1.5 \times 10^{-3}$  ph cm $^{-2}$  s $^{-1}$ . Statistically, the maps differ by  $\Delta\chi^2 \approx 10$ , which, accounting for the difference in degrees of freedom (1) is a significant difference. By considering the total number of data points in the analysis (129599), the two images are statistically indistinguishable. The maps, however, differ in the appearance of the galactic disk in 511 keV, which is not seen at all for

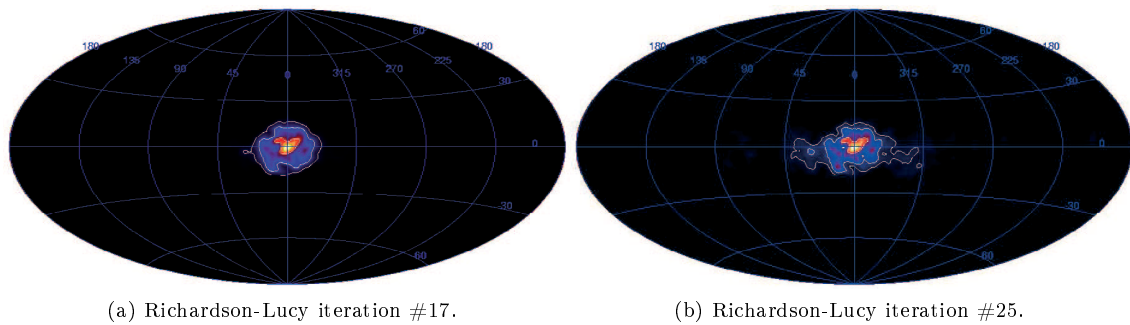


Figure 4.6: Positron annihilation sky map from Richardson Lucy deconvolution. Shown are two acceptable iterations (#17 left and #25 right) with a  $5^\circ \times 5^\circ$  boxcar smoothing. Contours are indicating levels of  $10^{-2}$ ,  $10^{-3}$ , and  $10^{-4}$   $\text{ph cm}^{-2} \text{s}^{-1} \text{sr}^{-1}$  from the centre outwards. From Knödlseider et al. (2005).

iteration #17. If the RL algorithm is pushed further, more and more emission is revealed, even in the far outskirts of the disk. Due to the apparently bad likelihood of images beyond iteration  $\approx$  #40, these have not been considered real in Knödlseider et al. (2005), also because it seemed that the exposure map partly correlated with the derived 511 keV map.

In general, it can be seen that there is a bright emission region in the centre of the galaxy whose longitudinal distribution (integrated over the latitude range) is slightly asymmetric. Empirically, these regions can be described by two 2D Gaussians with a compact component of  $5^\circ$  FWHM, and a broader component with a FWHM of  $10\text{-}20^\circ$  (Knödlseider et al. 2005). Knödlseider et al. (2005) also showed by simulations that low surface brightness regions will hardly be traced by the RL method at that time (low exposure in the disk), which could be one reason why the disk in 511 keV was seen only weakly.

### Maximum Entropy Method

The ME method exploits the information content of an image by penalising a goodness-of-fit criterion with a regularisation function. Because the goodness-of-fit criterion (e.g. the  $\chi^2$  measure) has many possible solutions, and because maximum-likelihood-based approaches (e.g. RL or gradient searches) tend to overfit gamma-ray data, another figure of merit is introduced which includes the image properties. This function is chosen to smooth the discretised pixel distribution of an image (Skilling 1989). In particular, the "best" set of proportions  $p_i$  (image brightness values) with  $i = 1, 2, \dots, N$  on  $N$  a priori equivalent cells (here: image pixels) is obtained by maximising the entropy of the image

$$S(\vec{p}) = - \sum_{i=1}^N p_i \log p_i. \quad (4.3)$$

This generalises in terms of measured data pixel  $d_i$  and proposed model pixel  $m_i$ , in which the prior knowledge about the sky intensity  $d_i$  is contained, to

$$\mathcal{S}(\vec{d}, \vec{m}) = \sum_{i=1}^N \left( d_i - m_i - d_i \log \left( \frac{d_i}{m_i} \right) \right). \quad (4.4)$$

From Eq. (4.4) it is evident that  $\mathcal{S}(\vec{d}, \vec{m})$  is maximal for  $\vec{d} = \vec{m}$ . In total, a Lagrangian method containing a regularisation with the entropy function,  $\mathcal{S}$ , and a fit quality function, describing the discrepancy between model and data,  $\mathcal{L}$ , is applied to the data set, aiming to maximise

$$Q(\vec{d}) = \alpha \mathcal{S}(\vec{d}) - \mathcal{L}(\vec{d}). \quad (4.5)$$

Here,  $\alpha$  is the Lagrange multiplier, balancing between the influence of the entropy and of the log-likelihood on the resulting image, and is iteratively adjusted during the ME procedure. The log-likelihood function is distributed according to the  $\chi^2$  distribution,  $\mathcal{L} = -\frac{1}{2}\chi^2$ , so that the expectation value of  $\mathcal{L}$  is  $-\frac{1}{2}N$  with  $N$  the number of data points, i.e. the "best fit" is found when  $\chi^2/N = 1$ . Historically, the maximum entropy method was hence defined as maximising the entropy function,  $\mathcal{S}$ , over the constraint that  $\chi^2 \stackrel{!}{=} N$ , which is finally expressed in Eq. (4.5) (e.g. Frieden 1972; Skilling 1989).

Although the ME method is based on "first principles", the application of the method is not unique. The entropy function can also take several forms of which Eq. (4.4) is the most popular one. Another problem is the correlation between adjacent pixels in "realistic" images, as their flux might have been emitted from the same (3D) source region in space. But these are treated independently in the ME method. In addition, the algorithm is sensitive to the first initial guess, i.e. the "reference" image upon which the entropy is evaluated, so that equivalently well "fitting" images can look quite different. This is true even if the images only slightly differ in the value of their entropy, and hence  $\alpha$ .

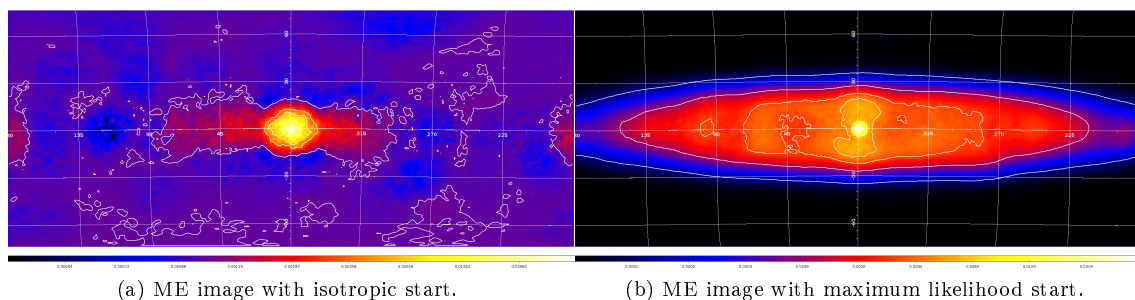


Figure 4.7: Maximum entropy images of the 511 keV sky as started from an isotropic map (a, bare isotropy maximum), and a "best fit" map (b, bare likelihood maximum) in logarithmic scaling. Contours indicate flux levels of 30, 10, 5, 3, 1, and  $0.1 \times 10^{-3} \text{ ph cm}^{-2} \text{ s}^{-1} \text{ sr}^{-1}$

In Fig. 4.7, the results of the ME method applied to the 511 keV data set described in Sec. 4.2 are compared for the central 508-514 keV, i.e. only representing the line dominant part of the spectrum. The reference image was set to an isotropic map, so that each pixel has the same intensity, i.e. the probabilities are equipartitioned, and the bare entropy is at maximum. Panel (a) shows the resulting image of iteration #66, with bright emission in the centre and a disk which gradually merges into an

almost omnipresent diffuse component. The 10% contours indicate a low surface-brightness disk-like component, extending at least from latitudes  $\approx -25^\circ$  to  $\approx +25^\circ$ . The Crab as the strongest continuum source in that band can also be identified at its correct position at  $(l/b) = (-175.44/-5.78)$ . The appearance of the Crab does not necessarily mean that there is annihilation emission from that direction, but rather that emission was found in the 508-514 keV band. There seems to be diffuse emission around that position, which may also be attributed to the Crab, but the ME algorithm does not have enough "leverage" to account for it correctly. This shows the limits of the ME method from the perspective of unknown prior knowledge. The faint diffuse emission above and below the disk (violet colour) may arise from a halo-like emission or even more so a large scale-height of disk emission. In Fig. 4.7b, the chosen reference image was the "best fitting" empirical model from Sec. 4.4.2. This image is already close to the maximum-likelihood, as it fits the data set well. In the ME result, the general shape of the starting image is rather conserved, but the smoothness is reduced towards a more patchy appearance of the disk structure. The Crab as a point source was not included in the starting image and is thus only weakly apparent. In iteration #220, shown in Fig. 4.7b, the formerly symmetric disk is now stretched towards negative longitudes, i.e. to where the Crab is located. The  $\chi^2$  values for the two images are 1215355 (a) and 1219534 (b), respectively, resulting in a  $\chi^2$  difference of  $\approx 4179$ . Considering the number of degrees of freedom, they are statistically only marginally distinguishable: The log-likelihood ratio follows a  $\chi^2$  statistic, for which the expectation value equals the number of degrees of freedom, here  $\nu = 1211027$ . Since this probability distribution has a width (standard deviation; second moment) of  $\sqrt{2\nu} \approx 1100$ , the  $n \times \sigma$  tolerance band for an adequate fit is  $1211027 \pm 1100n$ . In other words, depending on the realisation of the Poisson-distributed data,  $\chi^2$  differences for non-nested models<sup>2</sup> of the order of  $n \times \sigma$ , where  $n$  is to be chosen according to the number of data points<sup>3</sup>, are insignificant and compatible with statistical fluctuations that are expected. Formally, the image in panel (a) is favoured by  $< 4\sigma$  over the image in panel (b). But since the models / reconstructed images are non-nested, this formal criterion cannot be used. Only if large  $\Delta\chi^2$  values would occur, one could still argue that one or the other representation of the data should be preferred. In fact, neglecting the Crab in the best fitting likelihood map as a starting point for the maximum entropy algorithm misleads the ME imaging in this case. The total integrated flux for both images is  $4.0 \times 10^{-3}$  ph cm $^{-2}$  s $^{-1}$  (a) and  $3.4 \times 10^{-3}$  ph cm $^{-2}$  s $^{-1}$  (b), respectively<sup>4</sup>. Given the equivalence of both representations, an estimate of the systematic uncertainty on the line flux of the order of  $0.3 \times 10^{-3}$  ph cm $^{-2}$  s $^{-1}$ , i.e.  $\approx 10\%$ , can be derived.

Both reference images lead to a rather puffed up disk. This is new in respect to the positron annihilation morphology of the Milky Way (see Sec. 4.6.6 for further interpretation on the morphology). The conventional models for the central part of the Galaxy may also be reconsidered, as the ME results show structures in 511 keV

<sup>2</sup>Models or parametrisations of data which are not expressible by combinations or sub-model-components of another model are called non-nested. For example,  $ax^2 + bx + c$  and  $dx + e$  are nested models, whereas  $ax^2 + bx + c$  and  $\exp(dx) + e$  are not.

<sup>3</sup>In general, the value of  $n$  is arbitrary, depending on the wanted accuracy of the fit. For a small number of data points, say  $10^1 - 10^2$ ,  $n$  should be small, around 1, as higher values would allow any model to fit the data. However, for a large number of data points, say  $10^6$ , the expected number of outliers also rises, so that bigger numbers of  $n$  are also appropriate. In fact, this also depends on the number of fitted parameters, but as rule of thumb for number of data points  $10^N$ , and number of degrees of freedom  $\lesssim 10^N$ , the appropriate value for  $n$  to judge among models is  $n \approx N$ .

<sup>4</sup>This will turn out to be exactly the sum of 511 keV annihilation line fluxes and continuum in the 508-514 keV band from all sources in the Milky Way (see Sec. 4.6).

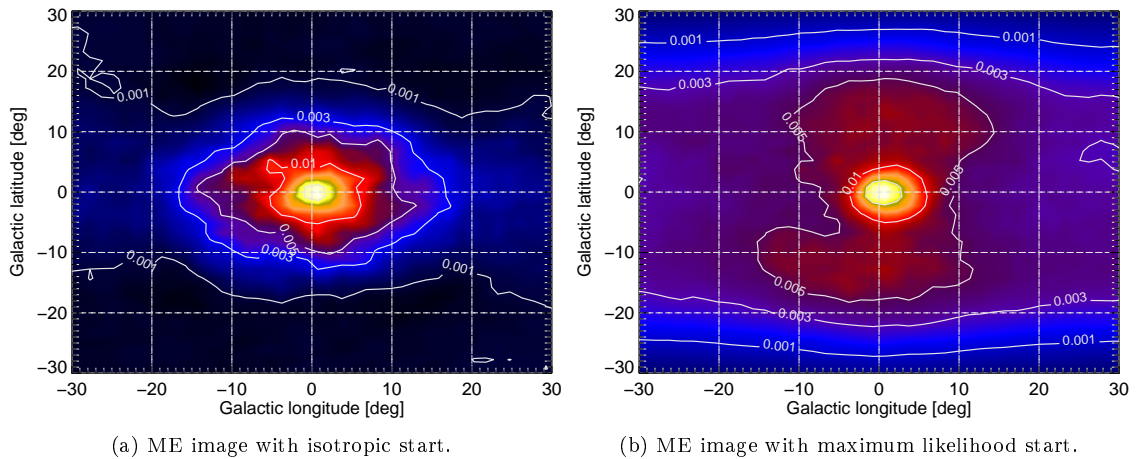


Figure 4.8: Maximum entropy images of the inner galactic ridge in 511 keV. Left and right panel are identical to Fig. 4.7, but zoomed into a region confined by  $|l| < 30^\circ$  and  $|b| < 30^\circ$  in now square-root scaling for illustration purpose.

emission which are deviant from the smooth Gaussian models, and are reminiscent of known astrophysical source configurations. In Fig. 4.8, the inner  $30^\circ \times 30^\circ$  of the ME images of the Milky Way are shown for both reference images. Comparing Fig. 4.8a with the RL deconvolution by Knödseder et al. (2005), Figs. 4.6a and b, the central part of the Milky Way bulge is represented in rather similar ways, with a symmetric shape in latitude, but slight deviations from spherical symmetry in longitude. Especially, an emission feature around  $(l/b) = (-5^\circ/5^\circ)$  is evident in both (RL and ME) reconstructions. The elongated and tilted emission region in the centre, which was interpreted as originating in the circumnuclear disk, appears less stretched in the ME reconstruction. It may be reminiscent of a galactic bar, viewed at a specific aspect angle (see also Sec. 4.6.6). The disk is now clearly detected and evident: It is indicated by the  $0.001 \text{ ph cm}^{-2} \text{ s}^{-1} \text{ sr}^{-1}$  contours in both the zoomed and unzoomed image. On the other hand, in Figs. 4.6a and b, the disk quickly fades away for larger longitudes. In the case of Fig. 4.8b, the central part looks again similar to a galactic bar, as the emission maximum is slightly offset towards negative longitudes ( $l_{max} \approx -1^\circ$ ), more extended towards positive longitude, and with increasing flux values for larger latitudes. But in addition to the disk, there is emission above and below the region of the galactic bulge, extending to latitudes  $|b| \approx 20^\circ$  with a higher intensity than the disk emission. This is, however, not seen in Fig. 4.8a. Such bipolar emission is reminiscent of the so-called "Fermi bubbles". These are two large bubble-like emission features, extending  $50^\circ$  above and below the galactic centre, with a longitudinal extent of  $40^\circ$ . They have been detected in gamma-rays between 0.3 and 300 GeV with Fermi/LAT (Su et al. 2010). If both emission features have a common origin, one reason why the latitudinal extent in 511 keV is not larger, may be due to the fact that the exposure time with SPI, Fig. 4.3, is only long enough to have detected such faint and low contrast emission below  $20^\circ$  latitude. In any case, the Fermi bubbles and the 511 keV emission from this ME reconstruction are spatially correlated. This may thus point towards the same physical origin, which will be discussed in more detail in Sec. 5.2.2. Another emission feature which is also thought to be related to the Fermi bubbles is the "WMAP haze". This is a microwave excess with a spherical, non disk-like morphology, visible up to at least  $|b| \approx 30^\circ$ , interpreted as synchrotron emission from cosmic-ray electrons (Finkbeiner 2004). A third, very similar emission

feature was revealed by the ROSAT 1.5 keV all sky map, showing a bipolar X-ray structure along the inner few tens of degrees towards the galactic centre (Snowden et al. 1997). This was, for example, interpreted as a superbubble, associated with a bipolar outflow from the galactic centre region, formed from a superwind with an energy of the order of  $10^{54}$ - $10^{55}$  erg (Sofue 2000; Sofue et al. 2016).

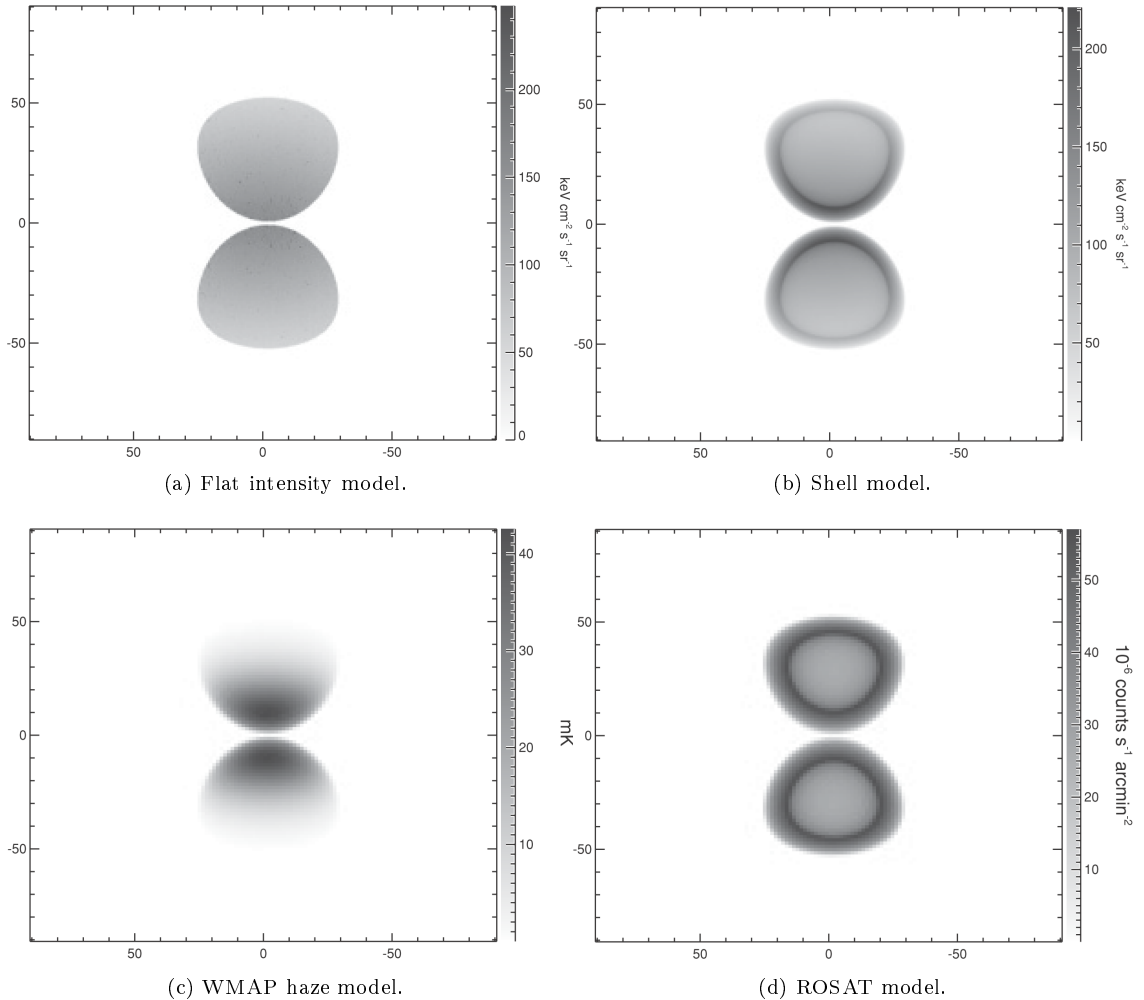


Figure 4.9: Projected emissivity distribution models for bipolar morphologies in the galactic centre. See text for details. From Su et al. (2010).

Su et al. (2010) presented different modelling approaches for the Fermi bubbles, based on the above mentioned measurements in different wavelengths. In Fig. 4.9, different emission models to explain the bipolar structures from the galactic centre are presented. In panel (a) a toy model for the Fermi bubbles with flat projected intensity is shown. The volume emissivity, assuming an optically thin interstellar medium, is proportional to  $(R^2 - r^2)^{-1/2}$  for  $r < R$ , where  $R = 3.5$  kpc is the radius of the bubble, and  $r$  the distance to the centres of the northern and southern bubble, respectively. Panel (b) describes a bubble model with compressed gas shells of 0.5 kpc thickness, that may originate from inverse Compton scattering of cosmic-ray electrons. In this model, the density distribution must be very non-uniform. The resulting morphology would then be limb-brightened. This, however, is in contrast to high-energy gamma-ray observations, but appears compatible with data from other wavelengths. The WMAP haze model, panel (c), is dominated by synchrotron emission, which depends also on the cosmic-ray electron density, and

the magnetic field, which was chosen as  $B = B_0 \exp(-z/z_0)$  with  $z_0 = 2$  kpc. Due to the decreasing magnetic field at larger heights above the galactic disk (higher latitudes), the emissivity also decreases for the microwave emission model. Panel (d) is a representation of a bipolar shell model from the ROSAT 1.5 keV measurements. The limb of the shell here is also brightened, as the gas is entirely contained in the shell "wall" with a thickness of 1 kpc, and no gas is assumed for the interior (see also Sofue 2000; Sofue et al. 2016). Disentangling the bubble-like emission feature from the 511 keV ME map, panels (a) and (c) would be favoured over the shell models (b) and (d). Reasons are: First, because the 511 keV emission is only seen up to  $|b| < 20^\circ$  which would indicate a connection with the magnetic field as the WMAP haze is also only dominant to this latitude scale. And second, because the 511 keV bubble intensity is rather flat, showing no large variations from the centre towards the ends. However, as already pointed out by Su et al. (2010), such a flat morphology is a challenge for many models.

It has to be cautioned, however, that such a discussion should not be carried out too far, since the systematic uncertainties on the morphology may also lead to biased or even false results, as shown by the different ME method starting images. In summary, the large scale structure of the 511 keV is consolidated to be bulge-dominated and accompanied by a low surface-brightness and thick disk. Peculiar small scale structures might be over-interpretation and should be treated with care.

### Information Field Theory

Both RL and ME methods yield results that depend on the guess of the very first (zeroth) iteration. This may lead the process into a "wrong" direction, and more so, the final result might be path-dependent. In addition, here the map is treated as single entity with integrated properties. Individual components are not distinguishable in the spectral domain because only one spectrum for the whole map is the end result. A more sophisticated analysis is possible by information field theoretical approaches, based on hierarchical Bayesian parameter models, and implemented in the Denoising, Deconvolving, and Decomposing Photon Observations (D<sup>3</sup>PO) algorithm (Selig & Enßlin 2015). Within an image, D<sup>3</sup>PO can separate (reconstruct) the point-like emission from the diffuse emission by using prior information of the spatial correlation structure of the diffuse part, and the brightness distribution of the uncorrelated point sources.

In particular, D<sup>3</sup>PO uses Bayes' theorem to judge how likely a potential signal (component) is, given the data and its prior. Based on only the likelihood, a data set could be described by either a congeries of point sources only, or entirely by diffuse emission, or any fitting combination of both. The weight of these components are determined according to the data, and their assigned prior probabilities. Diffuse emission, for example, can be patchy but with smooth variations across the sky, so that neighbouring emission spots can be expected to show similar flux values, being correlated with the other parts. A log-normal distribution for the diffuse photon flux fulfils these requirements (Oppermann et al. 2013; Selig & Enßlin 2015). The prior on the point source component was discussed based on geometrical and physical properties of the Universe (Fomalont 1968; Carvalho et al. 2009; Malyshev &

Hogg 2011; Carvalho et al. 2012; Guglielmetti et al. 2009; Selig & Enßlin 2015) and positivity arguments, leading to a product of independent inverse-Gamma distributions (Selig & Enßlin 2015). The posterior probability for both source components are calculated, and expectation values are determined by marginalising over the joint probability distribution<sup>5</sup>. At the time of writing this theses, D<sup>3</sup>PO is being implemented and applied to the SPI 511 keV data by Ghaempanah (2016, priv. comm.).

#### 4.4.2 Astrophysical Modelling

Based on prior knowledge from unbiased imaging and previous works, a full forward-modelling approach with a restricted number of pixons, here 2D Gaussians, is carried out. In previous studies, the centre of the Galaxy seen in 511 keV (simply called "the bulge", although this might have nothing to do with the definition of "the galactic bulge") was described by a combination of two 2D Gaussians. Table 4.3 summarises the extents of the bulge component from previous measurements.

Instrument	$l_0$	$b_0$	$\sigma_l^{\Gamma}$	$\sigma_b^{\Gamma}$	Flux	Reference
OSSE	-0.4(3)	-0.3(3)	4.1(7)	4.1(7)	0.35(4)	Purcell et al. (1997)
OSSE + TGRS + SMM	-0.4(3)	-0.1(3)	3.9(6)	3.9(6)	0.33(3)	Purcell et al. (1997)
SPI	0	0	6(1)	6(1)	0.85(15)	Churazov et al. (2005)
SPI	0	0	5	5	$\sim 1.1$	Knödlseder et al. (2005)
	0	0	15(5)	15(5)		
SPI	-0.6(3)	0.1(3)	8.1(9)	7.2(9)	1.09(4)	Knödlseder et al. (2005)
SPI	-0.1(2)	-0.2(2)	7.5(1.0)	6.0(1.0)	0.89(5)	Churazov et al. (2011)
SPI	0	0	14	6	0.89(5)	Churazov et al. (2011)
SPI	-1.25	-0.25	5.75	5.75	1.13	Skinner et al. (2014)
	0	0	20.55	20.55		
	-0.06	-0.05	0	0		

Table 4.3: Measured 511 keV bulge extents from previous studies. The parameters  $l_0$ ,  $b_0$ ,  $\sigma_l^{\Gamma}$ , and  $\sigma_b^{\Gamma}$  are longitude centroid, latitude centroid, longitude FWHM, and latitude FWHM in degrees, describing the bulge model dimensions as 2D Gaussians. If more than one component was found necessary to explain the bulge signal, they are listed one below the other. The flux is given in units of  $10^{-3}$  ph cm $^{-2}$  s $^{-1}$  for the entire bulge signal, i.e. summed over all components. Measurement uncertainties are given in brackets in units of the last digits. Churazov et al. (2011) found two equivalent descriptions: one almost spherical and one elongated in longitude but tilted by 12° counter-clockwise. An extent of zero means point-like emission.

In this thesis, the bulge as extracted and modelled by Skinner et al. (2014) is used. Their result was derived from a similar set of SPI observations. But they focussed on determining the proportions of bulge and disk in a 6 keV energy band between 508 and 514 keV, instead of using fine energy bins. The bulge is represented by the sum of three 2D Gaussians at different positions and with different widths in longitude and latitude. One of the Gaussians representing the bulge is offset to negative longitudes, while the other components are centred at the Galactic centre<sup>6</sup>. Point sources have to be added at the positions of the Crab, and Cygnus X-1 (Cyg X-1), because these are strong continuum sources which emit in the energy band between 490 and 530 keV. Additional point sources candidates will be discussed in Sec. 4.6.5 and 5.5.

<sup>5</sup>In detail, the expectation values and uncertainties are not analytically solvable so that elaborate techniques beyond Markov Chain Monte Carlo methods have to be applied which are beyond the scope of this thesis. See Selig & Enßlin (2015) for further information.

<sup>6</sup>In the case of the point-like component, the position is actually taken as that of Sgr A\*, the supermassive black hole in the centre of the Milky Way

In total,  $N_I = 6$  components were used to model the celestial emission in this energy range, in addition to the two-component background model ( $N_B = 2$ ), as described in Sec. 3.2.3.2. The celestial emission in the 490-530 keV energy range is dominated by the bright 511 keV line emission from the Galaxy's centre, modelled by the narrow bulge (NB) and the broad bulge (BB). To this, a yet to be determined disk is added. In general, the emission features are modelled as 2D Gaussians of the form

$$I(l, b; A_0^i, l_0^i, b_0^i, \sigma_l^i, \sigma_b^i) = A_0^i \exp\left(-\frac{(l - l_0^i)^2}{2\sigma_l^{i2}} - \frac{(b - b_0^i)^2}{2\sigma_b^{i2}}\right), \quad (4.6)$$

for each component  $i$ .

The disk component of the 511 keV positron annihilation in the Milky Way is uncertain. Previous studies reported detections of a disk-like component, but its extent and intensity was constrained only poorly. Therefore, the disk extent in this analysis will be determined by a 2D grid scan in the  $\sigma_l^{disk}$ - $\sigma_b^{disk}$  parameter space, maximising the total likelihood in all 80 energy bins, and holding the other components fixed. By scanning solutions with different disk extent, given a fixed/optimal configuration of the bulge, and point sources, a maximum likelihood solution in each energy bin is determined. For a grid of  $10 \times 10$  different longitude and latitude widths, ranging from  $\sigma_l^{disk} = 15^\circ, \dots, 150^\circ$ , and  $\sigma_b^{disk} = 1.5^\circ, \dots, 15^\circ$ , respectively, models have been calculated for each of the 80 energy bins, and then fitted together with the other five sky model components and the two background model components. All model scaling parameters have been re-optimised for each point of this model grid, in particular the flux per energy bin and component.

The fit could be improved significantly by an additional source in the centre of the Milky Way. Here, a point source or cusp, i.e. a point-like source that was recognised above the diffuse bulge emission, was used to describe the morphology. Such a component has also been found by Skinner et al. (2014), and is hereafter called Galactic Centre Source (GCS). The two strongest continuum sources in the gamma-ray sky, the Crab and Cygnus X-1, have also been added for an acceptable likelihood. In the model fitting, the model amplitudes  $A_0^i$  for each of the sky model components  $i$  is obtained in each of the 80 energy bins, thus comprising an individual spectrum of celestial emission per component. Hence, in this study, spectral information is inferred, and the analysis of cross correlations among components is performed. In this way, a bias towards any expected spectral shape from celestial emission is avoided. With the exception of exploring the effects of changing the disk parameters, the shape parameters of the other image model components (i.e. NB, BB, and CG) are not altered. An optimisation of all sky components in a single 6 keV wide energy bin was conducted by Skinner et al. (2014).

Such modelling includes correlations among components. It can be seen as an alternative to having a large number of pixels on the sky. Analysis through orthogonalised functions that have no astrophysical bias is an interesting method, as it associates image components with plausible and explicit source regions without a risk of this resulting from a possible bias within the method or its starting conditions. The aim is to build a minimal set of required parameters to describe the sky as accurate as the data provides it. The six components used for modelling the celestial emission

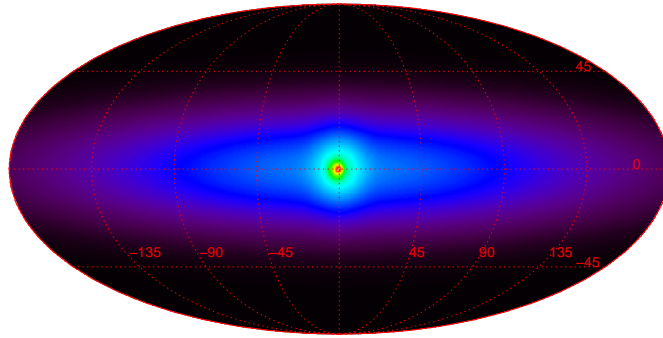


Figure 4.10: Image of the model components as assessed in the sky model fit study. The weighted sum of fluxes for each celestial component in the 80 bins in the analysed energy band from 490 to 530 keV is shown. Two additional point sources to improve the fit, the Crab and Cyg X-1, are not shown, focussing on the diffuse part. The image has been scaled by taking the cube root to emphasise the low surface-brightness and extent of the disk. See Tab. 4.4 for details.

in the 490 to 530 keV band are listed in Tab. 4.4 and illustrated in Fig. 4.10. Slices through  $l = 0$  and  $b = 0$ , respectively, are shown in Fig. 4.11. The disk encloses the entire bulge, NB and BB, in latitude, but extends far out in longitude. From the fitted brightness of the components, there is an apparent asymmetry in the global morphology, with higher flux values for negative longitudes. This was historically interpreted as an asymmetry in the disk of the 511 keV emission (Weidenspointner et al. 2008a), but is now attributed to the bulge component whose centroid is shifted to negative longitudes. The disk, however, is found to be symmetric. This is also resulting from the spectral analysis, Sec. 4.6.2.

Component	$l_0$ [deg]	$b_0$ [deg]	$\sigma_l^\Gamma$ [deg]	$\sigma_b^\Gamma$ [deg]
NB	-1.25	-0.25	5.75	5.75
BB	0.00	0.00	20.55	20.55
Disk	0.00	0.00	141.29	24.73
GCS	-0.06	-0.05	0.00	0.00
Crab	-175.44	-5.78	0.00	0.00
Cyg X-1	71.34	3.07	0.00	0.00

Table 4.4: Characteristics of the sky model components in the maximum likelihood model fitting analysis. The disk extent has been chosen according to a 2D grid scan for a total maximum likelihood over all 80 bins. An extent of  $0^\circ$  is equivalent to a point source. The Galactic Centre Source has been chosen to coincide with the position of Sgr A\* (see text for details).

The maximum likelihood values versus disk size parameters are shown for the 2D grid scan in Fig. 4.12b. A longitude extent of  $60_{-5}^{+10}$  degrees, and a latitude extent of  $10.5_{-1.5}^{+2.5}$  degrees ( $1-\sigma$  values) is found. In an independent analysis in a single 6 keV wide energy bin of the 511 keV line (Skinner et al. 2014), the disk extension parameters are found to lie in the range of  $30-90^\circ$  in longitude, and around  $3^\circ$  in latitude. Their study included the impact of different bulge parameters and different background methods. In the spectrally resolved analysis which uses the self-consistent background modelling approach, Sec. 3.2.3.2, and the above bulge model, the uncertainty on the (model-dependent) disk extent can be largely reduced. The best disk extent is obtained by optimising for both, the annihilation line and the galactic continuum components at the same time, for the energy region 490 to 530 keV.

The adequacy of the background model is demonstrated in Fig. 4.13, showing  $\chi^2$ -dof for each energy bin, subject to the optimised disk size. For the entire SPI-camera (black), the values scatter around a value of 1713 (corresponding to a reduced  $\chi^2$  of

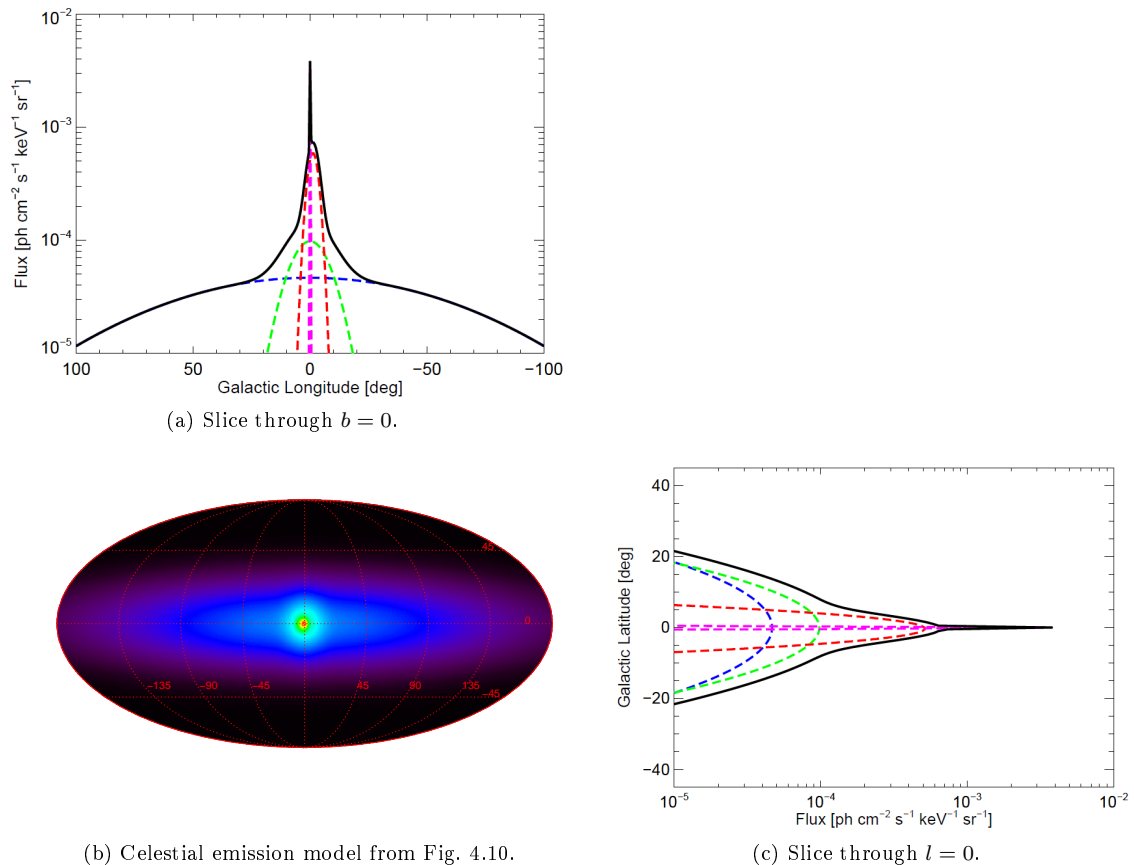


Figure 4.11: Annihilation emission profile in longitude and latitude. Shown are slices of the emission trough the map (panel b) at  $b = 0$  (a) and  $l = 0$  (c), respectively. The main model components are shown as blue dashed line for the disk, green for the BB, red for the NB, and magenta for the GCS in each panel. The total model is shown as black solid line. The profiles for point source components describing the Crab and Cyg are not shown.

1.0014 with 1211021 dof), and fall well within a  $3\sigma$  goodness-of-fit interval (orange area). No particular energy region is overemphasised in the maximum likelihood fits, nor are single detectors deviant. In total, the background model fitting determines 3772 parameters per energy bin.

Figure 4.14 shows the detection significance of the celestial signal for each energy bin, based on the best fit description of the sky in terms of the six components listed in Tab. 4.4. The significance is calculated using the likelihood-ratio between a background-only fit to the data, and a fit including the background plus six celestial sources. This leads to a difference of dof in each energy bin of 6. In the spectrum, the dominant annihilation line at 511 keV is very clear, with a total significance of  $58\sigma$ . Characteristic o-Ps continuum on the low-energy side of the line is also detected with high significance, as is the underlying diffuse Galactic continuum emission (Bouchet et al. 2011). The continuum emission part of the spectrum is predominantly from the disk, the Crab, and Cyg X-1 (see Sec.4.6).

The inner Galaxy is found to be the brightest region of the annihilation gamma-ray sky, confirming previous findings (e.g. Jean et al. 2006; Churazov et al. 2011). It is detected with a significance of more than  $56\sigma$ . The disk-like emission component has a significance of  $12\sigma$ . The surface brightness of annihilation radiation for this disk component is rather low. The diffuse gamma-ray continuum emission from the Galaxy (Bouchet et al. 2011) is the strongest signal in the disk, and is clearly detected

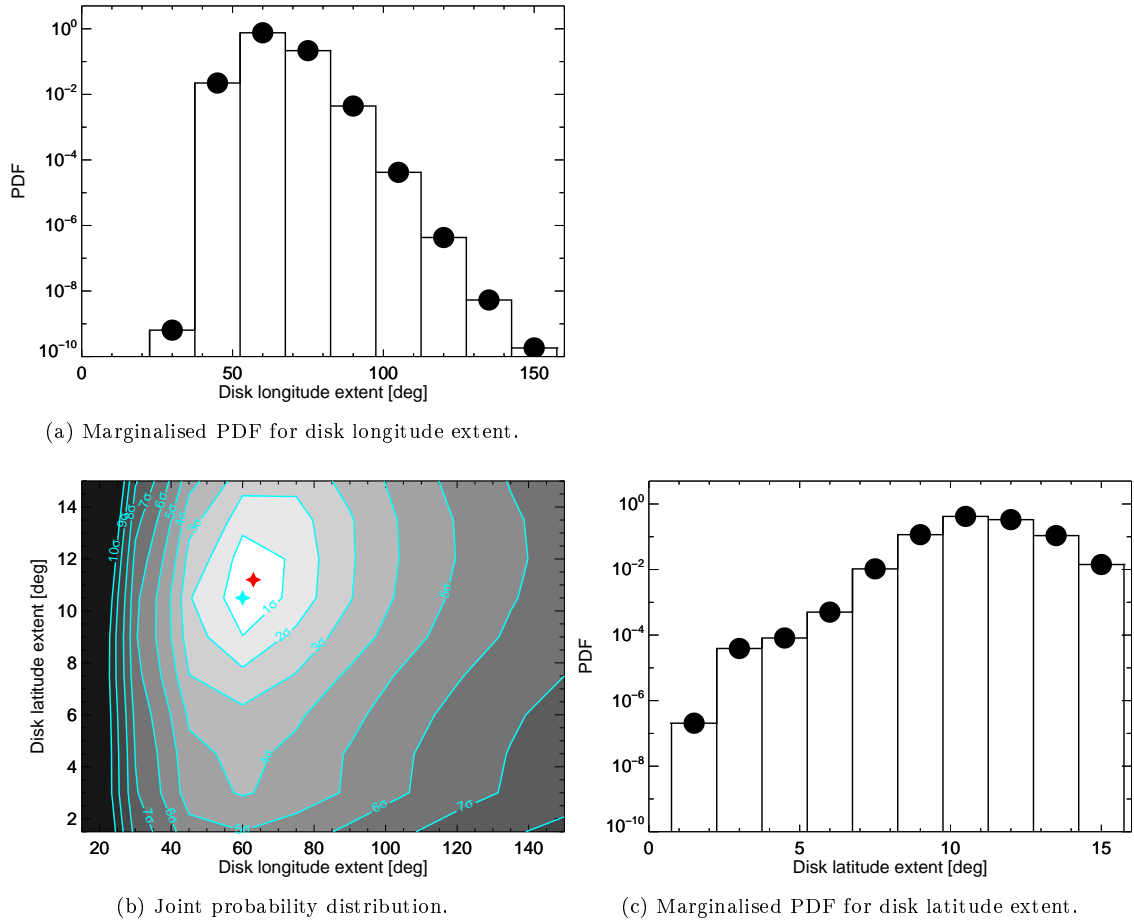


Figure 4.12: Maximum likelihood estimate for the disk extent. The contours in panel (b) indicate the uncertainty of the disk size with respect to the best fit using the fixed bulge and point-source component model. The cyan (red) star symbol indicates the best fit (most probable) disk extent. In panels (a) and (c), the marginalised probability distributions for the longitude and latitude extent of the disk is shown, respectively. From the likelihood maximisation on the specified grid, the disk longitude and latitude size are positively correlated with a coefficient of  $\rho = 0.253$ , meaning that a larger radial scale also favours a larger vertical scale and vice versa.

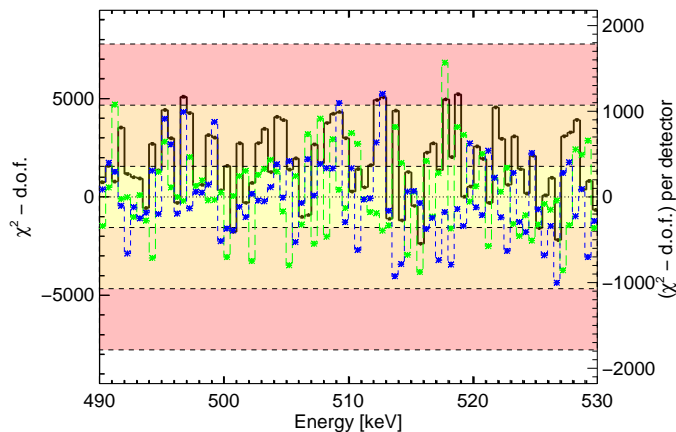


Figure 4.13: Background model performance measured by  $\chi^2$ -d.o.f. for each energy bin (i) for the entire SPI camera (left axis, black data points), and (ii) for two example detectors (right axis, detector 00 blue, detector 13 green). The ideal value of 0.0 (corresponding to a reduced  $\chi^2$  of 1.0) is shown as a dotted line, together with the 1, 3, and  $5\sigma$  uncertainty intervals for a  $\chi^2$ -statistic with 1211021 d.o.f. The majority of points fall into the  $3\sigma$  band. No excess is evident either in the energy domain or for particular detectors.

even in this 40 keV band. The two strongest continuum sources in this energy band, the Crab and Cyg X-1 (point sources), are detected at  $31\sigma$  and  $11\sigma$ , respectively; their spectral parameters are consistent with literature values (see Sec.4.6). In the

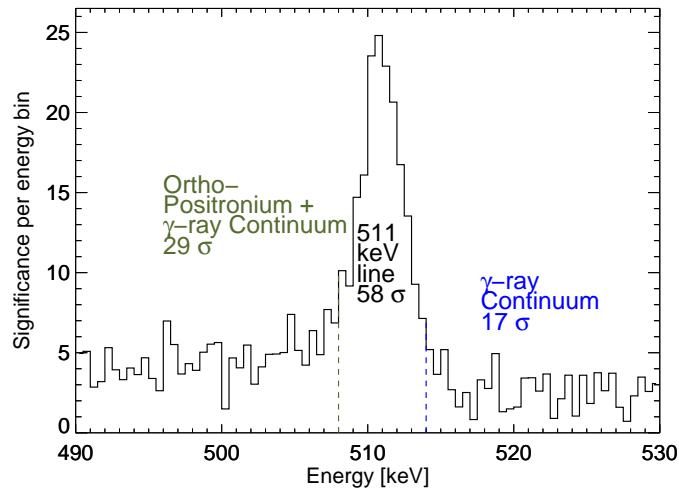


Figure 4.14: Detection significance of gamma-rays from positron annihilation in the Galaxy. The significance of detecting a signal from the sky, summed over all spatial components as described in the text, is given for each 0.5 keV wide bin in units of  $\sigma$ . The intense line at 511 keV, together with an ortho-positronium continuum from positron annihilation, and an underlying gamma-ray continuum emission component can be identified.

centre of the Galaxy, the GCS is detected with a statistical significance of  $5\sigma$  when fixing the positions and extents of the other components.

	NB	BB	Disk	GCS	Crab	Cyg X-1
NB	1.000					
BB	-.836	1.000				
Disk	.118	-.365	1.000			
GCS	-.535	.224	-.028	1.000		
Crab	-.018	.050	-.102	.004	1.000	
Cyg X-1	-.005	.003	.051	.001	-.004	1.000

Table 4.5: Correlation coefficients for the six simultaneously fitted sky components. Given are the mean coefficients across all energy bins.

The signals from the different sky components cannot be determined entirely independent as they partially overlap (e.g. bulge and disk). Thus, a correlation analysis is performed. Correlation coefficients for the intensities of the components have been calculated from the covariance matrix in the maximum likelihood fits, and are given in Tab. 4.5. Average values over the energy band are provided, since the energy dependence is negligible ( $< 0.01\%$ ). The intensity correlation between the NB and BB component is  $-0.836$ . This is plausible, because the NB is entirely surrounded by the BB. However, the (real, unknown) emission morphology does not allow the two component to interchange completely. Therefore, a single bulge component from the superposition of these two Gaussians, NB and BB, is defined. This definition represents an analytical description of an object's shape on the sky, independent and not based on astronomical, model-biased definitions of "the Galactic bulge", e.g. as defined by a stellar population or by infrared emission. This definition is preferred here as an alternative and complement to astrophysical model fitting, considering that such studies (Weidenspointner et al. 2008a; Higdon et al. 2009) remained questionable (see also Sec. 4.5). The disk only shows weak ( $-.365$  with BB) to almost no correlations with other components. For this reason, the disk component can be assumed to be a disentangled component on its own. "Disentangled" here means that the spectral description of the disk and other components can be treated as individual and not disturbing each other. The GCS is moderately anti-correlated with the NB ( $-.535$ ), weakly correlated with the BB ( $-.224$ ), and shows no cor-

relation with the other components. It is difficult to judge whether the GCS is a separate annihilation site or not. For the discussion and implications of the GCS, it is treated as an individual source of positron annihilation gamma-rays throughout this thesis. The continuum sources, both, are not correlated with other components as expected from the intensity of the sources being easily distinguishable with the point-source shadowgrams of SPI with respect to the diffuse emission.

## 4.5 Testing Astrophysical Tracers

A third alternative to "blind imaging" and "minimum number of components" analysis is to test astrophysical tracers. Instead of trying to deconvolve and reconstruct an image from SPI data space, or trying to express the data as a combination of an orthogonal basis of pixons, also known images can be convolved with the response and fitted to the data. In either case, this is the application of the coded mask imaging response to emission features from different perspectives. In doing so, the spatial distribution of astrophysical sources with their own mechanism is compared to the unknown annihilation morphology. This is greatly biased by the fact that only a limited amount of maps can be tested, which in return are chosen by plausibility arguments. Those astrophysically meaningful maps show a large variety of structured emission, for different regions, by different mechanism, and also weak and strong point sources.

### 4.5.1 Tracing by Photon Energy

In this analysis, the 490 to 530 keV energy band is used to test available all sky tracer maps that have been measured at different wavelengths. In particular, for each of the 80 half-keV energy bins, the likelihood ratio with respect to a background only fit,  $\Delta\chi^2 = -2(\ln(\mathcal{L}(\text{BG} + \text{SKY})) - \ln(\mathcal{L}(\text{BG})))$ , is calculated for each of the tracer maps, and compared to a "perfect" fit. This means a comparison to an improvement of a  $\Delta\chi^2$  value between  $\approx 20$  in the high-energy continuum band,  $\approx 30$ -40 in the o-Ps band, and up to  $\approx 600$  in the line, cf. Fig. 4.14. In Tab. 4.6, the tested tracers maps are presented, together with the respective photon energy, wavelength, and frequency, and also the responsible mechanisms for the emission at those energies.

In Fig. 4.15, the likelihood ratio test as a function of tracer map photon energy is shown for each energy bin. Around 511 keV, the fit is bad for all maps (dark blue shading). The continuum bands below and above the line can be fitted acceptably well by any of the maps, though the high energy side is generally better represented than the low energy side. It is, however, evident that one family of tracer maps indeed significantly improves the fit in the 511 keV band, though still not entirely acceptable by statistical means. The DIRBE maps at infrared wavelengths, between 1.25 and 4.9  $\mu\text{m}$ , are silhouetted against all other tracers in both, o-Ps and line bands. Another family of maps, which improves the low energy as well as the high energy part, Fig. 4.16, are the Swift/BAT 35-150 keV maps. At first glance the two families have nothing in common, but the level of contrast between galactic plane emission and other diffuse emission at higher latitudes is similar. This may be favoured by the o-Ps component. But because the centre of the galaxy is not as bright in the

$\lambda$	$\nu$	$E$	Tracer	Mechanism	Comment
73.5 cm	408 MHz	1.69 $\mu\text{eV}$	Magnetic field / Cosmic rays	Synch. emission	(1)
21.1 cm	1.42 GHz	5.90 $\mu\text{eV}$	Neutral hydrogen	H hyperfine transition	(2)
10.0 mm	30.0 GHz	124 $\mu\text{eV}$	Ionised gas / Cosmic rays	Free-free / Synch. / IC	(3a)
6.81 mm	44.0 GHz	182 $\mu\text{eV}$	-	-	(3b)
4.29 mm	70.0 GHz	290 $\mu\text{eV}$	-	-	(3c)
3.00 mm	100 GHz	414 $\mu\text{eV}$	-	-	(3d)
2.10 mm	143 GHz	591 $\mu\text{eV}$	-	-	(3e)
1.38 mm	217 GHz	898 $\mu\text{eV}$	-	-	(3f)
850 $\mu\text{m}$	353 GHz	1.46 meV	-	-	(3g)
550 $\mu\text{m}$	545 GHz	2.25 meV	-	-	(3h)
350 $\mu\text{m}$	857 GHz	3.54 meV	-	-	(3i)
240 $\mu\text{m}$	1.25 THz	5.17 meV	Dust ( $T \approx 12\text{K}$ )	Equilibrium grain heating	(4a)
140 $\mu\text{m}$	2.14 THz	8.86 meV	Dust ( $T \approx 21\text{K}$ )	-	(4b)
100 $\mu\text{m}$	3.00 THz	12.4 meV	Dust ( $T \approx 30\text{K}$ )	-	(4c)
60.0 $\mu\text{m}$	5.00 THz	20.7 meV	Dust ( $T \approx 50\text{K}$ )	-	(4d)
25.0 $\mu\text{m}$	12.0 THz	49.6 meV	Dust ( $T \approx 120\text{K}$ )	-	(4e)
12.0 $\mu\text{m}$	25.0 THz	103 meV	Dust ( $T \approx 250\text{K}$ )	-	(4f)
4.90 $\mu\text{m}$	61.2 THz	253 meV	Stars (red giants)	Starlight	(4g)
3.50 $\mu\text{m}$	85.7 THz	354 meV	-	-	(4h)
2.20 $\mu\text{m}$	136 THz	564 meV	-	-	(4i)
1.25 $\mu\text{m}$	240 THz	993 meV	-	-	(4j)
550 nm	545 THz	2.25 eV	Stars (M to A class)	-	(5)
49.6 $\text{\AA}$	60.4 PHz	250 eV	Hot gas (local)	Thermal bremsstrahlung	(6a)
16.5 $\text{\AA}$	181 PHz	750 eV	Hot gas	-	(6b)
8.27 $\text{\AA}$	363 PHz	1.50 keV	Hot gas / XRBs	-	(6c)
73.0 pm	4.11 EHz	17.0 keV	XRBs / SNRs / AGN	Brems. / Synch. / IC	(7a)
56.4 pm	5.32 EHz	22.0 keV	-	-	(7b)
42.1 pm	7.13 EHz	29.5 keV	-	-	(7c)
29.2 pm	10.3 EHz	42.5 keV	-	-	(7d)
19.9 pm	15.1 EHz	62.5 keV	-	-	(7e)
14.2 pm	21.2 EHz	87.5 keV	-	-	(7f)
9.93 pm	30.2 EHz	125 keV	-	-	(7g)
7.19 pm	41.7 EHz	173 keV	-	-	(7h)
686 fm	437 EHz	1.81 MeV	Massive stars	$^{26}\text{Al}$ decay	(8)
80.0 fm	3.75 ZHz	15.5 MeV	ISM / Cosmic rays	Nuclear interactions	(9)
17.7 fm	16.9 ZHz	70.0 MeV	-	-	(10a)
12.4 fm	24.2 ZHz	100 MeV	-	-	(11)
6.20 fm	48.4 ZHz	200 MeV	-	-	(10b)
1.77 fm	169 ZHz	700 MeV	-	-	(10c)
620 am	484 ZHz	2.00 GeV	-	-	(10d)
12.4 am	24.2 YHz	100 GeV	-	-	(10e)

Table 4.6: Summary of astrophysical tracer maps. Comments (1): Bandpass 406.25 – 409.75 MHz; mosaic of data from Jodrell Bank, Effelsberg, and Parkes telescopes (Haslam et al. 1981, 1982; Remazeilles et al. 2015); (2): Bandpass 1417.5 – 1423.5 MHz; Effelsberg-Bonn HI Survey (EBHIS) (Kerp et al. 2011; Winkel et al. 2016); (3a): Planck satellite measurements; Bandpass 20 – 33 GHz; (3b): Bandpass 39 – 58 GHz; (3c): Bandpass 60 – 80 GHz; (3d): Bandpass 85 – 130 GHz; (3e): Bandpass 130 – 160 GHz; (3f): Bandpass 190 – 250 GHz; (3g): Bandpass 310 – 410 GHz; (3h): Bandpass 450 – 650 GHz; (3i): Bandpass 750 – 1000 GHz; (Planck Collaboration et al. 2014a, 2016a); (4a): Diffuse InfraRed Background Experiment (DIRBE) measurements aboard the COsmic Background Explorer (COBE) satellite; Bandpass 193–288  $\mu\text{m}$ ; (4b): Bandpass 120–160  $\mu\text{m}$ ; (4c): Bandpass 84–116  $\mu\text{m}$ ; (4d): Bandpass 46 – 74  $\mu\text{m}$ ; (4e): Bandpass 20.7 – 29.3  $\mu\text{m}$ ; (4f): Bandpass 8.8 – 15.2  $\mu\text{m}$ ; (4g): Bandpass 4.57 – 5.23  $\mu\text{m}$ ; (4h): Bandpass 3.05 – 3.95  $\mu\text{m}$ ; (4i): Bandpass 2.02 – 2.38  $\mu\text{m}$ ; (4j): Bandpass 1.10 – 1.41  $\mu\text{m}$ ; (Hauser et al. 1998); (5): Bandpass 380 – 672nm all sky mosaic out of more than 3000 individual CCD frames (Mellinger 2009); (6a): ROentgen SATellit (ROSAT) measurements; Bandpass 0.1 – 0.4 keV; (6b): Bandpass 0.5 – 0.9 keV; (6c): Bandpass 0.9 – 2.1 keV; (Snowden et al. 1997; Voges et al. 1999); (7a): Burst Alert Telescope (BAT) measurements aboard the Swift satellite; Bandpass 14 – 20 keV; (7b): Bandpass 20 – 24 keV; (7c): Bandpass 24 – 35 keV; (7d): Bandpass 35 – 50 keV; (7e): Bandpass 50 – 75 keV; (7f): Bandpass 75 – 100 keV; (7g): Bandpass 100 – 150 keV; (7h): Bandpass 150 – 195 keV; (Krimm et al. 2013); (8): ME COMPTEL map Bandpass 1.7 – 1.9 MeV (Plüschke et al. 2001) and ME SPI map Bandpass 1805 – 1813 keV (Bouchet et al. 2015); (9): COMPTEL ME map; Bandpass 1 – 30 MeV; (Schoenfelder et al. 1993; Strong et al. 1994); (10a): Large Area Telescope (LAT) measurements aboard the Fermi satellite; Bandpass 30 – 100 MeV; (10b): Bandpass 100 – 300 MeV; (10c): Bandpass 300 – 1000 MeV; (10d): Bandpass 1 – 3 GeV; (10e): Bandpass 3 – 300 GeV; (Atwood et al. 2009); (11): Energetic Gamma-Ray Experiment Telescope (EGRET) measurement aboard CGRO; Bandpass 0.1 – 30 GeV; (Hartman et al. 1999).

Swift/BAT case as in the DIRBE maps, the line bins are extremely badly fitted by the hard X-ray maps. The infrared maps are very similar to the morphology found by modelling the 511 keV emission with 2D Gaussians, whereas the X-ray maps are dominated by point sources. This further supports the idea of stars being the true annihilation site for positrons. One possibility why the 1.25 to 4.9 micron maps do not fit the 511 keV SPI data perfectly is perhaps due to several point sources in the infrared images which come from nearby stars. In addition, the zodiac light, i.e.

sunlight either scattered by interplanetary dust (grain size  $\lesssim 4 \mu\text{m}$ ), or absorbed by it (grain size  $\gtrsim 4 \mu\text{m}$ ) and re-emitted as thermal infrared emission, might influence the fit. However, to what extent the zodiacal light worsens the fit - or even improves it - is hard to estimate, as the infrared emission from the solar system ecliptic in those maps (S-shapes in infrared maps of Fig. A.4) shows nearly no worsening of the fit in the case of the 4.9 micron map, but is hardly acceptable in the case of the 25 micron map, for example.

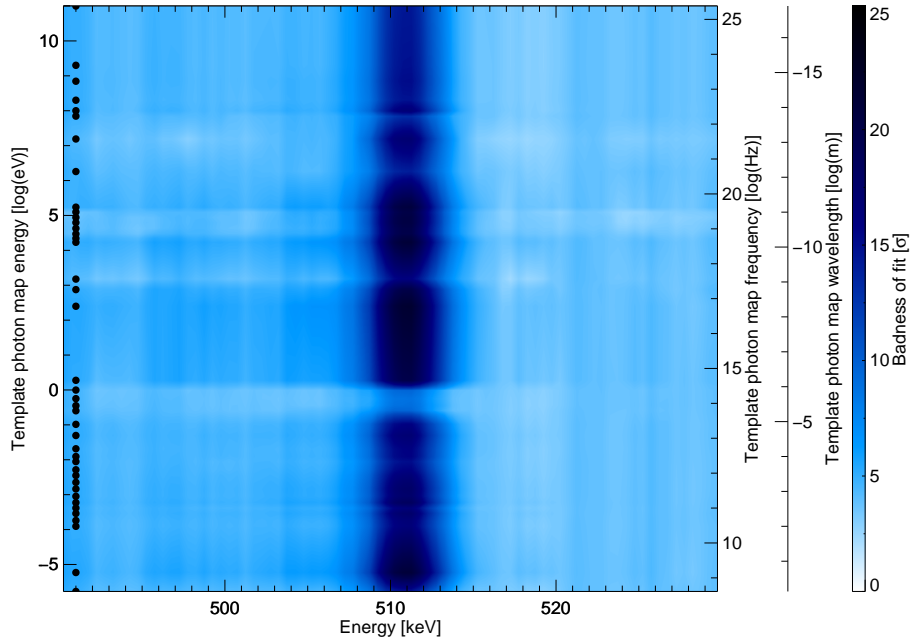


Figure 4.15: Likelihood of tracer maps as a function of photon energy. The y-axis shows the photon energy (wavelength, frequency) of the templated tracer maps versus the tested energy bins on the x-axis. The energies which have been tested in particular are indicated by the black dots on the left hand side, see also Tab. 4.6. The contours (blue shading, see colour bar on the right) indicate the badness of fit for each map and each energy bin, smoothed in x-direction by 2.5 keV. The fit badness is measured by a likelihood ratio test, comparing the template map plus background model against a background model only fit, and then set in respect to a perfect,  $\chi^2/\nu = 1.0$  fit. See text for detail.

Another map for which the o-Ps band is fitted as good as in the infrared and hard X-ray cases is the ROSAT 1.5 keV map. This map shows also the soft X-ray emission from X-ray binary (XRB) systems, in addition to the hot gas component in the Galaxy. This may provide an additional hint towards XRBs as a significant ingredient in the galactic positron annihilation picture. Similarly, the COMPTEL 1-15 MeV map fits both, the low- and the high-energy part of the spectrum well. In fact, both bands are best represented by this map. This is reasonable and expected, as the galactic diffuse gamma-ray spectrum is dominated by inverse Compton scattering of charged particles with the cosmic microwave background and stellar photons. Between  $\approx 50$  keV and few tens of MeV, the IC spectrum makes about 90% of the total gamma-ray flux in the inner Galaxy (Strong et al. 2005), excluding the 511 keV line. For this reason, the COMPTEL 1-15 MeV map is predestinated to fit those two bands below and above the 511 keV line exceptionally well. The low-energy band also contains o-Ps continuum gamma-rays, so that the fit does not reach a perfect  $\chi^2$  value. On the high-energy side, positrons are probably annihilating in flight, which adds to the spectrum, and might not be represented by the diffuse cosmic-ray gamma-ray map. This points towards an additional high-energy component, maybe originating from positrons. The 511 keV line is fitted as bad as by other tracer maps, so that the drawn conclusions and interpretations are only vague.

The emission morphology is not necessarily the source morphology of positrons in the Milky Way - except maybe for cosmic-ray positrons on the high-energy side of the spectrum - because of the large travelling paths of relativistic positrons, once escaped from their origins.

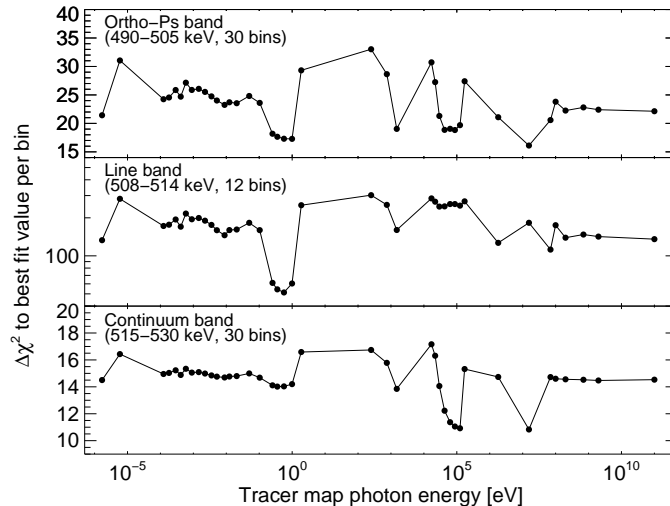


Figure 4.16: Likelihood ratio in different bands as a function of tested photon energy. The chosen bands are 490 – 505 keV for a focus on the ortho-positronium part, 508 – 514 keV for the line as the astrophysical line width is 2 – 3 keV, therefore capturing mainly the line photons, and 515 – 530 keV to have a measure of the high-energy continuum, coming from cosmic-rays and/or annihilation in flight. The shown  $\Delta\chi^2$  values indicate the distance to a perfect fit which would be  $\Delta\chi^2 = 0$  in this representation.

#### 4.5.2 Tracing by Physical Mechanism

An alternative to scan through all photon wavelengths is to be more specific on the physical process, which might trace the annihilation site. The Planck and WMAP satellites were designed to measure the cosmic microwave background, which is hidden by many foreground emissions. These are well measured in the Planck and WMAP radio bands. Similar to the analysis using different photon energy tracer maps, the scientific products of the Planck collaboration (Planck Collaboration et al. 2016b), and its predecessor mission WMAP (Bennett et al. 2013), are convolved with the SPI coded-mask imaging response, and fitted to the 511 keV in the same 40 keV band for each of the 80 half-keV bins. The tested maps are briefly illustrated in Tab. 4.7, explaining the physical origins of the emission, and special characteristics. Again, the likelihood ratio test with a background model only fit is performed, and then compared to a perfect fit. The resulting  $\Delta\chi^2$  values are shown in Fig. 4.17.

Map	Emission	Mechanism
CMB	Cosmic Microwave Background	Red shifted blackbody emission at $T = 2.7$ K.
CO	CO $J = 1 \rightarrow 0$ (115 GHz line emission)	Molecular rotation transition.
Syn	Synchrotron emission	Relativistic cosmic-ray electrons spiralling in galactic magnetic field.
SynPol	Polarised synchrotron	Intrinsically polarised emission of cosmic-ray electrons in regular magnetic field.
FF	Free-free emission	Bremsstrahlung from electron-ion collisions.
Dust	Thermal emission	Equilibrium dust grain heating.
AME	Anomalous Microwave Emission	Spinning dust with non-zero electric dipole moment.
SZ	Sunyaev-Zeldovich effect	Inverse Compton scattering of CMB photons with hot electrons in clusters.
XL	Additional line emission	Molecular transitions in HCN, CN, HCO <sup>+</sup> , CS, similar to CO.

Table 4.7: Summary of tracer maps with explicit physical mechanism as provided by Planck (Planck Collaboration et al. 2016b) and WMAP (Bennett et al. 2013). The given acronyms are linked to Fig. 4.17.

Comparing the "physical" tracer maps to the "wavelength" tracer maps, it is evident that the maps for the specific processes fit in general worse than the best guesses

from Fig. 4.16. This is not surprising, as most of those maps are combinations of the 30 to 857 GHz maps, which also generally fit bad. The only map which is significantly improving the fit in both, the line and the o-Ps band, is the Planck "Xline" map. This map combines the contributions of line emission from different molecules. In particular, it shows significant emission from HCN at 88.6 GHz from the direction of circumnuclear disk and Sgr A\* (Takekawa et al. 2014). While this map might relate to the GCS found by the component-wise analysis, this might only occur by chance as *any* point-like emission from the direction of the galactic centre improves the fit in the 511 keV line.

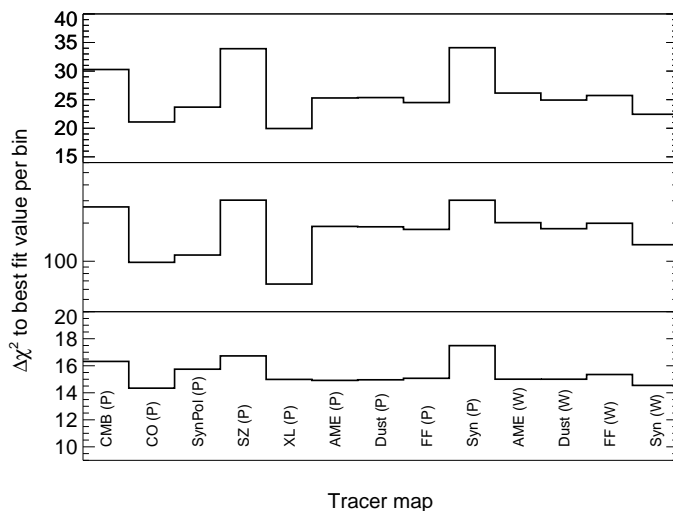


Figure 4.17: Likelihood ratio in different bands for maps with explicit physical mechanism. The chosen bands are equivalent to Fig. 4.16; maps are indicated by the acronyms as defined in Tab. 4.7. The letters in brackets refer to Planck (P) and WMAP (W) realisations. See text for details.

In summary, interpreting tracer maps towards the origin of galactic positrons remains questionable. It can, however, provide an estimate of the annihilation morphology, and tell where positrons predominantly annihilate. In addition, also the annihilation mechanism or conditions may be inferred, i.e. annihilation through intermediate Ps formation or not. If the fits are taken as blind candidates for the 511 keV morphology in space, a combination of hard X-ray emission (35-150 keV), infrared emission (1.25-4.9  $\mu\text{m}$ ), and point-like emission from the centre of the Galaxy, e.g. the "Xline" Planck map, would be sufficient to describe the dominating annihilation sites. But this heuristic approach should not be carried out too far, as the interpretation is not straightforward, and especially flukes and false arguments may lead to biased results.

## 4.6 Spectral Analysis

For each component of the component-wise celestial description with 2D Gaussians, a spectrum of sky emission is determined from the fits of intensity coefficients for each energy bin in the 40 keV wide range around the 511 keV line. These spectra are characterised in more detail by deriving the 511 keV line intensity ( $I_L$ ), the width, characterised as kinematic broadening ( $FWHM^{SKY}$ ), the centroid shift, interpreted as Doppler-shift from bulk motion ( $\Delta E_0 = E_{peak} - E_{lab}$ ), the o-Ps intensity ( $I_O$ ), and the Ps fraction ( $f_{Ps}$ ). The expected spectral components are represented by a

Gaussian 511 keV line, an o-Ps continuum (Ore & Powell 1949, see also Eq. (2.76)), and a power-law representing the diffuse Galactic gamma-ray continuum - each convolved with the SPI spectral response function plus the kinematic broadening, Eq. (3.19). Monte Carlo sampling is used to determine the uncertainties of the fitted spectral characteristics, parametrised through the 511 keV line centroid, width, and amplitude, the o-Ps amplitude at the measured line centroid, and the continuum flux-density at 511 keV. The power-law index for the diffuse Galactic continuum is fixed a priori to  $-1.7$  (Kinzer et al. 1999, 2001; Strong et al. 2005; Jean et al. 2006; Churazov et al. 2011; Bouchet et al. 2011). This is done because it is poorly determined in the used spectral band, and in any case has rather small impact on the annihilation component values ( $\lesssim 3\%$ ). Likewise, the power-law indices for the Crab and Cyg X-1 continua are set to the literature value for the Crab of  $-2.23$  (Jourdain & Roques 2009).

#### 4.6.1 The Bulge Component

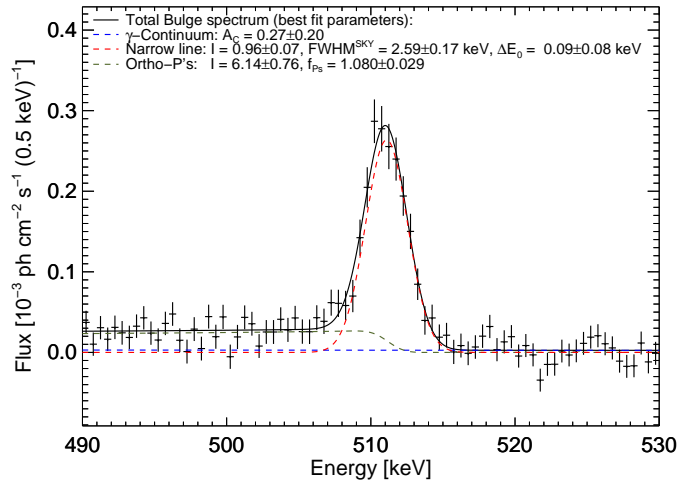


Figure 4.18: Spectrum of annihilation gamma-rays from the bulge (black crosses). The best fit spectrum is shown (continuous black line), as decomposed into a single 511 keV positron annihilation line (dashed red), the continuum from annihilation through ortho-positronium (dashed olive), and the diffuse gamma-ray continuum emission (dashed blue). Fitted and derived parameters are given in the legends. See text for details.

"The bulge" is defined as the superposition of the NB and BB component, because the central region of the Milky Way was shown to require two independent 2D Gaussian components whose intensities, however, strongly anti-correlate ( $-0.836$ ). The bulge shows a 511 keV line intensity of  $(0.96 \pm 0.07) \times 10^{-3} \text{ ph cm}^{-2} \text{ s}^{-1}$  and is detected with an overall significance of  $56\sigma$ . The bulge annihilation emission can be characterised by a 511 keV line of astrophysical width ( $2.59 \pm 0.17$ ) keV, and a Ps fraction of  $(1.080 \pm 0.029)$ , consistent with other studies (e.g. Jean et al. 2006; Churazov et al. 2011). The line peak appears at  $(511.09 \pm 0.08)$  keV. The diffuse Galactic gamma-ray continuum is a minor contribution in the bulge; its intensity is  $(0.27 \pm 0.20) \times 10^{-5} \text{ ph cm}^{-2} \text{ s}^{-1} \text{ keV}^{-1}$ . The spectral fit quality is found adequate from a  $\chi^2$  value of 66.47 with 74 degrees of freedom. Here, given the significant correlation between NB and BB, the propagation of uncertainties for each energy bin has to take the covariance between the two components into account when merging the bulge spectra:

$$\sigma_{Bulge,k} = \sqrt{\theta_{0,k}^2 \sigma_{0,k}^2 + \theta_{1,k}^2 \sigma_{1,k}^2 + 2\theta_{0,k}\theta_{1,k}\sigma_{01,k}} \quad (4.7)$$

In Eq. (4.7),  $\sigma_{Bulge,k}$  is the propagated uncertainty in energy bin  $k$ , as shown in Fig. 4.18,  $\sigma_{i,k}$  are the uncertainties for components  $i = 0$  (NB), and  $i = 1$  (BB), in energy bin  $k$  from the maximum-likelihood fit, Eqs. (3.12) and (3.14), and  $\sigma_{01,k}$  is the covariance between the NB and the BB for each energy bin. Neglecting the covariance term would overestimate the statistical uncertainties by about 250%.

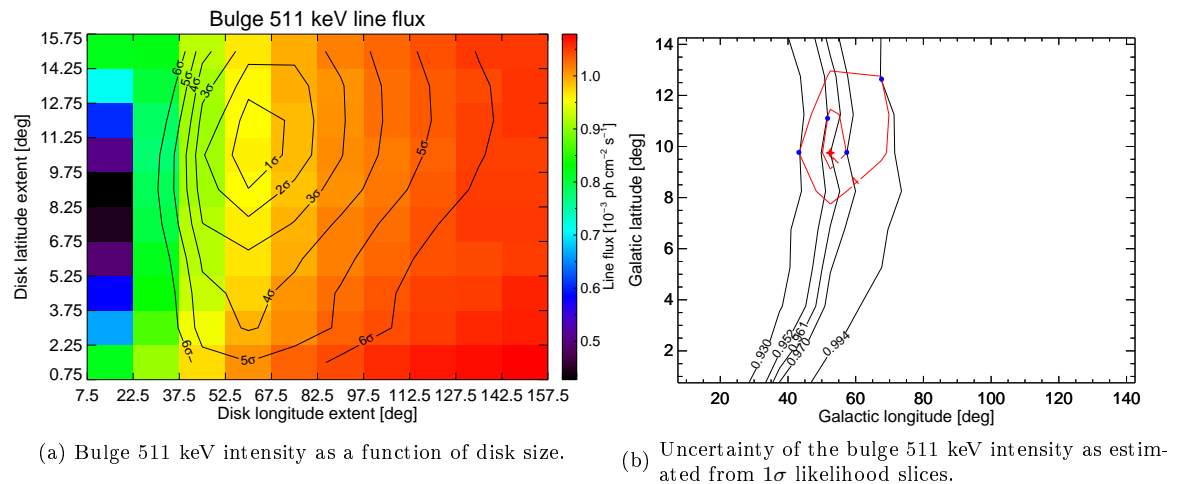


Figure 4.19: Dependence of the 511 keV line intensity in the bulge as a function of the choice of the disk extent ( $1\sigma$  Gaussian width value). Line intensities are shown as shading, see scale on right-hand axis. Overlaid are the uncertainty contours for the disk size, as derived from the maximum likelihood fits in the grid-scan (left panel). On the right panel, the uncertainty estimation procedure using likelihood slices in the disk size plane is shown. See text for details.

The size of the disk might have an influence on the intensities derived for the other sources. Its impact can be estimated by calculating the intersection of specific likelihood contours with the tangents of equal flux<sup>7</sup>. In Fig. 4.19, the dependence on the 511 keV line intensity in the bulge as a function of the disk extent is shown in the left panel, together with the procedure of how to estimate the uncertainty from that in the right panel. The star symbol is marking the point with the largest likelihood at  $0.961 \times 10^{-3} \text{ ph cm}^{-2} \text{ s}^{-1}$ . Lines of equal flux, touching the ( $2\Delta\mathcal{L} = 1$ )-, and ( $2\Delta\mathcal{L} = 4$ )-contours, respectively, are shown and marked by blue dots. These tangents correspond to the  $1$  and  $2\sigma$  uncertainties of the line flux in the bulge with respect to the disk size (longitude and latitude extent). The resulting  $1$  and  $2\sigma$ -uncertainties are  $(0.961 \pm 0.009) \times 10^{-3} \text{ ph cm}^{-2} \text{ s}^{-1}$ , and  $(0.961_{-0.031}^{+0.033}) \times 10^{-3} \text{ ph cm}^{-2} \text{ s}^{-1}$ , respectively. The uncertainty from the disk size influence can be compared to the "raw" statistical uncertainty from the measured counts. One realisation of the spectrum is shown in Fig. 4.18. It can be seen that the extent of the disk has a 1% effect on the estimate of the 511 keV line intensity of the bulge.

Other parameters of the bulge spectrum may also be influenced by the size of the disk. These are shown in Fig. 4.20. All other spectral parameters are hardly influenced by the chosen size of the disk, even within  $\approx 5\sigma$  uncertainty on the disk, with the exception of the gamma-ray continuum. In general, the spectral parameters

<sup>7</sup>This is not to be interpreted as "an error on an error" but rather the dependence on a particular - fitted or derived - value in another dimension, over which has to be marginalised to infer the correct uncertainty in the interesting parameter.

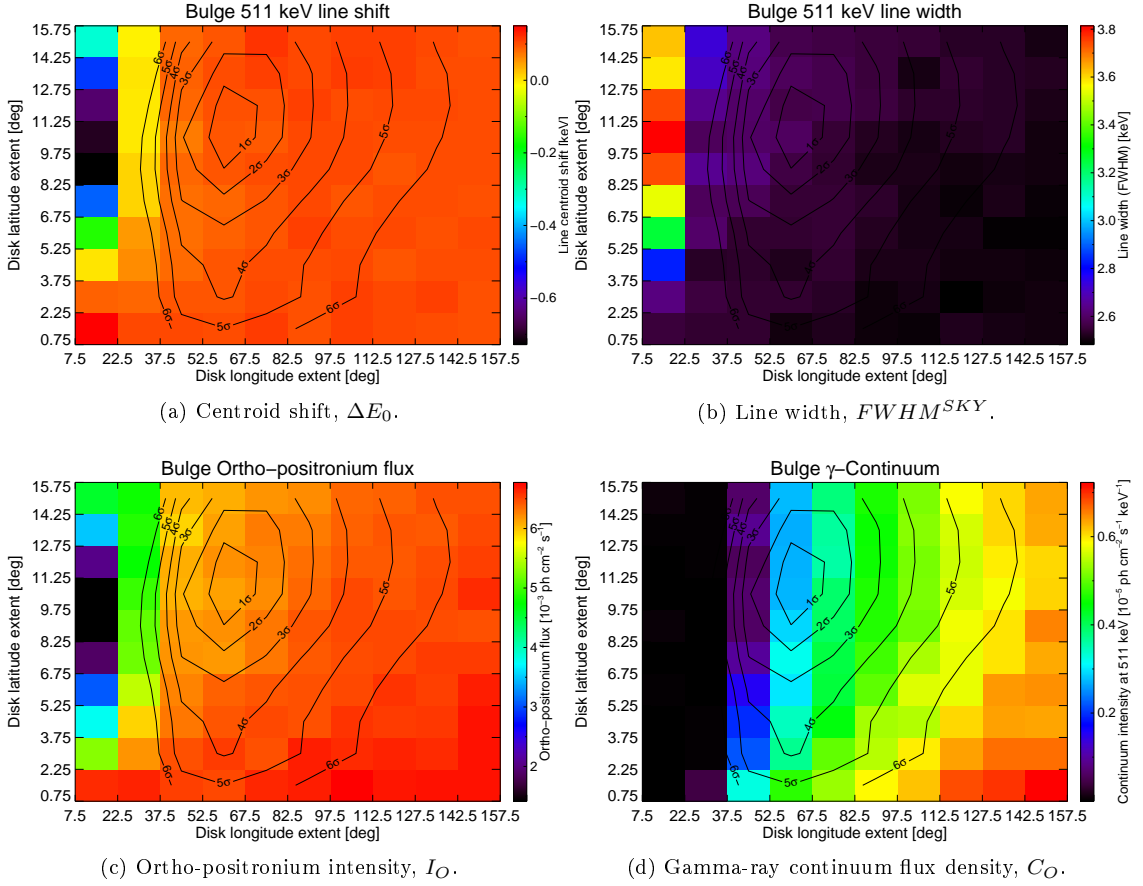


Figure 4.20: Dependence of spectral parameters of the bulge as a function of disk size. The notation is similar to Fig. 4.20. See text for details.

show a smooth dependence on the disk size. On the left-hand side of the panels in Fig. 4.20, i.e. when the disk is modelled with small longitude extents,  $\sigma_l^{disk} \lesssim 35^\circ$ , the maximum likelihood method cannot distinguish between the model components. Their overlap is large, and the increased degeneracy produces confusion also in the spectral domain. In the case of the galactic gamma-ray continuum, the overlap between bulge and disk increases the covariance in the continuum bins. For this reason, the continuum component in the bulge could be about twice as high. Especially the line shape parameters, i.e. centroid and width, are insensitive with respect to the disk extent.

#### 4.6.2 The Disk Component

The spectrum of the entire disk is shown in Fig. 4.21 for the best fitting disk model, with a longitude extent around  $60^\circ$  and a latitude extent around  $10.5^\circ$ . The 511 keV line intensity is  $(1.66 \pm 0.35) \times 10^{-3} \text{ ph cm}^{-2} \text{ s}^{-1}$ . The line width in the disk is  $(2.47 \pm 0.51) \text{ keV}$  (FWHM). This is in concordance with the bulge value. There might be systematic discrepancies between the spectral parameters of the single components, as discussed in Sec. 4.6.6. The 511 keV line shift,  $(0.16 \pm 0.18) \text{ keV}$ , is consistent with zero for the disk as an entity. The o-Ps continuum has an intensity of  $(5.21 \pm 3.25) \times 10^{-3} \text{ ph cm}^{-2} \text{ s}^{-1}$ , for which the Ps fraction obtains a value of  $(0.90 \pm 0.19)$ . The galactic gamma-ray continuum flux density amounts to  $(5.85 \pm$

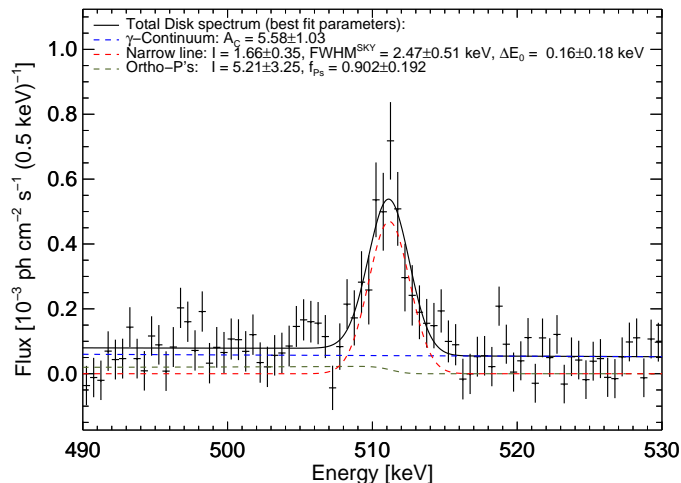


Figure 4.21: Spectrum of annihilation gamma-rays from the best fitting disk model (black crosses). The best fit spectrum is shown (continuous black line), as decomposed into a single 511 keV positron annihilation line (dashed red), the continuum from annihilation through ortho-positronium (dashed olive), and the diffuse gamma-ray continuum emission (dashed blue). Fitted and derived parameters are given in the legends. See text for details.

$1.05) \times 10^{-5} \text{ ph cm}^{-2} \text{ s}^{-1} \text{ keV}^{-1}$  at 511 keV. This value corresponds to  $(5.99 \pm 1.07) \times 10^{-6} \text{ ph cm}^{-2} \text{ s}^{-1} \text{ sr}^{-1} \text{ keV}^{-1}$  integrated across the full sky<sup>8</sup>, consistent with results by Strong et al. (2005) and Bouchet et al. (2011), for example<sup>9</sup>. The  $\chi^2$  value for the disk spectrum is 71.98 with 74 degrees of freedom, indicating a fully acceptable model to describing the data.

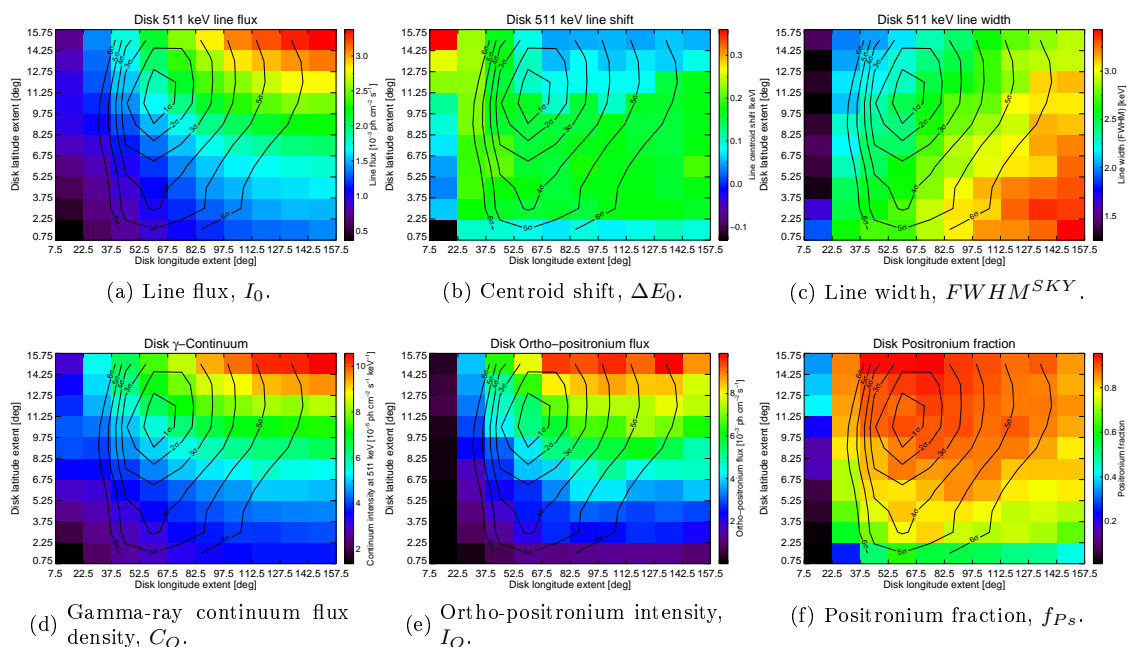


Figure 4.22: Dependence of spectral parameters of the disk as a function of disk size. The notation is similar to Fig. 4.20. See text for details.

The uncertainties of the derived spectral parameters are shown in Fig. 4.22, similar

<sup>8</sup>Here, the emission is truncated at 1% of the maximal surface brightness; along the galactic plane the intensity always is above that threshold and is therefore taken into account as  $2\pi$ ; towards higher latitudes, 99% of the emission are enclosed within  $\approx 70^\circ$ . Hence, the disk emission encloses a solid angle of  $3.11\pi$  sr. Note, that this value is therefore model and threshold dependent.

<sup>9</sup>Strong et al. (2005) and Bouchet et al. (2011) focused on a broader energy range and on the central part of the Milky Way.

to the bulge case. As expected from the nature of the fit, the spectral-shape parameters of the disk are the most varying ones. This results from the chosen shape to model the disk. At increasing disk size in longitude and latitude, the detection of low surface-brightness regions increases, and more line and continuum flux can be found. However, in the 80 bin spectral analysis, the longitude and latitude sizes are constrained very well, albeit biased by other parameters (e.g. bulge shape and number of components). This is evident by the  $1\sigma$  contours in the panels of Fig. 4.22, varying by 20% at most. The line shift is hardly influenced by the chosen disk size, whereas the line width could well be smaller, being formally consistent with the bulge value (see also further discussion of the line width below). The diffuse galactic gamma-ray and o-Ps continuum are difficult to disentangle in this energy band for the disk. Their general relative uncertainties, depending on the disk size, are of similar magnitude and shape. Likewise, the Ps fraction follows surprisingly the contours of the disk extent, being a function of the line intensity and o-Ps intensity only. Although this might be a coincidence, and over-interpretation of the shape of probability functions should be avoided, the value of the Ps fraction in the disk is always smaller than in the bulge, though formally consistent.

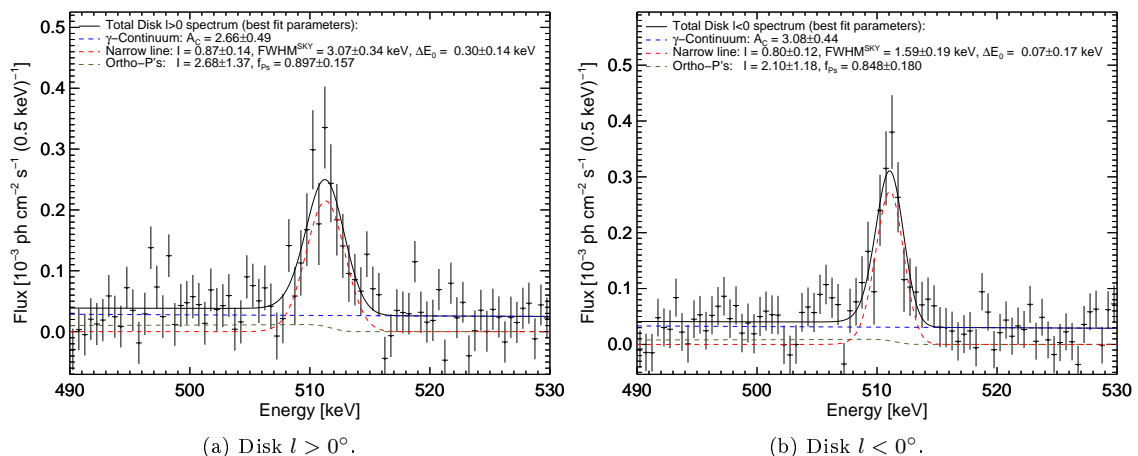


Figure 4.23: Spectrum of annihilation gamma rays from the eastern (a) and western (b) hemisphere of the Galaxy's disk. The fitted parameters are given in the legends, colours are the same as in Fig. 4.21. No flux asymmetry is found. See text for details.

The statistics from eleven years of data allow to derive spectral parameters separately for the eastern ( $l > 0^\circ$ ) and the western ( $l < 0^\circ$ ) hemisphere, see Fig. 4.23. Here, the Gaussian-shaped disk component is masked on alternate sides ( $l > 0^\circ$ , and  $l < 0^\circ$ ), which results in fitting now seven individual sky components. The  $\chi^2$  fit values are 83.79 and 68.42 for the  $l > 0^\circ$  and  $l < 0^\circ$  regions, respectively, with 74 degrees of freedom each. Although the value of 83.79 might indicate a bad fit for 74 degrees of freedom, it is still within the  $1\sigma$  tolerance band of the  $\chi^2$  statistics<sup>10</sup>. The 511 keV line intensities are  $(0.87 \pm 0.14) \times 10^{-3}$  ph  $\text{cm}^{-2}$   $\text{s}^{-1}$  for the ( $l > 0^\circ$ ) region, and  $(0.80 \pm 0.12) \times 10^{-3}$  ph  $\text{cm}^{-2}$   $\text{s}^{-1}$  for the ( $l < 0^\circ$ ) region. Thus, there is no disk asymmetry in the line fluxes, and the east-west ratio is  $1.09 \pm 0.24$ . This is in contrast to an earlier report by Weidenspointner et al. (2008a). The asymmetry is reduced, if not completely removed, as the narrow-bulge component is shifted away from the centre by about  $-1.25^\circ$  in longitude and  $-0.25^\circ$  in latitude (see also Skinner et al. 2014). The east/west ratio for the o-Ps continuum is  $(1.28 \pm 0.97)$ ,

<sup>10</sup>The expectation value of the  $\chi^2$  statistic equals the number of degrees of freedom, here  $\nu = 74$ . Since the probability distribution has a certain width (standard deviation; second moment) of  $\sqrt{2\nu} \approx 12.17$  the  $1\sigma$  tolerance band is  $74.00 \pm 12.17$  so that the value of 83.79 still represents an adequate fit quality.

and for the diffuse galactic gamma-ray continuum it is  $(0.86 \pm 0.20)$ . The western hemisphere of the disk shows a smaller line width (FWHM of  $(1.59 \pm 0.19)$  keV) than the eastern hemisphere ( $(3.07 \pm 0.34)$  keV). The two hemispheres have different spectra overall, with a statistical significance of  $2.8\sigma$ . Each of the two halves differ therefore from the combined disk spectrum by  $1.4\sigma$ .

In fact, the statistics in the central regions of the Galaxy allow to test for even more discriminations of emission regions. This leads to a measurement of the kinematical signatures in positron annihilation gamma-rays along the inner part of the Milky Way, and will be discussed in Sec. 4.7.3.

### 4.6.3 The Galactic Centre Source

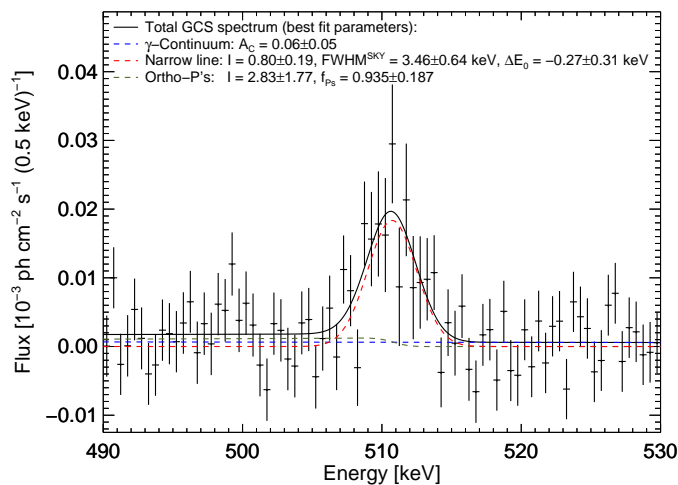


Figure 4.24: Spectrum of annihilation gamma rays from the point-like source (GCS) superimposed onto the extended bulge model in the Galaxy's centre. The fit and its components are indicated as above in Fig. 4.21.

The immediate vicinity in the direction of the centre of the Milky Way could be discriminated in Skinner et al. (2014) as a separate source. A point source at the position of Sgr A\* (the GCS) is detected with a significance of  $5\sigma$ . A first spectrum from the annihilation emission of this region is provided in Fig. 4.24. The 511 keV line intensity is  $(0.80 \pm 0.19) \times 10^{-4}$  ph cm $^{-2}$  s $^{-1}$ . Its annihilation emission is characterised by a broadened line with a width of  $(3.46 \pm 0.64)$  keV (FWHM above instrumental resolution), and a Ps fraction of  $(0.94 \pm 0.19)$ . This is still consistent within  $2\sigma$  uncertainties, compared to bulge and disk (total). There is a hint of an underlying broad continuum with a flux density estimate of  $(0.06 \pm 0.05) \times 10^{-5}$  ph cm $^{-2}$  s $^{-1}$  keV $^{-1}$ . There is no evident time variability down to scales of months. The annihilation line is centred at  $(510.73 \pm 0.31)$  keV if the spectrum is described by the above mentioned spectral model, indicating a red-shift. The o-Ps continuum is consistent with zero ( $< 2\sigma$ ), and assuming there is none leads to a smaller value for the line centroid of  $(510.59 \pm 0.35)$  keV. The fit quality as measured by  $\chi^2$  is 64.94 for 74 dof.

The influence of the disk extent on this component is hard to trace, as slight variations in the disk size may lead to strong effects in particular energy bins. As an example<sup>11</sup>, the GCS line flux is shown as a function of the disk size, similar to

<sup>11</sup> Additional figures concerning the other spectral parameters of the GCS with respect to the disk size can be found in Appendix A.

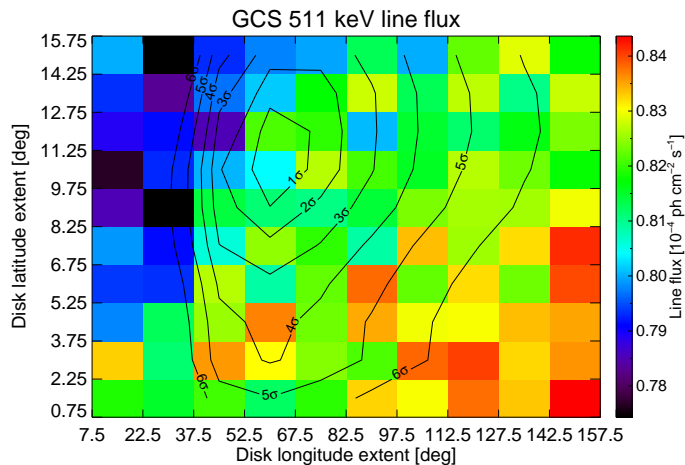


Figure 4.25: Dependence of GCS 511 keV line flux as a function of disk size. The notation is similar to Fig. 4.20. See text for details.

Fig. 4.25. Figure 4.25 shows the general trend of the GCS 511 keV line intensity, increasing from small disk axis ratios,  $\frac{a}{b}$ , (top left) towards higher disk axis ratios (bottom right). This is true for also the other parameters. However, the absolute magnitude of this effect is only of the order of 4% ( $< 3\sigma$ ).

#### 4.6.4 Continuum Sources

The Crab pulsar (Jourdain & Roques 2009) and Cygnus X-1 (Jourdain et al. 2012) are the only known Galactic sources strong enough to significantly influence the maximum likelihood analysis. They are thus included as constant point sources, i.e. not varying in time. The Crab is detected in the 40 keV energy band at  $31\sigma$  significance. The flux density found is  $(2.20 \pm 0.07) \times 10^{-5} \text{ ph cm}^{-2} \text{ s}^{-1} \text{ keV}^{-1}$  at 511 keV, sing a power-law with a fixed photon index of  $-2.23$  (Jourdain & Roques 2009). The flux in this energy band is consistent with the analysis across the full energy range of SPI (Jourdain & Roques 2009), though on the high side. This point source contribution is equivalent to about 40% of the total diffuse Galactic gamma-ray continuum emission.

Cygnus X-1 is also clearly detected at  $11\sigma$  significance. Its spectrum is described well by a single power-law spectrum with a (fixed) power-law index of  $-2.23$ , and a flux density of  $(0.65 \pm 0.06) \times 10^{-5} \text{ ph cm}^{-2} \text{ s}^{-1} \text{ keV}^{-1}$ . Cyg X-1 is known to be time variable, with a hard, a soft, and possibly an intermediate state (McConnell et al. 2002; Rodriguez et al. 2015b, see also Sec. 5.2). At 511 keV, the measured flux difference between the hard and the soft state is about  $1.5 \times 10^{-4} \text{ ph cm}^{-2} \text{ s}^{-1} \text{ keV}^{-1}$  (McConnell et al. 2002). The measured average of the different possible spectral states of Cyg X-1 are in good agreement with recent measurements of Rodriguez et al. (2015b). Cyg X-1 is only a weak source in the energy range around 511 keV, and included as a significant point source to optimise the maximum likelihood fit. No time variability has been tested.

The spectra of the Crab and Cyg X-1 are shown in Fig. 4.27. The chosen energy range is not enough to constrain the power-law index. The fitted values for the indices are  $(-1.41 \pm 1.52)$  for the Crab, and  $(-2.9 \pm 4.5)$  for Cyg X-1. These are

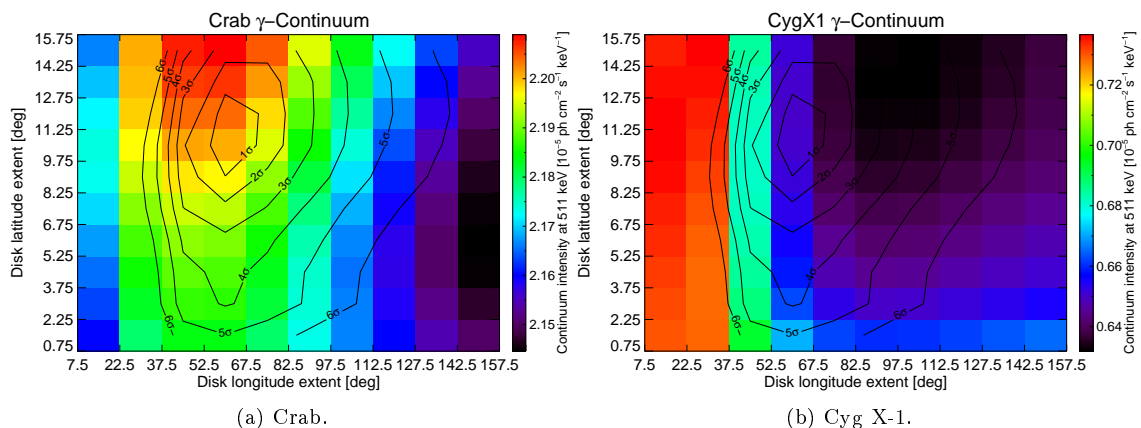


Figure 4.26: Dependence of the point source continuum fluxes as a function of disk size. Shown are the derived flux densities for the Crab (a) and Cyg X-1 (b) normalised to an energy of 511 keV. The notation is similar to Fig. 4.20. See text for details.

consistent with the literature values. The resulting flux values change by less than 0.3%, if the photon index is considered a free parameter. The correlations between the continuum sources and the other sky model components are negligible, except for the disk. The point source flux depends on the size of the disk emission model in either case, and more so for Cyg X-1. If the disk is chosen to be (unrealistically) short, the flux density of Cyg X-1 captures (erroneously) a part of this disk emission. The continuum flux densities of the two sources as a function of chosen disk size is shown in Fig. 4.26. The Crab flux does not show any strong correlations with the extent of the disk ( $< 2\%$ ).

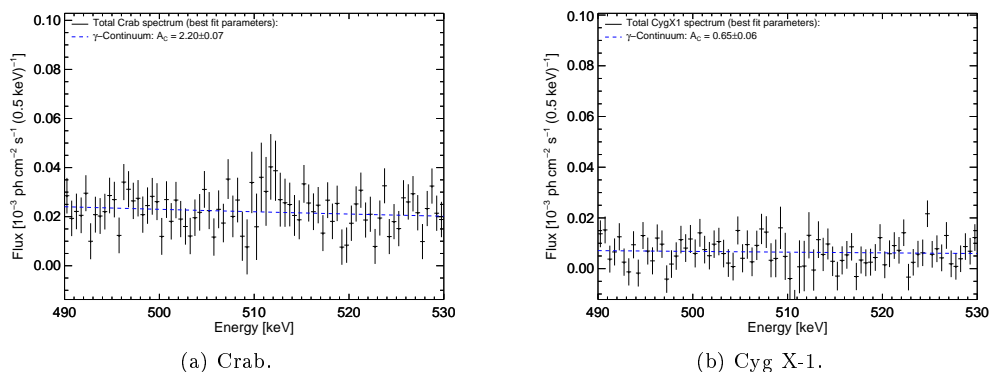


Figure 4.27: Spectrum of the Crab (a) and Cygnus X-1 (b) between 490 and 530 keV. The fitted parameters are given in the legends. There are no annihilation signals detected ( $< 2\sigma$ ). See text for details.

The Crab pulsar was historically identified to be an annihilation source but the measured signal was questionable (Agrinier et al. 1990; Massaro et al. 1991; Ulmer et al. 1994). Likewise, there is a high-energy "bump" measured for Cyg X-1 (McConnell et al. 2002) which either is due to positron annihilation or Comptonisation of the corona surrounding the black hole (see also Sec. 5.2 for more details on microquasars). There are no ( $< 2\sigma$ ) annihilation signals detected in these two point sources. Upper limits are given for both sources in Tab. 4.8, assuming either a "disk-like", i.e. narrow 511 keV line (1.6 keV FWHM), or a "GCS-like", i.e. broad 511 keV line (3.5 keV FWHM), respectively. Underlying broad erannihilation features ( $> 50$  keV FWHM) may still be compatible with the data.

	Narrow line	Broad line
Crab	6.62	7.44
Cyg X-1	1.27	1.89

Table 4.8: Upper limits ( $2\sigma$ , in units  $10^{-5}$  ph cm $^{-2}$  s $^{-1}$ ) for 511 keV gamma-ray line emission originating from the Crab or Cyg X-1. Limits for a narrow (1.6 keV FWHM), and a broad line (3.5 keV FWHM) are given.

#### 4.6.5 Additional Sources

A search for possible point-like annihilation emission in the satellite galaxies of the Milky Way was performed. This was done due to the hypothesis that light dark matter particles may also be a candidate source of positrons (Boehm et al. 2004; Gunion et al. 2006; Hooper et al. 2004; Picciotto & Pospelov 2005; Pospelov et al. 2008), and dwarf galaxies are believed to be dark matter dominated (e.g. Simon & Geha 2007; Strigari et al. 2008b). There was one  $3\sigma$  (six  $2\sigma$ ) sources among the 39 tested satellite galaxies. This finding and the implications for dark matter induced positrons will be thoroughly discussed in Sec. 5.5.

Taking the total Milky Way annihilation emission at a canonical distance of 8.5 kpc as a reference, the Andromeda galaxy (M31) should show a 511 keV line flux of the order  $10^{-7}$ - $10^{-6}$  ph cm $^{-2}$  s $^{-1}$  for its distance to the Sun of 783 kpc. Also a blue-shift of the order 0.5 keV is expected, as Andromeda is approaches the Milky Way at a velocity of 300 km s $^{-1}$ . The exposure around the position of M31 in this data set was  $\approx 400$  ks. It would, however, only be detectable with SPI when observing it for  $\approx 25$  Ms. Nevertheless, a search for point-like emission from the M31,  $(l/b) = (121.17/ - 21.57)^\circ$  (Evans et al. 2010) was performed, finding a  $2\sigma$  upper limit on the 511 keV flux of  $1 \times 10^{-4}$  ph cm $^{-2}$  s $^{-1}$ . M31 may be a prime target for future gamma-ray telescopes.

#### 4.6.6 Galactic Positron Annihilation Portrayal

The measured spectra at 0.5 keV binning in the 490-530 keV band around the 511 keV annihilation line allow a new look at Galactic positron annihilation, as separation among different components of bulge, disk, and central source has been achieved. A summary of the spectral parameters for all components included in the analysis is provided in Tab. 4.9. In addition, the results for a total, i.e. Galaxy-wide spectrum are listed. This may serve as a "conservative average" of positron annihilation throughout the Milky Way. The line and continuum intensities of the single components add up to the total Galaxy-wide intensities, as expected. The spectral parameters of the sky components are not too sensitive to the disk size, but the disk's spectral parameters are sensitive to the disk size itself. The cross correlations are almost negligible with respect to the flux uncertainties in each spectrum, and the fitted and derived parameters of each component are representative for the component itself.

The 511 keV line widths for the single components formally range from 1.59 keV to 3.46 keV, and are consistent with a mean value from the entire Galaxy, except for the eastern and western hemisphere of the disk (see above). The Doppler-shifts,  $\Delta E_0$ , are essentially consistent with zero within  $2\sigma$ . The Ps fractions are consistent

	Cont. flux dens.	Line Flux	FWHM	$\Delta E_0$	o-Ps Flux	Pos. frac.	$\chi^2/\text{d.o.f.}$
Bulge	0.27(20)	9.6(7)	2.59(17)	0.09(8)	61.4(7.6)	1.08(3)	66.47/74
Disk (total)	5.58(1.03)	16.6(3.5)	2.47(51)	0.16(18)	52.1(32.5)	0.90(19)	71.98/74
Disk ( $l > 0^\circ$ )	2.66(49)	8.7(1.4)	3.07(34)	0.30(14)	26.8(13.7)	0.90(16)	83.79/74
Disk ( $l < 0^\circ$ )	3.08(44)	8.0(1.2)	1.59(19)	0.07(17)	21.0(11.8)	0.85(18)	68.42/74
GCS	0.06(5)	0.8(2)	3.46(64)	-0.27(31)	2.8(1.8)	0.94(19)	64.94/74
Crab	2.20(7)	< 0.7	-(-)	-(-)	-(-)	-(-)	66.97/78
Cyg X-1	0.65(6)	< 0.2	-(-)	-(-)	-(-)	-(-)	73.38/78
Galaxy (total)	8.79(85)	27.4(3)	2.61(23)	0.15(9)	116.3(29.3)	0.99(7)	75.00/74

Table 4.9: Spectral parameters for each 511 keV sky model component and respective  $\chi^2$  fit values with degrees of freedom. Continuum flux densities are given as the value at 511 keV in units of  $10^{-5}$  ph cm $^{-2}$  s $^{-1}$  keV $^{-1}$ , line and ortho-positronium fluxes are given in  $10^{-4}$  ph cm $^{-2}$  s $^{-1}$ , FWHM of the celestial emission line in keV, the centroid shift  $\Delta E_0 = E_{peak} - E_{lab}$  in keV. The upper limits given for the line flux from the Crab and Cyg X-1 are  $2\sigma$  values and the corresponding  $\chi^2$  quoted are without fitting a line. One sigma uncertainties are given in brackets.

with 1.0 throughout the galaxy. The spectral fit quality is found adequate for all model components.

The differences of the derived spectra in their entireties is further investigated by comparing each spectrum with each other, and to the total spectrum of the Milky Way. Here, only the annihilation parts of the spectra are compared. The general question is how the best-fit spectrum of one component may be acceptable as a representation of data from another component. In detail, this is done by subtracting the best-fit power-law shaped gamma-continuum contribution,  $C(E)$ . The spectral model with the best-fit parameters ( $I_L$ ,  $I_O$ ,  $E_0$ ,  $\sigma$ ) of one spectrum is then fixed as a template spectrum, and fitted with only one global amplitude to all other spectra, separately. This leads to dof difference of 3. In Tab. 4.10, the significance in units of  $\sigma$  is shown, as calculated by a  $\chi^2$ -test with 3 dof. The table reads as follows: Line by line, the spectra (data points per energy bin) of the sky components are fitted by the templated spectrum (smooth function) of the other spectra (columns).

Sig. [ $\sigma$ ]	GCS	Bulge	Disk ( $l > 0$ )	Disk ( $l < 0$ )	Galaxy
GCS	0.0	0.6	1.0	1.5	0.8
Bulge	4.9	0.0	5.1	6.1	2.9
Disk ( $l > 0^\circ$ )	1.8	1.0	0.0	1.1	0.2
Disk ( $l < 0^\circ$ )	2.0	1.4	1.1	0.0	0.5
Galaxy	3.5	1.6	1.2	2.0	0.0

Table 4.10: Spectral model comparisons of the celestial components, GCS, Bulge, eastern and western hemisphere of the Disk, and the total/combined Milky Way (incorporating all correlations among different components, i.e. a mixture of all models). The probability values are given in units of  $\sigma$ , reflecting the tension of one templated best-fit spectrum being representative for another spectrum, or the combined Milky Way spectrum.

The spectrum for the GCS can easily be represented by the spectral shapes of the bulge ( $0.6\sigma$ ) and the two disk hemispheres ( $1.0\sigma$ ,  $1.5\sigma$ ). The opposite case is statistically discouraged ( $4.9\sigma$  bulge,  $1.8\sigma$  and  $2.0\sigma$  disk). The spectrum of the bulge cannot be represented by the spectrum of the disk ( $5.1\sigma$ ,  $6.1\sigma$ ), conversely, the disk spectrum can be represented by the bulge spectrum ( $1.0\sigma$  and  $1.4\sigma$ ). The two disk hemispheres are identical within  $1.1\sigma$ . The spectra, however, only differ in the widths of the spectral line and not in the centroid or o-Ps flux. If only the 511 keV line parameters are compared, the significance of a difference is actually higher ( $2.8\sigma$ ). The Galaxy as a whole cannot be represented by only the best-fit spectrum of the GCS ( $3.5\sigma$ ). For the bulge, and the two disk hemispheres, the tension is not as strong ( $1.6\sigma$  bulge,  $1.2\sigma$  and  $2.0\sigma$  disk). Summarising the spectral comparison in a different way: All individual spectral components can be

represented by the mixed Milky Way template spectrum, except for the bulge, where a  $2.9\sigma$  discrepancy appears significant.

### Annihilation Conditions in the Interstellar Medium

In view of the uncertainties, above results imply that the annihilation of positrons in the Milky Way looks the same in any place. This seems surprising, as the internal structures of the bulge and the disk, and especially the galactic nucleus, are different. Naturally, one would expect different line shapes, widths, Ps fractions, etc., from different annihilation sites as discussed in Sec. 2.4.3.4, considering the density, ionisation fraction and temperature of the ISM. From the above hints of spectral diversity, it is henceforth assumed that the annihilation conditions in the different components may be different. This can then provide new insights to how positrons propagate in the Milky Way, away from their sources towards annihilation at an unknown point in space and time.

The Ps fraction,  $f_{Ps}$ , is a prime diagnostic of annihilation conditions, Eq. (2.102).  $f_{Ps}$  is only a weak function of the 511 keV line intensity  $I_L$ , and the o-Ps continuum intensity  $I_O$ . Formation of a Ps atom is only efficient below energies of  $\sim 100$  eV and is facilitated in a partially neutral medium through charge exchange reactions with atoms and molecules, see Sec. 2.8. In particular, the ionisation state, temperature, and composition (H, He, gas/dust) influences the value of the Ps fraction. Using, for example, the model by Churazov et al. (2005), the measured Ps fraction in combination with the line width can be converted to the parameters of the ISM in which the annihilation took place. In Fig. 4.28, the different spectral parameters are superimposed on the Churazov et al. (2005) model, showing the uncertainties as shaded areas.

The measured Ps fractions and line widths in the bulge and in the disk as a whole are 1.0 and 2.59 keV, and 0.90 and 2.47, respectively. Comparing the eastern and western hemisphere of the disk separately, values of 0.90 and 3.07 keV, and 0.85 and 1.59 keV, respectively, are found. The GCS formally shows a Ps fraction of 0.94 with a line width of 3.46 keV. There is a tendency from inside the Galaxy outwards for a decreasing line width. The Ps fraction is largest in the bulge and has lower values in the very centre, and in the disk. Note that the choice of energy region (490 to 530 keV) may result in a bias towards high o-Ps fluxes, and thus large Ps fractions; however, the bias is the same for all spectra, so that the tendency for lower Ps fractions in the disk still applies, though with probably lower values. Based on  $f_{Ps}$  and the line width, and ignoring internal large scale motion (e.g. rotation) of the Milky Way, many different the annihilation conditions are possible concerning the spectral data, i.e. ISM phases in which the positrons annihilate.

The bulge region may be regarded as an annihilation site with a temperature between  $\approx 7700$  and  $10000$  K, and an ionisation fraction between 4 and 7%. The annihilation conditions of the Galaxy as a whole fall into the same region in that plot than the bulge. This suggests similar conditions, though in principle, also low temperature regions ( $< 300$  K) would be possible. This ambiguity is not new: Churazov et al. (2011) showed that the bulge spectrum may also favour the cold ISM phase. However, they ignored the fact that the statistical significance of favouring the low over

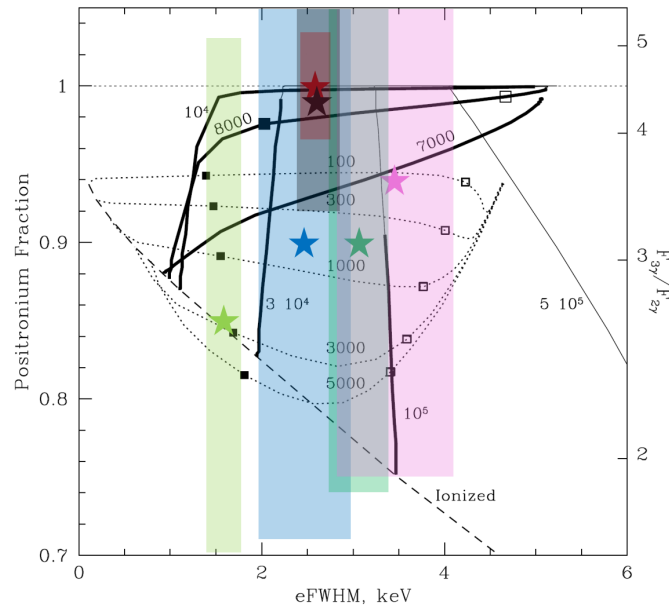


Figure 4.28: Annihilation conditions in different regions of the Milky Way. The underlying model is the same as Fig. 2.20. The star symbols mark the combinations of measured FWHM and positronium fraction for each component in the celestial emission model. The colours correspond to bulge (red), disk total (blue), disk west (green), disk east (light green), GCS (magenta), and Milky Way total (black). The value for the bulge measurement is set to the maximum physical value of 1.0. Shaded areas in the same colours represent the  $1\sigma$  measurement uncertain box. See text for detail.

the high temperature case was  $2.5\sigma$ , and overrode that due to background issues, and chose the high temperature case, rather arbitrarily. The disk as a whole entirely overlaps with the bulge measurements in its uncertainty box, although the total, as well as the two disk hemispheres, show quite different values, and therefore quite different annihilation conditions are possible. In particular, the western and eastern hemisphere have no overlap with the bulge, suggesting different phases of the ISM in disk and bulge for the positrons to annihilate. Indeed, the model allows the two disk hemispheres to share similar temperature values like in the bulge, but probably at different ionisation fractions, even allowing for annihilation in a completely ionised medium. This may be interpreted in at least two ways:

Either, the two regions indeed show different annihilation conditions. This would be surprising, as it would intuitively violate the naturalness of the Galaxy, and suggest a preference or uniqueness of a particular view. On the other hand, the apparent differences may simply be caused by line of sight integration effects of the whole eastern and western hemisphere. In fact, the  $l > 0$  region of the Milky Way is occulted by large dust clouds (cf. Fig. A.5a), for which the annihilation line shape is different, and unique across the temperature scale (Guessoum et al. 2005). The line width from Ps formation in dust grains contains two cases. Either the Ps formed in the grain leaves the dust particle for which the line width of the subsequent annihilation gamma-rays is around 1.4 keV (FWHM), or if the annihilation takes place inside the grain, the line width is estimated to be 2 keV. In fact, there are also lower values possible for the p-Ps annihilation line width, as measured in laboratory experiments (Biasini et al. 2000; Sasaki et al. 2003), and also higher values from annihilation in molecules (Iwata et al. 1997). The adopted value of 2.0 keV is a compromise between the higher value of the direct grain measurements and the lower value of the molecule measurements (Guessoum et al. 2005). The SPI instrument measures a superposition of annihilation gamma-rays from a particular line of sight,

and source intensities are weighted with the distances squared to the position where the annihilation took place. So, one or the other hemisphere may be more or less influenced by specific annihilation conditions, for example due to annihilation on dust grains.

It would be naive to assume that positrons choose a particular phase to annihilate: Each phase should contribute, weighted by the probability of annihilation therein, and the positron density. The measured line width is a superposition of many annihilation regions in the Galaxy. A single value of the line width and the Ps fraction is therefore not a too superior determinant of "the annihilation conditions". The instrumental resolution of gamma-ray detectors is sufficient to distinguish between several components. So, if the measurement uncertainties could be reduced to a level at which the statistical uncertainties only play a minor role, the full theoretical spectrum of a given ISM phase - and their superpositions - as given in Eq. (4.8) (e.g. Guessoum et al. 2005) could be disentangled.

$$\begin{aligned}
S(E) = \int dE & \left[ 3\frac{3}{4}F_{oPs}(E) + 2\frac{1}{4}\delta(E - E_0) \right] \{ X f_{PsF,H/H_2} G(E; E_0, \Gamma_{AiF,H/H_2}) + \\
& + Y f_{PsF,He} G(E; E_0, \Gamma_{PsF,He}) + (1 - X f_{PsF,H/H_2} - Y f_{PsF,He}) \times \\
& \times [ f_{CE,H/H_2} G(E; E_0, \Gamma_{CE,H/H_2}) + f_{CE,He} G(E; E_0, \Gamma_{CE,He}) + \\
& + f_{RR} G(E; E_0, \Gamma_{RR}) + f_{Gr,out} G(E; E_0, \Gamma_{Gr,out}) ] \} + \\
& + 2(1 - X f_{PsF,H/H_2} - Y f_{PsF,He}) [ f_{DA,e} G(E; E_0, \Gamma_{DA,e}) + \\
& + f_{DA,H/H_2} G(E; E_0, \Gamma_{DA,H/H_2}) + f_{DA,He} G(E; E_0, \Gamma_{DA,He}) + \\
& + f_{Gr,in} G(E; E_0, \Gamma_{Gr,in}) ] \tag{4.8}
\end{aligned}$$

In Eq. (4.8), the  $f_i$  denote the fractions of positrons undergoing a particular processes (probability) in an arbitrarily composed ISM of relative atomic/molecular hydrogen ( $X$ ) and helium ( $Y$ ) abundances. The indices are  $PsF$  for Ps formation in flight,  $CE$  for charge exchange,  $RR$  for radiative recombination with free electrons,  $Gr, in/out$  for Ps annihilating inside or outside a dust grain, and  $DA$  for direct annihilation (annihilation in flight) with free or bound electrons. The functions  $G(E; E_0, \Gamma_i)$  represent Gaussians as a function of photon energy  $E$ , line centroid  $E_0$ , and FWHM  $\Gamma_i$  for each process.  $F_{oPs}(E)$  is the shape of the o-Ps continuum, Eq. (2.76). The Lorentzian shape of the p-Ps annihilation line width has been approximated by a  $\delta$ -function.

The spectrum of the GCS yields annihilation conditions which are dissimilar to that of the bulge and the disk. Formally, the line width would suggest annihilation in a less ionised medium, compared to bulge and disk. But as the o-Ps continuum is only weakly detected, the Ps fraction is poorly constrained. In particular, the GCS spectrum is the only one where overlaps with regions of high temperatures ( $\gtrsim 10^5$ K) occur. This is naturally expected from thermal broadening of the line. Alternatively, this broadening provides a measure of the turbulence. The value of  $(2000 \pm 400)$  km s $^{-1}$  might reasonably be expected from non-equilibrium gas motion or past AGN activity in the centre of the Galaxy. Considering the imaging resolution of SPI ( $\sim 2.7^\circ$ ), the annihilate region could be compact, and may be related to the Galaxy's supermassive black hole Sgr A\*. Otherwise, the SPI point-spread-function

encompasses a physical region of the order of 350 pc at a distance of 8.5 kpc, which is reminiscent of the entire central molecular zone. Alexis et al. (2014) discussed the possibility that nucleosynthesis positrons produced in the central molecular zone travel into the galactic bulge, and could be responsible for the emission in the extended bulge. It is, however, not implausible that these positrons annihilate already locally there.

The supermassive black hole in the centre of the Milky Way with a mass of  $(4.31 \pm 0.38) \times 10^6 M_{\odot}$  (Gillessen et al. 2009), and its associated accretion disk extending up to 100 AU (Genzel et al. 2010, and references therein) have been discussed as positron sources (Totani et al. 2006; Cheng et al. 2006). Positrons can be produced in the vicinity of the supermassive black hole, from pair-production in the accretion disk, or in the hot corona above, or from the resulting jets (Beloborodov 1999a; Totani et al. 2006; Chernyshov et al. 2009). If Sgr A\* is assumed as the source of the positrons, a gravitational red-shift of at least 0.4 keV, and a temperature of  $\sim 10^3$  K (Shakura & Sunyaev 1973; Krolik 1999) is expected. These values are within the uncertainty limits of the measurement, see Tab. 4.9; see also Secs. 5.2, 5.2.2, 5.5, and 5.6 for further discussion.

### **Annihilation in the Interstellar Medium?**

The elementary assumption that positrons annihilate in the different phases of the ISM may be questioned. The measurements suggest a partially ionised medium, either in a cold environment ( $< 300$  K), which would point to the cold neutral (molecular clouds) phase of the ISM, or in a warm environment with a temperature around 8000 K, pointing to the warm neutral and warm ionised component of the ISM (see Tab. 2.4). The former would imply a positron number density of the order  $10^2$  to  $10^6$   $\text{cm}^{-3}$ , the latter a density between  $10^{-1}$  and  $10^0$   $\text{cm}^{-3}$ .

The required parameters of 8000 K, and being partially ionised do not only apply to the ISM, but also to stellar atmospheres. Here, the density may be as high as  $10^{10}$  to  $10^{14}$   $\text{cm}^{-3}$  above the photosphere of a star. In fact, it could well be possible that the entire 511 keV emission of the Galaxy originates from positron annihilation in stellar atmospheres only. If the annihilation rate of  $\sim 5 \times 10^{43}$   $\text{e}^+ \text{s}^{-1}$  in the Milky Way, at the galactic-centre distance of 8 kpc, is scaled to the distance of the Sun as one star, an annihilation rate of  $\sim 2 \times 10^{25}$   $\text{e}^+ \text{s}^{-1}$  would be required. It is known since the 1960s that interstellar positrons can enter the solar system, from measurements of cosmic-ray positrons with magnetic spectrometers above Earth's atmosphere (de Shong et al. 1964). Recently refined measurements with the Payload for Antimatter Matter Exploration and Light-nuclei Astrophysics satellite (Adriani et al. 2013) and the Alpha Magnetic Spectrometer aboard the International Space Station (Aguilar et al. 2013) provided high-precision positron energy spectra between 500 MeV and 300 GeV, i.e. highly relativistic positrons. These measurements identified an excess of high-energy positrons with respect to pure secondary production (Adriani et al. 2009). This is generally interpreted as evidence for a re-acceleration mechanism of cosmic-ray positrons. High-energy positrons obviously are captured and trapped in the magnetic field of Earth (Mikhailov et al. 2016), and can consequently also be captured, trapped, and maybe decelerated by the Sun. The number of high-energy

positrons seen by these experiments ( $\sim 2.5 \times 10^{-4} \text{ e}^+ \text{ s}^{-1}$  at Earth  $\Leftrightarrow \sim 2.5 \text{ e}^+ \text{ s}^{-1}$  at the Sun, scaled with geometrical cross section only), is, however, not sufficient to explain the required annihilation rate. But since the experiments are not sensitive to positrons already slowed down, and since they are restricted to Earth, the meaning of this number is rather uncertain. Typical solar flare events as measured with the Reuven Ramaty High Energy Solar Spectroscopic Imager produce annihilation gamma-rays from positrons of the order  $0.1 - 1.0 \text{ ph cm}^{-2} \text{ s}^{-1}$  (Share et al. 2004), and with varying line widths, changing from broad (4-8 keV FWHM) lines at the onset of the flare to narrow (1-2 keV) lines in the decline phase. This flux would convert to an annihilation rate of  $10^{25}$ - $10^{26} \text{ e}^+ \text{ s}^{-1}$  at the distance of the Sun. If the solar flare annihilation flux, and also if the cosmic-ray positron capture rate was scaling with the magnetic field strength of a star, the galactic positron annihilation rate could easily be met by stellar considerations only. In addition, this would already explain the morphology towards a thick and smooth stellar disk. In fact, Bisnovatyi-Kogan & Pozanenko (2016) estimated that the total number of G, K, and M dwarves in the Milky Way bulge ( $\sim 6 \times 10^{10}$ ) would explain about 1/3 of the annihilating positrons with only stellar flare events.

The most uncertain ingredient for the discussion of the positron annihilation in space, however, is the propagation from the sources to the sites where they annihilate with electrons. In a low density medium, for example, with a particle content of  $0.1 \text{ cm}^{-3}$ , the energy loss (Fig. 2.16) due to ionisation and Coulomb interactions of positrons, originally starting at MeV energies from  $\beta^+$ -decay for example, is as low as  $10^{-7} \text{ eV s}^{-1}$ . It may take several millions of years to slow down the positrons. But if it is possible for stars to capture positrons on their way through the Galaxy, these can lose their kinetic energy significantly faster in a stellar atmosphere, as the particle densities are many orders of magnitude larger than in the ISM. Only a few particle interactions are sufficient to slow the positrons down to create Ps by charge exchange in the photosphere of a star - not violating any measurement constraint.

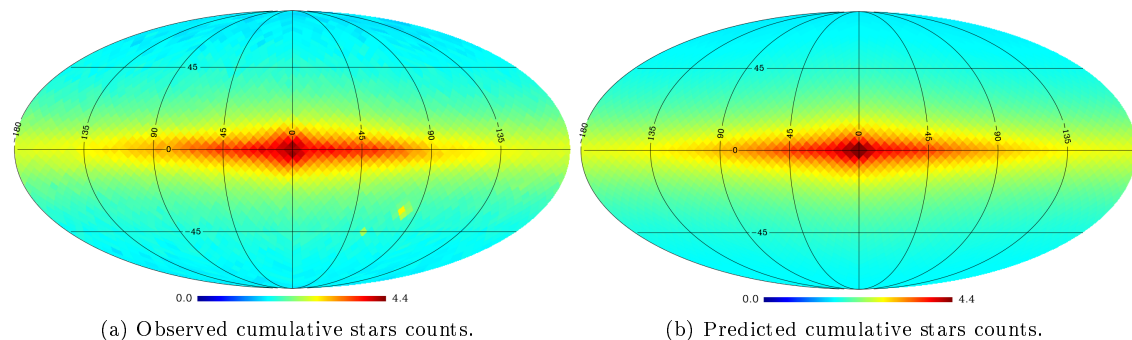


Figure 4.29: Star count map from the 2MASS survey. Panel (a) shows the integrated star counts in the 2MASS  $K_S$  band in logarithmic scaling and panel (b) the corresponding model by Polido et al. (2013). See text for details.

Annihilation in stellar atmospheres would naturally explain the smoothness and extent of the measured morphology of galactic annihilation gamma-ray emission. The 2MASS survey, for example, shows the integrated number of stars, radiating in three different wavelength band between  $1.07$  and  $1.40 \mu\text{m}$ ,  $1.41$  and  $1.91 \mu\text{m}$ , and  $1.90$  and  $2.42 \mu\text{m}$ , respectively (2MASS  $J$ ,  $H$ , and  $K_S$  bands (Carpenter 2001)). The 2MASS survey covers 99.8% of the near infrared sky with over 470 million point sources in those three bands (Cutri et al. 2003; Skrutskie et al. 2006). Polido

et al. (2013) used the "star count" method (Binney & Merrifield 1998, Eq. (4.9)) to investigate the Milky Way structure based on stellar statistics. Figure 4.29 shows the distribution of stars in the  $K_S$  band, and the corresponding model of Polido et al. (2013).

$$N_s(m_1, m_2, l, b)d\Omega = \int_{m_1}^{m_2} dm \int_0^{+\infty} dr r^2 \rho_s(r, M) \phi_s(M) dr d\Omega. \quad (4.9)$$

In Eq. (4.9),  $N_s$  is the number of stars of type  $s$  with apparent magnitude between  $m_1$  and  $m_2$  in a solid angle  $d\Omega$  around galactic longitudes  $l$  and latitudes  $b$ ;  $r$  is the distance of the objects to the Sun, as parametrised by the stellar density  $\rho_s$ , and the luminosity function  $\phi_s$ , which is number of stars per cubic parsec near the Sun with magnitudes in the range  $(M, M + dM)$ . Their parametrised model is compared to point objects with limiting apparent magnitudes of 15.8, 15.1, and 14.3 for the  $J$ ,  $H$ , and  $K_S$  band, respectively, depending on the line-of-sight, and source separation capability. The model consists of a thin and a thick disk, which are parametrised through their scale radii and scale heights. Central holes in both disks give way for the bulge region, consisting of a spheroid of certain radius, and a bar with specified length and orientation. In addition, the model includes a representation of the galactic spiral arms, with four logarithmic spirals, confined between 2 and 15 kpc (Polido et al. 2013). They did not model the LMC, SMC, or any other accumulation of stars, and also ignored O and B type stars.

The line-of-sight-integrated star counts, as a function of galactic longitude and latitude, are remarkably similar to the morphology of the 511 keV sky. A representation of the bulge as a combination of central spheroid plus bar component is close to the component-wise representation of the 511 keV sky with one central, narrow but offset 2D Gaussian, and a broader 2D Gaussian. The combination of the two empirical 2D model components reveals an offset in longitude in the 511 keV map of  $\approx 1^\circ$ ; the combination of a central spheroid with radius  $400 \pm 100$  pc, and a bar with a length of  $1250_{-250}^{+500}$  pc rotated  $12_{-1}^{+15}$  deg, yields an offset between  $0.1^\circ$  and  $0.9^\circ$ . In addition, the central spheric hole, which they included as a distinction between the bulge and the disk, is found with a radial size of  $2070_{-800}^{+2000}$  pc. This, converted to an angular scale, yields  $8.5^\circ$ - $25.6^\circ$  which is exactly the scale between the narrow and the broad bulge component of the 511 keV sky. The spirals arms are not very intense (low contrast) in the final model, similar to the 511 keV map. In the latter case, the spirals may be there, but are not detected with current exposure, probably being low contrast structures in the annihilation sky. The scale heights as measured from star counts are  $205 \pm 40$  pc and  $640 \pm 70$  pc for the thin and thick disk, respectively. From the 511 keV map in Fig. 4.10, scale height values between 500 and 2000 pc can be estimated. Note that estimating the 3D scale height from a 2D representation of the morphology includes systematic uncertainties<sup>12</sup>; note also that previous scale height measurements found values as high as 1600 pc (Reid & Majewski 1993). In any case, the positron annihilation morphology points to annihilation sites which are widespread in galactic height, and plausible candidates are stars as they are distributed up to very large heights, for example in the halo. However, the warm ionised

<sup>12</sup>The 511 keV scale height from the empirical 2D Gaussian disk model is geometrically estimated as  $h_{511} = d_{eff} \tan(\sigma_b)$ , where  $d_{eff}$  is the effective distance to "the disk" in all directions, and  $\sigma_b = 10.5^\circ \pm 1.5^\circ$  is the measured latitudinal extent of the disk. The effective distance is the weighted average of emission regions along all line of sights and is estimated to range between 3 and 12 kpc.

	Velocity spread	Bulk motion
The Bulge	1500(100)	53(47)
Disk (total)	1450(300)	94(106)
Disk $l > 0^\circ$	1800(200)	176(82)
Disk $l < 0^\circ$	950(100)	41(100)
GCS	2050(400)	-159(182)
Galaxy (total)	1550(150)	88(53)

Table 4.11: Doppler-velocity diagnostics of the main celestial emission model components. The values are quoted in units of  $\text{km s}^{-1}$ . One sigma uncertainties are given in brackets.

and the hot ionised phase of the ISM also have scale heights around 1000-3000 pc, so that distinguishing between the true annihilation sites has to be based on more parameters than only the scale height. In fact, the stars measured by the 2MASS survey are predominantly main sequence M class stars, and the positron flux which may come from those stars may not naturally correlate with the number of those stars. It may also be connected with the number of K and M class red giants, having more extended atmospheres and larger magnetic fields (Stello et al. 2016), and thus a probably larger geometrical positron capture cross section.

Further evidence for the scenario of stellar annihilation is provided by investigating astrophysical tracer maps. This is discussed in detail in Sec. 4.5. The 1.25 to 4.9 micron maps show predominantly these K to M class stars red giants, and significantly improve the fit to the 511 keV data over the background, though are still worse than the empirical model. In fact, those maps improve the fit in the line and not only in the continuum, pointing to a correlation of positron annihilation and the distribution of stars in the Galaxy. Also the kinematics of the inner Galaxy in 511 keV annihilation radiation, Sec. 4.7.3, shows a peculiar longitude-velocity profile which is similar to that of stars in the galactic bulge regions (Kunder et al. 2016), supporting the stellar atmosphere annihilation scenario even more.

### Morphology Diagnostics

A second order diagnostics of annihilation conditions is the width in combination with the centroid of the 511 keV annihilation line, as it can probe both, the kinematics of the positron population and the gas<sup>13</sup> dynamics. The velocity spread and bulk motion in the different parts of the Galaxy can be derived, ignoring the contribution to the line shape due to the local annihilation conditions. The parameters of the annihilation line for the different components are shown in Tab. 4.11 as converted to velocities.

For the two disk hemispheres, a velocity spread of  $(950 \pm 100) \text{ km s}^{-1}$  and  $(1800 \pm 200) \text{ km s}^{-1}$ , respectively, is found. This apparent difference in the line width in the two disk hemispheres can be interpreted in several ways, depending on the relative contributions of kinematic and thermal broadening. The contribution from Galactic kinematics is probably small, as the estimated velocity dispersion from interstellar gas is  $\sim 100 \text{ km s}^{-1}$  (Dame et al. 2001), or up to  $300 \text{ km s}^{-1}$  if the positrons originate in the  $\beta^+$ -decay of  $^{26}\text{Al}$  in the disk (Kretschmer et al. 2013). As before,

<sup>13</sup>Here, gas means the gas in which the positrons annihilate, be it in the interstellar medium or stellar atmospheres or both.

by performing line-of-sight integration over a whole hemisphere, peculiar sampling of different annihilation regions might influence the result. But then it would be surprising to observe the same flux. In general, it is not known how much of the line width is due to kinematics and how much is due to the annihilation conditions. The intrinsic velocity of "positrons annihilating with gas" may indeed be as high as  $1000 \text{ km s}^{-1}$  at the outskirts of the broad bulge component towards the disk. So, the fraction of the line width, attributed to Doppler shifts and broadenings, may be larger than expected, pointing possibly towards a more ionised gas component.

Connecting the individual-component line shapes with the morphology (extent) of the 511 keV emission will provide more insights to the annihilation sites, and may allow to trace back where the positrons originated. The bulge-to-disk (B/D) luminosity ratio was used historically to determine which sources may be responsible for the positrons leading to the annihilation emission. The measured B/D flux ratio is  $0.58 \pm 0.13$ , smaller than in previous studies (Knödlseeder et al. 2005; Weidenspointner et al. 2008b; Bouchet et al. 2010), although formally consistent, see Fig. 4.30. The annihilation luminosity for each component  $i$  is defined as the 511 keV line fluxes at effective distances to the annihilation site,  $L_{511}^i = 4\pi d_{eff}^{i,2} I_L^i$ . Based on effective distances<sup>14</sup> to the bulge of 8.5 kpc, and to the disk of 10.0 kpc, the (model-dependent) luminosity B/D ratio is  $0.42 \pm 0.09$ . This small value is probably due to the fact that the disk is now seen with a much larger extent than before, and may be amplified by the rough estimate of the effective distances. Additionally, the o-Ps continuum is also seen in the disk, and contributes significantly to the total annihilation luminosity as measured by B/D. Bouchet et al. (2010), for example, found an additional halo component, and attributed the halo flux to the bulge, which increased B/D. This approach, however, is not unique, as the galactic halo is neither part of the bulge nor the disk. In any case, it is hard to disentangle diffuse emission sites, and to attribute correct fluxes to the respective annihilation regions. Accounting for these systematic uncertainties, it can nevertheless be concluded that the luminosity B/D ratio is probably less than 1.0. This is in contrast to previous findings, using a narrower disk representation.

Most, if not all, of the candidate positron sources, Sec. 5, have B/D ratios of less than 1.0, formally ranging from around 0.1 to 0.5. Previous studies therefore suggested specific scenarios to explain the apparently large bulge to disk ratio. In general, the bright bulge would suggest origins of the positrons among old stellar populations, such as from SNe Ia, novae, LMXRBs, and microquasars (see Sec. 5). The best-fit latitude extent of the empirical disk model favours a rather large scale height, ranging from  $\approx 0.5$ -2.0 kpc. This suggests that positrons may be ejected from X-ray binaries and may annihilate further away from the sources, resulting in a low surface-brightness (Prantzos 2008; Prantzos et al. 2011). Accreting black-hole binaries may be more frequent in the bulge (3000 sources Bandyopadhyay et al. 2009) than in the disk, and could also reproduce the observed brightness distribution and disk extent (see also Sec. 5.2). However, the annihilation morphology may not be representative for the source distribution morphology in the Milky Way because of the propagation of the positrons through the ISM. From order of magnitude estimates, the life-time of positrons in the ISM can be several millions of years, of course depending on the

<sup>14</sup>Assuming the disk to be truncated at a radius  $R$ , i.e. full circle like, the mean distance of a point inside that circle as measured from the centre to every other point inside the circle is  $\frac{2}{3}R$  for distances smaller than  $\approx 0.5R$ , is  $1.131 \cdot R$  at the edge of the circle, and increases linearly for larger radii as expected. Assuming the Sun at a distance of 8.5 kpc to the galactic centre, the mean distance to any point in a disk of 15 kpc would be 10 kpc.

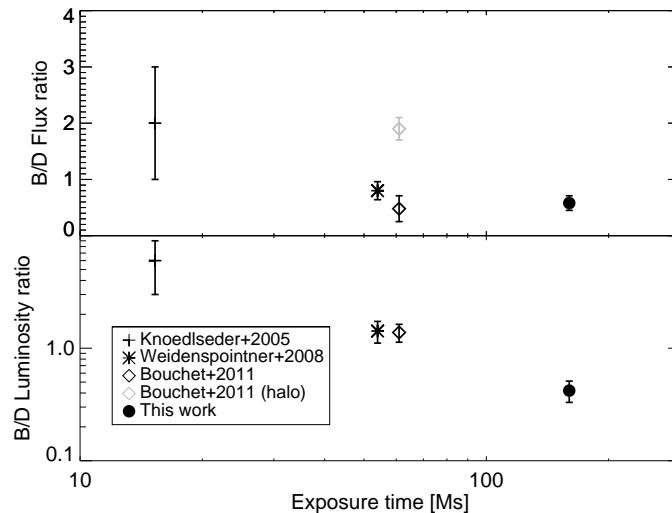


Figure 4.30: Comparison of bulge to disk ratios from SPI measurements. Shown are the estimated line flux (top panel) and annihilation luminosity (bottom panel) ratios derived from the bulge component and the disk component as a function of SPI/INTEGRAL exposure time in different studies. The flux B/D from this work is consistent with previous measurements, but the luminosity ratio is significantly lower compared to measurements with less exposure. See text for more details on the differences.

initial kinetic energy (injection energy). This can be translated to an estimate of the mean free path of positrons before annihilation or thermalisation of the order of kiloparsecs (Martin et al. 2012; Alexis et al. 2014, see also Sec. 4.1). Depending on the specific ISM phases, the annihilation may take place much later, and thus much further away from the sources. A deconvolution of the emission morphology with the mean propagation path of positrons from each source candidate would yield the source morphology. But this includes the injection energies of positrons and the environmental conditions on their way through the ISM, resulting in a circular argumentation.

Another possibility is therefore to "count" the positrons in specific annihilation regions, i.e. estimate the positron production / annihilation budget, and then consider how many positrons a specific source type could produce. This balancing approach will be carried out in Sec. 5, as most of the previous estimates for the different source types are mainly based on assumptions without direct evidence. In this thesis, direct measurements of several source types have been performed towards a more complete understanding of positron annihilation in the Milky Way, and its further implications. The positron annihilation rate,  $\dot{N}_{e^+}$ , is related to the annihilation luminosity and the  $P_s$  fraction by (Brown & Leventhal 1987)

$$\dot{N}_{e^+} = \frac{L_{511}}{2 - 1.5f_{P_s}}. \quad (4.10)$$

This is also equivalent to the positron production rate - modulo propagation effects - assuming a quasi steady state environment in the Milky Way. The obtained values for the different celestial emission model components are listed in Tab. 4.12. Note that the values depend on the effective distance to the components, which implies a systematic uncertainty of  $\approx 30\%$ . The order of magnitude estimates can help to discuss the contribution of each proposed source type in the Milky Way when measured in a coherent way. This means determining the absolute number of positrons

that may leave the local environments of their sources.

Component	$d_{eff}$	$I_{511}$	$f_{Ps}$	$L_{511}$	$\dot{N}_{e^+}$
Bulge	8.5	9.6(7)	1.08(3)	8.3(6)	1.7(2)
Disk (total)	10.0	16.6(3.5)	0.90(19)	19.9(4.2)	3.1(1.5)
Disk ( $l > 0^\circ$ )	10.0	8.7(1.4)	0.90(16)	10.4(1.7)	1.6(6)
Disk ( $l > 0^\circ$ )	10.0	8.0(1.2)	0.85(18)	9.6(1.4)	1.3(5)
GCS	8.5	0.8(2)	0.94(19)	0.7(2)	0.12(7)
Galaxy (total)	-	27.4(3)	0.99(7)	28.9(4.2)	4.9(1.5)

Table 4.12: Positron annihilation rates in different regions of the Milky Way as decomposed by the used celestial emission model components. The assumed effective distance,  $d_{eff}$ , is given in units of kpc, the 511 keV line flux,  $I_{511}$ , in units of  $10^{-4}$  ph cm $^{-2}$  s $^{-1}$ , the annihilation luminosity,  $L_{511}$ , in units of  $10^{42}$  ph s $^{-1}$ , and the positron annihilation rate,  $\dot{N}_{e^+}$ , in units of  $10^{43}$  e $^+$  s $^{-1}$ .  $f_{Ps}$  is the positronium fraction. The shown values for the entire Galaxy are adopted from the spectral fit ( $I_{511}$  and  $f_{Ps}$ ), and summed over the bulge, disk, and GCS components ( $L_{511}$  and  $\dot{N}_{e^+}$ ). Uncertainties are given in brackets in units of the last digits. Assuming a steady state, the positron annihilation rate equals the positron production rate in a particular component which must be supplied by the candidate sources discussed in the text.

## 4.7 Kinematics of the Galaxy Traced by Gamma-Rays

The spectral analysis of the positron annihilation gamma-ray data, Sec. 4.6, revealed clear signatures of Doppler-broadened and Doppler-shifted lines. Around photon energies of 511 keV, the total galactic signal is detected with a significance of more than  $58\sigma$ , so that gamma-ray line shapes provide information, not only about the annihilation conditions in interstellar gas, but also about kinematics. These are embedded in the superposition of many line-of-sights in such a large scale and component-wise analysis. With the high-resolution power of SPI, it is possible to analyse the angular variations of line widths and centroids along the Galaxy. This will provide an independent approach for a better understanding of where and how the positrons annihilate in the Galaxy.

As discussed in Sec. 4.6.6, the annihilation line for the Galaxy as a whole is Doppler-broadened by  $1550 \pm 150$  km s $^{-1}$  if interpreted as due to velocity variations only. Among the different components of the 511 keV Milky Way, bulge, disk, and GCS, the broadening ranges between 1000 and 2000 km s $^{-1}$ . This is much larger than what would be expected from galactic rotation, indicating probably two components. One may be due to galactic rotation, and one due to the intrinsic annihilation conditions. Large scale Doppler-shifts with respect to the laboratory energy are negligible for all components, except for the GCS. This is probably due to the fact that the solid angles, comprised by each of the components, is so large that positive and negative shifts cancel out each other, towards a broadened but not residually shifted line. The resolving power of SPI at 511 keV is  $R_{511} = 511/2.15 = 240$ . For a celestial gamma-ray line which is not intrinsically broadened, a signal to noise ratio of about 5 would hence be sufficient to determine line-shifts of the order of 75 km s $^{-1}$ , enough to decouple the intrinsic from the kinematic line broadening. However, the spatial extent and brightness profile of the Galaxy, compared to the angular resolution of SPI, will prevent significant line detections and also line shifts beyond  $\approx 25^\circ$ . In particular, the disk as seen in 511 keV shows such a low surface-brightness that a large area in the sky (large solid angle, see Sec. 4.7.1) has to be considered for a significant line detection. On the other hand, this will add the Doppler shifts for the large number of line-of-sights and will smear out residual shifts. Therefore, only

the inner galaxy will be discussed in Sec. 4.7.3, also because the surface-brightness in the inner Galaxy, and the SPI exposure, is highest in those regions.

In the case of  $^{26}\text{Al}$  (see Sec. 5.1.1.2 for a detailed discussion) which emits gamma-rays at 1809 keV when decaying, the morphology is not as constricted as in the 511 keV case. Consequently, a wider range in longitude can be investigated. In addition, the resolving power at 1809 keV is  $R_{1809} = 1809/3.16 = 570$ , and thus about 2.5 times better than at 511 keV, so that for equal signal strengths, the Doppler-shifts can be constrained better in the case of  $^{26}\text{Al}$ . This was used by Kretschmer et al. (2013) to create a longitude-velocity (l-v) diagram of the Milky Way in decay gamma-rays from  $^{26}\text{Al}$ . As shown in previous studies (e.g. Diehl et al. 2006; Wang et al. 2009; Kretschmer et al. 2013), and also in Sec. 5.1.1.3, the galactic  $^{26}\text{Al}$  1809 keV gamma-ray line is broadened by  $275 \pm 100 \text{ km s}^{-1}$ . This is thought to be caused by galactic rotation and feedback from massive stars, as their ejecta will be blown into large cavities, and change the dynamics of the ISM. These superbubbles may be as large as kiloparsecs, and superpositions of ejecta from many of those massive star regions, in different directions in the sky, will characterise the kinematics of interstellar gas. As the life-time of  $^{26}\text{Al}$  is 1.03 Myr, a million-year time scale will be traced by the 1809 keV emission. With more than nine years of INTEGRAL/SPI data, Kretschmer et al. (2013) showed that the gas motion from massive star ejecta is leading the molecular gas, as seen for example in CO, Fig. 4.31.

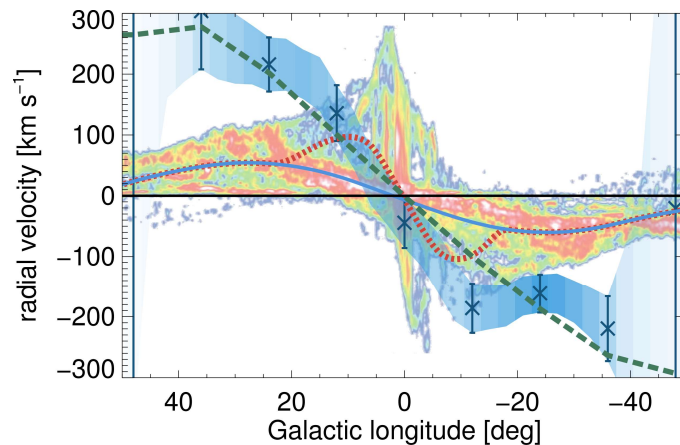


Figure 4.31: Longitude-velocity diagram of  $^{26}\text{Al}$  gamma-rays compared to molecular gas and other objects in the Galaxy. The  $^{26}\text{Al}$  line centroid energies were fitted to determine velocities in longitude bin widths of  $12^\circ$  and latitude ranges of  $\pm 5^\circ$  (blue data points and shading). For comparison, different models are shown in solid blue ( $^{26}\text{Al}$  distributed in the disk and spiral arms, closely following the CO emission, equivalent to a converted version of the radial rotation curve of Fig. 5.49), dotted red (additional bar contribution from the centre of the Galaxy), dashed green (spiral arms only plus leading-edge blow-out), and also the galactic CO emission as coloured contours. From Kretschmer et al. (2013).

In particular, Kretschmer et al. (2013) showed that excess velocities of  $\approx 100\text{--}300 \text{ km s}^{-1}$ , relative to the local standard of rest, are consistently (red- and blue-shifted on either galactic quadrant) observed in the inner  $80^\circ$  of the Milky Way. This is interpreted as preferential expansion of superbubbles towards the leading edges of spiral arms. The Galaxy in 1809 keV is best represented in this scheme as a two-arm spiral with a thickness of 0.5 kpc outside a radius  $r_0 \approx 4 - 5 \text{ kpc}$ , which would correspond to the tips of a bar-like distribution, rotated by about  $30 - 40^\circ$ . The general geometry of this scenario is that stars, formed in a spiral arm, propagate out of the spiral centre during their evolution, and create bubbles in their wind phases and supernovae. The ejecta, as traced by  $^{26}\text{Al}$ , expand more easily away from the arm than into it, as the density is increased in the arm. In the cumulative effect,

a more frequent forward ejection (away from the arms) than backward ejection is seen, which results in a residual excess velocity in the direction of the spiral arm. This is illustrated in Fig. 4.32.

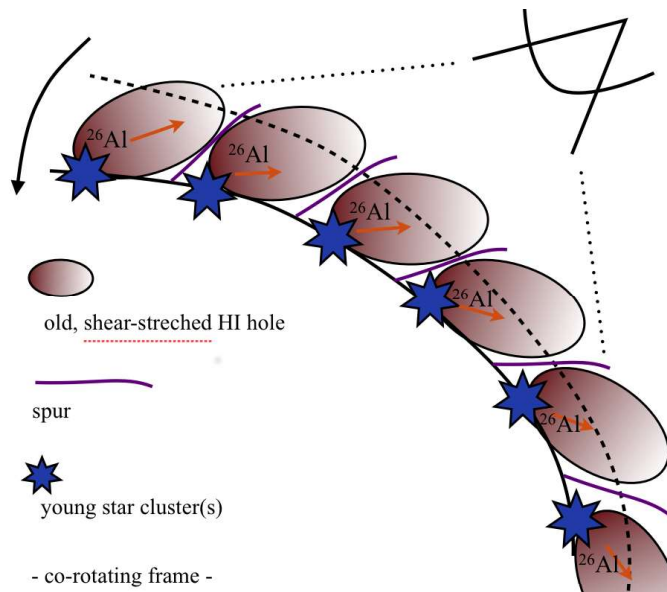


Figure 4.32: Sketch of  $^{26}\text{Al}$  rotation and blow-out geometry in co-rotating frame. Here, a spiral arm (solid line) moves anti-clockwise away from its previous position (dashed line) and stars created cavities / superbubbles (ellipses) during this time. Then, the young star clusters (blue stars) at the current spiral arm location feed  $^{26}\text{Al}$  (colour gradient in ellipses) into the old super bubbles for which reason the "rotation velocity" appears higher than what would be expected from galactic rotation only. From Krause et al. (2015).

As the analysis of Kretschmer et al. (2013) was done with another type of background method, using the temporal variance of onboard radiation monitors, the kinematic analysis of the  $^{26}\text{Al}$  data is repeated with the background modelling approach described in Sec. 3.2.3.2. This is done to consolidate and improve the results by using about 40% more data in Sec. 4.7.2. Then, an equivalent analysis is performed for the 511 keV data set as used in Sec. 4.2, towards a measure of the positron annihilation kinematics in Sec. 4.7.3. The general method to extract kinematic information from SPI data to use it in a position-velocity diagram for further analysis is explained in Sec. 4.7.1.

#### 4.7.1 Position-Velocity Diagrams

In order to create a position-velocity diagram from INTEGRAL/SPI data, the "sliding window method" from Kretschmer et al. (2013) is applied to the  $^{26}\text{Al}$  data set as described in Sec. 4.7.2. This method is extending the cutout method which is applied to the  $^{26}\text{Al}$  data in this thesis, Sec. 5.1.1.3.2, and also previous studies (e.g. Wang et al. 2009; Diehl et al. 2010), by scanning the gamma-ray emission with complementary but independent components. On the basis of the COMPTEL ME7 map, the sky is divided into two parts, one inside a spherical rectangle of  $l \in [l_0 - \Delta l/2, l_0 + \Delta l/2]$  and  $b \in [b_0 - \Delta b/2, b_0 + \Delta b/2]$  which defines the region of interest (ROI), and its complement, consisting of the full remaining sky map with this region cut out, Fig. 4.33.

The full complementary sky part is required because SPI has a large partially coded

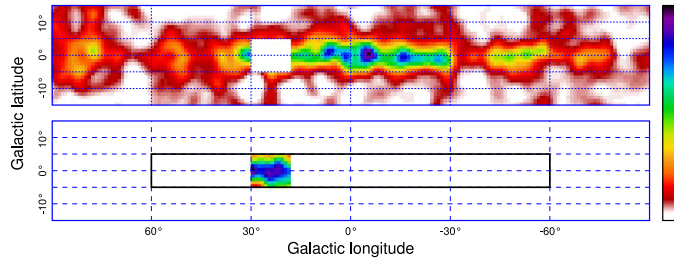


Figure 4.33: Definition of the region of interest in the sliding window method. In the bottom panel a ROI of  $l \times b = 12^\circ \times 10^\circ$  at  $l = 24^\circ$  is shown as cut out of the COMPTEL 1.8 MeV ME7 map, left with a hole as the complementary sky model in the top panel. The rectangular outline shows the region covered by the galactic plane scan. From Kretschmer et al. (2013).

field of view of  $30^\circ \times 30^\circ$ , so that many observations of the ROI also fall into the range outside of it. Then, the intensities of the two model components are determined simultaneously, in addition to the two-component background model, Sec. 4.7.2, using a maximum likelihood estimation for each half-keV energy bin, individually. This obtains two spectra, one for the ROI, and one for the coverage of the remaining Galaxy. This process is repeated by varying  $l_0$  to scan the ROI along the galactic plane. In this analysis,  $\Delta b$  is chosen so that the full expected scale height is covered for both, ejecta and gas streaming away from the plane in the direction of the halo. This converts to  $\Delta b = \pm \arctan(h_0/R_0)$  for a characteristic height  $h_0$  at a distance to the Sun  $R_0$ . Following Kretschmer et al. (2013), a latitude width of  $\Delta b = \pm 5^\circ$  is chosen, corresponding to a scale height of 300 pc at 3 kpc distance. In general such a ROI segment corresponds to a pyramid in 3D space, and covers many different distances from the galactic plane and from the Sun. Hence, nearby sources cover a larger solid angle and would only be partially sample. To account for this issue, an additional longitude-latitude-velocity diagram is constructed in Sec. 4.7.2.

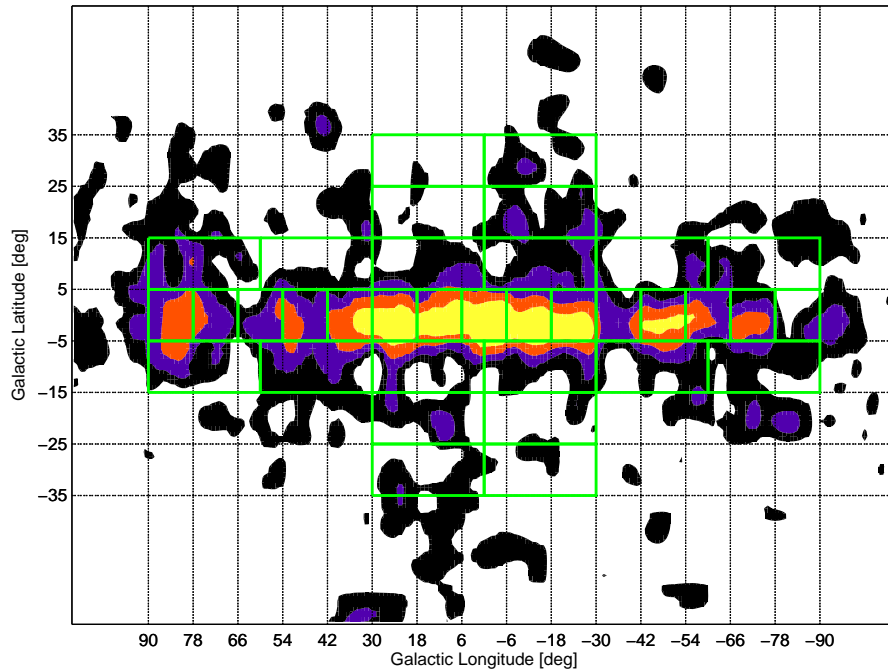


Figure 4.34: Region of interest scheme in the  $^{26}\text{Al}$  data analysis (green rectangles) on top of a coloured contour scheme of the COMPTEL 1.8 MeV ME7 map, showing the expected regions of strong (yellow  $10 \times 10^{-5} \text{ ph cm}^{-2} \text{ s}^{-1} \text{ sr}^{-1}$ ), moderate (red  $5 \times 10^{-5} \text{ ph cm}^{-2} \text{ s}^{-1} \text{ sr}^{-1}$ , purple  $2.5 \times 10^{-5} \text{ ph cm}^{-2} \text{ s}^{-1} \text{ sr}^{-1}$ ), and weak (black  $1.25 \times 10^{-5} \text{ ph cm}^{-2} \text{ s}^{-1} \text{ sr}^{-1}$ ) emission. In total, 35 ROIs are defined in this analysis. See text for details.

In particular, a ROI scheme as shown in Fig. 4.34 is used to first validate previous results, and then to extend the analysis of the  $^{26}\text{Al}$  emission. The broad longitude bins above and below the galactic plane have a latitudinal extent of  $\Delta l = 30^\circ$ , and are centred at  $l_0 = \pm 15^\circ$  for the latitude centres  $b_0 = \pm 20^\circ, \pm 30^\circ$ , and at  $l_0 = \pm 15^\circ, \pm 45^\circ, \pm 75^\circ$  for  $b_0 = \pm 10^\circ$ . In the galactic plane, the longitude extent can be smaller, as the signal is stronger. This leads to a ROI bin width of  $\Delta l = 12^\circ$  for  $l_0 = 0, \pm 12^\circ, \pm 24^\circ, \pm 36^\circ, \pm 48^\circ, \pm 60^\circ, \pm 72^\circ, \pm 84^\circ$  and  $b_0 = 0^\circ$ . The entire sky model map is constrained to  $|l| \leq 120^\circ$  and  $|b| \leq 60^\circ$ .

Each derived ROI spectrum is then fitted by a degraded Gaussian line shape, with instrumental resolution (FWHM) of 3.16 keV, on top of a constant offset, to account for celestial  $^{26}\text{Al}$  emission and galactic continuum. In the fit, the width is fixed at instrumental resolution, and centroid and amplitude of the line, as well as the amplitude of the continuum, are determined. Using the Doppler-formula, Eq. (2.103), with a laboratory energy of  $E_{lab} = 1808.63$  keV, the centroid is converted into a bulk Doppler-velocity from the direction of a particular ROI bin.

## 4.7.2 Kinematics from Al-26 Gamma-Rays

### Al-26 Data Set

The INTEGRAL/SPI data set that was used to study the  $^{26}\text{Al}$  1809 keV line in the Milky Way contains more than 13 years of data. The exposure map, Fig. 4.35, differs with respect to the 511 keV data set by the fact that newer observations focussed on closing exposure gaps, for a more complete coverage of the sky. This is ideal to study the entirety of the Milky Way, and also to have a closer look into regions of active star formation like ScoCen, Cygnus, and Orion. These regions have are mainly focussed as their distances, ages, and stellar contents are adequate to learn about the distribution of gas and kinematics in such stellar groups. An increased exposure will also help to constrain the gamma-ray emission spatially and spectroscopically towards a global interpretation of the signal.

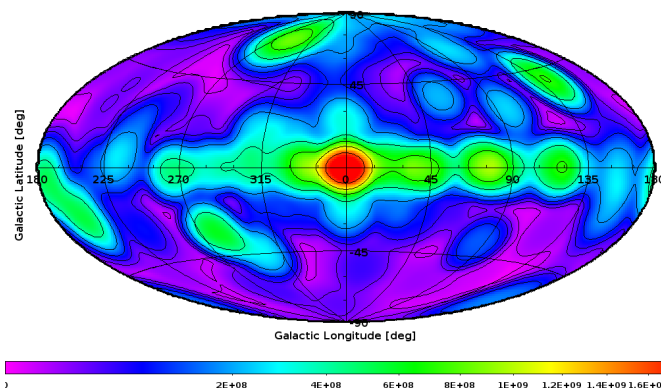


Figure 4.35: Exposure map of the 13-year  $^{26}\text{Al}$  1809 keV data set. The units are given in  $\text{cm}^2\text{s}$ ; the equivalent exposure time is calculated for 19 detectors with an effective area of  $\sim 44$   $\text{cm}^2$  for photon energies around 1809 keV. The contours, starting from the innermost, correspond to exposures of 36, 25, 16, 9, 4, 2, 1, 0.5, and 0.1 Ms, respectively. The total exposure time is 200.9 Ms.

The analysed data set consists of 92867 pointings for each of the 19 detectors of the

SPI camera. This amounts to 1503435 individual spectra (75171750 data points) to be analysed, taking the failed detectors into account. For active detectors, this corresponds to a dead-time corrected exposure of 200.9 Ms. The focus is put on the refinement of spectral parameters of the gamma-ray line at 1808.63 keV, originating in the decay of  $^{26}\text{Al}$ , which is produced in massive star regions (see Sec. 5.1.1.3.2). The chosen energy band for the study is between 1795 and 1820 keV, i.e. 50 energy bins of 0.5 keV width, forming the spectra. This is much less than the empirically determined instrumental resolution of 3.17 keV (FWHM, 13-years time-averaged mean, Fig. 3.18), towards high-precision gamma-ray spectroscopy. In addition, a larger energy band from 1745 to 1840 keV was analysed, which contains strong instrumental background lines, in order to consolidate the background modelling approach. Particular exposures for massive star regions are listed in Tab. 4.13.

Region	$l_0$	$b_0$	$r_0$	Time
Cygnus	80.5	1.5	16	12.9
ScoCen	340.0	23.0	16	5.3
Orion	198.0	-27.0	18	5.6
USco	350.0	20.0	10	6.8
UCL	332.0	18.9	9	6.1

Table 4.13: Mean exposure time in units of Ms for massive star regions as defined by a circular area around the associations' centres ( $l_0/b_0$ ) with radius  $r_0$  in units of degrees.

### Background Modelling Near 1.8 MeV

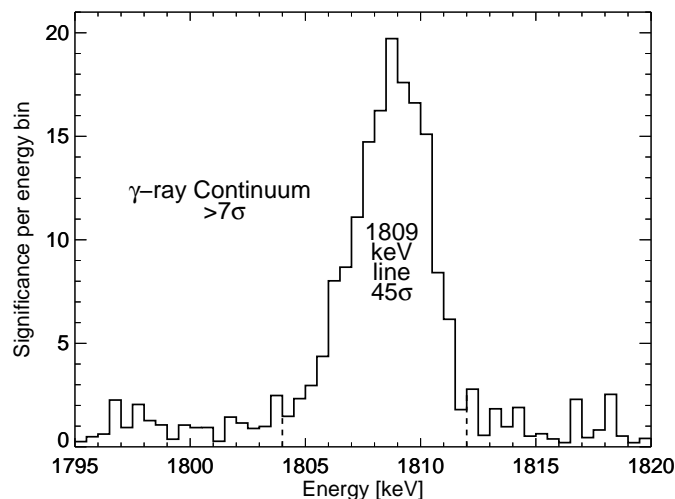


Figure 4.36: Detection significance of gamma-rays from  $^{26}\text{Al}$  in the Galaxy per 0.5 keV energy bin, similar to Fig. 4.14. The 1809 keV line is clearly seen at  $45\sigma$  significance over instrumental background and galactic gamma-ray continuum which is seen at more than  $7\sigma$ .

The instrumental background around the 1808.63 keV line in SPI exhibits a line complex, consisting of at least three lines at 1805.8, 1808.7, and 1811.3 keV. In addition, very strong lines at 1764 and 1779 keV are present from different origins inside the satellite. An energy range between 1745 and 1840 keV is used to validate the power of the background modelling method, Sec. 3.2.3. In total, 18 lines on top of a power-law like continuum are used to determine the background detector patterns for each energy bin. Here, this is done on a half-year time basis because the spectrum in this energy range is now statistics limited, see Fig. 3.14c.

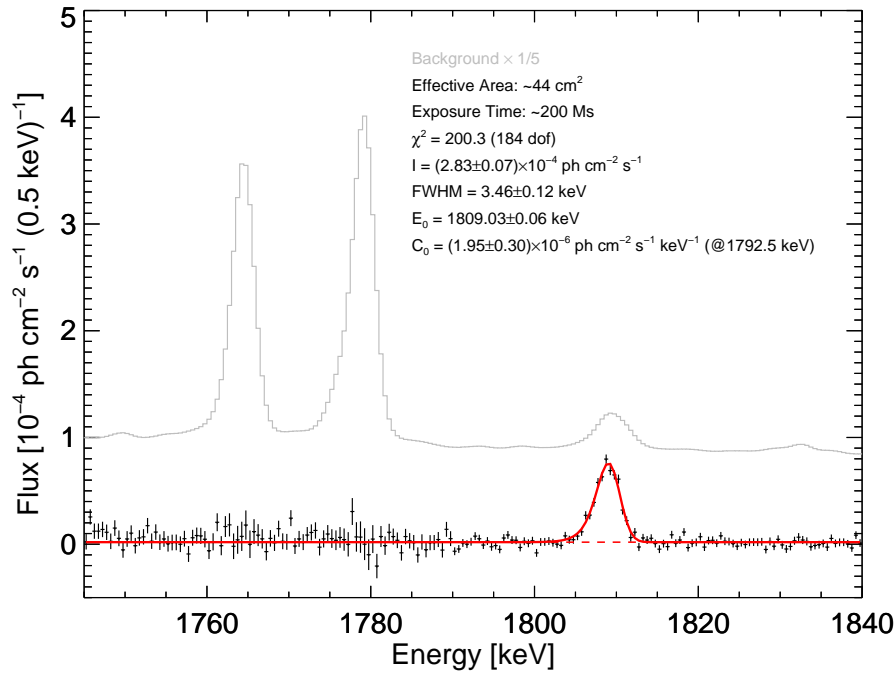


Figure 4.37: Spectrum of the inner Galaxy between 1745 and 1840 keV (black crosses). The raw background spectrum (grey histogram, scaled) in the is shown for comparison. The uncertainties in the range between 1745 and 1790 keV are larger because the maximum likelihood estimation tended to need more temporal intensity scaling parameters, as expected from the dominance of the strong instrumental lines, being 2-3 times more intense than the continuum beneath. The line features around 1764 and 1779 keV are completely removed, leaving only the celestial 1809 keV line and the galactic continuum. The spectral parameters have been derived by a fit of a degraded Gaussian line on top of a power-law like continuum, and are given in the legend. The  $\chi^2$  value of 200.3 for 184 dof proofs the adequacy of the fit.

In the maximum likelihood fit, the re-scaling has to be adjusted to shorter time-scales again, because of the detector degradation effects. This compensates the distorted detector patterns for single energy bins. Using a first-order morphology in the inner Galaxy for the description of the  $^{26}\text{Al}$  emission, here an exponential disk with scale radius 3.5 kpc and scale-height 85 pc, truncated at  $|l| < 30^\circ$  and  $|b| < 10^\circ$ , respectively, the significance per energy bin is derived and shown in Fig. 4.36. The resulting celestial spectrum is shown in Fig. 4.37, together with a superimposed total raw spectrum (background), down to an energy of 1745 keV. The total significance for the 1809 keV line as estimated from the range between 1804 and 1812 keV (due to the asymmetric line shape), is  $45\sigma$ . The high-energy continuum is seen with a significance of at least  $7.6\sigma$  in the energy band 1795 to 1820 keV, omitting the line. Only at the expected energy, an excess signal is seen over instrumental background and galactic continuum, confirming the presence of  $^{26}\text{Al}$  in the Milky Way. In addition, there are no artificial signals around the two major instrumental lines at 1764 and 1779 keV, which demonstrates the capabilities of the self-consistent background modelling approach, by exploiting the physical processes inside the space craft.

#### Al-26 Longitude-Velocity Diagram

This repeated analysis now covers a larger range in longitudes, up to the Cygnus region ( $l \approx 80^\circ$ ) in the first, and down to the Carina region ( $l \approx -70^\circ$ ) in the fourth galactic quadrant. One full Galactic rotation phase may thus be identified. For

the  $^{26}\text{Al}$  l-v-diagram, the inner ROIs with  $b_0 = 0^\circ$  are used for a consistency check with previous works, and to check the data quality by comparing raw spectra and celestial ROI spectra.

In Fig. 4.38, ten spectra from the galactic plane ROIs are shown, together with the respective raw background spectra from the same regions. As the background line centroid of the 1764 keV line is the same in all directions, varying by at most  $\pm 5 \text{ km s}^{-1}$ , the celestial  $^{26}\text{Al}$  line systematically varies. Also the fluxes of background and celestial lines change accordingly. The quoted flux values, Fig. 4.40, correspond to at least  $2\sigma$  detections, whereas for weaker signals, a  $2\sigma$  upper flux limit is given. If the line is not detected with high significance, the Doppler-velocity bulk-shift is not constrained, and is marked as grey data points in the l-v-diagram with "infinite" error bars, Fig. 4.39.

Between  $l = -40^\circ$  and  $l = +40^\circ$ , the derived Doppler velocities are fully consistent with those of Kretschmer et al. (2013). Especially the apparent blue-shift at  $l = 0^\circ$  is confirmed, and constrained to  $v = -85 \pm 28 \text{ km s}^{-1}$ . Either the rotation of the Galaxy, as seen in decay gamma-rays, involves peculiar sampling of massive star regions in different line-of-sights, which leads to an offset in the zero-point according to the bar-angle. Or the nearby OB association ScoCen is larger than expected from gamma-ray data only, and is distorting the line shape, so that the blue-shift is primarily due to streaming gas from this association towards the Sun. Furthermore, the velocity excess above pure galactic rotation is verified by a different analysis, using another background approach, and a 40% larger data set. In particular, the excess is between 150 and 250  $\text{km s}^{-1}$  in the direction of the spiral arms, consistent with cumulative massive-star-region ejecta blow-outs into large cavities, leading the spiral arms. The increased exposure also provides additional data points to the l-v-diagram around  $l = 66^\circ - 90^\circ$ . These coincide partially with the Cygnus region. Two more data points, with decreased velocities, validate galactic rotation as the driving mechanism. In the direction  $l \approx \pm 90^\circ$ , stars and gas move in the same direction as the solar system, and at the same speed. Thus, the relative velocity is expected to be nearly zero, with the exception of residual gas motion in cavities. In addition, the Sun is located at the corotation radius of the Milky Way (Mishurov & Zenina 1999), so that also the molecular gas velocity drops to zero at  $l \approx \pm 90^\circ$ .

In Fig. 4.40, the 1809 keV line flux along the galactic plane is shown. The derived relative flux values are consistent with Kretschmer et al. (2013) in the direction of the inner Galaxy. Furthermore, the absolute values from the direction of Cygnus are consistent with earlier studies (e.g. Martin et al. 2009,  $(6.0 \pm 1.0) \times 10^{-5} \text{ ph cm}^{-2} \text{ s}^{-1}$ ), when summed over the ROIs overlapping with Cygnus, i.e.  $(6.4 \pm 1.2) \times 10^{-5} \text{ ph cm}^{-2} \text{ s}^{-1}$ . From the direction of the Carina OB associations,  $70^\circ < l < 90^\circ$ , no significant  $^{26}\text{Al}$  line signal is detected, as may be expected from earlier measurements with COMPTEL, in which a weak signal of  $\approx 10^{-5} \text{ ph cm}^{-2} \text{ s}^{-1}$  is seen (Plüschke 2001). The  $2\sigma$  upper limit on the  $^{26}\text{Al}$  flux from the Carina region is  $2 \times 10^{-5} \text{ ph cm}^{-2} \text{ s}^{-1}$ , so that this massive star region will also be seen with INTEGRAL/SPI with increased exposure. In general, the fluxes in the inner galaxy strongly support the spiral arm blow-out in leading direction interpretation by Kretschmer et al. (2013) and Krause et al. (2015).

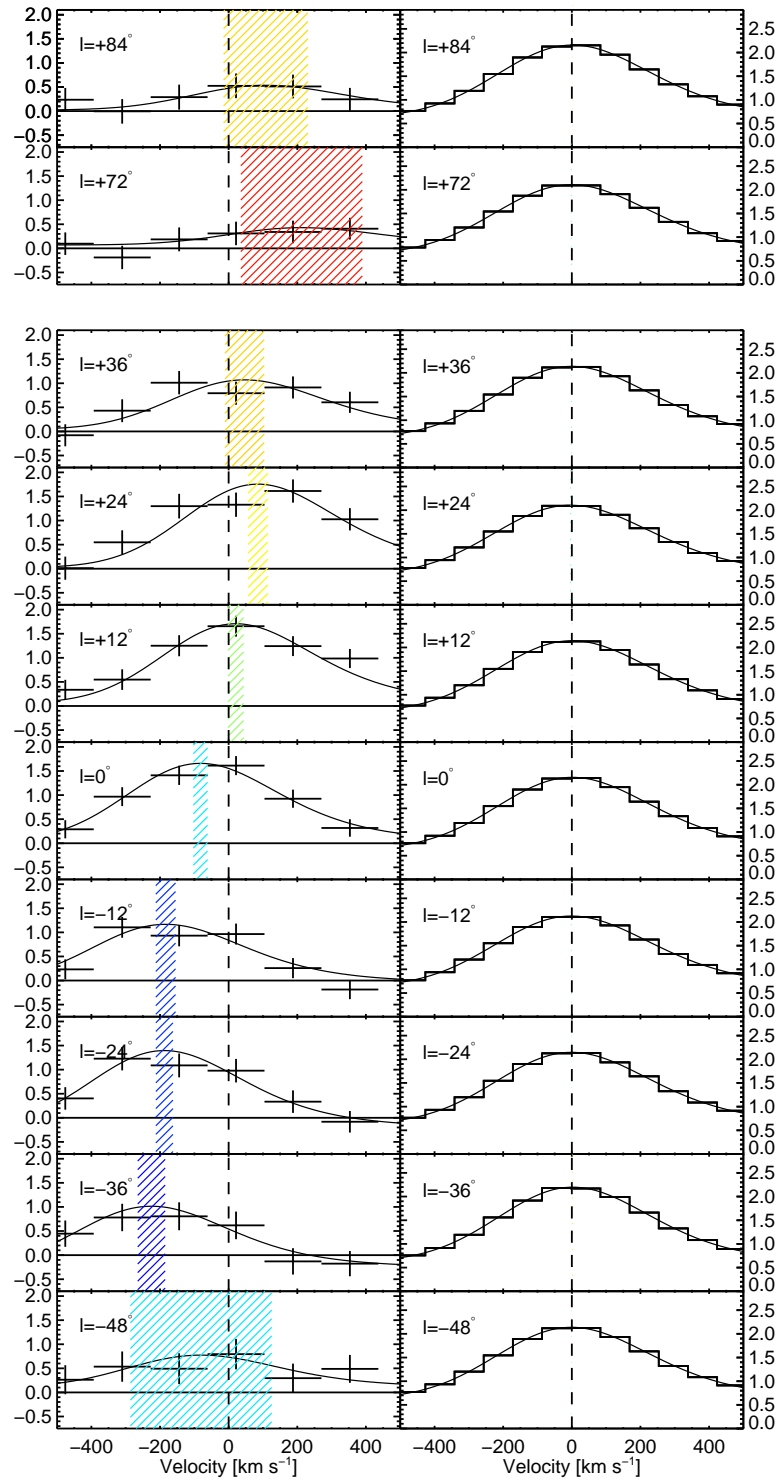


Figure 4.38: Comparison of celestial and background line centroids as a function of longitude. In the left column, the emission spectra (black crosses) from the  $^{26}\text{Al}$  1808.63 keV line is shown in velocity space for chosen longitude ROIs in the inner galaxy and the Cygnus region with size  $\Delta l \times \Delta b = 12^\circ \times 10^\circ$ . The spectral lines have been fitted by a degraded Gaussian with fixed width of 3.16 keV FWHM with varying centroid and amplitude (solid curved line). The zero-flux level is marked by a solid horizontal line, the zero-velocity which corresponds to a centroid of 1808.63 keV is marked by a dashed line. The left axes units are  $10^{-5} \text{ ph cm}^{-2} \text{ s}^{-1}$ . In each panel, the colour-hatched areas mark the measured Doppler-velocity with  $1\sigma$  uncertainties. In the right column, the respective background spectra (black histogram) for the same regions are shown. In particular, the strong background line at 1764.49 keV is normalised to the mean value of the respective spectrum and shown in velocity space. The uncertainties are smaller than the line thickness. Each spectrum is fitted by a degraded Gaussian in the same way as in the left panels (solid curved line). The determined systematic uncertainties from shifts of this line is of the order  $\pm 5 \text{ km s}^{-1}$ , consolidating the systematic longitudinal spectral shifts of the celestial  $^{26}\text{Al}$  line.

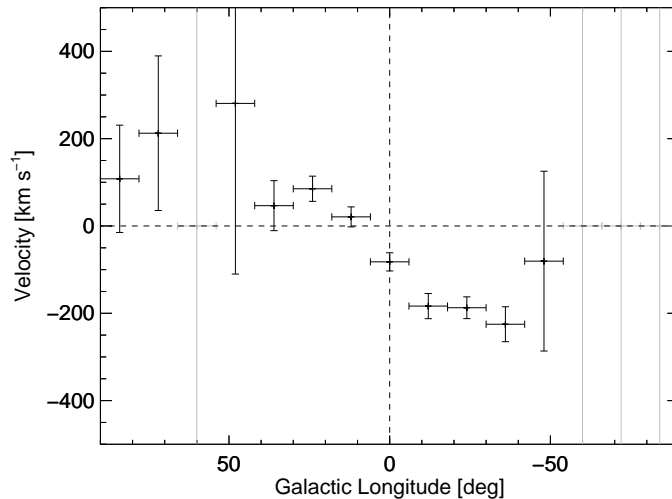


Figure 4.39: Longitude-velocity diagram of 1809 keV line emission in the Milky Way. Shown are the derived bulk-velocities from galactic plane ROIs ( $|b| \leq 5^\circ$ ) as defined in Fig. 4.34. Non-detections are marked with grey data points of infinite range. See text for details.

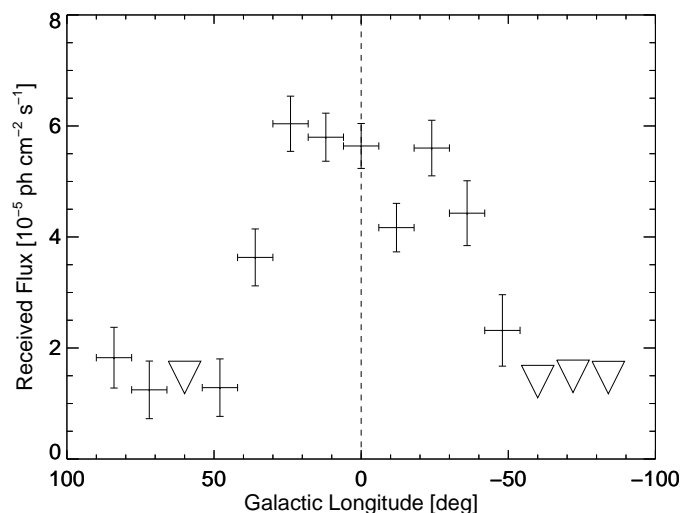


Figure 4.40: Longitude-flux diagram of  $^{26}\text{Al}$  emission in the galactic plane as derived from ROIs in Fig. 4.34. For non-detections, a  $2\sigma$  upper limit on the flux is derived and marked with downward triangles. See text for details.

## Al-26 Longitude-Latitude-Velocity Diagram

With increased exposures above and below the galactic plane, compared to previous studies (Kretschmer et al. 2013), also velocity estimates along galactic latitudes can be provided for the  $^{26}\text{Al}$  emission. In Fig. 4.41, the longitude-latitude-velocity-diagram of the Milky Way as seen in 1809 keV is shown.

The galactic rotation is clearly seen in the trend from blue-shifted spectral lines (bluish colours) for negative longitudes, over green and yellowish colours with nearly no line-shifts around  $l \approx +20^\circ$ , towards red-shifted lines (red colours) for positive longitudes. Grey shaded areas indicate non-detections of the  $^{26}\text{Al}$  line ( $< 2\sigma$ ). While at positive latitudes, the emission is found significant up to  $b = 25^\circ$ , at negative latitudes ( $b < 15^\circ$ ) no excess around 1809 keV is seen. This is probably due to the ScoCen association with its sub-groups, having a larger extent towards positive latitudes. The Upper-Scorpius association is only expected at negative longitudes above the

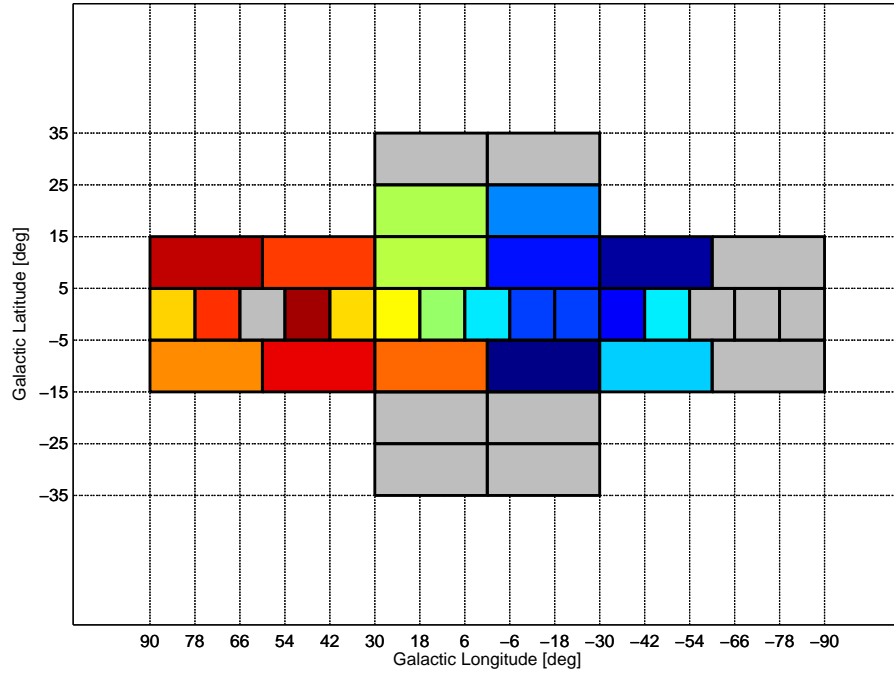


Figure 4.41: Longitude-latitude-velocity-diagram of the Milky Way at 1809 keV. Shown are measured Doppler bulk-velocities as derived from spectral fits to the ROIs as shown in Fig. 4.34. The colours indicate the shifts of the line-centroids with dark blue corresponding to a velocity of  $-300 \text{ km s}^{-1}$  (approaching Sun) and dark red of  $+300 \text{ km s}^{-1}$  (receding Sun). See text for details.

plane, whereas at positive longitudes, also significant emission is found. This emission origin is unknown. In particular, a line at  $1808.39 \pm 39 \text{ keV}$ , corresponding to a Doppler-velocity of  $+40 \pm 65 \text{ km s}^{-1}$ , with a flux of  $(5.3 \pm 1.0) \times 10^{-5} \text{ ph cm}^{-2} \text{ s}^{-1}$ , is detected with a statistical significance of  $5.3\sigma$  above instrumental background and gamma-ray continuum. This source may be distinct from the Upper-Scorpius association, because its Doppler-shift is significantly opposite, and also because the line intensity is about the same value as for USco. This would overestimate the  $^{26}\text{Al}$  content of USco by far, if the source was belonging to it (Diehl et al. 2010). For this reason, an additional or foreground source, maybe associated to ScoCen or even the local bubble (in which also the Sun is located), may cause this emission, which appears much weaker in COMPTEL analyses.

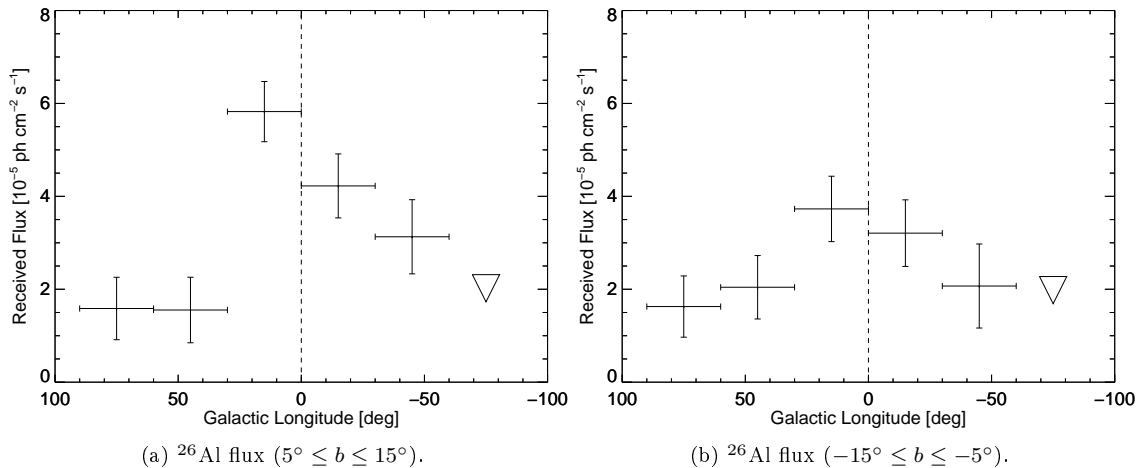


Figure 4.42:  $^{26}\text{Al}$  line flux variations with longitude and latitude as derived from ROIs defined in Fig. 4.34.

Even at high latitudes, the 1809 keV line fluxes are still strong compared to the galactic plane. This is shown in Fig. 4.42. These regions predominantly sample either the very close foregrounds, or the very distant, but already largely extended, cavities, filled with  $^{26}\text{Al}$ . This also supports the large scale height of the  $^{26}\text{Al}$  emission which is described in Sec. 5.1.1.3, and furthermore is in concordance with the superbubble blow-out interpretation. At larger vertical heights, above and below the plane, also the velocities seem to be larger. In Fig. 4.43, the average velocities of certain longitude ranges in and above/below the plane are compared. The velocity ratios are consistent with 1.0, but there is a clear trend for higher values above and below plane. This may be interpreted as gas, streaming out of the dense spiral arms into regions of less pressure and density, i.e. in the forward region of galactic rotation, and also out of the plane. The small ratios in the central parts of the Milky Way may again be due to foreground emission of the ScoCen association. Even more local emission would potentially explain the large velocity gradient of  $^{26}\text{Al}$  emission.

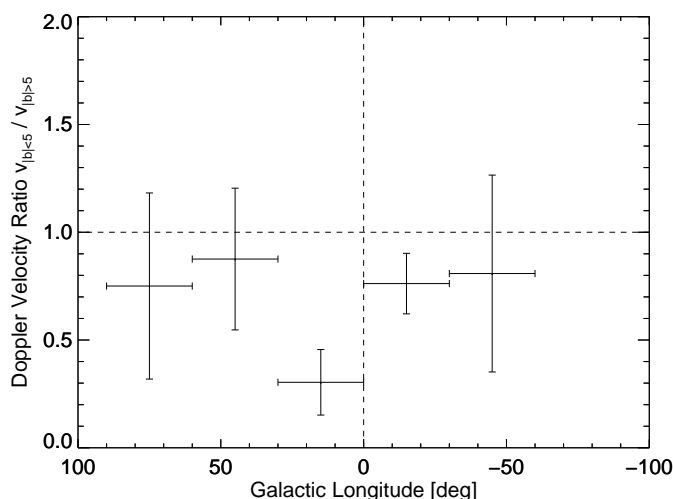


Figure 4.43: Doppler-velocity variations as a function of galactic latitude. Shown are the average values of bulk-velocities from Fig. 4.41 in  $\Delta l = 30^\circ$  bins along the galactic plane, in particular the ratio between velocities in the disk ( $|b| < 5^\circ$ ), and above and below the disk ( $|b| > 5^\circ$ ). In general, the ratios are below 1.0 so that gas in the plane of the disk seems to be slower than when blown out at large vertical heights.

### 4.7.3 Positron Annihilation Longitude-Velocity Diagram

The sliding window method has been shown to work also with another background modelling approach, and can thus be applied to the 511 keV data set. This will create a longitude-velocity diagram of positron annihilation in the inner Galaxy. The used data set is identical to the one described in Sec. 4.2, and also the background modelling is the same. Intensity scaling parameters of the background will be re-determined to account for enhanced or reduced emission in particular line-of-sights. The best fitting superposition of the four diffuse emission components (NB, BB, GCS, Disk) will be built as one representative model for the 511 keV emission, as the empirical six-component model is too degenerate in the inner Galaxy for an individual use. The Crab and Cygnus X-1 are still included in the fit as separate point-sources at their respective positions in the sky. The analysis of the diffuse positron annihilation emission showed that it is possible to detect point-like emission above the extended bulge and disk components. Furthermore, the signal is so strong,

that longitudinal variations of the order of less than  $1^\circ$  are identifiable. This allows to construct ROIs which are as small as possible to trace gradual variations in the velocity profile of positron annihilation. In particular, six different sets of ROIs have been chosen. They range from  $l = -31^\circ$  to  $l = +34^\circ$ , in steps of  $\Delta l = 3^\circ$  bins, for either  $\Delta b = 10.5^\circ$  or  $\Delta b = 21.0^\circ$ . For a particular choice of  $\Delta b$ , three sets are constructed, and named S1, S2, and S3, respectively. The set S1 begins at  $l_0 = -31^\circ$  towards positive longitudes in  $3^\circ$  steps, for a total of 22 individual data points. S2 (S3) is shifted by  $1^\circ$  ( $2^\circ$ ) to positive longitudes, so that it partially overlaps with S1, and ranges to  $l_0 = +33^\circ$  ( $l_0 = +34^\circ$ ). The latitude extent in the bulge region is well constrained, but the disk is only weakly seen. The analysis in Sec. 4.4.2 suggests a scale height of (latitudinal angular thickness) of  $10.5^\circ$ . Most of the emission is therefore expected to be contained within  $b = \pm 5.25^\circ$ , but as the scale height might vary across the longitudinal range, also an analysis with an enhanced extent of  $b = \pm 10.5^\circ$  is performed.

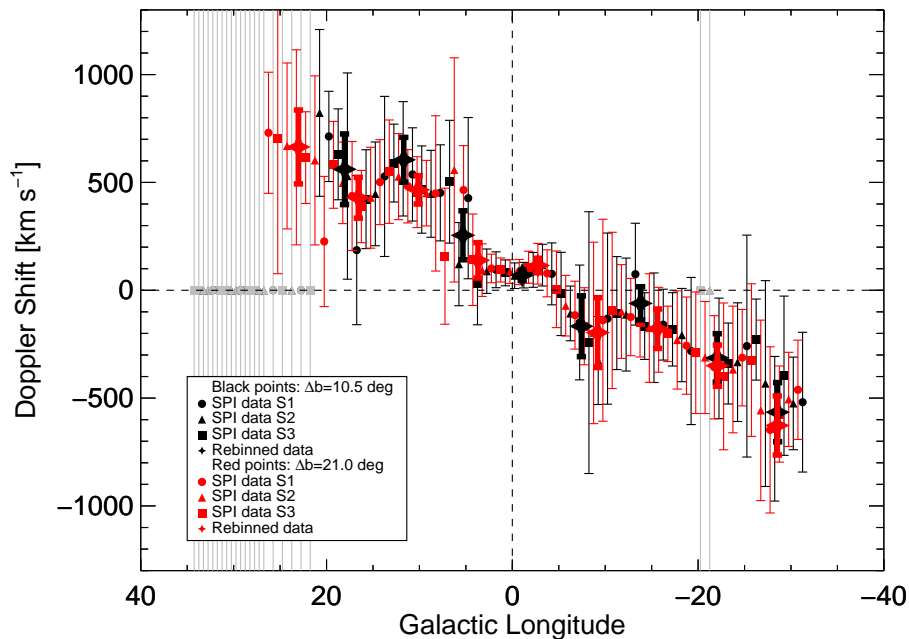


Figure 4.44: Longitude-velocity diagram of 511 keV emission in the Milky Way. Shown are the six ROI sets as described in the text for  $\Delta b = 10.5^\circ$  (black points) and  $\Delta b = 21.0^\circ$  (red points, offset by  $0.5^\circ$  for illustration purpose), respectively, with overlapping sets S1 (circles), S2 (triangles), and S3 (squares). As the data points of different ROI subsets correlate with each other, they have been combined to rebinned data-points (star symbols), partially abolishing the unknown degree of correlation but probably overestimating the uncertainty. Non-detections are marked with grey data points of infinite size. See text for details.

The longitude-velocity diagram of positron annihilation in the Milky Way is shown in Fig. 4.44. Gamma-ray lines are fitted with a Gaussian of fixed FWHM at instrumental resolution (2.15 keV) on top of a constant offset. The o-Ps continuum is not visible in the spectra of those small ROIs. The line amplitude and centroid is allowed to vary in order to determine the significance above the gamma-ray continuum, and the Doppler-velocity. Lines detected with  $2\sigma$  or above are taken into account in the analysis, whereas non-significant detections are marked with grey data points. The general trend of galactic rotation is visible in the 511 keV l-v-diagram: It shows a change from negative velocities (approaching Sun) at negative longitudes (fourth galactic quadrant) towards positive velocities (receding Sun) at positive longitudes (first galactic quadrant), and nearly no shift around  $l = 0^\circ$ . However, the absolute values are exceeding the line-of-sight velocities as would be expected from galactic

rotation only, similar to the  $^{26}\text{Al}$  case, and are even exceeding the bulk-velocities derived from the 1809 keV line, Sec. 4.7.2.

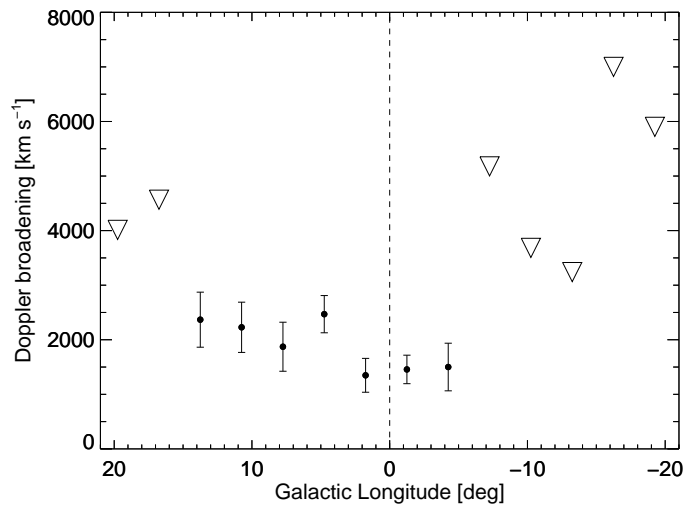


Figure 4.45: Dispersion profile (black dots) of positron annihilation in the inner Galaxy from  $\Delta b = 21.0^\circ$  ROIs. The lines are only well constrained between  $l = -5^\circ$  and  $l = +15^\circ$  and suggest an enhanced Doppler broadening in the inner parts of the Galaxy, although beyond this range the  $2\sigma$  upper limits (triangles) are still consistent with the inner parts. See text for details.

In the inner ridge of the Galaxy, between  $l = +5^\circ$  and  $l = -5^\circ$ , the rotation curve stays flat at a red-shifted value of  $80 \pm 50 \text{ km s}^{-1}$  (receding the Sun). This is surprising, as the bulge region as a whole, from the component-wise analysis, showed essentially no shift with a trend towards the blue side of the line. This indicates variation with galactic latitude, because individual NB and BB components might trace two different annihilation sites. The GCS also shows a residual red-shift of about  $240 \text{ km s}^{-1}$ , which may point to a connection between the inner bulge with an extent of  $\approx \pm 5^\circ$ , rather than to the outer bulge, with an extent of  $\approx \pm 9^\circ$ . A flat rotation curve of positron annihilation in the inner galaxy would suggest a separate region of annihilation in the centre of the Milky Way, which is not, or only marginally, connected to galactic rotation. A constant velocity implies a large dispersion in the region where the positrons annihilate. It would be surprising if the kinematic system in the inner 1.5 kpc of the Milky Way was moving away from Sun in an equilibrium (steady) state. In the range  $-5^\circ < l < 15^\circ$ , the Doppler-broadening can be determined with high significance, Fig. 4.45. The kinematic structure of positron annihilation in the inner Galaxy is reminiscent of a family of stars, which are commonly found in globular clusters, and also in the galactic centre, so-called RR Lyrae (RRL) stars. These stars are used as standard candles for distance measures up to a few hundred kiloparsecs, as their variability in luminosity follows a specific period. They have at most the mass of the Sun, and are about 50 times brighter on average, belonging predominantly to the spectral classes A and F. These stars contain very few other elements than H and He (i.e. small metallicity). This is understood as RRLs having formed in the early phase of the Milky Way, which would makes them to population II stars<sup>15</sup>. Using velocity profiles of RRLs, Kunder et al. (2016) showed that the Milky Way bulge is probably formed from the disk, and that RRLs have kinematics clearly distinct from other (giant) stars in the bulge, Fig. 4.46. The authors hence suggest, that RRLs in the central galactic region may

<sup>15</sup>Populations of stars are classified by their metallicities and ages. The first stars in the Universe, with essentially only hydrogen (no metals), are called population III stars. Population II stars are considered metal-poor. Young and recent stars show a higher metallicity and belong to the population I.

actually be from an inner-halo sample. As positron annihilation seems to follow the same kinematic shape than RRLs, annihilation in stellar atmospheres of such stars may be plausible. A preferred annihilation in such stars may not be physical, if those stars were not also the sources of positrons. This may again point to stellar flare events as major positron annihilation emission sources throughout the Galaxy. However, the absolute dispersion in 511 keV is hard to estimate, because intrinsic annihilation conditions also broaden the gamma-ray line.

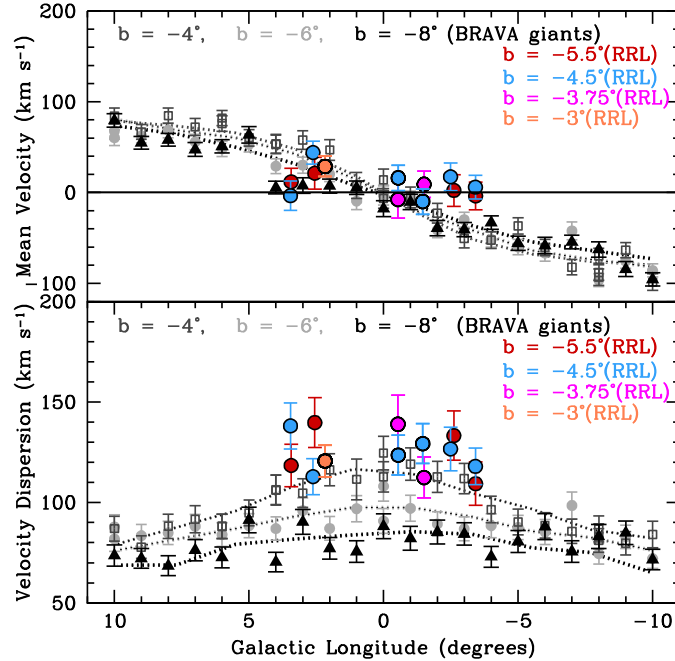


Figure 4.46: Kinematic profiles of RR Lyrae stars in the galactic centre. Shown is the velocity dispersion profile as a function of longitude (bottom) and the rotation curve (top) of RR Lyrae stars (coloured data points) at different latitudes. For comparison, giant stars from the Bulge Radial Velocity Assay (BRAVA) are shown in black and grey. The RR Lyrae stars have different kinematics compared to the remaining stars, pointing to a distinct population. From Kunder et al. (2016).

The longitude-flux profile is following the slice through  $b = 0^\circ$  (Fig. 4.11a), with an offset towards negative longitudes. Then, it follows the slowly declining disk component. The 511 keV line-to-continuum ratio is defined by the total annihilation line flux, divided by the continuum flux between 490 and 530 keV. It peaks at  $l = -9.5^\circ \pm 3.0^\circ$ , with a value of  $1.3 \pm 0.3$ , and decreases on both sides by  $\approx 75\%$  each  $10^\circ$  step. This decrease might again point towards different annihilation conditions in bulge and disk (cf. Sec. 4.6.6). This trend, however, may be questionable, because the gamma-ray continuum around the 511 keV line is composed of o-Ps continuum on the low-energy side, which is not detectable in the  $\Delta l = 3^\circ$  ROIs, and cosmic-ray gamma-continuum on both sides. The significant offset towards negative longitudes in the line-to-continuum ratio may be due to asymmetric galactic ridge emission, or gamma-rays from the nearby Norma spiral arm, increasing the signal.

In summary, the kinematics, annihilation conditions, as well as the gamma-ray morphology advocate for stellar atmospheres to be the true annihilation sites of positrons. This does not mean that the ISM may not be a prime target for positrons to annihilate, but the paradigm of annihilation gamma-rays from interstellar gas, instead of stellar gas, has to be thought over. This may be further explored by additional kinematics studies, and sophisticated modelling of positron transport, also taking into account stars, their magnetic fields, and their atmospheres.

## 5 Candidate Positron Sources

Positron production processes have been illustrated in Sec. 2.2 in a general way. In this chapter, different astrophysical sources will be discussed, which produce (or could produce) positrons in principle. As the true origins of galactic positrons are unknown, contributions from such plausible candidate sources will be estimated, based on both theoretical foundations and direct measurements. Essentially all astrophysical sources can produce positrons, and the fractions for different source types can range from nearly zero, to almost explaining the entire positron population. Here, the candidates are introduced, and gamma-ray measurements will be used to constrain each contribution.

### 5.1 Nucleosynthesis Origins

The most intuitive production mechanism of positrons in space is the  $\beta^+$ -decay of "proton-rich" nuclei. It is experimentally proven in the lab, that positrons are emitted in this process. Also, radioactive decay gamma-rays have been observed in the Universe from a variety of isotopes. Astrophysical positron emitters are listed in Tab. 5.1. During their evolution, massive stars produce heavy nuclei. These are accumulated in the ISM, by the ejection of stellar winds or from core-collapse supernova (CCSN) explosion. Among the most abundant isotopes which are  $\beta^+$ -unstable are  $^{26}\text{Al}$  and  $^{44}\text{Ti}$ . Also low-mass stars can be efficient positron producers, once they turned into a white dwarf (WD) after their main sequence phase. When a WD is disrupted in a thermonuclear type Ia supernova explosion (SN Ia), large amounts of  $^{56}\text{Ni}$  are created. In general, the environments in which those nuclei are produced need to have an excess number of protons, as positron emitters convert bound protons into bound neutrons, and positron emission requires that the mass difference between mother and daughter nucleus is greater than  $511 \frac{\text{keV}}{c^2}$ , Sec. 2.2.1. Radioactive decay of proton-rich nuclei has been one of the first proposed explanations of the galactic 511 keV emission (Clayton 1973). For an over-abundance of protons, hydrostatic equilibrium, like in the core of massive stars, or explosive nucleosynthesis, like in nova or supernova explosions, will lead to the production of such nuclei. In both cases, the requirement for the production is that the proton capture rate must be fast, i.e. it has to occur on shorter time scales than the decay of the corresponding  $\beta^+$ -unstable nuclei. In a typical SN Ia, or in the innermost region of a CCSN, the explosion has a canonical time scale of  $\approx 1$  s. The strong nuclear force, being responsible for the creation of new nuclei, dominates over the weak nuclear force, destroying new nuclei by decay. The initial stellar composition, shortly before the explosion, has predominantly a neutron-to-proton ratio ( $N/Z$ ) of 1.0, for example  $N = Z = 14$  in the case of  $^{28}\text{Si}$  for CCSN, or  $N = Z = 6$  and  $N = Z = 8$  in the case of  $^{12}\text{C}$  and  $^{16}\text{O}$ , respectively, for WDs in a SN Ia. This ratio is essentially conserved during the explosion, but since the last stable nucleus with  $N = Z$  ( $= 20$ ) is  $^{40}\text{Ca}$ ,

proton-rich nuclei which are created during such an explosion from  $\alpha$ -capture then decay to stable nuclei, by either electron capture or the emission of positrons at different branching ratios, depending on the species (Thielemann et al. 2011).

Nuc.	Decay	EC	$\beta^+$	$T_{1/2}$	$\gamma$ -rays	$\langle E_{kin} \rangle$	$E_{kin}^{max}$	Source
$^{13}\text{N}$	$^{13}\text{N} \rightarrow ^{13}\text{C}$	0.2	99.8	10 min	-	493.2	1198.5	Novae
$^{15}\text{O}$	$^{15}\text{O} \rightarrow ^{15}\text{N}$	0.1	99.9	2 min	-	736.7	1735.0	Novae
$^{18}\text{F}$	$^{18}\text{F} \rightarrow ^{18}\text{O}$	3.1	96.9	1.8 h	-	249.5	633.9	Novae
$^{22}\text{Na}$	$^{22}\text{Na} \rightarrow ^{22}\text{Ne}^*$	9.6	90.4	2.6 yr	1274.58 (1.00)	835.0	1821.0	Novae
$^{26}\text{Al}$	$^{26}\text{Al} \rightarrow ^{26}\text{Mg}^*$	18.3	81.7	717 kyr	1808.63 (1.00)	543.3	1173.5	Winds / CCSNe
$^{44}\text{Ti}$	$^{44}\text{Ti} \rightarrow ^{44}\text{Sc}^*$	100.0	0.0	60 yr	67.87 (1.01); 78.36 (1.00)	-	-	CCSNe
	$^{44}\text{Sc} \rightarrow ^{44}\text{Ca}^*$	5.7	94.3	3.97 h	1157.02 (1.00)	632.0	1474.3	CCSNe
$^{56}\text{Ni}$	$^{56}\text{Ni} \rightarrow ^{56}\text{Co}^*$	100.0	0.0	6.1 d	158.38 (0.99); 811.85 (0.86)	-	-	CCSNe / SNe Ia
	$^{56}\text{Co} \rightarrow ^{56}\text{Fe}^*$	80.4	19.6	77.2 d	846.77 (1.00); 1238.29 (0.66)	631.2	1458.9	CCSNe / SNe Ia

Table 5.1: Astrophysically important positron emitting nuclei. The most abundant nuclei from several source types are illustrated, together with the decay chain and branching ratio of the EC and  $\beta^+$  decay mode. If the decay is not proceeding into the ground state of the daughter nucleus, associated gamma-rays energies are given with number of photons per unit disintegration for the most important lines. If positron emission occurs in the decay chain, the average ( $\langle E_{kin} \rangle$ ) and end point ( $E_{kin}^{max}$ ) energy of the  $\beta^+$ -decay positron is given. Typical uncertainties on the line energies are of the order of 0.01 keV, and for the kinetic energies of the emitted positron of the order 0.1-1 keV. For additional gamma-ray lines, see Tab. A.1 in Appendix. A.

### 5.1.1 Positrons from Stars

During the majority of their evolution, stars produce He nuclei by the fusion of H in the so-called pp-cycles. In order to produce heavier nuclei, other, more energetic nuclear reactions have to take place, which is only possible if the initial mass of the star is large enough. For such massive stars ( $> 25M_{\odot}$ ), stellar winds become significant contributors to enrich the ISM with freshly produced nuclei. Also core-collapse supernovae play an important role to inject heavy nuclei into the Galaxy, once the star ran out of nuclear fuel. These nuclei will contribute to the galactic positron content, if they have the chance to escape from the star, and if they are  $\beta^+$ -unstable. This then depends on the isotope abundances and life-times. Therefore, stellar evolution, i.e. the processing of an initial composition of a star during its evolution towards heavier nuclei, the ejection of new elements into the ISM by winds and supernovae, and the interplay between many of such stars in groups, is a crucial factor in the contribution of radioactivities to the positron puzzle.

#### 5.1.1.1 Stellar Evolution

In general, a star can be considered a self-gravitating gas sphere in hydrostatic equilibrium,

$$\frac{dP}{dr} = -\frac{GM\rho}{r^2}, \quad (5.1)$$

where  $P$  is the star's pressure,  $M$  its mass, and  $\rho$  its density at a position  $r$  inside the stellar radius  $R$ . The mass of a virialised star as a function of density and radius is given by

$$dM = 4\pi\rho r^2 dr. \quad (5.2)$$

Assuming the equation of state of an ideal gas,

$$pV = Nk_B T \Leftrightarrow p\mu = \rho k_B T, \quad (5.3)$$

a zero-order estimation of the central temperature in a star can be derived:

$$T \propto \frac{M}{R} \quad (5.4)$$

As different nuclear reactions, i.e. burning phases of a star, critically depend on the temperature in a way that higher-order nuclei are usually created at higher temperatures, massive stars are the main producers of heavy elements. Typically, the energy production rate per mass and time,  $\epsilon_{it}^{nuc}$ , for initial particles  $i$  towards target particles  $t$ , is expressed as

$$\epsilon_{it}^{nuc} = \epsilon_0^{nuc} X_i X_t \rho T^\beta. \quad (5.5)$$

Here,  $\epsilon_0^{nuc}$  is a process-specific constant,  $X_{i/t} = \frac{M_{i/t}}{M_{tot}}$  are the relative mass-fractions of the incident and target nucleus with respect to the total mass of nuclei participating in that particular reaction,  $M_{tot}$ , and  $\beta = \beta(T)$  ranges between 1 and  $\approx 49$ , depending on the process.

Once a star exceeds a mass of  $0.08 M_\odot$ , the temperature in the centre can reach  $\approx 10$  MK, enough to start hydrogen burning via the PP-chain. The basic reaction is a conversion of four protons into one helium nucleus ( $\alpha$  particle), which can be subdivided into three different branches, as shown in Tab. 5.2. The energy production rate of the PP-chain is proportional to  $T^4$ , and is the main indicator of a star being on the main-sequence of stellar evolution. This main-sequence is defined as the time in which a star burns 10% of its initial hydrogen. In general, the evolutionary time scale of a star,  $t_E \approx 7.3 \times 10^9 \frac{M/M_\odot}{L/L_\odot}$  yr, describes that the more massive a star is, the higher is its burning rate  $\epsilon$ , and thus its luminosity  $L \propto \epsilon \propto T^\beta$ . In consequence, massive stars have a shorter main-sequence life-time, and can be considered efficient producers of positrons in the Galaxy. In fact, already in the PPI- and PPIII-chain, positrons are produced which, however, cannot escape the star's interior. These annihilate with electrons inside the star, and support the radiation pressure. At temperatures above  $\approx 23$  MK, the CNO cycle starts to provide nuclear energy with a production rate,  $\epsilon_{CNO} \propto T^{17}$ . In this burning phase, C, N, and O nuclei, predominantly built from earlier generations of stars, function as catalysts to produce further  $\alpha$  particles, cf. Tab. 5.2.

When a star is massive enough to reach a temperature of  $40 - 50$  MK, another CNO sub-branch, the NeNa-cycle, involving  $^{20}\text{Ne}$ ,  $^{21}\text{Ne}$ ,  $^{22}\text{Ne}$ , and  $^{23}\text{Na}$ , opens to produce even heavier nuclei. Around  $\approx 60$  MK, the equilibrium abundances of all nuclei between  $^{20}\text{Ne}$  and  $^{27}\text{Al}$  are reached, so that also the long-lived  $\beta^+$ -unstable isotope  $^{26}\text{Al}$  is produced. This happens during the NeNaMgAl-cycle, see Fig. 5.1. The  $^{26}\text{Al}$  nuclei are then either dredged up to the stellar surface and ejected by winds, for example in Wolf-Rayet stars, or injected into the ISM at the supernova explosion.

ppI, main sequence, all stars: $0.08 \leq M/M_{\odot} \leq M_{max}$ ; $10 \text{ MK} \leq T \lesssim 14 \text{ MK}$	He burning, triple- $\alpha$ -process: $T \gtrsim 100 \text{ MK}$ , He core masses $M_C \approx 0.2 - 0.45 M_{\odot}$
$p + p \rightarrow d + e^+ + \nu_e$ (1.442) $d + p \rightarrow {}^3\text{He}$ (1.442) ${}^3\text{He} + {}^3\text{He} \rightarrow {}^4\text{He} + 2p$ (12.860)	$\alpha + \alpha \rightarrow {}^8\text{Be}$ (-0.092) ${}^8\text{Be} + \alpha \rightarrow {}^{12}\text{C}$ (7.367)
ppII: $14 \text{ MK} \lesssim T \lesssim 23 \text{ MK}$	C burning, massive stars: $M \gtrsim 8M_{\odot}$ , $T \gtrsim 500 \text{ MK}$
${}^3\text{He} + {}^4\text{He} \rightarrow {}^7\text{Be}$ (1.587) ${}^7\text{Be} + e^- \rightarrow {}^7\text{Li} + \nu_e$ (0.862) ${}^7\text{Li} + p \rightarrow {}^8\text{Be} \rightarrow \alpha + \alpha$ (17.347)	${}^{12}\text{C} + {}^{12}\text{C} \rightarrow {}^{20}\text{Ne} + \alpha$ ${}^{12}\text{C} + {}^{12}\text{C} \rightarrow {}^{23}\text{Na} + p$ ${}^{23}\text{Na} + p \rightarrow {}^{20}\text{Ne} + \alpha$ ${}^{23}\text{Na} + p \rightarrow {}^{24}\text{Mg}$
ppIII: $T \gtrsim 23 \text{ MK}$	${}^{12}\text{C} + \alpha \rightarrow {}^{16}\text{O}$
${}^3\text{He} + {}^4\text{He} \rightarrow {}^7\text{Be}$ (1.587) ${}^7\text{Be} + p \rightarrow {}^8\text{B}$ (0.14) ${}^8\text{B} \rightarrow {}^8\text{Be} + e^+ + \nu_e \rightarrow \alpha + \alpha$ (18.069)	Ne burning: $T \gtrsim 120 \text{ MK}$
CNO main cycle: dominant for stars with $M \gtrsim 1.3M_{\odot}$ , $T \gtrsim 23 \text{ MK}$	${}^{20}\text{Ne} + \gamma \rightarrow {}^{16}\text{O} + \alpha$ ${}^{20}\text{Ne} + \alpha \rightarrow {}^{24}\text{Mg}$ ${}^{24}\text{Mg} + \alpha \rightarrow {}^{28}\text{Si}$
${}^{12}\text{C} + p \rightarrow {}^{13}\text{N}$ (1.944) ${}^{13}\text{N} \rightarrow {}^{13}\text{C} + e^+ + \nu_e$ (2.220) ${}^{13}\text{C} + p \rightarrow {}^{14}\text{N}$ (7.551) ${}^{14}\text{N} + p \rightarrow {}^{15}\text{O}$ (7.297) ${}^{15}\text{O} \rightarrow {}^{15}\text{N} + e^+ + \nu_e$ (2.754) ${}^{15}\text{N} + p \rightarrow {}^{12}\text{C} + \alpha$ (4.966)	O burning: $M \gtrsim 9M_{\odot}$ , $T \gtrsim (150..260) \text{ MK}$
CNO sub-cycle: $25 \text{ MK} \lesssim T \lesssim 30 \text{ MK}$	${}^{16}\text{O} + {}^{16}\text{O} \rightarrow {}^{28}\text{Si} + \alpha$ ${}^{16}\text{O} + {}^{16}\text{O} \rightarrow {}^{31}\text{P} + p$ ${}^{16}\text{O} + {}^{16}\text{O} \rightarrow {}^{31}\text{S} + n$ ${}^{31}\text{S} \rightarrow {}^{31}\text{P} + e^+ + \nu_e$
NeNaMgAl sequence, also AGB stars: $40 \text{ MK} \lesssim T \lesssim 60 \text{ MK}$	Si burning: $M \gtrsim 8..11M_{\odot}$ , $T \gtrsim (2.7..3.5) \text{ GK}$
${}^{15}\text{N} + p \rightarrow {}^{16}\text{O}$ (12.127) ${}^{16}\text{O} + p \rightarrow {}^{17}\text{F}$ (0.600) ${}^{17}\text{F} \rightarrow {}^{17}\text{O} + e^+ + \nu_e$ (2.761) ${}^{17}\text{O} + p \rightarrow {}^{14}\text{N} + \alpha$ (1.192) ${}^{17}\text{O} + p \rightarrow {}^{18}\text{F}$ (5.607) ${}^{18}\text{F} \rightarrow {}^{18}\text{O} + e^+ + \nu_e$ (1.656) ${}^{18}\text{O} + p \rightarrow {}^{15}\text{N} + \alpha$ (3.981) ${}^{18}\text{O} + p \rightarrow {}^{19}\text{F}$ (7.994)	${}^{28}\text{Si} + {}^{28}\text{Si} \rightarrow {}^{56}\text{Ni}$ ${}^{28}\text{Si} + (1..7)\alpha \rightarrow {}^{32}\text{S}..{}^{56}\text{Ni}$
${}^{20}\text{Ne} + p \rightarrow {}^{21}\text{Na}$ (5.979) ${}^{21}\text{Na} \rightarrow {}^{21}\text{Ne} + e^+ + \nu_e$ (3.548) ${}^{21}\text{Ne} + p \rightarrow {}^{22}\text{Na}$ (6.739) ${}^{22}\text{Na} \rightarrow {}^{22}\text{Ne} + e^+ + \nu_e$ (2.842) ${}^{22}\text{Ne} + p \rightarrow {}^{23}\text{Na}$ (8.794) ${}^{23}\text{Na} + p \rightarrow {}^{20}\text{Ne} + \alpha$ (2.377) ${}^{23}\text{Na} + p \rightarrow {}^{24}\text{Mg}$ (11.693) ${}^{24}\text{Mg} + p \rightarrow {}^{25}\text{Al}$ (6.548) ${}^{25}\text{Al} \rightarrow {}^{25}\text{Mg} + e^+ + \nu_e$ (4.277) ${}^{25}\text{Mg} + p \rightarrow {}^{26}\text{Al}$ (6.307) ${}^{26}\text{Al} \rightarrow {}^{26}\text{Mg} + e^+ + \nu_e$ (4.004) ${}^{26}\text{Al} + p \rightarrow {}^{27}\text{Si}$ (12.275) ${}^{26}\text{Mg} + p \rightarrow {}^{27}\text{Al}$ (8.271) ${}^{27}\text{Si} \rightarrow {}^{27}\text{Al} + e^+ + \nu_e$ (4.812) ${}^{27}\text{Al} + p \rightarrow {}^{28}\text{Si}$ (11.585) ${}^{27}\text{Al} + p \rightarrow {}^{24}\text{Mg}$ (1.601)	

Table 5.2: Excerpt of nuclear reactions inside stars. The PP-chains I, II, and III are representing the main-sequence phase of a star, i.e. also for low-mass stars. For each reaction,  $Q_{\text{tot}}$  is the released energy due to the mass defect in units of MeV, given in brackets if available. In addition, the mass ranges, star types, reaction rates, and temperatures at which the processes are dominant are listed for which these reactions can occur. After Lugaro & Chieffi (2011), Thielemann et al. (2011), and Karakas & Lattanzio (2014).

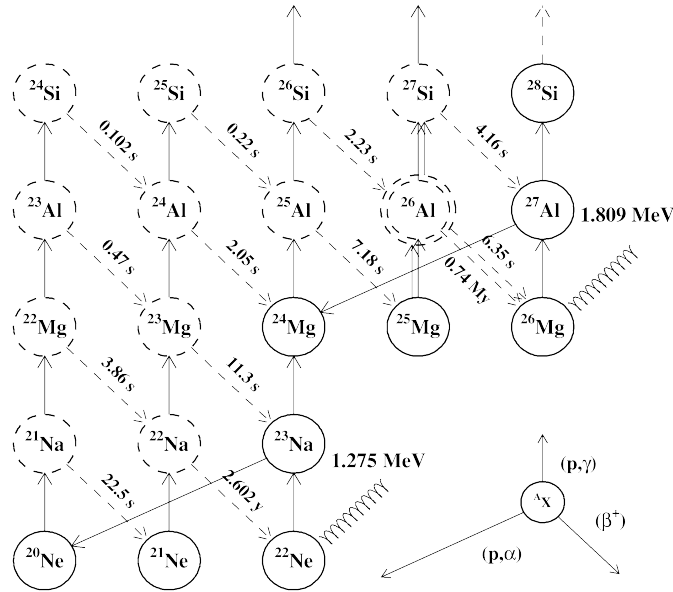


Figure 5.1: Main paths of the NeNaMgAl sequence from José et al. (2006). Shown are the participating isotopes towards the production of  $^{26}\text{Al}$ , where dashed circles denote unstable and closed circles stable isotopes. The half life time of the intermediate nuclei and characteristic gamma-ray energies are also given.

When a star burns towards heavier elements, its central density is increasing, and thus will also be hotter in its interior. The star does not cool efficiently by the emission of electromagnetic radiation then, which makes the emission of neutrinos an important process of cooling, as they can leave the surface nearly unhindered. The model paths of massive stars with  $15 M_{\odot}$  and  $25 M_{\odot}$  are illustrated in Fig. 5.2. In general, the  $\rho \propto T^3$  behaviour expected from fundamental stellar evolution equations is evident. Deviations from such an idealised path come from the ignition points of different burning stages. The triple- $\alpha$  reaction, burning three  $\alpha$ -particles to one carbon nucleus, then already proceeds at an energy production rate,  $\epsilon \propto T^{40}$ . Its ignition is accompanied by a large jump in luminosity and radius of the star. Stars have to be massive enough that, when they run out of hydrogen in their cores, they contract (i.e. they begin to collapse) until the central temperature rises up to  $10^8$  K. Then, also the density is high enough for  $\alpha$ -particles to fuse and to produce significant amounts of carbon directly. In addition, matter is ejected into the ISM, and the star can peel off itself, and may shorten its life as a burning star further.

Once the star ignites silicon burning towards iron, its fate has come, now containing all elements up to  $^{56}\text{Fe}$ . The iron-peak elements have the highest binding energy per nucleon of all isotopes, and the star cannot gain more energy by nuclear fusion. The pressure source from the interior runs dry and gravity wins - the star collapses. In 1D supernova models<sup>1</sup>, the interior, just before the collapse, is found as an onion like structure with layers of  $^1\text{H}$ ,  $^4\text{He}$  (with shares of  $^{12}\text{C}$ ,  $^{16}\text{O}$ , and  $^{22}\text{Ne}$ ), several  $^{16}\text{O}$  layers, also containing  $^{12}\text{C}$ ,  $^{20}\text{Ne}$ ,  $^{24}\text{Mg}$ ,  $^{28}\text{Si}$  and  $^{32}\text{S}$ , a Si-S-Ar layer, and the "iron"-core (Woosley et al. 2002). When the iron core reaches its Chandrasekhar mass-limit, it collapses by free-fall until the density reaches  $\gtrsim 2 \times 10^{16} \frac{\text{g}}{\text{cm}^3}$  in the case of a  $25 M_{\odot}$  star, for example. This will heat its interior up to temperatures of 5-10 GK. Thermal gamma-rays will photodisintegrate the iron-core nuclei, and a neutron star of  $\approx 10$  km size has emerged within typically one second. At that time,

<sup>1</sup>The onion like structure with heavy elements inside and lighter elements near the surface is not appropriate as 3D effects, rotation, and convection will lead to a more complicated scheme (Woosley et al. 2002).

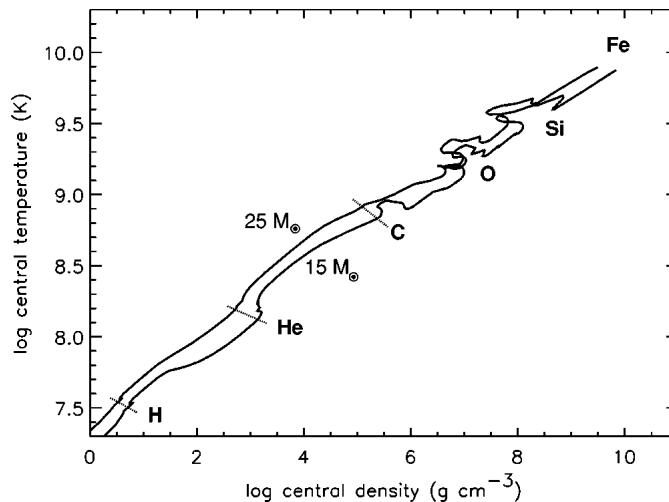


Figure 5.2: Evolution of massive stars as a function of density and temperature for a  $15M_{\odot}$  and  $25M_{\odot}$  star from hydrogen burning towards iron-core collapse; from Woosley et al. (2002). The zero-order ideal trajectory  $\rho \propto T^3$  is clearly seen as the star contracts to fuse heavier nuclei and thereby heats. Nonmonotonic behaviour is due to ignitions of higher burning phases.

the upper layers have not noticed that the core shrank to a compact object, which is sending out a shock-wave after the innermost layers bounced off the core. The ingoing layers are being photo-dissociated, and, if the shock-wave is strong enough, the remaining layers are peeled off, enriching the ISM with stellar produced nuclei. More details about CCSNe and nuclei produced and ejected will be discussed in Sec. 5.1.2. In the following Sec. 5.1.1.2, the contribution of  $^{26}\text{Al}$  to the galactic positron content will be discussed.

#### 5.1.1.2 Beta-Unstable Al-26 as Natural Positron Producer

The long-lived isotope  $^{26}\text{Al}$  is produced during the NeNaAlMg cycle, by not only massive stars but also AGB stars. The abundances of Mg and Al are altered in an H-burning shell via the activation of the MgAl-chain (upper right part of Fig. 5.1) at around 60 MK, rather than in the core of a massive star or at the bottom of convective envelopes in AGB stars. It is created by the proton-capture reaction  $^{25}\text{Mg}(p, \gamma)^{26}\text{Al}$ , which is very sensitive to temperature.  $^{26}\text{Al}$  can be easily destroyed again by neutron-capture reactions, such as  $^{26}\text{Al}(n, p)^{26}\text{Mg}$  or  $^{26}\text{Al}(n, \alpha)^{23}\text{Na}$ . In bottom layers of the H-burning shell, and during convective pulses, the temperatures can easily reach 90 MK and 200 MK, respectively, high enough for the neutron donating process  $^{13}\text{C}(\alpha, n)^{16}\text{O}$  to become very efficient. If the temperature increases beyond 250 MK in convective pulses, also the process  $^{22}\text{Ne}(\alpha, n)^{25}\text{Mg}$  originates more neutrons, which destroy even more of the  $^{26}\text{Al}$ -abundance. In general, the yield of  $^{26}\text{Al}$ , i.e. the amount of  $^{26}\text{Al}$  which is ejected into the ISM by winds and supernovae, depends on three factors. These are the reaction rate of converting  $^{25}\text{Mg}$  into  $^{26}\text{Al}$ , the amount of  $^{25}\text{Mg}$  initially available, and the amount of  $^{26}\text{Al}$  destruction.  $^{26}\text{Al}$  has to be dredged up into the stellar surface, and will eventually be ejected in the stellar winds during the Wolf-Rayet phase of a massive star, or during the supernova explosion. Calculated  $^{26}\text{Al}$  yields range from  $10^{-7}M_{\odot}$  for 1-4 $M_{\odot}$  AGB stars, and up to  $10^{-4}M_{\odot}$  for larger initial star masses. The contribution from AGB stars to the total galactic  $^{26}\text{Al}$  abundance is probably low compared to supernova yields. But

AGB stars have been undoubtedly identified as  $^{26}\text{Al}$  producers by the discovery of  $^{26}\text{Al}$  in meteorite grains and presolar dust. After stellar evolution, also a fraction  $^{26}\text{Al}$  is destroyed again, as a shock front, released by the core-collapse supernova explosion, will propagate through the stellar envelope. However, it might also be formed during explosive nucleosynthesis again (Thielemann et al. 2011).

The third dredge-up brings most of the newly produced nuclei to the stellar surface, where they are carried away by strong stellar winds. The origin of these winds are radiation pressure acting on large amounts of dust and gas that have been formed around AGB stars. Another origin is the luminosity variability of AGB stars, which is caused by stellar pulsation. During pulsations, the star contracts and expands, i.e. a de- and increase of the radius, and thus an in- and decrease of the temperature, will be followed by a change in luminosity. Stellar winds have different velocities depending on the origins; while strong and dense winds (called superwinds) have relatively low velocities of 5-30 km/s, with a huge mass loss rate of  $10^{-4} M_{\odot}/\text{yr}$ , normal hydrogen burning main sequence stars like the Sun show terminal velocities of a few 100 km/s, and a mass loss rate of  $10^{-11} M_{\odot}/\text{yr}$  (Lugaro & Chieffi 2011). Wolf-Rayet stars eject nuclei with even higher speeds of up to 4000 km/s, losing  $\sim 0.1\%$  of their mass per year (Kippenhahn & Weigert 1990). Due to the combined forces of radiation pressure and pulsation at the end of the AGB phase, the extended stellar envelopes where molecules like CO, TiO or ZrO found good conditions (temperatures  $\sim 1000$  K) to form, can be completely eroded (Willson 2000). An AGB star might also illuminate its own shell, which is then called a planetary nebula. At the end of a star's evolution, when no more fuel is available, the planetary nebula nucleus turns into a WD. However, the  $^{26}\text{Al}$  output of stellar winds is dominated by Wolf-Rayet stars, since they have by far the most intense winds.

Wolf-Rayet stars evolve very quickly as they are part of the normal evolutionary stages of O stars. For example, a typical  $25 M_{\odot}$  Wolf-Rayet star has a life-time around a few million years. Their strong stellar winds blow out the material into their surroundings, also including freshly produced  $^{26}\text{Al}$ . Depending on the initial mass, different evolution models are proposed: In the mass-range above  $\sim 30 M_{\odot}$ , every evolutionary sequence is starting with an O-type main-sequence star. Its next stage is either a red or blue supergiant (R/BSG), or a luminous blue variable (LBV) (Meynet et al. 2011). The extreme stellar winds in those phases are ejecting the unprocessed outer H-rich layer, for which reason the nitrogen-rich products of the CNO-cycle are uncovered (WN stars). Later, also the carbon-rich layers which originated from He-burning are uncovered (WC and WO stars), resulting in a complex internal structure. Whole layers can be repelled, which afterwards mix with the ISM, and make Wolf-Rayet stars to the main contributors to galactic  $^{26}\text{Al}$ . If the radiation pressure cannot prevent the remaining layers to fall into the centre (core-collapse supernova, see also Sec. 5.1.2), the supernova of the Wolf-Rayet star again ejects  $^{26}\text{Al}$  into the ISM.

Once  $^{26}\text{Al}$  is created and ejected, it accumulates inside large cavities ("superbubbles") which have been blown by previous supernova explosions and winds. These cavities are surrounded by shells of neutral hydrogen (HI). Usually, massive stars do not evolve separated from each other, but are created simultaneously in OB associations. With typical ages between  $\approx 1$  and 20 Myr, these regions are young, compared to

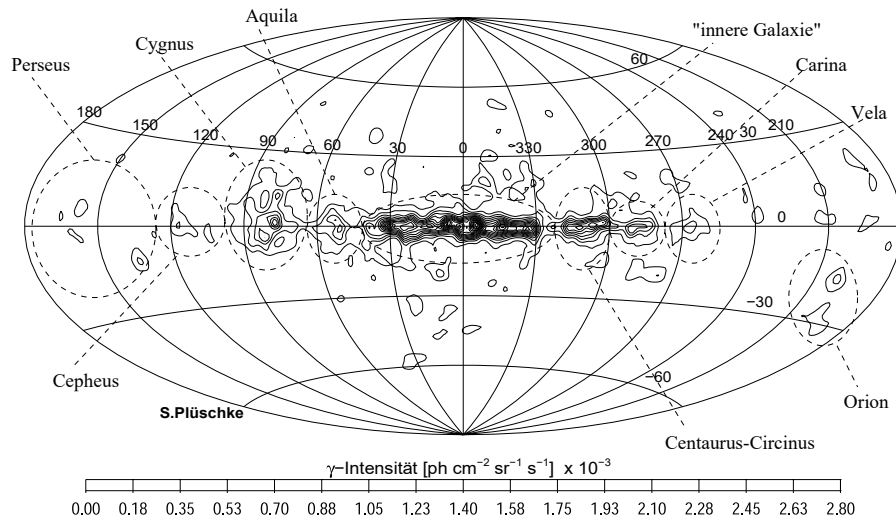


Figure 5.3: COMPTEL sky survey  $^{26}\text{Al}$  maximum entropy map iteration 7. The map shows the galactic 1809 keV emission (17 contour-lines) together with important, also probable foreground, emission regions, based on all COMPTEL observations. From Plüschke (2001).

the age of the Milky Way ( $> 10$  Gyr), and thus suitable to investigate and observe stellar formation and nucleosynthesis. Stars belonging to such an OB association have formed out of the same volume inside a molecular cloud, and at nearly the same time, with a distribution width of a million years. As O- and B-type stars are short-lived and will explode in a CCSN only a few million years after formation, OB associations are limited to tens of million years. O and B stars hence dominate the enrichment of the ISM, at least in the case of  $^{26}\text{Al}$ , albeit this short time scale. Supernovae may then trigger new star formation in neighbouring molecular clouds, if the gas pressure cannot counteract its own gravity any more. This situation can be estimated by the Jeans mass,  $M_J = \left(\frac{3}{4\pi\rho}\right)^{1/2} \left(\frac{5k_B T}{G\mu}\right)^{3/2}$ , i.e. the mass at which gravity wins against radiation pressure. Such a compression can either happen due to the accumulation of enough mass in the cloud (self-acting star formation), or by shock-waves, which are sent out by preceding supernova explosions (triggered star formation). The stellar content of an OB association can be described empirically by an initial mass function,

$$\frac{dN}{dM} \propto M^{-(\Gamma+1)}, \quad (5.6)$$

counting the number of stars in a given mass interval  $[M, M + dM]$ . The index  $\Gamma$  in Eq. (5.6) is of the order of 1 with dependencies in different mass regimes (Kroupa 2001). In general, there are only few massive stars among a large population of low-mass stars. Besides the mass and stellar content of OB associations, their sizes vary according to their ages and current shell velocity. The older an association is, the larger it is in general. Typical sizes are between 50 and 400 pc. The yield of  $^{26}\text{Al}$  from one star depends on its initial mass such that more massive stars tend to yield more  $^{26}\text{Al}$  ejecta. In groups of stars, the cumulative effect of many different initial masses have to be taken into account. Using gamma-ray observations of decaying  $^{26}\text{Al}$  with a half-life time of 717 kyr, Sec. 5.1.1.3, a snapshot of the current  $^{26}\text{Al}$  production can be determined. The temporal evolution of such an association is not

traced. The forward modelling of an entire population of stars can be studied in a population synthesis simulation. This includes an initial amount of stars, according to a specific initial mass function, and with different yields in wind phases and supernovae. Massive stars then happen to explode in the first million years after the creation of the star group, for which reason the further  $^{26}\text{Al}$  production is inhibited, as the remaining (AGB) stars only contribute  $\approx 1\%$  of the observed  $^{26}\text{Al}$ . Voss et al. (2009) modelled such a scenario for a group of 100 massive stars in the mass range between  $8\text{-}120M_{\odot}$ . The resulting yields are shown in Fig. 5.4. While  $^{26}\text{Al}$  is produced and ejected also during the wind phases after only  $\approx 1$  Myr, the radioactive isotope  $^{60}\text{Fe}$  which is only produced and ejected in explosive nucleosynthesis of a CCSN, shows a sharp ascent right at the time of the first explosion around 3.8 Myr. The total ejected  $^{26}\text{Al}$  mass is dominated by the wind phases within the first ten million years (Voss et al. 2009). Adjusting the stellar content to a realised OB association, such as Cyg OB2, and comparing the results with measurements, helps to constrain stellar evolution models of massive stars (Martin et al. 2010).

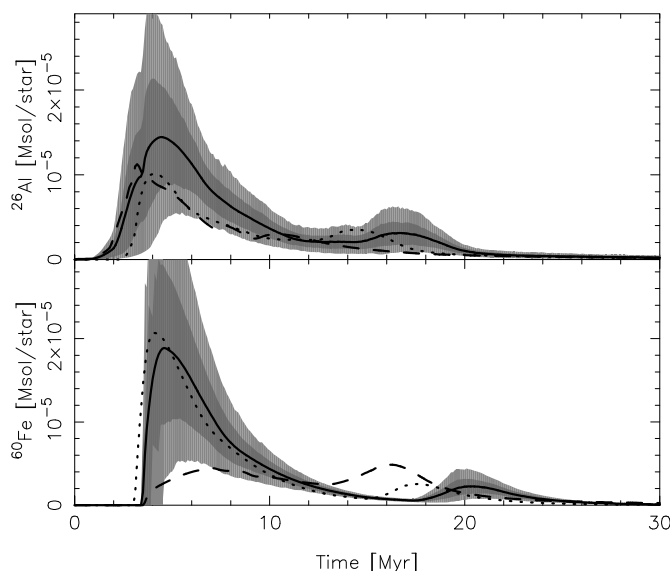


Figure 5.4: Time profiles of  $^{26}\text{Al}$  (top) and  $^{60}\text{Fe}$  (bottom) for a coeval population of stars. The solid, dashed, and dotted lines indicate average profiles for different stellar models and different yield models. The dark and light grey regions show the  $1\sigma$  and  $2\sigma$  uncertainties for a population of 100 stars between 8 and  $120M_{\odot}$ , based on Monte Carlo simulations. From Voss et al. (2009).

The decay scheme of  $^{26}\text{Al}$  is shown in Fig. 5.5. After it decayed to an excited state of  $^{26}\text{Mg}$  in a characteristic life time of  $\approx 1$  Myr,  $^{26}\text{Mg}^*$  de-excites by the emission of a 1808.63 keV gamma-ray to its ground state. Arnett (1969b) predicted a significant amount of  $^{26}\text{Al}$  from carbon burning of massive stars and supernovae (Arnett & Truran 1969; Arnett 1969b), of which gamma-rays, from the subsequent decay, should be detectable in the Milky Way (Clayton 1971, precisely from the decay of  $^{60}\text{Fe}$ ). This would show ongoing nucleosynthesis in the Universe. In 1984, the 1809 keV line from  $^{26}\text{Al}$  was detected by Mahoney et al. (1984) from the direction of the galactic centre, using the High Energy Astronomy Observatory (HEAO). A detailed map of the  $^{26}\text{Al}$  distribution in Milky Way was presented in Oberlack et al. (1996), showing the clear coincidence of 1809 keV emission with massive star groups, see Fig. 5.3. The COMPTEL map shows emission spots nearby, and at large distances. While at neighbouring OB associations like the Scorpius-Centaurus (ScoCen), Orion, or Cygnus associations, the gamma-ray flux is found within a rather defined region, the galactic ridge and extended plane is a superposition of

many stellar populations, emitting gamma-rays from the decay of  $^{26}\text{Al}$ .

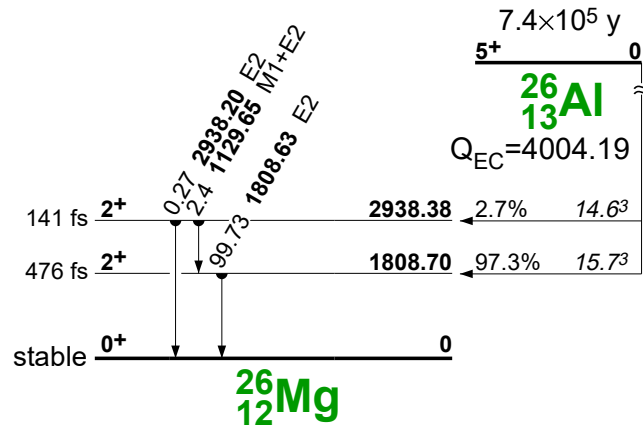


Figure 5.5: Decay scheme of  $^{26}\text{Al}$  with a half-life time of 717 kyr to  $^{26}\text{Mg}$  via positron emission (81.73%) or electron capture (18.27%) and a total energy of 4004.19 MeV. The main branch is the decay to a  $2^+$  state of  $^{26}\text{Mg}$  with a half life time of 476 fs, afterwards de-exciting by the emission of gamma-ray with an energy of 1808.63 keV. Other transitions are also shown; from Firestone et al. (1996).

Using the spectrometer SPI on INTEGRAL, it was then possible to provide high-resolution spectra of the 1809 keV gamma-ray line, thereby deriving exact kinematics of the Galaxy (Kretschmer et al. 2013), and individual associations (Diehl 2002; Diehl et al. 2010; Martin et al. 2010), by Doppler measurements (see also Sec. 4.7.2). In addition, exact line fluxes provided the current (i.e. on a time-scale of 1 Myr) mass of  $^{26}\text{Al}$  in the Milky Way, which contributes as a steady positron producer in the galactic plane. The  $\beta^+$ -decay (positron emission) of  $^{26}\text{Al}$  is hence accompanied by the emission a 1809 keV gamma-ray. However, the position from which the photon is detected does not coincide with where  $^{26}\text{Al}$  has formed, and also does not coincide with the position where the positron finally annihilates in the ISM, due to propagation (see Sec. 4.6.6). Therefore, the total mass will provide insights in how much  $^{26}\text{Al}$  actually contributes to the positron content in Galaxy. As gamma-rays are not hindered by galactic reddening or dust, they are detected from particular directions as superpositions of foreground and background sources. In order to estimate the total  $^{26}\text{Al}$  mass in the Milky Way, the foreground sources have to be taken into account, as their fluxes may dominate over the remaining galactic emission. In the following sections, the 13-year SPI data set, Sec. 4.7.2, will be used to disentangle different  $^{26}\text{Al}$  emission regions from each other, towards a total mass estimate of  $^{26}\text{Al}$  in the Milky Way. Parts of the results have been presented in Siegert & Diehl (2016).

### 5.1.1.3 Large- and Small-Scale 1809 keV Emission

#### 5.1.1.3.1 Galactic Structure

From previous studies (e.g. Diehl et al. 1995; Oberlack et al. 1996; Knödlseeder et al. 1999; Diehl et al. 2006), it is known that the 1809 keV emission is tracing massive star groups in the Milky Way. This young population of stars is found concentrated along the galactic plane (Diehl et al. 1995), but the associated gamma-ray emission from the decay of ejected  $^{26}\text{Al}$  seems to precede the massive star groups (Krause et al.

2015). This is derived from kinematic Doppler measurements (Kretschmer et al. 2013, see also Sec. 4.7.2). Out to a few kpc, the distribution and content of massive stars in the Galaxy is well known, but further away, many regions in the Milky Way are occulted by dust, so that direct measurements with optical telescopes are not possible. Gamma-rays pass such occulting regions, and thus provide information about the true content of this type of stars, and properties of the total population. Uncertainties arise about the Galaxy-wide interpretation of this gamma-ray signal, as there are localised and efficient  $^{26}\text{Al}$ -producing regions in the foreground. These emissions are superimposed in the data space.

As in the case for the 511 keV emission in the Galaxy, an astrophysically biased forward modelling approach will be conducted, as the emission morphology is already very well characterised, and sources are identified. In addition, three-dimensional emission models can be used as the structure and appearance of the Milky Way is also well known, at least up to several kpc. Also distant spiral galaxies can be used to find a valid description of the data. These show an exponential decreasing profile of their visible light further away from their centres, and a certain thickness (Longair 2008). An adequate first-order emission model for the galactic  $^{26}\text{Al}$  distribution is therefore an exponential disk with scale radius  $R_0$  and scale height  $z_0$ . Here, the Sun is located at a position  $(x_s/y_s/z_s)$  from the centre of the Galaxy, where  $s_0 = \sqrt{x_s^2 + y_s^2 + z_s^2} = 8.5$  kpc is the distance of the Sun to the centre. Without loss of generality,  $x_s$  can be chosen as 8.5 kpc and  $y_s$  then equals 0. The vertical distance of the Sun with respect to the galactic plane,  $z_s$ , is a matter of debate<sup>2</sup> (e.g. Humphreys & Larsen 1995; Dehnen & Binney 1998; Joshi 2007; Schönrich et al. 2010; Karim & Mamajek 2016) but is probably restricted to  $0 < z_s < 200$  pc. For this study,  $z_s$  is chosen as 0, i.e. the Sun is assumed to be exactly in the disk without an offset. The exponential disk model then reads

$$\rho(R, z) = A_0 \exp\left(-\left(\frac{R}{R_0} + \frac{|z|}{z_0}\right)\right) \text{ with } R^2 = x^2 + y^2, \quad (5.7)$$

and with  $A_0$  the fitted amplitude of the disk in each energy bin. From the 3D emission density profile, which is defined in the source frame (here centre of the Galaxy at  $(x/y/z) = (0/0/0)$ ), the sky intensity (emission morphology) in the direction  $(l/b)$  is calculated by the path integral (line-of-sight integration)

$$f(l/b) = \frac{1}{4\pi} \int_{s_{min}}^{s_{max}} \rho(x_s + s \cdot u_x, y_s + s \cdot u_y, z_s + s \cdot u_z) ds. \quad (5.8)$$

Here,  $\vec{u} = (\cos(l) \cos(b) / \sin(l) \cos(b) / \sin(b))$  is the unit vector of the line of sight in spherical (celestial galactic) coordinates, and  $s_{min/max}$  are the integration boundaries, deduced from the volume definition that is used to characterise the Milky Way and the maximum integration length about this volume. In Eq. (5.8), and for a certain pixel size,  $f(l/b)$  therefore defines a scalar (flux, intensity per pixel) for each position in the sky. The luminosity over the whole map with solid angle element  $d\Omega$  is then calculated from the density along the line-of-sight, weighted with the

<sup>2</sup>In fact, with such a 3D emission model, the relative position of the Sun with respect to the galactic plane, for a given radial distance, can be determined by gamma-ray measurements.

distance squared,

$$L = \int_{map} \int_{s_{min}}^{s_{max}} \rho(x_s + s \cdot u_x, y_s + s \cdot u_y, z_s + s \cdot u_z) s^2 ds d\Omega. \quad (5.9)$$

Earlier measurements from the inner Galaxy,  $|l| < 30^\circ$ ,  $|b| < 10^\circ$ , suggested that the scale height is around 80-200 pc (Diehl et al. 2006) or 60-250 pc (Wang et al. 2009), using a fixed scale radius of 4 kpc. In order to determine a galactic-wide measure for the  $^{26}\text{Al}$  emission, a grid of  $32 \times 64$  (=2048 disk models) combinations of  $R_0$  and  $z_0$  has been built, convolved with the coded-mask imaging response of SPI, and fitted to the 13-year data set. The scale radius  $R_0$  was chosen to range from 0.50 to 8.25 kpc in 250 pc steps, whereas  $z_0$  was chosen between 10 and 475 pc in 15 pc steps, and between 500 and 2050 pc in 50 pc steps. In Fig. 5.6, the best fit parameters from the maximum likelihood estimation is shown, together with the marginalised probability density functions for the scale radius and scale height, respectively. The tested grid points (upper right panel in Fig. 5.6) show the completeness of tested models in this two-dimensional parameter space.

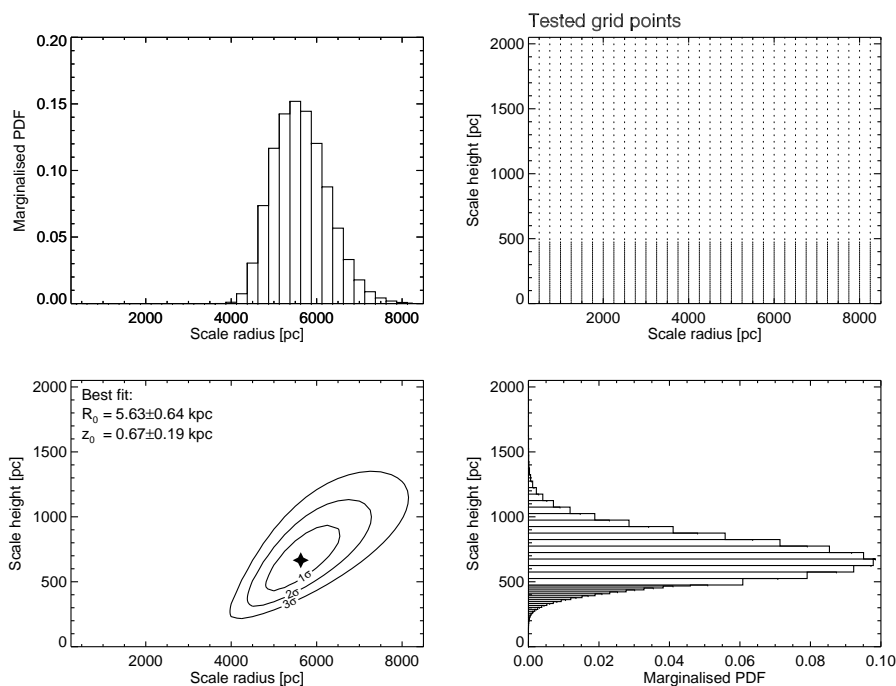


Figure 5.6: Fit results for  $^{26}\text{Al}$  data described by an exponential disk model. Shown are the 1, 2, and  $3\sigma$  uncertainty contours around the best fits values, given in the legend, and also the marginalised PDFs of the scale height and the radial scale. Tested grid points are given in the upper right panel.

The best fit parameters with  $1\sigma$  uncertainties are  $R_0 = 5.63 \pm 0.64$  kpc and  $z_0 = 670 \pm 190$  pc, respectively. This is much larger than in previous measurements. It is possible to constrain the scale height of the  $^{26}\text{Al}$  disk as a whole, but since foreground emission from prominent massive star regions like ScoCen (distance 140 pc,  $10\text{-}40^\circ$  above the plane), Orion-Eridanus (distance 400 pc,  $5\text{-}50^\circ$  below the plane) or extended emission from the Cygnus region (distance 1.4 kpc,  $\pm 20^\circ$  around the plane), glare into the line-of-sight, the 1809 keV height is not globally constrained. Superbubbles may indeed grow outside a thin stellar disk (Weaver et al. 1977; von Glasow et al. 2013), and it may hence not be surprising that a galactic  $^{26}\text{Al}$  scale

height would be larger than the scale height of the star population itself, as the 1809 keV emission is a superposition of many of such stellar groups in the Milky Way.

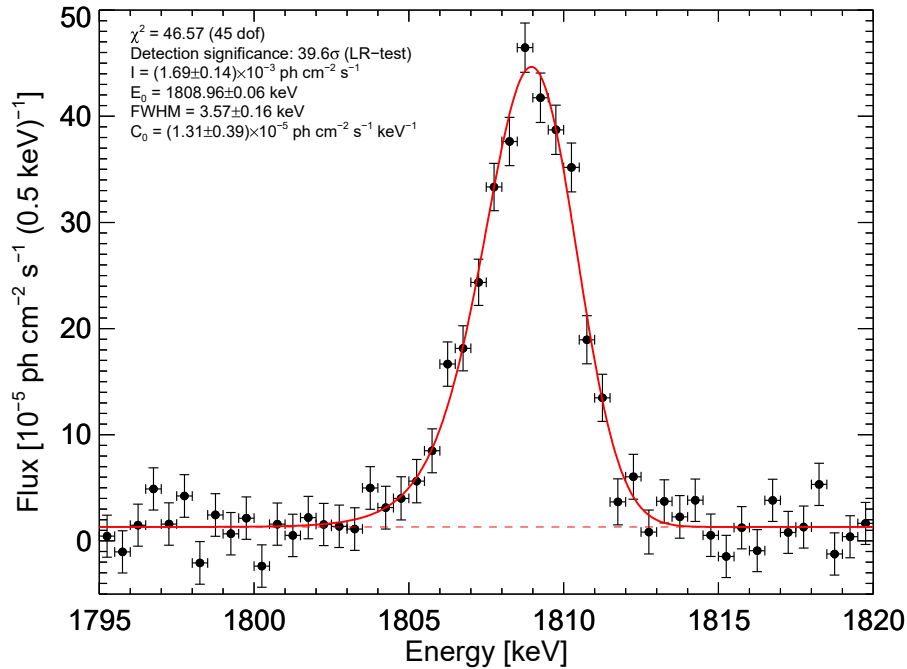


Figure 5.7: Spectrum (black crosses) of the 1809 keV  $^{26}\text{Al}$  emission in the Milky Way. The best fitting model of a degraded Gaussian (solid red line) on top of a constant offset representing the continuum (dashed red line) is also shown. Spectral parameters are given in the legend. See text for details.

The spectrum of the Milky Way in the energy range between 1795 and 1820 keV, as derived from the best fit exponential disk model, is shown in Fig. 5.7. The black data points are fitted with a degraded Gaussian line of fixed degradation parameter,  $\tau = 1.05$  keV, on top of a constant offset. Fitted parameters are the (symmetric Gaussian) line amplitude  $A_0$ , the central energy  $E_C$ , the line width  $\sigma$ , and the continuum amplitude  $C_0$ , in order to determine the derived parameters, line flux  $I$ , peak position  $E_C$ , and the FWHM of the line. The goodness-of-fit is described by a Pearson- $\chi^2$  value, and is  $\chi^2 = 46.57$  for 45 dof, indicating an excellent fit. The line is detected above the gamma-ray continuum with a significance of  $39.6\sigma$ , and has an intensity of  $(1.69 \pm 0.14) \times 10^{-3}$  pc cm $^{-2}$  s $^{-1}$ . Note that the  $^{26}\text{Al}$  line intensity in the inner Galaxy, as defined in previous studies (Diehl et al. 2006; Wang et al. 2009), is about six times smaller than in the total Galaxy, but the solid angle is 54 times smaller than the total sky, so that an increased flux is not surprising. Bouchet et al. (2015) found flux values ranging between 0.5 and  $3.2 \times 10^{-3}$  pc cm $^{-2}$  s $^{-1}$ , when using different emission templates from different wavelengths, similar to Sec. 4.5. Using the same set of astrophysical tracer maps as in the case of the 511 keV emission for the 1809 keV data set, an independent systematic uncertainty measure is derived, and shown in Fig. 5.8.

$^{26}\text{Al}$  line fluxes between  $0.9$  and  $2.4 \times 10^{-3}$  pc cm $^{-2}$  s $^{-1}$  are found acceptable for the current data set, implying a systematic uncertainty ( $2\sigma$ ) of 45%. The 1809 keV luminosity, as derived from the best fit line flux, is then  $(7.97 \pm 0.66) \times 10^{42}$  ph s $^{-1}$ . The line is Doppler blue-shifted with respect to the laboratory frame energy of 1808.63 keV to  $E_0 = 1808.96 \pm 0.06$  keV, equivalent to a Doppler line-of-sight velocity of  $-55 \pm 10$  km s $^{-1}$  towards the observer. This apparent blue-shift may be

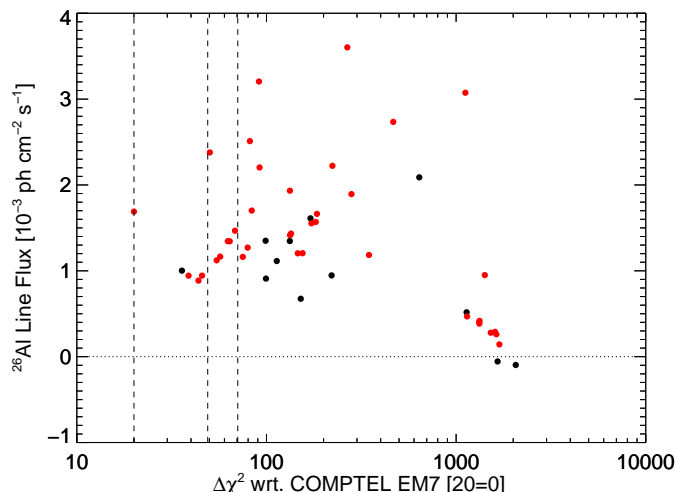


Figure 5.8: Systematics study of measured  $^{26}\text{Al}$  fluxes from different emission models, including a subset of astrophysical tracers (red) and exponential disk models (black). Shown are 1809 keV line fluxes from different models versus the  $\Delta\chi^2$  (likelihood) difference with respect to the COMPTEL ME7  $^{26}\text{Al}$  map which has been found to be the best tracer of the SPI  $^{26}\text{Al}$  data. For readability, a value of 20 has been added to the abscissa, so that 20 is equivalent to 0 (best fit). Values up to  $\Delta\chi^2 = 50$  (equivalent to 70 in the plot scale) are considered acceptable fits to the  $^{26}\text{Al}$  data.

due to a physical origin of gas streaming from the ScoCen association towards the Sun, which would skew the velocity measurement. But as the effect of a single OB association with respect to the flux and velocity of the entire remaining Galaxy is low, the measured velocity is more likely due to systematic effects in the energy calibration. Those may lead to line shifts of the order 0.2 keV around 1809 keV, corresponding to 33 km s<sup>-1</sup>. In addition, a meta-study of  $^{26}\text{Al}$  decay gamma-rays (Endt 1998) suggest a rest-frame photon energy of 1808.73 keV, which would correspond to another 16 km s<sup>-1</sup>. In total, this would imply a systematic uncertainty in the velocity of  $\approx 50$  km s<sup>-1</sup>. Together with the pure statistical uncertainty, the line would then be consistent with the lab energy, as expected from the integration along the entire sky. From fits of the astrophysical template, peak position between 1808.93 and 1808.99 keV are found. The FWHM of the line of  $3.57 \pm 0.16$  keV is larger than the instrumental resolution of 3.17 keV, equivalent to a velocity spread of  $272 \pm 58$  km s<sup>-1</sup>. The systematic uncertainty study suggests FWHM values between 3.55 and 3.67 keV. The velocity spread originates from the Doppler-shifts of galactic rotation at different line-of-sights, broadening the line by the superposition of red- and blue-shifted lines of instrumental resolution, Sec. 4.7.2, and also from gas, streaming (also turbulently) towards and away from the Sun from different massive star regions. A galactic gamma-ray continuum component is seen with a flux density of  $C_0 = (1.31 \pm 0.39) \times 10^{-5}$  ph cm<sup>-2</sup> s<sup>-1</sup> keV<sup>-1</sup>.

#### 5.1.1.3.2 Disentangling Gamma-Ray Foregrounds

As the inner Galaxy seems to be dominated by emission from a rather small scale height disk, the first approach to disentangle the foreground emission from the remaining Galaxy emission is to fit two exponential disks with different scale heights. One represents the "nearby" emission from neighbouring massive star groups, and also very local ( $< 100$  pc)  $^{26}\text{Al}$  radiation, which would be expected to show an almost

isotropic morphology. The local bubble, which also the Sun belongs to, may thus also be filled with  $^{26}\text{Al}$  gas. This disk would then be expected to show a large scale height, as such local emission might also be above and below the Sun. However, this value has no direct physical meaning, but may give clues about the true  $^{26}\text{Al}$  content and extent. The other disk is consequently the "thin" disk with a smaller scale height, probably similar to previous measurements from the galactic ridge only. In Fig. 5.9, the resulting best fit values are shown for a maximum likelihood analysis, using two exponential disks with the same scale radius  $R_0$ , but different scale heights  $z_{01}$  and  $z_{02}$ .

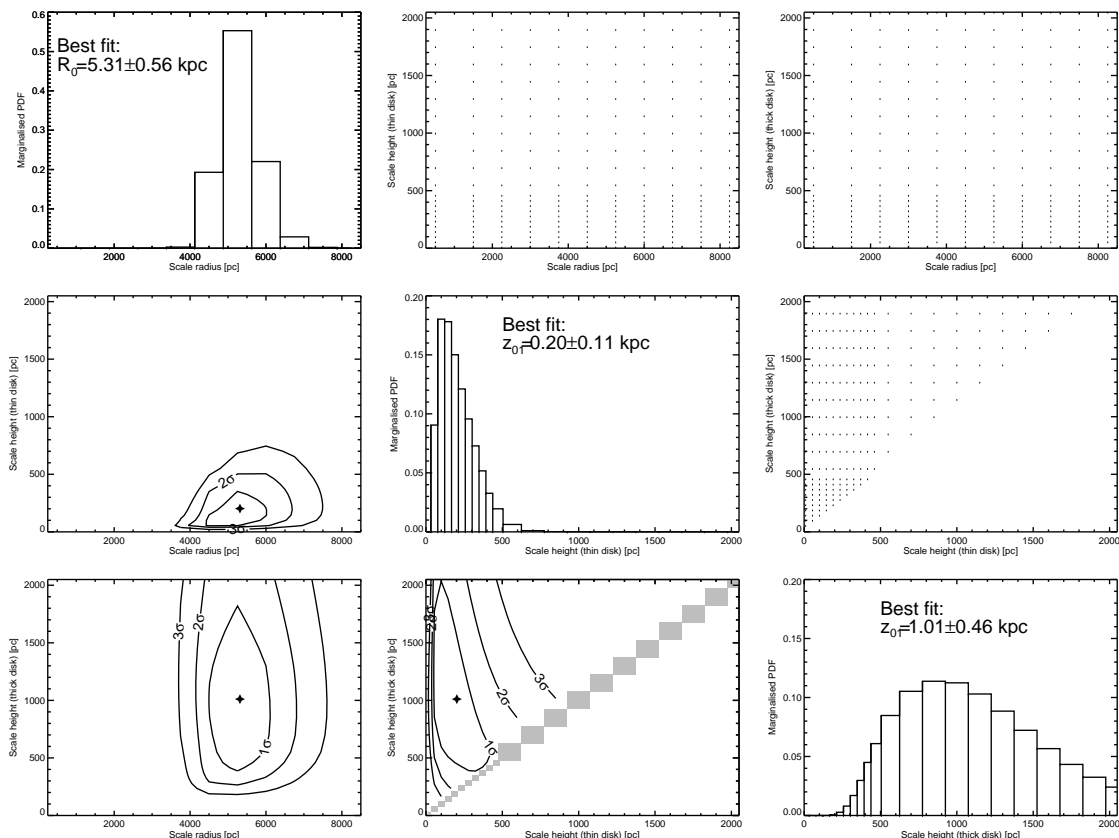


Figure 5.9: Fit results for  $^{26}\text{Al}$  data described by two exponential disk models. Shown are the 1, 2, and 3 $\sigma$  uncertainty contours around the best fits values, given in legends, and also the marginalised PDFs of the two scale heights and the radial scale. In the remaining panels, the tested grid points in the three-dimensional parameter space are given.

The best-fit scale radius for this two-component model in the three-dimensional parameter space is  $R_0 = 5.31 \pm 0.56$  kpc. The "thin" disk obtains a scale height value of  $z_{01} = 200 \pm 110$  pc, and the "thick" - local - disk has a scale height of  $1.01 \pm 0.46$  kpc. As expected from such a largely overlapping emission morphology, the intensity parameters are highly correlated  $\rho > 0.9$ , and also the scale heights show a significant covariance  $\rho = 0.76$ . Compared to a fit with a single exponential disk, the likelihood in the whole energy band between 1795 and 1820 keV improves by  $\Delta\chi^2 = 100.3$ . In the line range between 1804 and 1812 keV, no significant improvement is obtained ( $\Delta\chi_{line}^2 = 34.7$ ). The components are dispensably strong correlated, so that spectral line shapes are largely distorted. The intensities for both disks in the line band are  $(0.97 \pm 0.18) \times 10^{-3}$  pc cm $^{-2}$  s $^{-1}$  for the "thin" and  $(0.67 \pm 0.20) \times 10^{-3}$  pc cm $^{-2}$  s $^{-1}$  for the "thick" disk, respectively. This provides a first estimate of the foreground emission, which amounts to about 40% of the total emission. The remaining luminosity of the thin disk reduces to  $(3.06 \pm 0.57) \times$

$10^{42}$  ph s $^{-1}$  for an estimate of the galaxy-wide  $^{26}\text{Al}$  content. The local contribution has to assume an effective distance. For effective distance between 100 pc, for very local emission regions, and 500 pc averaging also over distant massive stars groups, a 1809 keV luminosity between  $10^{38}$  and  $10^{40}$  ph s $^{-1}$  is estimated. From this study, it can be concluded that one or more local components are necessary to describe the  $^{26}\text{Al}$  SPI data. As an order of magnitude, about 40% of the galaxy-wide emission can be considered local.

The two disk model implies large uncertainties of the local contributions. Previous studies already showed distinct emission from various OB associations (e.g. Diehl 2002; Diehl et al. 2010; Martin et al. 2010), and a next step is to refine the local contribution is to use information about the most prominent massive star groups, ScoCen with its sub-groups Upper Scorpius (USco) and Upper Centaurus Lupus (UCL), Cygnus with all its OB associations, and Orion with the Eridanus superbubble. This will provide an independent estimate of the  $^{26}\text{Al}$  content in the solar neighbourhood. The local bubble might also be filled with  $^{26}\text{Al}$ , but with unknown kinematics, for which reason a nearly isotropic  $^{26}\text{Al}$  background may be expected. The detection of an iso-intensity morphology with a coded-mask instrument like SPI is possible in principle, but as the celestial detector patterns from the instrumental response of such an emission looks the same for all directions, the only useful constraint in this context is the non-uniform exposure of SPI. In fact, such a model component will only be able to search for emissions that look similar to the exposure map. Since the exposure map is filled at different spots at different times, an isotropic component might be revealed with increased and non-uniform exposure. A fit of an isotropic map in addition to a smoothed and prepared<sup>3</sup> version of the COMPTEL ME7 map indeed found an excess. For this uniform map, a flux of the order of several  $10^{-3}$  ph cm $^{-2}$  s $^{-1}$  at around 1811 keV is found. But since the galactic contribution is still around  $1.7 \times 10^{-3}$  ph cm $^{-2}$  s $^{-1}$ , this excess may be considered an artefact from incomplete background treatment. The line peak is found at 1811 keV, similar to the background feature shown in Fig. 4.37. A refinement of such a study will be necessary to constrain the near foreground emission from  $^{26}\text{Al}$  gamma-rays.

In particular, the massive star groups as listed in Tab. 4.13 have been separated from the  $^{26}\text{Al}$  1809 keV COMPTEL ME7 map. This map is the best tracer of the  $^{26}\text{Al}$  emission itself (see Appendix Fig. A.3). Circular cut-outs from this map are used as best guesses for the emission morphologies of the associations, and then fitted to the data set, individually. In Fig. 5.10, the COMPTEL ME7 map and the respective cut-outs for Cygnus, ScoCen, and Orion-Eridanus are shown. The size of the circles are either based on the COMPTEL map itself and/or observations in other wavelengths, like the 21 cm HI data. In the case of Cygnus or ScoCen, the gamma-ray map comprises distinct emission features; in the case of ScoCen, Orion (see also Sec. 5.1.1.3.3) The HI maps provide a reasonable estimate of the extent of the cavities, which are filled with  $^{26}\text{Al}$ . In addition to these larger regions, also subgroups of the ScoCen OB association have been cut, and fitted separately (USco and UCL as coincidences in the COMPTEL map) as an alternative to ScoCen as one entity.

<sup>3</sup>In order to estimate the isotropic flux contribution in the COMPTEL ME7 map, a boxcar filter of  $5 \times 5$  degrees has been applied to the map so that a constant offset below the structured emission from individual regions is revealed. This offset has been subtracted from the map so that only the galactic emission and nearly no isotropic contribution is remaining.

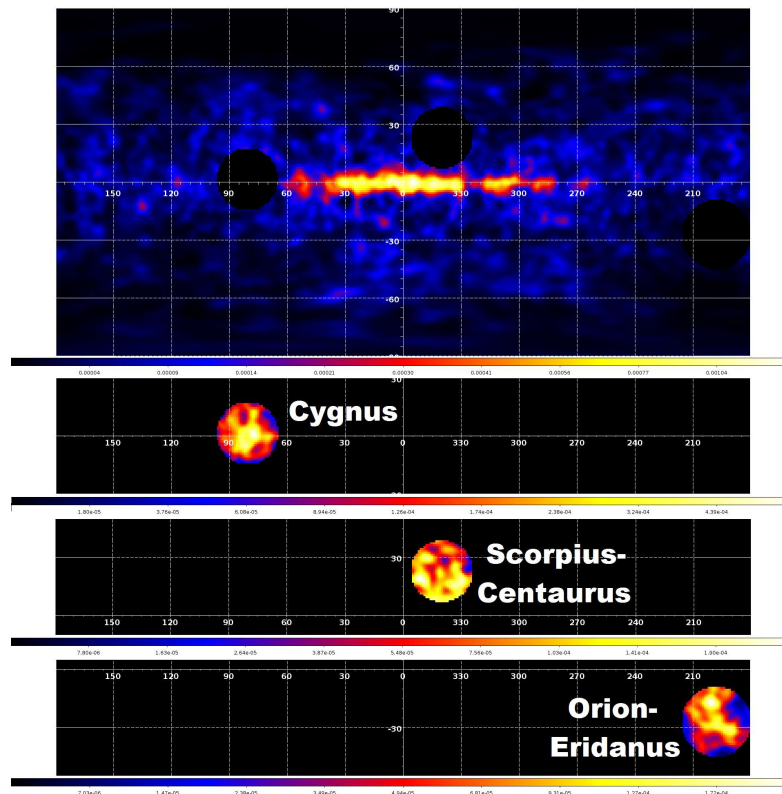


Figure 5.10: Massive star region definitions from the COMPTEL ME7 map. The top panel is equivalent to Fig. 5.3 but without the most prominent massive star regions (black circles). These are shown in the three lower panels as complementary sky model maps for the input in the maximum likelihood fitting. Note the different colourbar scale in each panel. See text for details.

Region	Flux	$M(^{26}\text{Al})$	FWHM	$v_{turb}$	$\Delta E_0$	$v_{bulk}$	Signi.
Cygnus	$9.28 \pm 1.75$	$154 \pm 29$	$3.66 \pm 0.46$	$300 \pm 275$	$0.00 \pm 0.19$	$0 \pm 32$	10.9
ScoCen	$7.58 \pm 1.43$	$1.3 \pm 0.3$	$< 3.61$	$< 275$	$-0.93 \pm 0.32$	$-154 \pm 53$	6.1
Orion	$3.65 \pm 1.19$	$5.0 \pm 1.6$	$< 4.06$	$< 600$	$-0.53 \pm 0.47$	$-88 \pm 78$	3.3
USco	$3.17 \pm 0.94$	$0.5 \pm 0.2$	$< 3.71$	$< 325$	$-0.77 \pm 0.44$	$-128 \pm 73$	3.2
UCL	$5.02 \pm 0.97$	$0.8 \pm 0.2$	$< 3.59$	$< 250$	$-1.11 \pm 0.33$	$-184 \pm 55$	5.0

Table 5.3: Spectral parameters of the  $^{26}\text{Al}$  1809 keV lines in massive star groups. Given are the line fluxes from different regions in units of  $10^{-5}$  ph  $\text{cm}^{-2}$   $\text{s}^{-1}$ , the corresponding apparent mass of  $^{26}\text{Ti}$  on a time scale of 1 Myr in units of  $10^{-4}M_{\odot}$ , the FWHM in units of keV, the resulting Doppler velocity spread interpreted as turbulent gas motion  $v_{turb}$  in  $\text{km s}^{-1}$ , the difference of the lab energy of the line with respect to the measured centroid in keV, the resulting bulk Doppler motion with respect to the Sun in  $\text{km s}^{-1}$ , and the detection significance above instrumental background and continuum in  $\sigma$  units. The  $^{26}\text{Al}$  has been calculated by using the flux as determined from the cutouts and determining the luminosity of 1808 keV gamma-rays from the distance of the OB association, not accounting for its angular extent, so that the mass estimates have to be considered as upper limits.

For each of the five regions, a spectrum is extracted in a maximum likelihood fit, simultaneously to the remaining Galaxy spectrum. The spectra are then fitted with a degraded Gaussian on top of a constant offset. The derived parameter are listed in Tab. 5.3. Each of the cut-outs shows a significant ( $> 3\sigma$ ) line flux, and the spectra are each well described by the line plus continuum model. This is evident from the  $\chi^2$  goodness-of-fit values. The resulting spectra are shown in Fig. A.6, and provide valuable information about ongoing nucleosynthesis for each of the massive star regions, and in the Milky Way. The focus of this thesis is to provide an estimate of the number of positrons which emerge from the decay of radioactive  $^{26}\text{Al}$ . The galactic-wide 1809 keV luminosity is necessary to determine the current mass of  $^{26}\text{Al}$  in the Galaxy as a whole, for which reason the fluxes of the neighbouring

massive star groups are needed to estimate the remaining flux. In particular, a galaxy-wide 1809 keV line flux of  $(1.48 \pm 0.14) \times 10^{-3}$  is obtained, by subtracting the derived foreground fluxes, listed in Tab. 5.3, from the total COMPTEL map intensity. Provided that the COMPTEL  $^{26}\text{Al}$  map is consistent with an exponential disk of scale radius of 5 kpc and scale height of 180 pc (e.g. Knoedlseder et al. 1996), the flux is converted to a luminosity of  $(4.47 \pm 0.42) \times 10^{42}$  ph s $^{-1}$ . This should be considered an upper limit, as there are more, but less-studied, close-by massive star groups whose  $^{26}\text{Al}$  content is unknown, also due to a lack of exposure time.

### 5.1.1.3.3 Characterising the Orion OB1 Association

In the case of the Orion-Eridanus region, and in particular the Orion OB1 association, the disentanglement can be approached in a more elaborate way. Orion is located below the galactic plane and in the galactic anti-centre, so that additional background emission from the Galaxy is not expected. The Orion OB1 association (Blaauw 1964; Warren & Hesser 1977; Brown et al. 1994) contains the largest groups of young massive stars in the vicinity of the solar system, at a distance of only 400 pc.

The stellar populations are well known, which allows for precise estimations of energy content of and mass flows into interstellar space. The  $^{26}\text{Al}$  ejecta, which are produced by massive stars in the Orion OB1 sub-groups, are a direct tracer of ongoing nucleosynthesis and enrichment of the ISM with heavy elements. Furthermore, the Orion A and B molecular clouds are located in an inter-arm region, and thus represent a high-density region "behind" the massive star groups (seen from the direction of the Sun). Between the solar system and stellar associations of Orion, there is a large cavity, enclosed by atomic hydrogen, and filled with hot X-ray gas, and which was blown presumably by the oldest subgroup 1a, several million years ago. This is called the Orion-Eridanus superbubble. The geometry and the conditions of Orion allow to test the galactic-wide superbubble interpretation of  $^{26}\text{Al}$  1809 keV emission. It would be expected, that nucleosynthesis ejecta should predominantly flow into the cavity, i.e. approaching the Sun, rather than in the opposite direction, as there is a large density, holding or reflecting the  $^{26}\text{Al}$  stream.

Name	( $l/b$ )	$r$	$T$	$d$	$N_{tot}$	$N_P$	$E_{out}$
a	(202.5° / -18.5°)	1.7°	11 ± 1	340 ± 20	190	53	70 ± 35
b	(205.0° / -17.0°)	1.5°	6 ± 2	470 ± 40	150	45	< 30
c	(208.5° / -19.5°)	2.0°	3 ± 2	510 ± 40	210	23	30 ± 20
d	(209.0° / -19.5°)	0.2°	< 1	410 ± 10	–	–	–

Table 5.4: Characteristics of the Orion OB1 stellar subgroups. The positions are given in galactic ( $l/b$ )-coordinates with radial extents  $r$ . The age  $T$  is given in units of Myr, the distances  $d$  in pc.  $N_{tot}$  is the total number of stars in the associations, and  $N_P$  the number of star present which are in the mass range 4 – 15 $M_{\odot}$  for a, 4 – 120 $M_{\odot}$  for b, and 7 – 36 $M_{\odot}$  for c, respectively. The energy output from the stars  $E_{out}$ , given in units of 10 $^{50}$  erg combines supernova, Wolf-Rayet, and O-star contributions. From Blaauw (1964) and Brown et al. (1994).

The Orion region can be defined by its molecular clouds, the OB association sub-groups, the Eridanus cavity, and several HII regions. The Orion A and B clouds range from ( $l/b$ ) = (217° / -21°) over (203° / -21°), (202° / -12°), (207° / -12°), (210° / -17°) to (217° / -17°) at a distance of 400 to 500 pc (seen in 100  $\mu\text{m}$  observations Brown et al. 1994). From HI data it is derived, that the Eridanus bubble spans

an area in the sky of  $\approx 2000 \text{ deg}^2$ , from  $l = -5^\circ$  to  $l = -55^\circ$ , and from  $b = 185^\circ$  to  $b = 225^\circ$  (Brown et al. 1995). It is touching the local bubble at a distance of 100 pc at  $(l/b) = (185^\circ-210^\circ / -28^\circ--50^\circ)$ , and measures 400 pc in size, elongated and parallel to the galactic plane. The characteristics of Orion OB1 association subgroups are listed in Tab. 5.4. The derived age for the subgroup 1a is significantly larger than for 1b and c, and much larger than for d. Thus, the expected  $^{26}\text{Al}$  signals from the subgroups should differ, also depending on their stellar contents.

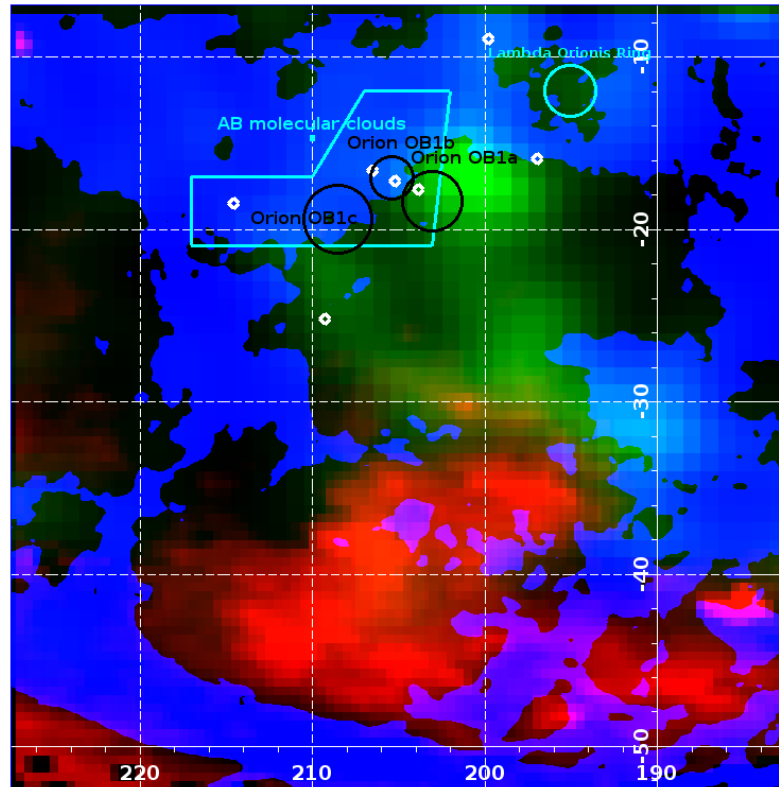


Figure 5.11: False-colour image of the Orion region. Shown are 21 cm atomic hydrogen data from the Effelsberg-Bonn HI survey (blue Kerp et al. 2011), 0.25 keV emission from the ROSAT all-sky survey (red Snowden et al. 1997), and the 1.8 MeV COMPTEL ME7 map (green Plüschke et al. 2001). The position of the stellar subgroups are marked with black circles, molecular cloud regions in cyan, and the star of the constellation of Orion with white diamond symbols. See text for details.

Using information from observations in various wavelengths, the superbubble hypothesis can be tested in the Orion region. In Fig. 5.11, the Orion region is shown as measured in 21 cm (atomic hydrogen, blue), 0.25 keV (hot plasma, red, ROSAT measurement), and 1.809 MeV ( $^{26}\text{Al}$ , green, COMPTEL ME7 map). In addition, the molecular cloud region as defined above is shown in cyan, together with the positions of the subgroups (black circles), and the brightest stars of the constellation of Orion (white diamonds). In the projected view towards Orion, the shell of atomic hydrogen entirely surrounds the 0.25 keV and 1.809 MeV emission. Furthermore, the hot plasma seems to be predominantly located at latitudes below  $\approx 34^\circ$ , whereas the  $^{26}\text{Al}$  is confined to the upper part of the bubble. The fading of X-ray emission towards the galactic plane may be explained by global oscillations of the hot gas, which is observed in hydrodynamic simulations of massive star feedback on the ISM (Krause et al. 2014). It appears that high-energy and soft emission alternate inside the superbubble, as the hot gas is sloshing on the full spatial scale of the bubble after interactions with shock fronts from supernovae. At a certain point in time, the projected luminosity of low- and high-energy emission may then be com-

pletely anti-correlated. A cooling process may have started around the position of the stars (supernovae, winds), which has not yet reached the far end of the bubble. In contrast to the X-ray gas, the  $^{26}\text{Al}$  ejecta should show a declining morphology, because the half-life time of  $^{26}\text{Al}$  restricts the emission region to absolute distances of  $1 \text{ pc} \frac{v}{1 \text{ km s}^{-1}}$ . Depending on the ejecta velocity, the emission may only be found several pc away or otherwise could have filled the whole bubble. The ejecta velocities may also decrease, once they left the local star or supernova environment.

The gamma-ray map has been derived with the maximum entropy method, and hence the large scale emission features can be considered correct. But on smaller scales, more pronounced spots should be considered with caution, as the method is prone to result in more point-like emission regions. With SPI, the assumed emission off the stellar groups can be tested by using different emission models, in addition to the best fit galactic plane model, derived in Sec. 5.1.1.3.1. Either the emission is located around the stars, which is tested by a symmetric 2D Gaussian model located at  $(l_{on}/b_{on}) = (-153.5^\circ / -19.5^\circ)$  with a radial extent of  $r_{on} = 4^\circ$ , or the emission is found at a projected distance off the stars, for example at the COMPTEL emission hot spot at  $(l_{off}/b_{off}) = (-159.5^\circ / -17.25^\circ)$ , which shows a radial extent of  $r_{off} = 3^\circ$ . The kinematic information from detected lines then first provides a consistency check, as emission only around the stars should show no significant Doppler-shifts. On the other hand, the Doppler-velocity should be equivalent to the projected distance of the emission, further away from the groups. Secondly, the discrete value of the Doppler-shift and the line broadening may help to falsify the superbubble hypothesis.

The spectra for both cases are shown in Fig. 5.12. It is evident from this analysis, that in the immediate vicinity of the stellar groups, no significant 1809 keV emission is found. The  $2\sigma$  upper limit on the flux from the direction of the stars is  $1.5 \times 10^{-5} \text{ ph cm}^{-2} \text{ s}^{-1}$ . More than  $6^\circ$  off the association, corresponding to a projected distance of about 50 pc, there is significant emission from the decay of  $^{26}\text{Al}$ . The line flux of  $(2.2 \pm 1.2) \times 10^{-5} \text{ ph cm}^{-2} \text{ s}^{-1}$  corresponds to an  $^{26}\text{Al}$ -mass, seen to decay, of  $(3.8 \pm 2.0) \times 10^{-4} M_\odot$ , at a distance of 450 pc. This is in concordance to the cumulative expected value of the four subgroups, derived from population synthesis models  $((2.5 - 6.6) \times 10^{-4} M_\odot$  Voss et al. 2010). If the entire Orion region as measured with COMPTEL is used as an emission template for SPI analysis, see Tab. 5.3, the 1809 keV line is detected with a significance of  $3.3\sigma$ , and shows a flux of  $(3.7 \pm 1.2) \times 10^{-5} \text{ ph cm}^{-2} \text{ s}^{-1}$ . This means there is also  $^{26}\text{Al}$  found inside the Eridanus cavity, far away from the stars, and with a flux of the order  $(1 - 2) \times 10^{-5} \text{ ph cm}^{-2} \text{ s}^{-1}$ . From the test emission spot spectrum, the line is blue-shifted. This would be expected from gas streaming into the direction of the Sun, rather than into the molecular clouds. The blue-shift is more significant when the COMPTEL cut-out of the region is used. A mean velocity of  $-88 \pm 78 \text{ km s}^{-1}$  is derived. The angular distance of  $\approx 6^\circ$  away from the stellar subgroups corresponds to a projected distance of  $\approx 50 \text{ pc}$ , and is reached if the line-of-sight velocity was of the order of  $-50 \text{ km s}^{-1}$ . This is fully consistent with the measured Doppler-shift. The width of the line constrains the turbulent motion of the streaming gas to less than  $600 \text{ km s}^{-1}$  ( $2\sigma$ ). This is of the order of the sonic speed of hot streaming gas in low-density medium, and far below the initial ejecta velocities of  $\approx 5000 \text{ km s}^{-1}$ , as would expected from supernova explosions. The nucleosynthesis products must have significantly slowed down after their ejection, so that supernovae have only a small probability of

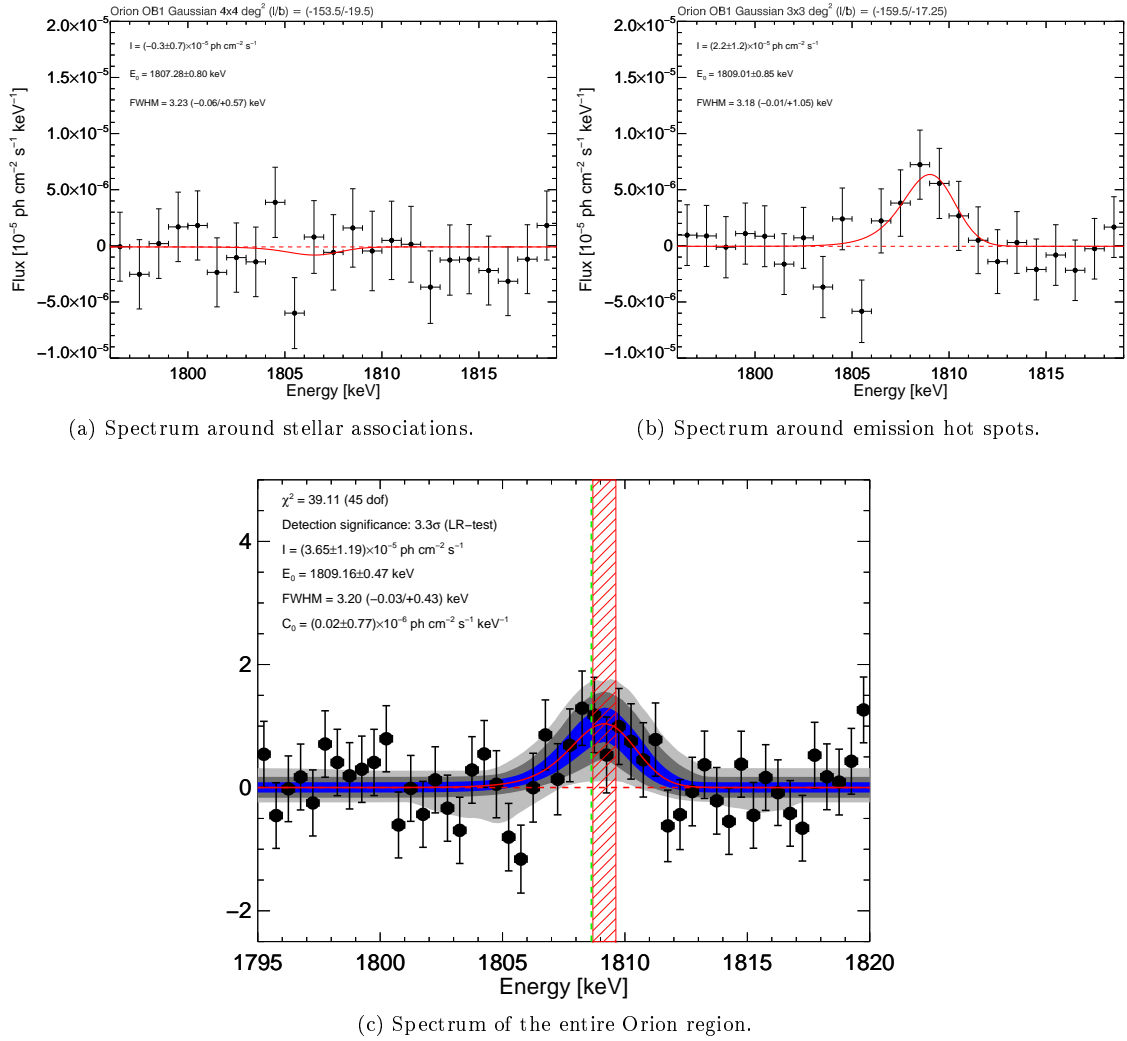


Figure 5.12: Spectra (black data points) from the Orion region. Panel (a) shows a spectrum from the position of the stellar groups as defined in the text around  $(l_{on}/b_{on}) = (-153.5^\circ/-19.5^\circ)$ , panel (b) from an emission hot spot around  $(l_{off}/b_{off}) = (-159.5^\circ/-17.25^\circ)$ , and panel (c) from the entire Orion region as defined in Tab. 5.3. The y-axis in (c) is given in units of  $10^{-5}$  ph  $\text{cm}^{-2}$   $\text{s}^{-1}$   $\text{keV}^{-1}$ . In each panel, the data has been fitted by a Gaussian (red solid lines) on top of a constant offset (red dashed lines). Fitted parameters are given in the legends. In (c), the 1, 2, and  $3\sigma$  uncertainty bands are indicated in blue, dark grey, and light grey. The laboratory energy is marked by a vertical green dashed line and the measured Doppler-shift as red hatched area. See text for detail.

enriching distant systems. These supernovae may have happened at distinct stellar associations, enclosed by a shell of atomic hydrogen, and several million years ago. . In fact, the scenario of one supernova 2.2 Myr ago in the association of ScoCen, which is suggested to have enriched Earth with  $^{60}\text{Fe}$  (e.g. Wallner et al. 2016), is hard to accomplish, if there was no "hole" in the HI shell, separating the local bubble from ScoCen. Instead, the enrichment of Earth with freshly produced nucleosynthesis material should have happened rather locally (e.g. Knie et al. 2004).  $^{26}\text{Al}$  ejecta are approaching the solar system, and do not diffuse into the molecular clouds or outside the Eridanus cavity. The superbubble hypothesis is hence supported by the gamma-ray measurements. The uncertainties on the gamma-ray data are still large, and detailed emission models should include exact 3D geometries. These may be derived from, for example, an elaborate treatment of HI data, or superbubble growth estimates as determined from Kompaneets model fitting (Pon et al. 2014), towards a realistic description of the Orion region. With increased INTEGRAL/SPI

exposure, improved  $^{26}\text{Al}$  emission models could then test different ejecta velocities from the Orion OB1 association, and determine the cumulative action of massive star groups.

#### 5.1.1.4 Determining the Al-26 Mass in the Galaxy

The steady-state amount of  $^{26}\text{Al}$  can be directly derived from the number of decay gamma-ray photons received. This is equivalent to the luminosity, measured in photons per second, from the activity of an amount of  $^{26}\text{Al}$  which is distributed in the Galaxy, or individual groups. The mass which is seen to decay, in units of solar masses, is determined by the rate of decay photons which have been measured by the telescope, i.e. the luminosity  $L$ , divided by the rate of photons at which one solar mass of pure  $^{26}\text{Al}$  atoms would emit,  $L_{\odot}^{26}$ ,

$$M(^{26}\text{Al}) [M_{\odot}] = \frac{L}{L_{\odot}^{26}}. \quad (5.10)$$

The luminosity of one solar mass of  $^{26}\text{Al}$  is calculated from the activity,  $A_{\odot}^{26}$ , of the number of  $^{26}\text{Al}$  atoms comprising one solar mass,  $N_{\odot}^{26}$ , and the probability that a gamma-ray emission at 1809 keV occurs, i.e.  $p_{1809}^{26} = 99.7\%$ :

$$\begin{aligned} L_{\odot}^{26} &= p_{1809}^{26} A_{\odot}^{26} = p_{1809}^{26} \lambda(^{26}\text{Al}) N_{\odot}^{26} = p_{1809}^{26} \frac{\ln 2}{T_{1/2}(^{26}\text{Al})} \frac{M_{\odot}}{M(^{26}\text{Al})} = \\ &= 1.41 \times 10^{42} \text{ ph s}^{-1}. \end{aligned} \quad (5.11)$$

In Eq. (5.11),  $\lambda(^{26}\text{Al})$  is the decay constant of  $^{26}\text{Al}$  ( $\lambda = \tau^{-1} = \frac{\ln 2}{T_{1/2}}$ ),  $M_{\odot} = 1.989 \times 10^{30} \text{ kg}$  is one solar mass, and  $M(^{26}\text{Al}) = 25.98689169u \approx 4.315 \times 10^{26} \text{ kg}$  is the atomic mass of one  $^{26}\text{Al}$  atom.

Using the luminosity values for the Milky Way as derived in Sec. 5.1.1.3, the total mass of  $^{26}\text{Al}$  from different estimates is given in Tab. 5.5. Depending on the assumptions of the emission morphology of the Galaxy, the estimates range between 2 and  $6M_{\odot}$  of  $^{26}\text{Al}$ . This can be considered a systematic uncertainty of the order of 50%, whereas the statistical uncertainty from one particular measurement itself is of the order of 10%. In fact, this statistical uncertainty can be further reduced if only data with high exposure like in the central radian of the Galaxy is used. Restricting the data set to the commonly used longitude and latitude extent of the galactic ridge,  $|l| < 30^{\circ}$ ,  $|b| < 10^{\circ}$ , and fitting the same cut-out of the COMPTEL ME7 map to this data, the spectrum of the inner Galaxy is derived, and shown in Fig. 5.13.

The 1809 keV line in the inner Galaxy is detected with a significance of  $41.3\sigma$  above the galactic gamma-ray continuum and instrumental background for an exposure of 42 Ms. The line contains a flux of  $(2.89 \pm 0.07) \times 10^{-4} \text{ ph cm}^{-2} \text{ s}^{-1}$ , corresponding to a luminosity of  $(3.90 \pm 0.09) \times 10^{42} \text{ ph s}^{-1}$ , and a total  $^{26}\text{Al}$  mass of  $2.77 \pm 0.06 M_{\odot}$ .

From the total  $^{26}\text{Al}$  mass in the Galaxy, the number of positrons which are con-

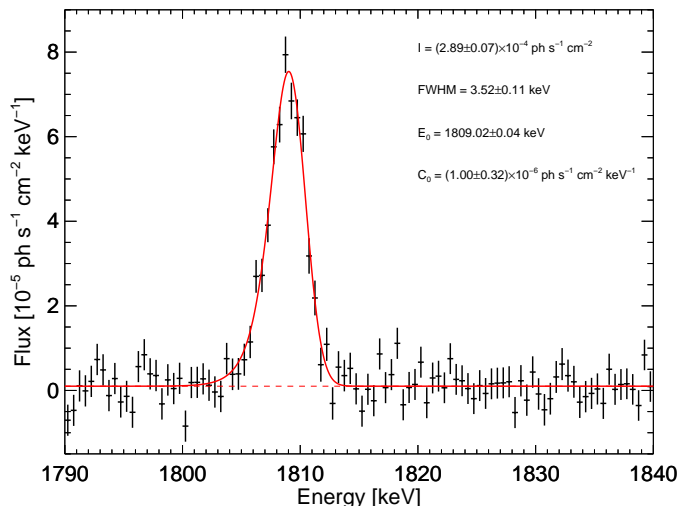


Figure 5.13: Spectrum (black crosses) of  $^{26}\text{Al}$  emission in the inner Galaxy as defined by the region  $|l| \leq 30^\circ$ ,  $|b| \leq 10^\circ$ , from the COMPTEL ME7 map. The best fit model of a degraded Gaussian on top of a constant offset is shown as red solid line with a dashed line for the continuum. Spectral parameters are given in the legend.

Model	Flux	Luminosity	$^{26}\text{Al}$ Mass
One exp. disk	$16.9 \pm 1.4$	$7.97 \pm 0.66$	$5.65 \pm 0.49$
Two exp. disks	$9.7 \pm 1.8$	$3.06 \pm 0.57$	$2.17 \pm 0.40$
COMPTEL cutouts	$14.8 \pm 1.4$	$4.47 \pm 0.42$	$3.17 \pm 0.30$
COMPTEL inner Galaxy	$2.89 \pm 0.07$	$3.90 \pm 0.09$	$2.77 \pm 0.06$
Weighted mean	-	-	$2.81 \pm 0.06$

Table 5.5: Estimates of the galactic  $^{26}\text{Al}$  mass in units of solar masses for different emission models and assumptions. The fluxes are given in units of  $10^{-4}$  ph  $\text{cm}^{-2}$   $\text{s}^{-1}$  and the luminosities in  $10^{32}$  ph  $\text{s}^{-1}$ . In the bottom line a uncertainty-weighted mean,  $\langle M \rangle = \frac{\sum_i (M_i \sigma_i^{-2})}{\sum_i \sigma_i^{-2}}$ , is given for the mass of  $^{26}\text{Al}$  in the Galaxy.

tributed by massive star ejecta on a time scale of 1 Myr can be estimated. With a probability  $p_{\beta^+}^{26} = 81.73\%$ , an  $^{26}\text{Al}$  atom is decaying via  $\beta^+$ -decay so that the number of positrons produced is

$$\dot{N}_{e^+}({}^{26}\text{Al}) = \frac{M_{MW}({}^{26}\text{Al})}{M_{atom}({}^{26}\text{Al})} \frac{1}{\text{Myr}} p_{\beta^+}^{26} = (3.35 \pm 0.07) \times 10^{42} \text{ e}^+ \text{ s}^{-1}, \quad (5.12)$$

which is  $10.8 \pm 5.2\%$  of the positron annihilation rate in the disk, and  $6.8 \pm 2.1\%$  in the total Galaxy. In consequence, the decay of  $^{26}\text{Al}$  in the Milky Way alone is not enough to explain the observed positron content. Note that the disk scale height of the  $^{26}\text{Al}$  emission morphology ( $\approx 500$  pc) is smaller than that of the positron annihilation emission ( $\approx 500\text{-}2000$  pc). This points towards a propagation effect of positrons away from their sources.

### 5.1.2 Core-Collapse Supernovae

Massive stars with  $M \gtrsim 8M_\odot$  follow a trajectory in the  $\rho - T$ -plane at which the central temperature, density, and mass are related by  $\frac{T_C^3}{\rho_C} \propto M_C^2 \sim \text{const.}$  (Janka 2012, see also Sec. 5.1.1). Once a massive stars leaves the H-burning main-sequence

of stellar evolution, the subsequent burning stages of He, C, Ne, O, and Si are proceeding faster and faster, so that the efficiency of energy production per time is decreasing, because the relative binding energy per nucleon for higher-order elements is also decreasing. At the same time, energy losses by neutrino-antineutrino pair-creation become dominant. At temperatures  $\gtrsim 10^9$  K, also electron-positron pair-creation sets in, so that at a certain point in time, neutrino losses are stronger than the radiation losses of a star, and the evolution of the produced He core decouples from that of the stellar envelope (Janka 2012).

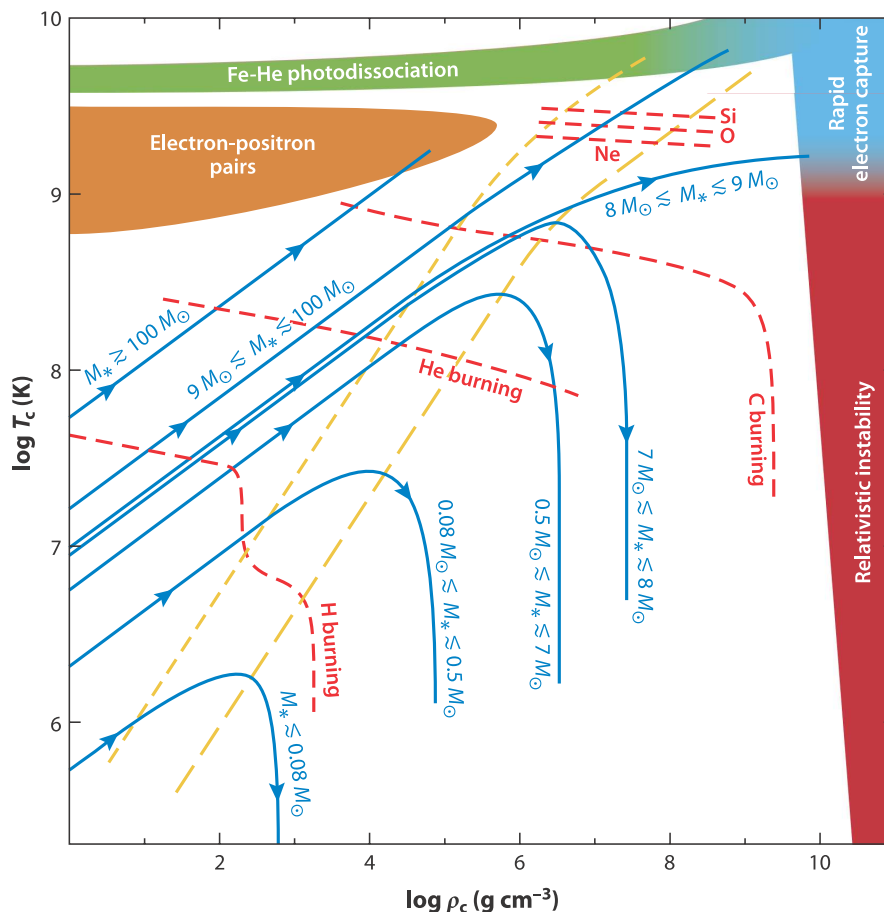


Figure 5.14: Final fates of stars with schematic evolutionary tracks in the  $\rho_C - T_C$ -plane, similar to Fig. 5.2. The coloured regions at the boundaries of the diagram are labelled by the instability process causing the collapse of the stellar core. Several stellar tracks (solid blue) as subdivided by initial stellar mass are shown as they pass different burning stages (red dashed). Short- and long-dashed yellow lines indicate beginning and strong degeneracy of the electron gas in the core, respectively. From Janka (2012).

This energy loss leads to an increase of gravitational binding energy as the star contracts. For larger He core masses, the central temperature can rise even more, and upper burning stages can set in, building heavier elements. Stars with an initial mass of  $\gtrsim 8M_\odot$  can climb up the  $\rho - T$ -diagram to a point where the stellar core becomes gravitationally unstable. Three different mechanism can start the implosion of a stellar core, leading to different final spots, and thus core-collapse subtypes, as shown in Fig. 5.14. Either electron-capture, iron-core dissociation, or electron-positron pair-creation can lead to the final fate of a massive star, depending on its initial mass (Fig. 5.14). The majority of stars with a mass between  $\approx 9$  and  $\approx 100M_\odot$  are believed to explode via an iron-core supernova. For such massive stars, Ne-burning and also later burning stages set in, finally creating core of Fe. At temperatures of the order  $10^{10}$  K, corresponding to  $k_B T \sim 1$  MeV, the Fe

core becomes gravitationally unstable, as thermal gamma-rays photodissociate the nuclei in the interiors, creating  $\alpha$ -particles, and a steadily rising number of free nucleons. As the density and temperature increases, electron captures on nuclei and free protons speed up the implosion. When the central density reaches the nuclear density of the order  $\rho \approx 2.7 \times 10^{14} \text{ g cm}^{-3}$ , the collapse is stopped promptly, because a homogeneous amount of nuclear matter, a neutron star, is formed, and in which strong nuclear repulsion forces inhibit further compression (Janka 2012; Burrows 2013).

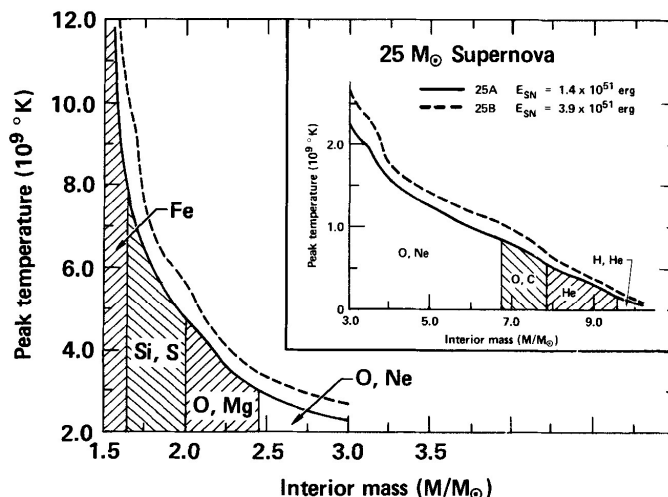


Figure 5.15: Peak explosion temperature as a function of mass fraction and burning zones, equivalent to pre-explosion composition for a  $25M_{\odot}$  supernova model. The peak temperature in each zone scales as  $E_{SN}^{1/4}$  as expected from Eq. (5.13). In particular, explosive burning of Ne, O, and Si are expected from this model calculation, whereas H, He, and C are not very abundant. Two models with different explosion energies are shown as solid and dashed line. From Weaver & Woosley (1980).

Due to this sudden stiffening of the equation of state, the collapse halts and reverses, commonly called a "rebound" or "overshooting", which bounces off the central core outwards in a shock wave. This shock wave then interacts with infalling layers which at that point fall freely towards to centre. The shock wave emerges to a shock front that finally leads to the complete disruption of the star in a core-collapse supernova explosion. In this shock region, explosive nucleosynthesis occurs. There, heavy nuclei may either be ejected from the supernova, or fall back onto the neutron star, depending on the mass cut, defining this region. For a given initial nuclear composition at the time of the explosion, and given density, nucleosynthesis yields for various isotopes can be estimated from only knowing the distribution of temperatures behind the shock front (Weaver & Woosley 1980; Thielemann et al. 2011). Thus, equating the explosion energy,  $E_{SN}$ , with the radiation energy inside the spherical volume of the shock front,

$$E_{SN} = \frac{4\pi}{3} r^3 a T^4(r), \quad (5.13)$$

where  $a = \frac{4\sigma}{c} = 7.5657 \times 10^{-15} \text{ erg cm}^{-3} \text{ K}^{-4}$  is the radiation density constant. Solving for the temperature  $T(r)$  will result in characteristic temperature zones of different explosive burning phases (Thielemann et al. 1996). In Fig. 5.15, the peak explosion temperature as a function of the mass fraction of massive stars is shown, in which the different explosive burning phases are indicated. In general, from the hottest regions near the iron core outwards, the temperature is decreasing with the

fourth root of the explosion energy. As the supernova, in particular the shock front, is expanding, some reactions might no longer be able to proceed fast enough to reach an equilibrium state. One particular effect of this explosive burning is the so-called  $\alpha$ -rich freeze-out, in which from the innermost created nuclei outwards, more and more nuclear reactions fall out of nuclear statistical equilibrium. Especially, three-body reactions like the triple- $\alpha$  process are suppressed. The conditions are then better described by an overabundance of  $\alpha$ -particles, leading to an overabundance of  $\alpha$ -multiple nuclei in the end. However, the mass cut cannot be derived from this kind of estimate, and has to be derived independently, e.g. by measuring the ejected  $^{56}\text{Ni}$  mass.

### 5.1.2.1 More Naturally Positron Producing Isotopes

In the context of the positron puzzle, one of the most important nuclei produced in this  $\alpha$ -rich freeze-out is  $^{44}\text{Ti}$ . It is also radioactive, and decays by electron capture to  $^{44}\text{Sc}$  which is then  $\beta^+$ -unstable, and decays to stable  $^{44}\text{Ca}$ . The yield of  $^{44}\text{Ti}$  in a core-collapse supernova strongly depends on the initial conditions of the star. As the nuclei are produced in the innermost regions in explosive Si-burning, and because of dynamical instabilities and simultaneous in- and outflows, it is uncertain where and how the separation between material accreting onto the compact remnant and the ejecta (mass cut) occurs (Fryer et al. 2008; Wongwathanarat et al. 2013; Popov et al. 2014). Typical yields per supernova event range around  $10^{-5}M_{\odot}$  of  $^{44}\text{Ti}$ , ejected into the surroundings (Timmes et al. 1996; The et al. 2006; Magkotsios et al. 2010). Wongwathanarat et al. (2016) illustrated in simulations that  $^{44}\text{Ti}$  yield of the order  $10^{-4}M_{\odot}$  are possible, and probably not uncommon when a supernova explodes asymmetrically. Earlier considerations were mainly based on 1D approaches, and hence could not take 3D effects into account.

After a half-life time of  $\approx 59$  yr,  $^{44}\text{Ti}$  is decay via 100% electron capture to an excited state of  $^{44}\text{Sc}$ , which is de-exciting by a cascade of gamma-ray emissions at energies 67.87 keV with a probability of 93.0%, 78.36 keV with 96.4%, or 146.22 keV with 0.1%.  $^{44}\text{Sc}$  then has a considerably shorter half-life time of 3.97 h, hence on astrophysical time-scales, both decays can be considered contemporaneous. It decays with a probability of 5.73% via electron capture, and with  $p_{\beta^+}^{44} = 94.27\%$  via positron emission, to an excited state of  $^{44}\text{Ca}$ . This again de-excites by the emission of gamma-rays, predominantly at 1157.02 keV (99.88%), to its stable ground state, Fig. 5.16.

Because  $^{44}\text{Ti}$  is that long-lived, it powers the late bolometric light curve of core-collapse supernovae (Seitenzahl et al. 2014), via the absorption of gamma-rays from radioactive decay. But as the supernova cloud is already diluted after several half-life times of  $^{44}\text{Ti}$ , many photons will escape the remnant, and be detectable with gamma-ray telescopes. Measuring these photons then provides direct information about the total  $^{44}\text{Ti}$  yield in an explosion and the kinematics of the expanding ejecta. The number of decayed  $^{44}\text{Ti}$  nuclei in one supernova explosion directly counts the number of positrons ejected into the ISM. Knowing the core-collapse supernova rate in the Milky Way then provides an estimate of the positron contribution from massive star explosions due to  $^{44}\text{Ti}$  decay. In the next section, the young supernova remnant Cassiopeia A (Cas A) will be investigated, determining the total ejected

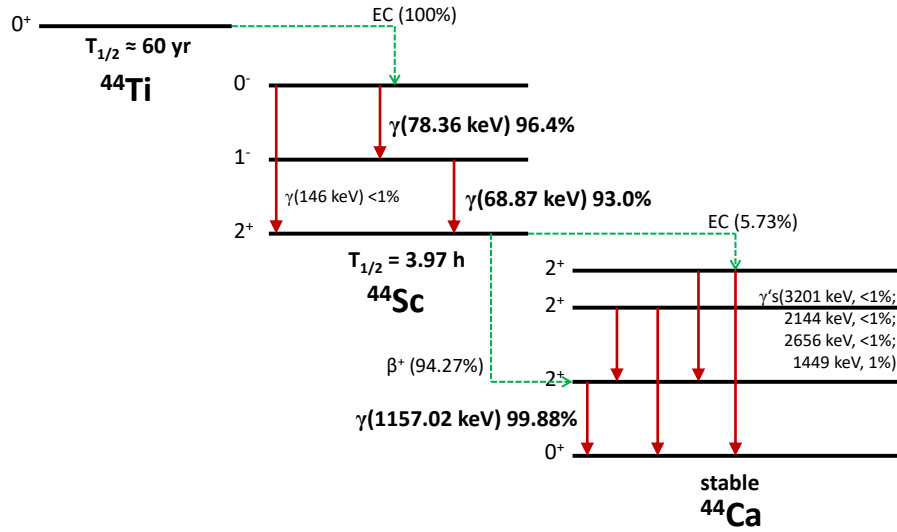


Figure 5.16: Decay scheme of the  $^{44}\text{Ti}$  decay chain. With a half-life time of  $\approx 59$  yr, first  $^{44}\text{Ti}$  is decaying with 100% probability via electron capture to an excited state of  $^{44}\text{Sc}$  which is de-exciting by the emission of a cascade of gamma-rays, and then also decaying after  $\approx 3.97$  h via positron emission with 94.27% probability to an excited state of  $^{44}\text{Ca}$ .  $^{44}\text{Ca}$  is then predominantly de-exciting by the emission of a 1157.02 keV gamma-ray.

$^{44}\text{Ti}$  mass, and thus the positron input of one explosion<sup>4</sup>. Utilising the measured  $^{26}\text{Al}$  mass in the Galaxy, an independent supernova rate can be derived towards an estimate of the positron population from core-collapse supernovae. The Cas A results have been presented in Siegert et al. (2015).

### 5.1.2.2 Measuring Ti-44 in Cassiopeia A

Cassiopeia A is the closest young remnant of a core-collapse supernova, and therefore a prominent study object in many wavelength regimes. It may have been seen in AD 1680 by Flamsted (Ashworth 1980; Green 2002), but was not as bright as expected from its proximity of  $3.4_{-0.1}^{+0.3}$  kpc (Reed et al. 1995). Apparently, the supernova itself was occulted by interstellar dust and gas, and its brightness could only be inferred indirectly (Eriksen et al. 2009). Thus, the date of the event is not precisely settled; Thorstensen et al. (2001) inferred the supernova event at  $\text{AD } 1671.3 \pm 0.9$  by measuring the proper motion of the supernova remnants' bright main shell, as well as faint, high-velocity, outer ejecta knots, and assuming free-expansion.

Cas A was the first supernova in which the characteristic line at 1157 keV from the second decay in the chain  $^{44}\text{Ti} \rightarrow ^{44}\text{Sc} \rightarrow ^{44}\text{Ca}$  had been reported by Iyudin et al. (1994) with COMPTEL. Later measurements focussed on the equally bright lines from the first decay (see Fig. 5.16). In particular, the studies with INTEGRAL/IBIS (Renaud et al. 2006) and NuStar (Grefenstette et al. 2014) settled the amount of  $^{44}\text{Ti}$  to  $\approx 1.4 \times 10^{-4} M_{\odot}$ , much larger than the 1D yield calculations predicted. Asymmetries in the explosion are now thought to cause a higher ejected  $^{44}\text{Ti}$  mass, as also revealed by the hard X-ray measurements of NuStar, providing a first resolved image of the Cas A supernova remnant in radioactive decay photons (Fig. 5.17 Nagataki et al. 1998; The et al. 2006; Wongwathanarat et al. 2016). In particular,  $^{44}\text{Ti}$  ejecta appear in

<sup>4</sup>Cassiopeia A is the only galactic supernova remnant young enough and close enough to study the gamma-rays from the  $^{44}\text{Ti}$  decay chain. One other supernova from which  $^{44}\text{Ti}$  decay gamma-rays have been detected is SN1987A in the Large Magellanic Cloud (Boggs et al. 2015).

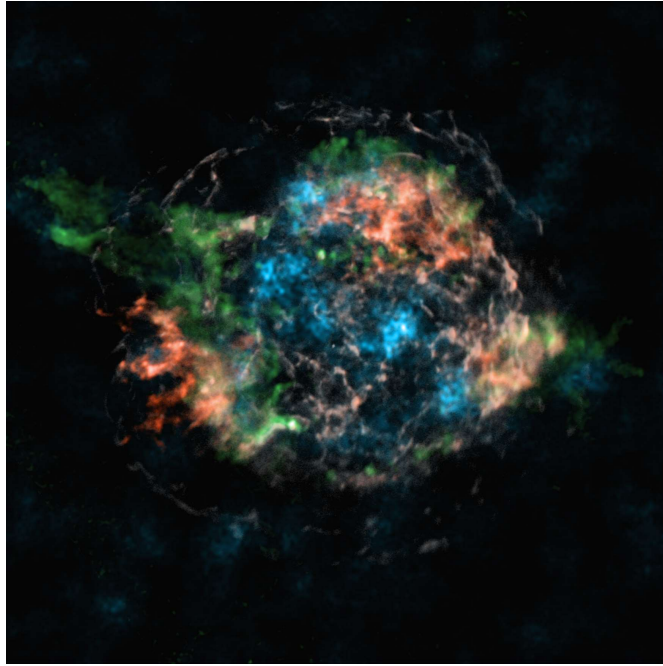


Figure 5.17: False-colour image of Cas A as seen at different wavelengths. In white, the 6 keV continuum emission is shown, the X-ray bright Fe emission in red, Si and Mg X-ray emission in green, and hard X-rays from  $^{44}\text{Ti}$  in blue. The  $^{44}\text{Ti}$  emission does not follow the distribution of Fe nor Si X-ray features as there may either be unshocked material left in the remnant or not seen, or the presupernova nucleosynthesis structure of elements in the star does not follow the standard picture. From Grefenstette et al. (2014).

clumps, re-affirming that Cas A did not explode as a spherical symmetric supernova. Not only this direct X-ray measurement showed the asymmetries but already from optical/infrared light echo spectra, asymmetries in the supernova photosphere have been revealed (Krause et al. 2005, 2008; Rest et al. 2008, 2011).

SPI on INTEGRAL is currently the only instrument which can observe the whole  $^{44}\text{Ti}$  decay chain gamma-rays at 68, 78, and 1157 keV in one coherent data set. In particular, exposures in which Cas A was at least in the partially-coded field of view of SPI, accumulated over ten years of the INTEGRAL mission are used to extract the spectra of this supernova remnant. This amounts to 5604 pointings, subdivided in an energy range covering the two low-energy lines and another energy range for the high-energy line, resulting in a total exposure of 10.84 Ms (partially-coded) in which Cas A was seen fully coded by the SPI coded mask aperture during 5.15 Ms, see Fig. 5.18.

The background is modelled in a slightly different manner as depicted in Sec. 3.2.3, as the source in the data set is always in the field of view of the instrument, so that the background tracing function has been derived from the data itself. Given the SPI imaging resolution of  $2.7^\circ$ , and the total supernova remnant diameter of  $\approx 5$  arcmin, the adopted sky intensity distribution (sky model) for Cas A is a point source, at the position of  $(l/b)_{\text{CasA}} = (111.74^\circ / -2.13^\circ)$ . In particular, the background modelling is done by fitting the known spectral shapes from the instrumental data base to a camera mean of one pointing with only one amplitude, which afterwards is assigned according to the background detector patterns to the raw spectrum of each detector. The maximum likelihood fit to determine the source strength from the data then requires less re-scaling parameters. This strongly suppresses the background but is also affected by systematics, e.g. over- or underestimating the continuum

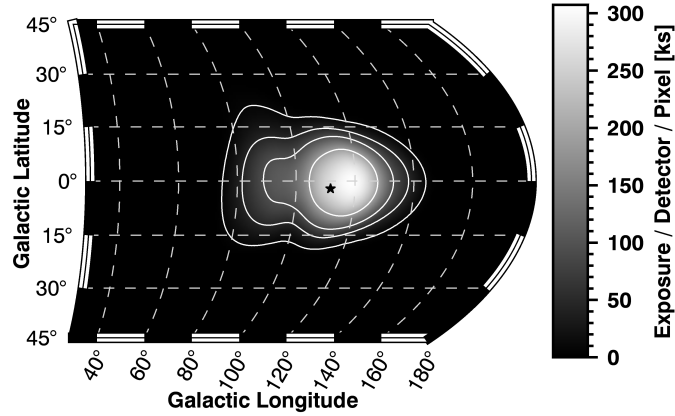


Figure 5.18: Exposure map of the Cas A SPI/INTEGRAL data set. Cas A is marked with a star at its position  $(l/b) = (111.74^\circ / -2.13^\circ)$ . Contours indicate the 0.1, 0.5, 1.0, and 2.0 Ms observation time boundaries.

contribution from the sky. However, any broadband resulting offset from zero in the finally derived spectra can be considered as a measure of systematics of this continuum treatment.

A priori, it is not assumed that the processes that lead to the low-energy lines from excited  $^{44}\text{Sc}$  (68, 78 keV) are the same for the high-energy line (1157 keV) from excited  $^{44}\text{Ca}$ . For example, cosmic-ray collisions with ambient  $^{44}\text{Ca}$  at several tens of MeV/nucleon effectively produce nuclear excitation, followed by de-excitation photons. Because  $^{44}\text{Sc}$  is short-lived, no corresponding excitation of  $^{44}\text{Sc}$  will occur through this cosmic-ray process, meaning that no additional emission is produced in the 68 and/or 78 keV lines. Therefore, the hard X-ray lines and the gamma-ray line is treated independently.

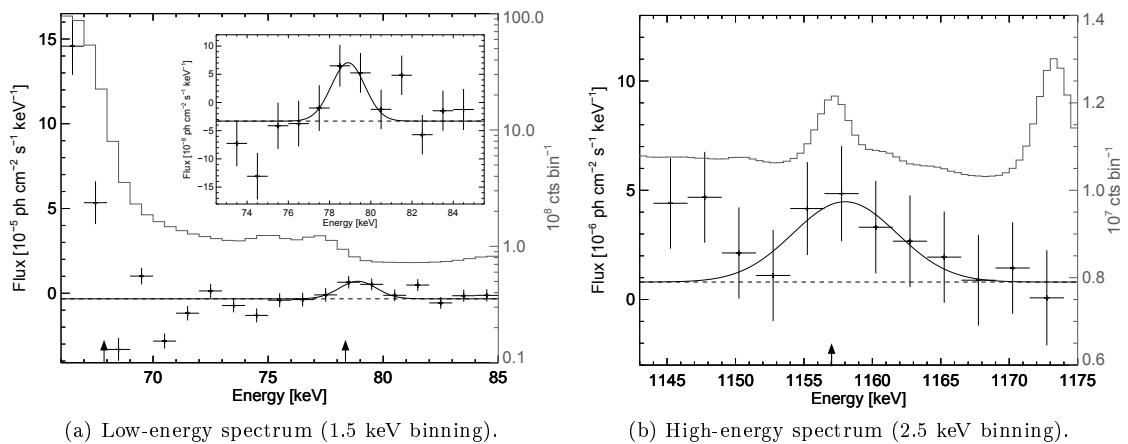


Figure 5.19: Spectra (black crosses) around the expected  $^{44}\text{Ti}$  lines from the position of Cas A. Both spectra have been fitted by a Gaussian-shaped line (solid lines) on top of a constant offset (dashed lines). The raw background spectrum is superimposed in both panels by a grey histogram with axes on the right. In panel (a), the background spectrum is shown in logarithmic scale as it increases by two orders of magnitude between 60 and 80 keV. The laboratory line energies are marked with arrows. See text for details.

The analysis shows the expected signature of a Gaussian-shaped line at the expected energies for the two independent spectra, as shown in Fig. 5.19. The significances of the lines are  $3.1\sigma$  (78 keV) and  $2.2\sigma$  (1157 keV), for a combined  $^{44}\text{Ti}$  detection significance of  $3.8\sigma$ . Systematic effects due to strong background features below 70 keV cannot be reliably modelled, and no constraint on the 68 keV line is obtained.

The mean reduced  $\chi^2$  of the maximum likelihood fit is 1.06 ( $\chi^2 = 98241, 92517$  dof), suggesting an additional systematic uncertainty. The spectra are well represented by a (symmetric) Gaussian on top of a constant offset. Spectral parameters for the 78 and 1157 keV line are given in Tab. 5.6.

Line	Flux	$M(^{44}\text{Ti})$	FWHM	$v_{exp}$	$\Delta E_0$	$v_{bulk}$	Signi.
$^{44}\text{Sc}^*(78.36)$	$3.5 \pm 1.2$	$2.4 \pm 0.9$	$8.6 \pm 1.4$	$2200 \pm 400$	$-1.0 \pm 3.6$	$-250 \pm 950$	3.1
$^{44}\text{Ca}^*(1157.02)$	$2.1 \pm 0.4$	$1.5 \pm 0.4$	$1.9 \pm 0.6$	$4300 \pm 1600$	$-0.7 \pm 1.1$	$-2700 \pm 4200$	2.2
Weighted mean	$2.3 \pm 0.4$	$1.6 \pm 0.4$	-	$2400 \pm 400$	-	$-350 \pm 950$	3.8

Table 5.6: Spectral parameters of the detected  $^{44}\text{Ti}$  line in Cas A. Given are the line origins with exact lab energy in keV, the measured flux in units of  $10^{-5}$  ph  $\text{cm}^{-2}$   $\text{s}^{-1}$ , the corresponding synthesised and ejected mass of  $^{44}\text{Ti}$  at the time of the explosion in units of  $10^{-4}M_\odot$ , the FWHM above instrumental resolution in units of keV, the resulting Doppler velocity spread interpreted as expansion velocity  $v_{exp}$  in  $\text{km s}^{-1}$ , the difference of the lab energy of the line with respect to the measured centroid in keV, the resulting bulk Doppler motion with respect to the Sun in  $\text{km s}^{-1}$ , and the detection significance above instrumental background and continuum in  $\sigma$  units. A weighted mean (inverse variance weighted) of the two lines is given in the last row. See text for details.

Formally, the flux values are consistent with each other, but the widths of the lines seem to differ by at least  $1000 \text{ km s}^{-1}$ . Also the previous high-energy line measurement by COMPTEL (Iyudin et al. 1994, 1997) shows a higher flux value than the hard X-ray line measurements. This systematic difference in " $^{44}\text{Ti}$ " flux is shown in Fig. 5.20a, illustrating the measurements of the  $^{44}\text{Sc}$  and  $^{44}\text{Ca}$  lines, taken with different instruments in the time between the years 1992 and 2014. The values are taken from The et al. (1996) with OSSE, Iyudin et al. (1997) with COMPTEL, Vink et al. (2001) with BeppoSAX, Renaud et al. (2006) with IBIS, this work with SPI, and Grefenstette et al. (2014) with NuStar (from left to right). These values only consider the fluxes measured with the mentioned instrument itself, hence no double-counting. When fixing the explosion date to AD 1671 an exponential decay law can be fit to the flux measurements of only the low- and high-energy line data points, respectively. Using the low-energy lines from the  $^{44}\text{Ti}$  decay as a direct estimate of the  $^{44}\text{Sc}$  flux, because it is uncontaminated by possible secondary processes that might mimic additional  $^{44}\text{Ti}$ , an additional flux of  $(2.29 \pm 0.62) \times 10^{-5} \text{ cm}^{-2} \text{ s}^{-1}$  can be estimated from a constrained fit of the high-energy line data points. This discrepancy has a statistical significance of  $3\sigma$ . About 340 yr after the explosion, the expected flux ratio  $F_{78}/F_{1157}$  is  $\sim 1$  but the measured flux ratio is  $0.6 \pm 0.24$ , suggesting an additional process which excites ambient  $^{44}\text{Ca}$ .

From the line fluxes, an observable  $^{44}\text{Ti}$  mass at the time of the explosion ( $t = 0$ ) can be estimated by

$$M(^{44}\text{Ti}, t = 0) = 4\pi d^2 F_i(t) \cdot 44m_u \cdot \tau(^{44}\text{Ti}) \cdot \exp(t/\tau(^{44}\text{Ti})) \cdot \frac{1}{p_i}, \quad (5.14)$$

similar to Eq. (5.11) but with the difference that a single object with known distance,  $d$ , and age,  $t = 337.2 \pm 6.4$  yr, is observed. In Eq. (5.14), for each detected line  $i$ , the flux  $F_i(t)$  is inserted and weighted with the probability  $p_i$  that a certain decay emits this photon during the de-excitation of the daughter nucleus. For the 1157 keV, a  $^{44}\text{Ti}$  mass of  $(2.4 \pm 0.9) \times 10^{-4}M_\odot$ , and for the 78 keV a mass of  $(1.5 \pm 0.4) \times 10^{-4}M_\odot$  is derived. Using also the measurements of previous studies in a weighted mean (inverse variance weighted), and combining them with the result of this work, a  $^{44}\text{Ti}$  mass of  $(1.37 \pm 0.19) \times 10^{-4}M_\odot$  is derived. The mass estimates from earlier measurements, corrected for distance and nuclear physics uncertainties,

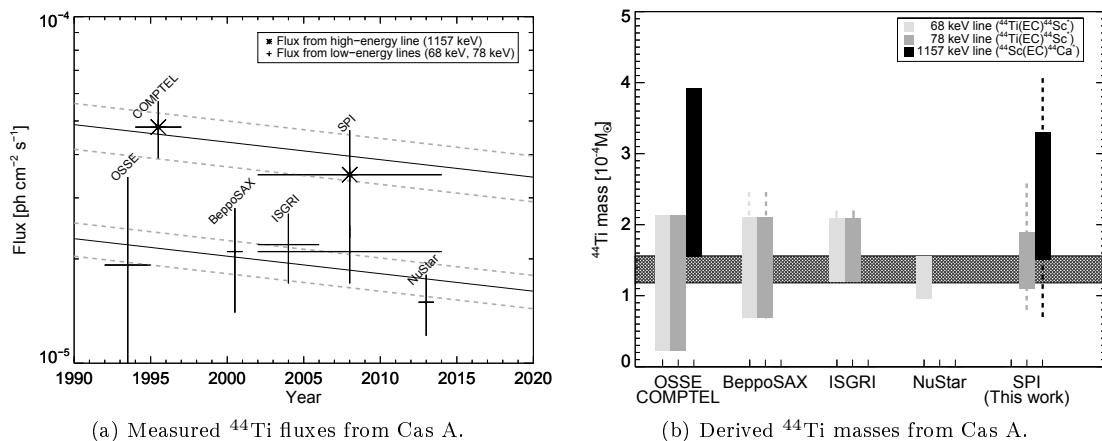


Figure 5.20: Comparison of Cas A measurements with different instruments. The left panel (a) shows a compilation of gamma-ray flux measurements in Cas A during the years 1992 to 2014 (see text). To each family of lines (low- and high-energy), an exponential decay function is fitted, fixing the characteristic life-time of  $^{44}\text{Ti}$  to 86 yr and the explosion date to AD 1671 (solid lines). The  $1\sigma$  uncertainties are shown separately by dashed grey lines for each fit. In panel (b), the derived  $^{44}\text{Ti}$  masses for each instrument are shown. The bars show the  $1\sigma$  uncertainty range of the estimated mass, including half-life time and explosion date. The OSSE and COMPTEL values are also corrected for the distance to Cas A. Upper limits (if given) are shown as dashed lines.

are illustrated in Fig. 5.20b, again showing that the "mass" estimates from the decay of  $^{44}\text{Sc}$  to  $^{44}\text{Ca}$  are systematically larger. Taking only the low-energy line measurements into account, the exponential fit, as above, obtains a  $^{44}\text{Ti}$  mass of  $(1.28 \pm 0.14) \times 10^{-4} M_{\odot}$ , whereas only the high-energy line measurements would reveal  $(2.72 \pm 0.43) \times 10^{-4} M_{\odot}$ .

Although the cosmic-ray acceleration, excitation and de-excitation scenario is plausible, its amplitude is probably over-estimated. Summa et al. (2011) simulated the nuclear excitation spectrum of Cas A, and suggested that the flux from de-exciting  $^{44}\text{Ca}^*$  would be of the order  $10^{-6} \text{ ph cm}^{-2} \text{ s}^{-1}$ , about one order of magnitude smaller than what is derived in work. As a consequence, the  $^{44}\text{Ti}$  mass estimate from the weighted mean of all previous and also this study is used as a robust yield from the Cas A supernova remnant,  $M_{\text{CasA}}(^{44}\text{Ti}) = (1.37 \pm 0.19) \times 10^{-4} M_{\odot}$ .

Taking into account that  $^{44}\text{Sc}$  decays with a probability of 94.27% via  $\beta^+$ -decay, the total  $^{44}\text{Ti}$  mass in Cas A converts to a total number of produced positrons of

$$N_{e^+}(\text{CasA}) = \frac{M_{\text{CasA}}(^{44}\text{Ti})}{M_{\text{atom}}(^{44}\text{Ti})} p_{\beta^+}^{44} = (3.52 \pm 0.49) \times 10^{51} e^+. \quad (5.15)$$

From the total mass of  $^{26}\text{Al}$  in the Milky Way, Sec. 5.1.1.4, a core-collapse supernova rate can be derived by using  $^{26}\text{Al}$  yield estimates from simulations, in particular from models of nuclear burning in stars during their evolution and terminal explosion. Diehl et al. (2006) calculated the galactic supernova rate,  $\dot{R}_{SN}$ , by assuming a steady-state  $^{26}\text{Al}$  maintenance, i.e. the decay of  $^{26}\text{Al}$  (destruction) is balanced by the production in winds and supernovae (supply), so that

$$\dot{R}_{SN} = \frac{M_{MW}(^{26}\text{Al})}{\tau(^{26}\text{Al}) \langle Y(^{26}\text{Al}) \rangle}. \quad (5.16)$$

Here,  $\langle Y(^{26}\text{Al}) \rangle$  is the initial-mass-function-averaged  $^{26}\text{Al}$  yield per supernova. This yield includes contributions from the explosive burning in supernova models, and also ejecta in the Wolf-Rayet wind phases. In the mass range between  $\approx 8$  and  $\approx 120M_{\odot}$ , the initial mass function scales as  $M^{-2.7}$ , which is enough to weight the dominant contribution of  $^{26}\text{Al}$  from massive stars, as intermediate-mass AGB stars only contribute a few per cent to the total mass. From a compilation of different models, Diehl et al. (2006) calculated an average  $^{26}\text{Al}$  yield of  $\approx 1.4 \times 10^{-4}M_{\odot}$  per supernova explosion. Using the galactic  $^{26}\text{Al}$  mass from Sec. 5.1.1.4, the core-collapse supernova rate in the Milky Way is  $\dot{R}_{SN} = 1.94 \pm 0.04$  per century. This value, however, is strongly affected by the total  $^{26}\text{Al}$  mass estimate of the Milky Way from which the supernova rate inherits a systematic uncertainty of the order of 25%. Also the yields are uncertain by a factor of  $\approx 30\%$ , so that the final core-collapse supernova rate in the Milky Way is

$$\dot{R}_{SN} = 1.94 \pm 0.04_{stat} \pm 0.76_{sys} \text{ century}^{-1}. \quad (5.17)$$

The main advantage of this method is that gamma-rays are not affected by extinction corrections, and thus provide an unlimited sample of the full disk of the Milky Way, and not only a small volume around the Sun. However, the systematic uncertainties of modelling yields, and finding the exact morphology, especially when disentangling fore- and background emission, Sec. 5.1.1.3.2, may result in biased estimates. Assuming the supernova rate in Eq. (5.17), the positron contribution from the decay of  $^{44}\text{Ti}$  can be estimated as

$$\dot{N}_{e^+}(^{44}\text{Ti}) = N_{e^+}(\text{CasA})\dot{R}_{SN} = (2.16 \pm 0.30) \times 10^{42} \text{ e}^+ \text{ s}^{-1}. \quad (5.18)$$

The value in Eq. (5.18) has to be considered as an upper limit, as, for example, the number of core-collapse supernovae that have been observed within the last 400 years (1) is significantly lower than was expected from a probabilistic approach of sampling  $^{44}\text{Ti}$  sources in the Galaxy (The et al. 2006). In particular, The et al. (2006) estimated how the  $^{44}\text{Ti}$  sky should appear in a gamma-ray survey, assuming a mean supernova rate of one per 30 years ( $3.33 \text{ century}^{-1}$ ), certain 1D model  $^{44}\text{Ti}$  yields for specific sub-types of core-collapse supernovae, and a parent spatial distribution for each sub-type. From their Monte Carlo treatment, they expect that for a gamma-ray telescope with a line sensitivity of  $10^{-5} \text{ ph cm}^{-2} \text{ s}^{-1}$ , about 4-7 sources should be detectable. The authors concluded that either the assumed rate of  $3.33 \text{ century}^{-1}$  is wrong, the assumed "typical" yields are underestimated (see also above), there are rare outliers, or the locations of core-collapse supernovae does not follow that of star formation (spiral arms). In fact, the rate is large compared to this work, even when accounting for the systematics. Also the yields might be underestimated as the only two observed remnants (Cas A, SN1987A) show  $^{44}\text{Ti}$  masses of more than  $10^{-4}M_{\odot}$ , so that also the peculiarity argument might not hold. However, there are observational indications that stars of certain masses may not explode, at all (Williams et al. 2014). This could also be supported by 3D supernova simulations, which "fail" to explode (e.g. Melson et al. 2015; Sukhbold et al. 2016; Janka et al. 2016), resulting in a skewed estimate of heavy-element yields, and in return of the core-collapse "supernova" (i.e. with nuclei ejecta) rate. Positrons may not escape from the young remnant shortly after the explosion, rather depositing

their energy inside the supernova cloud, as is the case of radioactive decay positrons from  $^{56}\text{Co}$ . In consequence, the positron contribution from radioactive  $^{44}\text{Ti}$  in core-collapse supernova explosions may be one order of magnitude below the estimate in Eq. (5.18).

Another way to evaluate the galactic  $^{44}\text{Ti}$  production rate is based on the solar ratio of  $^{44}\text{Ca}$  to  $^{56}\text{Fe}$ , which are the stable nuclei of the decay of  $^{44}\text{Ti}$  and  $^{56}\text{Ni}$  in supernova explosions. This ratio is known to be  $1.2 \times 10^{-3}$  (Lodders 2003), and functions as a conversion factor between the current rate of  $^{56}\text{Fe}$  production. This is given as the measured yield of a "typical" core-collapse supernova, here SN1987A with  $\langle Y(^{56}\text{Ni}) \rangle = 0.07 M_{\odot}$ , times the supernova rate  $\dot{R}_{SN}$ . The positron production rate is then

$$\dot{N}_{e^+}(^{44}\text{Ti}) = \left( \frac{^{44}\text{Ca}}{^{56}\text{Fe}} \right)_{\odot} \frac{\langle Y(^{56}\text{Ni}) \rangle \dot{R}_{SN}}{M_{atom}(^{44}\text{Ti})} p_{\beta^+}^{44} = (1.33 \pm 0.03) \times 10^{42} \text{ e}^+ \text{ s}^{-1}, \quad (5.19)$$

which is of the same order of magnitude as the estimate in Eq. (5.18), and is affected by the same systematic uncertainty in the galactic supernova rate. Adopting the value in Eq. (5.18) of  $(2.16 \pm 0.30) \times 10^{42} \text{ e}^+ \text{ s}^{-1}$ , the contribution of  $^{44}\text{Ti}$  to the galactic positron content amounts to  $4.4 \pm 1.5\%$ . The contribution to the disk positron annihilation rate is  $7.0 \pm 3.5\%$ . In total,  $^{44}\text{Ti}$  alone, and also in combination with  $^{26}\text{Al}$  (disk:  $17.8 \pm 6.3\%$ ; Galaxy:  $11.2 \pm 2.6\%$ ), is not enough to explain the observed positron content.

### 5.1.3 Thermonuclear Explosions

Low- to intermediate-mass stars ( $\lesssim 8M_{\odot}$ ) do not reach the upper burning stages, as also shown in Fig. 5.14, and hence do not explode in a core-collapse supernova. Instead, such stars only burn H, He, and possibly C, thereby expand to red giant stars, and are not heavy enough to ignite further stages, so that the source of hydrostatic pressure dries up. An amount of C and O builds up in the centre of a red giant which loses its outer layers. After the star lost all its layers and stops nuclear fusion, the remnant is called a white dwarf (WD), and is only stabilised against gravity by the Fermi pressure of a degenerate electron gas. WDs have high densities, of the order  $10^9 \text{ kg m}^{-3}$ , and are only stable up to the Chandrasekhar limiting mass of  $\approx 1.44M_{\odot}$ . Depending on the specific initial mass of the star, several compositions of WDs are possible. Very low mass stars,  $M \lesssim 0.5M_{\odot}$  will never be hot enough in their interiors during their evolution to burn He, and will probably end as He-only WDs. Since the evolution time of such a star is  $\approx 44 \text{ Gyr}$ , much higher than the age of the Universe of  $13.8 \text{ Gyr}$ , such He-only WDs are hard to observe as only interactions in a binary system would speed up the evolution of a very low-mass star. Up to an initial mass of  $\approx 8M_{\odot}$ , WDs obtain a "typical" final composition of C and O (CO-WDs). If the progenitor is even more massive than  $8M_{\odot}$ , up to  $\approx 10M_{\odot}$ , its core may end as a CONeMg-WD, provided that star does not collapse into a neutron star (Werner et al. 2005).

Once a WD formed, it is very hot compared to its progenitor, and as it has no

energy source, it will cool down steadily over time by radiating and thus becomes redder. If the WD is not in a binary system with another star, it will cool down for ever, finally becoming a "black dwarf" (Adams & Laughlin 1997). If, however, a WD has a companion star, it can accrete mass from it, which might at some point lead to a thermonuclear supernova of type Ia. This means, when the WD is exceeding its Chandrasekhar mass limit, or is ignited by another mechanism, a sudden rise in temperature will start nuclear reactions again, until the entire star is disrupted. The fast energy production forms a convective core in the centre, which grows very quickly, and as a consequence of the enhanced energy release, the temperature rises even further, and accelerates nuclear reactions - a thermonuclear runaway occurs, and a nuclear burning flame propagates outwards the WD. This sudden release of energy finally leads to an explosion and the mechanical disruption of the system. A WD explodes when enough mass, i.e.  $\gtrsim 0.3M_{\odot}$ , is completely burnt on a time scale of 1 s, which then ultimately exceeds the binding energy of the star,  $E_{grav} = \frac{5}{3} \frac{GM}{R^2} \approx 1.5 \times 10^{51}$  erg. This happens either due to a detonation (Arnett 1969a) or a deflagration (Nomoto et al. 1976), i.e. either caused by a shock-induced burning which propagates supersonically through the unburnt medium of the star, or caused by a thermal conduction burning front at subsonic velocities.

A type Ia supernova is commonly described by its light curve which originates in the decay gamma-rays of radioactive  $^{56}\text{Ni}$ . These are absorbed and/or down-scattered in the supernova cloud, and re-emitted at lower energies. The bolometric light curve shows a sudden rise in luminosity, followed by a steep decline, lasting for several weeks due to the decay of  $^{56}\text{Ni}$  with a half-life time of 6.1 d, and another gradual decline due to decay gamma-rays of the daughter nucleus  $^{56}\text{Co}$  with a half-life time of 77.1 d. Because of the fact that most of the WDs have the same mass when they explode, the peak luminosity and shape of the light curve of SNe Ia are characteristic and can be normalised to a common "standard candle". This uniformity can then act as a tool for cosmological distance measurements, by comparing the expected ("known") luminosity, e.g. in units of the absolute magnitude  $M$  of a typical SN Ia, normalised to a distance of 10 pc, with the measured, apparent magnitude  $m$ , via the distance modulus,  $m - M = 5 \lg(d) - 5$ .

The nuclear burning processes in SNe Ia depend on the peak temperature reached, and on the ratio between neutrons and protons, in general described as the neutron excess  $Y_e = Z/A$ . During such a thermonuclear event, nuclear-statistical equilibrium, Si-, O-, and C-Ne-burning<sup>5</sup> are encountered, which produce the nuclear yields of a SN Ia, depending on the initial composition. If  $Y_e$  obtains a value of 0.5, the majority of burnt material ends up in the form of  $^{56}\text{Ni}$ , whereas deviations from this value shifts the peak towards other nuclei like  $^{58}\text{Ni}$  and  $^{54}\text{Fe}$  ( $Y_e = 0.470 - 0.485$ ), or  $^{58}\text{Fe}$  and  $^{54}\text{Cr}$  ( $Y_e = 0.43 - 0.45$ ). The total amount of nucleosynthesised  $^{56}\text{Ni}$  ranges between 0.1 and  $1.0M_{\odot}$ , depending on the sub-type of the supernova, but averages to a common value of  $0.5 - 0.6M_{\odot}$ , ejected into the ISM for "normal" SNe Ia (Isern et al. 2011).  $^{56}\text{Co}$  decays with a probability of  $p_{\beta^+}^{56} = 19.58\%$  via  $\beta^+$ -decay to stable  $^{56}\text{Fe}$ . Thus, there is a large potential for SNe Ia to be a dominant positron producer in the Galaxy. But as the last nearby SN Ia in the Milky Way was probably Kepler's supernova<sup>6</sup>, SN1604, 412 years ago, all the  $^{56}\text{Ni}$  and  $^{56}\text{Co}$  from this event already decayed, and the galactic contribution of positron from such explosion must

<sup>5</sup>During the short time scale of such an event, all burning processes can be considered incomplete.

<sup>6</sup>The supernova remnant G1.9+0.3 is also believed to have exploded as a SN Ia only 120 - 150 years ago at a distance of more than 8 kpc, again too old and too far away to observe any remaining  $^{56}\text{Co}$ .

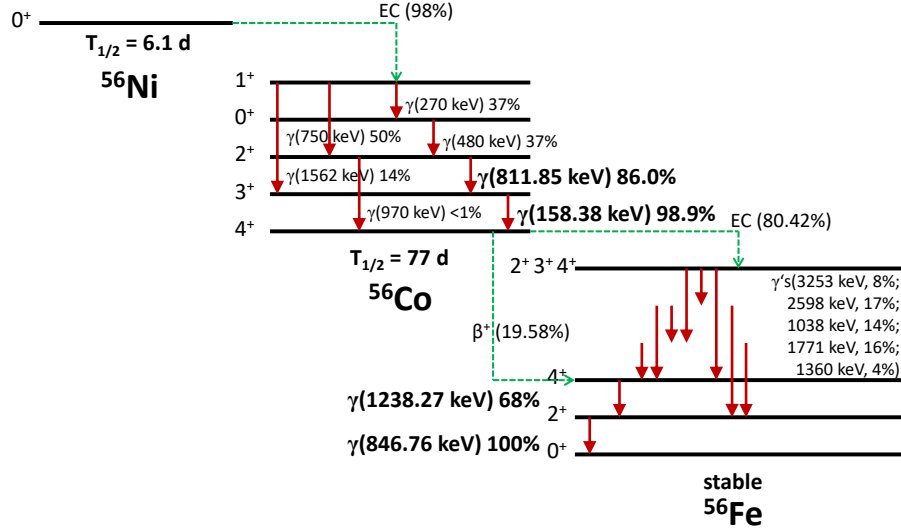


Figure 5.21: Decay scheme of the  $^{56}\text{Ni}$  decay chain. With a half-life time of 6.1 d, first  $^{56}\text{Ni}$  is decaying with 98% probability via electron capture to an excited state of  $^{56}\text{Co}$  which is de-exciting by the emission of a cascade of gamma-rays, and then also decaying after 77 d via positron emission with 19.58% probability to an excited state of  $^{56}\text{Fe}$ .  $^{56}\text{Fe}$  is then predominantly de-exciting by the emission of gamma-rays at 1238.27 keV and 846.76 keV.

be inferred indirectly. With Arnett's rule (Arnett 1982), the amount of  $^{56}\text{Ni}$  in a typical SNe Ia is also constrained observationally, to about  $0.1 - 1.0M_{\odot}$  (Stritzinger et al. 2006), using the bolometric light curve and its decline from distant SNe Ia. This amount is expected from the conversion of about one solar mass of C and O (WD), to mainly iron peak elements. From this mass, the number of positrons that are produced in total in such a supernova can be estimated to be around

$$N_{e^+}^{56}(\text{SN Ia}) = \frac{M_{\text{SN Ia}}(^{56}\text{Ni})}{M_{\text{atom}}(^{56}\text{Ni})} p_{\beta^+}^{56} = 4.2 \times 10^{53-54} e^+. \quad (5.20)$$

Because of the short decay time of  $^{56}\text{Co}$ , it is questionable whether the positrons can escape the local environment of the supernova, at all. During the early phases of the expanding supernova cloud, gamma-rays from the decay chain of  $^{56}\text{Ni}$ , Fig. 5.21, power the visible light curve, but as the envelope dilutes, gamma-rays may readily escape. The late light curve is thought to be powered by energy depositions of positrons. Milne et al. (1999) compared the average light curves of many distant SNe Ia to models in which a certain fraction of positrons are trapped, and found that  $f_{\text{norm}}^{\text{esc}} = 0.0 - 11.3\%$  of the positrons may escape the supernova until 2000 days after the explosion. They derived an average positron escape value of  $f_{\text{norm}}^{\text{esc}} \approx 3\%$ . In a follow-up study, Milne et al. (2001) also showed that a radial escape of positrons better describes the data of sub-luminous SNe Ia of generic type SN1991bg ( $f_{91bg}^{\text{esc}} = 100\%$ ), which are less frequent thermonuclear explosions ( $p_{91bg} \approx 15\%$  of the total number; "normal" SNe Ia occur<sup>7</sup> at  $p_{\text{norm}} \approx 70\%$ ), and only produce of the order of  $0.1M_{\odot}$  of  $^{56}\text{Ni}$ , or less. Combining the two types, the average yield of positrons from  $^{56}\text{Ni}$  in SNe Ia is

<sup>7</sup>There are also other sub-types of SNe Ia with another sub-luminous type, SN2002cx-like with  $p_{2002cx} \approx 5\%$  and a typical  $^{56}\text{Ni}$  of  $0.2M_{\odot}$ , and also super-luminous supernovae of generic type SN1991T with  $p_{91T} \approx 10\%$  and  $> 1.5M_{\odot}$  of  $^{56}\text{Ni}$  (Li et al. 2011; Hillebrandt et al. 2013). The sub-luminous types are henceforth assumed to not trap positrons and the normal and super-luminous ones to trap 97% of the positrons.

$$\langle N_{e^+}^{56}(\text{SN Ia}) \rangle = \sum_i N_{e^+}^{56}(i) p_i f_i^{\text{esc}} \approx 1.7 \times 10^{53} \text{ e}^+, \quad (5.21)$$

where the sum is over all  $i$  sub-types of supernovae of type Ia. The inferred SN Ia rate for the Milky Way is around  $R_{\text{SNIa}} = 0.5 \text{ century}^{-1}$ , based on extragalactic observations (e.g. van den Bergh & Tammann 1991; Mannucci et al. 2008; Prantzos et al. 2011). Thus, the positron production rate from  $^{56}\text{Ni}$  in WD explosions can be estimated as

$$\dot{N}_{e^+}(^{56}\text{Ni}) = \langle N_{e^+}^{56}(\text{SN Ia}) \rangle R_{\text{SNIa}} = 2.7 \times 10^{43} \text{ e}^+ \text{ s}^{-1}, \quad (5.22)$$

which would indeed just be enough to supply the whole positron content in the Milky Way, as was already pointed out by Prantzos (2006). However, the above estimates can be very defective, as they are all based on indirect measurements and assumptions. In particular, the yield of  $^{56}\text{Ni}$  is based on the uniformity of bolometric light curves, of which  $\approx 70\%$  can be normalised to a common scale. But assuming that the (peak) luminosity is only due to the decay  $^{56}\text{Ni}$  might overestimate the total yield. In fact, for so-called super-luminous supernovae, Arnett's rule (Arnett 1982) may not apply, as a single WD cannot exceed its Chandrasekhar limiting mass of  $\approx 1.4M_{\odot}$ , but yield estimates suggest  $1.5\text{-}2.0M_{\odot}$  of  $^{56}\text{Ni}$  for such events (see e.g. Hillebrandt et al. 2013). If instead of a single WD with a (giant) normal star companion, two WDs merge, the ejected mass could in principle be larger, as two stars may be burnt. The escape fraction of positrons from the  $^{56}\text{Co}$ -decay is also only measured indirectly. But this provides an order of magnitude estimate of the number of positrons, ejected into the ISM, of a few per cent from one such event. The diversity of SNe Ia has shown that, in principle, either all positrons could be trapped for certain 1D model calculations, or all could be ejected, for example, in the case of sub-luminous supernovae. Consequently, the escape fraction is the crucial point in determining the positron contribution of SNe Ia. A direct measurement of both, decay gamma-rays to determine the produced  $^{56}\text{Ni}$  mass, and annihilation gamma-rays to determine the number of positrons deposited in the supernova, can provide a reliable estimate of positrons from this type of explosion. This is then not based on assumptions and indirect inference. However, the thermonuclear supernova rate may be as inaccurate as the core-collapse supernova rate, and may only provide an upper limit.

On the 14th of January 2014, in the Galaxy M82 at a distance of  $\approx 3.5 \text{ Mpc}$ , a type Ia supernova went off - the closest since four decades, and within reach for observations with INTEGRAL. This unique opportunity was used to measure for the first time decay gamma-rays of  $^{56}\text{Ni}$  and  $^{56}\text{Co}$  from such a supernova type, thus determining the synthesised mass and kinematics of the explosion. In addition, the first gamma-ray light curve is measured, providing valuable clues about the still unsolved progenitor problem of SNe Ia. By determining the number of positrons annihilated in the envelope of SN2014J through its 511 keV gamma-rays, and comparing it to the derived mass of  $^{56}\text{Ni}$ , the positron escape fraction during the time of the INTEGRAL observation can be directly estimated. In the next Secs. 5.1.3.1 and 5.1.3.2, the SPI measurement of SN2014J will be described and used for a direct estimate of the positron content from SNe Ia in the Galaxy. These results have been presented in

Diehl et al. (2014), Diehl et al. (2015), Siegert & Diehl (2015), and Christodoulou, A. S. (2016).

### 5.1.3.1 Measuring the Ni-56 Decay-Chain in SN2014J

The INTEGRAL/SPI observation data set of SN2014J is subdivided in three parts. One early observation period, 16 days after the inferred explosion date, then until the expected maximum in gamma-ray light around days 60-100, and a late observation period when the supernova is expected to be completely optically thin for gamma-rays, around days 135 to 164. In particular, INTEGRAL orbits 1380 to 1428, with one major gap between 23 April and 27 May, are used for the analysis, for a main exposure of 2.8 Ms in the rising and maximum part of the gamma-ray light curve, and additional 1.4 Ms at late times. After data selections to suppress contaminations from solar flare events, for example, the data set consists of 4.2 Ms of exposure, spread over 1816 telescope pointings with a typical time of 3000 s. During the observation, SN2014J was always in the field of view of SPI, at its celestial position of  $(l/b)_{SN2014J} = (141.43^\circ/40.56^\circ)$ . The analysis is split into three targets, first searching for the dominant decay gamma-rays of  $^{56}\text{Ni}$ , at 158 and 812 keV, at early times, as the half-life time is only 6.1 d, then investigating the spectra for time-variable  $^{56}\text{Co}$  lines at 847 and 1238 keV, and finally determining the 511 keV flux of annihilation gamma-rays during the whole observation (Sec. 5.1.3.2).

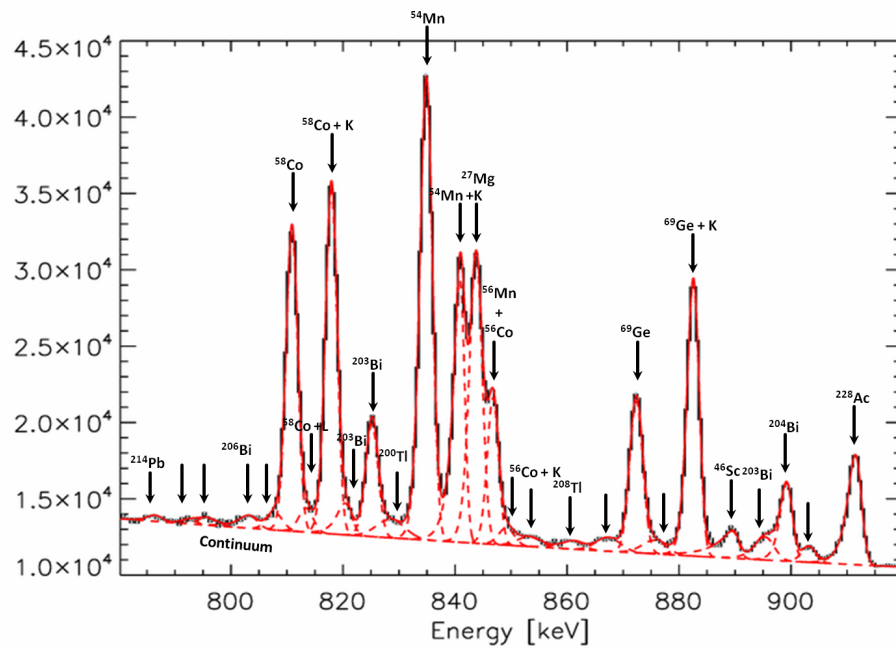


Figure 5.22: Background spectrum for the analysis of  $^{56}\text{Ni}$  decay gamma-rays. Shown is the raw orbit-integrated count spectrum of the SPI camera in the energy range between 780 and 920 keV per half-keV energy bin in black and superimposed a spectral fit in red, identifying 28 different components: a gamma-ray continuum, described by power-law, and 27 instrumental background lines, indicated with arrows and named if appropriate candidate source isotopes have been found.

The background around the target lines is modelled similarly to the Cas A case, Sec. 5.1.2.2. As SN2014J is at a distance of  $3.5 \pm 0.3$  Mpc with an intrinsic size of a few AU, the celestial emission model is also a point source. Because of the half-life time of  $^{56}\text{Co}$ , 77.1 d, the source is expected to be variable in time, and hence the maximum likelihood parameter estimation also includes several time nodes for the

celestial contribution, rather than only for the background. An example of a spectral background fit between 780 and 920 keV, covering the dominant  $^{56}\text{Ni}$  and  $^{56}\text{Co}$  lines, is shown in Fig. 5.22. In this spectrum, 27 individual instrumental background lines are fitted with the function of Eq. (3.19). Repeating this for each of the 15 working detectors of the data set, and for all observation revolutions, builds the basis of the instrumental background modelling towards precise detector patterns from different background sources in the satellite (Sec 3.2.3).

### 5.1.3.1.1 Early Time Spectra of Ni-56

Right at the onset of the maximum (visible) light of SN2014J, INTEGRAL started observations only 16.3 days after the inferred explosion date of January 14, UT  $14.75 \pm 0.21$  (Zheng et al. 2014). During this time, models (e.g. Isern et al. 2008) predict that the supernova envelope should still be opaque, even to penetrating gamma-rays from the  $^{56}\text{Ni}$  decay. It is expected that  $^{56}\text{Ni}$  is buried deeply in the supernova, and gamma-rays from the daughter nucleus  $^{56}\text{Co}$  only leak out of the expanding remnant several weeks after the explosion (e.g. Hillebrandt & Niemeyer 2000). It was hence surprising to measure a consistent signal of  $^{56}\text{Ni}$  decay gamma-rays, several weeks before they have been expected by most models. The  $^{56}\text{Ni}$  spectra are shown in Fig. 5.23.

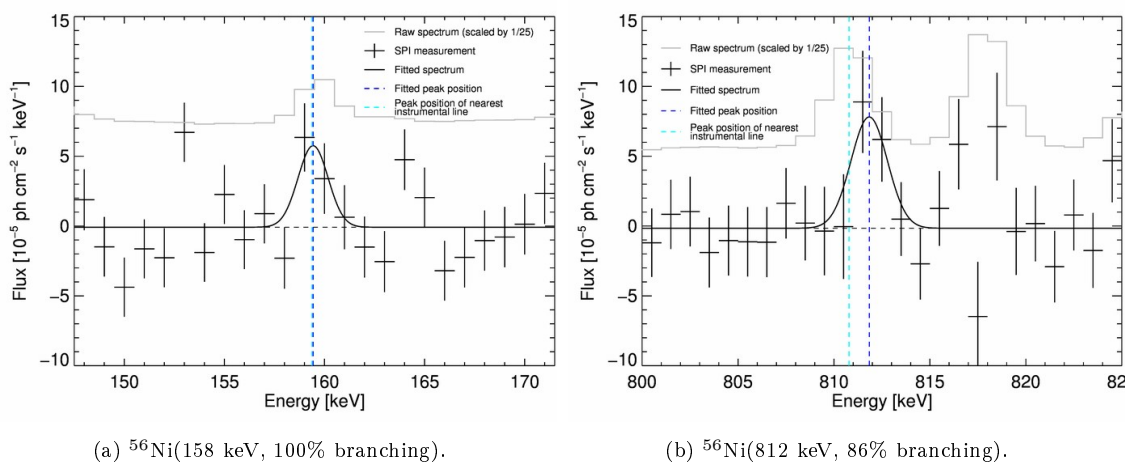


Figure 5.23: Gamma-ray spectra (black crosses) from SN2014J at maximum light, between days 16.6 and 19.2 after the explosion around 158 (left) and 812 keV (right), showing the two main  $^{56}\text{Ni}$  decay gamma-ray lines. The solid black lines are Gaussians on top constant offsets as fitted to the data points. The scaled raw spectrum is superimposed in grey, together with the peak positions of the fitted Gaussians compared to the peak of the nearest instrumental line. See text for details.

The two major lines at 158 and 812 keV are detected with a statistical significance of  $2.7\sigma$  and  $2.9\sigma$ , respectively, over instrumental background and celestial gamma-ray continuum, for a total  $^{56}\text{Ni}$  detection significance of  $4.0\sigma$ . Both spectra are extracted from a point source at the position of SN2014J, between days 16.6 and 19.2 after the explosion, and can well be described by a Gaussian on top of a constant offset. Within statistical uncertainties, the two lines are identical. Integrating the line profiles yields a gamma-ray flux of  $(1.10 \pm 0.42) \times 10^{-4} \text{ ph cm}^{-2} \text{ s}^{-1}$  (158 keV) and  $(1.90 \pm 0.66) \times 10^{-4} \text{ ph cm}^{-2} \text{ s}^{-1}$  (812 keV), respectively. The fitted centroids are  $159.43 \pm 0.43$  and  $811.84 \pm 0.42$  keV, respectively, consistent with the laboratory energies of 158.38 and 811.84 keV. This hence corresponding to a bulk velocity below

$\approx 2000 \text{ km s}^{-1}$  ( $2\sigma$  conf.). The measured intrinsic celestial line widths suggest no significant Doppler broadening, and although broader components could underlie the main signal, Fig. 5.24, velocity spreads are below  $\approx 2000 \text{ km s}^{-1}$  ( $2\sigma$  conf.).

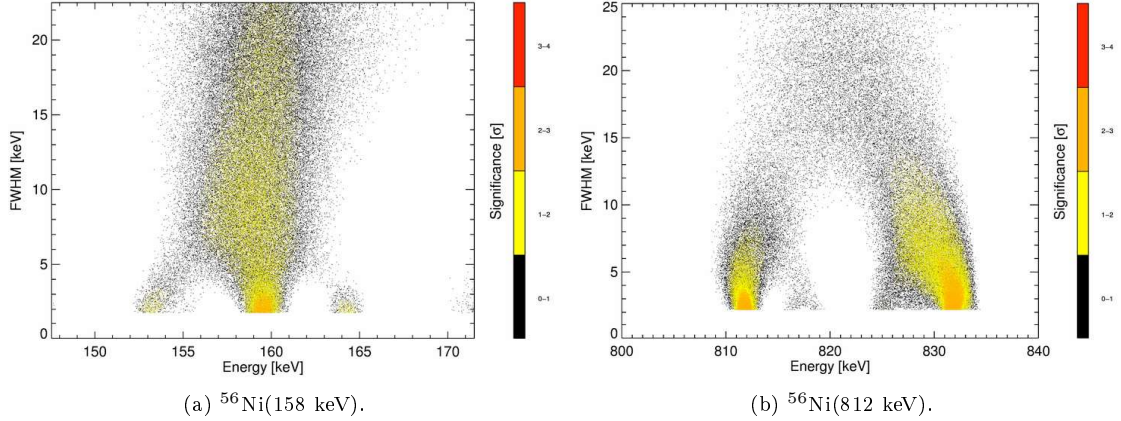


Figure 5.24: Monte-Carlo analysis of  $^{56}\text{Ni}$  spectra from SN2014J. Shown are the line parameter uncertainties as estimated from a random search around the the best fit values for the 158 keV (left) and 812 keV (right) lines in early SPI measurements. The only constraint is a minimum line width of the intrinsic instrumental width to cater for outliers of single data points from their neighbours. The absolute maxima of significance (=best fits) occur at (159.4 keV/1.77 keV) and (811.8 keV/2.23 keV), respectively. Both lines seem to have "satellite" lines at the same Doppler velocity of  $\approx 7500 \text{ km}^{-1}$  ( $\approx 4 \text{ keV}$  blue-shift at 158 keV and  $\approx 20 \text{ keV}$  blue-shift 812 keV). If an analysis with coarser energy binning (e.g. 10 keV) is performed, the lines are found consistently with a large broadening. However, the MCMC analysis suggests the lines to be rather narrow and not significantly Doppler-shifted.

The measured flux values can be converted to a  $^{56}\text{Ni}$  mass, seen to decay, at  $t \approx 18$  days past the explosion that corresponds to

$$\begin{aligned}
 M_{SN2014J}(^{56}\text{Ni}, t = 0) &= 4\pi d^2 F_{^{56}\text{Ni}}(t) \cdot 56m_u \cdot \tau(^{56}\text{Ni}) \cdot \exp(t/\tau(^{56}\text{Ni})) \cdot \frac{1}{p_{Ni}} = \\
 &= 0.06 \pm 0.03 M_{\odot}
 \end{aligned}
 \tag{5.23}$$

of  $^{56}\text{Ni}$  at the time of the explosion ( $t = 0$ ), where  $p_{Ni} = 98.8\%$  for the 158 keV and  $p_{Ni} = 86.0\%$  for the 812 keV line. This mass estimate is rather small for typical scenarios in which  $^{56}\text{Ni}$  is buried deeply in the supernova cloud where all gamma-rays should have been absorbed at this time. Therefore, the measurement implies that a substantial fraction of  $^{56}\text{Ni}$  must have been produced close to the surface of the exploding WD, and at a depth not exceeding a few  $\text{g cm}^{-2}$  in column density. Such a large amount of  $^{56}\text{Ni}$  freely exposed, together with the constraints on the kinematics, is unexpected in most explosion models. However, observations in other wavelengths also suggest SN2014J to be an unusual explosion, since the expected  $t^{-2}$ -behaviour (Nugent et al. 2011) in the rise of the optical light curve is not strictly represented by the data: Hours after the explosion, the light curve can be described by a broken power-law, showing a steeper rise and a possible "shoulder", which might also imply  $^{56}\text{Ni}$  near the surface (Goobar et al. 2014; Zheng et al. 2014).

Classical scenarios with a single WD being disrupted due to exceeding its Chandrasekhar limits mass have been excluded from upper limits of X-ray emission measurements (Nielsen et al. 2014). So-called sub-Chandrasekhar models, with a He-donating companion star, or a WD merger, seem to work better in the case of SN2014J,

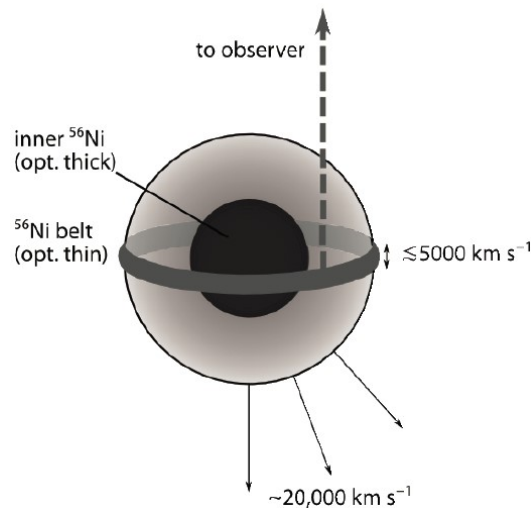


Figure 5.25: Sketch of a SN2014J ejecta configuration which is compatible with the INTEGRAL/SPI observations. Helium accreted in a belt before the explosion produces the  $^{56}\text{Ni}$  belt at the surface of the ejecta. The gamma-rays can escape from the belt material, while the  $^{56}\text{Ni}$  in the core (black) is still buried at high optical depths. The observer has to view the supernova nearly face-on.

and already explain the  $^{56}\text{Ni}$  located near the surface (Ruiter et al. 2014). Most of these double-detonation models, however, predict high velocity gamma-ray lines to be observed, if a shell of  $^{56}\text{Ni}$  was surrounding the supernova ejecta (Fink et al. 2007, 2010; Moll & Woosley 2013), and moreover should have an imprint on optical and infrared observables (Kromer et al. 2010), which are not seen in SN2014J (Nielsen et al. 2014). A plausible, though speculative configuration that explains the gamma-ray data, is an equatorial He belt, rather than a shell, accreted from a He donor. If this situation was observed essentially pole-on, the kinematic constraints can be met. Analogous to classical novae where this idea has already been discussed (Kippenhahn & Thomas 1978; Piro & Bildsten 2004), unstable mass transfer from a He companion to the WD is possible if the He donor is more massive than the WD and fills its Roche lobe. In order to conserve a belt and not to spread the accreted He over the WD before the He flash explosion, either the accretion rate must be of the order of  $10^{-5} M_{\odot} \text{ yr}^{-1}$  (Law & Ritter 1983), and/or the WD must be rapidly rotating, so that the accretion is faster than it loses angular momentum. Such a high accretion rate can be achieved if the material is mostly He and not H. When this He belt becomes dense enough, explosive He burning may be ignited, and the configuration as shown in Fig. 5.25 can be established. Remarkably, such a configuration would not violate optical nor gamma-ray observation data, and also radiation transfer simulations (see Diehl et al. 2014, supplementary information) do not produce easily distinguishable features from UV to IR wavelengths, when comparing the  $^{56}\text{Ni}$  belt to SN Ia standard models. In return, this makes SN2014J appear quite normal at any observation angle (Fig. 5.26).

#### 5.1.3.1.2 Variable Spectra of Co-56 Emission

In Fig. 5.27, the resulting spectra of a point source at the position of SN2014J between days 66.3 and 99.1 after the explosion are shown, i.e. when most explosion models predict the  $^{56}\text{Co}$  decay gamma-rays at predominantly 847 and 1238 keV to

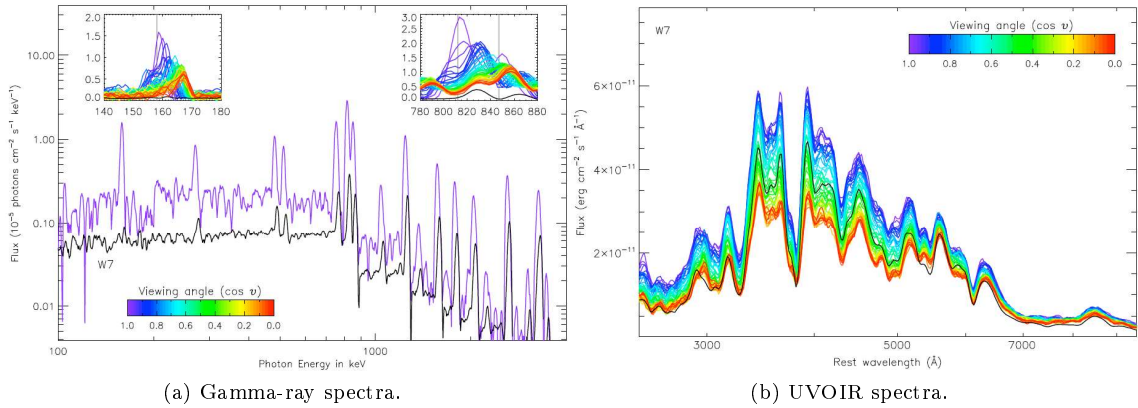


Figure 5.26: Expected model spectra of the supernova belt configuration from Fig. 5.25 as viewed from different observing angles (coloured spectra) and compared to the canonical W7 model (black) (Nomoto et al. 1984). In panel (a), a spectrum from a polar viewing angle is shown (violet) at day 18 after the explosion assuming a distance of 3.5 Mpc. In panel (b), the UV, O, and IR wavelengths are shown for the belt model configuration.

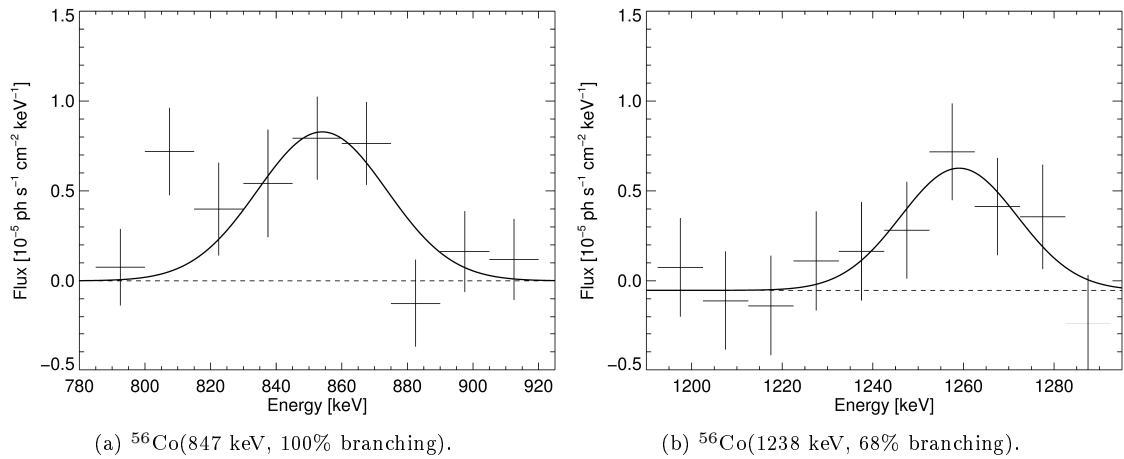


Figure 5.27: Spectra (black crosses) of  $^{56}\text{Co}$  decay gamma-rays from the position of SN2014J at expected gamma-ray line maximum between days 66.3 and 99.1 after the explosion around 847 (left) and 1238 keV (right). The solid black line represents Gaussians as fitted to the derived data points. See text for details.

have their maxima. The two  $^{56}\text{Co}$  lines are clearly detected in this time window, with statistical significances of  $4.4\sigma$  and  $3.0\sigma$  above instrumental background and continuum, respectively. During the total observation time, i.e. between days 16.3 and 164.0, gamma-ray emission is detected with  $9.5\sigma$  in the band between 780 and 920 keV, and with  $3.1\sigma$  in the band between 1190 and 1290 keV, respectively, consistent with expectations from models, predicting most of the flux below  $\approx 900$  keV as also shown in Fig. 5.26a. The measured flux values from the lines in Fig. 5.27 are  $(3.65 \pm 1.21) \times 10^{-4} \text{ ph cm}^{-2} \text{ s}^{-1}$  (847 keV) and  $(2.27 \pm 0.69) \times 10^{-4} \text{ ph cm}^{-2} \text{ s}^{-1}$  (1238 keV), respectively, for a branching ratio of  $0.62 \pm 0.28$ . This is consistent with the laboratory value of 0.68. The mass of  $^{56}\text{Ni}$  is  $0.50 \pm 0.12 M_{\odot}$ , as derived from the flux values, in analogy to Eq. (5.23), taking into account that  $\tau(^{56}\text{Ni}) \ll \tau(^{56}\text{Co})$ , and assuming the supernova is fully transparent. This mass estimation, the constraints of the Doppler broadening of about 40 to 50 keV (FWHM), corresponding to velocities of  $5500 \pm 1200 \text{ km s}^{-1}$ , and the lines to be blue-shifted about  $3000 \pm 1500 \text{ km s}^{-1}$ , are in good agreement with the majority of SN Ia model calculations.

The high-precision background modelling approach also allows to investigate the

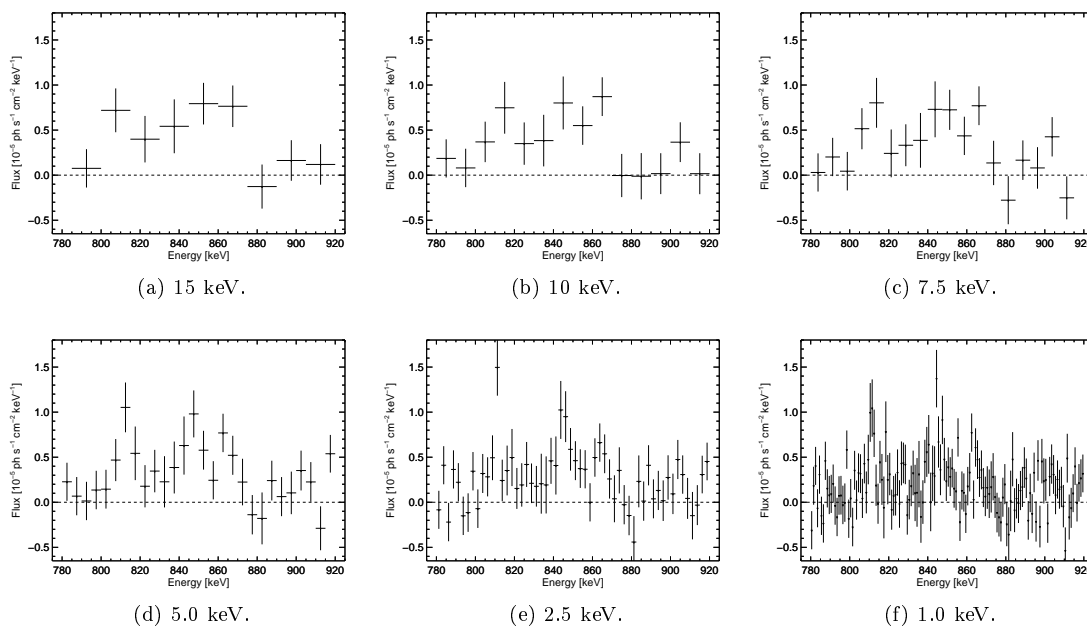


Figure 5.28: Spectral complexity in SN2014J revealed by different energy binning. Shown is a series of the same spectrum as shown in Fig. 5.27 (left panel) for different energy bin sizes. From top left to bottom right, the bin sizes are 15 keV, 10 keV, 7.5 keV, 5 keV, 2.5 keV, 1 keV, respectively. Accounting for the high resolution of SPI with its instrumental resolution of  $\approx 2.3$  keV at 850 keV, one single broad Gaussian is not representative for the observed data any more. Apparently, at least three separate features can be identified and followed in time.

spectral shapes of the  $^{56}\text{Co}$  lines in more detail. In Fig. 5.28, the same spectrum as shown in Fig. 5.27 (left panel) is shown at different energy binnings. Apparently, a single broad Gaussian does not capture the line shape properties any more, suggesting that SN2014J exploded indeed asymmetrically. In general, the  $^{56}\text{Co}$  gamma-rays should emerge gradually from the inner part of the supernova, as its envelope gets more and more transparent over time while expanding (Isern et al. 1997). Thus, spectral shapes determined from early times with respect to late times may be different. For example, the line-of-sight-integrated spectra move from a general blue-shift (near side of the remnant) towards the laboratory energy, as the whole object becomes visible. Furthermore, if ejecta would include major non-sphericities, velocity signatures could be even more complex. Therefore, the observation data set was split into four epochs, as shown in Fig. 5.29.

The first epoch, ranging from days 16.3 to 41.3 after the explosion, includes the optical light curve's maximum in which most of the gamma-rays from the inner core should be absorbed. Epoch (2), between days 41.3 and 66.3 is the phase in which the gamma-ray emission should gradually rise, and depending on the shape of the light curve, should provide clues about the progenitor system. The maximum gamma-ray light is found in epoch (3), from days 66.3 to 99.1 as described above. After an observation gap between days 100 and 134, the fourth epoch (days 134.8 to 164.0) should capture the gamma-ray emission of a rather transparent supernova. In particular, the epochs are chosen to be sensitive to different SN Ia model scenarios, towards a possible identification of the true mechanism. Epoch (4) is almost independent of the early evolution, and traces most directly the global dynamics of the  $^{56}\text{Ni}$  produced in the explosion, as it should follow pure radioactive decay after the gamma-ray maximum in a transparent supernova.

Tracing the 847 keV feature at 10 keV binning in Fig. 5.29 (centre panel), beginning

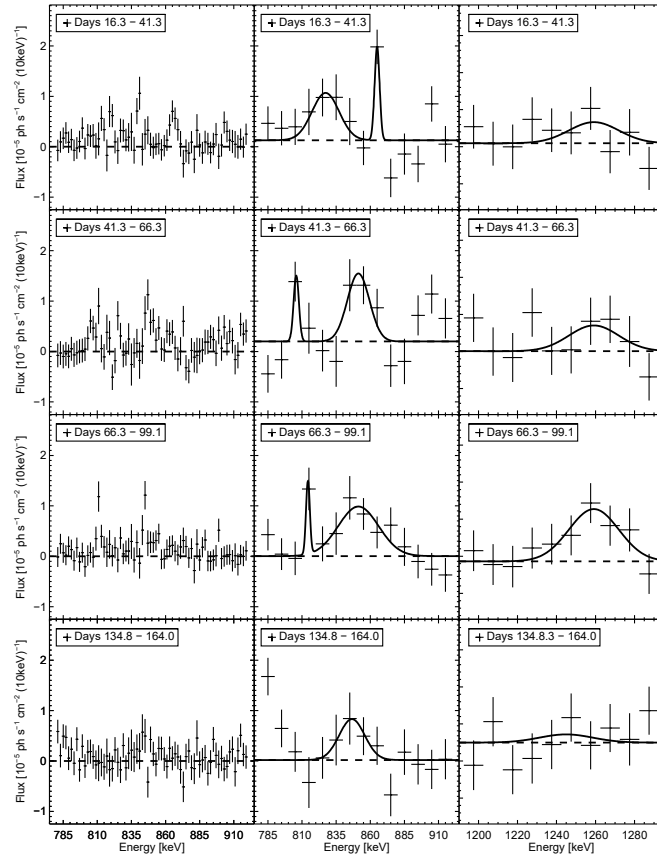


Figure 5.29: SN2014J signal intensity variations for the 847 keV line (centre) and the 1238 keV line (right) as seen in four consecutive epochs, and analysed with 10 keV energy bins. The 1238 keV fluxes have been scaled by the inverse branching ratio,  $1/0.68$ , for a direct comparison. For the 847 keV line, in addition, a high-spectral resolution analysis is shown at 2 keV energy bin width (left). Fitted line shapes are discussed in the text.

at epoch (4), a broadened line with a velocity spread of  $4750 \pm 1850 \text{ km s}^{-1}$  at rest is found, fully consistent with expectations. Towards earlier epochs (2) and (3), the line is found consistently, slightly blue-shifted and also broader. Epoch (1), in contrast, shows a red-shifted ( $\approx 7000 \text{ km s}^{-1}$ ) broad line, together with a narrow blue-shifted feature. Which component corresponds to the bulk or peculiar  $^{56}\text{Co}$  or  $^{56}\text{Ni}$  emission is arbitrary, and can only be figured out using smaller time bins, a higher spectral resolution, and a more sophisticated explosion model.

For the 847 keV line, it was possible to divide the data set into eleven time bins. Using too short time intervals will drown any information about the spectral shapes in statistical fluctuations, and makes the detection of the different component difficult. In addition to the 10 keV binning, the energy band between 780 and 920 keV was also analysed in 2 keV binning, resolving as narrow as the instrumental line width, for the eleven time bins, independently. All early time spectra show more than one spectral feature, which are all less broad, but which combine to the broad features which are apparent when using coarser energy bins. The last three time bins, corresponding to epoch (4), show a consistent picture of a broad  $^{56}\text{Co}$  emission line on top of a rather flat spectrum in its vicinity. In fact, this reassures the strange and complicated behaviour at early times, in which the discrimination between (blue-shifted)  $^{56}\text{Ni}$  and (red-shifted)  $^{56}\text{Co}$  is not unique. In any case, the structure of the exploding SN2014J is probably not symmetric, and might be sub-

ject to clumps and/or co-moving volume elements, carrying also  $^{56}\text{Co}$  which may lie along less-occulted line of sights at specific times. For this reason, as the supernova expands, different volume elements may thus contribute to the emission spectrum at different times and at different velocities as long as the occultation of gamma-rays is non-negligible.

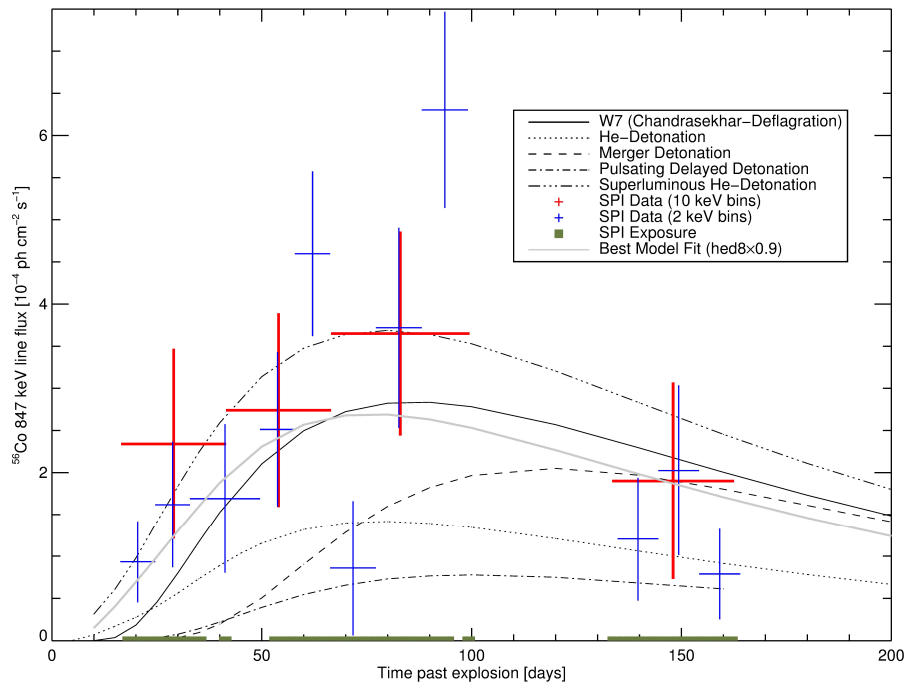


Figure 5.30: Gamma-ray line light curve of  $^{56}\text{Co}$  in SN2014J. Shown are the signal intensity variations for the 847 keV line as derived in two different spectral and temporal resolutions. The four-epoch results are consistent with the eleven-epoch analysis, both showing an initial rise and late decline of  $^{56}\text{Co}$  decay line intensity with a maximum at 60 to 100 days after the explosion. Shown are also several candidate progenitor models from The & Burrows (2014). The thick continuous line represents the best fit model of a helium detonation with one intensity scaling parameter, determining the  $^{56}\text{Ni}$  mass. See text for details.

In a last step, the derived flux values for different times build up the gamma-ray light curves for SN2014J as shown in Fig. 5.30. Comparing the data points to model light curves as prepared by The & Burrows (2014) specifically for SN2014J, another approach to determine the initially synthesised  $^{56}\text{Ni}$  mass is applied. Rather than tracing back the flux value at a specific time for an initial amount of  $^{56}\text{Ni}$ , all data points are subject to a statistical fit of models with only one global scaling parameter, corresponding to the  $^{56}\text{Ni}$  mass. The most plausible models, as judged by a  $\chi^2$  goodness-of-fit value, obtain a  $^{56}\text{Ni}$  mass in the range  $0.46\text{-}0.59(\pm 0.06)M_{\odot}$ . Interestingly, all well-fitting models imply a substantial fraction of  $^{56}\text{Ni}$  near the surface, though not as much as found in Sec. 5.1.3.1.1. However, distinguishing between different models from the fit-quality is difficult, as the models are not nested, and also because the  $\chi^2$  values are not varying much for most of the models. The detailed summary of fitting results can be found in Tab. 4 of Diehl et al. (2015). In general, the values range between  $0.4$  and  $0.8M_{\odot}$ , and a weighted average of the best fitting models for three different approaches obtains  $0.49 \pm 0.09M_{\odot}$  of  $^{56}\text{Ni}$  initially synthesised. This uses either the fluxes from the  $^{56}\text{Co}$  lines in 10 keV binning, or the total integrated flux in a band of 20 or 100 keV ignoring the line shape at all. The preference of specific models suggest He on the outside of the supernova, but these (1D) models all assume a single broad line to create their time profiles, which of course do not trace the details in the flux measurements.

### 5.1.3.2 Positron Annihilation in SN2014J

From the same data set, Christodoulou, A. S. (2016) performed an analysis of possible instantaneous positron annihilation in the expanding envelope of SN2014J. A direct measure of the positron escape fraction in a SN Ia can hence be derived, towards a gamma-ray-based estimate of the positron contribution from SNe Ia, Sec. 5.1.3.3. The focus was put on the energy range between 410 and 620 keV to detect a possible positron annihilation line at 511 keV, and also to identify possible contributions from an o-Ps continuum, if the positrons had the chance to significantly slow down before directly annihilating with ambient electrons. These spectral features are expected to be broadened according to the Doppler-broadening of the  $^{56}\text{Co}$  lines. In particular, the positrons which are emitted during the decay of  $^{56}\text{Co}$  have a mean kinetic energy of 631 keV. A significant detection of an o-Ps continuum would provide insights about the conditions of such a supernova event, as the positrons have to be decelerated fast below kinetic energies of about 1 keV to form o-Ps. If they do not form Ps, they either annihilate directly, broadening the 511 keV line due to the explosion kinematics, and due to the kinetic energy of the positrons, or they manage to escape the local environment of the supernova, and enrich the ISM.

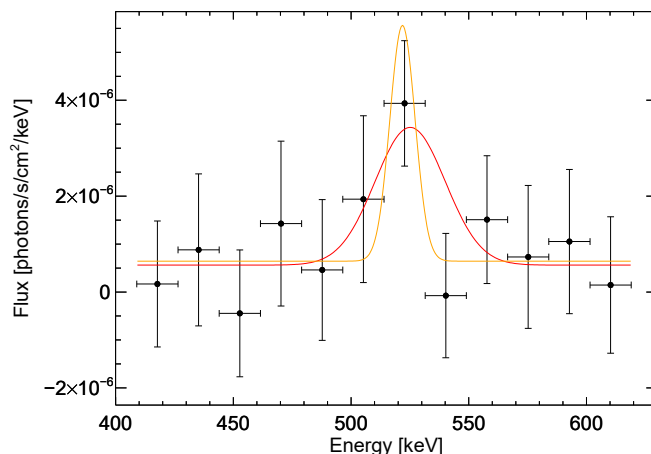


Figure 5.31: Annihilation line spectrum (black crosses) of SN2014J integrated over the entire observation period of INTEGRAL between days 16.3 and 164.0 after the explosion. Two model fits are shown, either with a fixed width from the decay gamma-ray of  $^{56}\text{Co}$  (green) or a free fit (red). See text for details. From Christodoulou, A. S. (2016).

In Fig. 5.31, the spectrum of the entire INTEGRAL/SPI observation data set in the vicinity of the 511 keV line is shown in 15 keV binning. The spectrum can be well described by a symmetric Gaussian on top of a constant offset. Depending on the assumptions on the line width, the line detection significance varies between 2 and  $3\sigma$  above instrumental background and gamma-ray continuum. The spectral description in Fig. 5.31 assumes either a fixed width, according to the Doppler-measurements of the  $^{56}\text{Co}$  lines of  $\approx 3000 \text{ km s}^{-1}$  (5.4 keV FWHM at 511 keV, orange line), or a freely determined width (here  $14.9 \pm 8.8 \text{ keV}$  FWHM, red line). In both cases, the positron annihilation line is significantly blue-shifted ( $521.8 \pm 3.3 \text{ keV}$  for fixed width,  $525.1 \pm 9.1 \text{ keV}$  for free width) by about  $6000\text{-}8000(\pm 5000) \text{ km s}^{-1}$ , which is then also concordance with the  $^{56}\text{Co}$  line measurements, Sec. 5.1.3.1.2. The annihilation line flux is  $(6.6 \pm 2.5) \times 10^{-5} \text{ ph cm}^{-2} \text{ s}^{-1}$  (fixed width) and  $(10.8 \pm 9.5) \times 10^{-5} \text{ ph cm}^{-2} \text{ s}^{-1}$ , respectively, suggesting a systematic uncertainty to the

511 keV flux of about 60%. An o-Ps continuum is not detected. A  $2\sigma$  upper flux limit of  $4 \times 10^{-4}$  ph cm $^{-2}$  s $^{-1}$  is derived.

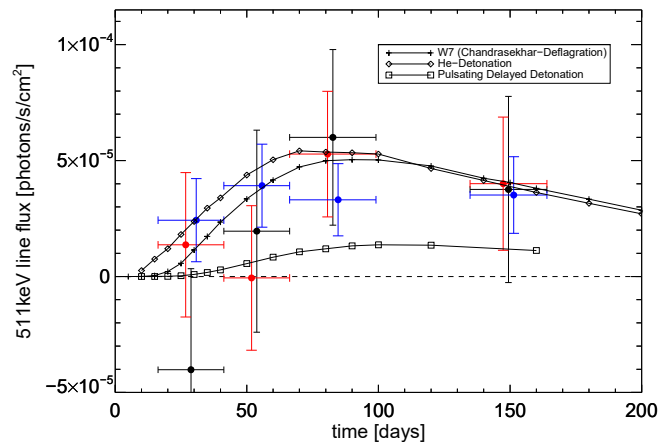


Figure 5.32: Annihilation line light curve of SN2014J. Shown are three different assumptions on the line shape with freely determined parameters (black), fixed width (red), and fixed width and centroid (blue) respectively. The time intervals are the same as in Fig. 5.30. For comparison, exemplary model predictions of the 511 keV line flux from The & Burrows (2014) are shown. See text for details. From Christodoulou, A. S. (2016).

As the 511 keV emission can be expected to at least follow the  $^{56}\text{Co}$  line intensity if the positrons annihilate instantaneously after the  $^{56}\text{Co}$  decay, also in the case of the 511 keV line, a gamma-ray line light curve is determined in the same time intervals. If the line showed a significantly different temporal behaviour than the  $^{56}\text{Co}$  lines, integrating over a long observation period might add periods of non-detections and background only, and will thus lead to a lower significance for the total spectrum. In Fig. 5.32, the light curve of the annihilation line is shown from three different assumptions on the spectrum, either by fixing width and centroid to the  $^{56}\text{Co}$  values (blue), or only fixing the width (red), or freely determining all spectral line parameters (black). For comparison, three model predictions from The & Burrows (2014) for the annihilation line are shown. The different spectral model assumptions are reflected in the size of the error bars for each epoch as the blue ones (two fixed parameters) are generally smaller than the red (one fixed parameter) and black (no fixed parameters) ones. In all three cases, the derived data points for the different epochs are consistent with a non-zero 511 keV flux when combined to one point. Essentially all supernova model predictions, and also a constant time profile, are consistent with the data. However, the time resolved analysis suggests somewhat lower flux values than the analysis using the entire observation time. This may be due to the fact that in the total spectrum, many different line-of-sights from also partly occulted  $^{56}\text{Co}$  clumps and co-moving volume elements may lead to different line shapes also in the case of the 511 keV line. On the other hand, the energy deposit of the positrons may not be instantaneous, and may lag the  $^{56}\text{Co}$  line emission. Alternatively, the 140-day integrated spectrum may also wrongly capture gamma-ray continuum into the 511 keV line, as is expected from the Compton-scattering of high-energy gamma-rays to smaller energies (see also Fig. 5.26a).

### 5.1.3.3 Positron Contribution from Type Ia Supernovae

Based on the results of Secs. 5.1.3.1.2 and 5.1.3.2, a new estimate of the contribution from thermonuclear supernovae to the galactic positron content can be obtained.

The measured positron escape fraction during the time  $\Delta t = t_2 - t_1 = 164.0 \text{ d} - 16.4 \text{ d} = 147.7 \text{ d} = 12.76 \text{ Ms}$  is defined as the number of positrons measured to annihilate during that time,  $N_{e^+}(\Delta t)$ , versus the number of positrons created by the  $\beta^+$ -decay of  $^{56}\text{Co}$  in that time,  $N_{56}(\Delta t)$ , and assuming instantaneous annihilation,

$$\eta = 1 - \frac{N_{e^+}(\Delta t)}{N_{56}(\Delta t)}. \quad (5.24)$$

Here,

$$N_{e^+}(\Delta t) = 4\pi d^2 \Delta t F_{511} = (1.23 \pm 0.47) \times 10^{54} \text{ e}^+, \quad (5.25)$$

with  $F_{511} = (6.6 \pm 2.5) \times 10^{-5} \text{ ph cm}^{-2} \text{ s}^{-1}$  is annihilation flux estimate from Sec. 5.1.3.2, and

$$\begin{aligned} N_{56}(\Delta t) &= \frac{M_{SN2014J}(^{56}\text{Ni}, t=0)}{M_{atom}(^{56}\text{Ni})} p_{\beta^+}^{56} = \\ &= N_{56,0} p_{\beta^+}^{56} (\exp(-t_1/\tau(^{56}\text{Co})) - \exp(-t_2/\tau(^{56}\text{Co}))) = \\ &= (1.30 \pm 0.24) \times 10^{54} \text{ e}^+, \end{aligned} \quad (5.26)$$

so that the positron escape fraction for SN2014J is

$$\eta = 1 - \frac{N_{e^+}(\Delta t)}{N_{56}(\Delta t)} = 0.06 \pm 0.33. \quad (5.27)$$

The derived estimate for the positron escape fraction is consistent with literature values (Milne et al. 1999, 2001), although the measurement uncertainties are quite large. In particular, all positrons in the observation time interval could have annihilated directly in the supernova cloud, but there is also a significant probability that a large amount of positrons may have escaped from remnant into the ISM of M82. Most of the positrons are believed to escape the remnant only years after the explosion, when the ejecta morphology is diluted, and positrons do not find enough ambient material to annihilate with. For this type of study, SN2014J is too far away to detect any signals with INTEGRAL/SPI beyond day  $\approx 200$ .

Using the measured escape fraction for an estimate of the positron content due to SNe Ia in the Milky Way, the question of the SN Ia rate is still a crucial point. Values between 0.1 and 1.0 thermonuclear explosions per century are plausible, so that the positron contribution from SNe Ia in the Galaxy is uncertain by at least one order of magnitude, as shown in Fig. 5.33. Within the  $1\sigma$  uncertainties of the escape fraction, and within plausible SNe Ia rates in spiral galaxies (van den Bergh & Tammann 1991; Mannucci et al. 2008), the positron production rate can range between 0 and several  $10^{44}$ , with an expectation value of

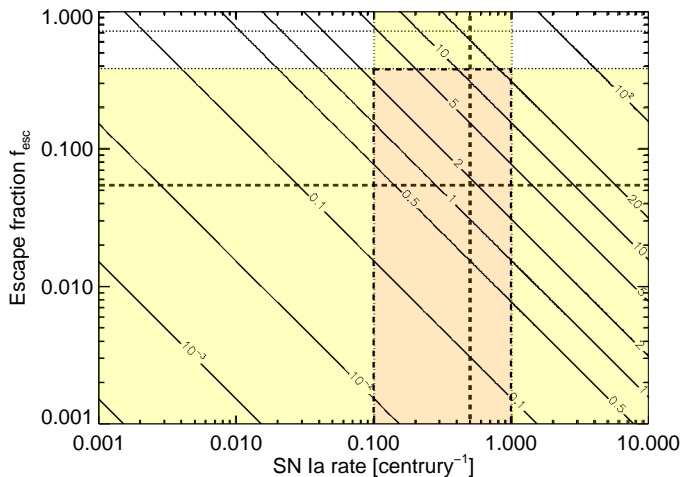


Figure 5.33: Positron production rate as a function of supernova SN Ia rate and positron escape fraction,  $f_{esc}$ . Shown are expected values of the positron production rate as contours in units of  $10^{43} \text{ e}^+ \text{ s}^{-1}$  and the measured values of the escape fraction in SN2014J (horizontal dashed line), together with its  $1$  and  $2\sigma$  uncertainties (horizontal dotted lines). Plausible values for the SN Ia rate are marked with the vertical dashed lines. Yellow regions define measured values and their  $1\sigma$  uncertainties and orange regions the overlap between both estimates. See text for details.

$$\dot{N}_{e^+}({}^{56}\text{Ni}) = N_{e^+}^{56}(\text{SN Ia})\eta R_{\text{SNIa}} = (1.9 \pm 11.9) \times 10^{43} \text{ e}^+ \text{ s}^{-1}. \quad (5.28)$$

This estimate used a rate of one SN Ia per 200 years, an escape fraction of 0.06, and an initially synthesised  ${}^{56}\text{Ni}$  mass<sup>8</sup> of  $0.49 \pm 0.09 M_{\odot}$ . This would explain  $61.3 \pm 127.0\%$  of the disk emission and  $38.8 \pm 126.8\%$  of the total galactic emission, assuming steady-state positron supply and annihilation. SNe Ia have the potential to be responsible for all of the positrons which are seen to annihilate in the Milky Way. But the secure contributions from  ${}^{26}\text{Al}$  and  ${}^{44}\text{Ti}$  also have to be taken into account.

In fact, SNe Ia may also be significant producers of  ${}^{44}\text{Ti}$ , either in normal SNe Ia with typical yields of the order of  $10^{-5} M_{\odot}$ , or in SN1991bg-like sub-luminous SNe Ia, with extremely high yields of to order  $0.03 M_{\odot}$ , as pointed out by Crocker et al. (2016). Assuming that all positrons from the decay chain of  ${}^{44}\text{Ti}$  escape into the ISM, an additional contribution to the positron content from thermonuclear supernovae of the order  $10^{40}$ - $10^{41} \text{ e}^+ \text{ s}^{-1}$  is plausible. This would only contribute to less than 1% of the total content. However, in the case of SN1991bg-like supernovae, the contribution to the galactic positron content may be almost 100%. The scenario Crocker et al. (2016) propose is based on a class of transient positron sources, occurring in stars of age  $\gtrsim 5$  Gyr. This may explain the global distribution of positrons, and at the same time the solar ( ${}^{56}\text{Fe}/{}^{44}\text{Ca}$ ) ratio which suggests more sources of  ${}^{44}\text{Ti}$  in the Galaxy, but which are apparently not seen. Such sources would occur at a present Galactic rate of  $\approx 0.2 \text{ century}^{-1}$ , and would typically synthesise about  $0.03 M_{\odot}$  of  ${}^{44}\text{Ti}$  whose daughter nucleus decays by positron emission. In a binary evolution model, they showed that mergers of He-only WDs with CO WDs satisfy

<sup>8</sup>The mass estimate from the early  ${}^{56}\text{Ni}$  measurement is ignored here, as the interpretation of such a large amount of  ${}^{56}\text{Ni}$  in the outskirts of one objects is probably an overestimation and/or based on false assumptions. Only a small amount of  ${}^{56}\text{Ni}$  of the order  $10^{-3} M_{\odot}$  is needed to ignite a white dwarf and furthermore the zero time of the  ${}^{56}\text{Ni}$  measurement is not unique as there might for example be a companion star at a distance of  $\approx 100$  AU whose surface might have been ignited and burnt to  ${}^{56}\text{Ni}$  by the real explosion of SN2014J several days later. This might have actually been seen by SPI/INTEGRAL in the early spectrum. This would also some the problem that no sharp low-velocity ionised Co-lines are seen in IR spectra of SN2014J as would be expected from the measurement in Sec. 5.1.3.1.

the age and rate constraints, and plausibly match the  $^{44}\text{Ti}$  yield requirements. As expected from the low  $^{56}\text{Ni}$  yields in this particular type of mergers, their delay time, and their merging rates, the evolution model would suggest sub-luminous thermonuclear supernovae, such as the SN1991bg subtype. Although the involvement of the delay time of different source types is an excellent step towards a more complete understanding of the positron puzzle, the scenario is on shaky grounds: It is not proven that SN1991bg-like events are the mergers of two WDs, and it is furthermore not proven that the merger of two WDs of a particular composition produce that much  $^{44}\text{Ti}$ . Such sub-luminous thermonuclear supernovae definitely contribute to the galactic positron content, but its magnitude has to be investigated further, and consolidated with measurements.

#### 5.1.3.4 Novae

Similar to type Ia supernovae, a nova explosion is resulting from a WD in a close binary system, accreting H-rich matter from a main-sequence companion star. But during a nova, the WD is not ignited in its centre, but rather on its surface when the accumulated matter reaches the H ignition conditions. This then leads to a thermonuclear runaway, and explosive H burning occurs. Nova scenarios suggest low mass-accretion rates, of the order  $\dot{M} = 10^{-10}\text{-}10^{-9}M_{\odot} \text{ yr}^{-1}$ , which leads to a compression of the accreted H to degenerate conditions until its ignition. Peak temperatures of the order of  $10^8$  K are reached. Explosive H burning is synthesising  $\beta^+$ -unstable nuclei with low half-life times such as  $^{13}\text{N}$ ,  $^{15}\text{O}$ , or  $^{18}\text{F}$ , with  $T_{1/2}$  no longer than minutes to hours (see Tab. 5.1). The nucleosynthesis products in novae are transported to the outer envelope by convection, which prevents the nuclei from destruction. The particle decays then lead to an energy release in the outer shells, which is seen as the nova outburst. This is accompanied by an increase of the visual luminosity, and a mass ejection of the order of  $10^{-4}M_{\odot}$ , with terminal velocities of  $10^2\text{-}10^3 \text{ km s}^{-1}$ . The accretion time scale,  $\tau_{acc} \propto M_{acc}/\dot{M}$ , is typically of the order  $10^4\text{-}10^5$  yr which is smaller than the nuclear burning time scale,  $\tau_{nuc} \propto C_p T/\epsilon_{nuc}$  where  $C_p$  is the specific heat, during the accretion phase. Thus, an H envelope can efficiently build up. When this envelope ignites, a thermonuclear runaway occurs as the degeneracy pressure prevents the envelope to expand, which would turn off the explosion. In explosive H burning, the CNO cycle (Tab. 5.1) is operating in equilibrium as long as the proton capture time scale is longer than the  $\beta^+$ -decays. When the temperatures rise above  $\approx 10^8$  K, proton captures are more frequent, and the resulting nucleosynthesis is limited by the time scale of  $\beta^+$ -decays (Hernanz 2005; José et al. 2006).

Depending on the composition of the WD, the nucleosynthesis products can be different. While CO WD novae mainly produce Li, C, N, O, and F isotopes, ONe novae also enrich the ISM with even heavier elements like Ne, Na, Al, up to Cl, from the hot NeNa cycle (NeNaMgAl cycle, Tab. 5.1 José et al. 2003; Hernanz & José 2006; José et al. 2006). The amount of radioactive short-lived nuclei synthesised in nova explosions could then be estimated from their decay gamma-rays. This is, however, only possible for  $^7\text{Be}$  (478 keV), which does not produce positrons, in the case of CO novae, and for  $^{22}\text{Na}$  (1275 keV) in ONe novae. The  $\beta^+$ -decays from the major positron producers  $^{13}\text{N}$ ,  $^{15}\text{O}$ , and  $^{18}\text{F}$  proceed directly to the ground states of their daughter nuclei, and no de-excitation gamma-rays are emitted. Additionally, the

question arises whether the positrons can actually escape from the novae or deposit all their energy in the envelope, similar to the SN Ia case. The commonly accepted mechanism is that the short-lived nuclei, especially  $^{13}\text{N}$  and  $^{18}\text{F}$ , produce burst like gamma-ray emission through their positron emissions and subsequent annihilations with electrons. This happens about one week before the visual flux maximum, i.e. when the nova is likely to be discovered. In Fig. 5.34, modelled gamma-ray light curves for CO and ONe novae are shown, together with a spectrum at the time of the gamma-ray flash, for a distance of 1 kpc.

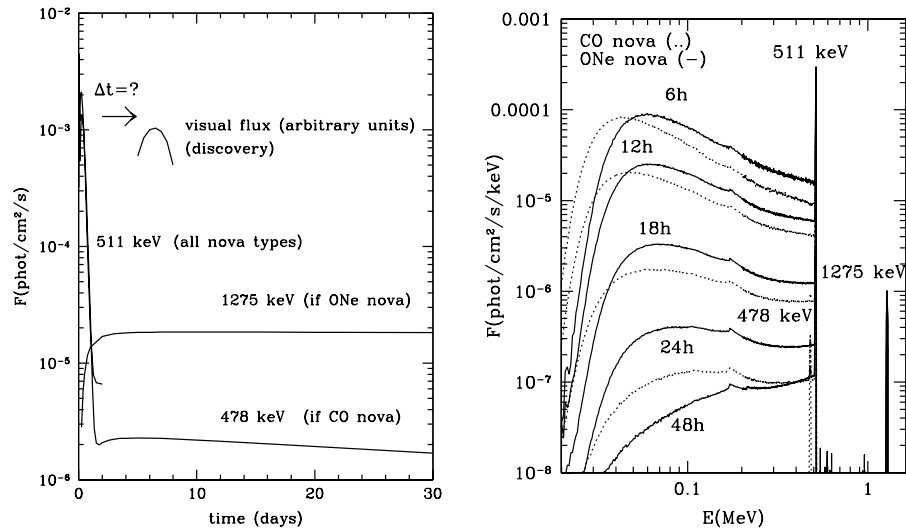


Figure 5.34: Evolution of gamma-rays emission from nova explosions. Shown are modelled gamma-ray light curves at a distance of 1 kpc from CO and ONe novae compared to the visual flux discovery one week later in the left panel, and the evolution of the soft gamma-ray spectrum during the first two days of the explosion with characteristic annihilation emission up to 511 keV, and gamma-ray lines at 478 keV from  $^7\text{Be}$  in CO novae and at 1275 keV from  $^{22}\text{Na}$  in ONe novae, respectively. From Hernanz (2005).

Nova explosions have never been observed in gamma-rays, and it is hence difficult to directly estimate their positron contribution to the galactic population. From the early phase during the gamma-ray flash, no independent measure is available to estimate the number of positron that could escape the nova, but as the life-times of  $^{13}\text{N}$  and  $^{18}\text{F}$ , 862 s and 158 min, respectively, are very short, most of the positrons can be expected to annihilate directly in the envelope. Only in the case of ONe novae with the longer-lived  $\beta^+$ -unstable isotope  $^{22}\text{Na}$  ( $T_{1/2} = 2.6$  yr), the positrons could potentially leave the local nova environment, and enrich the ISM. Knowing the initial abundance of  $^{22}\text{Na}$  in a nova explosion provides a direct measure of the positrons from novae in the Galaxy. This must take into account the galactic nova rate of  $20\text{--}60 \text{ yr}^{-1}$  (della Valle & Livio 1994; Shafter et al. 2000; Shafter 2002), and that about 1/3 of all novae are from ONe WDs (Gil-Pons et al. 2003). Della Valle & Livio (1998) pointed out, that most of the ONe novae occur near the galactic plane, but that there are also apparently faint novae at heights up to 1 kpc above the plane. Novae may thus not only contribute to disk population of positrons, but also to the bulge when considering propagation. From theoretical considerations and simulations, the amount of  $^{22}\text{Na}$  synthesised in ONe novae may be as large as  $10^{-8} M_{\odot}$  (Hernanz & José 2006), but may be also far less (José et al. 2003). The contribution from ONe novae can thus be estimated as

$$\dot{N}_{e^+}(\text{Novae}) = f_{\text{ONe}} p_{\beta^+}^{22} R_{\text{Novae}} \frac{M_{\text{Novae}}^{22}}{M_{\text{atom}}^{22}} = 1 \times 10^{38} - 3 \times 10^{41} \text{ e}^+ \text{ s}^{-1}. \quad (5.29)$$

Here,  $f_{\text{ONe}} = 1/3$  is the fraction of ONe novae among all novae,  $p_{\beta^+}^{22} = 90.4\%$  is the probability for  $^{22}\text{Na}$  to decay via  $\beta^+$ -decay,  $R_{\text{Novae}} = 20\text{-}60 \text{ yr}^{-1}$  is the galactic nova rate,  $M_{\text{Novae}}^{22} = 10^{-11}\text{-}10^{-8} M_{\odot}$  is the  $^{22}\text{Na}$  nova yield, and  $M_{\text{atom}}^{22} = 22 \text{ u}$  is the atomic weight of  $^{22}\text{Na}$ . Comparing the estimate from Eq. (5.29) with the total galactic positron annihilation rate, novae are at most contributing 1% to the positron content.

A consolidation of this estimate would be possible with gamma-ray observations. But as novae are only detected via optical measurements days after the initial outburst, only archival data could be used to identify gamma-ray flashes, prior to the nova identification. As for close-by novae ( $d < 0.5 \text{ kpc}$ ) annihilation flashes with fluxes of the order  $10^{-2} \text{ ph cm}^{-2} \text{ s}^{-1}$  can be expected, the 14 year data base of SPI/INTEGRAL spectra may be used for a gamma-ray identification of novae, and a possible estimate of the positron content, if the nova was of ONe type. Additionally, the ongoing nucleosynthesis in the Milky Way can be traced by gamma-ray measurements of all nova classes.

#### 5.1.4 Exotics

In the context of supernova explosions, hypernovae release an energy of the order  $10^{52} \text{ erg}$  and  $^{56}\text{Ni}$  masses of  $\gtrsim 0.5 M_{\odot}$  (Nomoto et al. 2010). This is about ten times more than in normal CCSN, and interpreted as aspherical explosions of massive stars with masses more than  $30 M_{\odot}$ . In the hypernova scenario, a rotating Fe/Ni core of a massive star directly collapses to a black hole at the end of its evolution. For a short time of 0.1 s, an accretion disk is forming, where the gravitational energy of accreted matter is transformed into two diametrically opposite jets along the rotation axis (see also Sec. 5.2). The mechanism how such jets are formed is unknown, but the jets, interacting with the infalling layers, may cause the visible supernova light. Around the basis of the jets, heavy nuclei, such as  $^{56}\text{Ni}$ , may be created and ejected into the ISM. Similar to the SN Ia case, about  $10^{55}$  positrons could be emitted by the  $\beta^+$ -decay of the daughter nucleus  $^{56}\text{Co}$ . But also here, the escape of positrons from the local hypernova environment is questionable. One such event could supply the Milky Way annihilation rate for a long time. If all positrons escape, a recurrence time of galactic hypernovae between  $10^4$  and  $10^5$  years would conform with the current annihilation rate. The morphology, however, would be hard to explain if only one event was responsible for the positrons. This model was also proposed to explain gamma-ray bursts, which release short flashes of gamma-rays, beamed along a jet direction (Woosley 1993). Alternative to the  $^{56}\text{Ni}$  decay, also pair creation from innermost regions of a launched gamma-ray burst jet with lower energy photons may provide substantial numbers of positrons (Parizot et al. 2005; Bertone et al. 2006). As the physics of super-luminous supernovae are not understood, also the positron contribution is unknown, and estimates are uncertain by several orders of magnitude.

Stars with initial masses above  $100 M_{\odot}$  may end up as pair-instability supernovae.

The interiors of those stars can reach to temperatures of GK and beyond, so that thermal gamma-ray photons may be created. These gamma-rays produce electron-positron pairs which rapidly annihilate again, being in thermal equilibrium with the photons. If the temperature is rising further, also the gamma-ray energies increase, and more gamma-rays are absorbed into electron-positron pairs. This reduces the radiation pressure of the star which is supporting the outer layers. In consequence, the star contracts and heats the inner core even further, leading to even more pair-creation. At one point, the conditions for O- and Si-burning could be met, and nuclear fusion sets in which counteracts gravity, and stabilises the star again. If the star was massive enough, typically between  $130$  and  $250M_{\odot}$ , pair-creation will lead to a strong reduction of the radiation pressure support, and the star collapses. This may ignite explosive nuclear burning, increasing the temperature towards even higher burning stages, and a thermonuclear runaway occurs. This pair-instability collapse releases an energy of the order  $10^{53}$  erg, more than the gravitational binding energy, and the star gets totally disrupted (Janka 2012). During such an event,  $20$  to  $40M_{\odot}$  of  $^{56}\text{Ni}$  may be created, as suggested in the case of the supernova SN2006gy in the galaxy NGC 1260, which is thought to have exploded by the pair-instability mechanism (Smith et al. 2007). This single event may have enriched the galaxy with  $10^{56}$  positrons, and would reproduce the Milky Way annihilation rate with a recurrence time of 1000 years, even for an escape fraction as small as  $\sim 1\%$ .

Another outstanding super-luminous supernova was ASASSN-15lh, at a distance of 1.2 Gpc (cosmological red-shift  $z = 0.233$ ), so far the brightest supernova ever detected (Dong et al. 2016). Kozyreva et al. (2016) estimated that if this supernova was powered by decay gamma-rays, about  $1500M_{\odot}$  of  $^{56}\text{Ni}$  would be required, which would imply  $10^{58}$  positrons created in only one event. But as the bolometric light curve of ASASSN-15lh is different compared to normal supernovae, showing a rapid decay after its maximum, the assumption of purely  $^{56}\text{Ni}$ -powered low-energy light is questionable. Instead, Kozyreva et al. (2016) suggests that ASASSN-15lh also was a pair-instability supernova, with a total  $^{56}\text{Ni}$  mass of  $55M_{\odot}$ , close to the upper limit expected from those objects. In any case, exotic explosive events could contribute significantly to the positron content in galaxies, but due to their unknown recurrence times and the uncertain escape fractions, gamma-ray bursts and pair-instability supernovae are still unidentified sources.

## 5.2 Compact Objects

Another mechanism to create electron-positron pairs is only possible in very compact regions, and in presence of a source of high-energy photons. Photon-photon self-absorption will lead to the creation of particle-antiparticle pairs, if the centre-of-momentum energy of the photon pair is larger than two times the rest mass of either particle. In the case of electron-positron pairs, the reaction cross section is of the order of the Thomson cross section  $\sim 10^{-25}$  cm<sup>2</sup>, so that photon-photon pair-creation should be a common process. However, in laboratory experiments, this process has never been observed due to the fact that high-energy and high-density photon beams would be required, see Sec. 2.2.4.1.

In astrophysical objects, such as neutron stars and black holes, these environmental

conditions can be met, as they have the potential for high-energy photons, and at the same time are compact, so that the emitted photons are concentrated in a small volume. In particular, the emitted gamma-ray photons have to be opaque to themselves, which means that the optical depth (in particular the attenuation cross section)  $\tau_{\gamma\gamma}$ , has to be of order of unity for photon-photon pair-absorption to become efficient,

$$\tau_{\gamma\gamma} = n_{\gamma}\sigma_{\text{pair}}r \stackrel{!}{\geq} 1. \quad (5.30)$$

In Eq. (5.30),  $n_{\gamma}$  is the number density of photons,  $\sigma_{\text{pair}}$  is the pair-creation cross section, and  $r$  the size dimension of the gamma-ray emitting source, cf. Eq. (2.98). The required photon number density, by means of electron-positron pair production, can be estimated from the energy density of a photon field with photon energies of  $m_e c^2$  on average, so that

$$n_{\gamma} = \frac{u_{\text{rad}}}{m_e c^2} = \frac{S}{m_e c^3} = \frac{L}{4\pi r^2 m_e c^3}. \quad (5.31)$$

Here,  $S$  is the Poynting flux, measuring the radiated power per unit area, and  $L$  is the corresponding source luminosity. It follows that pair-creation is efficient if

$$\tau_{\gamma\gamma} = \frac{L}{r} \frac{\sigma_{\text{pair}}}{4\pi m_e c^3} \stackrel{!}{\geq} 1. \quad (5.32)$$

The condition in Eq. (5.32) is often re-written in terms of the so-called compactness parameter (e.g. Lightman & Zdziarski 1987),

$$l \equiv \frac{L\sigma_T}{r m_e c^3} = 2\pi \left(\frac{m_p}{m_e}\right) \left(\frac{L}{L_E}\right) \left(\frac{r_S}{r}\right) \quad (5.33)$$

where  $m_p/m_e$  is the proton to electron mass ratio,  $L_E \equiv 4\pi GMcm_p/\sigma_T$  is the Eddington limit<sup>9</sup>,  $r_S \equiv 2GM/c^2$  is the Schwarzschild radius of a mass  $M$ , and  $\sigma_T$  is the Thomson cross section. As  $\sigma_T \approx \sigma_{\text{pair}}$ , the condition for efficient pair-production ( $\tau_{\gamma\gamma} \gtrsim 1$ ) can be stated as

$$l \stackrel{!}{\gtrsim} 10, \quad (5.34)$$

which means that objects with intrinsically small size  $r$  and/or large luminosity  $L$  are inevitably producing electron-positron pairs. In Fig. 5.35, the compactness of astrophysical objects is illustrated. Black holes and neutron stars can reach the  $l \gtrsim 10$  threshold, whereas white dwarves and stars are probably not sufficiently

<sup>9</sup>The Eddington luminosity limit is considered the maximum luminosity that an object can reach if and only if the object is in hydrostatic equilibrium of radiation pressure outwards and gravity inwards. If, for example, a star exceeds its Eddington limit, radiation-driven stellar winds will make the star lose its outer layers. For objects not in hydrostatic equilibrium such as accreting neutron star or black hole binaries, the Eddington limit has no direct physical meaning and only represents a particular value of the luminosity that is achieved in the system.

compact to produce pairs, except for solar flares or novae, for example. Isolated neutron stars or black holes will never reach a large enough luminosity to cross the compactness threshold, so that only in binary systems with ongoing mass accretion, positrons can be created. For this reason, the next Sec. 5.2.1 shortly illustrates the physics of X-ray binary systems in general, followed by a SPI measurement of a black hole binary system in outburst in Sec. 5.2.1.1.

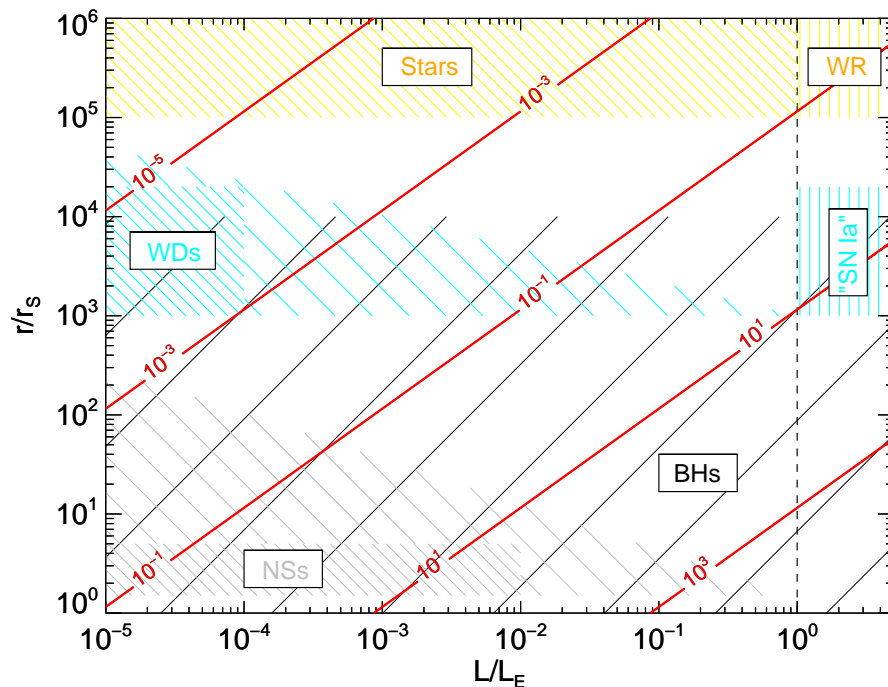


Figure 5.35: Compactness as a function of luminosity and size of astrophysical objects as defined in Eq. (5.33). The hatched areas show where different objects could be located in principle, taking either only the source itself into account (short-space hatched) or if it is accreting material (long-space hatched). The triangle shape of accreting white dwarves (WDs) and neutron stars (NSs) is due to the relation between mass accretion rate, luminosity, temperature, and radius,  $\dot{M} \propto L \propto T^4 \propto (r^{-3/4})^4 = r^{-3}$ , so that  $\lg(L) \approx -3 \lg(r)$ . Black holes (BHs) can in principle populate the whole  $L$ - $r$ -space but only if a donor is present. The Eddington luminosity  $L_E$  is indicated by a dashed vertical line: If stars exceeds this limit, they lose mass as the radiation pressure is producing strong winds like in Wolf-Rayet stars. In the case of degenerate stars, a single white dwarf can only cool so that its intrinsic luminosity is rather low but in accretion phases, they can also reach up to  $10^{38} \text{ erg s}^{-1}$  which is close to the Eddington luminosity of a  $1.4M_\odot$  star. Note that there is no radiation pressure in WDs so that the Eddington luminosity has no physical meaning. When a WD is ignited in its centre, it reaches several times the Eddington luminosity, but not in a stable configuration but rather in supernova of type Ia ("SN Ia"). Similarly, a NS may collapse to a BH if it accreted enough mass to exceed the TOV mass-limit, but this process does probably not produce any electromagnetic emission by itself. In red contours, the different values for the compactness are indicated. Above a value of  $\approx 10$ , Eq. (5.34), electron-positron pair production by photon-photon self-absorption is efficient. Only NSs and BHs can be efficient pair-producers, provided there is a gamma-ray source like an accretion disk or corona present.

## 5.2.1 X-Ray Binaries

Neutron stars and black holes are the compact remnants of core-collapse supernovae, Sec. 5.1.2. Because half of the stars in the Milky Way are found in binary systems (Longair 1994), it is not surprising to find neutron stars or black holes also in binary systems with either other compact objects (as measured by gravitational waves or so-called kilonovae Abbott et al. 2016; Tanvir et al. 2013), or normal stars (e.g. first measured X-ray binary with stellar companion Scorpius X-1 Giacconi et al. 1962). The compact objects can accrete matter from the companion star, usually modelled as a disk-like configuration (Shakura & Sunyaev 1973), in which the disk obtains

a certain temperature, of the order  $kT \lesssim 1$  keV. For this reason, these systems are called X-ray binaries (XRBs). Depending on the mass of the companion, an XRB can either be a low-mass XRB (LMXRB,  $M^* \lesssim 4M_\odot$ ) or a high-mass XRB (HMXRB,  $M^* \gtrsim 4M_\odot$ ), i.e. the star is either of O or B type (high mass), or any other star (low mass). On average, LMXRBs are about ten times brighter than HMXRBs, so that LMXRBs may tend to produce positrons easier than their high-mass analogues. If there is radio emission associated with an XRB, most probably due to synchrotron radiation from leptons which have been ejected from the compact object, and if this emission is also found to be diametrically opposite to the central source, the system is called a microquasar. Microquasars obtained their names due to their similarities with quasars, i.e. the central supermassive black hole engines in active galactic nuclei. These are  $10^6$  times brighter than microquasars but also  $10^6$ - $10^9$  times more massive than the stellar mass black holes with masses of the order  $10M_\odot$  (Mirabel & Rodríguez 1998). In addition, the time scales on which physical processes occur, and their durations, are much smaller in microquasars than in quasars, as the characteristic time, i.e. the light travel time as defined by the size of an object versus the speed of light, is directly proportional to the objects mass. Consequently, processes on a time scale of seconds in microquasars would take days or years in quasars.

The physics of neutron star and black hole XRBs can be treated equivalently in first order but with the difference that neutron stars have a solid surface, and black holes not. The objects have a similar gravitational potential, e.g. neutron stars radii are of the order of  $3r_S$ , which is equivalent to the innermost stable circular orbit of material accreted around a black hole, in a general relativistic description. In fact, processes such as X-ray bursts or pulsations require a surface, and thus can uniquely identify neutron stars. The behaviour of accretion flows in binary systems are given by the physical and geometrical parameters, such as the mass and spin of the compact object, the mass of the companion, and the distance and inclination to the donor star. The luminosity of the compact object is determined by the accreted mass per unit time (mass accretion rate), which depends on the gravitational potential, spin, and the properties of the accreted material itself. Thus, the luminosity is a non-linear measure of the total mass accretion rate (Körding et al. 2006). In general, the accretion flow is described by an unstable equilibrium between gravitational heating against radiative cooling. The heat is assumed to be caused by viscous stresses which convert the gravitational energy (Shakura & Sunyaev 1973). Cooling then happens locally, by blackbody radiation at different temperatures, depending on the radial length from the compact objects outwards as  $T(r) \propto r^{-3/4}$ . In consequence, the luminosity at smaller radii is larger, because also gravity is stronger. Likewise, the temperature is higher, as the heat is released on a smaller scale. This description is denoted as multi-colour disk model (Mitsuda et al. 1984), and exhibits a geometrically thin disk structure around the compact object.

The accretion disk is assumed to be constantly fed at low mass accretion rates, and composed of mainly neutral hydrogen. Changes in mass accretion rate or temperature, and consequently ionisation, will thus lead to instabilities in the accretion disk flow, which may trigger "outbursts" of XRBs. These are identified by the sudden and sometimes erratic release of energy in form of high-energy particles and gamma-rays. During the stable configuration of the Shakura-Sunyaev disk (Shak-

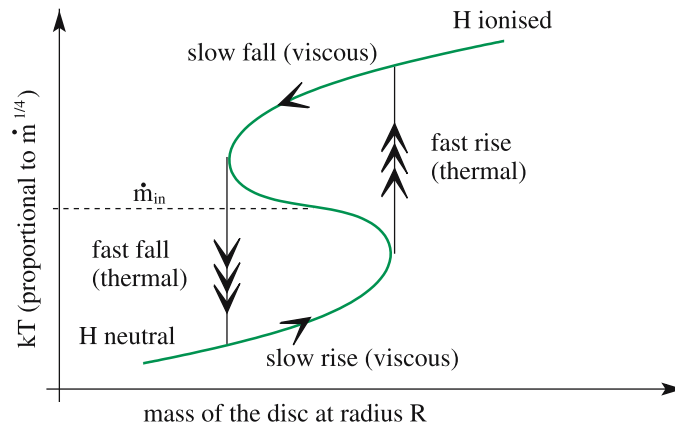


Figure 5.36: Scheme of the quasi-periodic hydrogen ionisation instability. Shown is the path through the accretion rate-mass-diagram as affected by the local effects of the instability. The mass accretion rate jumps (drops) discontinuously at a given radius of the disk when the temperatures are high (small) enough to ionise (recombine) hydrogen which leads to a thermal runaway. See text for more details. From Done et al. (2007).

ura & Sunyaev 1973), thermal photons are radiated away, so that the disk can cool again, which means that the opacity of the disk is rather low. When the temperature rises to  $10^4$ - $10^5$  K, some thermal photons in the far end of the Planck-spectrum may already ionise the hydrogen, so that the energy is not released but stays in the disk. A small increase of the temperature may thus yield a large increase in the opacity of the material, and the disk does not cool any more but only heats up. The higher photon energies than ionise more hydrogen, and a thermal runaway occurs, which is stopped when all the hydrogen is ionised. The fast increase in temperature is accompanied by an increase in mass accretion rate, now being larger than the initial mass accretion rate. The disk is then "eaten up" up to the radius where the hydrogen ionisation instability was triggered. As a consequence, the pressure (stress) decreases, the heat source dries up, and the temperature drops, which leads to hydrogen recombination. The disk can cool again, leading to more recombinations, and a cooling runaway will occur until most of the hydrogen is neutral again. The lower temperature is then accompanied by a decrease in mass accretion rate, so that the disk can finally build up again (Lasota 2001). This hysteresis-like behaviour is illustrated in Fig. 5.36.

Observationally, such an outburst is seen after a certain time of quiescence of the binary system, with a fast rise and exponential to linear decay (Fig. 5.37). There is a difference in recurrence time of neutron star outbursts and black hole outbursts, probably due to the fact that neutron star accretion disks are shorter, because neutron stars have a limited mass of  $\lesssim 2M_{\odot}$ . The binary companions must hence be closer in distance, so that more stable configuration could be established. Black holes have no upper mass limit, and the distance to the stellar companion can be quite large for also the disk to obtain a large extent. In fact, many of the LMXRB neutron stars are persistent and do not go into outburst, while all (known) LMXRB black holes are transient sources. Empirically, the recurrence time of neutron star outbursts is of the order of years, while the black hole binary outbursts may occur only once in  $\sim 100$  years, or even less frequent. The known HMXRB black holes are all persistent, and are believed to be powered by Roche lobe overflow, keeping the also the outer disk always above the hydrogen ionisation instability threshold temperature (Done et al. 2007). In both, persistent and non-persistent sources, the

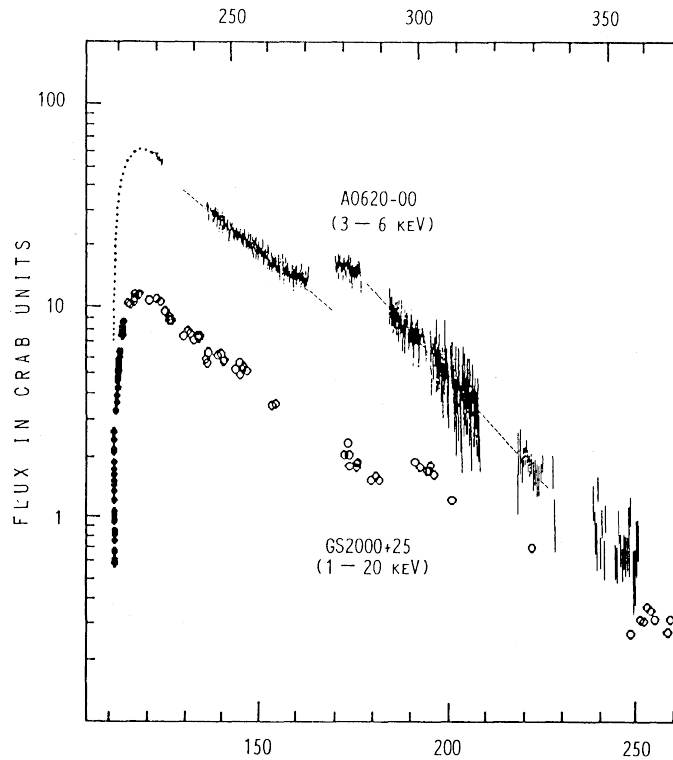
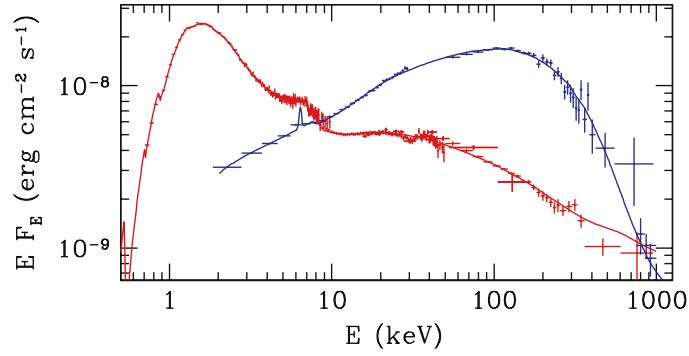


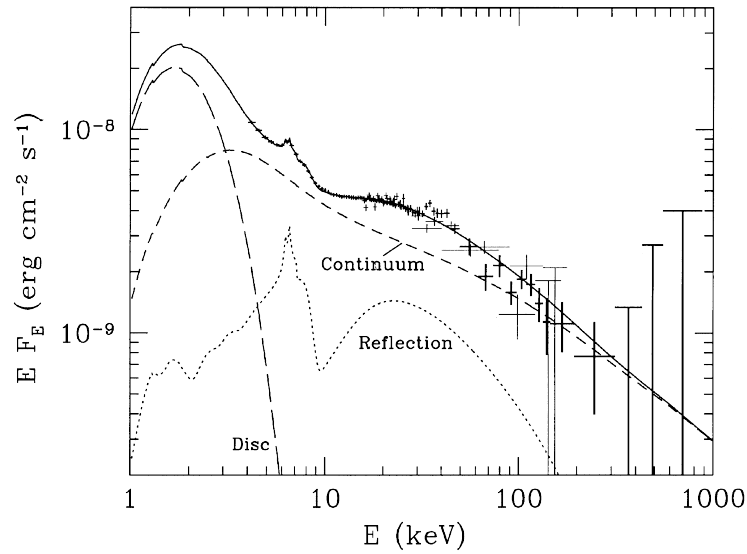
Figure 5.37: Typical light curves of X-ray binary outbursts. Shown are soft X-ray measurements from GS2000+25 in 1988 (days of year 1988, bottom axis) and A0620-00 in 1975 (days of year 1975, top axis). The sharp rise and exponential decay of the flux are clearly seen in both cases. See text for details. From Tanaka (1989).

change in accretion flow is generally accompanied by a change in spectral state and shape. Furthermore, the observed spectra, Fig. 5.38, are not simply explained by a multi-colour disk model, but require additional physical components to explain the non-thermal high-energy emission.

In the soft (thermal dominant) state (red points in Fig. 5.38a), the spectrum is described by thermal emission from an optically thick accretion disk around a black hole (multi-colour disk) below  $\approx 4$  keV. Emission from a hot and thin "corona" above (or surrounding) the accretion disk peaks at  $\approx 3$  keV, with a tail down to energies of  $\approx 100$  keV. In addition, a "reflection" component is found, i.e. light from the inner hot part of the disk, scattered and reflected at larger radii, Fig. 5.38b. However, there is also a strong high-energy tail in the photon spectrum of the soft state, and especially in the case of the hard state (blue points). There, the spectrum does not look like a disk at all, probably being dominated by bremsstrahlung and Compton scattering, as it is well described by a power-law shape with an exponential cut-off at high-energies (Remillard & McClintock 2006). There is no general or widely accepted model of the hard state as, for example, the hard state spectrum of the black hole binary source XTE J1118+480 can be described either by a thermal Comptonisation model (Frontera et al. 2001), a synchrotron emission dominated model (Markoff et al. 2001), or an advection dominated accretion flow (ADAF Narayan & Yi 1995) model (Esin et al. 2001). The emission spectra of black hole binaries in hard state cannot be associated with a disk, but rather with an extended structure, generally termed corona. There is an even larger variety of spectral states of black hole binaries, as the geometry and physics of the systems may invoke additional components beyond the disk, such as jets, active regions above the disk



(a) Spectral variance of the Cygnus X-1 as separated in soft state (red) and hard state (blue).



(b) Decomposition of soft state into thermal disk (long dash), continuum from the corona (short dash), and reflection component (dotted).

Figure 5.38: Classical definition of spectral states in X-ray binaries. Shown is a spectral decomposition of the HMXRB black hole Cygnus X-1 in different states, panel (a), and different emission regions and mechanisms during the soft state, panel(b). See text for details. From Gierliński et al. (1999).

(corona), or winds as shown in Fig. 5.39.

The formation, launch, composition, and central engine of jets is as yet unknown, as the physics of microquasars is complex. There is a consensus that high accretion rates are responsible for the thermal dominant state (soft state), with X-ray emission peaking around 1 keV, while hard X-ray and gamma-ray emission, peaking around 100 keV, is emitted during low-accretion rate phases (hard state). As there is radio emission associated and also correlated with X-ray emission in the hard state (Fender et al. 2004), with  $L_{\text{radio}} \propto L_{\text{X-ray}}^{0.7}$ , this coincidence is described as the existence of a persistent "jet", which is ejecting material into the surroundings. In the "very-high state", which can be seen as a combination of the soft and hard state, as the emission is strong in both soft and hard X-rays, see Fig. 5.39, there is reduced and sometimes burst-like radio emission observed. This is thought to be associated with unstable and discrete mass injection events in a flaring jets (Corbel et al. 2001; Fender et al. 2004). The observed synchrotron emission is most probably due to electrons, but charge-conservation implies also a positive component in jets, and whose nature is matter of debate. Either protons (in general ions) or positrons could be responsible

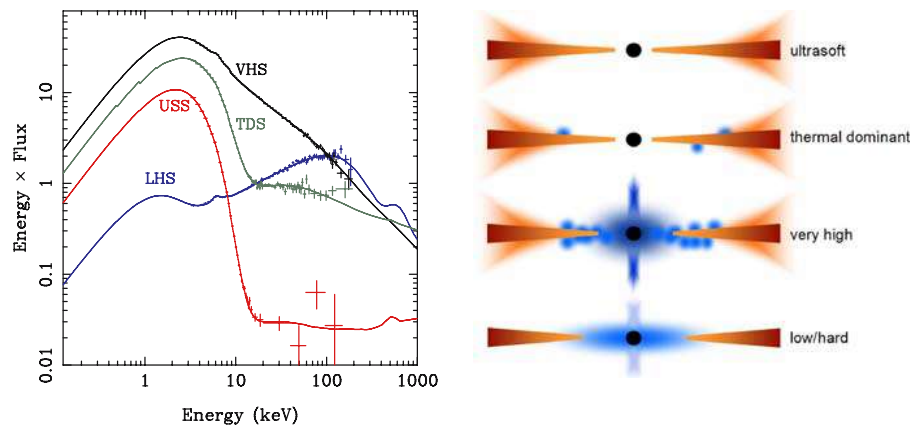


Figure 5.39: Spectral states of an outburst of GRO J1655-40. Shown are the measured spectra as decomposed to a very-high state (VHS), thermal dominant state (TDS), ultra-soft state (USS), and a low/hard state (LHS) up to 150 keV, together with fitted models as solid lines, derived from considerations as depicted in the right panel. In particular, the proposed accretion flow changes around the black hole (black dot) are shown to explain the different spectral shapes with varying contributions from the disk (red-orange), hot inner flow and jet (blue), and irregular or clumpy active regions above the disk (blue dots).

for the positive part. In the case of electron-positron pairs, the jet might eject (be composed of) them at relativistic energies (Gallo et al. 2003), and enrich the ISM with positrons, if they do not annihilate directly in the pair-plasma.

The pairs can easily and also efficiently be created in the vicinity of a black hole binary as shown in Fig. 5.35, either in the hot inner accretion disk, in the corona, or at the base of the jet. This requires a gamma-ray source present, to provide high-energy photons for gamma-gamma pair-absorption (Beloborodov 1999b). In the case of a jet, a fraction of the pairs may be released to the environment, and would not annihilate in the plasma. If the composition is rather electrons and protons instead of positrons, the plasma can also create secondary pairs, at the termination shock with the ISM (Heinz & Sunyaev 2002). An estimate of the positron production rate based on this scenario and the total kinetic luminosity of microquasars in the Milky Way yields  $4 \times 10^{43} \text{ e}^+ \text{ s}^{-1}$ . This is about the number that is required for the galactic positron content. The true duty cycle of such systems, i.e. the fraction of active positron production and ejection time versus the total time, is unknown, and furthermore, the true number of microquasars in the Milky Way is also unknown. Thus, the derived value by Heinz & Sunyaev (2002) may be uncertain by several orders of magnitude, in both directions. Based on theoretical models (e.g. Beloborodov 1999b), and the global energy content of XRB luminosities, Guessoum et al. (2006) estimated that of the order of  $10^{41} \text{ e}^+ \text{ s}^{-1}$  could be ejected into the ISM per microquasar. This would require of the order of 100 microquasars in the Galaxy, which is within reach from counting statistics of deep X-ray surveys of the galactic bulge (Sadowski et al. 2008; Bandyopadhyay et al. 2009; Tetarenko et al. 2016). In particular, the number of LMXRBs is estimated to be between  $3 \times 10^2$ - $3 \times 10^3$  (Bandyopadhyay et al. 2009, for the bulge only),  $10^3$ - $4 \times 10^4$  (Sadowski et al. 2008, for the entire Galaxy), and  $2 \times 10^4$ - $2 \times 10^8$  (Tetarenko et al. 2016, for the entire Galaxy, only BHBs). The galactic population of microquasars has the potential to explain all positrons annihilating in the Milky Way, and may also explain the large scale morphology, as it seems that microquasars are more concentrated in the bulge than elsewhere (Ribó 2002; Prantzos 2006). However, this is based on the low number statistics of actual detected microquasars only.

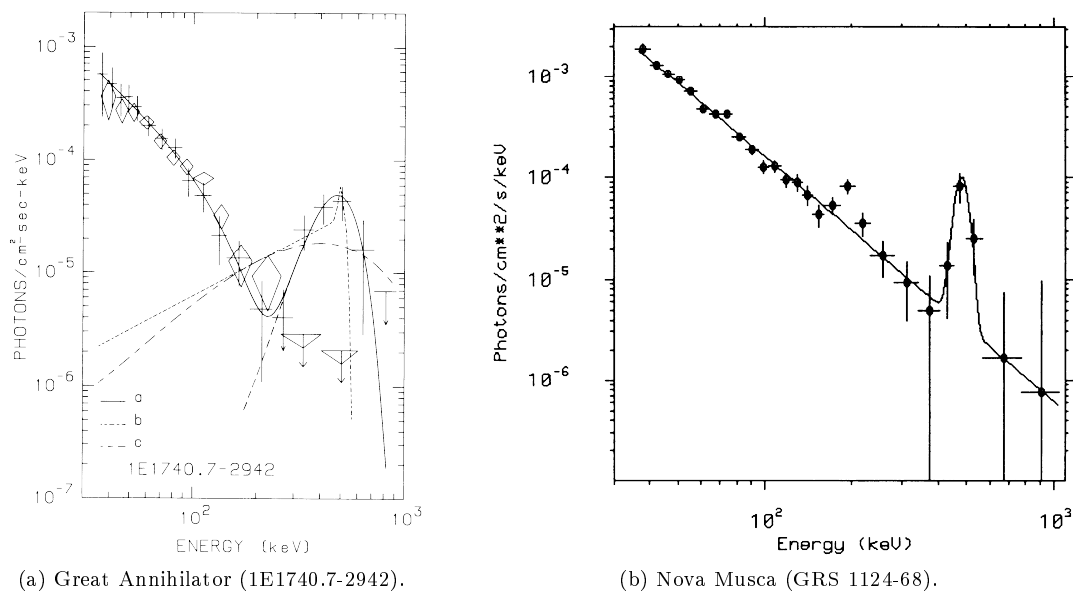


Figure 5.40: Measured high-energy spectra of microquasars. Shown are the photon spectra of the Great Annihilator, panel (a) from Bouchet et al. (1991), from October 1990 (black crosses) and March/April 1990 (diamonds), and of Nova Musca, panel (b) from Goldwurm et al. (1992), from January 1991. In both cases, a Gaussian-shaped emission feature around 500 keV is visible above the Comptonisation model (cut-off power-law (a) or single power-law (b)). Ortho-positronium or high-temperature Comptonisation does not fit for the Great Annihilator in particular. In Nova Musca, also another emission feature around 200 keV is seen and interpreted as Compton backscattering of 511 keV photons.

There are at least two previous measurements of high-energy spectra of microquasars in outburst, the so-called "Great Annihilator" (1E1740.7-2942) by Bouchet et al. (1991) in 1990, and "Nova Musca" (GRS 1124-68) by Goldwurm et al. (1992) in 1991, both with the SIGMA telescope aboard the GRANAT satellite. The spectra for both sources are shown in Fig. 5.40. In both cases, the cut-off power-law spectrum is evident, but in addition, there is a line-like high-energy excess at around 500 keV. This was interpreted as the annihilation of a hot electron-positron pair-plasma, created in the innermost parts of the accretion disk via photon-photon pair-absorption (Sunyaev et al. 1992). In the early 1990s, the galactic positron picture suffered from the incapability of resolving the gamma-ray sky around 511 keV, so that in consequence the annihilation line in the "centre" of the galaxy appeared time-variable<sup>10</sup>. Therefore, it was tried to find a source of positrons which varies in time and found 1E1740.7-2942, only about  $1^\circ$  off the galactic centre, and annihilating a large amount of positrons. For this reason, the source was then called the Great Annihilator. Follow-up observations in radio wavelengths (Mirabel et al. 1992) obtained an image as shown in Fig. 5.41. There is a diametrically opposite jet-like emission feature, observed around the position of the Great Annihilator, at a projected distance of  $\approx 1$  pc (Mirabel 1992). This is clear evidence for the injection of relativistic particles from a microquasar, and, based on the SIGMA findings, was directly interpreted as electron-positron pairs. However, since neither nearly contemporaneous (Jung et al. 1995; Smith et al. 1996b) nor long-term monitoring of the (transient) X-ray source (Harris et al. 1994; Smith et al. 1996a; Cheng et al. 1998) provided confirmation of such an activity and the annihilation feature, the positron interpretation remained contentious.

<sup>10</sup>This was resolved by OSSE on CGRO (Purcell et al. 1997), showing that there is an underlying morphology and that the emission feature is constant.

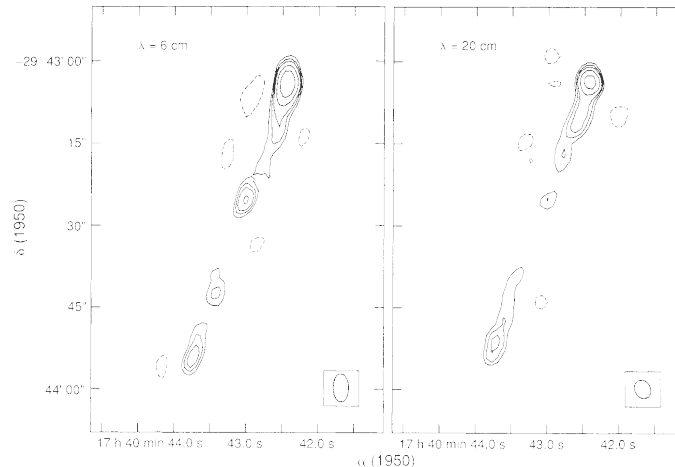


Figure 5.41: Radio maps of 1E1740.7-2942 at 6 and 20 cm wavelength. The Great Annihilator is located at (17 h 40 min 42.99 s /  $-29^{\circ}43'25.3''$ ), directly at the centre of a two-sided radio jet. Contours are  $-3, 3, 4, 7,$  and  $10$  in units of  $0.034$  mJy (left panel, 6 cm) and  $0.079$  mJy (right panel, 20 cm), respectively. From Mirabel et al. (1992).

In June 2015, the microquasar V404 Cygni (V404) went into outburst after 26 years of quiescence, becoming the strongest source in the X-ray sky. Unlike other most of the other black hole XRBs, V404 does not show the sharp rise and exponential decay behaviour in the X-ray light curve, but rather a flare-like and erratic emission, reminiscent of the very-high state with strong jets. V404 is therefore a prime candidate to search for positron annihilation in a microquasar, and to dispel previous doubts. INTEGRAL started to observe the source after a Swift/BAT trigger on the 17th of June, 2015, and was pointed to it during the entire outburst, until the 30th of June. The V404 analysis and results of Sec. 5.2.1.1 have been presented in Siegert et al. (2016b), Siegert et al. (2016a), and Rodriguez et al. (2015a).

### 5.2.1.1 Microquasar V404 Cygni

V404 Cygni is one of the best studied microquasars known today, as its binary system parameters are well measured. Because of its proximity of  $2.39 \pm 0.14$  kpc (Casares et al. 1992), multi-wavelength observations had been conducted. It is composed of a nine solar-mass black hole with a K3III companion star of  $0.7M_{\odot}$  (Khargharia et al. 2010), in a 6.5 day orbit (Miller-Jones et al. 2009). The plane of the binary system is spanned by the distance between the two orbiting objects of 0.15 AU, corresponding to a light-travel time of  $\approx 80$  s, and is inclined to the line-of-sight by  $67^{\circ}$  (Khargharia et al. 2010). In 1989, a source named GS2023+338 was detected by the GINGA satellite (Makino 1989; Kitamoto et al. 1989), but this source was actually known before as a "Nova Cygni 1938". It was measured with photographic plates from the Sonneberg Observatorium in Thüringen, Germany (Casares et al. 1991; Kimura et al. 2016). So, the source was actually "re-detected", and the outbursts in 1938, presumably 1956, 1989, and 2015, belong to the same source, V404 Cygni, at celestial coordinates  $(l/b) = (73.12^{\circ}/-2.09^{\circ})$ . V404 was the first black hole binary in which accurate proper motion studies could be performed, obtaining  $9.2 \pm 0.3$  mas yr $^{-1}$ , corresponding to a peculiar motion of  $40 \pm 5$  km s $^{-1}$ . This is consistent with a "kick" in a supernova explosion event, from which the black hole had emerged (Miller-Jones et al. 2009). Since all key parameters of the black hole binary system are known very precisely, V404 Cygni is an excellent

"laboratory" to study microquasar physics, in particular black hole accretion, jets, outflows, long-term behaviour, and the production of matter-antimatter pairs.

The INTEGRAL/SPI data set of V404 Cygni during the June 2015 outburst consists of 217 pointings from INTEGRAL revolutions 1554 to 1558, for a total dead-time corrected exposure time of 616 ks. Unlike for any other source, the activity of V404 was so strong that it became the strongest source in the gamma-ray sky, and furthermore was about five times stronger than the measured SPI background. This makes standard analysis, as described in Sec. 3.2.4.3, difficult as unknown systematic effects from a strong source might be introduced. The source was already identified in the raw count spectrum, and hence the background analysis was adjusted. The two preceding INTEGRAL orbits, 1552 and 1553, in which the instrument was pointed at high latitudes ( $b > 66^\circ$ ) being devoid of strong gamma-ray ( $> 300$  keV) sources, were used to determine the background patterns. The systematic uncertainty from gradual line-shifts, due to the energy calibration, are thus at most of the order 0.05 keV for the entire observation. The source is expected to predominantly show continuum emission, and broadened line emission. This systematic uncertainty is thus not a crucial point. During the observation, five other X-ray sources were in field of view of SPI, Cygnus X-1, Cygnus X-3, Cygnus A, 3A1954+319, and EXO2030+375, and have been taken into account in the maximum likelihood flux estimation.

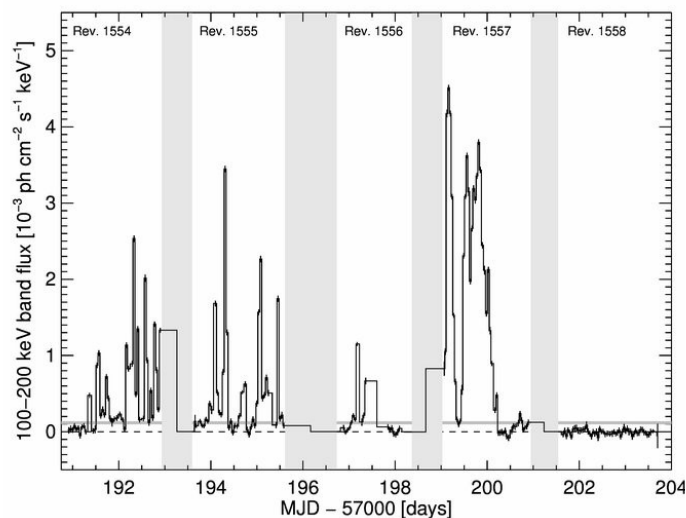


Figure 5.42: Light curve of hard X-rays during the V404 Cygni outburst. Shown is flux in the 100 and 200 keV band in  $\sim 1$  hour time binning (black histogram) with uncertainties in the five observing orbits. Grey shaded areas mark the regions where no data have been taken.

Due to the strong variability of this black hole binary system, not only the background scaling was determined on a short (pointing) time-scale, but also the source scaling. Unlike for other black hole XRBs, V404 does not show a smooth temporal behaviour, Fig. 5.37. Instead, the source shows high-energy flares, with a duration of the order of hours<sup>11</sup>, as shown in Fig. 5.42 for an energy band between 100 and 200 keV. This behaviour is unusual for most XRB sources with a few exceptions, and its nature is not understood. It might be associated with a "flickering" jet, emitting particle-antiparticle pairs (see below). For the spectral analysis, the data have been

<sup>11</sup>The timing resolution of SPI is restricted here to the duration of one pointing of about one hour. In principle, the timing resolution can be higher but as the instrument is "staring" when cutting a single pointing into sub-units, no additional coding information is available.

summed into three epochs of  $\sim 2$  days during the V404 flaring period, i.e. orbits 1554, 1555, and 1557, respectively, Fig. 5.43.

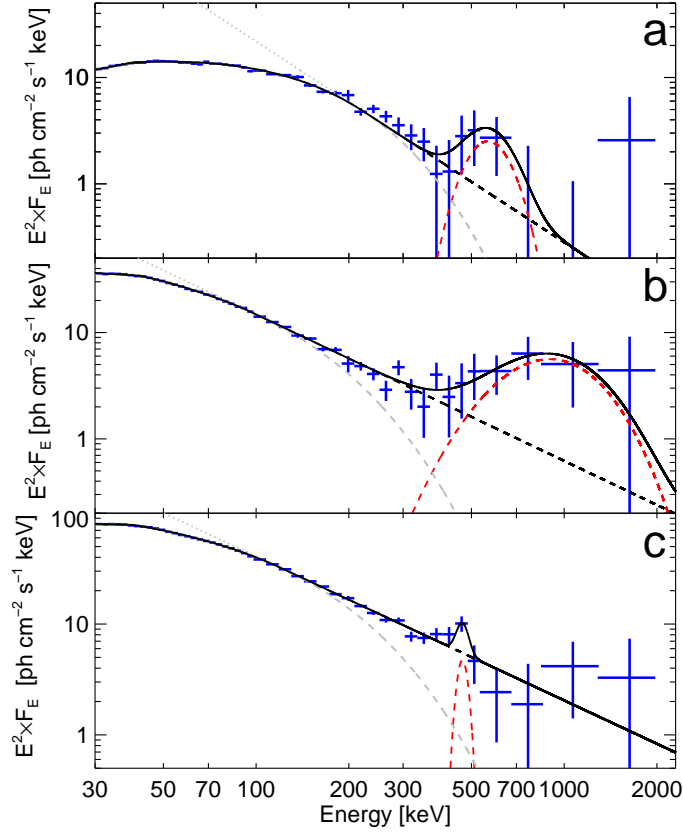


Figure 5.43: Spectral evolution of V404 Cygni during outburst. Shown are spectra (blue crosses) between 30 and 2000 keV in three different flaring epochs as defined by INTEGRAL orbits 1554 (top panel, a), 1555 (middle panel, b), and 1557 (bottom panel, c), respectively. In each panel, the individual spectral components are indicated as grey dashed lines for the Comptonisation model, black dashed for the power-law extension of the Comptonisation model, Eq. (5.35), and red dashed for annihilation radiation from a relativistic plasma. As the standard Comptonisation model falls short in describing data above  $\approx 200$  keV, a conservative power-law model has been added to extrapolate towards higher energies. In all three epochs, a significant flux excess is measured above the power-law extensions, which is interpreted as annihilation of a thermal pair plasma at different temperatures in flight.

The spectrum in each epoch is described by an empirical model function,

$$C(E) = \begin{cases} A_0 \left(\frac{E}{E_0}\right)^\alpha & : E < E_C \\ A_0 \left(\frac{E}{E_0}\right)^\alpha \exp\left(\frac{E_C - E}{E_F}\right) & : E_C \leq E \leq E_X \\ B_0 \left(\frac{E}{E_0}\right)^\beta & : E > E_X \end{cases} \quad (5.35)$$

with  $B_0 = A_0 \left(\frac{E_X}{E_0}\right)^{\alpha - \beta} \exp\left(\frac{E_C - E_X}{E_F}\right)$ , where  $E_0 = 100$  keV as a normalisation convention, and which is along with the spectral shape of Comptonisation. At energies below  $\approx 200$  keV, the spectra are well described by this standard spectral shape, but at higher energies, an  $18\sigma$  excess of above the high-energy tail is found. In order to quantify this excess, a thermal electron-positron pair-plasma model spectrum, Eq. (2.99), with two parameters describing the amplitude of the feature and the temperature of the plasma, is added. The temperature, denoted with  $kT$ , serves as a measure of the annihilation "line" width. The significance is calculated by a

$\chi^2$ -test of comparing a model involving only Eq. (5.35), versus a model with also thermal pair annihilation (TPA) in addition, Eq. (2.99). The characteristic curved shape of pair annihilation emission describes the excess in all three epochs well, for a total improvement of  $5\sigma$  above the power-law extension of the cut-off power-law, Eq. (5.35). The spectral parameters are listed in Tab. 5.7.

Orbit	$A_0$	$\alpha$	$E_C$	$E_F$	$B_0$	$\beta$	$F_{TPA}$	$E_X$	$kT_{TPA}$
1554	$2.31 \pm 0.11$	$-1.44 \pm 0.05$	$40 \pm 2$	$91 \pm 5$	$2.18 \pm 0.59$	$-3.89 \pm 0.09$	$220 \pm 113$	$1.9 \pm 1.2$	$29 \pm 14$
1555	$2.91 \pm 0.16$	$-2.18 \pm 0.05$	$42 \pm 1$	$86 \pm 3$	$1.48 \pm 0.03$	$-3.38 \pm 0.04$	$95 \pm 12$	$6.5 \pm 1.6$	$173 \pm 46$
1557	$7.30 \pm 0.05$	$-2.08 \pm 0.01$	$40 \pm 1$	$99 \pm 1$	$4.08 \pm 0.03$	$-3.30 \pm 0.02$	$122 \pm 7$	$1.2 \pm 0.9$	$2 \pm 1$
	$B_0$	$\beta$	$E_X$	$F_{TPA,hot}$	$kT_{TPA,hot}$	$F_{511}$	$E_{peak}$	$kT_{TPA,cool}$	
1557a	$4.27 \pm 0.42$	$-3.4 \pm 0.1$	$< 200$	$1.2 \pm 1.0$	$511 \pm 47$	$1.5 \pm 0.5$	$458 \pm 25$	$4 \pm 3$	
1557b	$5.73 \pm 1.20$	$-3.8 \pm 0.3$	$< 200$	$3.3 \pm 2.9$	$489 \pm 26$	$5.3 \pm 1.9$	$466_{-3}^{45}$	-	

Table 5.7: Spectral fit parameters for the flaring epochs of V404 Cygni as derived from a fit with the function in Eq. 5.35 and a thermal plasma annihilation (TPA) model. In the upper part, the parameters derived for the spectra in Fig. 5.43 are shown, in the lower part, parameters for two model alternatives of epoch 3 (orbit 1557, Fig. 5.44) are listed. The units are:  $10^{-3}$  ph cm $^{-2}$  s $^{-1}$  keV $^{-1}$  for the amplitudes  $A_0$  and  $B_0$  which are normalised to the flux at 100 keV,  $10^{-3}$  ph cm $^{-2}$  s $^{-1}$  for the integrated flux  $F_{TPA}$ , and  $F_{511}$ , respectively, denoting the area under the TPA, and the ortho-positronium (511) features, respectively. keV for  $E_C$ ,  $E_F$ ,  $E_X$ ,  $E_{peak}$ , and  $kT_{TPA}$ , denoting the spectral turning points (C, F, X), the centroid of the annihilation features, and the TPA temperature, respectively.

In epochs 1 and 2, the annihilation feature does not show any centroid shift although it appears blue-shifted. The apparent blue-shift is an implicit property of the TPA feature, mainly due to relativistic Doppler-shifts (see Sec. 2.4.3.3). For epoch 3, the annihilation feature is red-shifted by about 10% to  $458 \pm 25$  keV. The line width varies strongly between the three epochs, ranging between a few, to several hundreds of keV. Integrating over the flux of the annihilation features in all three epochs yields an average annihilation luminosity of  $L^{\gamma\gamma} = (2.19 \pm 0.50)10^{42}$  ph s $^{-1}$ , corresponding to  $L_{\pm} = (1.79 \pm 0.41)10^{36}$  erg s $^{-1}$ , and a positron production rate of  $\dot{N}_{e^+}^{\gamma\gamma} \approx (1.09 \pm 0.25)10^{42}$  e $^+$  s $^{-1}$ .

Electron-positron pair production is expected, in fact is inevitable, near luminous accreting black holes when their (seed) radiation spectra extent above  $E = m_e c^2 = 511$  keV (Svensson 1987; Maciolek-Niedzwiecki et al. 1995, see also Sec. 2.4.3.3). If the pairs produced in V404 Cygni are from photon-photon pair absorption, the processes has to take place at a distance to the black not greater than  $r \approx 11r_S \approx 300$  km. This constraints comes from total luminosity in photons of the required energy of up to  $L_1 \approx 10^{37}$  erg s $^{-1} \approx 0.01L_E$ , and the Schwarzschild radius of the black hole  $r_S \approx 27$  km, cf. Eq. (5.33). This leads to an efficient absorption of high-energy gamma-rays, as they can interact with the more numerous X-rays at lower energies, and consequently to a suppression of the photon spectrum at energies  $E \gg m_e c^2$ . This is supported by a tight upper limit on the GeV emission,  $F_{GeV} < 10^{-6}$  ph cm $^{-2}$  s $^{-1}$ , as obtained from an analysis of Fermi/LAT data (Siegert et al. 2016b). A significant fraction of the luminosity is hence converted into electron-positron pairs in form of a plasma, which is probably continually created and annihilated in the source. This plasma forms a broad annihilation feature with a width equivalent to temperature of  $\approx 100$  keV (Beloborodov 1999b), as seen in epoch 2, with a line width of  $kT \approx 170$  keV. On the other hand, photon collisions outside the source may create a pair outflow, in which the plasma would be in Compton equilibrium with temperatures of a few tens of keV from the accretion disk or corona. This is seen in epoch 1, with a line width of  $kT \approx 30$  keV. In fact, electron-positron pairs have already been invoked to explain the sometimes flat X-ray spectra of accreting black holes (Beloborodov 1999c; Fabian et al. 2015).

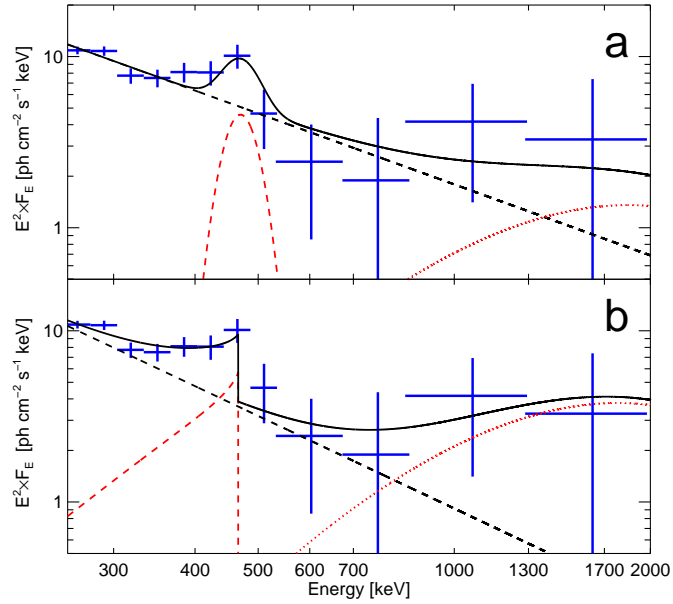


Figure 5.44: Alternative model spectra for V404 Cygni outburst epoch 3. Shown is the high-energy part of the spectrum in epoch 3 (orbit 1557) with different annihilation models. In both panels, black dashed curves indicate the Comptonisation continuum and red curves the annihilation components. In the top panel (a), the thermal pair plasma model as in Fig. 5.43 is shown with a 10% red-shifted line of an annihilating plasma at a temperature  $kT \approx 4$  keV. In the bottom panel (b), an alternative description by an ortho-positronium continuum is shown, also red-shifted by 10%. A high-temperature pair-plasma feature at  $kT \approx 500$  keV is indicated as red dotted lines in both panels.

The measured spectrum in epoch 3 shows a red-shifted excess with respect to 511 keV above the power-law shaped continuum, similar to what was observed for the Great Annihilator (Bouchet et al. 1991) or Nova Musca (Goldwurm et al. 1992). There is indication for a step decline below 511 keV, which is reminiscent of the o-Ps continuum, similar to the measured spectrum for galactic-wide positron annihilation, Sec. 4.6. In Fig. 5.44, two alternative spectral models for epoch 3 are shown. The top panel illustrates the data as fitted by a red-shifted and narrow annihilation feature, equivalent to Fig. 5.43. In the bottom panel, the o-Ps spectral shape is used instead, providing a marginally better fit, as also listed in Tab. 5.7. In addition, a broad component with a significance of  $< 2\sigma$  in both cases is indicated, which would imply a plasma temperature of more than 500 keV, then probably being separated from the cold plasma, as derived from the line width of 2 – 3 keV. The smaller line width in combination with the apparent red-shift in epoch 3 poses a problem to most model. If the 10% red-shift is interpreted as gravitational red-shift  $z$  (Einstein 1911) of photons in the strong gravitational field of a nine solar-mass black hole,

$$z(r_z) = \left(1 - \frac{2GM}{r_z c^2}\right)^{-1/2} - 1, \quad (5.36)$$

the emitting region,  $r_z$ , is constrained to  $r_z < 5r_S \approx 150$  km. But a TPA line emitted in this region would be expected to be significantly broader, owing to the relativistic bulk motions of the plasma and dispersion in gravitational red-shift. Likewise, the Ps interpretation is also difficult to explain as such a feature requires a dense plasma with a low temperature,  $T < 10^6$  K, to significantly slow down the pairs for the creation of the bound Ps state. But the lowest temperature a spherical surface of radius  $r_z$ , shining at a luminosity  $L$ , can achieve, is its black-body temperature, as

derived from Stefan-Boltzmann law,

$$L = A\sigma T^4 \stackrel{\text{sphere}}{=} 4\pi r^2 \sigma T^4 \Leftrightarrow T = \left( \frac{L}{4\pi r^2 \sigma} \right)^{1/4}, \quad (5.37)$$

with  $\sigma = 5.68 \times 10^8 \text{ W m}^{-2} \text{ K}^{-4}$  being the Stefan-Boltzmann constant. For a total measured luminosity of V404 of  $\approx 10^{38} \text{ erg s}^{-1}$ , the temperature would be restricted to  $T \gtrsim 5 \times 10^6 \text{ K}$ . The accretion flow at larger distances may indeed contain much cooler gas, especially if the central radiation is beamed and shielded by inner accretion disk. Then, the pair plasma which has to be created in the innermost regions, may be channelled outwards by a strong radiation field, and follows magnetic field lines towards cooler gas, decelerates there, and forms Ps before annihilation. This scenario would still be inconsistent with the measured red-shift, especially if interpreted as gravitational red-shift, but may be at least partly supported by independent measurements of the morphology of material near the black hole: High spectral resolution X-ray measurements with Chandra HETG (High Energy Transmission Grating King et al. 2015) suggest a high degree of ionisation, even out to a disk size of  $\approx 2 \times 10^6 \text{ km}$ . In combination with the high variability of X-ray line strengths, King et al. (2015) argue that the measured X-rays are not received directly, but rather as a result of reflection and/or reprocessing in the outer regions of the disk. In consequence, the outer edge of the disk must be elevated and blocks the direct view towards the inner disk, which may also result in a large variability of the X-ray continuum as seen in V404. Rather than rapid changes in the accretion rate of the black hole, the strong flares may be explained as a combination of line-of-sight effects from a re-structuring of the outer disk.

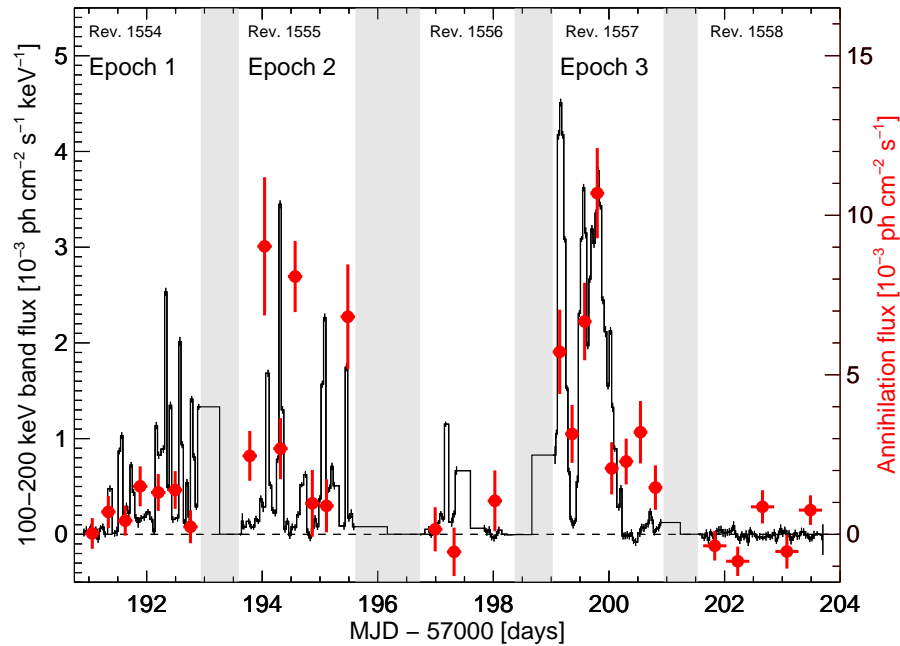


Figure 5.45: Annihilation flux light curve (red circles, right axis) of V404 Cygni during outburst in 6-7 hour time bins superimposed on the Comptonisation flux as measured with the 100-200 keV band flux (black histogram, left axis, similar to Fig. 5.42). The two high-energy emission components of the microquasar are either correlated and several times also lagged by tens of hours. See text for details.

Using the same time basis on which the 100 to 200 keV band is analysed, the flux

of pair annihilation is determined. As the statistics are rather low on the pointing time scale, the shapes of the annihilation features in each epoch are fixed, and only an amplitude is fitted to the spectra per one hour time bin, in addition to the Comptonisation model. In Fig. 5.45, the annihilation component is shown, rebinned to 6-7 hours for clarity. The Comptonisation flux as estimated from the 100-200 keV band and the annihilation flux seem to be correlated. The correlation as a function of the lag between X-rays and annihilation photons is shown in Fig. 5.46. The maximum correlation of  $\rho = 0.45$  is obtained for no lag which would mean that, whenever an X-ray flare occurs, on a time scale of  $< 1$  hour, pair plasma is created, ejected, and already annihilated again. However, there is also a second peak in the lag-correlation diagram around 20 hours, with a coefficient of  $\rho = 0.33$ . Albeit the correlation is weak and the significance is also only marginal, the X-ray emission may indeed lead the annihilation emission by almost one day. The timing resolution of SPI during this observation is not sufficient to probe the dynamical time scale of the inner accretion disk (milliseconds), nor the jet ejection time scale (minutes Mirabel & Rodríguez 1999), nor the light travel time between the two binary companions (80 s), but maybe the adiabatic expansion of ejected plasma blobs (minutes to hours Fender et al. 2004). Reducing the time-bin size could trace several time scales but would drown the annihilation signals entirely in the background. Thus, the time-averaged values do not resolve the rise-time of the annihilation flux, which may be much shorter than the six-hour bins. But since the apparent lag is measured at 20 hours, the responsible physical mechanism is probably not related to either of the mentioned time scales, but maybe to a resonant combination of them, similar to a feedback process. Especially in epoch 3, the trailing behaviour of annihilation photons with respect to the X-ray band is clearly visible as when the X-ray flux is completely gone, the annihilation flux needs about one day to fade. In fact, when the X-ray flaring of V404 stopped, the annihilation signal also vanished (orbit 1558).

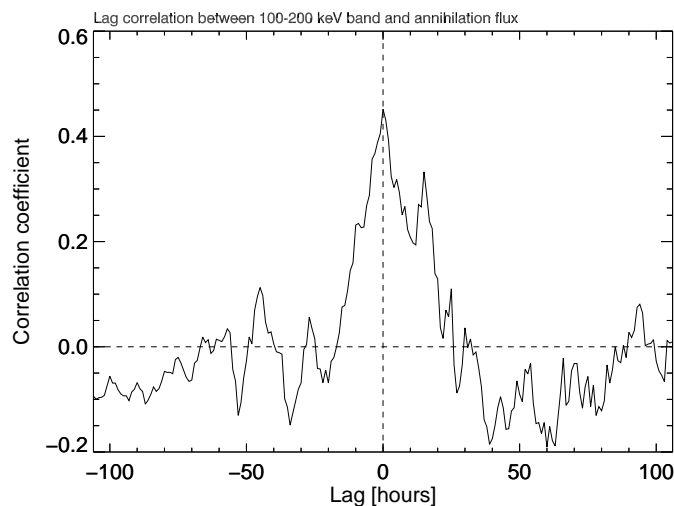


Figure 5.46: Correlation between the 100-200 keV band and annihilation flux in V404 Cygni as a function of the lag. The maximum correlation with a coefficient of  $\rho = 0.45$  is found with zero lag, meaning the Comptonisation emission occurs simultaneously to the annihilation emission. Around 20 hours, there is a second maximum with  $\rho = 0.33$  for which the annihilation emission could trail the hard X-rays. See text for details.

### 5.2.1.2 Positron Contribution from Microquasars

Based on the results of Sec. 5.2.1.1 and theoretical considerations, a new estimate of the contribution from microquasars to the galactic positron content can be obtained. Similar to the SN Ia case, the escape fraction of positrons in black hole binaries, i.e. the number of positrons not annihilating in the pair-plasma, is not known, but can be estimated from energy constraints.

In contrast to hadronic gas, pair plasma is easily accelerated and attains an equilibrium bulk velocity of  $v_{eject} \approx c/2$  away from the source. This is governed by the local radiation field anisotropy, forming the base of a relativistic outflow from the accretion disk (Beloborodov 1999b). Annihilation radiation around the source can be strongly affected by the magnetic field configuration, and may change the outflow speed and direction. This may be supported by the change in plasma temperature during the outburst, and also by measurements of optical counterparts of V404 flares (Gandhi et al. 2016). The power deposited in pair plasma alone of  $(1.79 \pm 0.44)10^{36}$  erg s<sup>-1</sup> would be sufficient to explain the observed typical radio luminosities associated with escaping blobs on larger scales (Gallo et al. 2003). As microquasars are now established as a positron producing source type, the link between ejected pair plasma, the non-detection of high-energy gamma-rays, and radio emission seen after the flares can be understood as follows:

Due to a probably magneto-hydrodynamic instability, the steady (quiescent) accretion of a black hole binary becomes irregular, and the sudden and abrupt changes in mass accretion rate leads to an increase in temperature and the formation of a compact gamma-ray source close to the black hole horizon. The disk morphology may be changed, and the outer parts may reflect the innermost radiation and thereby shield themselves, towards different line-of-sights with different column densities, and thus a flaring like appearance. The photon energy and density near the black hole will be so large that photon-photon pair-absorption becomes efficient, thereby reducing the number of high-energy photons, and electron-positron pair plasma is created, and continuously ejected in a jet. The jet's nature and mechanism is as yet unknown but probably related to electromagnetism in combination with general relativistic effects in the vicinity of black holes (Blandford-Znajek process Blandford & Znajek 1977). As the pair-plasma is escaping the black hole in the form of blobs, it is either annihilating very close (close to the horizon, broad line) or further away (few  $r_S$ , narrow line) from the black hole. The adiabatic expansion and inverse Compton cooling (Beloborodov 1999b) of pair-plasma blobs will lead to a reduced annihilation frequency, so that at some distance, the annihilation declines and synchrotron radiation from the constituents of the plasma is visible in radio emission.

The total maximum number of positrons that can be created in this picture can be estimated from the seed photons, i.e. the photons which are absorbed to create pairs, of an accretion disk in a simple flat geometry. As described in Eq. (5.35), the seed spectrum can be estimated as a power-law around 511 keV with a resulting luminosity above 511 keV of

$$L_1 = 4\pi d^2 \int_{m_e c^2}^{E_{max}} B_0 \left( \frac{E}{E_0} \right)^{\beta'} dE, \quad (5.38)$$

where  $E_{max}$  is the spectral break due to photon-photon pair absorption in the source (Beloborodov 1999b), and  $B'_0$  and  $\beta'$  are the spectral parameters of the "true" source spectrum before pair creation and annihilation. As the true source spectrum is not known,  $E_{max}$  is most conservatively set to  $+\infty$ , thereby ignoring other high-energy processes which could yield gamma-rays, and also spectral breaks. Hence,  $L_1$  is estimated from the flux value of the power-law component at 511 keV. This yields an average luminosity during the flaring epochs of V404 Cygni of  $\langle L_1 \rangle = (3.42 \pm 0.86) \times 10^{42}$  ph s $^{-1}$ , corresponding to  $(2.80 \pm 0.70) \times 10^{36}$  erg s $^{-1}$ , and a total positron production rate of  $\dot{N}_{e^+}^{\gamma\gamma, \text{tot}}(\text{V404}) = (1.71 \pm 0.43) \times 10^{42}$  e $^+$  s $^{-1}$ . The measured number of positrons annihilating in the pair plasma ejecta of V404, Sec. 5.2.1.1, account to  $\dot{N}_{e^+}^{\gamma\gamma} \approx (1.09 \pm 0.25) 10^{42}$  e $^+$  s $^{-1}$  so that the number of escaping positrons which enrich the ISM is estimated as

$$\dot{N}_{e^+}^{\gamma\gamma, \text{escape}} = \dot{N}_{e^+}^{\gamma\gamma, \text{tot}}(\text{V404}) - \dot{N}_{e^+}^{\gamma\gamma} = (0.62 \pm 0.50) \times 10^{42} \text{ e}^+ \text{ s}^{-1}. \quad (5.39)$$

This estimate may be uncertain by a factor of  $\sim 3$ , as from theoretical considerations (Beloborodov 1999b), the asymptotic ratio between  $L_1$  and  $L_{\pm}$  should be at most 20%, whereas in this study, the value is  $64 \pm 22\%$ . Hence, the number of escaping positrons can be larger, and the quoted number should be considered a lower limit. Together with the number of microquasars in the Milky Way and the duty cycle for each of the source, an estimate for the positron contribution from microquasars can be derived. Taking V404 as a standard microquasar, the duty cycle can be estimated from its previous outbursts and their durations, to  $\eta_{\mu Q} = (4.3 \pm 3.0) \times 10^{-3}$  where the variance between the outbursts are taken as an uncertainty estimate. The true population of microquasars in the Galaxy is unknown and may range between several 100 and millions. Thus, their contribution may be uncertain by several orders of magnitude. Here, a canonical value of  $N_{\mu Q} = 10000$  is used, as suggested by Romani (1992), Portegies Zwart et al. (1997), or Bandyopadhyay et al. (2009). Gilfanov (2004) pointed out that LMXRBs are good tracers of the stellar population, so that about 1/3 of all microquasars,  $N_{\mu Q}^{\text{bulge}} = \frac{1}{3} \cdot N_{\mu Q}$ , could be situated in the bulge regions of the Galaxy, and the remaining 2/3,  $N_{\mu Q}^{\text{disk}} = \frac{2}{3} \cdot N_{\mu Q}$ , in the disk (Bandyopadhyay et al. 2009). The total contribution of microquasars to the positron content in the disk thus amounts to

$$\dot{N}_{e^+}^{\gamma\gamma}(\mu Q) = N_{\mu Q} \eta_{\mu Q} \dot{N}_{e^+}^{\gamma\gamma, \text{escape}} = (2.67 \pm 2.85) \times 10^{43} \text{ e}^+ \text{ s}^{-1}. \quad (5.40)$$

The statistical uncertainty is probably overestimated as, for example, the duty cycle is only inferred from one source, and the luminosity values also includes uncertainties for the distance to V404 Cygni. Taking the derived value for granted, microquasars would contribute to  $54.5 \pm 60.5\%$  to the total galactic positron content, which converts to  $52.4 \pm 56.3\%$  of the bulge population and  $57.4 \pm 67.3\%$  of the disk. Within  $1\sigma$  uncertainties, microquasars alone can account for all positrons which are seen to annihilate in the Milky Way. However, there are also proven sources of positrons like the nucleosynthesis origins of radioactive nuclei, such as  $^{26}\text{Al}$  and  $^{44}\text{Ti}$ , whose presumably lesser contributions are yet much tighter constrained.

## 5.2.2 Supermassive Black Holes

Similar to stellar mass black holes, supermassive black holes (SMBHs) with masses of  $10^6$  to  $10^9 M_\odot$  could also produce electron-positron pairs in the vicinity of their event horizons, near the hot inner accretion disk, above in their coronae, or in relativistic jets. SMBHs are usually found in centres of spiral and elliptical galaxies. The escape fraction of positrons produced in steadily accreting SMBHs is only known up to a certain, model-dependent, limit, and the direct annihilation spectrum of thermal pair-plasma would be as broadened as in the case of V404 Cygni, Sec. 5.2.1.1. For the galactic centre SMBH Sgr A\*, the contribution in its current quiescent state is probably only a few per cent, as the accretion rate is only of the order  $10^{-8}$ - $10^{-6} M_\odot \text{ yr}^{-1}$  (Baganoff et al. 2003).

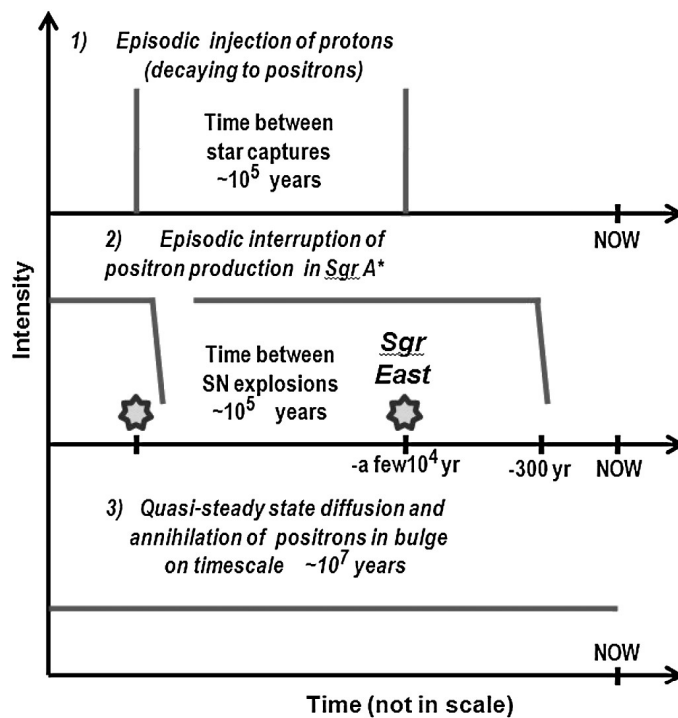


Figure 5.47: Scenarios for Sgr A\* as positron producer in the galactic centre. Shown are the periodic injection of positrons by tidal disruption events (1), periodic interruption of positron injection by accretion flow disturbances from supernova remnant encounters (2), and the steady matter accretion around SMBHs which leads to a constant production and annihilation of positrons in the bulge on time scales of  $10^7$  years. From Prantzos et al. (2011).

If the steady state assumption is dropped, and if Sgr A\* had phases of higher activity, an accretion rate of  $10^{-4} M_\odot \text{ yr}^{-1}$  may have increased the inner disk temperature<sup>12</sup>, up to  $10^{11}$  K (Totani 2006). Such an accretion rate may be due to tidal disruption events of low-mass stars (Cheng et al. 2007), massive star winds in the vicinity of Sgr A\* (Quataert 2004), or from the ionised halo surrounding Sgr A\* (Totani 2006). In either case, this may be enough to produce thermal MeV gamma-rays. As shown in Fig. 5.35, pair-production in the vicinity of compact objects like SMBHs is inevitable, provided gamma-ray photons are present. In consequence, an increased accretion rate could have produced a large amount of positrons on a much shorter time scale than the annihilation is expected to happen. Totani (2006) estimated that Sgr A\* alone could provide the observed  $1.8 \times 10^{-3} \text{ ph cm}^{-2} \text{ s}^{-1}$  from positron

<sup>12</sup>In radiatively inefficient advection flow (RIAF) models for accretion disks, the thermal energy can be as large as the gravitational energy close to the black hole, so that temperatures up to  $10^{12}$  K may result.

annihilation in the bulge region, if accretion rate about 300 years ago was about  $10^3$ - $10^4$  times higher than now. Further, Totani (2006) suggested that the accretion rate of Sgr A\* was predominantly at this level during the last  $10^7$  years, and that a supernova remnant shell, presumably from Sgr A East, disturbed the accretion flow around the SMBH. For this reason it is now in a quiescent state. The pair-production scenario around Sgr A\* is also in concordance with measurements of the galactic MeV continuum. Here, positron annihilation in flight should imprint at the injection energies of relativistic positrons (see also Sec. 5.3). The morphology could also be met, as the galactic centre source is consistent with the position of Sgr A\*, which would be expected as separate annihilation site in this scenario, from annihilation in the dense central molecular zone. Propagation of the positrons from Sgr A\* may extend as far as into the narrow bulge component, corresponding to radial scales of about 1 kpc (Totani 2006). The broad bulge component may thus correspond to a previous tidal disruption event around Sgr A\*, from which the positrons had the chance to propagate already further out.

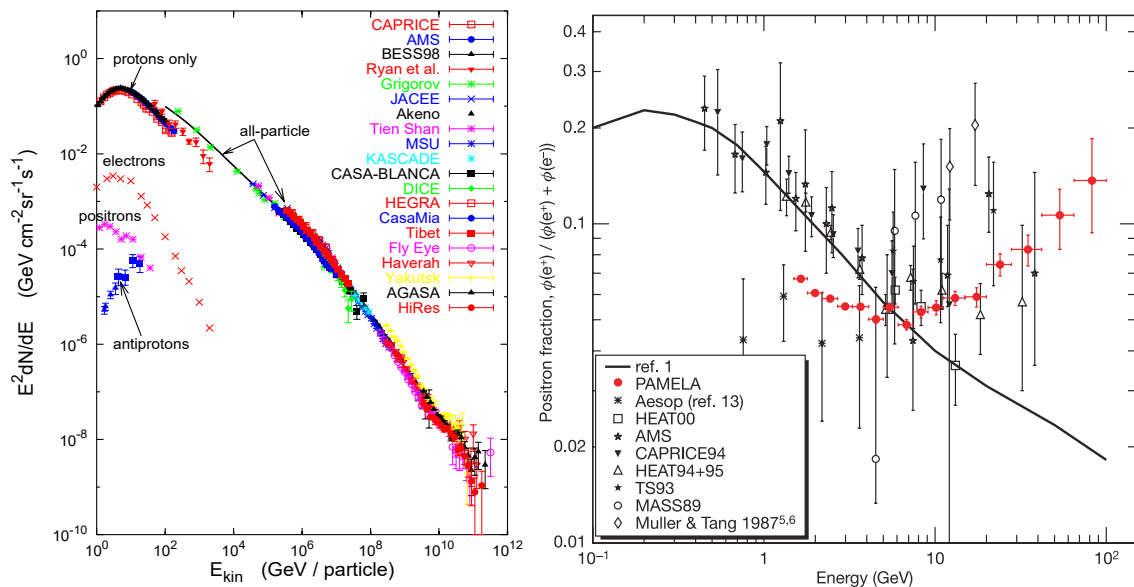
An alternative possibility to create positrons in the local environment of SMBHs is that proton-proton interactions from tidal disruption events lead to the production of charged pions, which subsequently decay into positrons. The rates at which such events are expected to occur are of the order  $10^{-5}$  to  $10^{-4}$  yr $^{-1}$ . Instead of maintaining a high accretion rate, Sgr A\* is then predominantly quiescent, and rises in luminosity for several tens of years (Rees 1988) when it is accreting the material of disrupted stars. Based on work of Fatuzzo et al. (2001), who noted that the 511 keV and GeV emission in the galactic centre may have a common origin due to hadronic interactions, Cheng et al. (2007) considered periodic tidal disruption events of many low-mass stars during the last  $10^7$  years. Each one them may have released an energy of the order  $10^{52}$  erg. The creation of positrons via relativistic proton-proton collisions also occurs on shorter time scales than the creation in the ISM, in this scenario. In consequence, the positrons are quasi-steadily produced, and diffuse into the extended bulge region. Most of the positrons are produced in the high-density regions, where the probability for proton interactions is largest, so that newly created positrons are also close to these dense regions, and should annihilate in flight on a short time scale. From the decay of secondarily produced charged pions, the positrons should have mean kinetic energies of several tens of MeV, which should then imprint in the gamma-ray spectrum at those energies. This is, however, inconsistent with observations in the MeV range (e.g. Bouchet et al. 2011), even though it should be noted that combined measurements with SPI, COMPTEL, and Fermi show a clear excess around 1 to 10 MeV.

The different scenarios for Sgr A\* as positron producer in the galactic centre are illustrated in Fig. 5.47. Additional discussion about Sgr A\* as the source of annihilation photons is provided in Sec. 5.6.

### 5.3 Cosmic Rays

Cosmic rays are high-energy particles which are propagating through interstellar space. The galactic composition of cosmic rays is mainly protons (88%),  $\alpha$ -particles (10%), and other nuclei (1%). This is similar to the solar element abundance with the

exceptions of Li, Be, and B, which are produced by spallation reactions of cosmic rays and measured to be  $5 \times 10^5$  times over-abundant with respect to the Sun (Berezinskii et al. 1990). The remaining 1% are mainly electrons with an energy-dependent fraction of positrons, and very few anti-protons (see Fig. 5.48b). The origin of cosmic rays and their acceleration mechanism are matter of debate, as there is a broad spectrum of cosmic-ray fluxes as a function of particle energies. The energy spectrum is changing abruptly at characteristic energies, Fig. 5.48a, and hence there may be different mechanisms to accelerate particles. Between  $\sim 10^9$  eV and  $\sim 4 \times 10^{15}$  eV, the spectrum can be described by a power-law function with index  $\gamma = 2.7$ , whereas between  $\sim 4 \times 10^{15}$  eV and  $\sim 10^{20}$  eV, the spectral index changes to  $\approx 3$ . Above this particle energy, the spectrum is limited by particle interactions with the cosmic microwave background, and cuts off around  $10^{20}$  eV, as predicted by Greisen (1966) and Zatsepin & Kuz'min (1966). Around and below 1 GeV, the measured spectrum at Earth is dominated by solar cosmic rays. The Sun is steadily releasing streams of charged particles with kinetic energies of the order of keV in all directions. In addition, solar flares and the associated magnetic reconnection of field lines near the surface of the Sun are responsible for the ejection of coronal mass. These particles are then interacting with the solar wind and magnetic fields, leading to a shock front. In this shock front, protons can be accelerated above energies of several tens of MeV by diffuse shock acceleration. The "true" cosmic-ray spectrum below 1 GeV is not easily determined, as direct measurements of particles outside the solar system is only possible with space probes, such as Voyager 1. Alternatively, gamma-ray measurements of nuclear de-excitation lines could be a direct tracer of the ongoing acceleration process, as particles with kinetic energies of MeV or more are required to excite nuclear levels.



(a) Broad band cosmic-ray spectrum as measured with different instrument and decomposed to particle species. The so-called "knee", indicating a change in spectral index from 2.7 to 3.0, appears around  $4 \times 10^{15}$  eV, and the "ankle" around  $5 \times 10^{18}$  eV with a cut-off at higher energies. From Hillas (2006).  
 (b) Close-up view of the cosmic-ray positron to electron ratio as a function of energy. A presumed model of primary positrons is included as solid black line as derived by Moskalenko & Strong (1998). Historic (black data points) and recent measurements (red data points) suggest an additional source of secondary positrons. From Adriani et al. (2009).

Figure 5.48: Cosmic-ray spectrum measured at Earth.

Supernovae and their remnants (Baade & Zwicky 1934), and to some extent pulsars

and compact objects, are made responsible for cosmic rays in the range below  $4 \times 10^{15}$  eV. The shock acceleration mechanism, also called Fermi-acceleration (Fermi 1949), is a stochastic acceleration process in which charged particles repeatedly cross a moving shock front and get reflected in magnetic irregularities by the magnetic mirror effect. Young supernova remnants expand at velocities of several  $1000 \text{ km s}^{-1}$  for several hundred years, and decelerate afterwards for a final merger with the ISM. This time scale and the velocity would correspond to a spectral index of at most 2.5 when diffusive shock acceleration is assumed. Thus, for energies above  $4 \times 10^{15}$  eV with a larger spectral index, supernova remnants may not come into consideration as cosmic-ray sources. High-energy cosmic rays, up to  $10^{18}$  eV, are believed to have their origins inside the Milky Way, probably from jets emerged in black hole binary systems or superbubbles. Above this energy, extragalactic accelerators, such as distant active galactic nuclei, could produce very-high-energy cosmic rays (George et al. 2008).

Once cosmic rays are ejected from their local environments, they propagate through the ISM at typical time scales of 10 to 100 Myr before escaping to intergalactic space (Berezinskii et al. 1990). Their transport is modelled as diffusion with different processes involved, such as energy losses by the galactic magnetic field, nuclear fragmentation, radioactive decay, or re-acceleration in the ISM. As cosmic rays also interact with interstellar gas, which is seen as high-energy gamma-ray emission, they are efficient producers of secondary particles like positrons and other isotopes. In the latter case, the light elements Li, Be, and B are mainly produced by cosmic-ray spallation interactions with heavier CNO ejecta. Especially the relative abundance of secondary to primary nuclei can be used to derive model-dependent propagation parameters, such as cosmic-ray confinement in the Galaxy, diffusion coefficient, or energy losses. Positrons may be created by, for example, charged pion-, kaon-, and anti-muon-decays (see Secs. 2.2.2 and 2.2.3), as the result of high-energy particle collisions. The primary to secondary abundance is then ill-defined because the escape of positrons from their sources, their acceleration, and their initial energies are unknown. The propagation of positrons may be equivalent to other species, especially electrons. But due to the fact that at any time, direct annihilation may occur, the true population of cosmic-ray positrons is unknown. However, the positron production rate can be estimated from propagation models, and, depending on the conditions, yield  $1\text{-}2 \times 10^{42} \text{ e}^+ \text{ s}^{-1}$ . Formally, this would correspond to a contribution to the galactic positron content of about 2 – 4% at energies of the order 100 MeV to GeV. The secondary electrons and positrons would imprint at high-energy gamma-ray spectra by their photon emissions from inverse Compton scattering and bremsstrahlung (Porter et al. 2008). During their slowing-down phases, however, there is also the possibility that positrons annihilate in flight, which should to some extent contribute as diffuse emission in the MeV range. Bouchet et al. (2011) showed that most of the galactic emission between 50 keV and 2 MeV, as measured with SPI, can entirely be explained by inverse Compton scattering of cosmic background photons with cosmic-ray electrons. Based on broad band spectra between  $10^{-2}$  and  $10^2$  MeV from the inner Galaxy at  $-10^\circ < l < +10^\circ$ ,  $-10^\circ < b < +10^\circ$ , Sizun et al. (2006) and Beacom & Yüksel (2006) concluded that the injection energy of positrons must be below several MeV, as otherwise, the MeV-GeV continuum should have imprints of annihilation in flight processes. In addition, Sizun et al. (2006) and Beacom & Yüksel (2006) constrained the dark matter particle mass to 3 – 7.5 MeV  $c^{-2}$ , if the source of the large scale diffuse 511 keV emission from the

galactic centre is assumed to be due to the annihilation light dark matter particles.

Although their implications are based on the dark matter hypothesis, the same argument applies for ejection energies of pulsars and cosmic rays. The cosmic-ray positron spectrum is shown in Fig. 2.17, based on a variety of energy-loss processes. Instead of showing a double-peaked annihilation profile as expected from the kinematics of fast positrons with nearly stationary electrons, there is only one peak around 255.5 keV and a power-law like spectrum up to ejection energy of the positron. If, however, one or more processes dominate during the energy loss, for example in an environment which may force rapid slowing down of positrons, the resulting spectral shape will vary. This may result in either a double-peaked profile, where the second peak will be around the kinetic positron energy, or a steeper power-law which will easily drown in statistical uncertainties. A re-analysis of the gamma-ray continuum with 14 years of SPI data, especially in the region between 100 and 8000 keV, would constrain the annihilation in flight spectrum, and provide a more reliable estimate of the cosmic-ray contribution to the galactic positron content.

## 5.4 Pulsars

Neutron stars are the remnants of massive stars of initial mass range between 8 and  $30M_{\odot}$ . When massive stars collapse under their own gravity, their cores get compressed until the density of nuclear matter is reached. This may lead to a rebound of infalling material from a compact object with a typical size of 10 km, containing one to two solar masses of material which is stabilised by neutron degeneracy pressure. Due to angular momentum conservation during the process of collapse, neutron stars are rotating with periods up to several hundred times per second. This is known from measurements of their electromagnetic radiation emitted in a beam, which, seen by an observer, looks like a pulsating emission. For this reason, rotating neutron stars are called pulsars. The radiation which pulsars emit is caused from particle acceleration near the magnetic poles. These do not have to be align with the rotational axis, so that large electrostatic fields may build up. Emitted electrons will be accelerated along the magnetic field lines of the neutron star, and emit synchrotron radiation, which is observed as pulsed radio emission. The origin of the magnetic fields are not known, but is believed to be due to magnetic flux-freezing as Gauss's law for magnetism conserves the magnetic flux through a surface. With decreasing surface, from a massive star of millions of km radius to a neutron star of 10 km radius, the magnetic field has to increase by several orders of magnitude to conform with Gauss's law (Lyne & Graham-Smith 2006).

There are mainly three sub-types of pulsars, depending on their rotation periods and magnetic fields: Crab-like pulsars with rotation periods of the order of few tenths of seconds and  $10^{12}$  G magnetic fields. These are rotation-powered objects and referred to as "normal" pulsars. Accretion-powered pulsars can spin up their rotation periods up to milliseconds, from accretion with a binary companion (millisecond pulsars). Magnetars are strongly magnetised objects with magnetic fields of up to  $10^{15}$  G (Lorimer 2005; Harding & Lai 2006).

Object	$B$ [G]	$P$ [s]	$N$
Normal pulsars	$10^{12}$	0.5	$1.5 \times 10^5$
Millisecond pulsars	$3 \times 10^8$	$3 \times 10^{-3}$	$3 \times 10^4$
Magnetars	$3 \times 10^{14}$	10	40

Table 5.8: Characteristic properties of pulsars. The values given are the magnetic field  $B$ , the period  $P$ , and the total number in the Milky Way  $N$ . All number are to be considered mean values and their realised ranges are within two orders of magnitudes for the magnetic field and the total number. From (Prantzos et al. 2011).

Interactions of high-energy photons with magnetic fields, Sec. 2.2.4.3, especially when the field strength is large, will lead to efficient electron-positron pair-production. The pairs may be accelerated in the electric field near the polar caps, and eventually leave the system if not bound to the pulsar by the magnetic bottle effect. If the accelerated particles annihilate again in the vicinity of the strong magnetic field, the subsequent gamma-ray photons will create more pairs, yielding a pair cascade. Again, the particles may either escape in the pulsar wind or will contribute to secondary radiation such as (high-energy) synchrotron emission. In general, only a few charged particles have to be accelerated up to high Lorentz-factors to start such a pair cascade (Harding 1981). Primary electron-positron pairs obtain energies which will be limited according the pulsars period as  $E_p \approx 6P^{1/3}$  TeV, with  $P$  being the pulsar rotation period in seconds (Halpern & Ruderman 1993; Zhang & Cheng 1997). Photons with energies around the critical energy,  $E_{cr} \approx 3B_{12}^{-1}$  MeV, will efficiently produce additional pairs, towards a total number of  $\dot{N}_{e^+}(\text{Pulsars}) = E_p/E_{cr}$  involved in the pair cascade (Prantzos et al. 2011). A more thorough analysis, also based on geometrical models (Cheng et al. 1986; Zhang & Cheng 1997; Prantzos et al. 2011), obtains a mean electron-positron pair-production rate of

$$\langle \dot{N}_{e^+}(\text{Pulsars}) \rangle \approx 2.8 \times 10^{37} B_{d,12}^{10/7} P^{-8/21} \text{ e}^+ \text{ s}^{-1}, \quad (5.41)$$

where  $B_{d,12}$  is the pulsar dipole magnetic field on the surface in units of  $10^{12}$  G. In case of millisecond pulsars, the dipole assumption is not given any more due to relativistic effects. There, the magnetic field must be scaled by the cube of the stellar radius  $r$ , versus the curvature of the magnetic field  $l \approx 1$  km,  $B_{d,12} \rightarrow B_{d,12}(r/l)^3$ . The contribution of positrons from pulsars is then determined as the production rate from Eq. (5.41), the number of pulsars  $N_i$  of each type  $i$  from Tab. 5.8, and the escape fraction for each type  $f_i^{esc}$ ,

$$\dot{N}_{e^+}(\text{Pulsars}) = \sum_i \langle \dot{N}_{e^+}(\text{Pulsars}) \rangle N_i f_i^{esc}. \quad (5.42)$$

The escape fraction is unknown in general but may be close to 1.0 for millisecond pulsars due to the lower magnetic field and lower than 1.0 for normal pulsars. In the case of magnetars, the pair-production may even be suppressed as noted by Harding & Lai (2006), as also their radio emission is weak. Using the values from Tab. 5.8 for typical pulsar properties, the galactic-wide contribution to the positron population may be estimated as

$$\begin{aligned}
\dot{N}_{e^+}(\text{Pulsars}) &= \dot{N}_{e^+}(\text{normal pulsars}) + \dot{N}_{e^+}(\text{ms pulsars}) + \dot{N}_{e^+}(\text{magnetars}) = \\
&= (2.7 \times 10^{42} + 1.4 \times 10^{42} + 0.8 \times 10^{42}) \text{ e}^+ \text{ s}^{-1} = \\
&= 4.9 \times 10^{42} \text{ e}^+ \text{ s}^{-1},
\end{aligned} \tag{5.43}$$

which is to be considered as an upper limit because the escape fraction is most uncertain. The pulsar population in the Milky Way could contribute about 10% to galactic positron content, mainly in galactic plane. Interestingly, pulsars are made responsible for the cosmic-ray positron excess, measured at Earth. In particular, one pulsar could have produced the number of high-energy positrons, if there was one pulsar at a distance of 100-200 pc to the solar system. Aharonian et al. (1995) noted that one (or few) nearby and young ( $\approx 0.1\text{Myr}$ ) object(s) could be the source of TeV positrons, and suggested the pulsar Geminga at a distance of 250 pc (Faherty et al. 2007) as probable source. With increased statistics from the AMS experiment, Yin et al. (2013) and Di Mauro et al. (2014) also found that Geminga significantly improves the description of the data. Also multiple pulsars may be possible. Among the seven most close-by pulsars, the source J1745-3040 is located at galactic coordinates  $(l/b) = (-1.45/-0.96)$ , reminiscent of the emission peak of the diffuse galactic 511 keV radiation, Sec. 4.4.2. This pulsar provides one of the best fits for the cosmic-ray positron excess (Boudaud et al. 2015), and is located only 200 pc away from the Sun in the direction of the galactic centre. One (or few) nearby pulsar(s) may also be responsible for the 511 keV emission measured with SPI: At a distance of  $\approx 200$  pc, the annihilation flux of  $10^{-3} \text{ ph cm}^{-2} \text{ s}^{-1}$  would correspond to only  $10^{40} \text{ e}^+ \text{ s}^{-1}$ , which could be maintained by one pulsar with  $B_{d,12}^{10/7} P^{-8/21} \approx 360$ . A single magnetar with a magnetic field of a few  $10^{14}$  G would be enough to supply the positron production and annihilation rate, if the created pairs slow down and annihilate sufficiently fast. This scenario, however, suffers from the morphology of the 511 keV emission. Although the pulsar J1745-3040 is located just at the correct position in the sky for the emission maximum, the extended emission around it would be hard to explain. Additionally, the disk-like 511 keV emission would contradict the geometry of such a pulsar system as the positrons, ejected at highly relativistic energies, would travel only a few tens of pc before annihilation, and in a preferred direction, aligned with the galactic plane. The kinematic information about the galactic annihilation radiation, Sec. 4.7.3, could on the other hand support a scenario with foreground emission. The central ten degrees in longitude show no signs of galactic rotation, and beyond this region, the velocities would be much too large to be due to rotation only. It is therefore not entirely excluded that one pulsar in the vicinity of the solar system is responsible for the "galactic" 511 keV emission.

## 5.5 Dark Matter

Historically, the term "dark matter" corresponds to an unseen mass in clusters of galaxies (Zwicky 1933, 1937). Already in 1933, Fritz Zwicky used observations of the Coma cluster to infer a "dynamical mass" of the cluster. From the application of the virial theorem, Zwicky found that this mass was at least two orders of magnitude larger, than what was expected from the visible light. He concluded that there was

an over-density of what he then named "dunkle Materie" (engl. dark matter), in contrast to the luminous matter of stars and gas (Zwicky 1933, 1937). There seemed to be an unseen mass, which does not shine, but only interacts gravitationally. In the 1930s, his theory of an additional mass component, which is not emitting nor absorbing photons, was completely ignored, but is today the state of the art prescription of most of the matter in the Universe.

Since the onset of imaging annihilation gamma-ray astronomy, the similarity of the 511 keV emission morphology and the presumed density profiles of dark matter has been suggested to consolidate both, the existence of dark matter, and the origin of antimatter in the Milky Way (e.g. Boehm et al. 2004). However, the existence of dark matter and associated physical processes still remain questionable. Direct searches for dark matter particles became very sensitive in recent years, that many mass ranges for WIMP particles could be excluded (e.g. Billard et al. 2014). Especially in the search for dark matter particles above  $\approx 1 \text{ GeV } c^{-2}$ , the initially believed easy direct detection suffers from evidence against WIMPs. For example, dark matter - matter interactions are at least eight orders of magnitude weaker than weak interactions (Lemrani 2006; Angle et al. 2008), and indirect (also astrophysical) detection experiments find no monochromatic line at  $E = m_{DM}c^2$  (Abdo et al. 2009; Aharonian et al. 2009). Also particle accelerator experiments find no hints of physics beyond the standard model (e.g. Piper 2009; Olive & Particle Data Group 2014; Mitsou 2015). But this does not entirely exclude the existence of dark matter, because its nature is almost entirely unknown, and it could well be that its interactions are much weaker than proposed in the standard model. This may point towards either heavy or light dark matter particles, or strong interacting particles at a different energy scale (Boehm & Silk 2008).

### 5.5.1 Appearance of Dark Matter

Dark matter is made responsible for the peculiar behaviour of large scale rotation in spiral galaxies. Instead of showing a decreasing rotation velocity, the rotation velocity remains at constant high speeds even for large radii,  $v_r \overset{measured}{\approx} const..$  It would be expected from only the baryonic content of galaxies that the kinematics should follow a Keplerian motion, i.e.  $v_r \overset{expected}{\propto} r^{-1/2}$ , from solving the equation of motion of a test particle in the gravitational field of a mass  $M_r$ . In particular, the velocity of a star at a distance  $r$  to the galactic centre should be given by equating the centrifugal force with the gravitational force of a mass  $M_r$ , interior to  $r$ , such that

$$\frac{v_r^2}{r} = \frac{GM_r}{r^2} \Leftrightarrow v_r = \sqrt{\frac{GM_r}{r}}. \quad (5.44)$$

But since the measured velocity is constant, there seems to be a non-visible component, whose mass has to increase linearly with radius,  $M_r \propto r$ . The innermost parts of galaxy rotation curves show steep rises, and then stay almost flat at a certain radius. This means that there is a particular density distribution, which determines the exact shape of the stars' (and gas) motions. By solving Eq. (eq:centriforcekepler)

for  $M_r$ , and differentiating with respect to  $r$  (assuming spherical symmetry), obtains the matter density distribution which is required for flat rotation curves,

$$\frac{dM_r}{r} = \frac{v_r^2}{G} \stackrel{!}{=} 4\pi r^2 \rho(r) \Leftrightarrow \rho(r) = \frac{v_r^2}{4\pi G r^2} \propto r^{-2}. \quad (5.45)$$

For consistency with the observational evidence for rigid-body-like rotation within the first few kpc, the derived density distribution has to be modified towards

$$\rho(r) = \frac{C_0}{a^2 + r^2}, \quad (5.46)$$

where  $C_0 \approx 4.6 \times 10^8 M_\odot \text{ kpc}^{-1}$  and  $a_0 \approx 2.8 \text{ kpc}$  are determined from the measured Milky Way rotation curve. The  $r^{-2}$ -behaviour is in contradiction to the number density of stars in the visible stellar halo, with  $r^{-3.5}$ , pointing again to an additional mass. Its total weight, however, is not known, as the sizes of galactic haloes are not known. Rotation curves up to several tens of kpc can be very well described by a combination of gas, bulge, disk, and a more general parametrisation of the dark matter halo density,

$$\rho(r)_{DM} = \frac{\rho(r_0)}{\left(\frac{r}{r_0}\right)^\gamma \left[1 + \left(\frac{r}{r_0}\right)^\alpha\right]^{\frac{\beta-\gamma}{\alpha}}}. \quad (5.47)$$

Here,  $\rho_0$  is the characteristic mass (or energy) density,  $r_0$  is the radial halo scale, and  $\alpha$ ,  $\beta$ , and  $\gamma$  are numerical parameters which are either measured, or found from simulations (e.g. Merritt et al. 2006). In Fig. 5.49, the rotation curve of the Milk Way is shown, as decomposed by the above-mentioned components.

The profiles of dark matter and the 511 keV emission are very similar, Fig. 5.50. Thus, the hypothesis can be stated, whether the emission is due to the interaction of dark matter particles. Such a test is not straightforward, as the emission morphology is not necessarily the source morphology, Sec. 4.6.6. A first step is to clarify whether the measured morphology is consistent with dark matter decay, annihilation, or de-excitation. Depending on the specific process, the expected flux would be proportional to the density to the power of  $n$ , where  $n = 1$  points to a single-particle process, i.e. decay, and  $n = 2$  points to two-particle process, i.e. either annihilation or de-excitation. Skinner et al. (2014) tested the Navarro-Frenk-White (NFW) dark matter density profile with  $\alpha = 1$ ,  $\beta = 3$ ,  $\gamma = 1$ , and  $r_0 = 20 \text{ kpc}$ . They used the resulting profile as an emission morphology template in a maximum likelihood fit to the same data set as described in Sec. 4.2, but only in the line band between 508 and 514 keV. They also used non-integer numbers of  $n$ , and found that  $n = 2.15 \pm 0.15$  is favoured over  $n = 1$ , by a  $\chi^2$  difference of 145. In fact, the authors found that the NFW profile "*can replace all three bulge components*", but did not quote the numbers for a goodness-of-fit measure, nor the received 511 keV flux from this template. The fitted NFW profile is assumed symmetric about the dynamical centre of the Milky Way, at  $(l/b) = (0/0)$ , but the empirically derived morphology shows an offset towards negative longitudes, Sec. 4.4.2. Kuhlen et al. (2013) showed that

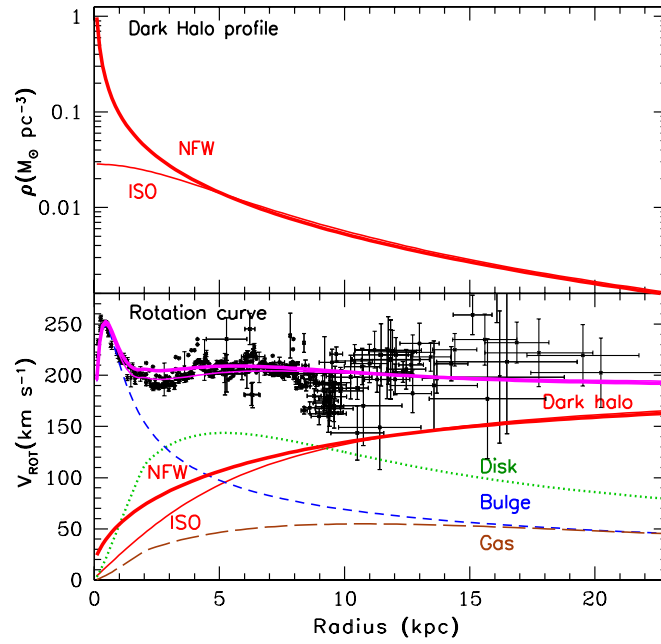


Figure 5.49: Rotation curve of the Milky Way (bottom panel) as decomposed to bulge, stellar disk, gas, and two possibilities of the dark halo (NFW and ISO). The flat rotation curve cannot be explained by the baryonic content of the Galaxy alone and a dark matter density profile (top panel) has to be assumed to account for the constant velocity beyond a radius of  $\approx 10$  kpc. An isothermal (ISO,  $\alpha = 2$ ,  $\beta = 2$ ,  $\gamma = 0$ ,  $r_0 = 5$  kpc) dark matter density profile is preferred for dwarf galaxies and avoids the strong cusp of the NFW profile. From Prantzos et al. (2011) with data points from Sofue et al. (2009).

the position of the central dark matter density peak can be expected to differ from the dynamical centre of a Galaxy, by several hundred pc. In return, the measured offset may be related to a shift of the dark matter density distribution (Skinner et al. 2014).

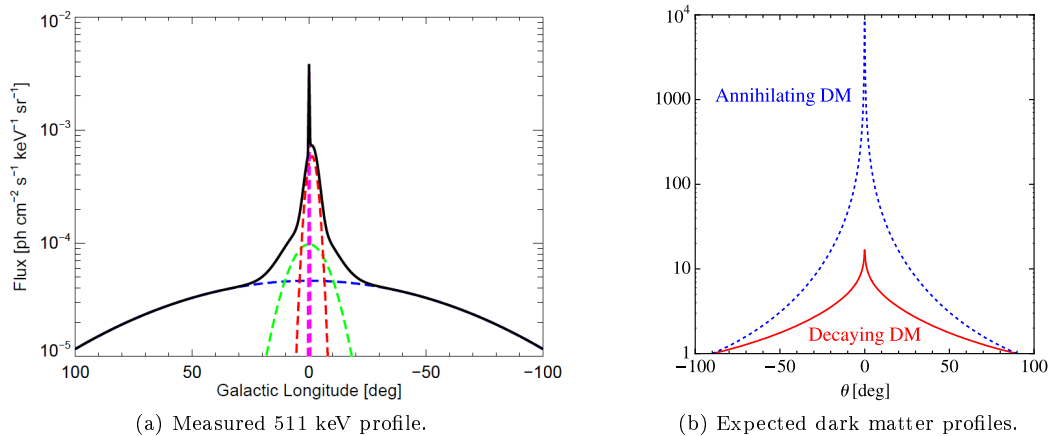


Figure 5.50: Angular profiles for 511 keV (left panel) and dark matter density profiles (right panel) of decaying (red) and annihilating (blue) dark matter particles as expected from a NFW profile in arbitrary units. Left panel equivalent to Fig. 4.11a; right panel from Dario Serpico & Hooper (2009).

### 5.5.2 Testing the Dark Matter Scenario with SPI

Assuming now the Milky Way 511 keV emission to be completely explained by the annihilation of dark matter particles, the second step of the before-mentioned hypothesis has to provide an independent proof. Results of this test have been presented

in Siegert et al. (2016d). Dark matter is a major ingredient for the standard model of cosmology<sup>13</sup>,  $\Lambda$ CDM. Dark matter is required to be "cold" for the formation of structures in the Universe, such as galaxy clusters, galaxies, and satellite galaxies. Following this type of cosmology, the corresponding galaxy formation model predicts large galaxies to have formed in such a dark matter halo. This should be surrounded by several smaller sub-haloes, in which the satellite galaxies of the parent should have formed. In several dark matter only simulations, e.g. the Millennium simulation or Via Lactea II, the cold dark matter paradigm inevitably forms structures hierarchically. Such simulations start from nearly isotropic dark matter densities, in which the particle constituents are non-baryonic, dissipationless, and collisionless. Structure formation then happens in a self-similar way. Giant dark matter complexes in such simulations are then believed to be superclusters or clusters of galaxies, which have formed by multiple mergers. On smaller scales (1 Mpc<sup>3</sup>), the structure of single galaxies are revealed, showing an overdensity in the centre, and a large number of smaller haloes. Note that those simulations do not include baryonic matter, so that conclusions about the visible structure are quite far-fetched. The large number of sub-haloes, Fig. 5.51, poses problems, as observationally, the number of known satellite galaxies of the Milky Way is about one order of magnitude lower than what would be expected from such simulations. This is known as the "missing satellite problem" (Moore et al. 1999; Klypin et al. 1999). At the time of writing this thesis, about 40 satellite galaxies of the Milky Way have been identified whereas about 400 are expected. Either these dark matter sub-haloes exist but did not accrete enough baryonic material to become visible, or dynamical processes, such as tidal stripping or mergers, prevent more identifications<sup>14</sup>. In any case, the satellite galaxies are then dominated by dark matter, so that large ratios of the dynamical mass to the visible light can be expected.

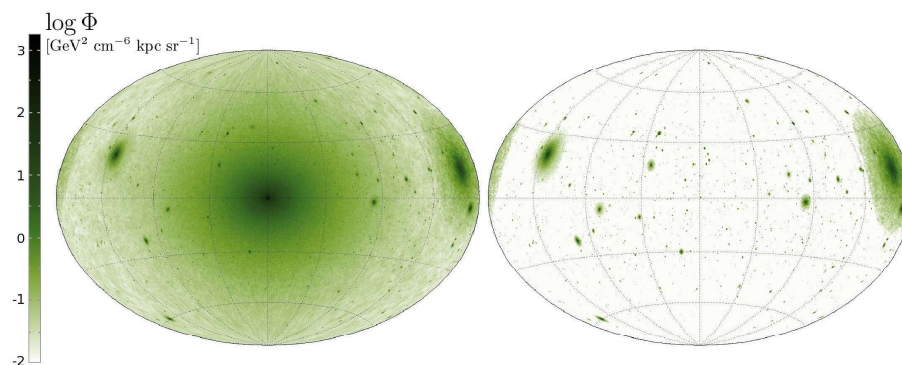


Figure 5.51: Simulated all-sky maps for dark matter annihilation signals from the Via Lactea simulation for an observer 8 kpc from the halo centre. The left panel shows the total expected dark matter signal from dark matter particle annihilation into heavy quarks as would be detectable by Fermi/LAT. In the right panel, the signal from only sub-haloes is shown, suggesting high-energy gamma-rays from satellite galaxies. From Kuhlen et al. (2008).

A good test of the annihilating dark matter hypothesis is thus to check in cumulative INTEGRAL/SPI data for a consistent 511 keV brightness from the known satellites of the Milky Way, depending on their dark matter content and their distance. Cordier et al. (2004) tested this for the case of the Sagittarius Dwarf

<sup>13</sup> $\Lambda$ CDM is a model of the evolution of the Universe, based on a Big Bang with the corresponding nucleosynthesis for the "seed" nuclei of hydrogen, helium, and lithium, a component termed "dark energy" ( $\Lambda$ ), and non-baryonic dark matter. Dark energy is associated with the vacuum energy of the Universe, and said to be responsible for the apparently-accelerated expansion of the Universe. Dark matter account for the large scale gravitational effects and must be cold to form structures (CDM).

<sup>14</sup>A third solution is that dark matter is not responsible for the formation of dwarf galaxies.

Spheroidal (Sag). A point-like emission, as expected from dark matter annihilation (see below) could not be detected, and a  $2\sigma$  upper limit on the 511 keV flux of  $2.5 \times 10^{-4}$  ph cm $^{-2}$  s $^{-1}$  was provided. Using this number, it was not possible to exclude nor corroborate dark matter as the cause of the 511 keV emission in the Milky Way, because the upper limit from Sag was not constraining enough. By using more than ten years of SPI data, covering the full sky, the until-then detected 39 dwarf satellite galaxies (DSGs) are tested to provide new constraints on a dark matter origin of the galactic positron signal.

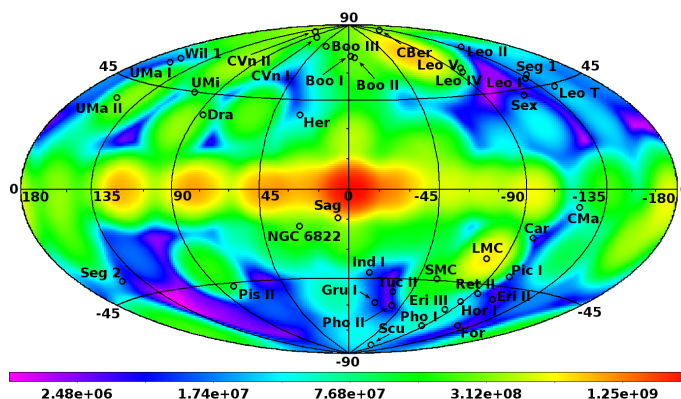


Figure 5.52: Sky exposure with SPI after 1258 orbits of the INTEGRAL mission, similar to Fig 4.3. Tested satellite galaxies of the Milky Way are marked with circles at their baryonic centres.

The used data set is identical to the one used in Sec. 4.2, and also the background modelling is applied in the same way. The galactic diffuse large scale emission is dominating the 511 keV signal, and has to be taken into account. Otherwise, the maximum likelihood method would attribute emission falsely to certain candidate sources. Therefore, the empirical six-component emission model from Sec. 4.4.2 is adopted as a baseline model. In addition to these six components, 39 DSGs, individually modelled as point-sources at their visible positions in the sky, Fig. 5.52, are included in the maximum likelihood parameter estimation. Here, each baseline model component is still allowed to vary in intensity, independently. Also the background scaling parameters are re-determined to account for possible contributions of the DSGs. In total, 39 more intensity scaling parameters are introduced for each energy bin, building an individual spectrum for each of the sources between 490 and 530 keV.

The emissivity of 511 keV photons produced per unit time is driven by the annihilation conditions in the Milky Way or in the DSGs, Sec. 4.6.6. These are the number densities of positrons and H-atoms, the ionisation fraction in the ISM, and its temperature. It is known that the number densities can be large in the Milky Way, but there is as yet no observational indication that there are similar large number densities in DSGs, also because most of these objects contain only a small number stars. If a detected signal is indeed from dark matter annihilation, the annihilation rate would be proportional to the integral over the line-of-sight, of the dark matter density squared. This is usually expressed in form of the so-called J-factor,

$$J \equiv \int_{\Delta\Omega} \int_{los} \rho_{DM}^2 dl, \quad (5.48)$$

where the first integral is over the solid angle of the region of interest, and the second

is over the line-of-sight (cf. also Eq. 5.8). The J-factor characterises the distribution of dark matter in an astrophysical system. Typical dark matter profiles follow a power-law in the innermost regions,  $\rho(r) \propto r^{-\gamma}$ , Eq. (5.47), where  $\gamma$  typically ranges between 0 and 2, Sec. 5.5.1. The  $\rho^2$ -dependence of the J-factor thus yields a very sharply peaked signal, in most cases. In general, compilations of dwarf galaxy J-factors from the literature (e.g. Ackermann et al. 2014; Evans et al. 2016) yield regions of interest, i.e. where dark matter annihilation is expected to be dominant, that are smaller than the imaging resolution of SPI. In consequence, the annihilation signals from DSGs are assumed to be point-like, and modelled as such. For example, the imaging resolution of SPI encompasses a physical region of about 400 pc for the closest of the DSGs in the sample, Canis Major (CMa), at a distance of 9 kpc. In the case of Sag, on the other hand, the galaxy is already in the process of tidal stripping, so that also its dark matter halo might have been influenced and stretched, and the derived fluxes could in principle be larger.

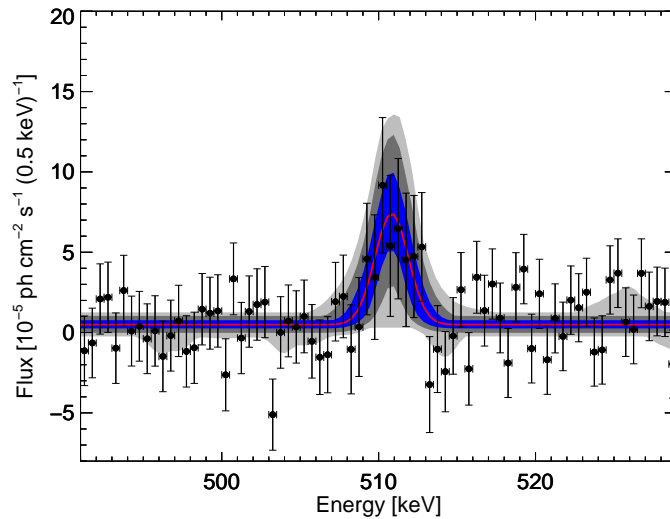


Figure 5.53: Spectrum from the position of Reticulum II. Shown are the derived data points from the maximum likelihood analysis (black data points) in half-keV binning, together with the best fitting model of a symmetric Gaussian on top of a constant offset (red solid line). The 1, 2, and 3 $\sigma$  uncertainty bands of such a model fit are shown in blue, dark grey, and light grey, respectively.

In the input catalogue of 39 sources, representing the satellite galaxies of the Milky Way within 500 kpc, the coordinates of the point sources are given by the baryonic centres of each source. The sources are at least separated by more than the imaging resolution of SPI (2.7 $^\circ$ ), and thus correlations between them (source confusion) is usually negligible. Exceptionally "close pairs" (Fig. 5.52) are CVn I - CVn II (6.5 $^\circ$ ), Leo I - Seg 1 (3.8 $^\circ$ ), Leo IV - Leo V (2.8 $^\circ$ ), and Boo I - Boo II (1.7 $^\circ$ ), so that the flux values derived from the latter pair only should be considered with caution. The extracted spectra for each of the DSGs are fitted by Gaussian-shaped lines with fixed FWHM of instrumental resolution (2.15 keV at 511 keV), on top of a constant offset. Their centroids may range between 508 and 514 keV, corresponding to bulk motions of  $|v_{bulk}| \approx 1750$  km s $^{-1}$ , to account for intrinsic motion of the satellite galaxies (several 100 km s $^{-1}$  McConnachie 2012), and also for statistical fluctuations. For non-positive results, a 2 $\sigma$  flux limit is estimated for a line at exactly 511 keV.

The strongest signal is found from the position of Reticulum II (Ret II,  $(l/b)_{Ret II} = (266.3^\circ / -49.7^\circ)$ , Fig. 5.53) with a significance of 3.1 $\sigma$  above instrumental background and continuum. The line flux derived for a point source coincident with Ret



in respect to a dark matter origin, for example.

Due to the individually low signals, an alternative stacking approach for a dark matter hypothesis test is performed. Instead of deriving 39 individual spectra, the relative fluxes according to the distances of the sources are fixed, and the sources are assumed to have the same mass scale (Strigari et al. 2008a). This obtains one spectrum for a reference DSG at a chosen canonical distance of  $d_0 = 100$  kpc, as the celestial distribution model now reads

$$F = \frac{\langle L_0 \rangle}{4\pi d_0^2} \sum_{i=1}^{39} \delta(l - l_i) \delta(b - b_i) \left( \frac{d_0}{d_i} \right)^2. \quad (5.49)$$

Here,  $\langle L_0 \rangle$  is the (fitted) intrinsic mean luminosity for a basic DSG at the canonical distance  $d_0$ , corresponding to 39 individual sources, at positions  $(l_i/b_i)$  in the sky, scaled by their distances  $d_i$ . The resulting spectrum would then be dominated by the closest galaxies as the flux  $F$  is proportional to the inverse distance squared. It may also be confused by diffuse emission in the galactic plane and bulge, due to their partial correlation in the maximum likelihood fit. In order to avoid such a bias in the stacking procedure, DSGs in the direction of the galactic plane ( $|b| < 10^\circ$ ) and galaxies closer than 25 kpc are ignored. Under these assumptions, a  $2\sigma$  upper limit on the 511 keV flux of  $1.4 \times 10^{-4}$  ph cm $^{-2}$  s $^{-1}$  is derived. Softening the restrictions and allowing all sources in the stack, the limit reduces to  $1.3 \times 10^{-4}$  ph cm $^{-2}$  s $^{-1}$ . If also the assumption of an identical mass for all DSGs is discarded, the celestial model is modified as

$$F = \frac{\langle L_0 \rangle M_0^2}{4\pi d_0^2} \sum_{i=1}^{39} \delta(l - l_i) \delta(b - b_i) \left( \frac{d_0}{d_i} \right)^2 \left( \frac{M_i}{M_0} \right)^2, \quad (5.50)$$

with  $M_0 = 10^6 M_\odot$  as the chosen canonical dynamical mass of one representative DSG at 100 kpc. Only for a subset of galaxies, the dynamical mass estimate is available (see Tab. 5.9), and could be included in this test. The derived  $2\sigma$  upper limit on the flux of  $2.3 \times 10^{-4}$  ph cm $^{-2}$  s $^{-1}$  would still be two orders of magnitude above the theoretically derived annihilation flux of  $\sim 2 \times 10^{-6}$  ph cm $^{-2}$  s $^{-1}$ , if the entire bulge signal of the Milky Way is due to dark matter alone (Vincent et al. 2012; Evans et al. 2016).

The stacking analysis may be affected by large systematic uncertainties, as the positions have to be assumed at the dynamical centres of the satellite galaxies, which might not be true (Kuhlen et al. 2013), and also the dark matter content is not known. Therefore, the individual signals may reveal an underlying physical process. The mass-to-light ratio,  $\Upsilon_V = M_{Dyn}/L_V$ , has been found to be a good indicator for dark matter in dwarf galaxies (Mateo 1998; Strigari et al. 2008a; McConnachie 2012), as shown in top panel of Fig. 5.55. Here, the mass-to-light ratio within the half-light radius of each galaxy is plotted against the absolute V-band magnitude from available literature data. For Pis II, Boo III, CMa, and the LMC, no dynamical mass estimate is available the the stellar masses have been used as lower limits. As shown by several studies (e.g. Mateo 1998; Strigari et al. 2008a; McConnachie 2012),  $\Upsilon_V$

Name	$d$	$F_{511}$	$M_{Dyn}$	$M_V$	$\sigma$	$l$	$b$	$T_{Exp}$	Ref.
Canis Major <sup>b</sup>	9	< 4.1	> 49	-14.4	—	239.99	-8.00	0.62	(1),(16),(17)
Segue 1 <sup>b</sup>	23	< 12.4	0.26	-1.5	—	220.48	50.43	0.16	(1),(12),(60),(61),(62),(63)
<b>Sagittarius Dwarf</b>	<b>28</b>	<b>2.2(1.0)</b>	<b>190</b>	<b>-13.4</b>	<b>2.3</b>	<b>5.57</b>	<b>-14.17</b>	<b>7.00</b>	(1),(44),(45),(46)
<b>Reticulum II<sup>c</sup></b>	<b>30</b>	<b>17.0(5.4)</b>	<b>0.24</b>	<b>-2.7</b>	<b>3.1</b>	<b>266.30</b>	<b>-49.73</b>	<b>0.55</b>	(22),(23),(27),(42),(43)
Ursa Major II <sup>c</sup>	34	4.1(2.3)	3.9	-4.2	1.9	152.46	37.44	1.67	(1),(57),(58),(59)
Segue 2 <sup>c</sup>	35	< 14.4	0.23	-2.5	—	149.43	-38.14	0.20	(1),(48)
Willman 1 <sup>c</sup>	42	7.3(7.1)	0.39	-2.7	1.0	158.58	56.78	0.45	(1),(62),(64),(65)
Coma Berenices <sup>c</sup>	44	1.6(1.7)	0.94	-4.1	1.0	241.89	83.61	2.93	(1),(6),(12),(18)
Boötes III	48	< 4.4	> 0.017	-5.8	—	35.41	75.35	1.93	(1),(8),(9),(10)
Boötes II <sup>a</sup>	49	< 5.8	3.3	-2.7	—	353.69	68.87	1.92	(1),(5),(6),(7)
Large Magellanic Cloud	50	< 3.6	> 1500	-18.1	—	280.47	-32.89	4.22	(1),(37),(38)
Tucana II <sup>c</sup>	57	3.8(8.4)	<i>N/A</i>	-3.8	0.5	328.08	-52.32	0.22	(22),(23)
Small Magellanic Cloud	61	0.6(2.8)	1400	-16.8	0.2	302.80	-44.30	1.38	(1),(37),(52),(53)
<b>Boötes I<sup>a,c</sup></b>	<b>62</b>	<b>8.5(2.9)</b>	<b>0.81</b>	<b>-6.3</b>	<b>3.0</b>	<b>358.08</b>	<b>69.62</b>	<b>1.85</b>	(1),(2),(3),(4)
Ursa Minor <sup>c</sup>	73	< 5.8	9.5	-8.8	—	104.97	44.80	1.30	(1),(29)
Horologium I <sup>c</sup>	79	6.7(4.4)	0.55	-3.4	1.6	271.39	-54.73	0.43	(22),(23),(27)
Draco <sup>c</sup>	82	< 3.8	11	-8.8	—	86.37	34.72	1.57	(1),(19),(20),(21)
Phoenix II	83	< 16.6	<i>N/A</i>	-2.8	—	323.68	-59.75	0.19	(22),(23)
Sculptor <sup>c</sup>	83	< 11.6	14	-11.1	—	287.54	-83.16	0.22	(1),(47)
Sextans <sup>c</sup>	85	6.5(5.3)	10.6	-9.3	1.2	243.50	42.27	0.12	(1),(49),(50),(51)
Eridanus III	87	7.3(5.1)	<i>N/A</i>	-2.0	1.5	274.95	-59.60	0.38	(22),(23)
Indus I	100	6.2(3.9)	<i>N/A</i>	-3.5	1.6	347.15	-42.07	0.26	(23),(23)
Ursa Major I <sup>c</sup>	101	< 9.2	11	-5.5	—	159.43	54.41	0.42	(1),(6),(54),(55),(56)
Carina <sup>c</sup>	103	0.6(3.6)	6.3	-9.1	0.2	260.11	-22.22	0.66	(1),(14),(15)
Pictoris I	114	< 7.4	<i>N/A</i>	-3.1	—	257.29	-40.64	0.46	(22),(23)
<b>Grus I<sup>c</sup></b>	<b>120</b>	<b>20.8(9.1)</b>	<b><i>N/A</i></b>	<b>-3.4</b>	<b>2.3</b>	<b>338.68</b>	<b>-58.25</b>	<b>0.12</b>	(22),(23)
Hercules	136	9.7(5.5)	2.6	-6.6	1.8	28.73	36.87	0.31	(1),(6),(12),(26)
Fornax <sup>c</sup>	139	16.9(9.6)	56	-13.4	1.8	237.10	-65.65	0.11	(1),(24),(25)
<b>Canes Venatici II<sup>c</sup></b>	<b>153</b>	<b>5.0(2.2)</b>	<b>0.91</b>	<b>-4.9</b>	<b>2.3</b>	<b>113.58</b>	<b>82.70</b>	<b>2.44</b>	(1),(6),(12),(13)
Leo IV <sup>c</sup>	155	< 5.4	1.3	-5.8	—	265.44	56.51	1.84	(1),(6),(12),(13)
Pisces II <sup>c</sup>	182	2.9(4.3)	> 0.0086	-5.0	0.7	79.21	-47.11	0.79	(1),(39),(40),(41)
Leo V <sup>c</sup>	186	3.7(3.3)	1.1	-5.2	1.1	261.86	58.54	1.96	(1),(35),(36)
Canes Venatici I <sup>c</sup>	216	1.2(2.2)	19	-8.6	0.6	74.31	79.82	1.84	(1),(6),(11)
Leo II <sup>c</sup>	218	5.0(5.5)	4.6	-9.8	0.9	220.17	67.23	0.35	(1),(31),(32)
<b>Leo I<sup>c</sup></b>	<b>246</b>	<b>15.8(7.4)</b>	<b>12</b>	<b>-12</b>	<b>2.2</b>	<b>225.99</b>	<b>49.11</b>	<b>0.12</b>	(1),(28),(29),(30)
Eridanus II	380	< 21.6	<i>N/A</i>	-6.6	—	249.78	-51.65	0.10	(22),(23)
Leo T <sup>c</sup>	412	6.1(6.5)	3.9	-8.0	1.0	214.85	43.66	0.19	(1),(33),(34)
Phoenix I	418	4.3(5.7)	9.7	-9.9	0.8	272.16	-68.95	0.36	(1),(66),(67),(68),(69)
NGC 6822	498	1.4(1.6)	3500	-15.2	0.9	25.34	-18.40	2.25	(1),(29),(69),(70),(71),(72)

Table 5.9: List of Milky Way satellites tested for 511 keV emission, ordered by distance. The measured line flux  $F_{511}$  is given in  $10^{-5}$  ph cm $^{-2}$  s $^{-1}$ .  $M_{Dyn}$  are the dynamical masses of the satellite in units of  $10^6 M_{\odot}$ ,  $M_V$  their absolute visual magnitude, and  $d$  the distance in kpc. The significance of a possible line detection is given in units of sigma.  $2\sigma$  or above detections are marked boldface. If a line is not present at all, a  $2\sigma$  upper limit on the flux is given. The positions of the assumed centres of the satellites are given in galactic longitude  $l$  and latitude  $b$  in units of degrees. The effective exposure time at the position of the sources  $T_{Exp}$  is given in Ms.  $M_{Dyn}$ ,  $M_V$ ,  $d$ ,  $l$ , and  $b$  are taken from the literature (references, last column). The distances have been chosen as the given mean value from the NASA/IPAC Extragalactic Database (NED), if available. (a) The values for Boo I may be over- or underestimated due to source confusion with Boo II, being not separated by at least one FWHM of the point-spread-function. Likewise, the value for Boo II may be wrong, too. (b) For the stacking analysis, these galaxies have been ignored to validate the flux limit. (c) These galaxies have been included in the mass- and distance-weighted stacking analysis due to available dynamical mass and J-factor estimates. References are: (1) (McConnachie 2012), (2) (Belokurov et al. 2006), (3) (Fellhauer et al. 2008), (4) (Dall’Ora et al. 2006), (5) (Walsh et al. 2007), (6) (Grcevich & Putman 2009), (7) (Walsh et al. 2008), (8) (Grillmair 2009), (9) (Carlin et al. 2009), (10) (Correnti et al. 2009), (11) (Zucker et al. 2006), (12) (Belokurov et al. 2007), (13) (Okamoto et al. 2012), (14) (Kraan-Korteweg & Tammann 1979), (15) (Mateo et al. 1998), (16) (Martin et al. 2004), (17) (Martin et al. 2005), (18) (Musella et al. 2009), (19) (Cotton et al. 1999), (20) (Falco et al. 1999), (21) (Tyler 2002), (22) (Koposov et al. 2015a), (23) (The DES Collaboration et al. 2015), (24) (Piatek et al. 2007), (25) (Poretti et al. 2008), (26) (Musella et al. 2012), (27) (Koposov et al. 2015c), (28) (Whiting et al. 2007), (29) (Young 2000), (30) (Caputo et al. 1999), (31) (Coleman et al. 2007), (32) (Gullieuszik et al. 2008), (33) (Irwin et al. 2007), (34) (Clementini et al. 2012), (35) (Belokurov et al. 2008), (36) (de Jong et al. 2010), (37) (Richter et al. 1987), (38) (Feast & Walker 1987), (39) (Belokurov et al. 2010), (40) (Kirby et al. 2015), (41) (Sand et al. 2012), (42) (Simon et al. 2015), (43) (Walker et al. 2015), (44) (Majewski et al. 2003), (45) (Ibata et al. 1994), (46) (Monaco et al. 2004), (47) (Queloz et al. 1995), (48) (Belokurov et al. 2009), (49) (Irwin et al. 1990), (50) (Battaglia et al. 2011), (51) (Lee et al. 2003), (52) (Matsunaga et al. 2011), (53) (Bekki & Stanimirović 2009), (54) (Willman et al. 2005b), (55) (Kleyna et al. 2005), (56) (Okamoto et al. 2008), (57) (Peñarrubia et al. 2006), (58) (Fellhauer et al. 2007), (59) (Dall’Ora et al. 2012), (60) (Norris et al. 2010), (61) (de Jong et al. 2008), (62) (Martin et al. 2008), (63) (Simon et al. 2011), (64) (Willman et al. 2005a), (65) (Willman et al. 2011), (66) (Cote et al. 1997), (67) (Zaggia et al. 2011), (68) (Gallart et al. 2001), (69) (Mateo 1998), (70) (Koribalski et al. 2004), (71) (Rogstad et al. 1967), (72) (Veljanoski et al. 2015).

shows a negative correlation with the brightness of the objects  $M_V$ . This is counter-intuitive, as naturally a nearly constant mass-to-light ratio would be expected, no matter how faint a galaxy is. The stellar mass-to-light ratio,  $\Upsilon_V^* = M^*/L_V$ , indeed shows a value of  $\sim 1.0$  across the entire magnitude scale. In particular, excluding the satellites in which no dynamical mass is available and also the Milky Way, the mass-to-light ratio is measured as  $\lg(\Upsilon_V) \propto a = +(0.22 \pm 0.02)M_V$ . As the galaxies become fainter,  $\Upsilon_V$  rises, which indicates an unseen mass and is generally interpreted as dark matter sub-haloes. Any tracer that would make dark matter "visible", e.g. by measuring its annihilation products, should show a similar trend, as the dynamical mass-to-positron-annihilation-luminosity,  $\Upsilon_{511} \equiv M_{Dyn}/L_{511}$ , would be proportional to  $M_{Dyn}^{-1}$  as  $L_{511} \propto M_{Dyn}^2$ , according to the hypothesis of dark matter annihilation. From

$$\Upsilon = \frac{M_{Dyn}}{L_V} \propto 10^{a \cdot M_V} \quad \& \quad L_V \equiv 10^{0.4(S-M_V)} \quad (5.51)$$

with  $S = 4.83$  being the absolute V-band magnitude of the Sun, serving as a reference points, the dynamical mass is empirically determined to follow

$$M_{Dyn} \propto 10^{(a-0.4)M_V} \Leftrightarrow -\lg(M_{Dyn}) \propto +(0.18 \pm 0.02)M_V := b^{exp} \cdot M_V. \quad (5.52)$$

Thus, the mass to 511 keV-light ratio,  $\Upsilon_{511}$ , would be expected to show also a positive correlation with  $M_V$ , with a tightly constrained expected slope  $b^{exp}$ . In the bottom panel of Fig. 5.55,  $\Upsilon_{511}$  is shown for galaxies whose flux estimates deviate from zero at the  $1\sigma$  level. For all other galaxies for which data are available,  $2\sigma$  lower limits are provided. The measured correlation is opposite to  $\Upsilon_V$ , with a fitted slope of  $b_{511} = -0.25 \pm 0.11$ . This is  $3.3\sigma$  away from the expected value when considering dark matter annihilation as the cause for the 511 keV emission. The reversed trend for  $\Upsilon_{511}$  versus  $M_V$  is thus in contradiction with what is expected from a dark matter origin, which may have several causes: The correlation is based on the high ratio derived from Sag, and may be further disturbed by large or small  $1\sigma$  values. Neglecting Sag, reduces the rank correlation coefficient from  $-0.35$  to  $-0.14$ , but is still far from the positive correlation in the top panel. Using rather only  $2\sigma$  values provides an even larger discrepancy, although only based on six values. The visually fainter galaxies like Ret II or Hor I, as seen in 511 keV, have dynamical mass estimates which are 2-3 orders of magnitude lower than for the bright galaxies (e.g. Sag, For). This automatically distorts the correlation in this direction, if the signals are not significant or strong. Most probably, though, it is not the dynamical mass which drives the apparent correlation, but rather the stellar mass as the corresponding correlation of  $\Upsilon_V^*$  versus  $M_V$  is completely gone, the respective correlation between  $\Upsilon_{511}^*$  and  $M_V$  is still there. Stars, compact objects, and their surrounding environments are a favoured explanation for any 511 keV emission. The positrons may come from very few sources and then annihilate after their propagations through the ISM of the satellites in stellar atmospheres, for example.

In the case of a dark matter origin of the 511 keV emission in the DSGs, the 511 keV flux,  $F_{511}$ , would follow  $F_{511} = \frac{1}{4\pi} \frac{\langle\sigma v\rangle}{m_{DM}^2} J$ , where  $\langle\sigma v\rangle$  is the thermally averaged cross

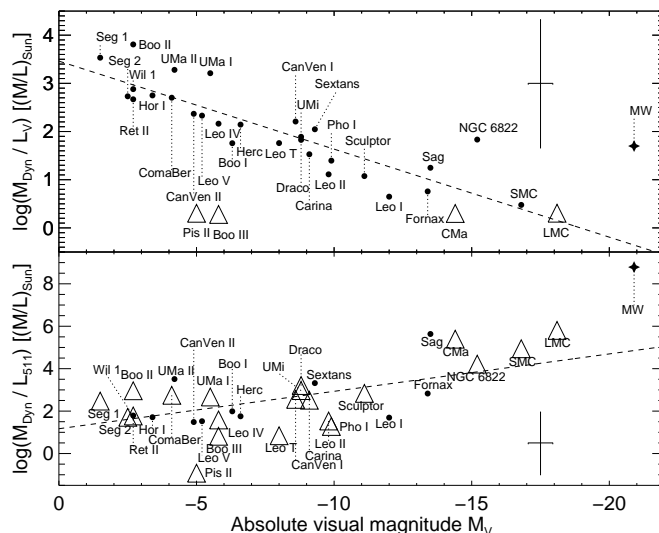


Figure 5.55: Mass-to-luminosity ratio in units of solar masses per solar luminosity as a function of absolute visual magnitude,  $M_V$ . Top panel shows the dynamical mass over the absolute V-band magnitude as already described by Mateo (1998), Strigari et al. (2008a), or McConnachie (2012). Towards fainter satellite galaxies,  $\Upsilon_V$  increases, which is generally interpreted as indirect evidence for dark matter (see text for details). Bottom panel shows the ratio of the dynamical mass and the 511 keV luminosity over the absolute visual magnitude. The trend is reversed when plotting  $\Upsilon_{511}$  versus  $M_V$ , in contradiction with what is expected for a dark matter origin. Typical error bars are shown;  $2\sigma$  lower limits are shown by triangles. For comparison,  $\Upsilon_V$  and  $\Upsilon_{511}$  for the Milky Way are shown with a star symbol in each panel.

section,  $m_{DM}$  the dark matter particle mass, and  $J$  the J-factor (Eq. 5.48). Hooper et al. (2004) estimated that if the whole 511 keV emission in the bulge of the Milky Way was due to annihilation of light dark matter particles into electron-positron pairs, an observable 511 keV emission from the direction of Sag would be about 3-6 times smaller than that of the bulge. In the analysis presented here, the measured ratio is  $42 \pm 19$ , ruling out the dark matter positron pair hypothesis by again  $\sim 2\sigma$ . Considering the flux from the emerged galactic centre source as due to dark matter, would provide a ratio of  $3.5 \pm 2.1$ , consistent with those expectations. If the Sag signal is entirely due to dark matter, this would indicate a dark matter contribution to the galactic signal of about 3%. However, recent studies found that a dark matter annihilation cross section of 5 (Ascasibar et al. 2006) to 10 (Vincent et al. 2012) times smaller than in the study of Hooper et al. (2004) would be a more reasonable estimate. In addition, the updated J-factor for Draco (Ackermann et al. 2014; Evans et al. 2016) is about 5 times smaller than what was used by Hooper et al. (2004). This in fact may also apply to Sag although its morphological structure is more complex due to tidal stripping. In any case, a 511 keV signal measured in Sag, even at higher significances does probably little to constrain the galactic centre signal.

Based on available J-factors (Evans et al. 2016) and assuming in-situ positron annihilation and negligible Ps formation, the strongest constraint on a possible dark matter origin can be obtained from the Ursa Major II dwarf galaxy, due to its large J-factor, and its proximity of 34 kpc. At a confidence level of  $2\sigma$ , the thermally averaged cross section is constrained to

$$\langle\sigma v\rangle < 5.6 \times 10^{28} \left(\frac{m_{DM}}{\text{MeV}}\right)^2 \text{ cm}^3 \text{ s}^{-1}, \quad (5.53)$$

which is still two orders of magnitude below the cross section required to explain

the entire Milky Way bulge signal. However, as the ultra-faint dwarf galaxy Ret II (Koposov et al. 2015b; Simon et al. 2015) is found with a significance of  $3.1\sigma$  to emit 511 keV photons, the galaxy might be special from the perspective of two different, but maybe unrelated, measurements: Ji et al. (2016) measured strong enhancements of neutron-capture elements in stars of Ret II, and interpret this as the result of nucleosynthesis of heavy elements from a single enrichment event only, which would then have to be a neutron star merger. The same enrichment event could be a potential positron source, e.g. through evolution into an accreting black hole system, towards the existence of one single microquasar in Ret II. On the other hand, Geringer-Sameth et al. (2015) reported a 2-10 GeV gamma-ray excess measured with Fermi/LAT at 2.3 to  $3.7\sigma$  significance. Such gamma-rays have been associated with star formation through cosmic-ray / gas interactions (Abdo et al. 2010; Ackermann et al. 2012, 2016). The effects of star formation are an inevitable prerequisite for the 511 keV emission in the Milky Way, as for example  $\beta^+$ -unstable nuclei are produced in massive stars and their supernovae, Sec. 5.1, and definitely contribute to the positron content in the Galaxy. At a distance of 30 kpc, Ret II shows a present-day annihilation rate of  $(3.7 \pm 1.2) \times 10^{43} \text{ e}^+ \text{ s}^{-1}$ , which is about as high as in the entire Milky Way, and would support both scenarios, the neutron star merger and/or the star formation picture. Either case may have produced or is still producing a large number of positrons, whose gradual and ongoing annihilation is seen in the ISM or stars of Ret II with SPI/INTEGRAL.

There is indeed a similarity between the 511 keV emission and the high-energy GeV emission. In both cases, there is an excess centred at around  $(l/b) \approx (-1^\circ/0^\circ)$ , and also an excess found in Ret II, which in fact may be related to each other, perhaps through dark matter. Although the GeV excess in Ret II may also be attributed to heavy dark matter particle annihilation into bottom-antibottom quark pairs, the Fermi/LAT data itself does not favour one or the other annihilation channel, also because of the large uncertainty in the dark matter content (J-factor) of Ret II (Geringer-Sameth et al. 2015). Furthermore, Ret II and the LMC are the only DSGs that show a high-energy excess, again disfavouring a dark matter explanation of the signals, as otherwise more DSGs should have already been detected (Ackermann et al. 2014). Using the J-factors from Evans et al. (2016), a dark matter only interpretation of the 511 keV signal from Ret II yields a cross section that would require a galactic bulge signal more than 100 times larger than what is observed with SPI (Siegert et al. 2016d). In return, this constrains the dark matter contribution to the galactic (Ret II and/or Milky Way) positron content to probably less than 1%.

This estimate is based on the assumption that positrons annihilate locally in the satellite galaxies. If the positrons were produced at relativistic energies from dark matter annihilations, they may not have enough time to slow down inside a galaxy, and may rather leave it. A detailed understanding of the propagation of positrons, away from their sources, and the subsequent slowing-down processes, is required to constrain the dark matter contribution for the galactic positron content.

## 5.6 A Galactic Centre Excess in 511 keV

The independent spectrum for the GCS is similar to that of the bulge as a whole and the disk spectrum as a whole, but spectral details differ. Especially the width and the centroid of the 511 keV line may give rise to an additional source and/or additional annihilation site of positrons. Considering the imaging resolution of SPI (2.7°), the source could be compact and related to the Galaxy's supermassive black hole Sgr A\*, or encompasses a region of the order of 350 pc, and thus includes the entire central molecular zone. If the entire galactic emission morphology is taken into account, the GCS may also representing the peak of a dark matter halo profile. In the following, the possible sources and annihilation conditions as implied by the GCS spectrum will be discussed.

### 5.6.1 Sagittarius A\*

If Sgr A\* is the source of the positrons, a gravitational red-shift of at least 0.4 keV, and a temperature of  $\sim 10^3$  K (Shakura & Sunyaev 1973; Krolik 1999) would be expected from the geometry and physical properties of the system. These values are within the uncertainty limits of the measurements in Sec. 4.6.3 as  $E_{peak}^{GCS} = -0.27 \pm 0.31$  keV and  $FWHM^{GCS} = 3.46 \pm 64$  keV. A simpler spectral model as used in Sec. 4.6, neglecting the o-Ps continuum in the fit, and assuming a constant offset instead of a power-law, obtains a red-shift of  $-0.41 \pm 0.35$  keV ( $z = (8.01 \pm 6.90) \times 10^{-4}$ ) for the GCS, and strengthens the apparent centroid shift. Statistically, the two spectral models are indistinguishable as an F-test, for example, yields a value of  $F = 1.54$  for one degree of freedom, which is equivalent for the models being distinguishable at  $1.2\sigma$  only. Given the measured red-shift, the mass of Sgr A\*, and assuming the gravity of Sgr A\* to be the cause of the measured red-shift, Eq. (5.36), the location of the emission can be constrained to  $R^* = 45_{-21}^{+115}$  AU. This would be fully consistent with the outer accretion zone of Sgr A\* (Genzel et al. 2010). The measured Doppler-broadening of the GCS annihilation line can be converted to an estimate of a temperature of  $(9.8 \pm 3.6) \times 10^4$  K in the interaction region. For the accretion disk of Sgr A\*, a mid-plane temperature of  $10^4$ - $10^5$  K is expected from viscous friction of the accreting material around a  $4 \times 10^6 M_\odot$  black hole (Shakura & Sunyaev 1973; Krolik 1999). This would again be consistent with the measurements. Direct pair-production automatically provides the kinetic energy constraint that is measured by the MeV continuum in the bulge (Sizun et al. 2006) in which annihilation in flight should imprint, but might not necessarily be also a constraint for the GCS. Assuming the GCS to be located at the position and distance of Sgr A\*, its 511 keV luminosity is  $(6.0 \pm 1.5) \times 10^{41}$  ph s $^{-1}$ . A steady state approach for this source obtains a positron production rate in the range  $0.3$ - $1.2 \times 10^{42}$  e $^+$  s $^{-1}$ . Positron production rates are hard to estimate for black holes in general, as this is based on poor assumptions, but could be in the range of  $0.16$ - $3.7 \times 10^{42}$  e $^+$  s $^{-1}$  (Totani 2006). Sgr A\* may already yield a consistent picture for the GCS, and can also contribute to the observed bulge emission. Alternatively, the Doppler broadening provides a measure of the turbulence of  $(2000 \pm 400)$  km s $^{-1}$ , which might reasonably be expected from non-equilibrium gas motion or past black hole activity.

### 5.6.2 Central Molecular Zone

Alexis et al. (2014) discussed the possibility that nucleosynthesis positrons produced in the central molecular zone travel into the galactic bulge, and could be responsible for the emission in the extended bulge. It is, however, not implausible that these positrons annihilate locally in the central molecular zone. Furthermore, Alexis et al. (2014) estimated the positron production from massive stars in that zone from  $^{26}\text{Al}$ , contributing to  $0.3 \times 10^{42} \text{ e}^+ \text{ s}^{-1}$ . In the bulge region of the Milky Way, the interstellar gas is approximately 50% neutral, i.e. atomic (10%) and molecular (90%), and 50% ionised. The molecular gas is accumulating in the central molecular zone (Morris & Serabyn 1996), and builds a thin disk, parallel to the galactic disk. Its extensions are 250 pc towards positive, and 150 pc towards negative longitudes, and a thickness of about 30 pc. In Fig. 5.56, the central molecular zone is shown schematically, and is compared to the NB measured with SPI, to the stellar bulge which is coincident with the BB, and the holed gaseous disk, holding also atomic and molecular gas. This gaseous disk has a physical size of  $3.2 \text{ kpc} \times 1.0 \text{ kpc}$ , is tilted counter-clockwise by  $13.5^\circ$  with respect to the galactic plane, and inclined by  $70^\circ$  near side down to the plane of the sky. In its hole, there is just about enough space to enclose the central molecular zone, being probably distinct from the disk, as also the densities and temperatures show a contrast. The ionised gas, however, seems to surround both regions, so that the morphology of bulge and GCS might correspond to the annihilation regions of the stellar bulge (cf. also Figs. 4.8a and 4.6a in which the HDG may be visible) and the central molecular zone. In the central regions of the bulge, there are at least three major stellar clusters which contain massive stars. This indicates recent star formation, which is probably fed from the central molecular zone. Adding the positrons produced by  $^{44}\text{Ti}$  from estimates of Alexis et al. (2014), the observed  $(1.0 \pm 0.5) \times 10^{42} \text{ e}^+ \text{ s}^{-1}$  are within reach for a nucleosynthesis interpretation. Possibly the central molecular zone has now emerged as a separate positron-producing source and annihilation site through the deeper exposure.

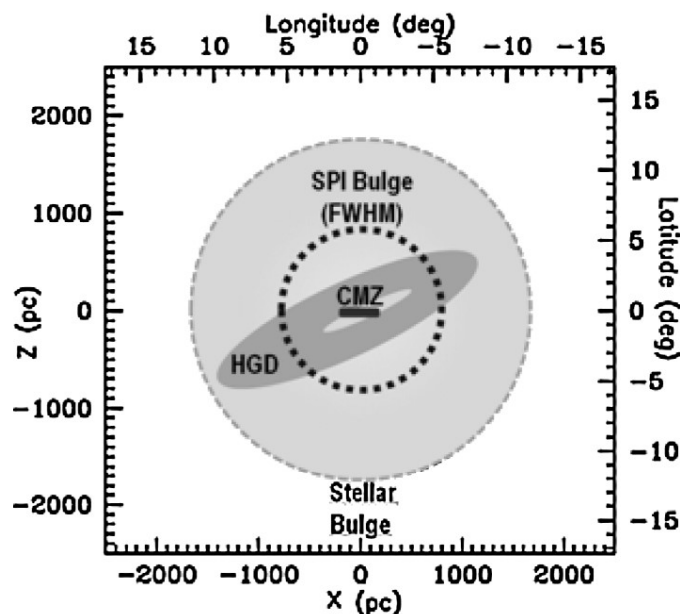


Figure 5.56: Schematic view of components in the inner Galaxy. Shown are stellar bulge which coincides with the broad bulge component of the empirical 511 keV emission model, the "SPI bulge" representing the narrow bulge component, the holed gaseous disk (HGD), and the central molecular zone (CMZ). See text for details. From Prantzos et al. (2011).

### 5.6.3 Dark Matter Annihilation

The more pronounced peak of the 511 keV emission towards the centre of the Galaxy also may revive interpretations of a dark matter origin, as already discussed in Sec. 5.5. Annihilating dark-matter particles have been proposed to create an annihilation photon emission profile, proportional to the square of the dark matter density profile (e.g. Burkert 1995; Navarro et al. 1996; Merritt et al. 2006), see also Ascasibar et al. (2006). The central cusp of such a distribution would be seen by SPI as a point-like source. As the nature of dark matter is entirely unknown, expected fluxes for the 511 keV line are based on rough estimates. These have to consider the annihilation cross section, the dark matter particle mass, and that the produced positrons may not propagate far. As satellite galaxies of the Milky Way are believed to be dark matter dominated, they should have revealed a detectable 511 keV annihilation signal which is not consistently seen with SPI, Sec. 5.5.2. However, this hypothesis is based on the assumption that the entire bulge signal is due to dark matter annihilation into electron-positron pairs, which may not be true at all. If the GCS emission is considered as only the tip of an annihilating dark matter profile, there is still chance for dark matter to contribute to the positrons, which are seen to annihilate in the centre of the Galaxy. In Sec. 5.5.2 it was shown that the dark matter contribution to the positron content in the Milky Way is probably less than 1%, based on the population of dwarf satellite galaxies of the Milky Way, and especially the dwarf galaxy Reticulum II. As the GCS has about 10% of the 511 keV luminosity of the entire bulge, the signal could be partially due to dark matter, but only of the order of 10%. Dark matter has also been invoked to explain the GeV signal in the centre of the Milky Way (e.g. Goodenough & Hooper 2009; Daylan et al. 2016) and also in Reticulum II (Geringer-Sameth et al. 2015). Interestingly, the only galaxies known to emit 511 keV radiation are the Milky Way and Reticulum II, for which reason there might be a link between the GeV and the 511 keV emission. Further investigation and more exposure is required to consolidate the signal in Ret II towards a more accurate characterisation of the annihilation emission there, and in the centre of the Galaxy, for a better understanding of the possible connection between high-energy gamma-rays and positrons.

## 5.7 Balancing the Galactic Positron Content

In the previous sections, the contributions of different astrophysical sources to the galactic positron content have been worked out, and consolidated and constrained with direct gamma-ray measurements, if possible. Assuming a steady state between positron annihilation and supply in the Milky Way, a production rate of  $(4.9 \pm 1.5) \times 10^{43} \text{ e}^+ \text{ s}^{-1}$  is required in the entire Galaxy, which splits into  $(1.8 \pm 0.2) \times 10^{43} \text{ e}^+ \text{ s}^{-1}$  for the bulge component ( $\approx 1/3$ ), and  $(3.1 \pm 1.5) \times 10^{43} \text{ e}^+ \text{ s}^{-1}$  for the disk ( $\approx 2/3$ ). These numbers assume only weak positron propagation away from their sources, so that residual contents in bulge or disk might directly point to propagation in the Galaxy. The identified sources of positrons in the Milky Way are stars and microquasars. Massive stars produce radioactive  $\beta^+$ -unstable nuclei, and eject them during their wind phases ( $^{26}\text{Al}$ ) or in core-collapse supernovae ( $^{26}\text{Al}$  and  $^{44}\text{Ti}$ ). White dwarf remnants of low-mass stars, are being disrupted in thermonuclear explosions, and produce major amounts of  $^{56}\text{Ni}$ . In microquasars,

the compactness of the black hole (or neutron star) will lead to photon-photon self-absorption, which is producing electron-positron pairs, and which are ejected in flares of such X-ray binary systems. There are also more frequent but maybe less efficient positron producers, such as novae, "normal" X-ray binaries, and pulsars with strong magnetic fields. But their contribution to the positron population in the Galaxy can so far only be based on theoretical estimates. All the remaining plausible sources have to be caught in action to produce either  $\beta^+$ -unstable nuclei in the case of novae, or ejecting jets of electron-positron pairs in the case of hard-state X-ray binaries. Future work and deeper observations will be needed to constrain the positron-production efficiency of the galactic population of X-ray binaries, pulsars, novae, and cosmic rays. The idea of having dark matter as the dominant positron source can be excluded. Its contribution is estimated to be probably less than 1%, Sec. 5.5.2.

Source	Galaxy	Bulge	Disk
$^{26}\text{Al}$	$3.35 \pm 0.07$	$0.35 \pm 0.01$	$3.00 \pm 0.06$
$^{44}\text{Ti}$	$2.16 \pm 0.30$	$0.22 \pm 0.03$	$1.94 \pm 0.27$
$^{56}\text{Ni}$	$19.0^{+119.0}_{-19.0}$	$4.6^{+28.8}_{-4.6}$	$14.4^{+90.2}_{-14.4}$
$\gamma\gamma$	$26.7^{+28.5}_{-26.7}$	$8.9^{+9.5}_{-8.9}$	$17.8^{+19.0}_{-17.8}$
$\sum$ Sources	$51.2^{+122.4}_{-32.8}$	$14.1^{+30.3}_{-10.0}$	$37.1^{+92.2}_{-22.9}$
Target Rate	$49.0 \pm 15.0$	$18.0 \pm 0.2$	$31.0 \pm 15.0$
	Galaxy %	Bulge %	Disk %
$^{26}\text{Al}$	$6.8 \pm 2.1$	$1.9 \pm 0.2$	$9.7 \pm 4.7$
$^{44}\text{Ti}$	$4.4 \pm 1.5$	$1.2 \pm 0.2$	$6.3 \pm 3.2$
$^{56}\text{Ni}$	$38.8^{+243.1}_{-38.8}$	$27.2^{+160.0}_{-27.2}$	$46.5^{+291.8}_{-46.5}$
$\gamma\gamma$	$54.5^{+60.5}_{-54.5}$	$49.4^{+53.1}_{-49.4}$	$57.4^{+67.3}_{-57.4}$
$\sum$ Sources	$104.5^{+250.5}_{-67.0}$	$79.7^{+168.6}_{-56.4}$	$119.9^{+299.5}_{-74.1}$
Target %	$100.0 \pm 30.6$	$100.0 \pm 11.1$	$100.0 \pm 48.4$

Table 5.10: Comparison between measured positron annihilation and production in the Milky Way. The contributions to bulge and disk have been estimated from the core-collapse supernova rates in the case of  $^{26}\text{Al}$  and  $^{44}\text{Ti}$  (10.3% bulge, 89.7% disk), from the thermonuclear supernova rate in the case of  $^{56}\text{Ni}$  (24.2% bulge, 75.8% disk), and from the stellar distribution in the case of  $\gamma\gamma$  (33.3% bulge, 66.7% disk).

The contributions from the above-mentioned sources are listed in Tab. 5.10. Here, also the respective contributions in bulge and disk are estimated. In fact, there are no additional sources needed beyond the nucleosynthesis and microquasars positrons, as the sum of all measured sources reaches to  $104.5^{+250.5}_{-67.0}$  %. This had been already pointed out by several authors based on theoretical considerations (e.g. Prantzos 2006; Guessoum et al. 2006; Prantzos et al. 2011). The escape of positrons from sources like microquasars and SNe Ia is the most uncertain factor in this estimate. In general, their contribution may be several times higher larger, or zero. In the case of the upper uncertainty limit, the measured sources could potentially produce 3.5 times more positrons than are required as measured from the annihilation rate. If true, the steady state annihilation/production scenario is probably unsustainable, and would point to a large reservoir of positrons thermalised in the ISM, or already escaped from the Galaxy into the intergalactic medium. On the other hand, the lower uncertainty limit may also suggest that there are additional sources required to meet the galactic annihilation rate. This would be only natural as novae, pulsars, X-ray binaries, and cosmic-rays are most certainly producing positrons, but to an unknown extent.

Taking the positron production estimates in bulge and disk as face values at 79.7% and 119.9%, respectively, this would indicate positron propagation from the disk into the bulge. This had also been suggested (e.g. Prantzos 2006; Higdon et al. 2009) and simulated (e.g. Martin et al. 2012; Alexis et al. 2014) by several authors. However, the uncertainties on positron escape and duty cycles in X-ray binaries and SNe Ia, and also the true distribution of sources do not allow stronger statements. In combination with the measured thick disk of the positron annihilation morphology in the Milky Way, Sec. 4.4.2, the propagation of positrons seems a plausible and probably inevitable mechanism. Once the positrons left their local production environments, which are predominantly found in the disk of the Galaxy, they may get trapped in the bulge and annihilate.

In summary, the positron annihilation signal in the Milky Way can be readily explained by a combination of several sources in the Galaxy, producing positrons predominantly by  $\beta^+$ -decay or photon-photon pair-creation, and not by one single source type. The morphology fits to a scenario in which positrons are ejected at relativistic energies from those sources, then propagate through the ISM, steadily lose energy, and finally annihilate after forming positronium.

## 5.8 Implications for the Positron Puzzle

Sophisticated calculations of propagation (Martin et al. 2012; Alexis et al. 2014) have been conducted to understand the peculiar bulge to disk ratio, i.e. in times when only the bright bulge was seen. Essentially all candidate sources, Chp. 5, are distributed in the disk of the Milky Way. An additional issue is that the observed annihilation rate is smaller than the combined production rate of all sources, especially in the disk. One way out is to move the positrons from the disk into the bulge, collect them and trap them there, until they finally annihilate. Such a propagation of positrons from the disk to the bulge would lead to a low-intensity and diffuse/extended disk emission for the few positrons annihilating during such propagation. This may happen, for example, along galactic magnetic field lines (e.g. Prantzos 2006, 2008; Heesen et al. 2009). But it is difficult to trap the positrons in the bulge, and requires peculiar magnetic field confinements. Another possibility has been proposed by Higdon et al. (2009). They assume that the intermediate region between disk and bulge is hot and ionised, so that positrons could diffuse over large distances. The gas density in the bulge region can be larger than in the disk, which may effectively reduce the propagation time. Positrons in the bulge might hence naturally annihilate faster. A more elaborate simulation was conducted by Alexis et al. (2014). They used a realistic and detailed distribution of matter and positron sources (here only assuming nucleosynthesis origins). In this case, the intensity of the disk could be met, as already pointed out by Prantzos (2006), based on order of magnitude estimations. However, the peakedness of the bulge is still not explained, then. In addition, the simulation results suggest that the spiral arms of the Milky Way should be visible, which is however not the case. This discrepancy lead to the hypothesis of a bulge emission with its own source type(s). Alexis et al. (2014) suggested such a population of sources in the bulge, from a forward modelling approach. Specifically, a star burst near the supermassive black hole Sgr A\* in the centre of the Galaxy would have produced  $10^{57}$ - $10^{60}$   $e^+ s^{-1}$  at MeV energies which,

and may have occurred 1-10 Myr ago. If all these positrons were produced at once, the commonly-accepted assumption of a steady-state production and annihilation rate of positrons is not given any more. A non-equilibrium and sudden injection of positrons would then explain the brightness of annihilation gamma-rays from the centre of the Milky Way. Such giant positron production flare might be also linked to the Fermi-bubbles, Sec. 4.4.1.

The time scale of galactic nucleosynthesis can differ significantly from the positron propagation time. An important question is hence whether the positrons actually escape the sources, and if so, how many. There is no way to trace positrons back from the point of annihilation to the positron sources, with current instrumentation. Candidate sources have to be caught "in flagranti" to emit positrons. The updated measurement of the 511 keV sky manifests the necessity of positron propagation in the Milky Way, not only from the bright bulge with its lack of candidate sources, but also as a thick, low-surface brightness, high annihilation rate, disk is revealed. The bulge is the most significant and distinct emission region which changed the point of view to the positron puzzle, in combination with the thick disk and the galactic centre source: Many sources produce a specific amount of positrons in the Milky Way, probably more than are seen to annihilate. The remaining positrons may be thermalised within the ISM, and may build reservoirs of charged particles in the Milky Way. The general question is: Where are the missing positrons?

### **Speculations**

The similarity between dark matter density profiles and the 511 keV emission morphology in the Milky Way has inspired speculations. One may think that positrons, or in general antimatter, could be responsible for the effects of dark matter, rather than being a result of dark matter decay. Such a hypothesis would require some mechanism to cause the non-Keplerian rotation curves in spiral galaxies. The annihilation kinematics show imprints of very large rotation velocities, beyond the dispersion-dominated bulge region. Therefore, this may not be too far-fetched, and this effect may be caused by the large scale effects of antimatter. The true content of thermalised positrons that may populate the Galaxy is unknown. But if it is possible to create quasi-steady reservoirs of antimatter, or a galaxy-wide distribution, the dark matter paradigm might stagger. As there is also matter inside a galaxy, the presence of antimatter effects will not disrupt the total system, but may rather induce the formation of density structures on galactic scales. Similarly, the giant intergalactic voids may not be entirely devoid of matter, but could instead be bubble-like accumulations of antimatter. These would then not annihilate because of the absence of matter, being concentrated in galaxies. Speculating even further, dark energy may then also be a relic of antimatter action. In total, the "dark" effects might, in general, only be the incarnations of an unknown population of anti-particles. The apparent baryon asymmetry of the Universe may be over-estimated by orders of magnitude in that case. This would be caused by the measurements, performed either only locally, or based on the indistinguishability of cosmic background photons from matter or from antimatter. Annihilation gamma-rays would be emitted at the boundaries of such matter-antimatter structured systems, but would be faint and may escape observations.

## 6 Summary and Conclusion

In this thesis, gamma-ray data from the SPI spectrometer aboard INTEGRAL were used to study the positron population in the Milky Way through their annihilation gamma-ray signature. Based on a detailed background modelling method, the celestial 511 keV emission was constrained, and separate annihilation regions have been identified, so that spectral information from different components was refined. The positron contents and annihilation conditions in the bulge and disk regions of the Galaxy were determined from characteristic spectral features of electron-positron annihilation and different emission tracers. As the origin of the majority of galactic positrons is unknown, source candidates have been investigated, from theoretical considerations, based on indirect evaluations, as well as by direct gamma-ray measurements. Nucleosynthesis contributions to the galactic positrons have been determined from the ejected masses of  $\beta^+$ -unstable nuclei from massive star winds and core-collapse supernovae, and also from thermonuclear supernovae, through their decay gamma-rays and trapped positrons. The microquasar V404 Cygni has been caught in action to produce electron-positron pair-plasma, as the characteristic annihilation spectrum could be observed. Dark matter, as plausible positron producer through dark matter particle annihilations, has been tested in satellite galaxies of the Milky Way. The constraints on the positron annihilation conditions, on different environments, and on different sources are complemented by kinematic studies of both, the 1809 keV sky from the decay  $^{26}\text{Al}$ , as positron seed distribution, as well as the 511 keV sky, as positron fate distribution.

From the diffuse large scale emission analysis of the galactic positron annihilation signal, at least two distinct annihilation sites were identified, the bulge and the disk. The bulge region had been found offset from the galactic centre by  $\approx 1^\circ$  towards negative longitudes, and could be represented by two extended emission features with radial extents of  $\approx 6^\circ$  and  $\approx 20^\circ$ , respectively. This essentially confirms previous studies. In addition, a disk like structure is apparent, extending  $\pm 10^\circ$  in galactic latitude and at least  $\pm 90^\circ$  in longitude. This consolidates a large and thick disk in which positrons annihilate in large numbers. A total number of positrons of  $5 \times 10^{43}$  annihilate per second in the Milky Way, of which  $\approx 1/3$  are found in the bulge, and  $\approx 2/3$  in the disk. The previously reported high bulge-to-disk ratio in 511 keV emission with values of 1.4-9.0 is now revised to a value significantly below, to  $\approx 0.5$ . This is more in concordance with expected positron source distributions, but still requires the effects of propagation because of the thickness of the disk. From deeper SPI observations at the very centre of the Galaxy, a previously unknown point-like source emerged. This could either be part of the bulge, with an increased annihilation rate due to larger gas densities, or even a separate source of positrons, such as the supermassive black hole Sgr A\*. From the spectroscopic analysis of each component, the 511 keV line, the three-photon continuum from positronium, and an underlying continuum are detected, and determined in their relative intensities. In the different regions, the line-to-continuum ratios, and in particular the line shape

parameters are different. This can be interpreted as due to variations of annihilation conditions in the interstellar medium of bulge and disk. Very different conditions in the interstellar medium may provide nearly-identical spectral parameters. So, one particular spectrum can result in different interpretations, ranging from partly ionised ( $\approx 1\text{-}5\%$ ) and warm gas ( $\approx 7000\text{-}40000$  K) conditions, to cold gas  $< 50$  K such as in molecular clouds. Warm and partly ionised conditions may also be found in stellar atmospheres. This is supported by testing astrophysical tracer maps, and also by the galactic annihilation kinematics. The best fitting maps for the ortho-positronium continuum and the 511 keV line are representations of the large-scale distribution of star light as emitted by red giants. The model fit of the high-energy continuum shows no improvement when trying to express its morphology with star light. Thus, the distribution of stars is indeed similar to that of positron annihilation gamma-rays only.

From the analysis of the 1809 keV gamma-ray line of  $^{26}\text{Al}$  decay, the total  $^{26}\text{Al}$  mass in the Milky Way had been determined to  $2.8M_{\odot}$ . This had been used to derive a core-collapse supernova rate of 1.9 per century and an estimate of the positron contribution from massive star nucleosynthesis ejecta. From  $^{26}\text{Al}$  and  $^{44}\text{Ti}$ , only 11% of the galactic positron content is explained, when assuming a steady state production and annihilation rate. Instead of having only one source of positrons in the Galaxy, multiple origins are required to fulfil the constraints of the 511 keV measurements. Gamma-rays from the type Ia supernova SN2014J provide valuable information about the  $^{56}\text{Ni}$  production and its positrons, from a thermonuclear explosion of a white dwarf. With SPI,  $0.5M_{\odot}$  of  $^{56}\text{Ni}$  have been directly measured from the decay gamma-rays, and a positron escape fraction of 6% has been determined. A significant fraction of galactic positrons, of the order of 40%, is estimated from this to be due to supernovae of type Ia. Black-hole binary systems are now also established as positron sources, as variable emission of pair-plasma annihilation could be measured from the microquasar V404 Cygni during an outburst. As seen here, high-energy photons may in general be efficient positron producers in suitable environments, such as in compact objects or high energy-density fields, when the threshold of pair-production is exceeded. The remaining 50% of galactic positrons can be explained by a population of stellar black-hole binaries, which undergo repeated outbursts on time scales of tens to hundreds of years. The large number of non-detections of 511 keV emission from Milky Way satellite galaxies reduces contributions from possible dark matter annihilation into electron-positron pairs to less than 1%. Surprisingly, the dwarf galaxy Reticulum II was seen in 511 keV gamma-rays, and also has been detected in GeV emission. This is true for only this galaxy and the Milky Way, so that there might be a link between positrons and high-energy photons. Understanding this coincidence might provide additional clues about the processes in the centres of galaxies.

Kinematic analysis of the 1809 keV sky confirms and strengthens the previous reports and interpretations of massive star blow outs into leading edges of spiral arms, by consolidating and improving the measurements from the inner Galaxy with a different background modelling method, and a larger data set. Galactic rotation is seen faster in decaying  $^{26}\text{Al}$  ejecta, as the streams away from massive star groups prefer low-density media, and not the molecular clouds at whose edges stellar associations are formed. The velocity gradients with galactic latitude also conform with this trend, as above and below the galactic plane, the velocities from gas streaming

inside superbubbles are also increased. This  $^{26}\text{Al}$  analysis paved the way towards a similar study for positrons. The positron annihilation kinematics in the inner galaxy are significantly different, however. Between  $l = -5^\circ$  and  $l = +5^\circ$ , the rotation curve is completely flat, and appears red-shifted, by about  $80 \text{ km s}^{-1}$ , yet with a large dispersion. This is reminiscent of the velocity profiles for RR Lyrae stars in the galactic centre, and would thus support the scenario of positron annihilation in stellar atmospheres. Further away from the stellar bulge, the Doppler-velocities for the 511 keV line can reach up to  $500 \text{ km s}^{-1}$  and beyond, which is larger than expected from galactic rotation, and also larger than the rotation curve from  $^{26}\text{Al}$  ejecta. This points to an additional process influencing the positron annihilation kinematics.

The positrons in the Milky Way tell about how matter and antimatter reacts, in a simple framework of lepton-antilepton systems. Although much is known about the microscopic processes which involve electrons and positrons, the large scale dynamics, which may be induced by antimatter in conjunction with matter, are hidden in unknown mechanisms. Dark matter could be largely excluded as the main source of galactic positrons. But the effect of an unseen mass in the Galaxy is still there, and the morphological similarities of positron annihilation and dark matter density profiles is tantalising. This coincidence may imply that dark matter is not a smooth and massive halo-like entity, but rather a result of antimatter interactions with matter. This might be seen as gradual and ongoing positron annihilation, concentrated in the bulge and to a lesser extent in the disk.

One single particular source type cannot be responsible for all the galactic positrons, seen to annihilate now: There are non-negligible and significant contributions from various candidate positron emitters in the Galaxy. Even when the assumption of quasi-steady state production and annihilation is dropped, the strong disk emission, in addition to the well characterised bulge, suggests distinct and multiple source populations. From the large extent of the disk, its annihilation flux, and the apparent under-production of positrons in the bulge, the required propagation of positrons is now consolidated, predominantly from the disk into the bulge. The disk annihilation rate may still be uncertain by 50%. This leaves room for additional sources, such as pulsars, cosmic rays, and novae, to contribute to the galactic-wide positrons from massive stars, supernovae Ia and II, and microquasars. Although there is a large variety of positron origins, the annihilation conditions throughout the Milky Way can be considered rather similar. There are spectral differences between the outskirts of the Galaxy, towards the bulge, and probably even towards the central hundreds of parsecs in the galactic centre. However, it should be noted that there is a degeneracy between spectral parameters and the parameters describing the annihilation conditions in the interstellar medium.

Sources of positrons throughout the Galaxy which are confirmed by measurements are massive stars, supernovae, and microquasars. Potential sources are pulsars, cosmic rays, and novae. Combining the positron production rates, the resulting total rate exceeds the rate of annihilating positrons. Consequently, there are positrons missing. Either there is a sea of thermal positrons, whose annihilation rate is too low to be measured, and out-shined by positronium annihilation, or the understanding of annihilation physics is deficient. These missing positrons need to be found by future gamma-ray telescopes, designed for the detection of annihilation radiation.

The irregular exposure from observations during 13 years of the INTEGRAL mission implies difficulties for firm statements about the detailed emission morphology and about the annihilation conditions beyond the bulge region. A more uniform, and especially a much deeper, exposure in the galactic plane and at higher latitudes would be necessary to test the physics of positrons and the galactic annihilation and production picture. Improved kinematic information of annihilating positrons in the inner ridge of the Galaxy would be helpful, and further out, the uncertainties exceed expectations from galactic rotation. Spectra determined outside the bulge suggest Doppler-velocities of up to  $1000 \text{ km s}^{-1}$ , larger than expected. An empirical emission model does well in describing the large scale morphology, without assumptions on physical or geometrical conditions. True 3D models may then be able to answer specific questions. It would be interesting to investigate stellar atmospheres, as alternatives to the interstellar medium, for the annihilation sites. This could be done, for example, by investigating the effect of solar activity with SPI. Archival inspection for nova signals in INTEGRAL data would also help to constrain the contributions from thermonuclear explosions, and would provide valuable information about nova physics in general. The possible link between a GeV excess and a 511 keV signal in dwarf galaxies, such as found for Reticulum II, and in the Milky Way itself, should be investigated further, as positrons might be a crucial ingredient, also for very high-energy emissions from interaction cascades which are typical for processes of GeV and TeV energies (AGN, jets, pulsars, etc.).

The propagation of positrons plays an important role in the galactic positron puzzle, and diffuse annihilation emission may be found on scales of tens to hundreds of parsecs. This may lead to a more structured morphology of the galactic 511 keV emission. Ejected at relativistic energies, positrons may annihilate in flight with a spectrum, characteristic for a particular source. Thus, also the spectral resolution must be sufficient for such an instrument, in order to discriminate between different annihilation mechanisms. Positrons in a thermal reservoir may also lead to significant annihilation emission. These low-energy positrons could be disentangled from the high-energy source positrons by detailed analyses of the annihilation spectra in the vicinity of positron sources. For this, a future instrument must also have high imaging capabilities in order to resolve emission close to positron sources.

# A Additional Figures and Tables

## Additional Annihilation Spectra

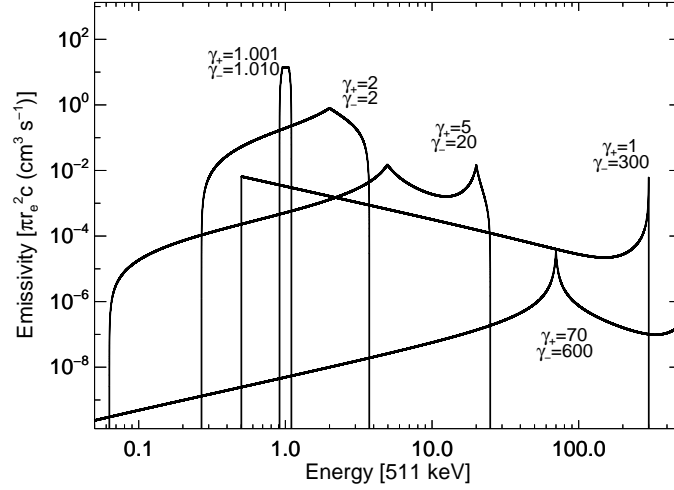


Figure A.1: Annihilation in flight spectra from Eq. (2.72) for various combinations of isotropic and mono-energetic particle populations,  $\gamma_+$  and  $\gamma_-$ , normalised to an emissivity of  $\pi r_e^2 c$ .

## Galactic Centre Source Parameters as a Function of Disk Size

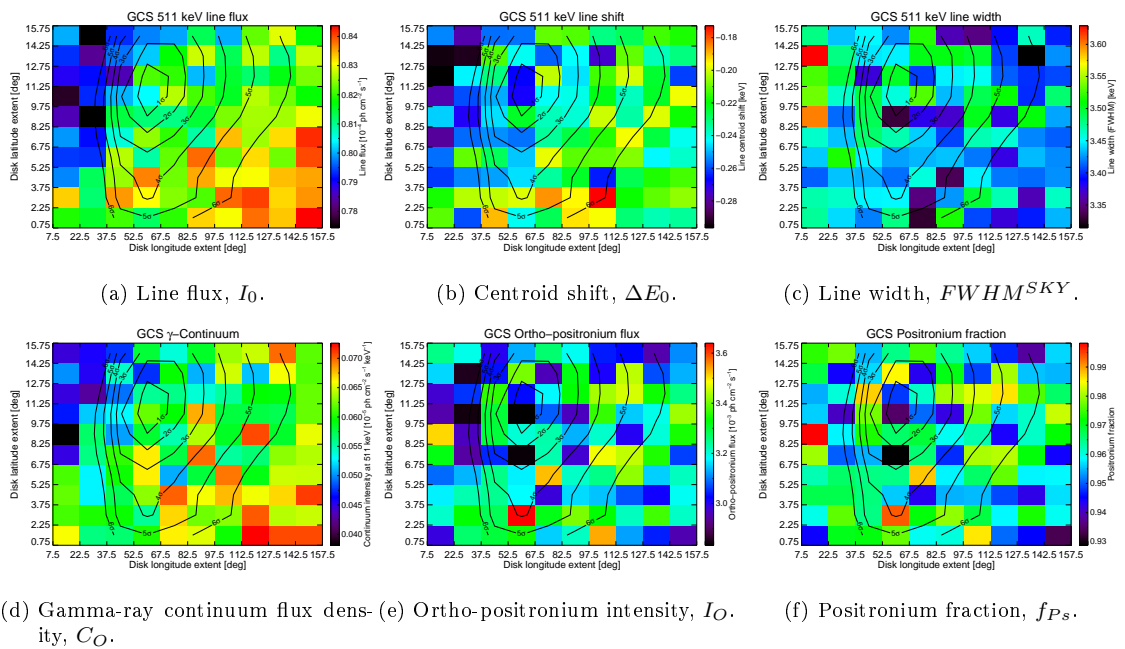


Figure A.2: Dependence of GCS spectral parameters as a function of disk size. The notation is similar to Fig. 4.20.

## Gamma-Ray Lines Associated with Positron-Emitting Nuclei

$^{26}\text{Al} \rightarrow ^{26}\text{Mg}^*$	1808.63(10) (0.998); 1129.67(10) (0.025); 2938(1) (0.002)
$^{56}\text{Ni} \rightarrow ^{56}\text{Co}^*$	158.38(3) (0.988); 269.50(2) (0.365); 480.44(2) (0.365); 749.95(3) (0.495); 811.85(3) (0.860); 1561.80(5) (0.140)
$^{44}\text{Ti} \rightarrow ^{44}\text{Sc}^*$	67.87(1) (1.009); 78.36(3) (0.995); 146.22(3) (0.001)
$^{44}\text{Sc} \rightarrow ^{44}\text{Ca}^*$	1157.02(2) (0.999); 1499.46(2) (0.009); 2656.44(3) (0.001)
$^{56}\text{Co} \rightarrow ^{56}\text{Fe}^*$	733.51(1) (0.002); 787.74(1) (0.003); 846.77(1) (1.000); 977.37(1) (0.014); 996.95(1) (0.001); 1037.84(1) (0.140); 1140.37(1) (0.001); 1175.10(1) (0.022); 1238.29(1) (0.664); 1335.40(1) (0.001); 1360.21(1) (0.043); 1442.75(1) (0.002); 1771.36(1) (0.155); 1810.76(1) (0.006); 1963.74(1) (0.007); 2015.21(1) (0.030); 2034.79(1) (0.077); 2113.14(1) (0.004); 2212.94(1) (0.004); 2276.13(1) (0.001); 2598.50(1) (0.170); 3009.65(1) (0.010); 3202.03(1) (0.032); 3253.50(1) (0.079); 3273.08(1) (0.019); 3451.23(1) (0.009); 3548.06(6) (0.002)

Table A.1: Additional gamma-ray lines from astrophysical positron emitters. For each reaction, gamma-ray lines in units of keV with an emission probability of more than 0.1 per 100 decays (in brackets) are given.

## Astrophysical Tracer Maps

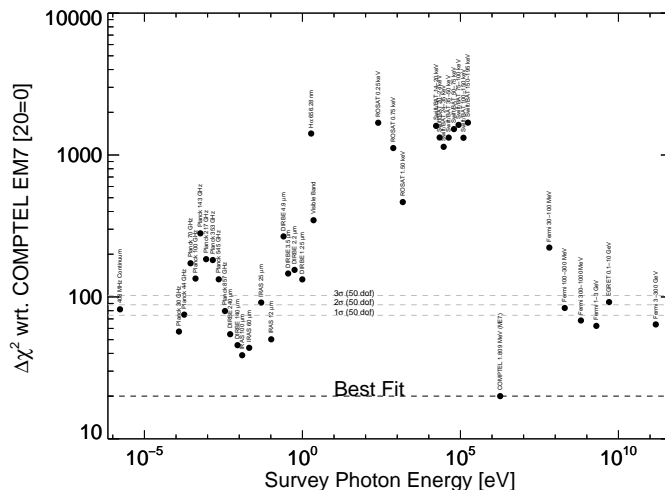


Figure A.3: Likelihood of tracer maps as a function of photon energy for the 1809 keV line, similar to Fig. 4.15. Shown is the negative log-likelihood ratio  $\Delta\chi^2(\text{BG}+\text{Sky model vs. BG only})$ , with respect to the COMPTEL ME7 map. A value of 20 has been added to each point for illustration purpose only so that 20 is the best fit value ( $\Delta\chi^2 = 0$ ).

See Figs. A.4 and A.5 on the following pages for images of the tracer maps.

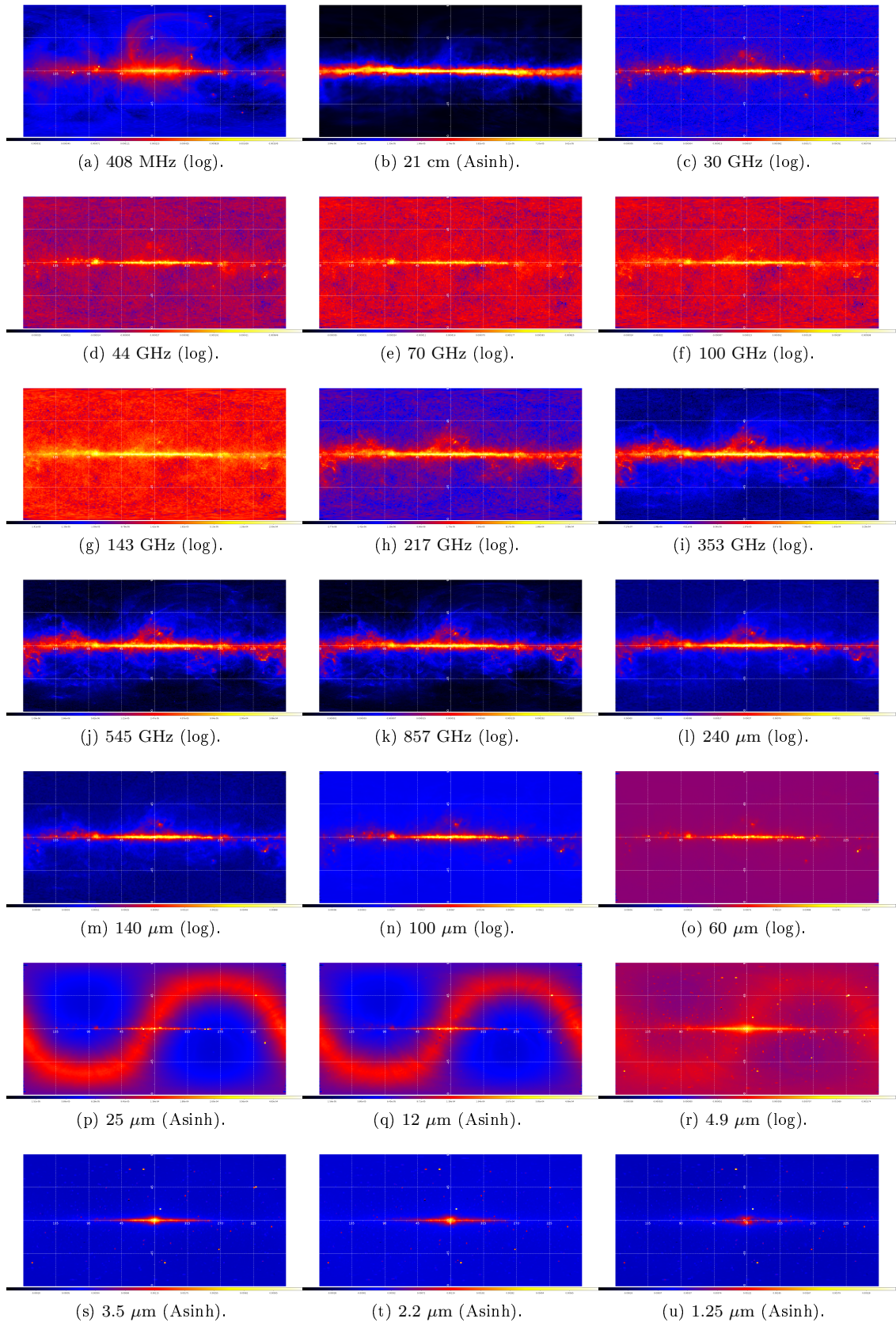


Figure A.4: Astrophysical tracer maps 1-21, sorted by photon energy. The colour indicate the relative flux in each pixel from black (zero) over blue, red, yellow, to white (maximum intensity). The image scaling is given in brackets.

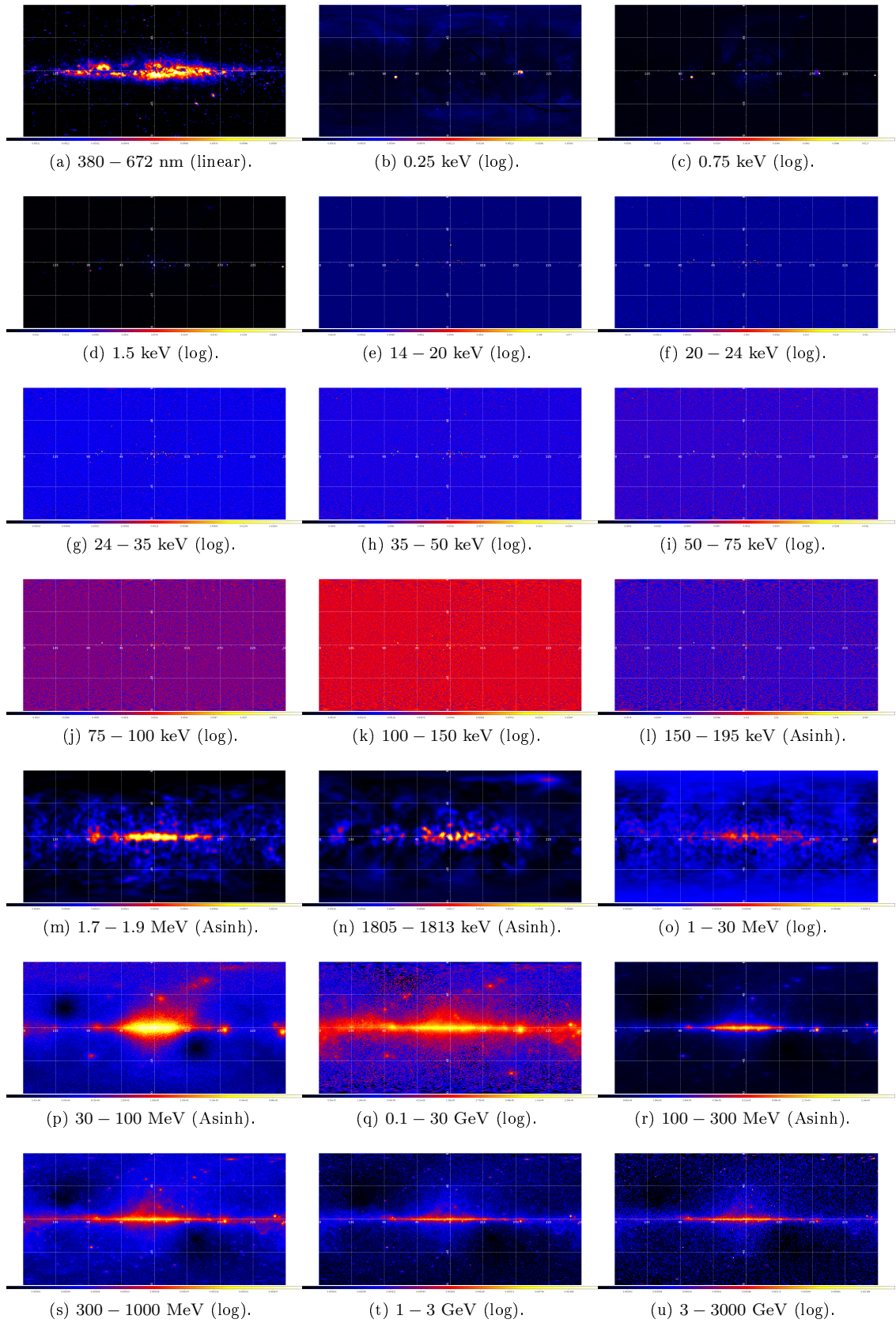


Figure A.5: Astrophysical tracer maps 21-42, sorted by photon energy. The colour indicate the relative flux in each pixel from black (zero) over blue, red, yellow, to white (maximum intensity). The image scaling is given in brackets.

## Gamma-Ray Spectra from Massive-Star Regions

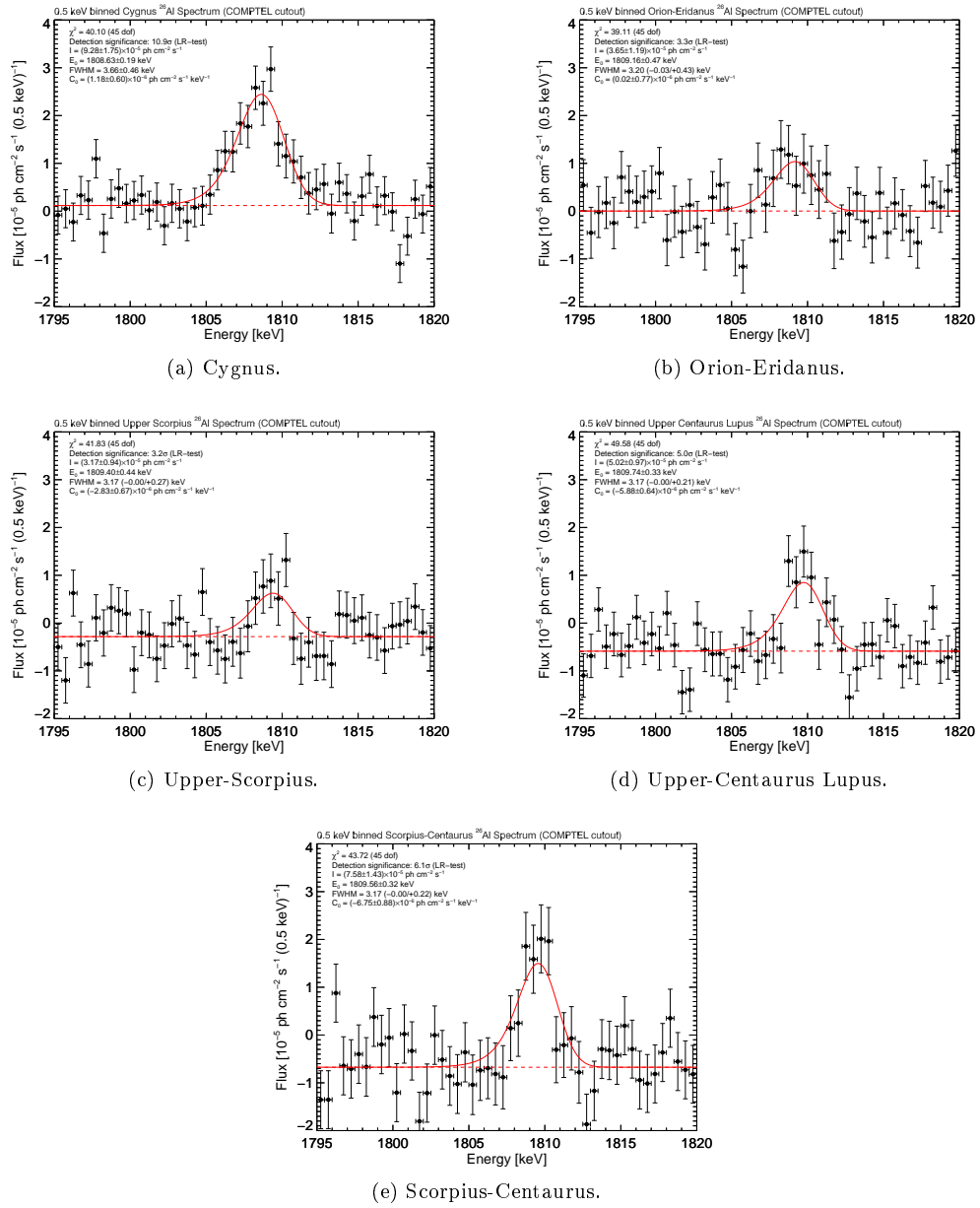


Figure A.6:  $^{26}\text{Al}$  decay gamma-ray spectra from massive star groups. Each spectrum (black data points) is fitted by a degraded Gaussian with fixed degradation parameter  $\tau$  of 1.05 keV (red solid line) on top of a constant offset (red dashed line). Spectral parameters are given in the legends.

## B Additional Equations and Derivations

### Pair Creation Thresholds

Assuming a stationary particle or photon interacting with another particle or photon, the threshold energies to create an electron-positron pair is estimated by considering the invariant masses of educts and products (at rest), respectively.

#### Photon-Electron Interaction

$$\begin{aligned}
 \gamma + e^- &\rightarrow e^- + e^- + e^+ \\
 m_e^2 + 2E_1 m_e &\geq 9m_e^2 \\
 E_1 &\geq 4m_e
 \end{aligned} \tag{B.1}$$

#### Photon-Proton Interaction

$$\begin{aligned}
 \gamma + p &\rightarrow p + e^- + e^+ \\
 m_p^2 + 2E_1 m_p &\geq m_p^2 + 4m_e^2 + 4m_p m_e \\
 E_1 &\geq 2m_e + \frac{m_e^2}{m_p} \gtrsim 2m_e
 \end{aligned} \tag{B.2}$$

#### Electron-Electron Interaction

$$\begin{aligned}
 e^- + e^- &\rightarrow e^- + e^- + e^- + e^+ \\
 2m_e^2 + 2E_1 m_e &\geq 16m_e^2 \\
 E_1 &\geq 7m_e
 \end{aligned} \tag{B.3}$$

#### Proton-Proton Interaction

$$\begin{aligned}
 p + p &\rightarrow p + p + e^- + e^+ \\
 2m_p^2 + 2E_1 m_p &\geq (2m_p^2 + 2m_e^2)^2 = 4m_p^2 + 4m_e^2 + 8m_p m_e \\
 E_1 &\geq m_p + 2\frac{m_e^2}{m_p} + 4m_e \gtrsim m_p + 4m_e
 \end{aligned} \tag{B.4}$$

### Photon-Photon Interaction

The 4-momentum vectors of the incoming photons are defined as

$$P_1 = P_1^\mu = \begin{pmatrix} E_1 \\ \vec{p}_1 \end{pmatrix}, \quad P_2 = P_2^\mu = \begin{pmatrix} E_2 \\ \vec{p}_2 \end{pmatrix}.$$

The 4-momentum vectors of the outgoing electron-positron pair are defined as

$$P_+ = P_+^\mu = \begin{pmatrix} E_+ \\ \vec{p}_+ \end{pmatrix}, \quad P_- = P_-^\mu = \begin{pmatrix} E_- \\ \vec{p}_- \end{pmatrix}.$$

The invariant masses are given by

$$P_1^2 = P_{1\mu}P_1^\mu = E_1^2 - \vec{p}_1^2 = 0,$$

$$P_2^2 = P_{2\mu}P_2^\mu = E_2^2 - \vec{p}_2^2 = 0,$$

$$P_+^2 = P_{+\mu}P_+^\mu = E_+^2 - \vec{p}_+^2 = m_e^2,$$

$$P_-^2 = P_{-\mu}P_-^\mu = E_-^2 - \vec{p}_-^2 = m_e^2.$$

The invariant mass of the centre of mass frame is given by

$$\begin{aligned} E_{CM}^2 &= \\ (P_1 + P_2)^2 &= (E_1 + E_2)^2 - (\vec{p}_1 + \vec{p}_2)^2 = \\ &= E_1^2 + 2E_1E_2 + E_2^2 - (\vec{p}_1^2 + \vec{p}_2^2 + 2\vec{p}_1 \cdot \vec{p}_2) = \\ &= E_1^2 + 2E_1E_2 + E_2^2 - E_1^2 - E_2^2 - 2E_1E_2 \cos(\phi) = \\ &= 2E_1E_2(1 - \cos(\phi)), \end{aligned}$$

$$\begin{aligned} E_{CM}^2 &= \\ (P_+ + P_-)^2 &> 4m_e^2, \end{aligned}$$

so that

$$2E_1E_2(1 - \cos(\phi)) > 4m_e^2,$$

and consequently

$$E_2 > \frac{2m_e^2c^4}{E_1(1 - \cos(\phi))}. \quad (\text{B.5})$$

### Two-Photon Annihilation Kinematics

Energy and momentum conservation in the centre of momentum frame of an annihilating electron-positron pair into two photons;  $\theta$  is the angle between the incoming positron and outgoing photon 2:

$$E_+ + E_- = E_1 + E_2 = E_{tot} \quad (\text{B.6})$$

$$\vec{p}_+ + \vec{p}_- = \vec{p}_1 + \vec{p}_2 = 0 \quad (\text{B.7})$$

Each photon energy,  $E_{1/2}$ , will be expressed as a function of the incident particle energies,  $E_+$   $E_-$ , respectively, as a function of the Lorentz-factors  $\gamma_\pm = E_\pm/m$ , where  $m$  is the electron mass.

$$E_1 = E_+ + E_- - E_2 \Leftrightarrow \gamma_1 = (\gamma_+ + \gamma_-) - \gamma_2 \quad (\text{B.8})$$

$$\begin{aligned} E_1^2 &= (E_+ + E_- - E_2)^2 = \\ &= E_+^2 + E_-^2 + E_2^2 + 2E_+E_- - 2E_+E_2 - E_-E_2 \equiv |\vec{p}_1|^2 = p_1^2 \end{aligned} \quad (\text{B.9})$$

$$\begin{aligned}
|\vec{p}_1|^2 &= (\vec{p}_+ + \vec{p}_- - \vec{p}_2)^2 = \\
&= p_+^2 + p_-^2 + p_2^2 - 2p_+p_- - 2p_+p_2 \cos(\theta) + 2p_-p_2 \cos(\theta) = \\
&= E_+^2 + E_-^2 + E_2^2 - 2m^2 - 2\sqrt{(E_+^2 - m^2)(E_-^2 - m^2)} + \\
&+ 2E_2 \cos(\theta) \left( \sqrt{E_-^2 - m^2} - \sqrt{E_+^2 - m^2} \right) \tag{B.10}
\end{aligned}$$

In Eqs. (B.9) and (B.10), the relativistic energy-momentum relation for massive,  $\sqrt{E^2} = p^2 + m^2$ , and massless particles,  $E = p$ , respectively, was used to obtain pure energy equations.

Equating Eq. (B.9) and (B.10), and solving for  $E_2$  gives

$$E_2 = \frac{m^2 + E_+E_- + \sqrt{(E_+^2 - m^2)(E_-^2 - m^2)}}{(E_+ + E_-) + \cos(\theta) \left( \sqrt{E_-^2 - m^2} - \sqrt{E_+^2 - m^2} \right)},$$

which converts to the energy of photon 2 in units of the electron mass:

$$\gamma_2 = \frac{1 + \gamma_+\gamma_- + \sqrt{(\gamma_+^2 - 1)(\gamma_-^2 - 1)}}{(\gamma_+ + \gamma_-) + \cos(\theta) \left( \sqrt{\gamma_-^2 - 1} - \sqrt{\gamma_+^2 - 1} \right)} \tag{B.11}$$

In the special case of a stationary electron (positron),  $\gamma_{\mp} = 1$ , hit by a relativistic positron (electron),  $\gamma_{\pm} = \gamma$ , Eq. (B.11) becomes

$$\gamma_2 = \frac{1 + \gamma}{1 + \gamma - \sqrt{\gamma^2 - 1} \cos(\theta)}. \tag{B.12}$$

In Eq. (B.12),  $\gamma_2(\theta)$  as a function of  $\theta$  obtains a maximum for  $\theta_{max} = 0$  and a minimum for  $\theta_{min} = \pi$ , which describes roughly the high- and low-energy cut-off of the resulting annihilation spectrum for a given particle energy,  $\gamma$ , respectively:

For  $\theta_{max/min} = 0, \pi$  this results to

$$\begin{aligned}
\gamma_2^{max} &= \frac{1 + \gamma}{1 + \gamma \mp \sqrt{\gamma^2 - 1}} = \\
&= \frac{\gamma + 1}{\sqrt{(\gamma + 1)(\gamma + 1)} \mp \sqrt{(\gamma - 1)(\gamma + 1)}} = \\
&= \frac{\sqrt{\gamma + 1}}{\sqrt{\gamma + 1} \mp \sqrt{\gamma - 1}} = \\
&= \frac{\sqrt{\gamma + 1} (\sqrt{\gamma + 1} \pm \sqrt{\gamma - 1})}{(\sqrt{\gamma + 1} \mp \sqrt{\gamma - 1}) (\sqrt{\gamma + 1} \pm \sqrt{\gamma - 1})} = \\
&= \frac{\gamma + 1 + \sqrt{\gamma^2 - 1}}{\gamma + 1 + \sqrt{\gamma^2 - 1} - \sqrt{\gamma^2 - 1} - \gamma + 1} = \\
&= \frac{1}{2} \left( 1 + \gamma \pm \sqrt{\gamma^2 - 1} \right) = \tag{B.13}
\end{aligned}$$

$$\begin{aligned}
&= \frac{1}{2} \left( 1 + \gamma \pm \gamma \sqrt{1 - \frac{1}{\gamma^2}} \right) = \\
&\stackrel{\gamma \gg 1}{\approx} \frac{1}{2} (1 + \gamma \pm \gamma) = \\
&= \begin{cases} \gamma + \frac{1}{2} & \text{for } \theta = \theta_{max} = 0 \\ \frac{1}{2} & \text{for } \theta = \theta_{min} = \pi, \end{cases} \tag{B.14}
\end{aligned}$$

so that the maximum energy a photon can carry away from the direct annihilation of a fast positron (electron) with a stationary electron (positron) is  $E_{1/2}^{max} \approx E_{\pm} + \frac{1}{2}m_e c^2$ , and the minimum energy is  $E_{2/1}^{min} \approx \frac{1}{2}m_e c^2$ .

### Three-Photon Annihilation Kinematics

Energy conservation in ortho-positronium decay for three photons, numbered 1, 2, and 3, respectively:

$$E_1 + E_2 + E_3 = 2m \Leftrightarrow \gamma_1 + \gamma_2 + \gamma_3 = 2$$

In Eq. (2.64), the energy of photon 1 and 2 as a function of photon energy 3 in units of the Lorentz-factors is given as:

$$\begin{aligned}
\gamma_1 &= 2 - (\gamma_2 + \gamma_3) \\
\gamma_2 &= \frac{1 - \gamma_3}{1 + \frac{\gamma_3}{2} (\cos(\phi) - 1)}
\end{aligned}$$

Now consider a photon energy  $\gamma_3 = 1 + \epsilon$ , where  $\epsilon > 0$  and small:

$$\gamma_2 = -\frac{2\epsilon}{(1 - \epsilon) + (1 + \epsilon) \cos(\phi)}$$

In order to fulfil energy conservation, photon energy 2 must be less than  $1 - \epsilon$ :

$$\begin{aligned}
\gamma_2 &\stackrel{!}{<} 1 - \epsilon \\
\Rightarrow -\frac{2\epsilon}{(1 - \epsilon) + (1 + \epsilon) \cos(\phi)} &\stackrel{!}{<} 1 - \epsilon \\
\Rightarrow \cos(\phi) &\stackrel{!}{>} -\frac{1 + \epsilon^2}{1 - \epsilon^2} \\
\Rightarrow \phi &\stackrel{!}{>} \arccos\left(-\frac{1 + \epsilon^2}{1 - \epsilon^2}\right) \tag{B.15}
\end{aligned}$$

In Eq. (B.15),  $\phi$  is only defined if  $\epsilon = 0$ , which is in contradiction to the assumption  $\epsilon > 0$ . It follows that one photon may not carry more energy than the rest mass of one electron.

### Approximating the Peak Position of Asymmetric Spectral Lines

According tot Eq. (3.19), the instrumental line shape including degradation effects is given by

$$\begin{aligned}
L(E) &= (G \otimes T)(E) = \\
&= \sqrt{\frac{\pi}{2}} \frac{A_0 \sigma}{\tau} \exp\left(\frac{2\tau(E - E_0) + \sigma^2}{2\tau^2}\right) \operatorname{erfc}\left(\frac{\tau(E - E_0) + \sigma^2}{\sqrt{2}\sigma\tau}\right) = \\
&= \sqrt{\frac{\pi}{2}} \frac{A_0 \sigma}{\tau} \mathcal{X}(E) \mathcal{Y}(E), \tag{B.16}
\end{aligned}$$

with  $A_0$ ,  $E_0$ , and  $\sigma$  the amplitude, centroid, and width of a symmetric Gaussian shape, and  $\tau$  the degradation parameter. In the last line of Eq. (B.16), the auxiliary functions  $\mathcal{X}(E) = \exp\left(\frac{2\tau(E - E_0) + \sigma^2}{2\tau^2}\right)$  and  $\mathcal{Y}(E) = \operatorname{erfc}(\mathcal{Z}(E)) = \operatorname{erfc}\left(\frac{\tau(E - E_0) + \sigma^2}{\sqrt{2}\sigma\tau}\right)$  have been introduced. Formally, the line peak is given for the value of  $E = E_{peak}$  when

$$\left. \sqrt{\frac{2}{\pi}} \frac{\tau}{A_0 \sigma} \frac{\partial L(E)}{\partial E} \right|_{E=E_{peak}} = \left. \frac{\partial \mathcal{X}}{\partial E} \mathcal{Y} + \frac{\partial \mathcal{Y}}{\partial E} \mathcal{X} \right|_{E=E_{peak}} \stackrel{!}{=} 0. \tag{B.17}$$

The derivatives are given by

$$\frac{\partial \mathcal{X}}{\partial E} = \frac{\mathcal{X}}{\tau} \tag{B.18}$$

$$\frac{\partial \mathcal{Y}}{\partial E} = -\sqrt{\frac{2}{\pi}} \frac{1}{\sigma} \exp(-\mathcal{Z}^2) \tag{B.19}$$

$$\frac{\partial \mathcal{Z}}{\partial E} = \frac{1}{\sqrt{2}\sigma}, \tag{B.20}$$

so that the condition of Eq. (B.17) reduces to

$$\mathcal{F}(E) \equiv \frac{\mathcal{X}(E)}{\mathcal{Y}(E)} \exp(-\mathcal{Z}^2(E)) - \sqrt{\frac{\pi}{2}} \frac{\sigma}{\tau} \stackrel{!}{=} 0. \tag{B.21}$$

Eq. (B.21) is a non-linear transcendental function which is approximately solved with the Newton-Raphson method

$$E_{peak} \approx E_{n+1} = E_n - \frac{\mathcal{F}(E_n)}{\mathcal{F}'(E_n)}, \tag{B.22}$$

where the starting point  $E_{n=0}$  is assumed to be the centroid of the symmetric Gaussian  $E_0$  to which the peak position reduces in the limiting case  $\tau \rightarrow 0$ . The derivative of  $\mathcal{F}(E)$  is given by

$$\mathcal{F}'(E) = \exp(-\mathcal{Z}^2(E)) \left[ \frac{\mathcal{X}'(E)\mathcal{Y}(E) - \mathcal{X}(E)\mathcal{Y}'(E)}{\mathcal{Y}^2(E)} - 2 \frac{\mathcal{X}(E)\mathcal{Z}(E)\mathcal{Z}'(E)}{\mathcal{Y}(E)} \right]. \quad (\text{B.23})$$

Inserting the functions  $\mathcal{X}(E)$ ,  $\mathcal{Y}(E)$ ,  $\mathcal{Z}(E)$ , and their derivatives, and then evaluating the function  $\mathcal{F}'(E)$  at  $E = E_0$  obtains

$$\mathcal{X}(E_0) = \exp\left(\frac{\sigma^2}{2\tau^2}\right) \quad (\text{B.24})$$

$$\mathcal{X}'(E_0) = \frac{1}{\tau} \quad (\text{B.25})$$

$$\mathcal{Y}(E_0) = \operatorname{erfc}\left(\frac{\sigma}{\sqrt{2\tau}}\right) \quad (\text{B.26})$$

$$\mathcal{Y}'(E_0) = -\sqrt{\frac{2}{\pi}} \frac{1}{\sigma} \exp\left(-\frac{\sigma^2}{2\tau^2}\right) \quad (\text{B.27})$$

$$\mathcal{Z}(E_0) = \frac{\sigma}{\sqrt{2\tau}} \quad (\text{B.28})$$

$$\mathcal{Z}'(E_0) = \frac{1}{\sqrt{2\sigma}}, \quad (\text{B.29})$$

with auxiliary variable  $\omega \equiv \frac{\sigma}{\sqrt{2\tau}}$

$$\mathcal{F}(E_0) = \frac{1}{\operatorname{erfc}(\omega)} (1 - \sqrt{\pi}\omega \operatorname{erfc}(\omega)) \quad (\text{B.30})$$

$$\mathcal{F}'(E_0) = \frac{1}{\sqrt{\pi}\omega\tau \operatorname{erfc}(\omega)^2} \exp(-\omega^2) \quad (\text{B.31})$$

so that

$$\frac{\mathcal{F}(E_0)}{\mathcal{F}'(E_0)} = \frac{\sqrt{\pi}\omega\tau \operatorname{erfc}(\omega) (1 - \sqrt{\pi}\omega \operatorname{erfc}(\omega))}{\exp(-\omega^2)} = \mathcal{I}_1(E_0). \quad (\text{B.32})$$

For large values of  $\omega$ , equivalent to small values of  $\tau$ , the complementary error-function has the asymptotic behaviour

$$\operatorname{erfc}(\omega) \approx \exp(-\omega^2) \left( \frac{1}{\sqrt{\pi}\omega} - \mathcal{O}(\omega^{-3}) \right), \quad (\text{B.33})$$

so that the first iteration step,  $\mathcal{I}_1(E_0)$  simplifies to

$$\mathcal{I}_1(E_0) \approx \frac{\sqrt{\pi}\omega\tau \frac{\exp(-\omega^2)}{\sqrt{\pi}\omega} \left( 1 - \sqrt{\pi}\omega \frac{\exp(-\omega^2)}{\sqrt{\pi}\omega} \right)}{\exp(-\omega^2)} = \tau (1 - \exp(-\omega^2)) \stackrel{\omega \rightarrow \infty}{\approx} \tau, \quad (\text{B.34})$$

from which it follows that to first order approximation for small  $\tau$ , the line peak is given by

$$E_{peak} \approx E_0 - \tau. \quad (\text{B.35})$$

## Average Background Model for Variable Patterns

The arithmetic mean may also be tried to infer a background model (pattern) from the data in the case of time-variable instrumental line and continuum patterns:

$$\begin{aligned} \frac{1}{N_p} \sum_{p=1}^{N_p} D(p) &= \frac{\alpha}{2} N_S \frac{N_{obs}}{N_p} \begin{pmatrix} 1 \\ 1 \end{pmatrix} + \\ &+ \beta_C N_{BGC} \begin{pmatrix} 1 \\ 1 \end{pmatrix} + \\ &+ \beta_L N'_{BGL} \lambda_1 \begin{pmatrix} 1 \\ \lambda_2/\lambda_1 \end{pmatrix} + \\ &+ \frac{\beta_L}{2} N'_{BGL} (N_p + 1) l_1 \begin{pmatrix} 1 \\ l_2/l_1 \end{pmatrix} = \end{aligned} \quad (\text{B.36})$$

$$= \beta' N_{BGM} \begin{pmatrix} 1 \\ 1 + \delta' \end{pmatrix} \equiv \beta' R_{BGM} \quad (\text{B.37})$$

In Eq. (B.36),  $N'_{BGL}$  includes the normalisation of the background line response, averaged over all times  $N_p$ , and  $\delta'$  is the pointing averaged deviation from a (1/1) detector pattern. It can be seen that the derived detector pattern,  $R_{BGM}$ , Eq. (B.37), is wrong for both, continuum and line backgrounds at the same time, because the line and the continuum pattern have different time behaviours. This is illustrated in Fig. 3.24a. Due to the degradation, the detector pattern of the data in one energy bin changes with time, but the background model pattern is fixed for all times.  $R_{BGM}$  only fits well for particular pointings, here between  $p = 25$  and  $p = 65$ . A statistical fit with only background yields a systematic deviation from zero which would then be interpreted as a false (probably time dependent) celestial signal. In this way, artefacts are created.

## Total Pair Creation Cross Section in the Field of a Nucleus

Bethe & Heitler (1934) calculated the differential cross section for pair production by a photon in the field of a nucleus. The total cross section involved elliptical integrals and cannot be given in an analytical form. An approximation was first given by Racah (1936); Jost et al. (1950) calculated the total cross section again, agreeing with Racah (1936) provided the formula in a more readable form for  $\eta = \frac{2m_e}{E} \leq 1$  (see also Jauch & Rohrlich 1955):

$$\sigma_{Z,pair}(E) = \alpha Z^2 r_e^2 \{ 2\eta^2 [2C_2(\eta) - D_2(\eta)] + 2/27 [(109 + 64\eta^2)E_2(\eta) - (67 + 6\eta^2)(1 - \eta^2)F_2(\eta)] \} \quad (\text{B.38})$$

$$C_2(\eta) = \int_1^{1/\eta} \frac{\text{Arcosh}(x)}{x} \text{Arcosh}((\eta x)^{-1}) dx \quad (\text{B.39})$$

$$D_2(\eta) = \int_1^{1/\eta} \frac{\text{Arcosh}((\eta x)^{-1})}{\sqrt{x^2 - 1}} dx \quad (\text{B.40})$$

$$E_2(\eta) = F(\sqrt{1 - \eta^2}) - E(\sqrt{1 - \eta^2}) \quad (\text{B.41})$$

$$F_2(\eta) = F(\sqrt{1 - \eta^2}) \quad (\text{B.42})$$

$$F(x) = \int_0^{\frac{\pi}{2}} \frac{d\theta}{\sqrt{1 - x^2 \sin^2(\theta)}} \quad (\text{B.43})$$

$$E(x) = \int_0^{\frac{\pi}{2}} \sqrt{1 - x^2 \sin^2(\theta)} d\theta \quad (\text{B.44})$$

$E(x)$  and  $F(x)$  are the complete elliptical integrals of first and second kind, respectively.

## Neutralino Self-Annihilation Cross Section

In the non-relativistic limit, the neutralino self-annihilation cross section into fermion-antifermion pairs in the minimal is given by (Jungman et al. 1996, and references therein)

$$\sigma(\chi\chi \rightarrow f\bar{f})_{v \rightarrow 0} = \frac{c_f \beta_f}{128\pi m_\chi^2} |\mathcal{A}(\chi\chi \rightarrow f\bar{f})_{v \rightarrow 0}|^2, \quad (\text{B.45})$$

where  $\mathcal{A}(\chi\chi \rightarrow f\bar{f})_{v \rightarrow 0}$  is the annihilation helicity amplitude for small relative velocities.

$$\mathcal{A}(\chi\chi \rightarrow f\bar{f})_{v \rightarrow 0} = \mathcal{A}_{sf} + \mathcal{A}_Z + \mathcal{A}_H \quad (\text{B.46})$$

where

$$\mathcal{A}_{sf} = \sqrt{2} \sum_{j=1}^6 \frac{1}{P_j} \left\{ [(X'_{fij0})^2 + (W'_{fij0})^2] \frac{m_{f_i}}{m_\chi} + 2X'_{fij0}W'_{fij0} \right\} \quad (\text{B.47})$$

is the sfermion exchange contribution, where the sum is over six sfermion states which can couple to a fermion  $f_i$ ,  $P_j = 1 + \left(\frac{m_{\bar{f}_i}}{m_\chi}\right)^2 - \left(\frac{m_{f_i}}{m_\chi}\right)^2$ , allowing that the produced fermions are not necessarily particle-antiparticle pairs of the same family,  $X'_{fij0}$  and  $W'_{fij0}$  are the fermion ( $f$ ) coupling matrices between fermions ( $i$ ), sfermions ( $j$ ), and the lightest neutralino (index 0),  $m_{f_i}$  is the fermion mass, and  $m_\chi$  is the neutralino mass;

$$\mathcal{A}_Z = 2\sqrt{2} \frac{g^2}{\cos^2(\theta_W)} O_{00}^{\prime\prime L} T_3(f_i) \frac{m_{f_i} m_\chi}{m_Z^2} \quad (\text{B.48})$$

is the  $Z$  boson contribution, with  $g$  being the weak coupling constant,  $\theta_W$  being the Weinberg angle,  $O_{00}^{\prime\prime L}$  being the neutralino-neutralino couplings,  $T_3(f_i)$  being the weak isospin of the fermion, and  $m_Z$  is the  $Z$  boson mass; and

$$\mathcal{A}_H = 4\sqrt{2} T_{H00} h_{Hff} \frac{1}{4 - (m_H/m_\chi)^2 + i\Gamma_H m_H/m_\chi^2} \quad (\text{B.49})$$

is the Higgs boson contribution to the amplitude, where  $T_{H00}$  is the Higgs-neutralino-neutralino coupling,  $h_{Hff}$  are the Yukawa Higgs-fermion couplings,  $m_H$  is the Higgs mass, and  $\Gamma_H$  is the decay width of the Higgs.

## Mandelstam Variables

Regarding Fig. 2.11, showing the annihilation of a positron with an electron, the Mandelstam variables are defined as (Olive & Particle Data Group 2014):

$$s = (P_-^\mu + P_+^\mu)^2 = (P_1^\mu + P_2^\mu)^2 = 2m_e^2 + 2E_- E_+ - 2\vec{p}_- \cdot \vec{p}_+ \quad (\text{B.50})$$

$$t = (P_-^\mu - P_2^\mu)^2 = (P_+^\mu - P_1^\mu)^2 = m_e^2 - 2E_- E_2 + 2\vec{p}_- \cdot \vec{p}_2 \quad (\text{B.51})$$

$$u = (P_-^\mu - P_1^\mu)^2 = (P_+^\mu - P_2^\mu)^2 = m_e^2 - 2E_- E_1 + 2\vec{p}_- \cdot \vec{p}_1 \quad (\text{B.52})$$

where

$$\cos(\theta) = \frac{\vec{p}_- \cdot \vec{p}_2}{|\vec{p}_-| |\vec{p}_2|} \quad (\text{B.53})$$

and

$$s + t + u = 2m_e^2 \quad (\text{B.54})$$

since  $m_\gamma = 0$

## Radiative Recombination of Hydrogen

Full expression for low and high kinetic temperature regimes of the radiative recombination rate of protons with electrons to hydrogen from Gould (1989):

$$y = \frac{Ry}{kT}$$

$$\alpha_H(T) = C \sqrt{\frac{2kT}{\pi m}} y \phi(y) \bar{g}(y) \quad \text{for } y \geq 0.5 \quad (\text{B.55})$$

$$C = 2^6 3^{-3/2} \alpha^3 \pi a_0^2 \approx 4.21 \times 10^{-22} \text{ cm}^2$$

$$\phi(y) = \frac{1}{2} (1.735 + \ln y + (6y)^{-1})$$

$\bar{g}(y)$  is tabulated in Gould (1989)

$$\alpha_H(T) = C \sqrt{\frac{2kT}{\pi m}} y \phi^{(2)}(y) \bar{g}^{(2)}(y) \quad \text{for } y < 0.5 \quad (\text{B.56})$$

$$\phi^{(2)}(y) = \phi^{(0)}(y) - \phi^{(1)}(y)$$

$$\phi^{(0)}(y) = \sum_{k=1}^{\infty} (a_k - b_k \ln y) y^k$$

$$\phi^{(1)}(y) = \sum_{k=1}^{\infty} (c_k - d_k \ln y) y^k$$

$\bar{g}^{(2)}(y)$ ,  $a_k$ ,  $b_k$ ,  $c_k$ , and  $d_k$  are tabulated in Gould (1989)

## One-Quantum Annihilation Cross Section

Full expression for the single-quantum annihilation of a positron with a bound electron of an atom with charge number  $Z$  in lowest order Born approximation from Johnson et al. (1964):

$$\sigma_{\gamma}^{bound} = 4\pi r_e^2 \alpha^4 Z^5 f(\eta)$$

$$f(\eta) = \frac{\eta^2 - \frac{1}{3}\eta + \frac{4}{3}}{\sqrt{\eta^2 - 1}(\eta + 1)^2} \quad (\text{B.57})$$

$$\eta = \frac{E_+}{m_e c^2} \quad \text{for } \eta \geq 1 \quad (\text{B.58})$$

## Positron Annihilation Rate

Analytical expression for the angle-averaged annihilation rate,  $\bar{\sigma v}$ , as a function of electron and positron energy, given as Lorentz-factors,  $\gamma_-$  and  $\gamma_+$ , respectively (Svensson 1982):

$$\bar{\sigma v}(\gamma_+, \gamma_-) = \pi r_e^2 c \frac{F(\gamma_{cm})}{\beta_+ \gamma_+^2 \beta_- \gamma_-^2} \quad (\text{B.59})$$

$$F(\gamma_{cm}) = \left[ \beta_{cm}^3 \gamma_{cm}^2 L(\beta_{cm}) - 2\gamma_{cm}^2 + \frac{3}{4} L^2(\beta_{cm}) \right]_{\gamma_{cm}=\gamma_{cm}^{min}}^{\gamma_{cm}=\gamma_{cm}^{max}} \quad (\text{B.60})$$

$$L(\beta) = \ln \left( \frac{1 + \beta}{1 - \beta} \right) \quad (\text{B.61})$$

$$\gamma_{cm}^{min} = \sqrt{\frac{1}{2} (1 + \gamma_+ \gamma_- - \gamma_+ \gamma_- \beta_+ \beta_-)} \quad (\text{B.62})$$

$$\gamma_{cm}^{max} = \sqrt{\frac{1}{2} (1 + \gamma_+ \gamma_- + \gamma_+ \gamma_- \beta_+ \beta_-)} \quad (\text{B.63})$$

## Positron Annihilation Spectra

Analytical expression for the spectral shape,  $v \frac{d\sigma_{\gamma\gamma}}{dE}$ , as a function of  $E$ , normalised to the electron mass  $m_e$ ,  $\gamma_+$ , and  $\gamma_-$  from Svensson (1982). Each spectrum is defined in the interval  $[E_L, E_U]$ , where  $E_{L/U} = \frac{1}{2}[\gamma_+(1 \mp \beta_+) + \gamma_-(1 \mp \beta_-)]$ , and equals zero elsewhere:

$$v \frac{d\sigma_{\gamma\gamma}}{dE}(E, \gamma_+, \gamma_-) = \pi r_e^2 c \frac{S(E, \gamma_+, \gamma_-, \gamma_{cm})}{\beta_+ \gamma_+^2 \beta_- \gamma_-^2} \quad (\text{B.64})$$

$$S(E, \gamma_+, \gamma_-, \gamma_{cm}) = \left[ \sqrt{(\gamma_+ + \gamma_-)^2 - 4\gamma_{cm}^2} + H_+ + H_- \right]_{\gamma_{cm}=\gamma_{cm}^{(L)}}^{\gamma_{cm}=\gamma_{cm}^{(U)}} \quad (\text{B.65})$$

$$H_{\pm} = \left( 2 + \frac{1 - \gamma_{cm}^{*2}}{c_{\pm}} \right) I_{\pm} + \left[ \frac{1}{\gamma_{cm}} - \frac{\gamma_{cm}}{c_{\pm}} + \frac{\gamma_{cm}}{2\gamma_{cm}^{*2}} (2c_{\pm} - d_{\pm}) \right] \frac{1}{u_{\pm}} + \frac{\gamma_{cm}}{c_{\pm}} u_{\pm} \quad (\text{B.66})$$

$$I_{\pm} = \begin{cases} \frac{1}{\sqrt{c_{\pm}}} \ln(\gamma_{cm} \sqrt{c_{\pm}} + u_{\pm}) & (c_{\pm} > 0) \\ \frac{1}{\sqrt{-c_{\pm}}} \arcsin\left(\frac{\gamma_{cm}}{\gamma_{cm}^*}\right) \sqrt{-c_{\pm}} & (c_{\pm} < 0) \end{cases} \quad (\text{B.67})$$

$$H_{\pm} = \left( \frac{2}{3} \gamma_{cm}^3 + 2\gamma_{cm} + \frac{1}{\gamma_{cm}} \right) \frac{1}{\gamma_{cm}^*} + \frac{1}{2} \left( \frac{2}{3} \gamma_{cm}^3 - d_{\pm} \gamma_{cm} \right) \frac{1}{\gamma_{cm}^{*3}} \quad (c_{\pm} = 0) \quad (\text{B.68})$$

$$\gamma_{cm}^{(L)} = \gamma_{cm}^{min} = \sqrt{\frac{1}{2} (1 + \gamma_+ \gamma_- - \gamma_+ \gamma_- \beta_+ \beta_-)} \quad (\text{B.69})$$

$$\gamma_{cm}^{(U)} = \max \{ \gamma_{cm}^{max}; \gamma_{cm}^* \} = \max \left\{ \sqrt{\frac{1}{2} (1 + \gamma_+ \gamma_- + \gamma_+ \gamma_- \beta_+ \beta_-)}; \gamma_{cm}^* \right\} \quad (\text{B.70})$$

$$\gamma_{cm}^* = \sqrt{E(\gamma_+ + \gamma_- - E)} \quad (\text{B.71})$$

$$d_{\pm} = \gamma_{\mp}(\gamma_+ + \gamma_-) \pm E(\gamma_+ - \gamma_-) \quad (\text{B.72})$$

$$c_{\pm} = (\gamma_{mp} - E)^2 - 1 \quad (\text{B.73})$$

$$u_{\pm} = \sqrt{c_{\pm} \gamma_{cm}^2 + \gamma_{cm}^{*2}} \quad (\text{B.74})$$

## Positron Energy Loss Rate due to Ionisation

According to Eq. 2.82 as described in Berger & Seltzer (1964), the energy loss rate of electrons or positrons passing through matter with electron density  $n_e$ , charge number  $Z$ , and relative atomic mass  $A$  is given by

$$\frac{dE}{dx} = 2\pi r_e^2 m_e c^2 n_e \frac{1}{\beta^2} \left[ \ln \left( \frac{\beta^2 \gamma^2 (\gamma - 1)}{2(I/m_e c^2)^2} \right) + F^{\pm}(\beta\gamma) - \delta(\beta\gamma) \right] \quad (\text{B.75})$$

$$\text{with} \quad (\text{B.76})$$

$$F^+(\tau) = 2 \ln(2) - \frac{\beta^2}{12} \left[ 23 + \frac{14}{\tau + 2} + \frac{10}{(\tau + 2)^2} \frac{4}{(\tau + 2)^3} \right] \text{ for positrons,}$$

and

$$F^-(\tau) = 1 - \beta^2 + \frac{\left[\frac{\tau^2}{8} - (2\tau + 1) \ln(2)\right]}{(\tau + 1)^2} \text{ for electrons, respectively, where}$$

$$\tau = \gamma - 1. \quad (\text{B.77})$$

## Line Background Model Weighting Coefficients

In Eq. (3.34), the parameters  $\Delta_1^{i+1}$  and  $\Delta_2^{i+1}$  are weighting functions for the changing line ratios during a particular background block  $i + 1$ , resulting in a complicated way to write down the mean of the line pattern (vector/matrix) times its time dependent normalisation during the  $m_{i+1}$  observations, where  $f_i = s_i + m_{i+1} - 1$ , see Sec. 3.2.4.2. They are given by

$$\Delta_1 = \psi(a + f_i + 1) - \psi(a + s_i) = \quad (\text{B.78})$$

$$= \psi(a + s_i + m_{i+1}) - \psi(a + s_i) = \sum_{k=0}^{m_{i+1}-1} \frac{1}{a + s_i + k} \quad (\text{B.79})$$

$$\Delta_2 = \Delta_2^1 + \Delta_2^2 + \Delta_2^3 \quad (\text{B.80})$$

where

$$\Delta_2^1 = a [\psi(a + s_i + 1) - \psi(a + f_i + 1)] \quad (\text{B.81})$$

$$= a [\psi(a + s_i + 1) - \psi(a + s_i + m_{i+1} + 1 - 1)] = \sum_{k=0}^{m_{i+1}-2} \frac{-a}{a + s_i + k + 1} \quad (\text{B.82})$$

$$\Delta_2^2 = s_i [\psi(a + s_i + 1) - \psi(a + s_i)] = \sum_{k=0}^0 \frac{s_i}{a + s_i + k} = \frac{s_i}{a + s_i} \quad (\text{B.83})$$

$$\Delta_2^3 = f_i - s_i = m_{i+1} - 1. \quad (\text{B.84})$$

Here,  $\psi(x)$ , is the digamma-function where

$$\psi(x) = \frac{d}{dx} \ln(\Gamma(x)) = \frac{\Gamma'(x)}{\Gamma(x)}, \quad (\text{B.85})$$

$$\psi(x + 1) = \psi(x) + \frac{1}{x}, \quad (\text{B.86})$$

$$\text{and} \quad (\text{B.87})$$

$$\psi(x + N) - \psi(x) = \sum_{k=0}^{N-1} \frac{1}{x + k}. \quad (\text{B.88})$$

## C Energy Calibration of SPI

SPI calibration is routinely and automatedly performed at the INTEGRAL Science Data Centre (ISDC) which is attached to the Astronomical Observatory of the University of Geneva. The raw data from the low- (18-2000 keV) and high-energy (2000-8000 keV) range are binned into spectra of 16384 physical channels each for all detectors. ISDC is using a set of 16 known instrumental background lines to calibrate the low-energy range, and two to three lines for the high-energy range. In particular, for a each of the lines with known laboratory peak energies, pre-defined windows of channels are selected for each revolution and each detector in order to fit the spectra with one symmetric Gaussian on top of a straight line. For one revolution and detector, this obtains 16 peak positions in channel space which are calibrated against the 16 known laboratory energies with the function

$$E = \sum_{i=-1}^2 C_i x^i, \quad (\text{C.1})$$

where  $x$  is the channel number, and the  $C_i$  are the determined calibration gain factors. Due to cosmic-ray bombardment, the detectors degrade over time which results in asymmetric gamma-ray line shapes. As a consequence of the calibration with symmetric Gaussians, the peak positions in energy space shift over time as shown in Fig. 3.19. Annealing phases twice a year restore the lattice structures of the Ge detectors, the lines become more symmetric again, and the shift is reset. During the normal operations, however, the line drift is of the order of 0.01% or  $30 \text{ km s}^{-1}$  which has to be taken into account as systematic uncertainty. Compared to the statistical uncertainties, the systematics outweigh by a factor of 2 to 5. The drift is caused by the fact that also in channel space, the lines degrade and the peak positions are shifted towards smaller values. As the now off centred lines are assumed to still be aligned with the laboratory energies, the calibration leads to line shifts in the opposite direction so that with ongoing mission duration, the line peaks are found at larger and larger energies.

An alternative to using the symmetric Gaussians in pre-defined channels, the physically motivated degraded line shape,  $L(x)$ , from Eq. 3.19 could be used already in the calibration step to counteract the energy drift and to reduce the systematic uncertainty. The function  $L(x)$  has the advantage that the true peak position, i.e. where the line should actually be centred on, can be inferred from the fitted parameters. For small values of the degradation parameter  $\tau$ , the peak position of the degraded Gaussian line is determined by  $E_{peak} \approx E_0 - \tau$ , Eq. (3.21). The true laboratory energy in this approximation would then be exactly the fitted parameter  $E_0$  so that a calibration using this parameter instead of  $E_{peak}$  (which is the same when using the symmetric or the asymmetric Gaussian for small enough windows)

would avoid the energy drift to first order. As  $\tau$  is increasing with energy, the approximate formula is not appropriate at higher energies, and a thorough calibration requires a more precise treatment. In addition to one degraded Gaussian for the determination of the strongest line peak, several low-intensity lines should be used to stabilise the fit and not skew the peak position if there are line complexes. Finally, there should be consistency in the usage of line shape parameters over energy and time during the calibration so that in principle,  $\tau$  should increase with energy and time at least linearly, and  $\sigma$  should show its typical square-root behaviour along the energy scale, and as the intrinsic detector resolution should stay constant in time, except that over the long mission duration, also the intrinsic line widths become broader. Using the instrumental response line data base in a re-processing step to disentangle the time- and energy-dependent coefficients for  $\sigma$  and  $\tau$ , a well-defined energy calibration could be provided in future works.

## D Bibliography

- Abbott, B. P., Abbott, R., Abbott, T. D., et al. 2016, *Physical Review Letters*, 116, 061102
- Abdo, A. A., Ackermann, M., Ajello, M., et al. 2009, *Physical Review Letters*, 102, 181101
- Abdo, A. A., Ackermann, M., Ajello, M., et al. 2010, *ApJ*, 709, L152
- Ackermann, M., Ajello, M., Allafort, A., et al. 2013, *Science*, 339, 807
- Ackermann, M., Ajello, M., Allafort, A., et al. 2012, *ApJ*, 755, 164
- Ackermann, M., Albert, A., Anderson, B., et al. 2014, *Phys. Rev. D*, 89, 042001
- Ackermann, M., Albert, A., Atwood, W. B., et al. 2016, *A&A*, 586, A71
- Adams, F. C. & Laughlin, G. 1997, *Reviews of Modern Physics*, 69, 337
- Adkins, G. S. & Brown, F. R. 1983, *Phys. Rev. A*, 28, 1164
- Adkins, G. S., Fell, R. N., & Sapirstein, J. 2000, *Physical Review Letters*, 84, 5086
- Adriani, O., Barbarino, G. C., Bazilevskaya, G. A., et al. 2013, *Physical Review Letters*, 111, 081102
- Adriani, O., Barbarino, G. C., Bazilevskaya, G. A., et al. 2009, *Nature*, 458, 607
- Agrinier, B., Masnou, J. L., Parlier, B., et al. 1990, *ApJ*, 355, 645
- Aguilar, M., Alberti, G., Alpat, B., et al. 2013, *Physical Review Letters*, 110, 141102
- Aharonian, F., Akhperjanian, A., Barrio, J., et al. 2001, *A&A*, 370, 112
- Aharonian, F., Akhperjanian, A. G., Anton, G., et al. 2009, *A&A*, 508, 561
- Aharonian, F. A. & Atoyan, A. M. 1981, *Physics Letters B*, 99, 301
- Aharonian, F. A. & Atoyan, A. M. 2000, *A&A*, 362, 937
- Aharonian, F. A., Atoyan, A. M., & Voelk, H. J. 1995, *A&A*, 294, L41
- Al-Ramadhan, A. H. & Gidley, D. W. 1994, *Physical Review Letters*, 72, 1632
- Alexis, A., Jean, P., Martin, P., & Ferrière, K. 2014, *A&A*, 564, A108
- Alpher, R. A., Bethe, H., & Gamow, G. 1948, *Phys. Rev.*, 73, 803
- Ambrosanio, S. & Mele, B. 1996, *Phys. Rev. D*, 53, 2541
- Anderson, C. D. 1933, *Physical Review*, 43, 491
- Andresen, G. B., Ashkezari, M. D., Baquero-Ruiz, M., et al. 2010, *Nature*, 468, 673
- Angle, J., Aprile, E., Arneodo, F., et al. 2008, *Phys. Rev. Lett.*, 100, 021303
- Antipov, Y. M. et al. 1970, *Yad. Fiz.*, 12, 311
- Armour, E. A. G., Baker, D. J., & Plummer, M. 1990, *Journal of Physics B Atomic Molecular Physics*, 23, 3057
- Arnett, W. D. 1969a, *Ap&SS*, 5, 180
- Arnett, W. D. 1969b, *ApJ*, 157, 1369
- Arnett, W. D. 1982, *ApJ*, 253, 785
- Arnett, W. D. & Truran, J. W. 1969, *ApJ*, 157, 339
- Arsenescu, R., Baglin, C., Beck, H. P., et al. 2003, *New Journal of Physics*, 5, 1
- Asai, S., Orito, S., & Shinohara, N. 1995, *Physics Letters B*, 357, 475
- Ascasibar, Y., Jean, P., Boehm, C., & Knödseder, J. 2006, *MNRAS*, 368, 1695
- Ashworth, Jr., W. B. 1980, *Journal for the History of Astronomy*, 11, 1
- Attíe, D., Cordier, B., Gros, M., et al. 2003, *A&A*, 411, L71
- Atwood, W. B., Abdo, A. A., Ackermann, M., et al. 2009, *ApJ*, 697, 1071

- Baade, W. & Zwicky, F. 1934, Contributions from the Mount Wilson Observatory, vol. 3, pp.79-83, 3, 79
- Baganoff, F. K., Maeda, Y., Morris, M., et al. 2003, ApJ, 591, 891
- Bandyopadhyay, R. M., Silk, J., Taylor, J. E., & Maccarone, T. J. 2009, MNRAS, 392, 1115
- Bardon, M., Norton, P., Peoples, J., Sachs, A. M., & Lee-Franzini, J. 1965, Physical Review Letters, 14, 449
- Battaglia, G., Tolstoy, E., Helmi, A., et al. 2011, MNRAS, 411, 1013
- Baur, G., Boero, G., Brauksiepe, S., et al. 1996, Physics Letters B, 368, 251
- Bařer, V. N. & Katkov, V. M. 1968, Soviet Journal of Experimental and Theoretical Physics, 26, 854
- Bé, M.-M., Chisté, V., Dulieu, C., et al. 2016, Monographie BIPM-5, Vol. 8, Table of Radionuclides (Pavillon de Breteuil, F-92310 Sèvres, France: Bureau International des Poids et Mesures)
- Beacom, J. F. & Yüksel, H. 2006, Physical Review Letters, 97, 071102
- Bekki, K. & Stanimirović, S. 2009, MNRAS, 395, 342
- Beloborodov, A. M. 1999a, in Astronomical Society of the Pacific Conference Series, Vol. 161, High Energy Processes in Accreting Black Holes, ed. J. Poutanen & R. Svensson, 295
- Beloborodov, A. M. 1999b, MNRAS, 305, 181
- Beloborodov, A. M. 1999c, ApJ, 510, L123
- Belokurov, V., Walker, M. G., Evans, N. W., et al. 2008, ApJ, 686, L83
- Belokurov, V., Walker, M. G., Evans, N. W., et al. 2010, ApJ, 712, L103
- Belokurov, V., Walker, M. G., Evans, N. W., et al. 2009, MNRAS, 397, 1748
- Belokurov, V., Zucker, D. B., Evans, N. W., et al. 2007, ApJ, 654, 897
- Belokurov, V., Zucker, D. B., Evans, N. W., et al. 2006, ApJ, 647, L111
- Bennett, C. L., Larson, D., Weiland, J. L., et al. 2013, ApJS, 208, 20
- Berezinskii, V. S., Bulanov, S. V., Dogiel, V. A., & Ptuskin, V. S. 1990, Astrophysics of cosmic rays
- Berger, M. J. & Seltzer, S. M. 1964, NASA Special Publication, 3012
- Bergstrom, Jr., P. M., Kissel, L., & Pratt, R. H. 1996, Phys. Rev. A, 53, 2865
- Berko, S. & Pendleton, H. N. 1980, Annual Review of Nuclear and Particle Science, 30, 543
- Bertone, G., Kusenko, A., Palomares-Ruiz, S., Pascoli, S., & Semikoz, D. 2006, Physics Letters B, 636, 20
- Bethe, H. & Heitler, W. 1934, Proceedings of the Royal Society of London Series A, 146, 83
- Bethe, H. A. 1935, Proceedings of the Royal Society of London Series A, 150, 129
- Bhabha, H. J. 1936, Proceedings of the Royal Society of London Series A, 154, 195
- Bhatia, A. K., Drachman, R. J., & Temkin, A. 1974, Phys. Rev. A, 9, 223
- Bhatia, A. K., Drachman, R. J., & Temkin, A. 1977, Phys. Rev. A, 16, 1719
- Biasini, M., Ferro, G., Monge, M. A., Di Francia, G., & La Ferrara, V. 2000, Journal of Physics Condensed Matter, 12, 5961
- Billard, J., Figueroa-Feliciano, E., & Strigari, L. 2014, Phys. Rev. D, 89, 023524
- Billoire, A., Lacaze, R., Morel, A., & Navelet, H. 1978, Physics Letters B, 78, 140
- Binney, J. & Merrifield, M. 1998, Galactic Astronomy
- Bisnovatyi-Kogan, G. S. & Pozanenko, A. S. 2016, ArXiv e-prints
- Blaauw, A. 1964, ARA&A, 2, 213
- Blandford, R. D. & Znajek, R. L. 1977, MNRAS, 179, 433
- Bœhm, C. & Fayet, P. 2004, Nuclear Physics B, 683, 219

- Boehm, C., Hooper, D., Silk, J., Casse, M., & Paul, J. 2004, *Physical Review Letters*, 92, 101301
- Bøehm, C. & Silk, J. 2008, *Physics Letters B*, 661, 287
- Boggs, S. E., Harrison, F. A., Miyasaka, H., et al. 2015, *Science*, 348, 670
- Bouchet, L., Jourdain, E., & Roques, J.-P. 2015, *ApJ*, 801, 142
- Bouchet, L., Mandrou, P., Roques, J. P., et al. 1991, *ApJ*, 383, L45
- Bouchet, L., Roques, J. P., & Jourdain, E. 2010, *ApJ*, 720, 1772
- Bouchet, L., Strong, A. W., Porter, T. A., et al. 2011, *ApJ*, 739, 29
- Boudaud, M., Aupetit, S., Caroff, S., et al. 2015, *A&A*, 575, A67
- Bray, J. C. & Eldridge, J. J. 2016, *MNRAS*, 461, 3747
- Broda, K. W. & Johnson, W. R. 1972, *Phys. Rev. A*, 6, 1693
- Brown, A. G. A., de Geus, E. J., & de Zeeuw, P. T. 1994, *A&A*, 289, 101
- Brown, A. G. A., Hartmann, D., & Burton, W. B. 1995, *A&A*, 300, 903
- Brown, B. L. & Leventhal, M. 1987, *ApJ*, 319, 637
- Burkert, A. 1995, *ApJ*, 447, L25
- Burrows, A. 2013, *Reviews of Modern Physics*, 85, 245
- Burrows, D. N., Michael, E., Hwang, U., et al. 2000, *ApJ*, 543, L149
- Bussard, R. W., Ramaty, R., & Drachman, R. J. 1979, *ApJ*, 228, 928
- Campbell, C. P., McAlinden, M. T., Kernoghan, A. A., & Walters, H. R. J. 1998, *Nuclear Instruments and Methods in Physics Research B*, 143, 41
- Campeanu, R. I. & Humberston, J. W. 1977, *Journal of Physics B Atomic Molecular Physics*, 10, L153
- Caputo, F., Cassisi, S., Castellani, M., Marconi, G., & Santolamazza, P. 1999, *AJ*, 117, 2199
- Carlin, J. L., Grillmair, C. J., Muñoz, R. R., Nidever, D. L., & Majewski, S. R. 2009, *ApJ*, 702, L9
- Caroli, E., Stephen, J. B., Di Cocco, G., Natalucci, L., & Spizzichino, A. 1987, *Space Sci. Rev.*, 45, 349
- Carpenter, J. M. 2001, *AJ*, 121, 2851
- Carvalho, P., Rocha, G., & Hobson, M. P. 2009, *MNRAS*, 393, 681
- Carvalho, P., Rocha, G., Hobson, M. P., & Lasenby, A. 2012, *MNRAS*, 427, 1384
- Casares, J., Charles, P. A., Jones, D. H. P., Rutten, R. G. M., & Callanan, P. J. 1991, *MNRAS*, 250, 712
- Casares, J., Charles, P. A., & Naylor, T. 1992, *Nature*, 355, 614
- Cash, W. 1979, *ApJ*, 228, 939
- Cassidy, D. B., Hisakado, T. H., Tom, H. W. K., & Mills, Jr., A. P. 2012, *Physical Review Letters*, 108, 133402
- Cassidy, D. B. & Mills, A. P. 2007, *Nature*, 449, 195
- Castor, J. I., Abbott, D. C., & Klein, R. I. 1975, *ApJ*, 195, 157
- Chandrasekhar, S. 1931, *The London, Edinburgh, and Dublin Philosophical Magazine and Journal of Science*, 11, 592
- Charman, A. E. 2013, *Nature Communications*, 4, 1785
- Cheng, K. S., Chernyshov, D. O., & Dogiel, V. A. 2006, *ApJ*, 645, 1138
- Cheng, K. S., Chernyshov, D. O., & Dogiel, V. A. 2007, *A&A*, 473, 351
- Cheng, K. S., Ho, C., & Ruderman, M. 1986, *ApJ*, 300, 500
- Cheng, L. X., Leventhal, M., Smith, D. M., et al. 1998, *ApJ*, 503, 809
- Chernyshov, D., Cheng, K. S., Dogiel, V., Ko, C. M., & Ip, W. H. 2009, in *The Extreme Sky: Sampling the Universe above 10 keV*, 75
- Christodoulou, A. S. 2016, *Positron Annihilation Spectroscopy of SN2014J*
- Churazov, E., Sazonov, S., Tsygankov, S., Sunyaev, R., & Varshalovich, D. 2011,

- MNRAS, 411, 1727
- Churazov, E., Sunyaev, R., Sazonov, S., Revnivtsev, M., & Varshalovich, D. 2005, MNRAS, 357, 1377
- Clayton, D. D. 1971, Nature, 234, 291
- Clayton, D. D. 1973, Nature Physical Science, 244, 137
- Clementini, G., Cignoni, M., Contreras Ramos, R., et al. 2012, ApJ, 756, 108
- Coleman, M. G., Jordi, K., Rix, H.-W., Grebel, E. K., & Koch, A. 2007, AJ, 134, 1938
- Corbel, S., Kaaret, P., Jain, R. K., et al. 2001, ApJ, 554, 43
- Cordier, B., Attié, D., Cassé, M., et al. 2004, in ESA Special Publication, Vol. 552, 5th INTEGRAL Workshop on the INTEGRAL Universe, ed. V. Schoenfelder, G. Lichti, & C. Winkler, 581
- Cork, B., Lambertson, G. R., Piccioni, O., & Wenzel, W. A. 1956, Phys. Rev., 104, 1193
- Correnti, M., Bellazzini, M., & Ferraro, F. R. 2009, MNRAS, 397, L26
- Cote, S., Freeman, K. C., Carignan, C., & Quinn, P. J. 1997, AJ, 114, 1313
- Cotton, W. D., Condon, J. J., & Arbizzani, E. 1999, ApJS, 125, 409
- Craig, N. 2013, ArXiv e-prints, arXiv:1309.0528v2
- Crannell, C. J., Joyce, G., Ramaty, R., & Wertz, C. 1976, ApJ, 210, 582
- Crivelli, P., Cooke, D. A., & Friedreich, S. 2014, International Journal of Modern Physics Conference Series, 30, 1460257
- Crocker, R. M., Ruitter, A. J., Seitenzahl, I. R., et al. 2016, ArXiv e-prints, arXiv:1607.03495
- Cutri, R. M., Skrutskie, M. F., van Dyk, S., et al. 2003, VizieR Online Data Catalog, 2246
- Czarnecki, A. & Karshenboim, S. G. 1999, ArXiv High Energy Physics - Phenomenology e-prints
- Czarnecki, A., Melnikov, K., & Yelkhovsky, A. 1999, Physical Review Letters, 83, 1135
- Dall’Ora, M., Clementini, G., Kinemuchi, K., et al. 2006, ApJ, 653, L109
- Dall’Ora, M., Kinemuchi, K., Ripepi, V., et al. 2012, ApJ, 752, 42
- Dame, T. M., Hartmann, D., & Thaddeus, P. 2001, ApJ, 547, 792
- Dario Serpico, P. & Hooper, D. 2009, New Journal of Physics, 11, 105010
- Daugherty, J. K. & Harding, A. K. 1983, ApJ, 273, 761
- Daylan, T., Finkbeiner, D. P., Hooper, D., et al. 2016, Physics of the Dark Universe, 12, 1
- De Angelis, A., Galanti, G., & Roncadelli, M. 2013, MNRAS, 432, 3245
- de Jong, J. T. A., Martin, N. F., Rix, H.-W., et al. 2010, ApJ, 710, 1664
- de Jong, J. T. A., Rix, H.-W., Martin, N. F., et al. 2008, AJ, 135, 1361
- de Shong, J. A., Hildebrand, R. H., & Meyer, P. 1964, Physical Review Letters, 12, 3
- Dehnen, W. & Binney, J. J. 1998, MNRAS, 298, 387
- della Valle, M. & Livio, M. 1994, A&A, 286, 786
- Della Valle, M. & Livio, M. 1998, ApJ, 506, 818
- Deutsch, M. 1951, Physical Review, 82, 455
- Di Mauro, M., Donato, F., Fornengo, N., Lineros, R., & Vittino, A. 2014, J. Cosmology Astropart. Phys., 4, 006
- Diehl, R. 2002, New A Rev., 46, 547
- Diehl, R., Dupraz, C., Bennett, K., et al. 1995, A&A, 298, 445
- Diehl, R., Halloin, H., Kretschmer, K., et al. 2006, Nature, 439, 45

- Diehl, R., Lang, M. G., Martin, P., et al. 2010, *A&A*, 522, A51
- Diehl, R., Siegert, T., Hillebrandt, W., et al. 2014, *Science*, 345, 1162
- Diehl, R., Siegert, T., Hillebrandt, W., et al. 2015, *A&A*, 574, A72
- Dirac, P. A. M. 1926, *Proceedings of the Royal Society of London Series A*, 112, 661
- Dirac, P. A. M. 1928, *Proceedings of the Royal Society of London A: Mathematical, Physical and Engineering Sciences*, 117, 610
- Dirac, P. A. M. 1930, *Proceedings of the Cambridge Philosophical Society*, 26, 361
- Dirac, P. A. M. 1930, *Proceedings of the Royal Society of London A: Mathematical, Physical and Engineering Sciences*, 126, 360
- Djouadi, A., Mambrini, Y., & Mühlleitner, M. 2001, *European Physical Journal C*, 20, 563
- Done, C., Gierliński, M., & Kubota, A. 2007, *A&A Rev.*, 15, 1
- Dong, S., Shappee, B. J., Prieto, J. L., et al. 2016, *Science*, 351, 257
- Dorfan, D. E., Eades, J., Lederman, L. M., Lee, W., & Ting, C. C. 1965, *Phys. Rev. Lett.*, 14, 1003
- Drachman, R. J. 1983, in *American Institute of Physics Conference Series*, Vol. 101, *Positron-Electron Pairs in Astrophysics*, ed. M. L. Burns, A. K. Harding, & R. Ramaty, 242–252
- Drachman, R. J., Omidvar, K., & McGuire, J. H. 1976, *Phys. Rev. A*, 14, 100
- Drees, M. & Nojiri, M. M. 1993, *Phys. Rev. D*, 47, 376
- Dudziak, W. F., Sagane, R., & Vedder, J. 1959, *Physical Review*, 114, 336
- Einstein, A. 1905, *Annalen der Physik*, 323, 639
- Einstein, A. 1911, *Annalen der Physik*, 340, 898
- Elwert, G. 1939, *Annalen der Physik*, 426, 178
- Endt, P. M. 1998, *Nuclear Physics A*, 633, 1
- Erber, T. 1966, *Reviews of Modern Physics*, 38, 626
- Eriksen, K. A., Arnett, D., McCarthy, D. W., & Young, P. 2009, *ApJ*, 697, 29
- Esin, A. A., McClintock, J. E., Drake, J. J., et al. 2001, *ApJ*, 555, 483
- Evans, I. N., Primini, F. A., Glotfelty, K. J., et al. 2010, *ApJS*, 189, 37
- Evans, N. W., Sanders, J. L., & Geringer-Sameth, A. 2016, *Phys. Rev. D*, 93, 103512
- Fabian, A. C., Lohfink, A., Kara, E., et al. 2015, *MNRAS*, 451, 4375
- Faherty, J., Walter, F. M., & Anderson, J. 2007, *Ap&SS*, 308, 225
- Falco, E. E., Kurtz, M. J., Geller, M. J., et al. 1999, *PASP*, 111, 438
- Fatuzzo, M., Melia, F., & Rafelski, J. 2001, *ApJ*, 549, 293
- Feast, M. W. & Walker, A. R. 1987, *ARA&A*, 25, 345
- Fellhauer, M., Evans, N. W., Belokurov, V., et al. 2007, *MNRAS*, 375, 1171
- Fellhauer, M., Wilkinson, M. I., Evans, N. W., et al. 2008, *MNRAS*, 385, 1095
- Fender, R. P., Belloni, T. M., & Gallo, E. 2004, *MNRAS*, 355, 1105
- Fermi, E. 1926, *Rend. Accad. Lincei*, 3, 145
- Fermi, E. 1949, *Physical Review*, 75, 1169
- Fermi, E., ed. 1950, *Nuclear physics*
- Ferrell, R. A. 1956, *Reviews of Modern Physics*, 28, 308
- Ferrer, F. & Vachaspati, T. 2005, *Physical Review Letters*, 95, 261302
- Ferrer, F. & Vachaspati, T. 2007, *International Journal of Modern Physics D*, 16, 2399
- Ferrière, K. M. 2001, *Reviews of Modern Physics*, 73, 1031
- Feynman, R. P. 1949, *Physical Review*, 76, 749
- Fields, B. & Sarkar, S. 2006, *ArXiv Astrophysics e-prints*, arXiv:0601514
- Filippenko, A. V. 1997, *ARA&A*, 35, 309
- Filk, T. & Close, F. 2010, *Antimaterie* (Spektrum Akademischer Verlag)

- Fink, M., Hillebrandt, W., & Röpke, F. K. 2007, *A&A*, 476, 1133
- Fink, M., Röpke, F. K., Hillebrandt, W., et al. 2010, *A&A*, 514, A53
- Finkbeiner, D. P. 2004, *ApJ*, 614, 186
- Finkbeiner, D. P. & Weiner, N. 2007, *Phys. Rev. D*, 76, 083519
- Firestone, R. 2003, Overview of Nuclear Data, Website, available online at <http://www.escholarship.org/uc/item/7p80t5p0>; visited on August 14th 2013.
- Firestone, R., Shirley, V., Baglin, C., Chu, S., & Zipkin, J. 1996, *Table of Isotopes* (Wiley)
- Fomalont, E. B. 1968, *Bull. Astron. Inst. Netherlands*, 20, 69
- Fox, P. J., Jung, G., Sorensen, P., & Weiner, N. 2014, ArXiv e-prints, arXiv:1401.0216
- Frieden, B. R. 1972, *Journal of the Optical Society of America* (1917-1983), 62, 511
- Friedman, A. 1922, *Zeitschrift für Physik*, 10, 377
- Frontera, F., Zdziarski, A. A., Amati, L., et al. 2001, *ApJ*, 561, 1006
- Fryer, C., Young, P., Bennet, M. E., et al. 2008, in *Nuclei in the Cosmos (NIC X)*, 101
- Gallart, C., Martínez-Delgado, D., Gómez-Flechoso, M. A., & Mateo, M. 2001, *AJ*, 121, 2572
- Gallo, E., Fender, R. P., & Pooley, G. G. 2003, *MNRAS*, 344, 60
- Gamow, G. 1946, *Phys. Rev.*, 70, 572
- Gandhi, P., Littlefair, S. P., Hardy, L. K., et al. 2016, *MNRAS*, 459, 554
- Genzel, R., Eisenhauer, F., & Gillessen, S. 2010, *Reviews of Modern Physics*, 82, 3121
- George, M. R., Fabian, A. C., Baumgartner, W. H., Mushotzky, R. F., & Tueller, J. 2008, *MNRAS*, 388, L59
- Geringer-Sameth, A., Walker, M. G., Koushiappas, S. M., et al. 2015, *Physical Review Letters*, 115, 081101
- Ghaempanah, M. 2016, 511 keV D3PO SPI Analysis, personal communication
- Giacconi, R., Gursky, H., Paolini, F. R., & Rossi, B. B. 1962, *Physical Review Letters*, 9, 439
- Gierliński, M., Zdziarski, A. A., Poutanen, J., et al. 1999, *MNRAS*, 309, 496
- Gil-Pons, P., García-Berro, E., José, J., Hernanz, M., & Truran, J. W. 2003, *A&A*, 407, 1021
- Gilfanov, M. 2004, *MNRAS*, 349, 146
- Gillessen, S., Eisenhauer, F., Fritz, T. K., et al. 2009, *ApJ*, 707, L114
- Ginzburg, V. L. 1979, *Theoretical physics and astrophysics*
- Gninenko, S. N., Krasnikov, N. V., Matveev, V. A., & Rubbia, A. 2006, *Physics of Particles and Nuclei*, 37, 321
- Goldwurm, A., Ballet, J., Cordier, B., et al. 1992, *ApJ*, 389, L79
- Goobar, A., Johansson, J., Amanullah, R., et al. 2014, *ApJ*, 784, L12
- Goodenough, L. & Hooper, D. 2009, ArXiv e-prints, arXiv:0910.2998
- Gould, R. J. 1989, *ApJ*, 344, 232
- Grcevich, J. & Putman, M. E. 2009, *ApJ*, 696, 385
- Green, D. A. 2002, *Highlights of Astronomy*, 12, 350
- Grefenstette, B. W., Harrison, F. A., Boggs, S. E., et al. 2014, *Nature*, 506, 339
- Greiner, W., Bromley, D., & Reinhardt, J. 2012, *Quantum Electrodynamics* (Springer Berlin Heidelberg)
- Greisen, K. 1966, *Physical Review Letters*, 16, 748
- Griffiths, D. 1987, *Introduction to Elementary Particles*, 400
- Grillmair, C. J. 2009, *ApJ*, 693, 1118

- Guessoum, N., Jean, P., & Gillard, W. 2005, *A&A*, 436, 171
- Guessoum, N., Jean, P., & Prantzos, N. 2006, *A&A*, 457, 753
- Guessoum, N., Ramaty, R., & Lingenfelter, R. E. 1991, *ApJ*, 378, 170
- Guglielmetti, F., Fischer, R., & Dose, V. 2009, *MNRAS*, 396, 165
- Gullieuszik, M., Held, E. V., Rizzi, L., et al. 2008, *MNRAS*, 388, 1185
- Gunion, J. F., Hooper, D., & McElrath, B. 2006, *Phys. Rev. D*, 73, 015011
- Halpern, J. P. & Ruderman, M. 1993, *ApJ*, 415, 286
- Harding, A. K. 1981, *ApJ*, 247, 639
- Harding, A. K. & Lai, D. 2006, *Reports on Progress in Physics*, 69, 2631
- Harris, M. J., Share, G. H., & Leising, M. D. 1994, *ApJ*, 433, 87
- Hartman, R. C., Bertsch, D. L., Bloom, S. D., et al. 1999, *ApJS*, 123, 79
- Haslam, C. G. T., Klein, U., Salter, C. J., et al. 1981, *A&A*, 100, 209
- Haslam, C. G. T., Salter, C. J., Stoffel, H., & Wilson, W. E. 1982, *A&AS*, 47, 1
- Haug, E. 1975, *Zeitschrift Naturforschung Teil A*, 30, 1099
- Haug, E. & Nakel, W. 2004, *The Elementary Process of Bremsstrahlung*. Series: World Scientific Lecture Notes in Physics, ISBN: 9789812795007. World Scientific Publishing Co. Pte. Ltd., ed. Eberhard Haug & Werner Nakel, 73
- Hauser, M. G., Arendt, R. G., Kelsall, T., et al. 1998, *ApJ*, 508, 25
- Haymes, R. C., Ellis, D. V., Fishman, G. J., Glenn, S. W., & Kurfess, J. D. 1969, *ApJ*, 157, 1455
- Heesen, V., Beck, R., Krause, M., & Dettmar, R.-J. 2009, *A&A*, 494, 563
- Heinz, S. & Sunyaev, R. 2002, *A&A*, 390, 751
- Heisenberg, W. 1927, *Zeitschrift für Physik*, 43, 172
- Heitler, W. 1954, *Quantum theory of radiation*
- Hernanz, M. 2005, in *Astronomical Society of the Pacific Conference Series*, Vol. 330, *The Astrophysics of Cataclysmic Variables and Related Objects*, ed. J.-M. Hameury & J.-P. Lasota, 265
- Hernanz, M. & José, J. 2006, *New A Rev.*, 50, 504
- Higdon, J. C., Lingenfelter, R. E., & Rothschild, R. E. 2009, *ApJ*, 698, 350
- Hillas, A. M. 2006, *ArXiv Astrophysics e-prints*, arXiv:0607109
- Hillebrandt, W., Kromer, M., Röpke, F. K., & Ruiter, A. J. 2013, *Frontiers of Physics*, 8, 116
- Hillebrandt, W. & Niemeyer, J. C. 2000, *ARA&A*, 38, 191
- Hofstadter, R. 1948, *Phys. Rev.*, 74, 100
- Hooper, D., Ferrer, F., Boehm, C., et al. 2004, *Physical Review Letters*, 93, 161302
- Hooper, D. & Wang, L.-T. 2004, *Phys. Rev. D*, 70, 063506
- Hubble, E. 1929, *Proceedings of the National Academy of Sciences*, 15, 168
- Huh, J.-H., Kim, J. E., Park, J.-C., & Park, S. C. 2008, *Phys. Rev. D*, 77, 123503
- Humberston, J. W., Van Reeth, P., Watts, M. S. T., & Meyerhof, W. E. 1997, *Journal of Physics B Atomic Molecular Physics*, 30, 2477
- Humberston, J. W. & Wallace, J. B. G. 1972, *Journal of Physics B Atomic Molecular Physics*, 5, 1138
- Humphreys, R. M. & Larsen, J. A. 1995, *AJ*, 110, 2183
- Ibata, R. A., Gilmore, G., & Irwin, M. J. 1994, *Nature*, 370, 194
- Irwin, M. J., Belokurov, V., Evans, N. W., et al. 2007, *ApJ*, 656, L13
- Irwin, M. J., Bunclark, P. S., Bridgeland, M. T., & McMahon, R. G. 1990, *MNRAS*, 244, 16P
- Isern, J., Bravo, E., & Hirschmann, A. 2008, *New A Rev.*, 52, 377
- Isern, J., Gómez-Gomar, J., Bravo, E., & Jean, P. 1997, in *ESA Special Publication*, Vol. 382, *The Transparent Universe*, ed. C. Winkler, T. J.-L. Courvoisier, &

- P. Durouchoux, 89
- Isern, J., Hernanz, M., & José, J. 2011, in *Lecture Notes in Physics*, Berlin Springer Verlag, Vol. 812, *Lecture Notes in Physics*, Berlin Springer Verlag, ed. R. Diehl, D. H. Hartmann, & N. Prantzos, 233–308
- Iwata, K., Greaves, R. G., & Surko, C. M. 1997, *Phys. Rev. A*, 55, 3586
- Iyudin, A. F., Diehl, R., Bloemen, H., et al. 1994, *A&A*, 284, L1
- Iyudin, A. F., Diehl, R., Lichti, G. G., et al. 1997, in *ESA Special Publication*, Vol. 382, *The Transparent Universe*, ed. C. Winkler, T. J.-L. Courvoisier, & P. Durouchoux, 37
- Janka, H.-T. 2012, *Annual Review of Nuclear and Particle Science*, 62, 407
- Janka, H.-T., Melson, T., & Summa, A. 2016, *ArXiv e-prints*, arXiv:1602.05576
- Jauch, J. & Rohrlich, F. 1955, *Theory of Photons & Electrons*, Addison-Wesley Series in advanced physics (Addison-Wesley Publishing Company)
- Jean, P., Knödlseeder, J., Gillard, W., et al. 2006, *A&A*, 445, 579
- Jean, P., Naya, J. E., & von Ballmoos, P. 1997, in *ESA Special Publication*, Vol. 382, *The Transparent Universe*, ed. C. Winkler, T. J.-L. Courvoisier, & P. Durouchoux, 635
- Ji, A. P., Frebel, A., Chiti, A., & Simon, J. D. 2016, *Nature*, 531, 610
- Jinnouchi, O., Asai, S., & Kobayashi, T. 2003, *Physics Letters B*, 572, 117
- Johnson, M. H. & Lippmann, B. A. 1949, *Physical Review*, 76, 828
- Johnson, W. N., Kurfess, J. D., Kinzer, R. L., Purcell, W. R., & Strickman, M. S. 1989, *NASA STI/Recon Technical Report N*, 91
- Johnson, III, W. N., Harnden, Jr., F. R., & Haymes, R. C. 1972, *ApJ*, 172, L1
- Johnson, W. R., Buss, D. J., & Carroll, C. O. 1964, *Physical Review*, 135, 1232
- José, J., Hernanz, M., García-Berro, E., & Gil-Pons, P. 2003, *ApJ*, 597, L41
- José, J., Hernanz, M., & Iliadis, C. 2006, *Nuclear Physics A*, 777, 550
- Joshi, Y. C. 2007, *MNRAS*, 378, 768
- Jost, R., Luttinger, J. M., & Slotnick, M. 1950, *Phys. Rev.*, 80, 189
- Jourdain, E. & Roques, J. P. 2009, *ApJ*, 704, 17
- Jourdain, E., Roques, J. P., & Malzac, J. 2012, *ApJ*, 744, 64
- Jung, G. V., Kurfess, D. J., Johnson, W. N., et al. 1995, *A&A*, 295, L23
- Jungman, G., Kamionkowski, M., & Griest, K. 1996, *Phys. Rep.*, 267, 195
- Kadyrov, A. S. & Bray, I. 2002, *Phys. Rev. A*, 66, 012710
- Karakas, A. I. & Lattanzio, J. C. 2014, *PASA*, 31, e030
- Karim, M. T. & Mamajek, E. 2016, *ArXiv e-prints*, arXiv:1610.08125
- Karshenboim, S. G. 1993, *Soviet Journal of Experimental and Theoretical Physics*, 76, 541
- Karshenboim, S. G. 2002, *Applied Surface Science*, 194, 307
- Karshenboim, S. G. 2004, *International Journal of Modern Physics A*, 19, 3879
- Kataoka, Y., Asai, S., & Kobayashi, T. 2009, *Physics Letters B*, 671, 219
- Kernoghan, A. A., Robinson, D. J. R., McAlinden, M. T., & Walters, H. R. J. 1996, *Journal of Physics B Atomic Molecular Physics*, 29, 2089
- Kerp, J., Winkel, B., Ben Bekhti, N., Flöer, L., & Kalberla, P. M. W. 2011, *Astronomische Nachrichten*, 332, 637
- Khan, P. & Ghosh, A. S. 1983, *Phys. Rev. A*, 27, 1904
- Khargharia, J., Froning, C. S., & Robinson, E. L. 2010, *ApJ*, 716, 1105
- Kimura, M., Isogai, K., Kato, T., et al. 2016, *Nature*, 529, 54
- King, A. L., Miller, J. M., Raymond, J., Reynolds, M. T., & Morningstar, W. 2015, *ApJ*, 813, L37
- Kinzer, R. L., Milne, P. A., Kurfess, J. D., et al. 2001, *ApJ*, 559, 282

- Kinzer, R. L., Purcell, W. R., & Kurfess, J. D. 1999, *ApJ*, 515, 215
- Kippenhahn, R. & Thomas, H.-C. 1978, *A&A*, 63, 265
- Kippenhahn, R. & Weigert, A. 1990, *Stellar Structure and Evolution*
- Kirby, E. N., Simon, J. D., & Cohen, J. G. 2015, *ArXiv e-prints*, arXiv:1506.01021
- Kitamoto, S., Tsunemi, H., Miyamoto, S., Yamashita, K., & Mizobuchi, S. 1989, *Nature*, 342, 518
- Klein, O. & Nishina, T. 1929, *Zeitschrift fur Physik*, 52, 853
- Klemperer, O. & Chadwick, J. 1934, *Proceedings of the Cambridge Philosophical Society*, 30, 347
- Kleyna, J. T., Wilkinson, M. I., Evans, N. W., & Gilmore, G. 2005, *ApJ*, 630, L141
- Klypin, A., Kravtsov, A. V., Valenzuela, O., & Prada, F. 1999, *ApJ*, 522, 82
- Knie, K., Korschinek, G., Faestermann, T., et al. 2004, *Physical Review Letters*, 93, 171103
- Knödlseeder, J., Bennett, K., Bloemen, H., et al. 1999, *A&A*, 344, 68
- Knödlseeder, J., Jean, P., Lonjou, V., et al. 2005, *A&A*, 441, 513
- Knoedlseeder, J. 2005, in *Internal INTEGRAL Science Workshop*, 28
- Knoedlseeder, J., Prantzos, N., Bennett, K., et al. 1996, *A&AS*, 120, 335
- Knoll, G. 2010, *Radiation Detection and Measurement* (John Wiley & Sons)
- Komatsu, E., Smith, K. M., Dunkley, J., et al. 2011, *The Astrophysical Journal Supplement Series*, 192, 18
- Koposov, S. E., Belokurov, V., Torrealba, G., & Evans, N. W. 2015a, *ApJ*, 805, 130
- Koposov, S. E., Belokurov, V., Torrealba, G., & Evans, N. W. 2015b, *ApJ*, 805, 130
- Koposov, S. E., Casey, A. R., Belokurov, V., et al. 2015c, *ArXiv e-prints*, arXiv:1504.07916
- Körding, E. G., Fender, R. P., & Migliari, S. 2006, *MNRAS*, 369, 1451
- Koribalski, B. S., Staveley-Smith, L., Kilborn, V. A., et al. 2004, *AJ*, 128, 16
- Kozyreva, A., Hirschi, R., Blinnikov, S., & den Hartogh, J. 2016, *MNRAS*, 459, L21
- Kraan-Korteweg, R. C. & Tammann, G. A. 1979, *Astronomische Nachrichten*, 300, 181
- Krane, K. 1987, *Introductory Nuclear Physics* (Wiley)
- Krause, M., Diehl, R., Böhringer, H., Freyberg, M., & Lubos, D. 2014, *A&A*, 566, A94
- Krause, M. G. H., Diehl, R., Bagetakos, Y., et al. 2015, *A&A*, 578, A113
- Krause, O., Birkmann, S. M., Usuda, T., et al. 2008, *Science*, 320, 1195
- Krause, O., Rieke, G. H., Birkmann, S. M., et al. 2005, *Science*, 308, 1604
- Kretschmer, K., Diehl, R., Krause, M., et al. 2013, *A&A*, 559, A99
- Kretschmer, K. A. 2011, *Dissertation*, Technische Universität München, München
- Krimm, H. A., Holland, S. T., Corbet, R. H. D., et al. 2013, *ApJS*, 209, 14
- Krolik, J. H. 1999, *Active galactic nuclei : from the central black hole to the galactic environment*
- Kromer, M., Sim, S. A., Fink, M., et al. 2010, *ApJ*, 719, 1067
- Kroupa, P. 2001, *MNRAS*, 322, 231
- Kuang, Y. R. & Gien, T. T. 1997, *Phys. Rev. A*, 55, 256
- Kuhlen, M., Diemand, J., & Madau, P. 2008, *ApJ*, 686, 262
- Kuhlen, M., Guedes, J., Pillepich, A., Madau, P., & Mayer, L. 2013, *ApJ*, 765, 10
- Kunder, A., Rich, R. M., Koch, A., et al. 2016, *ApJ*, 821, L25
- Kuraev, E. A. & Lipatov, L. N. 1974, *Yad.Fiz.*, 20, 112
- Landau, L. D. & Lifshitz, E. M. 1975, *The classical theory of fields*
- Larsson, S., Ryde, F., Borgonovo, L., et al. 2004, in *ESA Special Publication*, Vol. 552, 5th INTEGRAL Workshop on the INTEGRAL Universe, ed. V. Schoenfelder,

- G. Lichti, & C. Winkler, 649
- Lasota, J.-P. 2001, *New A Rev.*, 45, 449
- Law, W. Y. & Ritter, H. 1983, *A&A*, 123, 33
- Lee, M. G., Park, H. S., Park, J.-H., et al. 2003, *AJ*, 126, 2840
- Leibniz, G. 1714, *Leibniz' sogenannte Monadologie und Principes de la nature et de la grâce fondés en raison*. Herausgegeben von Clara Strack, etc. (Unveränderter photomechanischer Nachdruck, 1967.), Seminar B. Erdmann (Walter de Gruyter & Company)
- Lemaître, G. 1927, *Annales de la Société Scientifique de Bruxelles*, 47, 49
- Lemrani, R. 2006, *Physics of Atomic Nuclei*, 69, 1967
- Leventhal, M., MacCallum, C. J., & Stang, P. D. 1978, *ApJ*, 225, L11
- Li, W., Bloom, J. S., Podsiadlowski, P., et al. 2011, *Nature*, 480, 348
- Lichti, G. & Georgii, R. 2001, *Instruments*, ed. V. Schönfelder, 27–76
- Lightman, A. P. & Zdziarski, A. A. 1987, *ApJ*, 319, 643
- Lodders, K. 2003, *ApJ*, 591, 1220
- Longair, M. S. 1992, *High energy astrophysics. Vol.1: Particles, photons and their detection*, 436
- Longair, M. S. 1994, *High energy astrophysics. Vol.2: Stars, the galaxy and the interstellar medium*
- Longair, M. S. 2008, *Galaxy Formation*
- Lorimer, D. R. 2005, *Living Reviews in Relativity*, 8, 7
- Lucy, L. B. 1974, *AJ*, 79, 745
- Lugaro, M. & Chieffi, A. 2011, in *Lecture Notes in Physics*, Berlin Springer Verlag, Vol. 812, *Lecture Notes in Physics*, Berlin Springer Verlag, ed. R. Diehl, D. H. Hartmann, & N. Prantzos, 83–152
- Lund, N., Budtz-Jørgensen, C., Westergaard, N. J., et al. 2003, *A&A*, 411, L231
- Lyne, A. G. & Graham-Smith, F. 2006, *Pulsar Astronomy*
- Maciolek-Niedzwiecki, A., Zdziarski, A. A., & Coppi, P. S. 1995, *MNRAS*, 276, 273
- Madsen, N. 2010, *Philosophical Transactions of the Royal Society of London Series A*, 368, 3671
- Magkotsios, G., Timmes, F. X., Hungerford, A. L., et al. 2010, *ApJS*, 191, 66
- Mahoney, W. A., Ling, J. C., Wheaton, W. A., & Jacobson, A. S. 1984, *ApJ*, 286, 578
- Majewski, S. R., Skrutskie, M. F., Weinberg, M. D., & Ostheimer, J. C. 2003, *ApJ*, 599, 1082
- Makino, F. 1989, *IAU Circ.*, 4782
- Malyshev, D. & Hogg, D. W. 2011, *ApJ*, 738, 181
- Mandrou, P., Vedrenne, G., Jean, P., et al. 1997, in *ESA Special Publication*, Vol. 382, *The Transparent Universe*, ed. C. Winkler, T. J.-L. Courvoisier, & P. Durouchoux, 591
- Mannucci, F., Maoz, D., Sharon, K., et al. 2008, *MNRAS*, 383, 1121
- Markoff, S., Falcke, H., & Fender, R. 2001, *A&A*, 372, L25
- Martin, N. F., de Jong, J. T. A., & Rix, H.-W. 2008, *ApJ*, 684, 1075
- Martin, N. F., Ibata, R. A., Bellazzini, M., et al. 2004, *MNRAS*, 348, 12
- Martin, N. F., Ibata, R. A., Conn, B. C., et al. 2005, *MNRAS*, 362, 906
- Martin, P., Knödseder, J., Diehl, R., & Meynet, G. 2009, *A&A*, 506, 703
- Martin, P., Knödseder, J., Meynet, G., & Diehl, R. 2010, *A&A*, 511, A86
- Martin, P., Strong, A. W., Jean, P., Alexis, A., & Diehl, R. 2012, *A&A*, 543, A3
- Mas-Hesse, J. M., Giménez, A., Culhane, J. L., et al. 2003, *A&A*, 411, L261
- Massam, T., Muller, T., Righini, B., Schneegans, M., & Zichichi, A. 1965, *Il Nuovo*

- Cimento A, 63, 10
- Massaro, E., Matt, G., Salvati, M., et al. 1991, *ApJ*, 376, L11
- Mateo, M., Hurley-Keller, D., & Nemec, J. 1998, *AJ*, 115, 1856
- Mateo, M. L. 1998, *ARA&A*, 36, 435
- Matsunaga, N., Feast, M. W., & Soszyński, I. 2011, *MNRAS*, 413, 223
- McConnachie, A. W. 2012, *AJ*, 144, 4
- McConnell, M. L., Zdziarski, A. A., Bennett, K., et al. 2002, *ApJ*, 572, 984
- Meiksin, A. A. 2009, *Reviews of Modern Physics*, 81, 1405
- Mellinger, A. 2009, *PASP*, 121, 1180
- Melson, T., Janka, H.-T., Bollig, R., et al. 2015, *ApJ*, 808, L42
- Merritt, D., Graham, A. W., Moore, B., Diemand, J., & Terzić, B. 2006, *AJ*, 132, 2685
- Meynet, G., Georgy, C., Hirschi, R., et al. 2011, *Bulletin de la Societe Royale des Sciences de Liege*, 80, 266
- Michel, L. 1950, *Proceedings of the Physical Society A*, 63, 514
- Mikhailov, V. V., Adriani, O., Barbarino, G., et al. 2016, *Journal of Physics Conference Series*, 675, 032003
- Milgrom, M. 1983, *ApJ*, 270, 365
- Miller-Jones, J. C. A., Jonker, P. G., Dhawan, V., et al. 2009, *ApJ*, 706, L230
- Mills, A. P. 1981, *Phys. Rev. Lett.*, 46, 717
- Mills, A. P. 1983, *Phys. Rev. Lett.*, 50, 671
- Mills, A. P. & Crane, W. S. 1985, *Phys. Rev. A*, 31, 593
- Milne, P. A., The, L.-S., & Leising, M. D. 1999, *ApJS*, 124, 503
- Milne, P. A., The, L.-S., & Leising, M. D. 2001, *ApJ*, 559, 1019
- Mirabel, I. F. 1992, *The Messenger*, 70, 51
- Mirabel, I. F. & Rodríguez, L. F. 1998, *Nature*, 392, 673
- Mirabel, I. F. & Rodríguez, L. F. 1999, *ARA&A*, 37, 409
- Mirabel, I. F., Rodriguez, L. F., Cordier, B., Paul, J., & Lebrun, F. 1992, *Nature*, 358, 215
- Mishurov, Y. N. & Zenina, I. A. 1999, *A&A*, 341, 81
- Mitsou, V. A. 2015, *Journal of Physics Conference Series*, 651, 012023
- Mitsuda, K., Inoue, H., Koyama, K., et al. 1984, *PASJ*, 36, 741
- Mogensen, O., Pedersen, N., & Andersen, J. 1982, *Chemical Physics Letters*, 93, 115, cited By 9
- Mohapatra, R. N. 2009, *Journal of Physics G Nuclear Physics*, 36, 104006
- Mohorovičić, S. 1934, *Astronomische Nachrichten*, 253, 93
- Mohr, P. J., Newell, D. B., & Taylor, B. N. 2015, *ArXiv e-prints*, arXiv:1507.07956
- Moll, R. & Woosley, S. E. 2013, in *American Astronomical Society Meeting Abstracts*, Vol. 221, *American Astronomical Society Meeting Abstracts #221*, #253.22
- Møller, C. 1932, *Annalen der Physik*, 406, 531
- Monaco, L., Bellazzini, M., Ferraro, F. R., & Pancino, E. 2004, *MNRAS*, 353, 874
- Monge, M. A., Pareja, R., González, R., & Chen, Y. 1996, *Journal of Radioanalytical and Nuclear Chemistry*, 211, 23
- Moore, B., Ghigna, S., Governato, F., et al. 1999, *ApJ*, 524, L19
- Morris, M. & Serabyn, E. 1996, *ARA&A*, 34, 645
- Moskalenko, I. V., Porter, T. A., & Strong, A. W. 2006, *ApJ*, 640, L155
- Moskalenko, I. V. & Strong, A. W. 1998, *ApJ*, 493, 694
- Murphy, R. J., Share, G. H., Skibo, J. G., & Kozlovsky, B. 2005, *ApJS*, 161, 495
- Musella, I., Ripepi, V., Clementini, G., et al. 2009, *ApJ*, 695, L83

- Musella, I., Ripepi, V., Marconi, M., et al. 2012, *ApJ*, 756, 121
- Muta, T. & Niuya, T. 1982, *Progress of Theoretical Physics*, 68, 1735
- Nagataki, S., Hashimoto, M.-a., Sato, K., Yamada, S., & Mochizuki, Y. S. 1998, *ApJ*, 492, L45
- Namba, T. 2012, *Progress of Theoretical and Experimental Physics*, 2012, 04D003
- Narayan, R. & Yi, I. 1995, *ApJ*, 452, 710
- Navarro, J. F., Frenk, C. S., & White, S. D. M. 1996, *ApJ*, 462, 563
- Nielsen, M. T. B., Gilfanov, M., Bogdán, Á., Woods, T. E., & Nelemans, G. 2014, *MNRAS*, 442, 3400
- NNDC. 2016, National Nuclear Data Center - Table of Nuclides, Website, information extracted from the NuDat 2 database <http://www.nndc.bnl.gov/nudat2/>; visited 2016 August 29.
- Nomoto, K., Sugimoto, D., & Neo, S. 1976, *Ap&SS*, 39, L37
- Nomoto, K., Tanaka, M., Tominaga, N., & Maeda, K. 2010, *New A Rev.*, 54, 191
- Nomoto, K., Thielemann, F. K., & Sheeler, J. C. 1984, *ApJ*, 283, L25
- Norris, J. E., Gilmore, G., Wyse, R. F. G., Yong, D., & Frebel, A. 2010, *ApJ*, 722, L104
- Nugent, P. E., Sullivan, M., Cenko, S. B., et al. 2011, *Nature*, 480, 344
- Oberlack, U., Bennett, K., Bloemen, H., et al. 1996, *A&AS*, 120, C311
- Okamoto, S., Arimoto, N., Yamada, Y., & Onodera, M. 2008, *A&A*, 487, 103
- Okamoto, S., Arimoto, N., Yamada, Y., & Onodera, M. 2012, *ApJ*, 744, 96
- Olive, K. A. & Particle Data Group. 2014, *Chinese Physics C*, 38, 090001
- Oppenheimer, J. R. & Volkoff, G. M. 1939, *Physical Review*, 55, 374
- Oppermann, N., Selig, M., Bell, M. R., & Enßlin, T. A. 2013, *Phys. Rev. E*, 87, 032136
- Ore, A. & Powell, J. L. 1949, *Physical Review*, 75, 1696
- Parizot, E., Cassé, M., Lehoucq, R., & Paul, J. 2005, *A&A*, 432, 889
- Pauli, W. 1925, *Zeitschrift für Physik*, 31, 765
- Peñarrubia, J., McConnachie, A., & Babul, A. 2006, *ApJ*, 650, L33
- Penin, A. A. 2004, *International Journal of Modern Physics A*, 19, 3897
- Perl, M. L., Abrams, G. S., Boyarski, A. M., et al. 1975, *Physical Review Letters*, 35, 1489
- Perlmutter, S., Aldering, G., Goldhaber, G., et al. 1999, *ApJ*, 517, 565
- Piatek, S., Pryor, C., Bristow, P., et al. 2007, *AJ*, 133, 818
- Picciotto, C. & Pospelov, M. 2005, *Physics Letters B*, 605, 15
- Piper, J. 2009, *ArXiv e-prints*, arXiv:0906.3676
- Piro, A. L. & Bildsten, L. 2004, *ApJ*, 610, 977
- Planck Collaboration, Adam, R., Ade, P. A. R., et al. 2016a, *A&A*, 594, A1
- Planck Collaboration, Adam, R., Ade, P. A. R., et al. 2016b, *A&A*, 594, A10
- Planck Collaboration, Ade, P. A. R., Aghanim, N., et al. 2014a, *A&A*, 571, A1
- Planck Collaboration, Ade, P. A. R., Aghanim, N., et al. 2014b, *A&A*, 571, A16
- Plüschke, S. 2001, Dissertation, Technische Universität München, München
- Plüschke, S., Diehl, R., Schönfelder, V., et al. 2001, in *ESA Special Publication*, Vol. 459, *Exploring the Gamma-Ray Universe*, ed. A. Gimenez, V. Reglero, & C. Winkler, 55–58
- Polido, P., Jablonski, F., & Lépine, J. R. D. 2013, *ApJ*, 778, 32
- Pon, A., Johnstone, D., Bally, J., & Heiles, C. 2014, *MNRAS*, 444, 3657
- Popov, M. V., Filina, A. A., Baranov, A. A., Chardonnet, P., & Chechetkin, V. M. 2014, *ApJ*, 783, 43
- Poretti, E., Clementini, G., Held, E. V., et al. 2008, *ApJ*, 685, 947

- Portegies Zwart, S. F., Verbunt, F., & Ergma, E. 1997, *A&A*, 321, 207
- Porter, T. A., Moskalenko, I. V., Strong, A. W., Orlando, E., & Bouchet, L. 2008, *ApJ*, 682, 400
- Pospelov, M., Ritz, A., & Voloshin, M. 2008, *Physics Letters B*, 662, 53
- Prantzos, N. 2006, *A&A*, 449, 869
- Prantzos, N. 2008, *New A Rev.*, 52, 457
- Prantzos, N., Boehm, C., Bykov, A. M., et al. 2011, *Reviews of Modern Physics*, 83, 1001
- Pritchard, D. E. 1983, *Phys. Rev. Lett.*, 51, 1336
- Purcell, W. R., Cheng, L.-X., Dixon, D. D., et al. 1997, *ApJ*, 491, 725
- Quataert, E. 2004, *ApJ*, 613, 322
- Queloz, D., Dubath, P., & Pasquini, L. 1995, *A&A*, 300, 31
- Racah, G. 1936, *Il Nuovo Cimento (1924-1942)*, 13, 66
- Ramaty, R., Kozlovsky, B., & Lingenfelter, R. E. 1979, *ApJS*, 40, 487
- Ramaty, R. & Meszaros, P. 1981, *ApJ*, 250, 384
- Reed, J. E., Hester, J. J., Fabian, A. C., & Winkler, P. F. 1995, *ApJ*, 440, 706
- Rees, M. J. 1988, *Nature*, 333, 523
- Reid, N. & Majewski, S. R. 1993, *ApJ*, 409, 635
- Remazeilles, M., Dickinson, C., Banday, A. J., Bigot-Sazy, M.-A., & Ghosh, T. 2015, *MNRAS*, 451, 4311
- Remillard, R. A. & McClintock, J. E. 2006, *ARA&A*, 44, 49
- Renaud, M., Vink, J., Decourchelle, A., et al. 2006, *ApJ*, 647, L41
- Rest, A., Foley, R. J., Sinnott, B., et al. 2011, *ApJ*, 732, 3
- Rest, A., Welch, D. L., Suntzeff, N. B., et al. 2008, *ApJ*, 681, L81
- Ribó, M. 2002, PhD thesis, Departament d'Astronomia i Meteorologia, Universitat de Barcelona, Av. Diagonal 647, E-08028 Barcelona, Spain
- Richardson, W. H. 1972, *Journal of the Optical Society of America (1917-1983)*, 62, 55
- Richter, O.-G., Tammann, G. A., & Huchtmeier, W. K. 1987, *A&A*, 171, 33
- Riess, A. G., Filippenko, A. V., Challis, P., et al. 1998, *AJ*, 116, 1009
- Rodriguez, J., Cadolle Bel, M., Alfonso-Garzón, J., et al. 2015a, *A&A*, 581, L9
- Rodriguez, J., Grinberg, V., Laurent, P., et al. 2015b, *ArXiv e-prints*, arXiv:1505.02786
- Rogstad, D. H., Rougoor, G. W., & Whiteoak, J. B. 1967, *ApJ*, 150, 9
- Romani, R. W. 1992, *ApJ*, 399, 621
- Roques, J. P., Schanne, S., von Kienlin, A., et al. 2003, *A&A*, 411, L91
- Roth, J., Primbsch, J. H., & Lin, R. P. 1984, *IEEE Transactions on Nuclear Science*, 31, 367
- Ruiter, A. J., Belczynski, K., Sim, S. A., Seitenzahl, I. R., & Kwiatkowski, D. 2014, *MNRAS*, 440, L101
- Rybicki, G. B. & Lightman, A. P. 1979, *Radiative processes in astrophysics*
- Ryzhikh, G. G. & Mitroy, J. 2000, *Journal of Physics B Atomic Molecular Physics*, 33, 2229
- Sadowski, A., Ziółkowski, J., Belczyński, K., & Bulik, T. 2008, in *American Institute of Physics Conference Series*, Vol. 1010, *A Population Explosion: The Nature & Evolution of X-ray Binaries in Diverse Environments*, ed. R. M. Bandyopadhyay, S. Wachter, D. Gelino, & C. R. Gelino, 404–406
- Saito, S. L. 2000, *Nuclear Instruments and Methods in Physics Research Section B: Beam Interactions with Materials and Atoms*, 171, 60, low Energy Positron and Positronium Physics

- Sakharov, A. D. 1967, *Soviet Journal of Experimental and Theoretical Physics Letters*, 5, 24
- Sand, D. J., Strader, J., Willman, B., et al. 2012, *ApJ*, 756, 79
- Sasaki, Y., Nagai, Y., Ohkubo, H., et al. 2003, *Radiation Physics and Chemistry*, 68, 569
- Satapathy, U. C., Tripathy, D. N., & Rao, B. K. 1982, *Phys. Rev. A*, 25, 1431
- Sauter, F. 1934, *Annalen der Physik*, 412, 404
- Schoenfelder, V., Aarts, H., Bennett, K., et al. 1993, *ApJS*, 86, 657
- Schönrich, R., Binney, J., & Dehnen, W. 2010, *MNRAS*, 403, 1829
- Schrader, D. M., Jacobsen, F. M., Frandsen, N.-P., & Mikkelsen, U. 1992, *Phys. Rev. Lett.*, 69, 57
- Seaton, M. J. 1959, *MNRAS*, 119, 81
- Seitenzahl, I. R., Timmes, F. X., & Magkotsios, G. 2014, *ApJ*, 792, 10
- Selig, M. & Enßlin, T. A. 2015, *A&A*, 574, A74
- Shafter, A. W. 2002, in *American Institute of Physics Conference Series*, Vol. 637, *Classical Nova Explosions*, ed. M. Hernanz & J. José, 462–471
- Shafter, A. W., Ciardullo, R., & Pritchett, C. J. 2000, *ApJ*, 530, 193
- Shakura, N. I. & Sunyaev, R. A. 1973, *A&A*, 24, 337
- Shapiro, M. 2012, *Cosmic Radiation in Contemporary Astrophysics*, *Nato Science Series C: (Springer Netherlands)*
- Share, G. H., Murphy, R. J., Smith, D. M., Schwartz, R. A., & Lin, R. P. 2004, *ApJ*, 615, L169
- Shepp, L. A. & Vardi, Y. 1982, *IEEE Transactions on Medical Imaging*, 1, 113
- Siegert, T. & Diehl, R. 2015, *ArXiv e-prints*, arXiv:1501.05648
- Siegert, T. & Diehl, R. 2016, *ArXiv e-prints*, arXiv:1609.08817
- Siegert, T., Diehl, R., Greiner, J., et al. 2016a, *ArXiv e-prints*, 1603.01169v2
- Siegert, T., Diehl, R., Greiner, J., et al. 2016b, *Nature*, 531, 341
- Siegert, T., Diehl, R., Khachatryan, G., et al. 2016c, *A&A*, 586, A84
- Siegert, T., Diehl, R., Krause, M. G. H., & Greiner, J. 2015, *A&A*, 579, A124
- Siegert, T., Diehl, R., Vincent, A. C., et al. 2016d, *ArXiv e-prints*, arXiv:1608.00393
- Simon, J. D., Drlica-Wagner, A., Li, T. S., et al. 2015, *ApJ*, 808, 95
- Simon, J. D. & Geha, M. 2007, *ApJ*, 670, 313
- Simon, J. D., Geha, M., Minor, Q. E., et al. 2011, *ApJ*, 733, 46
- Sizun, P., Cassé, M., & Schanne, S. 2006, *Phys. Rev. D*, 74, 063514
- Skilling, J. 1989, *Classic Maximum Entropy*, ed. J. Skilling (Dordrecht: Springer Netherlands), 45–52
- Skinner, G., Diehl, R., Zhang, X., Bouchet, L., & Jean, P. 2014, in *Proceedings of the 10th INTEGRAL Workshop: "A Synergistic View of the High-Energy Sky"* (INTEGRAL 2014). 15-19 September 2014. Annapolis, MD, USA. Published online at <http://pos.sissa.it/cgi-bin/reader/conf.cgi?confid=228, id.054, 054>
- Skinner, G. K. 2004, *New A Rev.*, 48, 205
- Skinner, G. K. 2008, *Appl. Opt.*, 47, 2739
- Skrutskie, M. F., Cutri, R. M., Stiening, R., et al. 2006, *AJ*, 131, 1163
- Smith, D. M., Leventhal, M., Cavallo, R., et al. 1996a, *ApJ*, 471, 783
- Smith, D. M., Leventhal, M., Cavallo, R., et al. 1996b, *ApJ*, 458, 576
- Smith, N., Li, W., Foley, R. J., et al. 2007, *ApJ*, 666, 1116
- Snowden, S. L., Egger, R., Freyberg, M. J., et al. 1997, *ApJ*, 485, 125
- Sodickson, L., Bowman, W., Stephenson, J., & Weinstein, R. 1961, *Physical Review*, 124, 1851
- Sofue, Y. 2000, *ApJ*, 540, 224

- Sofue, Y., Habe, A., Kataoka, J., et al. 2016, *MNRAS*, 459, 108
- Sofue, Y., Honma, M., & Omodaka, T. 2009, *PASJ*, 61, 227
- Star Collaboration, Agakishiev, H., Aggarwal, M. M., et al. 2011, *Nature*, 473, 353
- Stecker, F. W. 1969, *Ap&SS*, 3, 579
- Stecker, F. W. 1971, NASA Special Publication, 249
- Stecker, F. W. 2002, ArXiv High Energy Physics - Phenomenology e-prints, arXiv:0207323
- Steigman, G. 2010, ArXiv e-prints, arXiv:1008.4765
- Stello, D., Cantiello, M., Fuller, J., et al. 2016, *Nature*, 529, 364
- Street, J. C. & Stevenson, E. C. 1937, *Phys. Rev.*, 52, 1003
- Strigari, L. E., Bullock, J. S., Kaplinghat, M., et al. 2008a, *Nature*, 454, 1096
- Strigari, L. E., Koushiappas, S. M., Bullock, J. S., et al. 2008b, *ApJ*, 678, 614
- Stritzinger, M., Leibundgut, B., Walch, S., & Contardo, G. 2006, *A&A*, 450, 241
- Strong, A. W., Bennett, K., Bloemen, H., et al. 1994, *A&A*, 292, 82
- Strong, A. W., Diehl, R., Halloin, H., et al. 2005, *A&A*, 444, 495
- Sturmer, S. J., Shrader, C. R., Weidenspointner, G., et al. 2003, *A&A*, 411, L81
- Su, M., Slatyer, T. R., & Finkbeiner, D. P. 2010, *ApJ*, 724, 1044
- Sukhbold, T., Ertl, T., Woosley, S. E., Brown, J. M., & Janka, H.-T. 2016, *ApJ*, 821, 38
- Summa, A., Elsässer, D., & Mannheim, K. 2011, *A&A*, 533, A13
- Sunyaev, R., Churazov, E., Gilfanov, M., et al. 1992, *ApJ*, 389, L75
- Svensson, R. 1982, *ApJ*, 258, 321
- Svensson, R. 1983, *ApJ*, 270, 300
- Svensson, R. 1987, *MNRAS*, 227, 403
- Svensson, R., Larsson, S., & Poutanen, J. 1996, *A&AS*, 120, 587
- Takekawa, S., Oka, T., Tanaka, K., et al. 2014, *ApJS*, 214, 2
- Tanaka, Y. 1989, in *ESA Special Publication, Vol. 296, Two Topics in X-Ray Astronomy, Volume 1: X Ray Binaries. Volume 2: AGN and the X Ray Background*, ed. J. Hunt & B. Battrick
- Tanvir, N. R., Levan, A. J., Fruchter, A. S., et al. 2013, *Nature*, 500, 547
- Tao, S.-J. & Green, J. H. 1969, *The Journal of Physical Chemistry*, 73, 882
- Tetarenko, B. E., Bahramian, A., Arnason, R. M., et al. 2016, *ApJ*, 825, 10
- The, L.-S. & Burrows, A. 2014, *ApJ*, 786, 141
- The, L.-S., Clayton, D. D., Diehl, R., et al. 2006, *A&A*, 450, 1037
- The, L.-S., Leising, M. D., Kurfess, J. D., et al. 1996, *A&AS*, 120, C357
- The DES Collaboration, Bechtol, K., Drlica-Wagner, A., et al. 2015, ArXiv e-prints, arXiv:1503.02584
- Thielemann, F.-K., Hirschi, R., Liebendörfer, M., & Diehl, R. 2011, in *Lecture Notes in Physics, Berlin Springer Verlag, Vol. 812, Lecture Notes in Physics, Berlin Springer Verlag*, ed. R. Diehl, D. H. Hartmann, & N. Prantzos, 153–232
- Thielemann, F.-K., Nomoto, K., & Hashimoto, M.-A. 1996, *ApJ*, 460, 408
- Thomson, J. J. 1897, *Philosophical Magazine Series 5*, 44, 293
- Thorstensen, J. R., Fesen, R. A., & van den Bergh, S. 2001, *AJ*, 122, 297
- Timmes, F. X., Woosley, S. E., Hartmann, D. H., & Hoffman, R. D. 1996, *ApJ*, 464, 332
- Toll, J. S. 1952, PhD thesis, PRINCETON UNIVERSITY.
- Tolman, R. C. 1939, *Physical Review*, 55, 364
- Totani, T. 2006, *PASJ*, 58, 965
- Totani, T., Oda, T., Sumi, T., et al. 2006, in *Astronomical Society of the Pacific Conference Series, Vol. 360, Astronomical Society of the Pacific Conference Series*,

- ed. C. M. Gaskell, I. M. McHardy, B. M. Peterson, & S. G. Sergeev, 55
- Tsai, W.-Y. & Erber, T. 1974, *Phys. Rev. D*, 10, 492
- Tsai, Y.-S. 1974, *Reviews of Modern Physics*, 46, 815
- Tyler, C. 2002, *Phys. Rev. D*, 66, 023509
- Ubertini, P., Lebrun, F., Di Cocco, G., et al. 2003, *A&A*, 411, L131
- Ulmer, M. P., Lomatch, S., Matz, S. M., et al. 1994, *ApJ*, 432, 228
- Vallery, R. S., Zitzewitz, P. W., & Gidley, D. W. 2003, *Physical Review Letters*, 90, 203402
- van den Bergh, S. & Tammann, G. A. 1991, *Annual Review of Astronomy and Astrophysics*, 29, 363
- Varracchio, E. F. & Girardeau, M. D. 1983, *Journal of Physics B Atomic Molecular Physics*, 16, 1097
- Va'vra, J. 2013, ArXiv e-prints, arXiv:1304.0833
- Vedrenne, G., Roques, J.-P., Schönfelder, V., et al. 2003, *A&A*, 411, L63
- Veljanoski, J., Ferguson, A. M. N., Mackey, A. D., et al. 2015, *MNRAS*, 452, 320
- Vincent, A. C., Martin, P., & Cline, J. M. 2012, *J. Cosmology Astropart. Phys.*, 4, 022
- Vink, J., Laming, J. M., Kaastra, J. S., et al. 2001, *ApJ*, 560, L79
- Vishnevsky, N. K. et al. 1974, *Yad. Fiz.*, 20, 694
- Voges, W., Aschenbach, B., Boller, T., et al. 1999, *A&A*, 349, 389
- von Glasow, W., Krause, M. G. H., Sommer-Larsen, J., & Burkert, A. 2013, *MNRAS*, 434, 1151
- von Kienlin, A., Rau, A., Beckmann, V., & Deluit, S. 2004, in *American Institute of Physics Conference Series*, Vol. 727, *Gamma-Ray Bursts: 30 Years of Discovery*, ed. E. Fenimore & M. Galassi, 622–625
- Voss, R., Diehl, R., Hartmann, D. H., et al. 2009, *A&A*, 504, 531
- Voss, R., Diehl, R., Vink, J. S., & Hartmann, D. H. 2010, *A&A*, 520, A51
- Walker, M. G., Mateo, M., Olszewski, E. W., et al. 2015, *ApJ*, 808, 108
- Wallner, A., Feige, J., Kinoshita, N., et al. 2016, *Nature*, 532, 69
- Walsh, S. M., Jerjen, H., & Willman, B. 2007, *ApJ*, 662, L83
- Walsh, S. M., Willman, B., Sand, D., et al. 2008, *ApJ*, 688, 245
- Wang, W., Lang, M. G., Diehl, R., et al. 2009, *A&A*, 496, 713
- Warren, Jr., W. H. & Hesser, J. E. 1977, *ApJS*, 34, 115
- Watson, L. J., Mortlock, D. J., & Jaffe, A. H. 2011, *MNRAS*, 418, 206
- Weaver, R., McCray, R., Castor, J., Shapiro, P., & Moore, R. 1977, *ApJ*, 218, 377
- Weaver, T. A. & Woosley, S. E. 1980, in *Annals of the New York Academy of Sciences*, Vol. 336, *Ninth Texas Symposium on Relativistic Astrophysics*, ed. J. Ehlers, J. J. Perry, & M. Walker, 335–357
- Weidenspointner, G., Kiener, J., Gros, M., et al. 2003, *A&A*, 411, L113
- Weidenspointner, G., Skinner, G., Jean, P., et al. 2008a, *Nature*, 451, 159
- Weidenspointner, G., Skinner, G. K., Jean, P., et al. 2008b, *New A Rev.*, 52, 454
- Weigmann, H., Hansen, H., & Flammersfeld, A. 1963, *Nucl. Phys. A*, 45, 555
- Werner, K., Hammer, N. J., Nagel, T., Rauch, T., & Dreizler, S. 2005, in *Astronomical Society of the Pacific Conference Series*, Vol. 334, *14th European Workshop on White Dwarfs*, ed. D. Koester & S. Moehler, 165
- Wheeler, J. A. 1946, *Annals of the New York Academy of Sciences*, 48, 219
- Whiting, A. B., Hau, G. K. T., Irwin, M., & Verdugo, M. 2007, *AJ*, 133, 715
- Williams, B. F., Peterson, S., Murphy, J., et al. 2014, *ApJ*, 791, 105
- Willman, B., Blanton, M. R., West, A. A., et al. 2005a, *AJ*, 129, 2692
- Willman, B., Dalcanton, J. J., Martinez-Delgado, D., et al. 2005b, *ApJ*, 626, L85

- Willman, B., Geha, M., Strader, J., et al. 2011, *AJ*, 142, 128
- Willson, L. A. 2000, *ARA&A*, 38, 573
- Winkel, B., Kerp, J., Flöer, L., et al. 2016, *A&A*, 585, A41
- Winkler, C., Courvoisier, T. J.-L., Di Cocco, G., et al. 2003, *A&A*, 411, L1
- Witten, E. 1985, *Nuclear Physics B*, 249, 557
- Wongwathanarat, A., Janka, H.-T., Mueller, E., Pllumbi, E., & Wanajo, S. 2016, ArXiv e-prints, arXiv:1610.05643
- Wongwathanarat, A., Janka, H.-T., & Müller, E. 2013, *A&A*, 552, A126
- Woosley, S. E. 1993, *ApJ*, 405, 273
- Woosley, S. E., Heger, A., & Weaver, T. A. 2002, *Rev. Mod. Phys.*, 74, 1015
- Yahel, R. Z. 1982, *ApJ*, 252, 356
- Yin, P.-F., Yu, Z.-H., Yuan, Q., & Bi, X.-J. 2013, *Phys. Rev. D*, 88, 023001
- Young, L. M. 2000, *AJ*, 119, 188
- Zaggia, S., Held, E. V., Sommariva, V., et al. 2011, in *EAS Publications Series*, Vol. 48, *EAS Publications Series*, ed. M. Koleva, P. Prugniel, & I. Vauglin, 215–216
- Zannoni, A. 1999, ArXiv e-prints, arXiv:cond-mat/9912229
- Zatsepin, G. T. & Kuz'min, V. A. 1966, *Soviet Journal of Experimental and Theoretical Physics Letters*, 4, 78
- Zdziarski, A. A. 1980, *Acta Astron.*, 30, 371
- Zhang, L. & Cheng, K. S. 1997, *ApJ*, 487, 370
- Zheng, W., Shivvers, I., Filippenko, A. V., et al. 2014, *ApJ*, 783, L24
- Zucker, D. B., Belokurov, V., Evans, N. W., et al. 2006, *ApJ*, 643, L103
- Zwicky, F. 1933, *Helvetica Physica Acta*, 6, 110
- Zwicky, F. 1937, *ApJ*, 86, 217